203(4), 2025

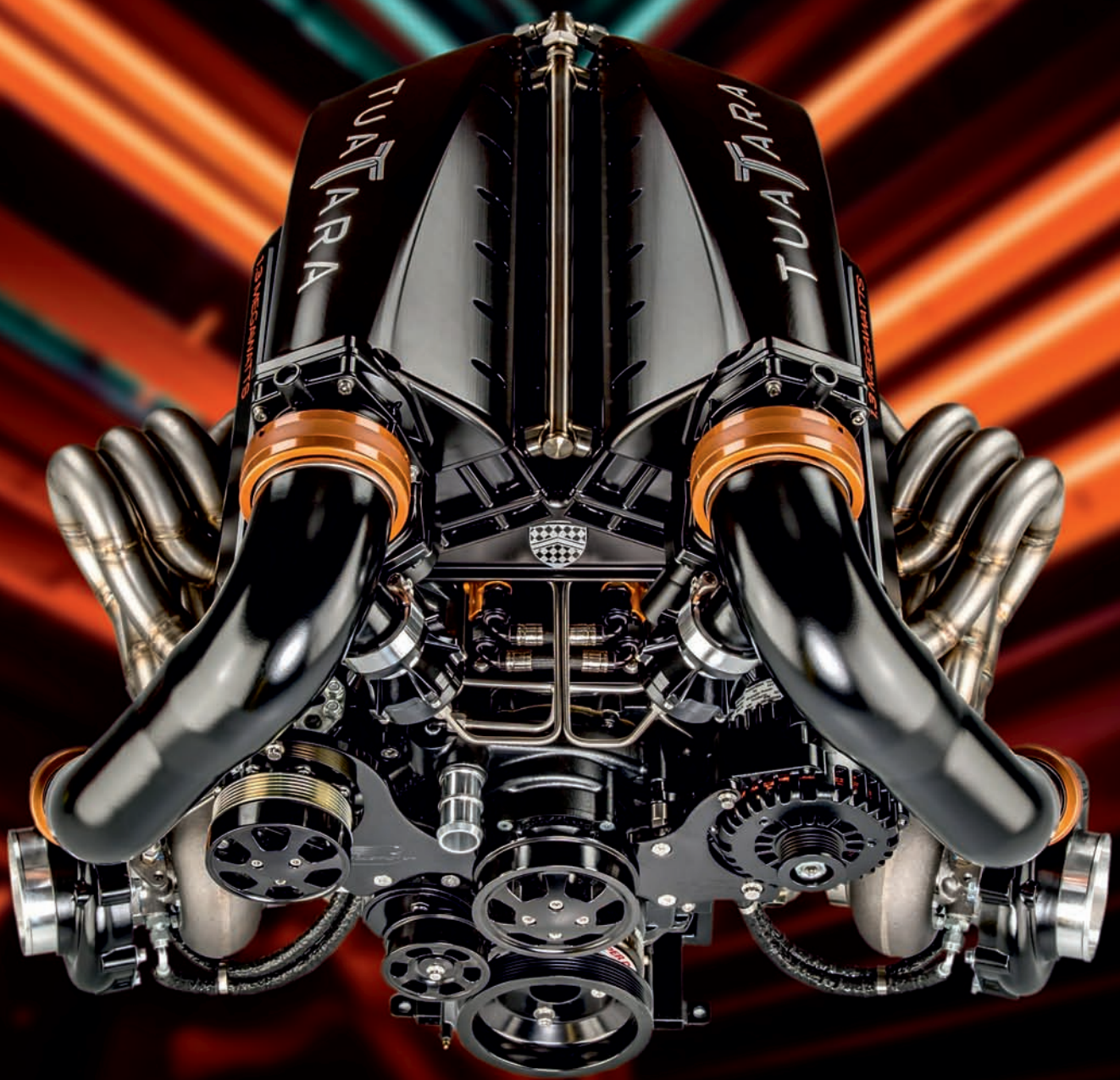

COMBUSTION ENGINES

Ergonomics and automation

Compliance: UE regulations 2017/1151, EN 12341:2014, US EPA 40CFR 1065, 40CFR part 50

- Automation of measurement processes
- On-line measurement
- Air buoyancy correction
- Dynamic analysis of the quality of weighing
- Environmental conditions module

Automotive laboratories

RADWAG Wagi Elektroniczne
26-600 Radom, ul. Toruńska 5
tel. 48 386 60 00, e-mail: radom@radwag.pl

radwag.com

Due to the dynamic development of machine and vehicle powertrains, the "Combustion Engines" scientific journal, while retaining its historical title, currently publishes works related not only to internal combustion engines, but also other powertrains, including hybrid drives, electric drives and fuel cells.

PTNSS Supporting Members
Członkowie wspierający PTNSS

BOSMAL Automotive Research and Development Institute Ltd
Instytut Badań i Rozwoju Motoryzacji BOSMAL Sp. z o.o

Motor Transport Institute
Instytut Transportu Samochodowego

Institute of Aviation
Sieć Badawcza Łukasiewicz – Instytut Lotnictwa

Automotive Industry Institute
Sieć Badawcza Łukasiewicz – Przemysłowy Instytut Motoryzacji

Sieć Badawcza Łukasiewicz – Poznański Instytut Technologiczny

AVL List GmbH

Air Force Institute of Technology
Instytut Techniczny Wojsk Lotniczych

Military Institute of Armoured & Automotive Technology
Wojskowy Instytut Techniki Pancernej i Samochodowej

Toyota Motor Poland Ltd. Sp. z o.o.

RADWAG Balances and Scales
RADWAG Wagi Elektroniczne

FOGO Sp. z o.o.

Horus Energia Sp. z o.o.

John Deere Polska Sp. z o.o.

COMBUSTION ENGINES
A Scientific Magazine

2025, 203(4)

Year LXIV

PL ISSN 2300-9896
PL eISSN 2658-1442

Publisher:
Polish Scientific Society of Combustion Engines
60-965 Poznan, pl. M. Skłodowskiej-Curie 5, Poland
tel.: +48 61 6475959, fax: +48 61 6652204
E-mail: sekretariat@ptnss.pl
WebSite: http://www.ptnss.pl
Papers available on-line: http://combustion-engines.eu

Contents

Publisher:

Polish Scientific Society of Combustion Engines
60-965 Poznan, pl. M. Sklodowskiej-Curie 5, Poland
tel.: +48 61 6475959, fax: +48 61 6652204
E-mail: sekretariat@ptnss.pl
WebSite: http://www.ptnss.pl

Subscriptions
Send subscription requests to the Publisher's address.
Cost of a single issue PLN 100.

Preparation for print
ARS NOVA Publishing House
60-782 Poznan, ul. Grunwaldzka 17/10A

Circulation: 60 copies

Printing and binding

Zakład Poligraficzny Moś i Łuczak, sp. j.,
Poznań, ul. Piwna 1

The journal is under the patronage of the Transport Committee and the Machine Building Committee of the Polish Academy of Sciences

The journal is registered and listed in the Polish and international database

Papers published in the
Combustion Engines
quarterly receive 70 points as stated by the Notification of the Minister of Science dated 5 January 2024.

Declaration of the original version
The original version of the Combustion Engines journal is the printed version.

Cover
I – Twin-turbo SSC Tuatara V8 engine
(www.nelsonracingengines.com);
background (Kehn Hermano, Person Holding a Glass Ball – pexels.com)
IV – Porsche 911 hybrid with exhaust energy recovery
(www.automotivepowertraintechnologyinternational.com)

Article citation info:
Graba M, Hennek K, Mamala J, Prażnowski K, Mueller M. Acceleration dynamics of a passenger vehicle with an electric powertrain and their impact on the mileage energy consumption. Combustion Engines. 2025;203(4):3-8. https://doi.org/10.19206/CE-206090

Mariusz GRABA
Krystian HENNEK
Jarosław MAMALA
Krzysztof PRAŻNOWSKI
Maximilian MUELLER

Combustion Engines
Polish Scientific Society of Combustion Engines

Acceleration dynamics of a passenger vehicle with an electric powertrain and their impact on the mileage energy consumption

ARTICLE INFO

Received: 8 April 2025
Revised: 30 May 2025
Accepted: 9 June 2025
Available online: 22 July 2025

The aim of the paper was to analyse the effect of an electric vehicle's acceleration intensity on energy consumption in a real road test. The research involved the urban Skoda Citigo-e iV equipped with a proprietary measurement system. Acceleration tests were carried out at different accelerator pedal positions, analysing kinematic and energy parameters, including energy consumption, speed, acceleration, and power. The paper introduces a dynamics index, combining powertrain capacity with specific energy consumption, allowing an objective comparison of vehicle energy and traction efficiencies. The results indicate that moderate acceleration up to about 40% pedal position is the most energy efficient. Further increases in power result in a significant increase in energy consumption with little dynamic acceleration. The electric vehicle's acceleration dynamics were compared to those of an internal combustion vehicle, which showed similarity in terms of the moderate acceleration area. The results show that moderate acceleration is the most energy-efficient, and the presented acceleration dynamics index allows for an objective comparison of the efficiency of different powertrains.

Key words: *acceleration dynamics, energy consumption, electric vehicle, dynamic index, powertrain efficiency*

1. Introduction

Vehicles are an integral part of everyday life for many of us; Poland featured 723 cars per 1000 inhabitants at the end of 2024, according to Statistics Poland. This score is the highest among European Union members, as many car users use their cars for daily commuting or leisure. However, a passenger car has two main tasks. The first is to be designed to have good traction, and the second is to ensure the road user safety. The first task is simple in that, for technical reasons, a person can design any powertrain, but in light of the requirements to reduce carbon emissions and the carbon footprint, this is forcing a lot of improvements, modifications, and optimisation of the power units on car manufacturers. This applies equally to internal combustion (ICEV), hybrid (HEV), and electric (BEV) passenger vehicle, which produces zero emissions in the TTW system. On the other hand, ensuring the powertrain's good technical performance associated with achieving accelerations of the order of 5 m/s^2 or the ability to develop high travel speeds requires the powertrain to have a large power reserve [8, 11]. Power is needed not only to drive the vehicle's wheels, but also to power the vehicle's increasingly sophisticated and extensive range of accessories, securing not only travel comfort, but also road user safety by ensuring adequate controllability related to the acceleration required for manoeuvres such as merging into traffic or overtaking [1, 6, 10].

Therefore, the authors used this paper to analyse the acceleration intensity of an electric vehicle on the energy consumption in a road test. The passenger vehicle acceleration was carried out in a flexibility test from an assumed initial speed, for various constant accelerator pedal positions providing constant power in the powertrain, until reaching a speed at which acceleration reached values close to 0 m/s^2 or relatively 120 km/h. The analysis covered basic indices characterising the vehicle's movement, such as the speed profile's kinematic parameters or energy parameters in the form of energy consumption. In the energy balance of a vehicle in motion, the measure of the consumed electrical energy supplied from the traction batteries to the vehicle's powertrain and auxiliary equipment is the realised speed profile describing its movement dynamics [3].

2. Acceleration as a fundamental phase of vehicle motion

The maintenance of good traction performance during acceleration is one of the most important phases of movement in terms of energy consumption, which is a consequence of the conversion of electrical energy stored in the traction batteries into driving force at the wheels[4]. At full acceleration intensity, it is required to feed the full power from the vehicle's electric motor into the powertrain. The acceleration achieved depends on a number of different factors, including external conditions such as wind or external temperature, the road surface condition, weight distribution, tyre type, frontal area, and body aerodynamics, all of which directly affect energy consumption [2, 9]. When analysing the acceleration process for an electric powertrain on a level road at a given intensity, the energy supplied from the traction batteries is balanced by the sum of its expenditure to overcome the resistance to motion, including rolling (E_R) and air (E_A), powertrain losses (E_L) and also its expenditure to overcome the vehicle's inertia (E_I), which is directly proportional to the acceleration achieved [5]. The energy balance can be written as an equation (1):

$$E_e = E_R + E_A + E_I + E_L. \quad (1)$$

When considering the individual components, the energy to overcome rolling resistance and air resistance, on a horizontal road, can be determined by completing a run-

down test. Hence, in order to analyse the acceleration process, it is a good idea to perform a two-phase cycle, consisting of an acceleration phase immediately followed by a rundown phase. Thus, knowing the test vehicle's mass and also its deceleration during the rundown phase, the resistance to motion becomes balanced with its inertia resulting from kinetic energy. We can therefore determine the rundown energy in accordance with equation (2)

$$E_{R+A} = \frac{m\delta_w(V_1^2 - V_2^2)}{2} \quad (2)$$

where: m – road test vehicle mass; δ_w – rotating mass from the wheels; V_n – instantaneous speed of the vehicle in motion.

Similarly, by knowing the vehicle's mass and, in this case, the acceleration during the acceleration phase, we can determine the energy required to overcome the vehicle's inertia (3):

$$E_I = \frac{m\delta_w(V_1^2 - V_2^2)}{2} \quad (3)$$

where: m – road test vehicle mass; δ_w – rotating mass from the wheels; V_n – instantaneous speed of the vehicle in motion.

Electric energy (E_e) supplied to the powertrain during the acceleration phase depends on the instantaneous electrical power from the powertrain E_e when supplied with current (4) [12].

$$E_e = \int_{t_1}^{t_2} U(t) \cdot I(t) dt \quad (4)$$

where: U(t) – instantaneous voltage supplied from the traction battery to the electric motor; I(t) – instantaneous current supplied from the traction battery to the electric motor; t – time of acceleration.

Taking the above into account, it is possible to determine the efficiency of the vehicle's powertrain during the acceleration phase as the ratio of the useful energy transferred to vehicle motion (E_L) to the total electric energy supplied from the traction batterie (E_e), as shown in equation [6] (5):

$$\eta = \frac{E_L}{E_e} \quad (5)$$

At the same time, for a fixed vehicle speed, in which the acceleration is equal to 0 m/s^2, the energy balance features no inertia, thereby enabling the determination of the powertrain's efficiency under steady-state conditions.

In order to compare the different powertrains of electric vehicles, one can determine the total specific energy consumption Q_{je} expressed as the ratio of the energy output from the traction batteries to the product of the mass and the distance travelled.

$$Q_{je} = \frac{E_e}{m \cdot L} \quad (6)$$

In order to objectively address the comparison of acceleration dynamics, the authors of [7] proposed a dynamics index, which can be presented with relation (7):

$$I_D = \frac{P}{Q_E} \quad (7)$$

The proposed passenger vehicle dynamics index combines the available power of the powertrain and the specific energy consumption. This provides a versatile and objective tool for measuring traction parameters during the acceleration process. This index takes into account the powertrain's capacity, the vehicle's mass, and the distance travelled.

3. Methodology, test object, and research tools

The paper contains an analysis of a passenger vehicle's acceleration process from a fixed initial speed to a fixed final speed in a road test on a horizontal road. The final vehicle speed results from the energy balance between the powertrain and the resistance to motion, or from the vehicle reaching an assumed final speed of 120 km/h. The acceleration intensity was determined by a constant acceleration pedal use with which constant power was applied to the powertrain during the road test for a given fixed gear ratio. Each road test was repeated a minimum of three times on the same road section, driving in both directions on a given measuring section, from which mean values were taken.

The Skoda Citigo-e iV electric passenger vehicle was used during the road tests conducted as part of the author's own research. The vehicle is equipped with a proprietary measurement data recording system using the onboard data transmission network. It is a front-wheel drive electric urban vehicle with a 61 kW motor with 212 Nm of torque. The electric motor's maximum rotation speed is 12,000 rpm. The transmission system features a single gear transmission, while the total ratio is equal to i_c = 8.16. The mean energy consumption on the WLTP combined cycle is 16.4 kWh per 100 km at a range of 260 km. The car's top speed is limited to 130 km/h, and the mass during testing is 1381 kg.

An important component of the road test is the appropriate selection of the measuring section, which was a 2.2 km section with a slope of 0.05°. A proprietary measurement system developed in the LabVIEW environment was used to record the Skoda Citigo-e iV vehicle's kinematic parameters. It enables the recording of kinematic parameters in the time domain from the on-board CAN BUS-based data transmission network, recording other drivetrain parameters, such as electric motor's rotational speed, energy consumption, vehicle load and speed, battery capacity, accelerator pedal, distance, battery voltage and current, electric motor power, current to drive auxiliary equipment. In addition, a device recording GPS data – speed, acceleration, distance travelled – was used.

4. Acceleration process analysis

The acceleration process analysis was based on the measurement of the kinematic parameters of the passenger vehicle's motion in real traffic conditions on a paved asphalt surface, from a constant linear speed of 40 km/h, regardless of the selected acceleration pedal position (10%, 20%, 30%, 40%, 50%, 55%, 60%, 70%, 100%). The acceleration flexibility test for initial acceleration pedal positions was carried out until a constant speed was reached (acceleration equal to 0 m/s^2) and in other cases until a speed of 120 km/h was reached. Changes in the powertrain's basic indices during

the acceleration test for the initial acceleration pedal position are shown in Fig. 1.

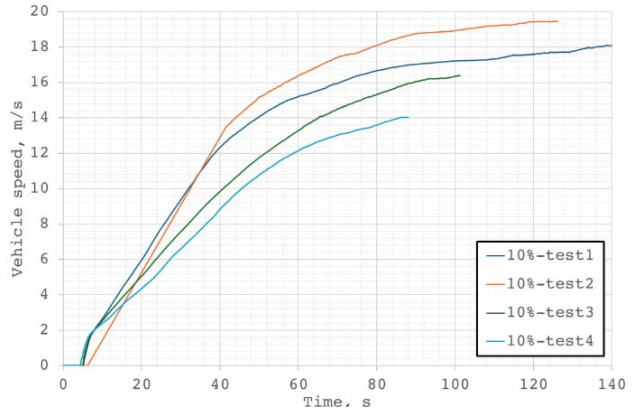

Fig. 1. Diagram of the speed vs time dependency for the 10% acceleration pedal position

Figure 2 shows the time dependence of current and energy consumption. As expected, the current increases during acceleration and then takes on a fixed value until the end of the acceleration phase. This current waveform results in a linear increase in energy consumption, while the voltage, at the same time, changes slightly from 318 V to 312 V.

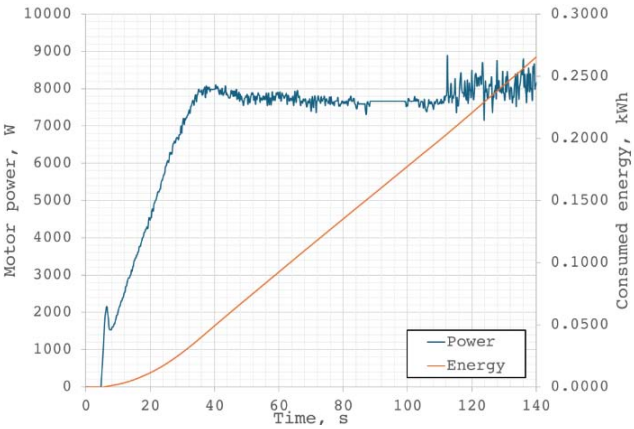

Fig. 2. Diagram of the motor power P and energy consumed E_n vs time dependency for the 10% acceleration pedal position

The acceleration tests were carried out in both directions on the road and their progression is comparable for different acceleration pedal positions, but the specific initial "peak" in the graphs for the 10% acceleration pedal position is important. It appears as soon as the acceleration pedal is depressed – the power momentarily rises to around 2.2 kW, before dropping to 1.5 kW and continuing to rise almost linearly. This is caused by the inertia in the powertrain, the so-called power jerk, which is clearly visible in Fig. 2, and also the large increase in acceleration values and their oscillation in the subsequent course (Fig. 4). Figure 3 shows the cumulative averaged waveforms from all Skoda Citigo-e iV road tests.

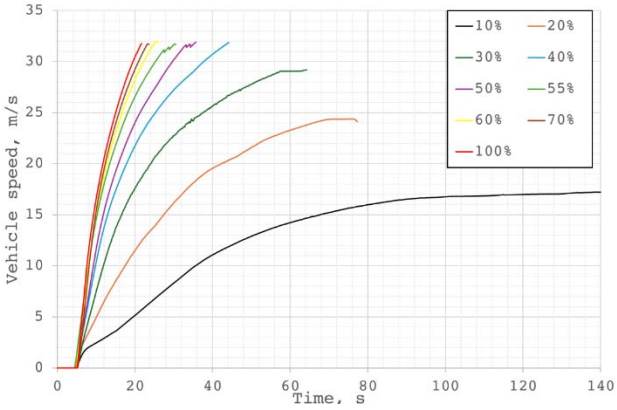

Fig. 3. Cumulative diagrams of the speed vs time dependency

The speed vs time dependency diagram in Fig. 3 shows that only in the first three runs (10%, 20% and 30% acceleration pedal positions) the road test came to an end due to the speed stabilisation and an acceleration drop to 0 m/s^2, as shown by the final acceleration waveform in Fig. 6. Despite the very slight differences in the speed profile for the acceleration pedal position of 55% and above, this recorded acceleration shows increasing values (Fig. 6), and this can be illustrated even better as a function of the change in acceleration vs speed (Fig. 7).

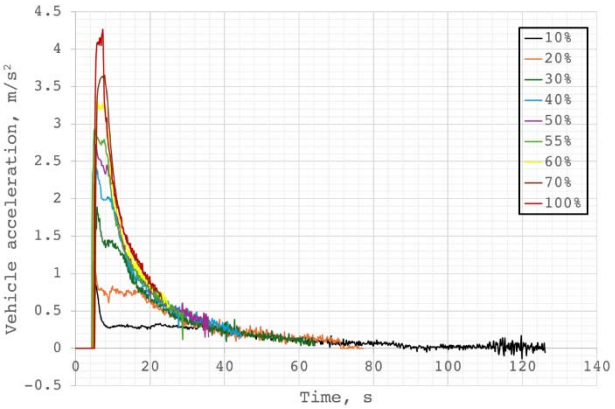

Fig. 4. Cumulative diagrams of the acceleration vs time dependency

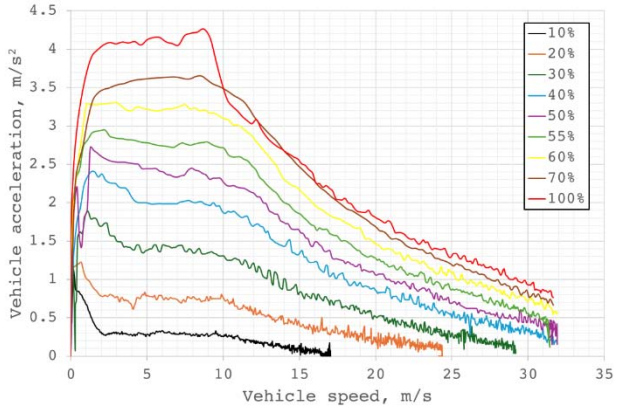

Fig. 5. Cumulative diagrams of the acceleration vs speed dependency for Skoda Citigo-e iV

Figure 5 shows that once the speed reaches 10 m/s, it starts to reduce acceleration in each case, regardless of the

powertrain's set power. The higher the power value, the more intense the acceleration drop during the initial phase, and this is mainly due to the inertia and resistance to motion.

Summarising the acceleration process, the specific values of the acceleration process from its start to end can be compiled as presented in Table 1. The table shows mean power P, mean energy consumption, specific energy consumption Q_e, and others. It is worth noting that power values close to maximum power do not significantly reduce acceleration power and distance.

Table 1. Summary for driving

Pedal position	Instantaneous energy consumed E_n	Mean consumption per 100km	Mean power P	Specific energy consumption Q_e	Measurement time	Distance	Average acceleration	Maximum acceleration
%	kWh	kWh/ 100 km	kW	J/(kg·m)	s	m	m/s^2	m/s^2
10	0.18	15.7	5.8	1.5	106.8	1304	0.16	1.78
20	0.27	26.4	13.9	3.0	69	1185	0.35	2.22
30	0.35	37.7	23.3	3.3	54.7	1144	0.56	2.03
40	0.35	52.6	32.6	6.6	38.7	851	0.82	2.62
50	0.32	65.7	39.0	7.9	29.6	632	1.08	2.6
55	0.30	77.1	44.1	9.6	24.5	514	1.30	2.99
60	0.29	91.5	51.0	12.1	20.7	432	1.55	3.39
70	0.28	100.6	56.1	13.4	18.3	373	1.74	3.67
100	0.27	111.8	59.2	13.5	16.3	327	1.93	4.45

The values between the initial and maximum power increments are significant, and the difference in distance travelled between the 10% and 100% acceleration pedal position is nearly 1000 m. The mean power and specific energy consumption, on the other hand, are almost 10 times greater. The energy consumed from the battery during each test, except the first, oscillates around 0.3 kWh; the mean energy consumption increases as the distance travelled shortens considerably. Drawing attention to the energy consumed from the battery, one can observe that the car travelled a different distance in each test, preventing the use of this value to make a direct comparison between each acceleration process and partial power. Therefore, referring to Figs. 3 and 4, and Table 1, the authors further analysed a distance of 300 m and an acceleration time of approximately 16 seconds for the full power input to the powertrain. A diagram of the vehicle's speed vs road dependency for the Skoda Citigo-e iV is shown below in Fig. 6.

The values shown in Table 2 represent the mean values for the acceleration process over a distance of 300m so that an acceleration dynamics index can be calculated for an electric vehicle. The presented dependencies prove that the considered acceleration process on a shorter representative section is characterised by established dependencies in terms of available power and mean mileage energy consumption. However, the values for specific energy consumption and the calculated dynamics index indicate that once a certain acceleration pedal power value is exceeded, the index no longer increases, but only the energy consumption increases.

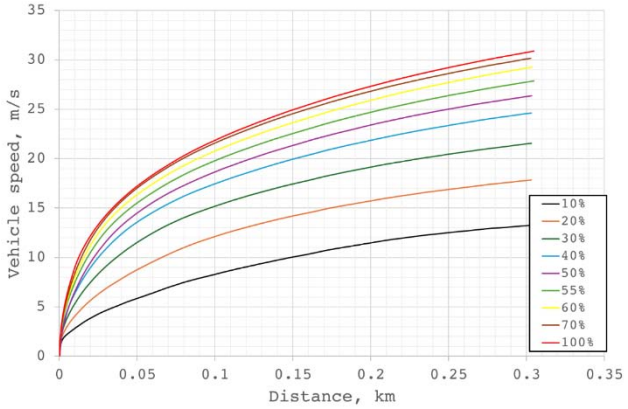

Fig. 6. Diagram for the speed vs distance travelled dependency for a 300 m distance – Skoda Citigo-e iV

Table 2. Summary for a 300 m distance travelled – Skoda Citigo-e iV

Pedal position	Instantaneous energy consumed En	Mean consumption per 100 km	Calculated mean power	Mean resistance	Mean driving power	Specific energy consumption	Measurement time	Distance	Average acceleration	Maximum acceleration	Dynamics index Id
%	kWh	kWh/ 100 km	kW	kW	kW	J/(kg·m)	s	m	m/s^2	m/s^2	kg·m/s
10	0.05	19.4	4.4	2.1	2.3	1.7	44.3	300.2	0.27	1.78	1.39
20	0.09	36.3	11.8	3.8	8.0	3.8	28.4	301.0	0.63	2.22	2.09
30	0.13	53.8	22.2	5.4	16.8	3.7	22.7	301.0	0.97	2.03	2.41
40	0.17	71.2	30.6	6.8	23.8	8.8	19.7	300.9	1.26	2.62	2.77
50	0.19	81.5	37.4	7.5	29.8	9.5	18.5	301.4	1.44	2.53	3.14
55	0.21	90.6	43.0	8.3	34.7	11.0	17.5	301.4	1.60	2.99	3.16
60	0.23	102.6	50.3	9.0	41.2	13.1	16.5	300.8	1.78	3.39	3.22
70	0.25	107.5	55.7	9.6	46.1	14.2	16.1	302.1	1.89	3.67	3.24
100	0.25	114.5	59.1	10.0	49.1	13.8	15.6	301.1	1.99	4.45	3.57

5. Passenger vehicle acceleration dynamics index

Figures 7 and 8 show graphs of the mean energy consumption and acceleration pedal position vs dynamics index dependency, according to the values shown in Table 2.

The dynamics index was calculated, which determines the energy required to accelerate a passenger vehicle with a mass of 1 kilogram over a distance of 1 metre in 1 second, based on calculations according to equation 7. According to the unit's designation, it is a value defined as per the unit of momentum. The presented dependency between the dynamics index with values such as mean energy consumption (Fig. 7) or acceleration pedal position (Fig. 8) allows for determining the moderate acceleration area associated with the energy consumption minimisation. The moderate acceleration area covers the acceleration process up to the acceleration pedal position of 40%, while the dynamic acceleration area covers the range exceeding this value. The boundary between these areas can be established based on trend lines – a point which is then projected onto the axes is es-

tablished at their intersection. In the case of the diagram in Fig. 7, the limit point has a value of approximately I_d = 3.12 kg·m/s with an energy consumption value of approximately 80 kWh per 100 km.

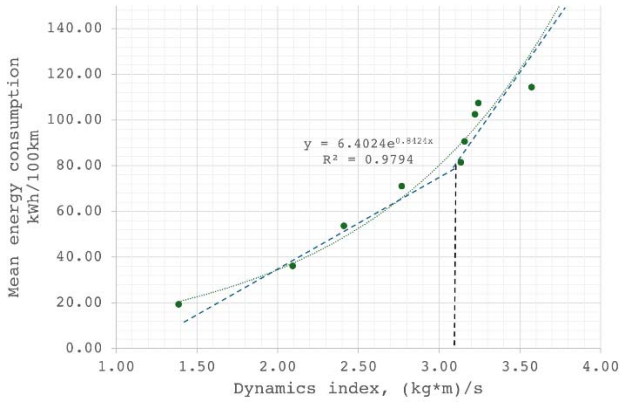

Fig. 7. Diagram of the energy consumption vs dynamics index dependency

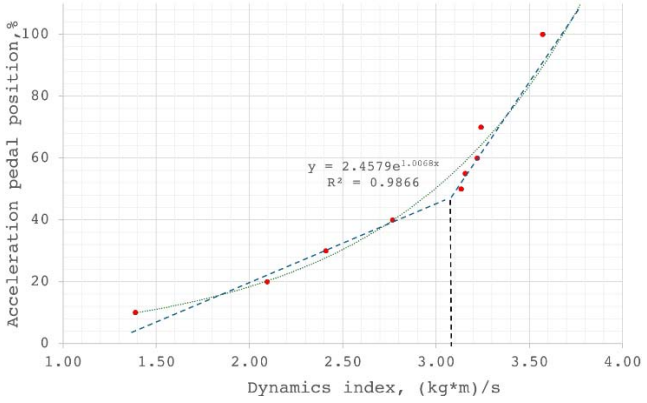

Fig. 8. Diagram of the acceleration pedal position vs dynamics index dependency

These values were compared to the results presented by the authors in paper [3] for a passenger vehicle with an indirect-injection combustion engine and a homogeneous combustion system with a power output of 110 kW, i.e. almost twice the power output of the tested electric vehicle. A comparison of the dynamics index shows that, for both the internal combustion and electric vehicles, the moderate acceleration area occurs at no more than 40% of the acceleration pedal position. In the case of internal combustion motors, the increment in fuel expenditure is steeper in relation to the dynamics index, which takes on higher values due to the internal combustion motor's power output.

6. Conclusions

The paper presents the results of tests on the acceleration dynamics of an electric vehicle on the Skoda Citigo-e iV, with a particular focus on the effect of acceleration intensity on energy consumption in real road tests. The results show that moderate acceleration, at around 40% of the acceleration pedal position, is the most energy efficient. Further increases in power lead to a significant increase in energy consumption with a slight increase in acceleration dynamics index.

The paper introduces a dynamics index that combines the powertrain's available capacity with specific energy consumption, thereby allowing an objective comparison of the vehicles' energy and traction efficiencies. This index is a versatile tool for assessing vehicle traction performance, thereby allowing for the comparison of different powertrains. A comparison of the dynamics index with the internal combustion vehicle showed similarity in the moderate acceleration area. Acceleration as the primary phase of a vehicle's motion is a key element in the analysis of energy consumption, and the research results indicate that moderate acceleration is the most energy efficient, which is important for increasing the range of electric vehicles. The results suggest that drivers should avoid pressing the power pedal rapidly beyond 45% to optimise power consumption, which may also have a positive impact on powertrain durability and battery life. Research on the impact of acceleration intensity on the total energy consumption of electric vehicles is essential to optimise driving strategies and extend vehicle range. Understanding this relationship also supports the development of more efficient powertrain control systems.

Nomenclature

BEV	battery electric vehicle
E_R	rolling resistance energy
E_A	air resistance energy
E_I	inertia resistance energy
E_L	losses in powertrain energy
HEV	hybrid electric vehicle
ICEV	internal combustion engine vehicle
I_d	dynamics index
I(t)	instantaneous current supplied from the traction battery to the electric motor
m	road test vehicle mass
t	time of acceleration
TTW	tank-to-well
U(t)	instantaneous voltage supplied from the traction battery to the electric motor
V_n	instantaneous speed of the vehicle in motion
δ_w	wheels rotating mass

Bibliography

[1] Badin F, Le Berr F, Briki H, Dabadie J-C, Petit M, Magand S et al. Evaluation of EVs energy consumption influencing factors: driving conditions, auxiliaries use, driver's aggressiveness. 2013 World Electric Vehicle Symposium and Exhibition (EVS27). 2013;6(1):112-123. https://doi.org/10.1109/EVS.2013.6914723

[2] Berry M. The effect of driving style and vehicle performance on the real-world fuel consumption of US light-duty

Vehicles. Doctoral Thesis. 2010. https://dspace.mit.edu/handle/1721.1/58392
[3] Cieślik W, Szwajca F, Golimowski J. The possibility of energy consumption reduction using the ECO driving mode based on the RDC test. Combustion Engines. 2020;182(3): 59-69. https://doi.org/10.19206/CE-2020-310
[4] Davari MM, Jerrelind J, Trigell AS. Energy efficiency analyses of a vehicle in modal and transient driving cycles including longitudinal and vertical dynamics. Transport Res D-Tr E. 2017;53:263-275. https://doi.org/10.1016/j.trd.2017.04.019
[5] Ferreira H, Rodrigues CM, Pinho C. Impact of road geometry on vehicle energy consumption and CO_2 emissions: an energy-efficiency rating methodology. Energies. 2020;13: 119. https://doi.org/10.3390/en13010119
[6] Fic B. Samochody elektryczne (in Polish). Wydawnictwo KABE. Krosno 2009.
[7] Graba M, Bieniek A, Prażnowski K, Hennek K, Mamala J, Burdzik R et al. Analysis of energy efficiency and dynamics during car acceleration. Eksploat Niezawodn. 2023;25(1): 17. https://doi.org/10.17531/ein.2023.1.17
[8] Kropiwnicki J, Gawłas T. Evaluation of the energy efficiency of electric vehicle drivetrains under urban operating conditions. Combustion Engines. 2023;195(4):28-34. https://doi.org/10.19206/CE-169492
[9] Mamala J, Graba M, Bieniek A, Prażnowski K, Hennek K, Kołodziej S et al. Evaluation of energy consumption in the acceleration process of a passenger car. Combustion Engines. 2022;190(3):35-44. https://doi.org/10.19206/CE-142553
[10] Mamala J, Graba M, Stasiak P. Energy efficiency of the electric drive system of a passenger car under normal operation conditions. In: Rackov M, Miltenović A, Banić M. (eds) Machine and Industrial Design in Mechanical Engineering. KOD 2024. Mechanisms and Machine Science. 2024;174. Springer, Cham. https://doi.org/10.1007/978-3-031-80512-7_90
[11] Shuklinov S, Uzhva A, Lysenko M, Tishenko A, Novikova Y. Maximum automobile acceleration. Automobile Transport. 2021;49:13-22. https://doi.org/10.30977/AT.2219-8342.2021.49.0.02
[12] Siłka W. Energy consumption of car movement (in Polish). WNT. Warszawa 1997.

Mariusz Graba, DEng. – Faculty of Mechanical Engineering, Opole University of Technology, Poland.
e-mail: *m.graba@po.edu.pl*

Krzysztof Prażnowski, DEng. – Faculty of Mechanical Engineering, Opole University of Technology.
e-mail*: k.praznowski@po.edu.pl*

Krystian Hennek, DEng. – Faculty of Mechanical Engineering, Opole University of Technology, Poland.
e-mail: *k.hennek@po.edu.pl*

Maximilian Mueller, MEng. – student at Opole University of Technology, Poland.

Prof. Jarosław Mamala, DSc., DEng. – Faculty of Mechanical Engineering, Opole University of Technology, Poland.
e-mail: *j.mamala@po.edu.pl*

Article citation info:
Bogdanowicz A, Socik P, Zadrąg R, Zacharewicz M, Wirkowski P. Multi-criteria analysis of the emission of harmful compounds from a marine diesel engine fueled with a mixture of marine fuel and n-butanol. Combustion Engines. 2025;203(4):9-15. https://doi.org/10.19206/CE-207151

Artur BOGDANOWICZ
Paweł SOCIK
Ryszard ZADRĄG
Marcin ZACHAREWICZ
Paweł WIRKOWSKI

Combustion Engines
Polish Scientific Society of Combustion Engines

Multi-criteria analysis of the emission of harmful compounds from a marine diesel engine fueled with a mixture of marine fuel and n-butanol

ARTICLE INFO

Received: 11 March 2025
Revised: 27 April 2025
Accepted: 14 June 2025
Available online: 26 June 2025

The article analyses in detail the impact of adding n-butanol to marine fuel on the emission of harmful compounds in diesel engines used in maritime transport. The applied multi-criteria analysis showed that introducing n-butanol as a fuel additive can significantly reduce the emission of substances such as nitrogen oxides (NO_x), carbon monoxide (CO), and carbon dioxide (CO_2), which consequently reduces the negative impact on the natural environment. In addition, the studies confirm that the mixture does not affect the operational efficiency of engines, which means that it can be used without the need to introduce major changes to the infrastructure or to the vessels themselves. Nevertheless, the authors emphasise that further research is necessary, especially at higher concentrations of n-butanol, to optimise this method in terms of long-term ecological and economic benefits and to ensure its full effectiveness. The conclusions indicate the potential of this technology, but they emphasise that it will be crucial to carry out additional tests to minimise the risk of possible negative side effects.

Key words: *marine diesel engine, emission, engine efficiency, multicriteria analysis*

1. Introduction

Butanol, also known as butyl alcohol, is one of many chemicals that play a key role in today's world in terms of reducing emissions of harmful compounds from marine combustion engines. This organic compound, an alcohol, has many uses and interesting properties that attract the attention of scientists, industrialists, and chemistry enthusiasts. Butanol has long been an important element of the chemical industry and other economic sectors, and also plays an important role in scientific research, especially in the context of alternative energy sources and sustainable development. The paper is a continuation of the team's previous research on the composition of marine fuel n-butanol. In addition to testing exhaust emissions, the team also investigated engine vibration characteristics [1, 5, 13, 14]. Similar studies are being conducted in other facilities around the world. An interesting approach to the topic of blended fuels was presented by Yu et al. [20]. Their work is based on a three-dimensional simulation model of an engine cylinder developed using the commercial simulation software AVL-Fire, with its accuracy validated against experimental data. The impact of diesel/biodiesel/n-butanol fuel blends on engine performance, combustion behavior, and emission characteristics was examined through simulations conducted on the model. The combustion process was analyzed for fuel mixtures containing 0%, 5%, 10%, 15%, and 20% n-butanol at different loads. Despite the engine's brake power decreasing, brake-specific fuel consumption rose, and NO_x emissions increased. Furthermore, across all load conditions, soot and CO emissions were observed to decline as the proportion of n-butanol in the fuel blend increased. The authors presented an interesting approach in the paper [6, 7]. The effect of oxygenated diesel fuel containing n-butanol on the exhaust emissions of passenger cars was described, which was tested on the NEDC transition cycle. The tests carried out showed that a diesel/butanol blend containing 10% n-butanol caused a significant reduction in PM and smoke emissions, had no effect on NO_x and CO_2 emissions, and caused higher CO and HC emissions. Tipanluisa et al. reached similar conclusions [17, 19]. This research explored the use of a single-zone combustion model combined with triple Wiebe functions to evaluate the effects of diesel/n-butanol blends as drop-in fuels for a four-cylinder heavy-duty diesel engine. Commercial diesel fuel served as the baseline for comparison with n-butanol blends containing 5%, 10%, and 20% by volume. The study examined combustion behavior, engine performance, and emission characteristics across various speed and load conditions in accordance with the World Harmonized Steady-State Cycle (WHSC). All n-butanol blends led to a reduction in CO and particulate emissions across all operating conditions. However, emissions of THC and NO_x increased, particularly at full load. Among the tested blends, 10% concentration demonstrated superior engine performance as well as favorable combustion and emission characteristics, highlighting its potential as a promising fuel blend. It should be noted that despite many publications showing that n-butanol mixtures improve combustion processes, also susceptible to changes in ambient temperature. The authors of the publication [4, 5, 8, 9, 18] pointed out that the inclusion of n-butanol as a component of the mixture is beneficial for both efficiency and particulate emissions, but the concentration of the mixture is limited by problems with starting at very low ambient temperatures, which should be carried out on marine combustion engines. The authors [7, 11, 12, 15] of the paper also reach the same conclusions by conducting experiments on a four-stroke, single-cylinder, air-cooled diesel engine

due to its transition from neat rapeseed oil biodiesel to fuel blends prepared by mixing in various proportions (by volume) of rapeseed methyl ester and butanol [4]. At full (100%) load conditions, the lowest NO_x emission was obtained with the engine running on a biofuel blend. The lowest level of carbon monoxide emissions (CO) was observed when the engine was running with the most butanol-oxygenated biofuel blend. The highest smoke opacity of the exhaust was obtained when the engine was fueled with neat biodiesel and at full load. However, when examining the concentrations of individual compounds together with the engine parameters, it is difficult to assess the impact of the tested mixture on marine engine work, especially under different loads. Therefore, this opens the way for other multi-criterion tools that can be very helpful in drawing conclusions.

2. Research plan and object

The research on the composition of marine fuel was carried out on the Cegielski-Sulzer 6AL20/24 marine diesel engine [3].

Fig. 1. The marine diesel engine Cegielski-Suzer 6AL20/24 laboratory stand

Engine operating parameters were recorded using an engine monitoring system and the TESTO 350 analyzer [16] was used to measure emissions of harmful compounds. During the measurements, the engine's fuel consumption was also recorded. Technical data were shown in Table 1.

The complete three-valued plan was selected for the experiment, consisting of 1 block and 27 measuring points. The tests were carried out for a mixture of marine fuel and n-butanol at concentrations of 0, 15, and 30 percent.

Table 1. Marine diesel engine Sulzer type 6AL20/24 [3]

Specification	
Piston arrangement	Inline
Cylinder diameter	200 mm
Piston stroke	240 mm
Displacement volume	1 cyl. – 7.54 dm^3
Nominal power	420 kW
Starter	pressure compressed air – 3 MPa
Number of cylinders	6
Number of valves per cylinder	4

The value of the stoichiometric constant of the fuel was calculated based on the equation:

$$L_T = 11.84 \cdot c + 34.214 \cdot h \left[\frac{kg}{kg_{fuel}}\right] \quad (1)$$

The composition of the fuel used on Navy ships is: c = 0.87 and h = 0.13. The following values were adopted for mixture of n–butanol and marine fuel: But15 – c = 0.8367; h = 0.1309; o = 0.0324; But30 – c= 0.8034; h = 0.1318; o = 0,0648. The calculations were made on the basis of a program calculating calorific values and theoretical air demand. The calorific values were adopted based on the previous research conducted and described in the paper [21]. Substituting the theoretical mass air demand into the excess air coefficient formula:

$$\lambda = \frac{L_R}{L_T} \quad (2)$$

After transformation, the determined actual air demand:

$$L_R = \lambda \cdot [11.84 \cdot c + 34.214 \cdot h] \left[\frac{kg}{kg_{fuel}}\right] \quad (3)$$

The excess air coefficient is calculated based on the relationship:

$$\lambda = \frac{C_{CO_2max}}{C_{CO_2}} \quad (4)$$

where: C_{CO_2} – carbon dioxide concentration in exhaust gases [%].

The air flow rate is calculated as:

$$\dot{m_{air}} = G_e \cdot L_R \left[\frac{kg}{s}\right] \quad (5)$$

Exhaust mass flow rate:

$$\dot{m_{ex}} = G_e + \dot{m_{air}} \left[\frac{kg}{s}\right] \quad (6)$$

The next step was calculation emission intensity of individual harmful compounds calculated on the basis of equation:

$$e_j = u \cdot c_j \cdot \dot{m}_{ex} \quad (7)$$

where: $\dot{m}_{ex}$ – exhaust mass flow rate, c_j – concentration of the exhaust component, u – the coefficient depending on the exhaust component: NO_x – 0.001587, CO – 0.000966, CO_2 –15.19.

The relative emission to the registered engine power was calculated:

$$e_m = \frac{e_j}{P_e} \quad (8)$$

Finally, the overall engine efficiency was determined from the data recorded from the engine (from each measurement point).

3. Multi-criteria ranking

3.1. Optimization using multi-criteria methods

Multi-criteria ranking is used to compare many options or solutions, taking into account criteria that are supposed to facilitate decision making. It is useful when a decision has to be made based on various factors. The main assumption is to unify the examined factors and structure the evaluation of various options, which in turn facilitates the analysis. The final result of the analysis depends on the weights

that will be assigned to individual criteria. The search for an optimal solution using a single criterion is rather rare, so it is important that the decision maker precisely defines the criteria and their weights.

In multi-criteria optimization problems, there are two groups of solutions [10]:

– dominated: binding criteria that cannot be improved without simultaneously deteriorating the value of the other criteria. There is no clear answer in this group, but a group of favorable solutions can be distinguished
– non-dominated: it is possible to find one solution, but it requires parameterization and application of all criteria. One of the advantages of such a solution is reducing the multi-criteria problem to a single-criteria problem, while the disadvantage is subjectivism in normalization and difficulties in estimating the weights of individual criteria.

In the search for a single solution, the weighted sum method is most often used, where the criteria are combined into one objective function according to a specific formula. Then, the zero unitarization method can be used, which is used to evaluate a finite number of variants to choose from. In this method, all variables are used in evaluating individual criteria and divided into three classes: stimulants (increase in the evaluation of the phenomenon), destimulants (decrease in the evaluation of the phenomenon), and nominants (favorable value). When specifying a variable as a stimulant or a destimulant, the direction of the function (minimum or maximum) is important.

3.2. Zero unitarization method

Fixed reference points should be assumed in the zero unitarization method. For this purpose, the range of the normalized variable was determined [2]:

$$G(X_j) = \max_i x_{ij} - \min_i x_{ij} \tag{9}$$

The following relationship was used to calculate the value of stimulants:

$$z_{ij} = \frac{x_{ij} - \min_i x_{ij}}{G(X_j)} \quad \begin{pmatrix} i = 1, 2, \dots, r \\ j = 1, 2, \dots, s \end{pmatrix}, \; X_j \in S \tag{10}$$

However, determining the value of the destimulant:

$$z_{ij} = \frac{\max_i x_{ij} - x_{ij}}{G(X_j)} \quad \begin{pmatrix} i = 1, 2, \dots, r \\ j = 1, 2, \dots, s \end{pmatrix}, \; X_j \in D \tag{11}$$

It should be noted that in the zero unitarization method, values in the <0;1> range are obtained. The normalization of diagnostic features is the initial stage that allows to obtain a joint multi-criteria assessment of each of the considered objects, which are then summed up to obtain an aggregate (synthetic) variable:

$$Q_i = \sum_{j=1}^{s} z_{ij} \quad (i = 1, 2, \dots, r) \tag{12}$$

Variable Q_i is a synthetic variable that is a large-criteria evaluation of a complex phenomenon characterizing the i-th object. Knowledge of this variable allows for the construction of a ranking, i.e., a system of objects ordered in relation to non-increasing values of Q_i. The objects with the best values are at the beginning, while the objects with the worst values are at the end of the ranking. In order to divide the set of objects into three parts (best, average, worst), the following relation should be used to calculate the limit value of average objects:

$$U = \frac{\max_i Q_i - \min_i Q_i}{3} \tag{13}$$

The following subgroups were obtained in this way:

– best object:

$$Q_i \in < \max_i Q_i - U, \max_i Q_i > \tag{14}$$

– average objects

$$Q_i \in (\max_i Q_i - 2U, \max_i Q_i - U) \tag{15}$$

– worst-case objects:

$$Q_i \in < \min_i Q_i, \max_i Q_i - 2U > \tag{16}$$

Table 2. The Q and UQ coefficient values based on calculations [2]

Rotational speed [1/min]	Load [kNm]	Butanol concentration [%]	Q	UQ
450	0.98	0	2.24	0.55
450	1.9	0	2.42	0.59
450	2.81	0	2.36	0.58
600	0.98	0	1.29	0.32
600	1.9	0	2.57	0.63
600	2.81	0	2.98	0.73
600	4.65	0	3.16	0.77
675	0.98	0	1.91	0.47
675	2.81	0	3.22	0.79
675	4.65	0	3.37	0.83
750	0.98	0	1.87	0.46
750	1.9	0	2.70	0.66
750	2.81	0	3.68	0.91
750	4.65	0	3.87	0.95
450	0.98	15	3.21	0.79
450	1.9	15	2.31	0.57
450	2.81	15	2.28	0.56
600	0.98	15	1.55	0.38
600	1.9	15	2.69	0.66
600	2.81	15	2.96	0.72
600	4.65	15	3.29	0.81
675	0.98	15	1.85	0.45
675	2.81	15	3.24	0.79
675	4.65	15	2.95	0.72
750	0.98	15	1.75	0.43
750	1.9	15	2.66	0.65
750	2.81	15	3.64	0.89
750	4.65	15	3.85	0.94
450	0.98	30	3.86	0.94
450	1.9	30	2.16	0.53
450	2.81	30	2.10	0.52
600	0.98	30	1.58	0.38
600	1.9	30	2.55	0.62
600	2.81	30	3.08	0.75
600	4.65	30	3.05	0.75
675	0.98	30	1.86	0.454
675	2.81	30	3.61	0.89
675	4.65	30	3.39	0.83
750	0.98	30	1.82	0.45
750	1.9	30	2.48	0.61
750	2.81	30	3.78	0.93
750	4.65	30	4.08	1

Based on the results of engine parameters and concentrations of harmful compound emissions: nitrogen oxides, carbon monoxide, and carbon dioxide, the emission of individual harmful compounds was calculated. Then, the values of overall engine efficiency were calculated at the tested measurement points. The values of overall engine efficiency are considered as stimulants, and the emission of individual harmful compounds is assumed as a destimulant. On this basis, the Q coefficient was determined as a result of calculations (Table 2).

From the data obtained: maximum value maxQ = 4.08, average value U = 0.93, and minimum value minQ = 1.29. Dividing into subgroups, the following results are presented:

- best object: $Q_b \in < 3.15,\ 4.08 >$
- average objects $Q_a \in (2.22, 3.15)$
- worst-case objects: $Q_w \in < 1.29, 2.22 >$.

Due to the fact that the determined values do not clearly explain the influence of stimulants and destimulants on Q value, it is necessary to perform a statistical analysis. For this purpose, the unit values are adopted for the next steps (Table 2):

$$UQ = \frac{Q_i}{maxQ} \tag{17}$$

3.3. Statistical analysis

The statistical analysis of the determined unit values of UQ factor was carried out in the Statistica program [2]. All 42 measurement points were taken into account, appropriately divided by the concentration of n-butanol in ship fuel (14 points each for But0 – 0%, But15 – 15%, and But30 – 30% concentration). Descriptive statistics determined characteristics describing the properties of the distribution of UQ value characteristics. The location of the feature (mean, median, lower and upper quartile), its measures of dispersion (quartile range, variance, standard deviation), measures of asymmetry (skewness), and measures of concentration (Kurtosis) were examined. The results of the statistical analysis were presented in the form of Fig. 2 and Fig. 3 and Table 3 and Table 4.

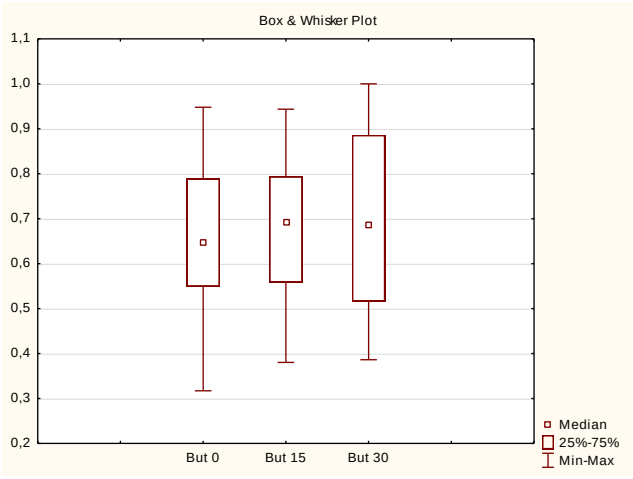

Fig. 2. The box plots represent the median values with upper and lower quartiles of UQ factor

The mean and median values of the UQ factor are close to each other. Mean values increase with increasing n-butanol concentrations. The highest median value of the UQ factor is at a n-butanol concentration of 15%. The median values for concentrations of 15% and 30% in blended fuel are higher than the median value of marine fuel.

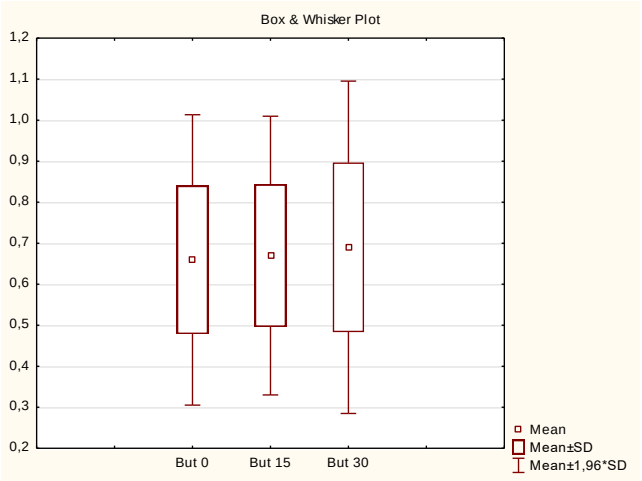

Fig. 3. The box plots represent the mean values with the standard deviation of UQ factor

The set of UQ coefficient values is not very diverse, as evidenced by small variance values. The coefficient of skewness is close to zero for all concentrations. However, at concentrations of 0 and 15, it takes negative values (slight left-side asymmetry), and at a concentration of 30%, it takes a positive value (slight positive asymmetry). Kurtosis values are negative, which indicates a flattened distribution.

Table 3. Descriptive statistics for UQ factor

Variable	Descriptive statistics				
	Valid N	Mean	Median	Minimum	Maximum
But0	14	0.66	0.65	0.32	0.95
But15	14	0.67	0.69	0.38	0.94
But30	14	0.69	0.68	0.39	1.00

The quartile range is similar for marine fuel and 15% n-butanol concentration. For the concentration of 30% butanol is the highest.

Table 4. Descriptive statistics for UQ factor (continued)

Variable	Descriptive statistics						
	Lower quartile	Upper quartile	Quartile range	Variance	Std. dev.	Skewness	Kurtosis
But0	0.55	0.79	0.24	0.033	0.180	–0.159	–0.54
But15	0.56	0.79	0.23	0.03	0.17	–0.21	–0.9
But30	0.52	0.89	0.37	0.04	0.2	0.05	–1.49

The lower quartile for But0 and But15 is 0.55, while for But30 it is 0.51. The upper quartile for But0 and But15 is 0.79, while for But30 it is 0.88. A quartile range of 0.23 (But 0 and 15) indicates that the middle 50% of the data is

narrowed to within 0.23 units of the data. This means that the data in this range are relatively close together, suggesting low variability in this central region of the data set. For the concentration value of But30, the quartile range interval with a width of 0.36 units, and the data range is the largest.

The variance for the cases studied ranges from 0.17 to 0.2. This means that the data values are fairly close to the mean, but are not completely clustered at one point. The values in the set do not deviate too far from the mean, but are not clustered very closely together either.

In the case of But0 and But15 concentrations, negative skewness indicates that the data is shifted to the left, with a long left tail and fewer extremely low values. Weak skewness, i.e., the dispersion of data around the mean, is still relatively equal. Such a distribution is characterized by a greater concentration of data to the right of the mean, and the mean is smaller than the median.

Concentration But30 has low positive skewness. This indicates that the distribution is close to symmetric, but with minimal right shift. The mean is only slightly higher than the median, and the right tails are relatively short.

In each analyzed case, negative values of kurtosis were presented. Negative kurtosis (platykurtic) indicates a data distribution that is flat, with short tails and rare outliers. UQ factor data in such a distribution is more evenly distributed, and extreme values are less common. In the context of statistical analysis, this can mean that the data is less "noisy" and does not contain many exceptions, which can simplify analysis.

The UQ factor distribution was presented in graphical (Fig. 4–6) and tabular form (Table 4–6). The histogram distribution was divided into 14 parts.

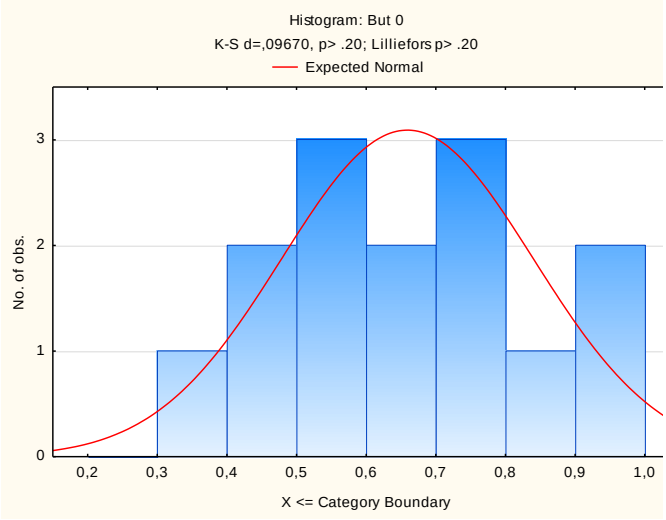

Fig. 4. Histogram UQ factor distribution for concentration But0

The highest UQ factor values for But0 concentration were observed in the ranges from 0.5 to 0.6 and 0.7 to 0.8, while the lowest were in the ranges from 0.3 to 0.4 and from 0.8 to 0.9. A slight fit to the normal distribution can be seen, but it deviates in the range of values from 0.9 to 1.

Table 4. Frequency table UQ factor for concentration But0

Category	Frequency table: But 0; K-S d = 0.09670. p > 0.20; Lilliefors p > 0.20					
	Count	Cumulative count	Percent of valid	Cumul % of valid	% of all cases	Cumulative % of all
0.2 < x ≤ 0.3	0	0	0	0	0	0
0.3 < x ≤ 0.4	1	1	7.14286	7.1429	7.14286	7.1429
0.4 < x ≤ 0.5	2	3	14.28	21.43	14.28	21.43
0.5 < x ≤ 0.6	3	6	21.43	42.8	21.43	42.86
0.6 < x≤ 0.7	2	8	14.28	57.14	14.28	57.143
0.7 < x ≤ 0.8	3	11	21.43	78.57	21.43	78.57
0.8 < x ≤ 0.9	1	12	7.143	85.714	7.143	85.71
0.9 < x ≤ 1.0	2	14	14.28	100.00	14.28	100
Missing	0	14	0		0	100

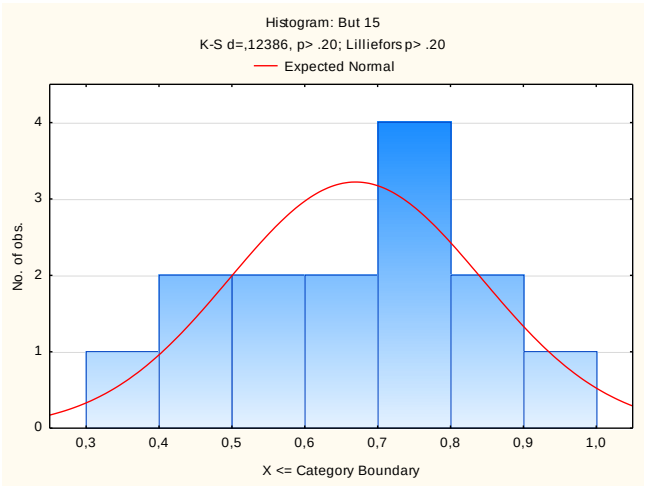

Fig. 5. Histogram UQ factor distribution for concentration But 15

Table 5. Frequency table UQ factor for concentration But 15

Category	Frequency table: But 15; K-S d = 0.12386; p > 0.20; Lilliefors p > 0.20					
	Count	Cumulative count	Percent of valid	Cumul % of valid	% of all cases	Cumulative % of all
0.3 < x ≤ 0.4	1	3	7.143	7.143	7.143	7.14
0.4 < x ≤ 0.5	2	5	14.28	21.43	14.28	21.43
0.5 < x ≤ 0.6	2	7	14.28	35.71	14.28	35.71
0.6 < x≤ 0.7	2	11	14.28	50.00	14.28	50.00
0.7 < x ≤ 0.8	4	13	28.57	78.57	28.57	78.57
0.8 < x ≤ 0.9	2	14	14.28	92.85	14.29	92.85
0.9 < x ≤ 1.0	1	14	7.15	100	7.15	100
Missing	0	1	0.0		0.0	100.0

For the case of But15 concentration, the largest number is located in the range from 0.7 to 0.8 of the UQ factor value. The smallest number is located on the border of the ranges, i.e., in the ranges from 03 to 0.4 and from 0.9 to 1.

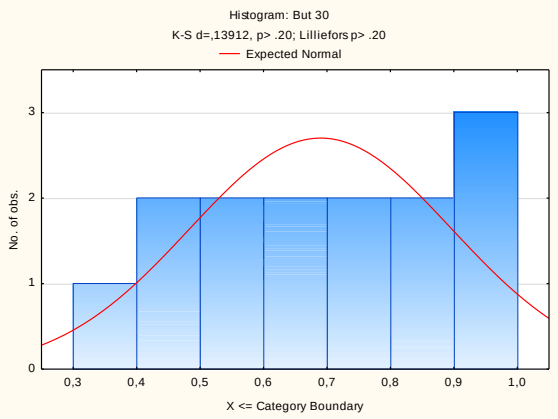

Fig. 6. Histogram UQ factor distribution for concentration But30

Table 6. Frequency table UQ factor for concentration But30

Category	Frequency table: But30; K-S d = 0.13912; p > 0.20; Lilliefors p > 0.20					
	Count	Cumulative count	Percent of valid	Cumul % of valid	% of all cases	Cumulative % of all
0.3 < x ≤ 0.4	1	1	1	7.14	7.14	7.14
0.4 < x ≤ 0.5	2	2	3	14.28	21.42	14.28
0.5 < x ≤ 0.6	2	2	5	14.28	35.71	14.28
0.6 < x≤ 0.7	2	2	7	14.28	50	14.28
0.7 < x ≤ 0.8	2	2	9	14.28	64.28	14.28
0.8 < x ≤ 0.9	2	2	11	14.28	78.57	14.28
0.9 < x ≤ 1.0	3	3	14	21.42	100	21.42
Missing	0	0	14	0		0

UQ factor values distribution for concentration But30 shows the highest number in the range from 0.9 to 1, while the lowest number is in the range from 0.3 to 0.4. In the range from 0.4 to 0.9, the numbers are at a constant level.

4. Summary

The paper presents a comprehensive analysis of the impact of a marine fuel and n-butanol mixture on the emissions of harmful substances from marine diesel engines. Research conducted using multicriteria analysis has shown that such a mixture could become a promising alternative to traditional fuels. The key conclusions can be divided into several main areas:

1. Impact on pollutant emissions. Experimental results show that adding n-butanol to marine fuel leads to a significant reduction in emissions of harmful compounds. The reduction in emissions helps reduce the negative environmental impact of shipping.
2. Operational efficiency of the engines. Despite the introduction of an alternative fuel mixture, the operational efficiency of diesel engines has been maintained. This means that environmental benefits go hand in hand with maintaining efficient performance, which is crucial for practical marine transportation applications.
3. Eco-economic potential. The authors emphasize that fuel blending has the potential to contribute to improved environmental performance by reducing emission harmful compounds from exhaust gases. At the same time, because of the maintained engine performance, its use can also be economically viable. This dual approach – environmental protection combined with operational profitability – is an attractive direction for further research and implementation.
4. Need for further research and optimization. Although the results are promising, the article indicates that the use of a mixture with higher n-butanol concentrations requires further research. Optimization of engine performance and precise determination of fuel mixing conditions are essential to fully realize the eco-economic potential of this technology.

Nomenclature

CO	carbon oxide
CO_2	carbon dioxide
GHG	greenhouse gas
MDF	marine diesel fuel
NO_x	nitrogen oxides
THC	hydrocarbons

Bibliography

[1] Agarwal AK, Das LM. Biodiesel development and characterization for use as a fuel in compression ignition engines. J Eng Gas Turb Power. 2001;123:440-447. https://doi.org/10.1115/1.1364522

[2] Bąk I, Cheba K, Szczecińska B. The statistical analysis of road traffic in cities of Poland. Transp Res Procedia. 2019; 39:14-23. https://doi.org/10.1016/j.trpro.2019.06.003

[3] Instrukcja techniczno-ruchowa silnika okrętowego H. Cegielski-Sulzer typu 6AL20/24. Poznań: Cegielski-Sulzer.

[4] Khan IA, Singh SK, Yadav AK, Ghosh U, Sharma D. Enhancement in the performance of a diesel engine fuelled with Pongamia methyl ester and n-butanol as oxygenated additive. Int J Ambient Energy. 2019;40:842-846. https://doi.org/10.1080/01430750.2018.1437559

[5] Kluczyk M. Influence of butanol-diesel oil fuel blends on marine engine vibration characteristics. Adv Sci Technol Res J. 2024;18(5):372-384. https://doi.org/10.12913/22998624/190834

[6] Kozak M. Exhaust emissions from a diesel passenger car fuelled with a diesel fuel-butanol blend. SAE Technical Paper 2011-28-0017. 2011. https://doi.org/10.4271/2011-28-0017

[7] Kozak M, Merkisz J. Oxygenated diesel fuels and their effect on PM emissions. Appl Sci. 2022;12(15):7709. https://doi.org/10.3390/app12157709

[8] Labeckas G, Slavinskas S, Mickevičius T. Experimental investigation of biodiesel-n-butanol fuels blends on performance and emissions in a diesel engine. Combustion Engines. 2022;188(1):90-95. https://doi.org/10.19206/CE-142030

[9] Lapuerta M, Ramos Á, Barba J, Fernández-Rodríguez D. Cold- and warm-temperature emissions assessment of n-butanol blends in a Euro 6 vehicle. Appl Energy. 2018;218: 173-183. https://doi.org/10.1016/j.apenergy.2018.02.178
[10] Nisbet R, Miner G, Yale K. Handbook of statistical analysis and data mining applications. 2017;1-792.
[11] Rodríguez CG, Lamas MI, Rodríguez JdD, Abbas A. Multi-criteria analysis to determine the most appropriate fuel composition in an ammonia/diesel oil dual fuel engine. J Mar Sci Eng. 2023;11(4):689. https://doi.org/10.3390/jmse11040689
[12] Rodríguez CG, Lamas MI, Rodríguez JdD, Abbas A. Possibilities of ammonia as both fuel and NO_x reductant in marine engines: a numerical study. J Mar Sci Eng. 2022;10(1): 43. https://doi.org/10.3390/jmse10010043
[13] Singh R, Kumar R. Insights into the influence of n-butanol with neat biodiesel and biodiesel diesel blends on diesel engine characteristics: review. Int J Energy Res. 2022;46: 5441-5466. https://doi.org/10.1002/er.7550
[14] Sirman MB, Owens EC, Whitney KA. Emissions comparison of alternative fuels in an advanced automotive diesel engine. SAE Technical Paper. 2000;109:2166-2176. https://doi.org/10.4271/2000-01-2048
[15] Tat ME, Van Gerpen JH. The kinematic viscosity of biodiesel and its blends with diesel fuel. J Am Oil Chem Soc. 1999;76:1511-1513.
[16] Testo 350 Maritime Instruction Manual. Lenzkirch: Testo; 2010.
[17] Tipanluisa L, Thakkar K, Fonseca N, López JM. Investigation of diesel/n-butanol blends as drop-in fuel for heavy-duty diesel engines: combustion, performance, and emissions. Energy Convers Manag. 2022;255:115334. https://doi.org/10.1016/j.enconman.2022.115334
[18] Voniati G, Dimaratos A, Koltsakis G, Ntziachristos L. Ammonia as a marine fuel towards decarbonization: emission control challenges. Sustainability. 2023;15(21):15565. https://doi.org/10.3390/su152115565
[19] Wander PR, Altafini CR, Colombo AL, Perera SC. Durability studies of mono-cylinder compression ignition engines operating with diesel, soy and castor oil methyl esters. Energy. 2011;36:3917-3923. https://doi.org/10.1016/j.energy.2010.10.037
[20] Yu S, Cao C, Lv W. Combustion and emission characteristics investigation of a marine diesel engine powered by diesel/biodiesel/n-butanol blends. Energy Sci Eng. 2022;10(9): 3317-3330. https://doi.org/10.1002/ese3.1220
[21] Zacharewicz M, Socik P, Wirkowski P, Zadrąg R, Bogdanowicz A. Evaluation of the impact of supplying a marine diesel engine with a mixture of diesel oil and n-butanol on its efficiency and emission of toxic compounds. Combustion Engines. 2023;195(4):40-47. https://doi.org/10.19206/CE-169484

Artur Bogdanowicz, DEng. – Faculty of Mechanical and Electrical Engineering, Polish Naval Academy, Poland.
e-mail: *a.bogdanowicz@amw.gdynia.pl*

Paweł Socik, MEng. – Faculty of Mechanical and Electrical Engineering, Polish Naval Academy, Poland.
e-mail: *p.socik@amw.gdynia.pl*

Prof. Ryszard Zadrąg, DSc., DEng. – Faculty of Mechanical and Electrical Engineering, Polish Naval Academy, Poland.
e-mail: *r.zadrag@amw.gdynia.pl*

Prof. Marcin Zacharewicz, DSc., DEng. – Faculty of Mechanical and Electrical Engineering, Polish Naval Academy, Poland.
e-mail: *m.zacharewicz@amw.gdynia.pl*

Paweł Wirkowski, DSc., DEng. – Faculty of Mechanical and Electrical Engineering, Polish Naval Academy, Poland.
e-mail: *p.wirkowski@amw.gdynia.pl*

Article citation info:
Danielak A, Kozak M, Cierniewski M. Prospects for the development of fuel cells in railway applications. Combustion Engines. 2025;203(4):16-22. https://doi.org/10.19206/CE-208507

Anna DANIELAK
Miłosław KOZAK
Maksymilian CIERNIEWSKI

Combustion Engines
Polish Scientific Society of Combustion Engines

Prospects for the development of fuel cells in railway applications

ARTICLE INFO

Received: 6 June 2025
Revised: 8 July 2025
Accepted: 22 July 2025
Available online: 18 September 2025

In recent years, there has been a huge increase in interest in fuel cell technology, which has undergone a period of rapid development. In the automotive market and in the railway industry, there is a growing trend in the production of transport containing fuel cells. The European Union is also striving to minimize greenhouse gas emissions in order to achieve climate neutrality by 2050. The article discusses the current use of hydrogen fuel cells in the railway industry. It shows groundbreaking projects of hybrid rail vehicles in the last few years. It also presents a brief overview of hydrogen fuel cell technology, its advantages and further challenges that need to be addressed to develop the market.

Key words: *fuel cells, rail vehicles, hydrogen, greenhouse gas emissions, hybrid vehicles*

1. Introduction

Nowadays, in the 21st century, one of the biggest challenges has become global warming. The whole world is striving to minimize the use of fossil gases and the emission of greenhouse gases (GHGs) that cause them. Legislation (Directive 2003/87/EC) suggests that new vehicles should be zero emission by 2035. In 2050, the European Union is to achieve climate neutrality - zero net emissions (NZE). To achieve this, the International Energy Agency (IEA) informs that CO_2 emissions in the transport sector must decrease radically by more than 3% per year by 2030 [29].

Railways are considered to be an economical, environmentally friendly form of transport. They have a very large load capacity, and the tracks take up very little space compared to roads [16]. However, this method of transport can also be improved to become zero-emission. It is equally important to continue to encourage more and more passengers to use this form of transport. Diesel-powered railway vehicles, which burn oil, are currently very popular on low-frequency long-distance routes. These engines are characterized by high thermodynamic efficiency and high torque [4]. However, burning oil causes very large greenhouse gas emissions (approx. 2,69 kg CO_2/dm^3). So far, electric or hybrid vehicles have been designed to minimize carbon monoxide emissions into the atmosphere [33]. However, electric vehicles have many disadvantages, including long charging time, low cell life, and the existing hybrid systems do not meet CO_2 emission limits. Currently, in order to reduce greenhouse gas emissions in railways, they are being electrified.

The history of the first electric railways dates back to the 19th century, when the first electric train designed by Werner von Siemens was presented in Berlin in 1879 [33]. However, the electrification of railway lines and the related construction of new infrastructure (supply lines, power substations, rectifier stations) are associated with very high costs. Therefore, the electrification of railways took place only in places with high traffic, mainly in urban railways. Such drastic zero emission requirements dictated by the European Union force the creation of new hybrid systems containing hydrogen fuel cells. An increase in the interest of manufacturers in investing in the electric drive sector can be observed in the automotive and railway markets [3]. Currently, there are several types of hydrogen cells, depending on the type of fuel used. However, hydrogen has found the greatest application in transport due to its high reactivity both at high temperatures (even 500°C) and low temperatures [26]. Initially, fuel cells were mainly used in road transport – cars and buses. However, currently there are also attempts to implement hybrid drives using hydrogen fuel cells in rail transport [33]. There are studies [8, 22] that show that the diesel rail vehicles used so far can be replaced by a hybrid drive using hydrogen fuel cells and a cooperating battery energy storage unit. The only additional element related to infrastructure and the related cost is refueling stations.

The principle of the fuel cell was discovered by chemist Christian Friedrich Schoenbein in 1838. The scientist discovered it by accident during an experiment related to electrolysis. He disconnected the battery from the electrolyzer and connected two electrodes. He observed that the current flowed in the opposite direction, and oxygen and hydrogen were consumed. However, the chemist could not cope with the corrosion of the electrodes, which is why it was commonly believed that it was useless. At that time, he used sulfuric acid as an electrolyte. Several decades later, chemical engineer Francis Bacon resumed work on fuel cells. He changed the acid electrolyte to alkaline (KOH solution) and used powdered nickel as electrodes. Thanks to this, he obtained a higher power density of the cell and dealt with the problem of electrode corrosion [13].

2. Principle operation of hydrogen fuel cells and their types

2.1. Introduction

The operation of a fuel cell is based on the reverse electrolysis process. Hydrogen fuel cells convert chemical energy into electrical energy as an exergonic reaction of hydrogen with oxygen (oxidation-reduction reaction-redox). The principle of their operation was known in the 19th century, but they did not find application until the use of a

cell with polymer membranes in the Gemini and Apollo space missions to power NASA satellites and space capsules [37].

A hydrogen fuel cell consists of an anode, a cathode, and an electrolyte. Hydrogen is continuously supplied to the anode, and oxygen is continuously supplied to the cathode. Theoretically, during the oxidation-reduction (redox) reaction, each atom changes its oxidation state. The catalyst at the anode splits the hydrogen into protons and electrons. Then the electrolyte allows only protons to pass to the cathode. And the electrons move to the cathode via an external electrical circuit. At the cathode, electrons and protons combine with oxygen to form steam of water, which escapes from the cell [23, 32].

Basic chemical reactions occurring in a hydrogen fuel cell:

– Near the anode in an acidic solution, a hydrogen molecule is adsorbed on the catalyst surface and dissociates into a proton and an electron:

$$H_2 \overleftarrow{\rightarrow} 2H^+ 2e^- \qquad E_a^0 = 0\ V \tag{1}$$

– The protons then flow through the electrolyte; at the cathode, oxygen is reduced and steam of water molecules are formed:

$$\frac{1}{2}O_2 + 2H^+ + 2e^- \overleftarrow{\rightarrow} H_2O \qquad E_e^0 = 1.23V \tag{2}$$

The total reaction can be written using the equation:

$$H_2 \overleftarrow{\rightarrow} 2H^+ 2e^- \qquad E_a^0 = 0\ V \tag{3}$$

There are several types of hydrogen fuel cells currently in use and they may differ depending on the way the fuel is used, the operating temperature of the cells and the type of electrolyte used [18, 23, 38].

Table 1. Classification of hydrogen fuel cells

Fuel cell	Electrolyte	Catalyst	Fuel	Operating temperature (0°C)
LT PEMFC	Polymer membrane (H^+)	Fri	H_2	40–90
HT PEMFC	PFSA (H^+)	Fri/Fri	H_2	90–1000
AFC	Alkaline solution (most often KOH solution), (OH^-)	Fri/Mon Sun	H_2	60–220
MCFC	Li or K carbonates (CO_3^{2-})	No	H_2	600–700
SOFC	Zr oxides (O^{2-})	–	H_2	600–1000

Types of cells and their classification:

a) Depending on fuel use:
   – direct hydrogen supply
   – indirect – the fuel is obtained in the reforming process.
b) Depending on the operating temperature of the cells:
   – low temperature 25–100°C
   – high temperature – above 100°C
c) Depending on the type of electrolyte used:
   – with polymer membrane (PEMFC)
   – alkaline (AFC)
   – carbonate (MCFC)
   – oxide ceramic (SOFC)

Table 1 presents the classification of hydrogen fuel cells taking into account their characteristic features. The type of electrolyte used, the temperature range at which the cell operates, and the catalysts used (both on the anode and cathode) are taken into account [18, 37].

2.2. Low temperature fuel cells

The most popular due to safety and energy efficiency is the low-temperature hydrogen cell with polymer membrane LT PEMFC. The electrolyte is a polymer containing sulfonic groups (most often Nafion) [1, 5]. It is formed into a membrane covered with porous platinum, acting as a catalyst. The electrodes are two graphite sheets. The whole is pressed at a high temperature. Due to the presence of platinum in the electrolyte, PEMFC cells are very sensitive to carbon monoxide – at a CO concentration of 10–20 ppm and an operating range of 60–80°C, the catalyst is "poisoned" [5]. Hydrogen used as fuel in these cells must be very pure (≥ 99.97% – the maximum content of pollutants must not exceed 300 ppm); it cannot come from reforming. Therefore, another, better application may be HT PEMFC cells operating at temperatures above 100°C LT PEMFC cell stacks provide energy efficiency of up to about 60% [15].

The oldest, one of the first fuel cells, is the alkaline AFC cell. It was thanks to alkaline fuel cells that the first American space missions were successful. Traditional AFC cells, like PEMFC, can also operate at room temperature (40–75 °C). However, they have an electrolyte that is highly sensitive to CO_2 (35–85% wt. KOH solution); it degrades when in contact with carbon monoxide. In addition to traditional cells with a liquid electrolyte, alkaline fuel cells also include more modern solutions – fuel cells with a polymer anion exchange membrane (AEMFC). AEMFC cells can be used in a slightly wider temperature range of 50–90 °C and are characterized by a much higher current density of 300–9700 mA cm^{-2} (compared to traditional cells, 100–300 mA cm^{-2}). However, to date, they have only found laboratory applications [12, 18]. Compared to other fuel cells operating at low temperatures, alkaline cells do not have noble metals such as Pt or Pd used as a catalyst.

2.3. High temperature fuel cells HT PEMFC

Higher operating temperature fuel cells are attracting increasing attention because they do not require expensive metal catalysts and because the exhaust heat can be efficiently managed by other thermal cogeneration systems. High-temperature fuel cells also have higher efficiency compared to low-temperature fuel cells [23]. Such fuel cells include polymer membrane HT (PEMFC), carbonate MCFC, oxide ceramic (SOFC), and zinc air (ZAFC) [34, 46].

One type of hydrogen-polymer cells with a polymer membrane, but suitable for use at temperatures above 100°C, are HT PEMFC cells. The best solution for PEMFC cells is to use pure hydrogen as fuel, but currently, this is a very expensive solution. Hydrogen is most often obtained by reforming organic fuels, including natural gas and gasoline. Hydrogen produced in this way usually contains about

0.1–2% of impurities. HT PEMFC cells, compared to LT PEMFC, are more resistant to catalyst poisoning. The entropy of the adsorption phenomenon of carbon monoxide on Pt is negative, so adsorption preferentially occurs at low temperatures. At the same time, at higher temperatures, when using high-temperature cells, the adsorption of harmful gases on the catalyst is slower, which is why they show greater tolerance to these gases. Another challenge for PEMFC cells is their efficiency. The use of HT PEMFC cells reduces the problem of the need for cooling technology, because they can operate at higher temperatures. However, the main problem with using PEMFC cells at higher temperatures is that the membranes and catalysts degrade much faster. HT PEMFC cells do not have platinum as a catalyst. They can also be powered by hydrogen produced by the reforming process. The energy efficiency of the fuel cell is typically 35–60% [4, 18, 46].

The generated electricity from fuel cells is transferred directly to the rail vehicle drive system or to energy storage (most often batteries). The use of hydrogen fuel cells as the only source of energy is associated with many disadvantages, including their high cost, shorter service life, and slow response to changes in dynamics. Therefore, in rail vehicles, in order to minimize gas emissions and demand for fossil fuels, a hybrid system is usually designed, in which the primary power source is hydrogen fuel cells, and the storage is batteries. A hybrid system is designed, consisting of a fuel cell and an ESS (energy storage system); additionally, appropriate control algorithms are needed to manage energy from these sources [4, 31, 35]. There are various energy storage devices, most often currently these are lithium-ion Li-on batteries, nickel-cadmium NiCd batteries, and newer solutions, such as $LiFePO_4$ and titanium batteries. Lithium-ion batteries are a very good solution due to their high energy density and low weight.

The EMS energy management system efficiently manages the energy between the PEMFC cells and the batteries to minimize fuel consumption and achieve high charging efficiency [22]. The PEMFC and the battery together provide power to the vehicle. There are three driving modes:

- Battery Drive Mode – When the total power requirement is supplied solely by the battery
- Fuel Cell Driving Mode – The battery charges, and the entire power requirement is supplied by the fuel cell
- Fuel cell and battery-powered driving mode – when the total power requirement is supplied by the fuel cell and battery.

There are many advantages to using hydrogen fuel cells in rail transport. These include:

- quiet operation of railway vehicles
- energy independence of states
- reduction of greenhouse gas emissions, including CO_2 (g)
- if hydrogen production and the entire hydrogen technology are introduced on a wide scale, the costs of hydrogen fuel cells will be reduced [23] (from USD 2.5 per kilogram to as much as USD 6.8)
- high efficiency of fuel cells (ok. 40–50%).

3. Overview of hydrogen drives in rail vehicles

3.1. Light Rail Vehicles (LRV) and suburban and regional multiple units running on non-electrified tracks

Taking into account all the given requirements and features of hydrogen cells, four types of rolling stock require a change of system. These are: light rail vehicles (LRV), suburban and regional trains running on non-electrified tracks, switch locomotives, and mining locomotives [20]. Over the years, there has been a tendency towards a growing interest in the topic of hydrogen-powered railways. In 2016, over 70 publications were written on the subject of "Hydrogen Trains", and in 2022, scientists undertook to write about 200 publications [16].

In 2017, the Chinese Tangshan Railway presented the first prototype of a light rail vehicle (LRV) powered by hydrogen fuel cells with batteries and ultracapacitors. This combination ensures completely wireless operation of the railway. The power of the hydrogen cells used was 150 kW. The supplier of hydrogen fuel cells was the Canadian company Ballard Power Systems. The LRV prototype has hydrogen tanks with a capacity of 12 kg, thanks to which it has a range of 40 km on a single refueling [20].

The first hydrogen traction unit was introduced to the market by Alstom [2, 39], which showed it at an event held in Munich in 2018 (Fig. 1). Alstom entered into cooperation with other companies producing fuel cells, batteries, and hydrogen tanks, including Selectron Systems, Hydrogenics, Hexagon Xperion, and Akasol [39]. Two prototypes underwent field tests on the Elbe-Weser line in Germany. The train, called Coradia iLint, is capable of reaching a distance of 1175 km without refueling at a maximum speed of 140 km/h. The fuel cells and hydrogen tank are situated on the roof of the train, while the rest of the hydrogen drive is located in the lower part of the train. The kinetic energy generated during braking is stored in lithium-ion batteries.

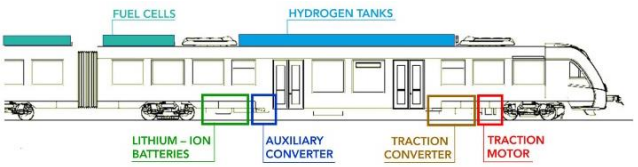

Fig. 1. A trainset manufactured by Alstom, using a hydrogen drive system [26]

Table 2 presents the basic data of selected Light Rail Vehicles (LRV) [11, 28, 29, 43, 44].

3.2. Shunting locomotives

In recent years, there has also been a development of large-scale prototypes of high-power traction vehicles. In 2009, Vehicle Projects LLC, a company consisting of leading US hydrogen production and storage companies, created a large-scale prototype of a hybrid shunting locomotive powered by hydrogen fuel cells and lead-acid batteries for use in cities and military bases [7, 15]. At 127 tons, the power reached 250 kW using a PEM fuel cell drive, and the transient power significantly exceeded 1 MW. This was the largest hydrogen fuel cell vehicle to date. Miller [6] de-

scribed that the fuel cell stacks provide a mean power of 75 kW, with lead-acid batteries as an additional energy storage device, which provides peak power. The hydrogen was stored in compressed gas cylinders at a pressure of 350 bar [6, 17, 27]. The locomotive was tested at the Pueblo Test Facility. It was used as a shunting locomotive in Southern California and then transferred to the Oklahoma Railroad Museum in 2023 [6, 27].

Table 2. Basic data of selected Light Rail Vehicles (LRV)

Name of the traction unit	Year of production	Maximum speed	Maximum distance without refueling	Additional information
Mireo Plus H	2024	160 km/h	1200 km	Fuel cell power: 2 × 200 kW Traction power: 544 kW
Coradia Ilint	2018	140 km/h	1175 km	Traction power: 1.7 MW (battery and fuel cell)
Cinova H2	2024	200 km/h	1200 km	Fuel cell power: 4 × 960 kW
Hydro Flex	2019	130 km/h	1000 km	Fuel cell power: 200 kWh Hydrogen storage: 20 kg
FLIRT H2	2022	127 km/h	2803 km	Fuel cell power: 6 × 100 kW The fuel cells are placed in an additional car in the middle of the train

In 2012, China also began to take action to protect the environment and reduce greenhouse gases. The first PEMFC-based shunting locomotive was developed (Fig. 2). The locomotive's energy source is hydrogen, and the additional power source is lithium-ion batteries. The hydrogen storage system consists of nine 35 MPa cylinders that can store about 23 kg of compressed hydrogen. The hydrogen propulsion system is placed in the second half of the engine room. It consists of: a PEMFC stack module, an air supply module, a cooling module, and an auxiliary power module. The PEMFC stack has a rated power of 150 kW at 570–640 V. The locomotive was tested on a test line in Chengdu, Sichuan. Satisfactory results were obtained, which formed the basis for further modifications and development of hybrid locomotives [10].

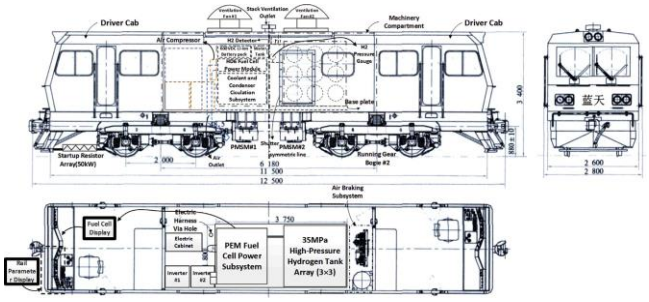

Fig. 2. System layout of the PEM fuel cell locomotive [10]

The next Chinese hybrid locomotive was designed by CRRC Datong and State Power Investment Corporation (SPIC) in 2021. The locomotive is designed for both shunting and regular line service. It is capable of operating continuously without refueling for 24.5 hours at a maximum speed of 80 km/h. The company claims that the locomotive reduces greenhouse gas emissions by about 80 kg per 1000 ton-km compared to a diesel locomotive [14].

3.3. Mining locomotives

Mining vehicles, due to their specific nature and closed workplace, should have be safe; an explosion could threaten a tragic accident. The advantage of a vehicle using hydrogen fuel cells compared to a locomotive using crude oil is the lack of extracted pollutants. The first prototype (Fig. 3) of a hydrogen-powered locomotive was developed and demonstrated in the USA by Vehicle Projects Inc. in 2002 [27, 36, 42]. The vehicle was powered by a polymer membrane fuel cell, and the energy was stored using metal hydrides and batteries. The vehicles were to be used in mining for platinum extraction. In 2012, the first commercial introduction of four 10-ton locomotives took place in South Africa as a mining vehicle. The locomotives have a metal hydride storage system, 22 kW fuel cells and a lithium-ion battery. The mining vehicle has a maximum power of 17 kW. Due to the use of a metal hydride energy storage system, it operates at a pressure of 10–15 bar, unlike other energy storage systems [19, 27].

Fig. 3. First hydrogen fuel cell-powered mining vehicle [25]

4. Challenges for hydrogen fuel cells

The biggest challenge for fuel cells is the cost of producing the fuel cells themselves, the cost of hydrogen production, its storage and transport, the cost of hydrogen power plants and the cost of investing in hydrogen fuel stations. The main factor contributing to the increase in the cost of fuel cells is the cost of, among others, the catalyst (usually platinum). Considering the use of fuel cells in transport, the cell systems would have to have a similar service life to alternative, current systems. Comparing the durability of current car engines, the durability of fuel cells after approx. 1000 h decreases significantly [9]. As for the costs of the technology itself and the hydrogen infrastructure, it depends on its mass production and hydrogen production. The assumption is based on the statement that long-term costs will be reduced with the increase in the number of hydrogen refuelling stations built

and the entire infrastructure. Hydrogen refuelling stations are much more problematic to build compared to conventional stations due to the physical properties of hydrogen. Special tanks, cooling units, and compressors are needed [16]. Considering means of transport, the lack of commercialization of the entire hydrogen-based technology, including hydrogen refueling stations, will result in a lack of demand for fuel cell vehicles. However, if the automotive industry does not produce hydrogen fuel cell vehicles, there will be no demand for companies to build hydrogen refueling stations. The entire issue is called a "chicken and egg" by the automotive industry and research institutes [30]. This is one of the reasons why governments around the world are currently strongly supporting and subsidizing the fuel cell industry. If the entire hydrogen investment gains momentum, the cost of cells and hydrogen itself should drop significantly. Another important challenge is waste management technology towards sustainable and low-emission transport [30].

One of the biggest controversies is also the aspect of the safety of using hydrogen. Hydrogen is stored in special tanks under pressure, usually 70 MPa. For safety reasons, they are placed separately on the roofs of trains or in separate carriages [45].

5. Conclusions

The examples of existing hydrogen fuel cell technologies in rail transport presented in this article clearly show that hydrogen cells are a beneficial alternative to existing common solutions based on, among others, fossil fuel engines or electric motors.

There are a number of advantages to hydrogen fuel cells, including:

– elimination of greenhouse gases (GHGs) – if hydrogen is produced only from renewable energy sources [46]
– the speed of refueling vehicles with hydrogen (compared to charging electric vehicles)
– low noise level compared to combustion engines
– high efficiency of fuel cells compared to diesel engines (fuel cell vehicles can reduce energy consumption by up to 58% compared to diesel engine vehicles) [45].

However, there are also a number of challenges that are still waiting to be solved. The biggest of them are: the high costs of hydrogen, the entire technology of hydrogen production and fuel cells, hydrogen refueling stations, and the durability of fuel cells. Thanks to government support, many countries have decided to introduce hydrogen vehicles and develop hydrogen infrastructure on their territory. Recently, there has been a large development of rail transport powered by hydrogen fuel cells. Currently, the leading companies that are involved in the production and introduction of rail transport powered by hydrogen cells include Alstom, Siemens Mobility, Vehicle Projects, and Stadler.

Most often, rail vehicles are designed as hybrid vehicles with both hydrogen fuel cells as the main source of energy and batteries (most often lithium-ion) as an additional energy storage. Fuel cells themselves as an energy source have a slow response to changes in dynamics, so during acceleration, for example, additional energy comes from batteries.

Nomenclature

AEMFC	anion exchange membrane fuel cell
AFC	alkaline hydrogen fuel cell
EMS	energy management system
HT PEMFC	high temperature hydrogen proton exchange membrane fuel cell
IEA	International Energy Agency
$LiFePO_4$	lithium iron phosphate battery
LRV	light rail vehicle
LT PEMFC	low temperature hydrogen proton exchange membrane fuel cell
MCFC	carbonate hydrogen fuel cell
NZE	net zero emissions
Pd	palladium
Pt	platinum
SOFC	solid oxide fuel cell

Bibliography

[1] Adroher XC, Chen KS, Mishler J, Cho SC, Wang Y. A review of polymer electrolyte membrane fuel cells: Technology, applications, and needs on fundamental research. Appl Energy. 2011;88(4):981-1007. https://doi.org/10.1016/j.apenergy.2010.09.030

[2] Alstom Coradia iLint – the world's 1st hydrogen powered passenger train. (accessed on 20.11.2023) https://www.alstom.com/solutions/rolling-stock/alstom-coradia-ilint-worlds-1st-hydrogen-powered-passenger-train

[3] Andaloro L, Antonucci V, Dispenza G, Napoli G, Sergi F. Design of a hybrid electric fuel cell power train for an urban bus. Int J Hydrogen Energy. 2013;38(18):7725-7732. https://doi.org/10.1016/j.ijhydene.2012.08.116

[4] Anwar M, Cole C, Hassan NMS, Spiryagin M, Sun Y. A review of hydrogen technologies and engineering solutions for railway vehicle design and operations. Railway Engineering Science. 2021;29(3):212-232. https://doi.org/10.1007/s40534-021-00257-8

[5] Badwal SPS, Giddey S, Kulkarni A, Munnings C. A comprehensive review of direct carbon fuel cell technology. Prog Energy Combust Sci. 2012;38(3):360-399. https://doi.org/10.1016/j.pecs.2012.01.003

[6] Barnes DL, Erickson TL, Hess KS, Miller AR. System design of a large fuel cell hybrid locomotive. J Power Sources. 2007;173(2):935-942. https://doi.org/10.1016/j.jpowsour.2007.08.045

[7] BNSF, Vehicle projects demonstrate fuel cell switch locomotive. Fuel Cells Bull. 2009;8:4. https://doi.org/10.1016/s1464-2859(09)70245-7

[8] Bryk K, Cierniewski M, Radziszewski P. Selection of parameters for the hydrogen power-supply system of an auxiliary rail vehicle. Materials Science and Welding Technologies. 2024;68(6):1-6. https://doi.org/10.32730/mswt.2024.68.6.5

[9] Chalk SG, Miller JF. Key challenges and recent progress in batteries, fuel cells, and hydrogen storage for clean energy systems. J Power Sources. 2006;159(1):73-80. https://doi.org/10.1016/j.jpowsour.2006.04.058
[10] Chen W, Dai C, Liu Z, Li Q, Peng F. System integration of China's first proton exchange membrane fuel cell locomotive. Int J Hydrogen Energy. 2014;39(25):13886-13893. https://doi.org/10.1016/j.ijhydene.2014.01.166
[11] China Unveils 'Groundbreaking' Hydrogen High Speed Train. (accessed on 27.08.2024) https://www.newsweek.com/china-unveils-groundbreaking-hydrogen-high-speed-train-1960349
[12] Cifrain M, Enzinger P, Faleschini G, Gsellmann J, Hacker V, Kordesch K et al. Alkaline fuel cells applications. J Power Sources. 2000;86:162-165. https://doi.org/10.1016/S0378-7753(99)00429-2
[13] Cook B. Introduction to fuel cells and hydrogen technology. Eng Sci Educ J. 2002;11(6):205-216. https://doi.org/10.1049/esej:20020601
[14] CRRC hydrogen locomotive enters service in Inner Mongolia. (accessed on 07.12.2021) https://www.railjournal.com/freight/crrc-hydrogen-locomotive-enters-service-in-inner-mongolia
[15] Dincer I, Siddiqui O. A review on fuel cell-based locomotive powering options for sustainable transportation. Arabian Journal for Science and Engineering. 2018;44(2):677-693. https://doi.org/10.1007/s13369-018-3607-2
[16] Ding D, Wu XY. Hydrogen fuel cell electric trains: technologies, current status, and future. Applications in Energy and Combustion Science. 2024;17:100255. https://doi.org/10.1016/j.jaecs.2024.100255
[17] Dippo JL, Erickson TL, Hess KS, Miller AR. Demonstration of a hydrogen fuel-cell locomotive. Rail Conf. 2010;1:1-6. http://www.apta.com/mc/rail/previous/2010/Papers/Demonstration-of-a-Hydrogen-Fuel-Cell-Locomotive.pdf
[18] Ferriday TB, Middleton PH. Alkaline fuel cell technology – a review. Int J Hydrogen Energy. 2021;46(35):18489-18510. https://doi.org/10.1016/j.ijhydene.2021.02.203
[19] Fourie F, Valicek P. Fuel cell technology in underground mining. 6th Int Platin Conf. 2014.
[20] Fowler M, Fraser R, Haji Akhoundzadeh M, Panchal S, Samadani E, Raahemifar K. Investigation and simulation of electric train utilizing hydrogen fuel cell and lithium-ion battery. Sustainable Energy Technol Assess. 2021;46:101234. https://doi.org/10.1016/j.seta.2021.101234
[21] Gallucci M. Hydrogen trains roll into service: a new hybrid locomotive signals a growing push for zero-emission rail technologies. IEEE Spectrum. 2019;56(8):6-7. https://doi.org/10.1109/MSPEC.2019.8784110
[22] Ganguly S, Sarma U. Determination of rating requirement for fuel-cell-battery hybrid energy system to substitute the diesel locomotives of Indian Railway. 2017;1-6. https://doi.org/10.1109/INDICON.2017.8487471
[23] Green Energy and Technology. Bentham Science Publishers eBooks. 2006. https://doi.org/10.2174/97816080528511060101
[24] Haller P, Kaźmierczak A, Matla J, Trocki M. Hydrogen as a fuel for spark ignition combustion engines – state of knowledge and concept. Combustion Engines. 2024;196(1):73-79. https://doi.org/10.19206/CE-171541
[25] Hillmansen S, Hoffrichter A, Miller AR, Roberts C. Well-to-wheel analysis for electric, diesel and hydrogen traction for railways. Transportation Research Part D: Transport and Environment. 2012;17(1):28-34. https://doi.org/10.1016/j.trd.2011.09.002
[26] Hillmansen S. The application of fuel cell technology to rail transport operations. Proc Inst Mech Eng F-J Rail Rapid Transit. 2003;217(4):291-298. https://doi.org/10.1243/095440903322712900
[27] Hoffrichter A. Hydrogen as an energy carrier for railway traction. PhD Thesis. Universit of Birmingham. 2013. http://etheses.bham.ac.uk/id/eprint/4345
[28] IK Gjerdingen, Hydrogen technology experimentation for sustainable mobility. A case study of hydrogen fuel cell experimentation in Lower Saxony in Germany. 2020. https://www.duo.uio.no/bitstream/handle/10852/79221/Hydrogen-technology-experimentation-for-sustainable-mobility---A-case-study-of-hydrogen-fuel-cell-experimentation-in-Lower-Saxony-in-Germany.pdf?sequence=1&isAllowed=y
[29] International Energy Agency; Energy System Transport. (accessed on 11.07.2023) https://www.iea.org/energy-system/transport
[30] Janicka A, Hamid M, Mońka P, Wesołowski M. Analysis of the potential of electro-waste as a source of hydrogen to power low-emission vehicle powertrains. Combustion Engines. 2024;196(1):126-133. https://doi.org/10.19206/ce-169494
[31] Jermsittiparsert K, Li H, Xiao C, Zhang G. Optimal size selection for fuel cell and battery in a hybrid power system of the intercity locomotives. J Clean Prod. 2021;317:128498. https://doi.org/10.1016/j.jclepro.2021.128498
[32] Kordesch KV, Simader GR. Environmental impact of fuel cell technology. Chem Rev. 1995;95(1):191-207. https://doi.org/10.1021/cr00033a007
[33] Koseki T. Technologies for saving energy in railway operation: general discussion on energy issues concerning railway technology. IEEE Trans Electr Electron Eng. 2010;5(3):285-290. https://doi.org/10.1002/tee.20531
[34] Lanzini A, Mehr AS, Rosen MA, Santarelli M. Polygeneration systems based on high temperature fuel cell (MCFC and SOFC) technology: system design, fuel types, modeling and analysis approaches. Energy. 2021;228:120613. https://doi.org/10.1016/j.energy.2021.120613
[35] Li J, Xu L, Zhang W. Ouyang M. Optimization for a fuel cell/battery/capacity tram with equivalent consumption minimization strategy. Energy Convers Manag. 2017;134:59-69. https://doi.org/10.1016/j.enconman.2016.11.007
[36] Miller AR. Tunneling and mining applications of fuel cell vehicles. Fuel Cells Bull. 2000;3(22):5-9. https://doi.org/10.1016/S1464-2859(00)88922-1
[37] Mosetlhe TC, Nqodi A, Yusuff AA. Advances in hydrogen-powered trains: a brief report. Energies. 2023;16(18):6715-6725. https://doi.org/10.3390/en16186715
[38] Neef HJ. International overview of hydrogen and fuel cell research. Energy. 2009;34(3):327-333. https://doi.org/10.1016/j.energy.2008.08.014
[39] Palmer C. Hydrogen-powered trains start to roll. Engineering. 2022;11:9-11. https://doi.org/10.1016/j.eng.2022.02.003
[40] Pawłowski K. Analiza porównawcza technologii wytwarzania wodoru (in Polish). Gaz Woda i Tech Sanit. 2023;1(4):4-12. https://doi.org/10.15199/17.2023.4.1
[41] Rail Engineer; Hydrogen trains coming soon? (accessed on 16.12.2020) https://www.railengineer.co.uk/hydrogen-trains-coming-soon/
[42] Setiawan IC, Setiyo M. Fueling the future: the case for heavy-duty fuel cell electric vehicles in sustainable transportation. Automotive Experiences. 2024;7(1):1-5. https://doi.org/10.31603/ae.11285

[43] Siemens Mobility's first hydrogen fleet at the Wildenrath test center. (accessed on 11.12.2023) https://www.mobility.siemens.com/pl/pl/o-firmie/newsroom/pierwsza-flota-wodorowa-siemens-mobility-w-wildenrath.html
[44] Stadler's hydrogen-powered train FLIRT H2 achieves a new Guinness World Records title. (accessed on 25.03.2024) https://stadlerrail.com/en/media/article/stadler%E2%80%99s-hydrogen-powered-train-flirt-h2-achieves-a-new-guinness-world-records-title/1656/
[45] Wang J. Barriers of scaling-up fuel cells: cost, durability and reliability. Energy. 2015;80:509-521. https://doi.org/10.1016/j.energy.2014.12.007
[46] Wu J, Zhang H, Zhang J. High-temperature PEM fuel cells (Chapter 10). PEM fuel cell testing and diagnosis. 2013;243-282. https://doi.org/10.1016/b978-0-444-53688-4.00010-3

Anna Danielak, MEng. – Faculty of Civil and Transport Engineering, Poznan University of Technology, Poland.
email: *anna.danielak@doctorate.put.poznan.pl*

Maksymilian Cierniewski, DEng. – Poznań Institute of Technology, Łukasiewicz Research Network, Poland.
email:
maksymilian.cierniewski@pit.lukasiewicz.gov.pl

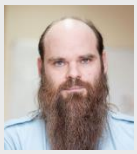

Prof. Miloslaw Kozak, DSc, DEng. – Faculty of Civil and Transport Engineering, Poznan University of Technology, Poland.
email: *miloslaw.kozak@put.poznan.pl*

Article citation info:
Ślusarczyk K, Jurecki R. The use of a vehicle simulator for eco-driving research. Combustion Engines. 2025;203(4):23-31. https://doi.org/10.19206/CE-207006

Katarzyna ŚLUSARCZYK
Rafał JURECKI

Combustion Engines
Polish Scientific Society of Combustion Engines

The use of a vehicle simulator for eco-driving research

ARTICLE INFO

Received: 11 May 2025
Revised: 24 May 2025
Accepted: 11 June 2025
Available online: 30 August 2025

The study presents the use of a driving simulator as a tool for evaluating driver behavior in the context of eco-driving. A group of 37 drivers of varying age and experience completed a predefined urban driving scenario under controlled conditions. Based on four operational variables, each weighted by its assumed impact on fuel efficiency, the WEco indicator was developed to enable a quantitative assessment of driving style. Drivers were classified into three groups representing different levels of eco-driving performance. The results showed clear differences in fuel consumption and engine RPM, confirming the validity of the classification model. The proposed indicator offers practical applications in fleet management, driver training, and environmental impact monitoring.

Key words: *eco-driving, vehicle simulator, driving style classification, fuel consumption, driver behavior analysis*

1. Introduction

Due to growing environmental awareness and the constant rise in fuel costs, the search for effective strategies to reduce fuel consumption and greenhouse gas emissions is becoming a priority and an integral part of responsible vehicle use. The search for alternative energy sources to improve efficiency, reduce toxic emissions into the atmosphere, and prevent global warming are currently key areas of development in the energy sector, including the design of internal combustion engines [30]. Road transport accounts for over 85% of total freight transport. In this process, motor vehicles are primarily used for transport operations [33]. Transport accounts for a significant portion of energy consumption and emissions of environmentally harmful dust and gases [22]. Reducing carbon dioxide emissions to mitigate climate change has become a key focus of research and development in the sector in recent years [10, 26, 29]. As a result, the concept of eco-driving, or eco-friendly driving, is gaining in importance and popularity. Eco-driving is not only a way of driving, but also a comprehensive strategy involving the application of special techniques and driving behaviour in order to minimise the vehicle's negative impact on the environment, while at the same time reducing fuel consumption and operating costs. The main principles of eco-driving are based on smooth driving, reducing unnecessary acceleration and braking. The technique involves driving the car in the highest possible gear, at the lowest possible engine speed. It is also important to brake the engine by reducing gears – e.g. when approaching traffic lights (idling) [4]. Eco-driving appears to be an effective way to achieve energy savings and emission reductions in the short term [27]. It is becoming increasingly common and is thought to improve driving behaviour. Research results presented in papers such as [32] show that the use of eco-driving not only has environmental benefits but also reduces operating costs through lower fuel consumption, which is particularly important in this day and age. The issue of eco-driving is currently very popular and is addressed in numerous publications. Researchers have noted the potential impact of eco-driving on improving the safety of transport users. Studies [2, 6, 8, 28] show a link between eco-driving and safe driving, as safe driving includes, among other things, observing speed limits and avoiding rapid acceleration or braking. Many studies on eco-driving have shown potential reductions in fuel consumption and CO_2 emissions ranging from 5% to 40% [2]. The authors focus on the implementation of eco-driving into fleet driver training. They emphasise that eco-driving not only reduces costs and environmental impacts, but also improves driving safety – through smoother driving, reduced speed and earlier response to traffic situations, among other benefits [6]. Deliberate reductions in greenhouse gas and particulate emissions have been shown to contribute to climate change mitigation [7, 8, 11], as well as generating economic benefits through reduced fuel consumption of vehicle engines [8]. Driving according to eco-driving principles can have a significant impact on reducing fuel consumption by up to 10%, thereby reducing CO_2 emissions while driving by the same amount [7]. The concept of eco-driving may be relevant and is often studied and analysed, especially in the context of companies operating large fleets of vehicles [6, 15, 13]. According to research findings, it can be concluded that the application of eco-driving principles brings tangible benefits such as reduced fuel consumption, lower emissions of greenhouse gases and air pollutants, reduced vehicle operating costs, and extended vehicle life [4, 14]. Compared to normal driving, eco-driving resulted in a reduction in fuel consumption of 0.44 dm³/100 km (–6.6%), while aggressive driving led to an increase of 1.64 dm³/100 km (+24.6%) [4]. In order to carry out effective research in the context of eco-driving, it is necessary to select appropriate parameters such as road conditions [16], route choice [24], traffic volume, and other relevant factors. It should be noted, not under all conditions will eco-driving principles produce noticeable benefits [5, 9, 23, 24]. In the literature, researchers often mention routes with a high number of intersections with traffic lights because they force the driver to brake, accelerate and idle frequently [17], which provides a realistic context for evaluating the effectiveness of eco-driving strategies.

Vehicle simulators offer the possibility of programming routes in such a way that consistent and repeatable measurement conditions, e.g. the number of intersections with traffic lights, environmental conditions, and traffic behaviour, remain consistent across all test drives. Achieving such standardisation in actual road tests would be extremely difficult. Therefore, the use of driving simulators allows controlled experimentation with identical traffic scenarios, enabling analysis and comparison of driver performance under repeatable conditions. According to the literature, the greatest environmental and economic benefits of eco-driving are observed in urban and suburban traffic (e.g. on national, regional, and local roads), while the least benefits are reported for driving on motorways and expressways due to the relatively smooth flow of traffic and fewer stops [5, 9, 23, 24]. This article presents potential applications of vehicle simulators in eco-driving-related research. By discussing various aspects of eco-driving and presenting research results, the aim is to highlight the importance of this concept as an effective strategy to reduce fuel consumption and greenhouse gas emissions in the context of modern road transport. The article presents selected aspects of measurement methodologies in the field of eco-driving using a vehicle simulator. Simulators play a key role and are frequently used tools in many studies [18, 21, 24]. Simulators provide a safe, controlled and precise environment for testing and improving driving techniques [19, 21]. They enable not only the collection of research data, but also the effective training of drivers [25] and the testing of new technologies to support sustainable transport development. They also provide reproducible and safe testing conditions. This allows testing under controlled conditions and strict traffic scenarios, eliminating the risks associated with real-world traffic. This makes it possible to test different driving situations and techniques without endangering drivers. Simulators also offer highly precise data acquisition capabilities. They are equipped with advanced measurement systems that enable detailed tracking of vehicle dynamics and parameters characterising driving behaviour, such as acceleration, braking, gear changes, engine revolutions, and fuel consumption. This data is essential for analysing the effectiveness of various eco-driving techniques. One of the biggest advantages of simulators is the ability to reproduce identical test conditions for different drivers. Through the use of simulators, the same route and driving conditions can be accurately reproduced for each participant, allowing reliable comparisons and evaluation of the impact of different factors on eco-driving efficiency. This approach eliminates potential errors due to route variability or changing road conditions. Simulators are also widely used in driver training. Through practical exercises, drivers can learn and improve their eco-driving techniques, which then directly translates into improved driving behaviour in real-world conditions. Testing in a vehicle simulator also allows new technologies to be tested, including driver assistance systems and systems that support eco-driving, such as fuel-optimised navigation, intelligent speed management systems and different engine modes. In addition, simulators facilitate the study of the behavioural aspects of driving. They allow researchers to analyse how factors such as stress or fatigue, for example, affect driver behaviour and the ability to apply eco-driving techniques effectively. The aim of this study is to develop indicators to analyse driver behaviour and to investigate selected eco-driving techniques using a vehicle simulator. The study also focuses on developing and testing an indicator-based model to classify drivers' driving styles according to eco-driving principles. This research responds to current socio-economic needs related to reducing transport emissions, promoting fuel efficiency, and improving drivers' technical competence. The importance of sustainability in the transport sector is constantly growing and requires effective tools to assess and influence driver behaviour. The classification model proposed in this thesis is practical and flexible, making it potentially useful both in training processes (e.g. for professional drivers) and in monitoring fleet performance. Basing the analysis on real measurement data collected from the simulator increases the reliability of the results and opens up prospects for further research and implementation of solutions in practice.

2. Methods

2.1. Research equipment

The research was conducted using the Oktal™ driving simulator, located at the Laboratory of Vehicles and Tractors of the Kielce University of Technology (Fig. 1).

Fig. 1. Oktal™ Vehicle Simulator

The simulator's motion system platform has six degrees of freedom and is driven by six electric actuators, working in conjunction with electronically controlled gear systems. It allows angular oscillations of up to ±10° and linear displacements of up to ±50 mm. The simulator cab is a section of the actual vehicle cab. It is equipped with all the necessary components for driving. It includes a steering wheel with an angle sensor and active force feedback up to 15 Nm, capable of ±540° rotation and simulating uneven road surfaces. The accelerator, brake, and clutch pedals feature passive force feedback, which mimics real pedal resistance, and are equipped with pressure and position sensors. The manual gearshift lever includes a gear position sensor (supporting up to five or six forward and reverse gears), passive resistance, and a mechanical function that simulates clutch engagement by locking the gear when disengaged. Additional cabin features include a keyed ignition, manual parking brake, indicator lever, light switches, hazard warning button, horn, and programmable dashboard. The dashboard can display parameters such as vehicle speed, engine crank-

shaft speed, fuel consumption, brake pedal pressure, steering angle, and more. The cabin is equipped with an adjustable driver's seat, seat belts, and an audio system that generates dynamic vehicle sounds (such as engine operation, tyre-road interaction, and skidding), as well as ambient sounds [20]. The simulator allows customised measurement routes to be programmed to suit research needs. It also allows full control over environmental conditions, including time of day, weather, and traffic volume. During the experiments, the system records hundreds of parameters such as vehicle speed, position, acceleration, fuel consumption, gear selection, crankshaft speed, accelerator and brake pedal pressure, clutch engagement, and total simulation time. The ability to record and analyse these parameters under reproducible and controlled conditions enables a comprehensive assessment of driver behaviour, particularly in relation to eco-driving practices. For the purpose of the study, a route was chosen that represented driving conditions typical of an urban environment. The total length of the route was 2.5 km. It was programmed to allow repeated testing of driver behaviour under identical environmental conditions. Each driver had to drive the exact same route. The route included, among other things, intersections with traffic lights, which required drivers to stop and start frequently, creating convenient conditions for assessing driver behaviour in terms of eco-driving efficiency. The choice of a relatively short test route (2.5 km) was dictated by the need to ensure consistent, controlled, and repeatable experimental conditions. The main objective of the study was to compare driver behaviour in well-defined and repeatable urban traffic scenarios, which required minimising the variability of external factors such as traffic volumes, signalling patterns, and road infrastructure layout. The limited distance also facilitated the efficient conduct of multiple repetitions of the test within a limited time and under stable environmental conditions, thus increasing the reliability and comparability of the results obtained by the participants. Nevertheless, the authors recognise the limitations of the short route length. Therefore, future research will consider implementing longer and more varied routes that more accurately reflect the complexity of real traffic conditions and allow for more precise statistical averaging of driver behaviour indicators. The programmed route is shown in Fig. 2.

Fig. 2. Route map of the driving simulation

2.2. Participants

A total of 37 drivers aged between 21 and 67 years participated in the study. The age of the drivers averaged 28.22 years (standard deviation = 9.54), and the median age was 25 years. Table 1 shows the characteristics of the study group.

Table 1. Characteristics of the driver study group

Length of holding a driving licence			
Up to a single year	1–5 years	6–10	> 10
2.70%	35.14%	32.43%	29.73%
Frequency of vehicle use			
Daily	Several times a week	Several times a month	
72.97%	21.62%	5.41%	
Distance travelled per month			
Up to 100 km	101–300 km	301–1000 km	1001–3000	Up to 100 km
8.11%	5.41%	43.24%	35.14%	8.11%
Total distance travelled			
5–50 thousand kilometres	50–150 thousand kilometres	150–300 thousand kilometres	> 300 thousand kilometres
16.22%	37.84%	24.32%	21.62%
Is their work related to driving a vehicle?			
Yes		No	
24.32%		75.68%	

The results indicate that the group of drivers participating in the study was diverse in terms of age and driving experience, as measured by monthly driving distance and time since obtaining their licence. The task assigned to each participant was to drive a designated, pre-programmed route in a driving simulator. The route was designed to elicit various driving behaviours typical of urban traffic, such as stopping at intersections.

2.3 Parameters for eco-driving analysis

Tests carried out using the Oktal™ vehicle simulator allowed data to be collected that could be used to assess driving style. During the experiment, participants were asked to drive through urban areas at a speed typical of urban traffic, while choosing a pace they considered safe. Participants were first given a test drive to familiarise themselves with the simulator and the route. While driving, participants had to remain alert to their surroundings, including other road users. The route included intersections with traffic lights, intersections without traffic lights, and roundabouts. Figure 3 shows a screenshot of a sample simulation drive.

The figures below show examples of the characteristics that can be obtained during simulation studies. These example profiles illustrate the measurement capabilities of the simulator in eco-driving research and demonstrate its potential for use in larger-scale statistical analyses.

Fig. 3. Screenshot of a representative location during the simulation drive

The following variables were analyzed:

– Vehicle velocity [km/h] (Fig. 4a)
– Selected gear [-] (Fig. 4b)
– Engine crankshaft speed [rpm] (Fig. 4c)
– Fuel consumption [l/s] (Fig. 5).

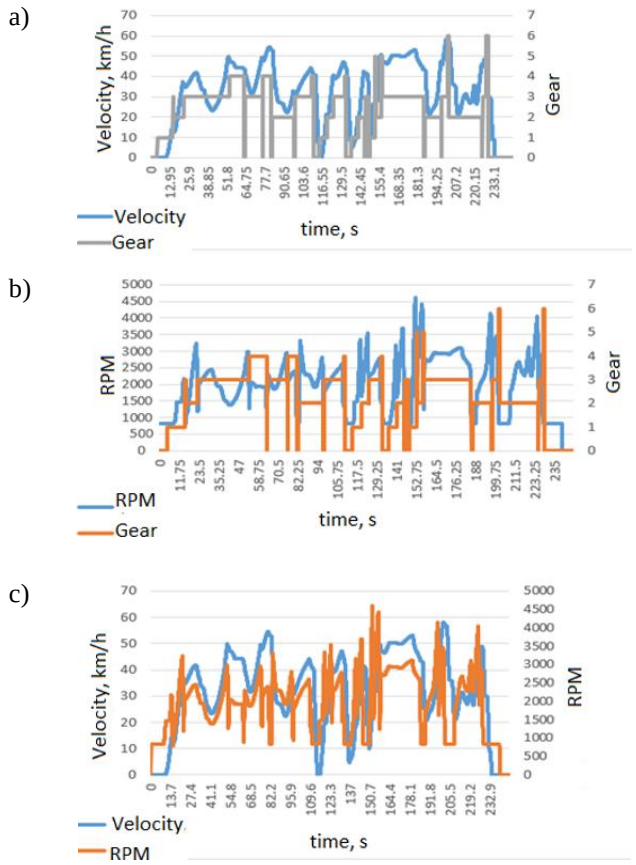

Fig. 4. Sample profiles obtained during the simulation drive: a) vehicle velocity and gear selection during the drive, b) engine crankshaft rotational velocity and corresponding gear, c) engine crankshaft rotational velocity and the vehicle velocity at the given moment

Analysis of the graphs above indicates that the test route was relatively dynamic and required frequent speed changes. In eco-driving, the optimal approach is to maintain a smooth and steady driving style that minimises the need for frequent gear changes. It is generally recommended to keep the vehicle speed as constant as possible, to avoid rapid acceleration or braking, and to select gears that keep the engine crankshaft speed within the optimum operating range. Interpreting these profiles makes it possible to assess whether the driver has chosen the right gears in relation to the vehicle speed. A common problem among drivers is keeping the engine speed excessively high or too low, which is inefficient in terms of fuel consumption and mechanical performance. The sample profiles allow the driver's behaviour to be assessed in the context of eco-driving principles, particularly in terms of gear selection on a specific test route. The data reveal moments when the driver failed to reduce gears in a timely manner – particularly in situations where he or she continued to drive in a higher gear despite a significant drop in vehicle speed and engine speed.

Figure 5 shows the vehicle speed profile in combination with engine crankshaft speed and fuel consumption during the simulation drive.

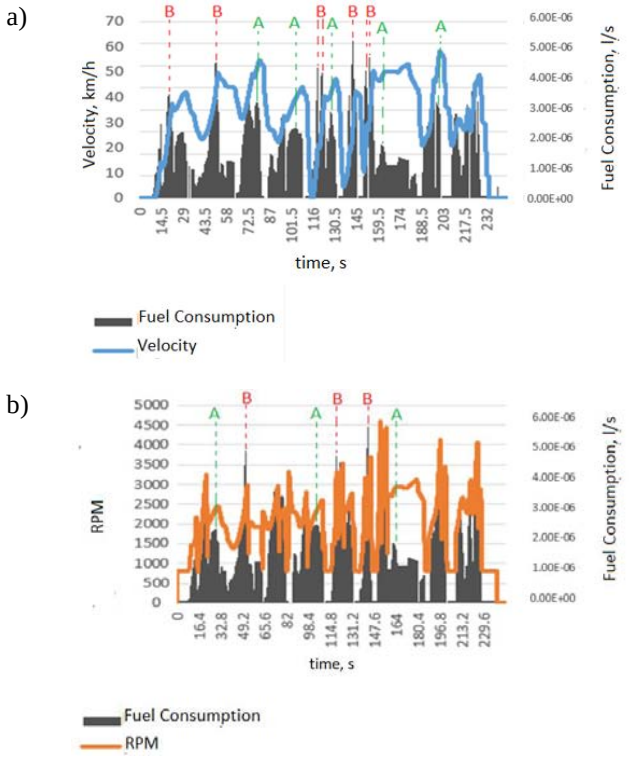

Fig. 5. Fuel consumption during the simulation drive: a) in relation to vehicle velocity, b) in relation to engine crankshaft rotational velocity

Analysis of the vehicle speed profile (Fig. 5a) identifies points where fuel consumption was particularly high (labelled point A), and points where it remained relatively low despite maintaining adequate vehicle speed and crankshaft speed (labelled point B). Dynamic changes in engine speed are associated with an increase in fuel consumption. Any rapid acceleration results in a sharp increase in fuel consumption. By analysing the engine crankshaft speed profile (Fig. 5b), it is possible to identify periods when fuel consumption remained relatively low under relatively stable revving conditions. To assess drivers from an eco-driving perspective, the following indicators were defined (Fig. 6).

Over-speed indicator (W1): expressed as a percentage of the total driving time in which the vehicle exceeded the speed limit. This indicator provides information on whether

a driver complies with traffic regulations and how often and to what extent he or she exceeds the speed limit. Exceeding the speed limit not only constitutes a legal offence but can also lead to increased fuel consumption.

High Engine RPM Indicator (W2): expressed as a percentage of the time that the engine crankshaft speed exceeded 3,000 revolutions per minute (rpm). High engine speeds, especially in the context of unreasonably aggressive driving, lead to higher fuel consumption and increased emissions. A well-defined indicator makes it possible to assess how often the engine operates in the excessive rev range, which is a key aspect of driving style analysis in the context of eco-driving principles.

Engine Idling Time Indicator (W3): expressed as a percentage of the total time the vehicle remains idling (e.g. during traffic jams or stopping at traffic lights). Longer engine idling results in unnecessary fuel consumption and increased CO_2 emissions. While this may be due to factors beyond the driver's control – such as road infrastructure – it can be remedied by implementing Intelligent Transport Systems (ITS), which improve traffic flow, and by equipping vehicles with Start-Stop systems. Reducing this rate is a key element in improving economic driving performance.

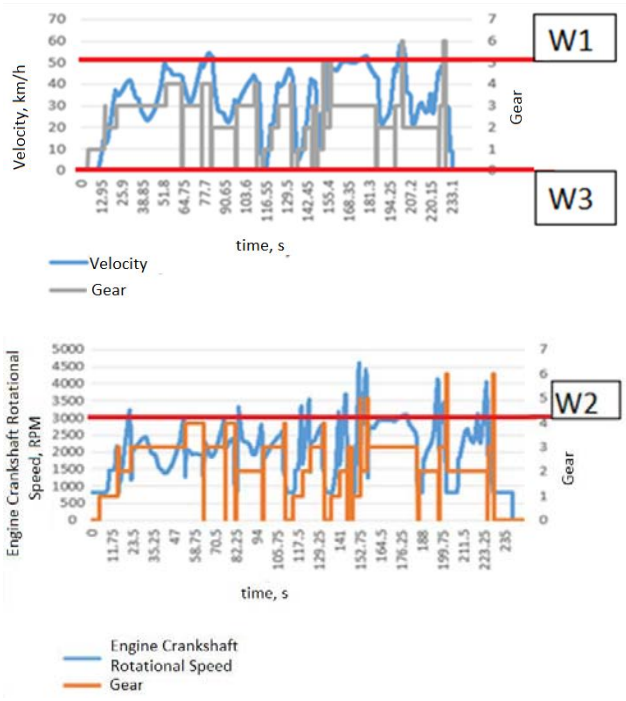

Fig. 6. Diagram of the applied indicators

Fuel Consumption Indicator (W4) is a direct measure of driving efficiency, representing the amount of fuel consumed relative to the distance travelled. Analysis of this indicator makes it possible to assess the impact of driver behaviour on vehicle fuel efficiency. These indicators make it possible to identify common mistakes made by drivers that can lead to increased fuel consumption. As part of the study conducted, each participant drove in urban conditions using a driving simulator, covering the same route. The following parameters were recorded for each participant during the drive: instantaneous speed, selected gear, engine crankshaft speed and instantaneous fuel consumption. Indicators W1 to W4 were calculated from the collected data. Weights were then assigned to each of these indicators, allowing the WEco index to be calculated for each driver. Based on the WEco index value, participants were classified into one of three driver profile groups.

3. Results

3.1. Characterisation of driving sessions in terms of eco-driving

In order to initially characterise the data used to calculate the WEco index, an analysis of the distribution of the four operational variables was carried out. For this purpose, box plots were used to graphically assess the dispersion, asymmetry and presence of outliers in the data set.

Figure 7 shows the distributions of the previously mentioned parameters.

The first variable analysed, representing the percentage of time driving at speeds exceeding 50 km/h (Fig. 7a), had a median of 12.48%.

The interquartile range was from 9.11% to 18.5%, with non-outliers ranging from 1.44% to 32.26%.

Numerous outliers were observed, indicating significant variation in driving speed among drivers, with some participants displaying a much more dynamic driving style.

The second variable, illustrating the percentage of time driving with an engine crankshaft speed above 3000 rpm (Fig. 7b), had a median of 16.54% and an interquartile range from 5.95% to 24.29%.

Nevertheless, the presence of outliers suggests significant differences in acceleration techniques and gear selection strategies, which have a direct impact on fuel economy.

The third variable, the proportion of idling time (Fig. 7c), showed a median of 7.1%.

Most observations fell between 3.36% and 11.38%, while non-outlier values ranged from 0.64% to 18.5%.

This distribution may reflect differences in driving smoothness and frequency of stops – such as during traffic congestion or while waiting at signalized intersections.

Extended engine idling is an undesirable phenomenon from an energy efficiency perspective.

The last analyzed variable – fuel consumption in liters per 100 km (Fig. 7d) – had a median value of 12.63 l/100 km, with quartiles ranging from 12.03 to 13.95 l/100 km.

Numerous outlier observations were recorded, reaching up to 22–25 l/100 km.

This highlights significant variation in vehicle operating intensity, resulting from factors such as driving dynamics, acceleration behavior, and engine RPM usage.

The relatively high median confirms that urban conditions – combined with certain driving styles – can lead to substantial fuel consumption.

In summary, the analysis of the four partial indicators revealed notable variability in driver behavior, with the presence of both typical and outlier values.

Particularly pronounced variation was observed in indicators W2 and W4, confirming their critical role in constructing the WEco indicator and in the overall assessment of eco-driving performance.

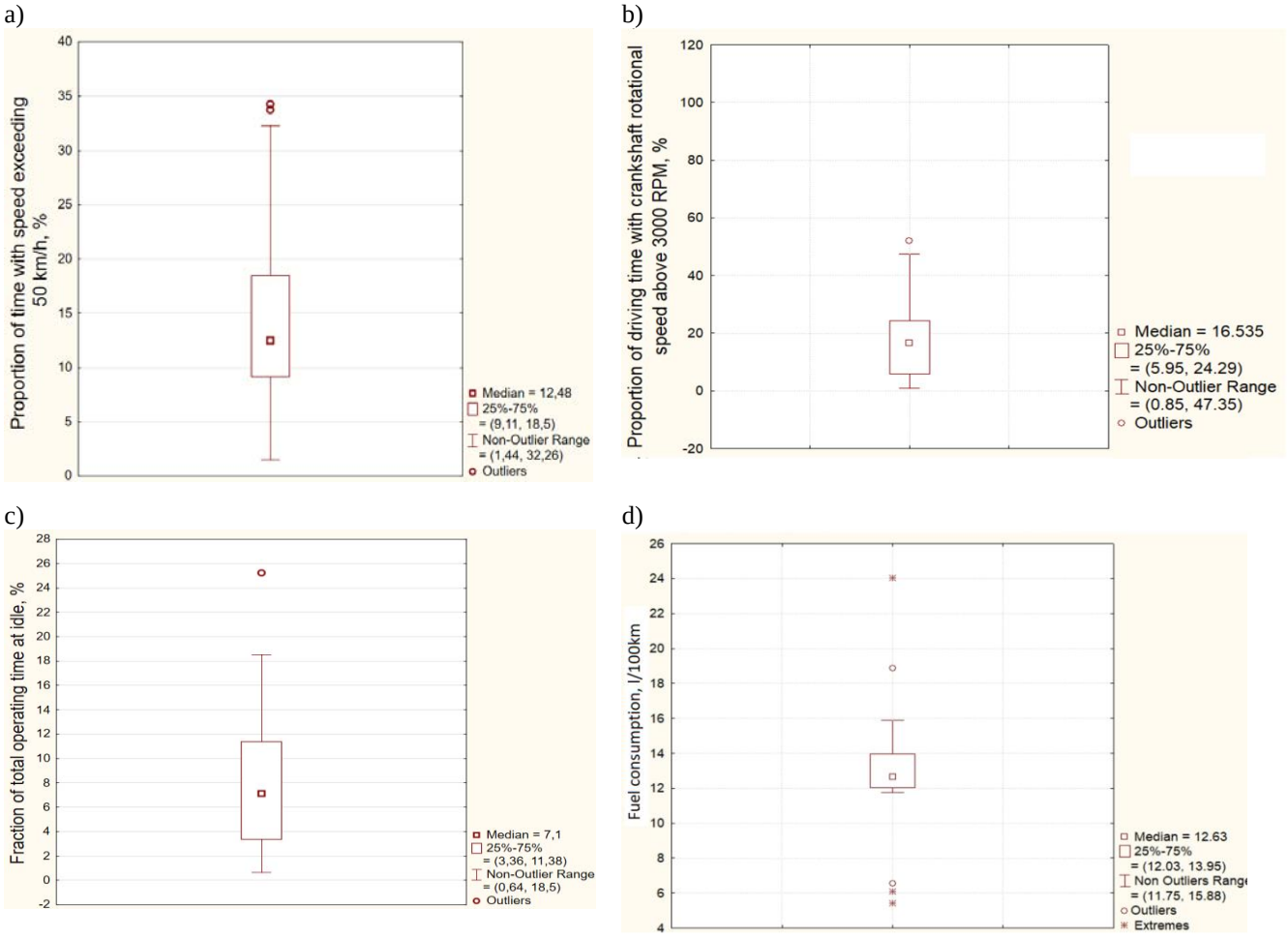

Fig. 7. Indicator values: a) W1 – proportion of time with speed exceeding 50 km/h, b) W2 – proportion of driving time with crankshaft rotational speed above 3000 rpm, %, c) W3 – fraction of total operating time at idle, %, d) W4 – fuel consumption, $dm^3/100$ km

3.2. Indicator-based assessment of driving style

The presented driver classification model is a proposal and can be modified according to research and practical needs. Four key eco-driving indicators, defined in Chapter 2.3, were analyzed. To construct a synthetic WEco index that takes into account various aspects of driver driving style, each indicator was assigned a weight corresponding to its potential impact on economic and environmental performance. By multiplying the indicator values by the weights, adjusted values were obtained, reflecting the importance of a given parameter in the overall assessment of driving style. The choice of weights presented in this article is a proposal and can be modified depending on the adopted methodology, available data, or the purpose of the analysis. Different scenarios may place greater emphasis on, for example, CO_2 emissions, fuel consumption, or acceleration intensity. The presented classification method is open-ended and can be modified depending on the specifics of the case study, research assumptions, or practical requirements—for example, in the context of specific vehicle fleet types or training systems. The choice of weights was based on the assumption that individual indicators differ in their importance in terms of their impact on economic and environmental performance. A high WEco value, according to the adopted criteria, may indicate a less economical/ecological driving style, while a lower value may indicate a smoother and more economical driving style.

The fuel consumption index (W4) received the highest weight of 0.4 because it was considered the most critical component of the combined score. Fuel consumption is a direct and tangible consequence of inefficient driving, and its impact on the final score was deliberately emphasized [31].

The second most important variable was the percentage of time the engine crankshaft speed exceeded 3000 rpm (W2), which was assigned a weight of 0.3. High engine speeds typically correlate with aggressive acceleration and frequent operation above optimal speeds for a given gear, which negatively impacts fuel economy and exhaust emissions.

The engine idling time index (W3) was assigned a weight of 0.2. This parameter indirectly reflects driving smoothness and the driver's ability to effectively manage idle times – long idling times are associated with lower energy efficiency, especially in urban conditions. This is particularly important for pollutant emissions, and modern vehicles often use start-stop systems to mitigate this issue. The lowest weight, 0.1, was assigned to W1, the percentage of time driving at speeds exceeding 50 km/h. Although this variable relates to road safety and provides information

about driver behavior, its direct impact on fuel consumption in an urban environment is relatively limited and more difficult to interpret compared to other indicators.

Based on the calculated WEco values, drivers were divided into three groups. The decision to use a three-level classification was made to ensure transparency and analytical usefulness of the results. This division distinguishes between drivers with low, medium, and high WEco scores, corresponding to three general profiles: eco-driving, average driving, and non-ecological driving. This simplification allows for simple interpretation and facilitates further statistical comparisons between groups.

Classification thresholds were determined based on the empirical distribution of WEco values (i.e. a histogram), taking into account a uniform distribution of participants and the presence of clear natural breakpoints in the data. The aim was to maintain a balanced group size (as far as possible), while reflecting the actual variability in driving behaviour. Interval grouping, based on data-driven cut-off values, is shown in Fig. 8.

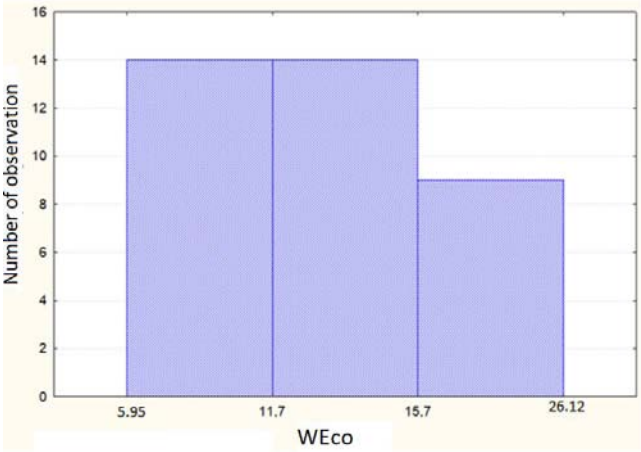

Fig. 8. Histogram of the WEco indicator (sum of operational parameters) divided into 3 classes

Based on the calculated WEco values, drivers were assigned to the appropriate classification group.

Group 1 (n = 14) comprises drivers with the lowest WEco values (≤ 11.7), indicating the relatively most economical and environmentally friendly driving style.

Drivers in this group are characterised by moderate speed, a low proportion of driving at high crankshaft speeds, short idling times, and moderate fuel consumption. Their driving style can be described as smooth, calm and energy-efficient.

Group 2 (n = 14) represents an average level of efficiency, with WEco values ranging from 11.71 to 15.70.

Drivers in this group show an average level of adherence to eco-driving. Their driving behaviour is more variable, which may reflect an inconsistent driving style or a lack of dominance of fuel-saving habits.

Group 3 (n = 9) includes drivers with the highest WEco values (> 15.70), indicating the least economical driving style in the sample. Their driving style was associated with more frequent use of high engine speeds, higher fuel consumption and longer idling periods.

The style of this group can be characterised as more dynamic and potentially less environmentally friendly.

In order to assess the relevance of the classification adopted and the contribution of the individual WEco components, a statistical analysis of the differences between the groups (groups 1–3) was carried out for four sub-indices: W1, W2, W3, and W4.

For this purpose, the non-parametric Kruskal-Wallis test was used.

The analysis confirmed that the WEco indicator was effective in differentiating drivers according to their driving style.

Significant differences, especially at W1 ($H = 13.42$, $p = 0.0012$) and W2 ($H = 28.73$, $p = 0.00000058$), indicate that a more dynamic driving style – characterised by higher speeds and increased engine crankshaft speed – clearly differentiates the classification groups.

The results confirm the usefulness of the WEco index as a tool for assessing driving efficiency and further benchmarking.

4. Discussion

The aim of this study was to develop and evaluate an indicator model for classifying driving styles in urban environments, with particular emphasis on eco-driving principles using a vehicle simulator. The study defined four key indicators, which were assigned arbitrarily determined weights based on their assumed impact on eco-driving and environmental friendliness. These values were used to calculate the WEco index, which provided an overall assessment of driver behavior behind the wheel. The WEco index was then used to classify drivers into three groups representing different levels of driving efficiency and eco-friendliness. The obtained values revealed noticeable variation among participants, enabling the identification of both highly efficient and decidedly unsustainable driving styles. The largest number of drivers was recorded in groups 1 and 2, suggesting that a moderate approach to vehicle operation may be the dominant trend among the drivers studied. Although the proposed model is still in development, it demonstrates potential for practical application – for example, in fleet management systems, driver behavior monitoring applications, eco-driving training programs, and in assessing progress in reducing fuel consumption and exhaust emissions. Based on easily measurable vehicle parameters obtained during actual driving using telematics systems, it is possible to identify drivers who effectively employ eco-driving techniques in practice. It should be emphasized, however, that the presented concept remains open to adaptation – both the indicators themselves and the weights assigned to them can be adapted to specific applications, available datasets, or transport policy goals. Further work in this area is planned. Driver classification based on the WEco indicator is consistent with existing literature on eco-driving and driver behavior analysis. Research indicates that variables such as fuel consumption, engine idling time and high-rpm operation are key to assessing energy efficiency and emissions [3, 31]. The literature also highlights the effectiveness of simple standarised indicators as tools for monitoring driving style, especially in the context of vehicle fleets or driver education programmes [1, 12].

Therefore, the WEco indicator proposed in this study is in line with current knowledge and offers a useful analytical tool for future research and practical applications.

5. Conclusions

In this study, a composite WEco index was developed and initially validated to classify drivers' driving style in terms of compliance with eco-driving principles. Analysis of four component indices (W1–W4) enabled effective differentiation of driver behavior in simulated urban traffic conditions. The results confirm the potential of WEco as a tool for assessing the energy efficiency of driving style, with potential applications in driver training and assistance systems. Despite limitations – such as the short test route – the obtained data were consistent and repeatable. Future plans include expanding the study to include longer and more diverse driving scenarios, which will enable a more comprehensive assessment of the stability and usefulness of the WEco index. As a result of the analyses, the WEco index was developed, enabling not only a qualitative but also a quantitative assessment of driving style in relation to eco-driving principles. Based on this index, participants were assigned to three efficiency classes, including drivers with smooth and energetic driving styles, as well as those with a more dynamic and less economical driving style. The Kruskal-Wallis test results confirmed statistically significant differences between the groups, particularly in terms of engine operation at high speed and fuel consumption, which confirms the validity of the proposed classification approach.

The model presented can be applied both in research and in practice – for example, in driver training programmes or fleet management systems. With climate change on the rise, the concept of eco-driving is gaining importance. Eco-driving is a driving style that not only reduces fuel consumption but also reduces the emission of harmful pollutants into the atmosphere, such as carbon dioxide (CO_2) and nitrogen oxides (NO_x). Environmental responsibility in everyday activities, including vehicle operation, is becoming a key factor in the fight against global warming and air pollution. This highlights the importance of promoting appropriate driving behaviour, starting with driver education.

Driving simulators are an innovative tool that plays a significant role in promoting and teaching eco-driving. These technologies make it possible to assess driver behaviour in terms of eco-driving. Thanks to advanced systems, simulators can accurately reflect road conditions and driving dynamics, enabling a detailed analysis of an individual's driving style. They assess aspects such as driving fluidity, use of gears, braking, and acceleration technique. As a result, simulators can effectively identify areas where drivers can improve their habits to become more environmentally responsible behind the wheel.

For young drivers just starting their driving adventure, simulators provide particularly valuable educational support. In a controlled and safe environment, they can learn the principles of eco-driving from the very beginning. Regular simulator training allows them to acquire and reinforce habits that not only reduce their environmental impact but also improve road safety. Young drivers learn how to avoid sudden acceleration and braking, maintain a constant speed, and optimally use gears to reduce fuel consumption.

Eco-driving brings not only environmental but also economic benefits. Reduced fuel consumption translates into savings, providing additional motivation for drivers to implement eco-driving principles in their daily practice. Furthermore, simulators allow drivers to familiarize themselves with various realistic driving scenarios where eco-driving techniques are particularly beneficial – for example, in urban environments, where frequent stop-and-go driving often leads to increased fuel consumption.

In the face of climate challenges, eco-driving education is becoming an essential part of both new driver training and the ongoing development of experienced drivers. Thanks to their advanced capabilities, simulators offer a unique opportunity for both learning and assessment, making them a very valuable tool in promoting sustainable and responsible driving behaviour.

Bibliography

[1] Ahn K, Rakha H, Trani A, Van Aerde M. Estimating vehicle fuel consumption and emissions based on instantaneous speed and acceleration levels. J Transp Eng. 2002;128(2): 182-190. https://doi.org/10.1061/(ASCE)0733-947X(2002)128:2(182)

[2] Alam MS, McNabola A. A critical review and assessment of eco-driving policy & technology: Benefits & limitations. Transp Policy. 2014;35:42-49. https://doi.org/10.1016/j.tranpol.2014.05.016

[3] Andrieu C, Saint Pierre G. Comparing effects of eco-driving training and simple advices on driving behavior. Procedia Soc Behav Sci. 2012;54:211-220. https://doi.org/10.1016/j.sbspro.2012.09.740

[4] Andrzejewski M, Nowak M. Wpływ stylu jazdy według zasad eco-drivingu na emisję substancji toksycznych z lekkiego samochodu użytkowego (in Polish). Autobusy. 2019; 20(6):33-37. https://doi.org/10.24136/atest.2019.121

[5] Andrzejewski M. Wpływ stylu jazdy kierowcy na zużycie paliwa i emisję substancji szkodliwych w spalinach. PhD thesis. Repozytorium Naukowe Politechniki Poznańskiej; Poznań 2013.

[6] Auerbach P, Kukla W. Istota i zasady ekojazdy, czyli integralna część szkolenia w przedsiębiorstwach świadczących usługi transportowe (in Polish). Zesz Nauk Politech Pozn Org Zarz. 2013;60:5-19.

[7] Barkenbus JN. Eco-driving: an overlooked climate change initiative. Energy Policy. 2010;38:762-769. https://doi.org/10.1016/j.enpol.2009.10.021

[8] Caban J, Sopoćko M, Ignaciuk P. Eco-driving, przegląd stanu zagadnienia (in Polish). Autobusy. 2017;18(6).

[9] Casanova J, Barrios C, Espinosa F. Capability of on-board emission measurement systems for driver behavior assessment. Int Conf on Transport and Environment. Milan 19-21.03.2007.

[10] De Abreu VHS, Santos AS, Monteiro TGM. Climate change impacts on the road transport infrastructure: A systematic review on adaptation measures. Sustainability. 2022;14(14): 8864. https://doi.org/10.3390/su14148864

[11] Delhomme P, Cristea M, Francoise P. Self-reported frequency and perceived difficulty of adopting eco-friendly driving behaviour according to gender, age, and environmental concern. Transp Res Part D. 2013;20:55-58. https://doi.org/10.1016/j.trd.2013.02.002
[12] Ericsson E. Independent driving pattern factors and their influence on fuel-use and exhaust emission factors. Transport Res D-Tr E. 2001;6(5):325-345. https://doi.org/10.1016/S1361-9209(01)00003-7
[13] Farion E, Zbadyński M. Analysis and evaluation of the implementation of ecodriving in a transport company. TransLogistics. 2019;5(1):183-198.
[14] Gorzelańczyk P, Michaś D. The impact of eco-driving on the operation of vehicles. Autobusy. 2019;20. https://doi.org/10.24136/atest.2019.039
[15] Hennig W. Ford eco-driving: the clever move, vehicle environmental engineering & Ford Europe. Cologne 2004.
[16] Huang Y, Yan X, Li X, Rakotonirainy A. Evaluating the safe and eco-driving performances of car-following behaviors in a vehicle platoon under foggy conditions. J Transp Saf Secur. 2024;16(2):204-229. https://doi.org/10.1080/19439962.2023.2201173
[17] Jayawardana V, Wu C. Learning eco-driving strategies at signalized intersections. Proc Eur Control Conf. 2022:383-390. https://doi.org/10.23919/ECC55457.2022.9838000
[18] Jukiewicz M, Orszulak B. Stanowisko laboratoryjne do pomiaru wybranych parametrów psychofizycznych kierowców (in Polish). Przegl Elektrotech. 2015;91(12):281-283. https://doi.org/10.15199/48.2015.12.72
[19] Jurecki R. Research the reaction time of young drivers in different conditions of driver work realized in a driving simulator. Logistyka. 2014;6:5003-5014.
[20] Jurecki R, Poliak M, Jaśkiewicz M. Young adult drivers: simulated behaviour in a car-following situation. Promet-Traffic Transp. 2017;29(4):381-390. https://doi.org/10.7307/ptt.v29i4.2305
[21] Jurecki RS, Jaśkiewicz M. The driving simulator as a teaching position used to improve the road safety and learning eco-driving. Gen Prof Educ. 2015;4:3-13.
[22] Liu Y, Gao J, Qin D, Zhang Y, Lei Z. Rule-corrected energy management strategy for hybrid electric vehicles based on operation-mode prediction. J Clean Prod. 2018;188:796-806. https://doi.org/10.1016/j.jclepro.2018.04.024
[23] Merkisz J, Andrzejewski M, Pielecha J. The effect of applying the eco-driving rules on the exhaust emissions. Combustion Engines. 2013;155(4):66-74.
[24] Merkisz J, Orszulak B, Andrzejewski M. The selection of a route for a vehicle simulator in terms of eco-driving. Symul Bad Rozw. 2013;4(2).
[25] Orszulak B, Merkisz J, Andrzejewski M. Evaluate the usefulness of research using a passenger vehicle simulator to verify the application of the eco-driving guidelines by drivers. Combustion Engines. 2015;54.
[26] Ravi SS, Osipov S, Turner JW. Impact of modern vehicular technologies and emission regulations on improving global air quality. Atmosphere. 2023;14(7):1164. https://doi.org/10.3390/atmos14071164
[27] Tanvir S, Chase RT, Roupahil NM. Development and analysis of eco-driving metrics for naturalistic instrumented vehicles. J Intell Transp Syst. 2021;25(3):235-248. https://doi.org/10.1080/15472450.2019.1615486
[28] Vaezipour A, Rakotonirainy A, Haworth N, Delhomme P. A simulator study of the effect of incentive on adoption and effectiveness of an in-vehicle human machine interface. Transport Res F-Traf. 2019;60:383-398. https://doi.org/10.1016/j.trf.2018.10.030
[29] Wegener M, Koch L, Eisenbarth M, Andert J. Automated eco-driving in urban scenarios using deep reinforcement learning. Transport Res C-Emer. 2021;126:102967. https://doi.org/10.1016/j.trc.2021.102967
[30] Wierzbicki S, Mikulski M, Śmieja M. Effect of CO_2 content in CNG on the combustion process in a dual-fuel compression ignition engine. Combustion Engines, 2015;54(3);91-101. https://doi.org/10.19206/CE-116869
[31] Zarkadoula M, Zoidis G, Tritopoulou E. Training urban bus drivers to promote smart driving: a note on a Greek eco-driving pilot program. Transport Res D-Tr E. 2007;12(6): 449-451. https://doi.org/10.1016/j.trd.2007.05.002
[32] Zhang L, Zhu Z, Zhang Z, Song G, Zhai Z, Yu L. An improved method for evaluating eco-driving behavior based on speed-specific vehicle-specific power distributions. Transport Res D-Tr E. 2022;113:103476. https://doi.org/10.1016/j.trd.2022.103476
[33] Ziółkowski A, Fuć P, Jagielski A, Bednarek M. Analysis of emissions and fuel consumption from forklifts by location of operation. Combustion Engines. 2022;189(2):30-35. https://doi.org/10.19206/CE-141741

Katarzyna Ślusarczyk, MEng. – Department of Automotive Engineering and Transport, Kielce University of Technology, Poland.
e-mail: *khaberka@tu.kielce.pl*

Prof. Rafał Jurecki, DSc., DEng. – Department of Automotive Engineering and Transport, Kielce University of Technology, Poland.
e-mail: *rjurecki@tu.kielce.pl*

Article citation info):
Szwajca F, Pielecha I, Mielcarzewicz D. Experimental investigation on the influence of passive/active pre-chamber injection strategy on the hydrogen knock limit. Combustion Engines. 2025;203(4):32-41. https://doi.org/10.19206/CE-207382

Filip SZWAJCA
Ireneusz PIELECHA
Dawid MIELCARZEWICZ

Combustion Engines
Polish Scientific Society of Combustion Engines

Experimental investigation on the influence of passive/active pre-chamber injection strategy on the hydrogen knock limit

ARTICLE INFO

Received: 9 May 2025
Revised: 29 May 2025
Accepted: 20 June 2025
Available online: 7 July 2025

Hydrogen combustion in an engine is related to the high speed of the process, the wide variability of the excess air ratio, and the high intensity of knock combustion. This paper presents analyses of knock combustion in a TJI engine under passive and active pre-chamber fuelling. The tests were conducted on a single-cylinder AVL 5804 test engine at n = 1500 rpm and medium load (IMEP = 3–4 bar). Attention was focused on the knock indicator – MAPO at different excess air ratio values. The possibilities of reducing this phenomenon in the TJI engine during different pre-chamber fuel injection strategies and at different excess air ratio values are presented. The probability of knock occurrence was determined cycle by cycle for several combustion cases (including a further 2 to 5 engine cycles). The paper shows that knock occurs differently in the main chamber and pre-chamber when the engine is actively or passively fed.

Key words: *hydrogen engine, TJI combustion system, active and passive pre-chamber, knock intensity*

1. Introduction

1.1. Carbon and carbon-free fuels

The search for substitutes for fossil fuels leads to a reduction in greenhouse gas emissions (mainly CO_2), while at the same time increasing the conversion efficiency of energy sources. Hydrogen as a fuel for transport is used in fuel cells (high-purity hydrogen – 99.97% according to ISO 14687:2025, ISO 19880-8:2024, and ISO 19880-9:2024) and in internal combustion engines (hydrogen with limited purity) in the form of a single-component fuel or multi-component fuel. Dual-fuel systems mainly involve the co-combustion of hydrogen with the following fuels:

– petrol, LPG, ethanol
– natural gas or in the form of HCNG (methane, H_2–CNG blend)
– diesel
– ammonia.

1.2. Turbulent Jet Ignition combustion system

An interesting way of burning hydrogen in combination with the above-mentioned fuels is to use a two-stage Turbulent Jet Ignition system. An engine equipped with such a system is characterised by having two combustion chambers. A pre-chamber and a main chamber. The prechamber usually does not exceed 5% of the volume of the main chamber [20]. Ignition takes place in the prechamber, then flames enter the main chamber through the prechamber orifices to ignite the remaining fuel-air mixture there. The TJI ignition system is divided into two types, with an active prechamber and a passive prechamber. The passive pre-chamber is filled during the compression stroke with homogeneous fuel-air mixtures available in the main chamber. The active pre-chamber system is integrated with an auxiliary fuel-metering device to accurately control the equivalence ratio of the stratified mixture [27]. The influence of the pre-chamber design (number and diameter of holes) on the combustion process was investigated by Wakasugi et al. [24]. The results of the research showed that a small number of orifices was advantageous for getting longer penetration into the main chamber. The number of orifices hardly affects the cone angle of the torch flame. The study also shows that the cone angle is consistently larger for larger orifices diameter. Excessively high jet velocity at a small-sized nozzle increases flame stretching and cooling losses at the orifice hole. The effect of pre-chamber orifices diameter on combustion parameters in a hydrogen-fuelled TJI engine was also analysed by Górzyńska et al. [6]. The research was a numerical simulation using CFD analysis of the combustion process inside the prechamber and main chamber. The study showed that increasing the diameter of the holes led to an increase in the maximum pressure in the cylinder and the rate of heat release. An important conclusion of the study is also that the maximum temperature value in the cylinder increased with the increase in the diameter of the holes. The presented properties of the TJI ignition system mean that it has the potential to be used during the combustion of dual fuels, especially in the case of an active prechamber.

1.3. Co-combustion of hydrogen with other fuels

The combustion of pure hydrogen is usually carried out using indirect injection (PFI) or direct injection (DI). An analysis of direct injection of hydrogen into an engine was presented by Liu et al. [11]. The central hydrogen injection at medium load (10 bar) and 1500 rpm without exhaust gas recirculation was used. The maximum indicated combustion efficiency was obtained at 45% with four injector orifices.

Research carried out by Gürbüz et al. [9] involved the use of a two-stage combustion system during the combustion of hydrogen with petrol. Hydrogen was injected into the intake manifold, and petrol was injected into the pre-chamber (it accounted for about 2% of the total volume). Tests were carried out with varying values of λ (0.8–1.2) at n = 2300 rpm. Increasing the excess air ratio results in an

extension of the combustion duration in the range of 0–10% mass fraction burned (MFB) with a corresponding increase in the fuel dose to the pre-chamber. Increasing the dose to the prechamber at different excess air ratios led to settling of the load at 6.3 bar. At lower values of λ a higher load was observed (about 6.6 bar), at λ = 1.2 the IMEP value equaled 5.1 bar. The unevenness of the combustion process (as determined by CoV(IMEP)) was greatest when using the passive combustion chamber and increased from 0.8% to 3.0% when increasing the excess air ratio.

The study by Shi et al. [19] was conducted on a TJI engine at a relatively high compression ratio (17.5:1), excess air ratio λ = 2.1, and n = 3000 rpm. The pre-chamber was fuelled with hydrogen, and the main chamber with gasoline. This fuel injection strategy resulted in low NO_x concentrations (approximately 20–30 ppm) being recorded at 1–2 MPa hydrogen injection pressure. This value increases with the advance of the ignition angle.

Vehicle simulation studies (AVL Cruise) performed by Rimkus et al. [17] show that a small addition of hydrogen (5%) to petrol results in a large increase in nitrogen oxides concentration (by about 20%) during the WLTC test. The addition of hydrogen also resulted in a reduction of other gaseous components: CO by 22%, CO_2 by 15% and hydrocarbons by more than 35%.

The combustion of diesel fuel with additions of hydrogen and natural gas was studied by Menaa et al. [13] in the research, a dual-fuel (diesel-natural gas) was used with various hydrogen additions (from 0 to 20% H_2). The lack of natural gas addition in the fuel resulted in a higher maximum thermal efficiency of the engine (30%) than the system with natural gas addition. In the second case, only at maximum load was greater efficiency achieved (around 32%).

Yang et al. [26] investigated the effect of varying hydrogen content in the pre-chamber, while feeding the main chamber with methane, on engine performance. Feeding the pre-chamber with hydrogen resulted in an increase in thermal efficiency of up to 46% (with a passive chamber, the result was about 45%). The use of the passive pre-chamber also resulted in an increase in nitrogen oxide emissions of approximately 70%. Fueling the pre-chamber with methane or hydrogen rapidly reduced NO_x emissions. (at λ = 2.0–2.1).

Combined combustion of hydrogen and ammonia (despite much worse thermodynamic performance) is becoming more and more important. Research by Guo et al. [8] conducted with a TJI engine involved feeding the main chamber with NH_3 + H_2 and pre-chamber with H_2 at λ = 1 (in the main chamber). With an increase in the hydrogen blending ratio from 10% to 50%, the ammonia combustion efficiency improves from 96.9% to 98.6%, accompanied by a significant reduction in the unburned ammonia emissions.

A simulation study of the combustion of hydrogen with ammonia was conducted by Zue et al. [28]. Analyses were conducted with direct mixture injection (λ = 2.0–3.0) in the range of 10–30% ammonia content. A higher value of the excess air ratio increases the combustion duration while sharply reducing IMEP. The highest thermal efficiency (47.5%) was obtained at 20% NH_3 and λ = 2.5 (increase or decrease of λ resulted in a deterioration of efficiency).

Consideration of the use of hydrogen in combination with conventional and alternative fuels shows that its high reactivity can bring benefits in terms of thermal efficiency. Hydrogen as a carbon-free fuel may also prove to be a way of reducing emissions of harmful carbon compounds such as unburned hydrocarbons, CO_2 and CO. An engine with a TJI ignition system is a promising way to use hydrogen together with previously mentioned fuels, but it is important to first investigate the effects of TJI engine operating conditions on knocking combustion during hydrogen combustion.

1.4. Knock during combustion of hydrogen

Knock combustion is assumed to be incorrect combustion of air-fuel mixture resulting in the generation of uncontrolled pressure waves acting against the main combustion source leading to a decrease in overall engine efficiency [12]. For conventional liquid fuels, an octane number is determined which indicates the resistance of the fuel to knocking combustion. The octane number scale is determined by comparing fuels with two standards, heptane, which has an octane value of 0, and iso-octane, which has an octane value of 100. In the case of liquid hydrogen, a laboratory octane number in excess of 130 has been recorded, meaning that in this form it has a high resistance to knocking. However, it is noteworthy that for the methane number used for gaseous fuels, hydrogen is used as a standard, which has a 0 on this scale, meaning that in its gaseous state of matter it is a fuel susceptible to knock combustion [23]. Hydrogen as a fuel has a wide flammability range (λ = 0.14–10), a low minimum ignition energy (0.017 mJ), and a high laminar combustion rate (2.91 m/s) [2, 4, 5]. However, the process of hydrogen combustion in an internal combustion engine generates some problems, and the main reason for that is the dual nature of hydrogen knock. It consists of two mechanisms, heavy and light knock. The first one is described as air-fuel autoignition at the end of the combustion stroke caused by high temperature and pressure in the combustion chamber. Light knock is the unstable combustion of an ignited air-fuel mixture initiated by a controlled source of combustion [12]. Investigating the range of occurrence and intensity of knocking combustion during hydrogen combustion in a TJI engine with active and passive injection modes is an important element in considering it use as a fuel.

2. Materials and methods

2.1. Test bench

The pre-chamber injection strategy was examined using a single-cylinder AVL 5804 research engine. The technical data are shown in Table 1. The engine was equipped with a pre-chamber with a volume of V_{PC} = 2.1 cm^3 and 6 orifices with a mean diameter of 1.7 mm. The engine was fed with hydrogen in two variants: with a passive pre-chamber (without fuel supply to the PC), with an active pre-chamber (with fuel supply to the PC).

The engine is equipped with an 8-channel AVL IndiSmart high-speed measurement system. The test bench includes flow meters for intake air (Sensyflow ABB), hydrogen in the main chamber (Bronkhorst 111AC-70K), and hydrogen in the pre-chamber (Bronkhorst 111B-100).

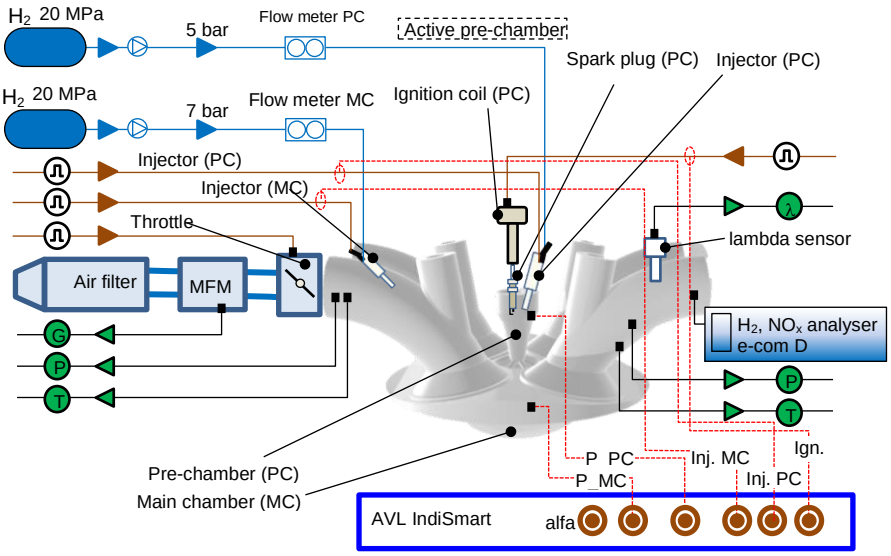

Fig. 1. Schematic diagram of the test bench for hydrogen combustion in a two-stage combustion system (with an active or passive pre-chamber)

A broadband LSU 4.9 lambda sensor was used to measure the oxygen content in the exhaust gases. Along with the LSU 4.9 sensor, an LCP80 controller, adapted for oxygen measurement during hydrogen fueling, was employed. The ECU Master EMU Black system was used to control the electronic throttle and ignition timing. Basic information on the control and measurement equipment is provided in Table 2.

Table 1. Engine specification

Engine type	AVL 5804; 4-valve; TJI, passive, active pre-chamber
Bore × stroke	85 × 90 mm
Compression ratio	14.5:1
Pre-chamber volume	2.1 cm^3
Main chamber volume	510 cm^3

Table 2. Measurement equipment used during the knock combustion experiment

Equipment	Producer, measurement range	Resolution
Air flow meter	ABB SensyFlow 0–720 kg/h	error < ±0.8%
Fuel flow meter PC	Bronkhorst 111B-100 0.16–25 ln/min	±0.1% FS
Fuel flow meter MC	Bronkhorst 111AC-70K 0.4–100 ln/min	±0.1% FS
Acquisition system	AVL IndiSmart; 8-channels	0.1 deg
Pressure sensor PC	Kistler M3.5 6081 AQ22	0–25 MPa
Pressure sensor MC	AVL GH14D	0–25 MPa
Inlet air temp.	Linuatherm Pt 100	–30–180°C
Inlet air pressure	Wika A-10	0–10 bar
Exhaust temperature	Czaki K thermocouple	0–1000°C
Exhaust pressure	Wika A-10	0–10 bar
Lambda sensor	LSU 4.9 + LCP 80 λ = 0.7 to 12.5	0.1
Injection control system	Mechatronika	0–20 ms, ±0.1 ms
Ignition control system	ECU Master EMU Black	0.5 deg
Throttle control system	Bosch ETB 32 mm 0–90 deg	1 deg

High-speed measurements were carried out during the analysis of 100 consecutive engine cycles. Measurements were taken of the combustion pressure in both engine chambers, the ignition point, fuel injection into the intake manifold, and the pre-chamber. In addition, the excess air ratio, throttle position, pressure, and temperature in the engine intake and exhaust systems were recorded.

2.2. Scope of the research

The research work aimed to analyse hydrogen combustion in an engine with a two-stage combustion system, focusing on knock combustion. For both combustion cases (passive, active), the ranges of the knock combustion defined by the MAPO coefficient were determined. The full scope of the research work is shown in Table 3.

Table 3. Scope of work on knock combustion of the TJI engine

Passive pre-chamber	
λ	1.25; 1.35; 1.50; 1.60; 2.00
CoC	var; 2 deg; each successive one was due to an increase in ignition delay
Ignition	regulated, CoC-dependent
IMEP	3.5–4.0 bar
n	1500 rpm (const)
Active prechamber	
λ	1.6; 2.0; 2.5; 3.0
CoC	2 deg; each successive one was due to an increase in Δqo_PC = 2 ms
Ignition	const
IMEP	3.5–4.0 bar
n	1500 rpm (const)
MC injection control strategy qo_MC	mode: const; mass flow: 166.7 g/h injection time: 7 ms injection pressure: 7 bar fuel dose: 3.76 mg/inj fuel dose energy: 450 j/inj
MC injection control strategies qo_PC	mode: var mass flow: 0–10 g/h injection time: 0–10 ms (Δt = 2 ms) injection pressure: 5 bar fuel dose: 0–0.23 mg/inj fuel dose energy: 0–28 J/inj

Hydrogen combustion in the passive combustion system was achieved by adjusting the ignition timing to obtain a 2-degree delay in the Center of Combustion (CoC). In this manner, measurements were taken from CoC = 2 deg to CoC = 18 deg aTDC. The excess air ratio was kept constant.

Hydrogen combustion in the active mode was carried out with a constant ignition timing and a simultaneous increase of the fuel dose to the pre-chamber. The amount of fuel dose to the main chamber was constant. Increasing the amount of fuel injected into the pre-chamber accelerated the combustion centre towards TDC, for which reason the dose was reduced at several test points. Increasing the dose to the pre-chamber resulted in a change in the magnitude of the global excess air ratio, which varies in the range where knock combustion occurs. This range of global excess ratio was also taken into account in the results of the study.

2.3. Methodology for interpreting knock combustion

MAPO (maximum amplitude of pressure oscillation) is the most commonly used evaluation indicator in knock tests [3, 10]. It indicates the intensity of the impact generated by the abnormal combustion:

$$\mathrm{MAPO} = \frac{1}{\mathrm{N}}\sum_{1}^{\mathrm{N}} \max_{\mathrm{IGN,IGN+KN}} |\tilde{\mathrm{p}}| \qquad (1)$$

where N – number of cycles, $|\tilde{\mathrm{p}}|$ – filtered cylinder pressure (explained further), IGN – ignition angle, KN – duration of knock combustion.

As MAPO increases, the tendency and intensity of knock combustion rise. There is currently no clear MAPO value that indicates knock combustion. The threshold level depends on the type of engine [3, 10]. The magnitude of the limit has been defined differently: Szwaja and Naber [22] set the value of the knock combustion border at 1 bar. The same value is used by many authors in their studies [14, 21, 25]. Aramburu et al. [1] used a knock combustion limit of MAPO = 4 bar in their study on a 6-cylinder engine with a displacement of 5883 cm^3. The same MAPO limit was used by Pla et al. [15], despite the fact that the displacement of the indirect-injection engine was only 1300 cm^3. For engines with a large displacement (5 dm^3/cyl.), the MAPO value was increased to 5 bar [7]. Otherwise, the parameter depended on the filter size. Puzinauskas [16] highlighted two ranges: 4–9 kHz, with MAPO limit = 0.15 bar, and at 4–12 kHz, with MAPO limit = 0.23 bar. Shi et al. [18] attempted to correlate MAPO with the maximum value of average luminance, achieving an R-squared fitting value of 0.67. This indicates that MAPO follows a moderate exponential relationship with the peak average flame brightness, and that greater knock resistance results in a higher peak average flame intensity brightness.

The knock combustion analysis was carried out according to the scheme shown in Fig. 2. The cylinder pressure curve recorded during the combustion process (1) was digitally filtered at 4 kHz. Then, deviations from the mean value within the 4–20 kHz range were extracted in the form of MAPOx (2). Positive and negative oscillations were presented as absolute values – PP (3). Based on this, the maximum oscillation changes – PPmx – were determined for each cycle (from the 100 cycles analyzed – (4)).

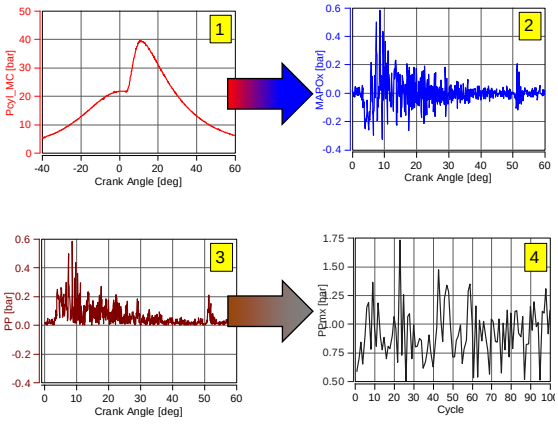

Fig. 2. Calculation process of MAPO

3. Results and discussion

3.1. Combustion with passive pre-chamber

The combustion process was analysed at different values of λ and varying CoC settings. Pressure changes in both chambers are shown in Fig. 3.

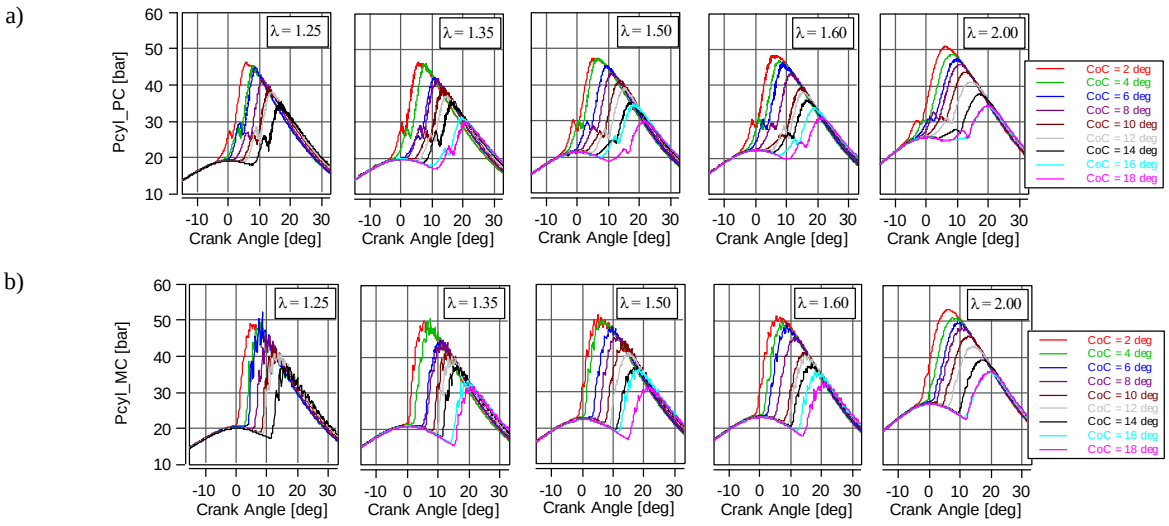

Fig. 3. Combustion pressure: a) in the pre-chamber PC; b) in the main chamber MC, at different CoC values at n = 1500 rpm; λ = 1.25, passive pre-chamber

The initiation of the combustion process in the pre-chamber (Fig. 3a) occurs near TDC. Then flames from the pre-chamber enter the main chamber, thereby igniting the fuel-air mixture. Significant pressure oscillations are observed in the main chamber, which are indicative of knock combustion (Fig. 3b). An analysis of the operating point λ = 1.25 with varying CoC is shown in Fig. 3a. The occurrence of knock combustion is visible at each CoC value. Even a significant ignition delay (CoC = 14 deg aTDC) indicates the presence of knock combustion.

3.2. Combustion with active pre-chamber

Figure 4 shows the pressure in the cylinder (main chamber) during use of the active pre-chamber with variable λ and changing fuel dose to the pre-chamber. Increasing the fuel injection to the PC (Fig. 4a) results in a reduction of λ with a simultaneous rise in combustion pressure at the PC and MC (Fig. 4b). At the same time, an enhancement of the pressure peak responsible for ignition in the prechamber is observed.

The absence of fuel injection into the pre-chamber causes combustion to deteriorate at low λ, although the process can still occur. For a lean air-fuel mixture and no injection into the pre-chamber, a lack of combustion is observed.

3.3. Knock combustion analysis during passive pre-chamber use

To obtain the MAPO magnitude (equation 1), a digital filtering process was performed on the cylinder pressure signal (at f = 4 kHz, in the angular range 0–70 deg with pressure signal resolution Δα = 0.1 deg). The results of the high-pass filter were used for further analyses.

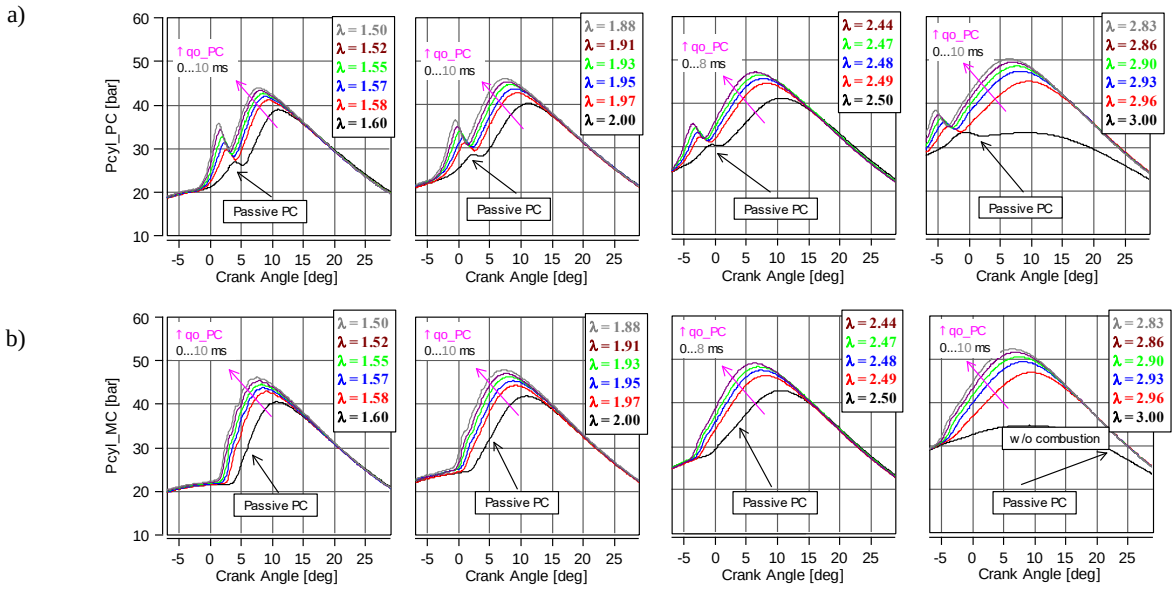

Fig. 4. Combustion pressure: a) in the pre-chamber; b) in the main chamber, at different excess air ratio values resulting from changes in the fuel dose supplied to the pre-chamber at n = 1500 rpm; active pre-chamber; each graph shows the basic excess air ratio and the adjusted excess air ratio (coloured), which change as the changes of fuel dose in pre-chamber (Δt = 2 ms)

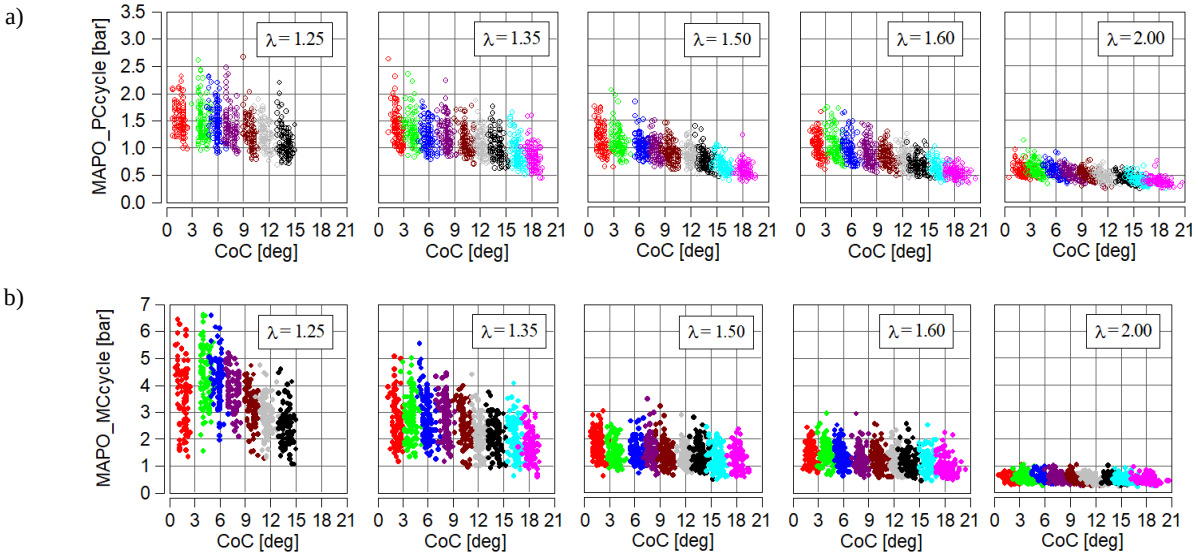

Fig. 5. Maximum MAPO value for each of the 100 cycles: a) in the pre-chamber (MAPO_PCcycle), b) in the main chamber (MAPO_MCcycle), for different CoC and various excess air ratios (passive pre-chamber)

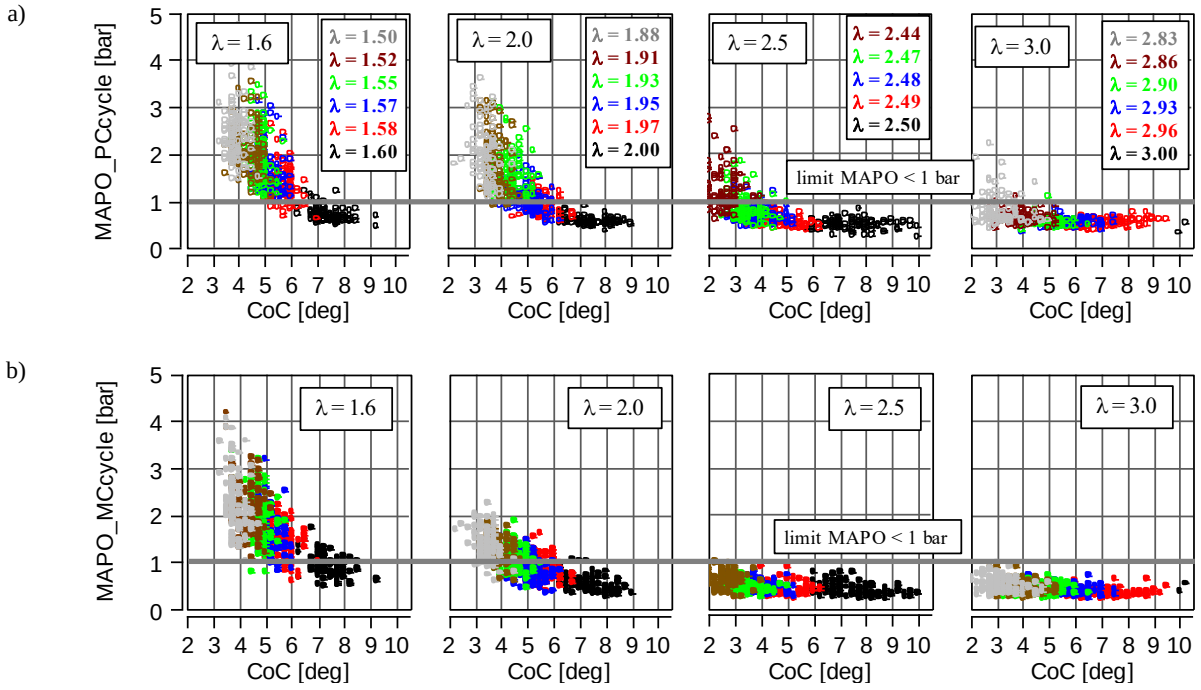

Fig. 6. Maximum MAPO value for each of the 100 cycles: a) in the pre-chamber (MAPO_PCcycle), b) in the main chamber (MAPO_MCcycle), for different CoC and various excess air ratios (active pre-chamber). Each graph shows the basic excess air ratio and the adjusted excess air ratio (colored), which change as the changes of fuel dose in the pre-chamber (Δt = 2 ms)

During the combustion pressure analysis, it was observed that MAPO reaches lower values in the pre-chamber (Fig. 5a) than in the main chamber (Fig. 5b). The study used a passive pre-chamber, so the amount of fuel was not regulated directly inside this chamber. The amount of fuel in the pre-chamber was determined only by the global value of λ obtained by injecting fuel into the intake of the engine. A reduction in pressure oscillations has been achieved in the pre-chamber compared to the main chamber. The absolute maximum values of MAPO_PC relative to MAPO_MC are more than doubled in the range of λ < 1.5. At higher values of λ these changes are smaller and at λ = 2.0 the maxima are the same.

In the following section, a full MAPO_MC analysis was carried out for each engine cycle at λ = var and CoC = var (Fig. 5a). Figure 5b shows that increasing the excess air ratio reduces knock combustion. In addition, in the range of each value of λ, increasing the CoC also limits the maximum oscillation of the combustion pressure. It is worth noting that when knock combustion occurs during hydrogen combustion, it is more effective to temporarily reduce the excess air ratio than to delay its ignition (or CoC).

As mentioned earlier, the papers [21, 22, 25] assume that the MAPO limits indicating the occurrence of knock are MAPO > 1 bar. Taking the above conclusions into account, it can be stated that in the passive pre-chamber, both normal and abnormal (knock combustion) cycles occurred under all conditions. However, it can be assumed that at λ > 1.5 and high CoC values, knock combustion in the pre-chamber is almost non-existent. For λ = 2.0, knock combustion in the pre-chamber did not occur – regardless of the CoC. Analysis of the same conditions in the main chamber (MC) indicates the absence of knock combustion only at λ = 2.0.

3.4. Knock combustion analysis during active pre-chamber use

The next step of the research was to analyse the identification and evaluation of the intensity of knock combustion in the active pre-chamber and main chamber at different engine operating parameters. Figure 6 shows the calculated MAPO values for PC and MC, respectively.

From the results, it can be concluded that the leaner the mixture is, the lower the tendency for knock combustion to occur. Furthermore, usually knock combustion is more intense in the pre-chamber than in the main chamber. This is particularly evident for λ = 2.5 and λ = 3.0. Moreover, more intensive knock combustion was recorded at lower CoC values, which means that better combustion conditions occur when an active pre-chamber with a higher dose of injected hydrogen is used. In the case of a fuel-air mixture with λ = 1.6, knock combustion occurs in most of the engine operating conditions. When CoC occurs after 7 degrees aTDC, knock combustion no longer occurs in the prechamber, while it continues to occur in the main chamber.

3.5. Average MAPO analysis with passive PC

Analysis of the global MAPO index for both combustion chambers (Fig. 7a) shows significantly higher values in the main chamber than in the pre-chamber. The highest MAPO values of 4.5 (at λ = 1.25) were recorded when CoC = 4 deg aTDC. When increasing the excess air ratio, the MAPO index obtains almost constant values with a tendency to decrease slightly with increasing CoC. When λ = 2.0, the MAPO remains constant at 0.5 bar, indicating the absence of knock combustion.

Analysis of MAPO in the pre-chamber (passive) shows much smaller variations in this indicator. The maximum

MAPO is 1.5 bar at λ = 1.25 (and then decreases to around 1.0 bar). A similar trend of decreasing MAPO is observed when increasing λ.

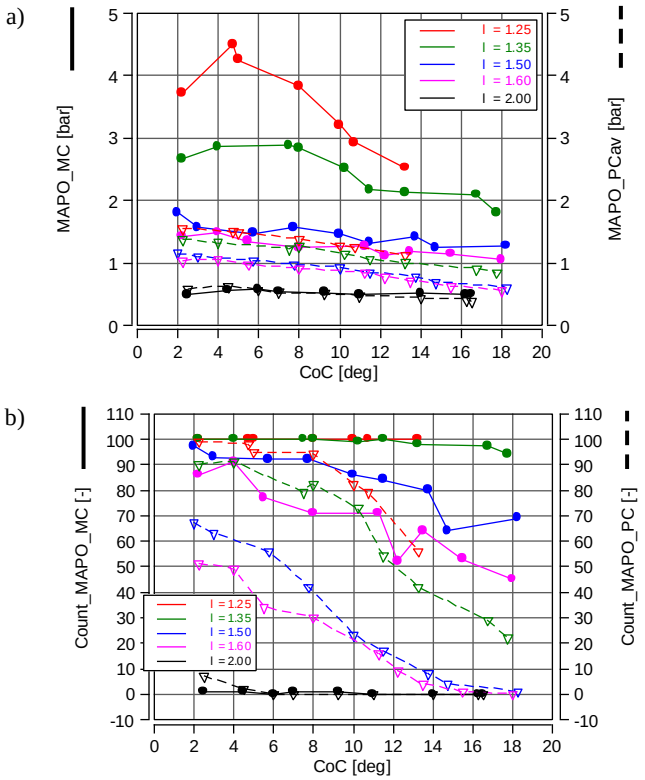

Fig. 7. Knock combustion analysis of the passive chamber: a) average MAPO_MC vs. average MAPO_PC indicators; b) knock combustion occurrence based on threshold values (referenced to 100 analyzed cycles)

Then the number of cycles during which knock combustion occurred (cycles at which MAPO > 1 bar) was counted. With 100 measuring cycles, the percentages correspond to the absolute number of cycles.

The analysis carried out with the AVL Concerto system indicates that at low excess air ratio (λ < 1.5) the number of knock cycles in the main chamber is almost 100% (Fig. 7b). While λ = 1.35 and CoC > 12 deg aTDC, the occurrence of knock decreases slightly and reaches 95%. When λ = 1.5, the highest number of knock cycles occurs at CoC = 2 deg aTDC and equals Count_MAPO_MC = 97%. When λ = 1.6 the number of knock cycles ranges from 86% (CoC = 2 deg aTDC) to 44% (at CoC = 18 deg aTDC). The minimum number of knock combustion cycles was recorded at λ = = 2.0: it is only 1% at several operating points, regardless of the CoC.

In the pre-chamber, the number of knock combustion cycles was never 100%. At λ = 1.25, the occurrence of knock combustion was 99%. When CoC occurred at 18 deg aTDC the number of knock cycles was 56%. With each higher value λ – the number of knock combustion cycles was lower. When λ = 1.5 and λ = 1.6 the number of knock combustion cycles in the pre-chamber was about 40% less than in the main chamber – and decreased with increasing CoC. When λ = 2.0 in the pre-chamber, only at CoC = 2 deg aTDC and at CoC = 4 deg aTDC, the number of knock cycles was higher than in the main chamber. For the higher CoC, there was no knock in the pre-chamber during any of the analysed engine cycles.

3.6. Average MAPO analysis with active PC

Controlling the combustion in the active pre-chamber system involved increasing the fuel dose in the PC, which had the effect of reducing CoC. This type of regulation results in an increasing MAPO in the PC and MC while limiting the CoC. For λ = 1.6 and λ = 2.0 MAPO value is well above the 1 bar (Fig. 8a). When combusting a very lean air-fuel mixture (λ = 2.5 and λ = 3.0) MAPO was limited. However, it was always higher in PC than in MC.

An analysis of the number of knock combustion cycles (Fig. 8b) shows the high occurrence of knock combustion when λ ≤ 2.0. A higher number of knock cycles was recorded under these conditions in PC than in MC. When λ = = 3.0 knock combustion is completely eliminated in MC, while it still occurs in PC (at low CoC values).

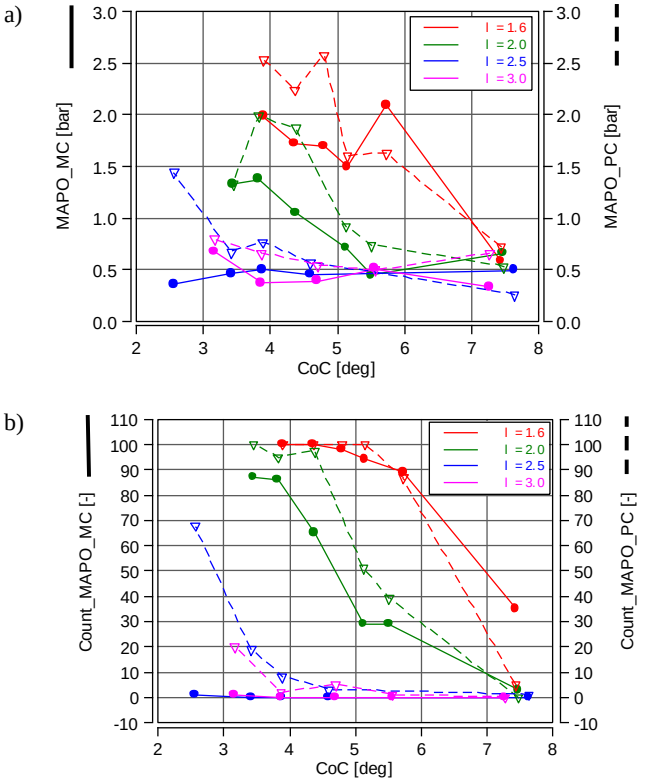

Fig. 8. Knock combustion analysis of the active chamber: a) average MAPO_MC vs. average MAPO_PC indicators; b) number of knock combustion events based on threshold values (referenced to 100 analyzed cycles)

3.7. Assessment of the probability of knock combustion occurrence

The analysis of knock combustion was presented in the previous chapter. An assessment of the occurrence of knock combustion per 100 engine cycles is also included there. The probability of knock combustion occurring cycle-by-cycle is analysed below. The following analysis covers knock combustion of two, three, four and five cycles occurring in sequence. This comparison was made for passive and active pre-chamber.

The probability of knock combustion of two cycles occurring in succession was determined as cycle-to-cycle → CTC(2). Similarly, the subsequent values of the 100-cycle combustion were determined cycle-by-cycle.

The probability of cycle-by-cycle knock combustion in the passive chamber was carried out during combustion at λ = 1.25; 1.35; 1.5 and 1.6. Cycle-by-cycle combustion at λ = 2.0 was not analysed, because the occurrence of knock in this case was very low (Fig. 7b).

An analysis of the probability of knock combustion at λ = 1.25 shows the virtually continuous occurrence of this phenomenon. The number of knock cycles in the MC was 99, so the probability of abnormal combustion is CTC(2) = = 98%. The value for five consecutive knock cycles is CTC(5) = 95%. These values barely change when delaying the occurrence of the combustion centre (Fig. 9a). Analysis of knock combustion in the pre-chamber shows slightly different figures. As the CoC increases, the number of knock combustion cycles decreases. The probability of obtaining 50% of the cycles with CTC(5) combustion does not occur at CoC = 14 deg aTDC. For the remaining (lower CTC values), knocking combustion with a probability of 50% occurs for all other CTC values.

Analysis at λ = 1.35 reveals that in the main chamber, the change in CTC value is linear (Fig. 9b). In contrast, in the pre-chamber, the CTC(3) value takes on a much lower probability than CTC(2). A linear decrease in probability is observed during CTC(4) and CTC(5).

During combustion at λ = 1.5, a linear decrease in the probability of successive knock cycles is observed with increasing CoC. A similar trend is also observed in the pre-chamber. With a CoC above 8 deg, the probability of knock combustion with a CTC(2) value reaches less than 40%.

When λ = 1.6, the analysis shows that knock combustion is significantly less probable at CTC = 2. In the pre-chamber at CTC(2), knock combustion reaches 50% (at CoC = 2 deg aTDC). With an active pre-chamber, knock combustion has the highest probability when the centre of combustion occurs earlier (Fig. 10a). In this case, it is observed that the probability of cycle-by-cycle knock combustion is higher in PC than in MC. This is caused by the fact that a small CoC is achieved by increasing the fuel dose to the pre-chamber.

Figure 10b also shows the above trend. At λ = 2.0, knock combustion in PC is much more likely than in MC. These values are independent of CoC.

At high values of λ (Fig. 10c), knock combustion occurs only in the pre-chamber. In the worst-case scenario, it has a probability of more than 60% (regardless of the following cycles. However, CTC(2) analysis shows that the probability is reduced to 40% (at CoC = 3 deg aTDC).

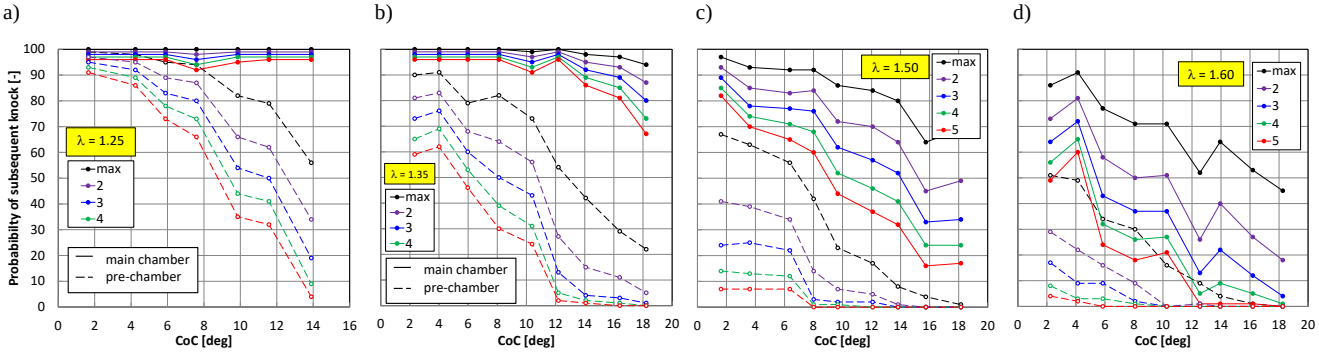

Fig. 9. Probability of two to five subsequent knock cycles at different excess air ratio values (passive pre-chamber): a) at λ = 1.25, b) at λ = 1.35, c) at λ = 1.5, d) at λ = 1.6

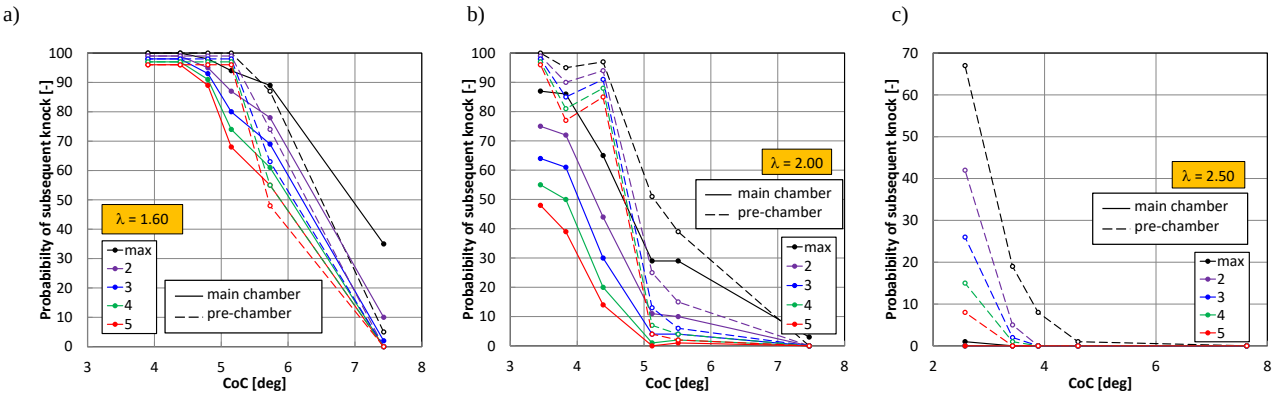

Fig. 10. Probability of two to five subsequent knock cycles at different excess air ratio values (active pre-chamber): a) at λ = 1.6, b) at λ = 2.0, c) at λ = 2.5

4. Conclusions

1. During tests with a passive pre-chamber, MAPO is more than 2 times higher in the MC chamber than in the PC. It decreases with an increase in the excess air ratio.
2. During tests with the active pre-chamber, the MAPO value reached a similar value in both chambers (for λ = = 1.6). However, for more lean air-fuel mixtures, MAPO in the PC is higher than in the MC. This situation persists until λ = 3.0, after which knock occurs only in the pre-chamber.
3. Knock combustion in the passive pre-chamber system occurs when λ reaches low values and remains high up to λ = 1.6. When λ = 2.0, knock combustion is strongly limited by the excess air ratio. A significant reduction of knock combustion is possible by delaying the combustion centre (independent of the excess air ratio).
4. Knock combustion in the active combustion chamber system occurs up to λ = 2.0; it is more frequent in PC than in MC.
5. In the passive pre-chamber system, the probability of knock combustion in 3 consecutive cycles (CTC(3)) is strongly reduced when an increase in λ and does not occur at λ > 3 and CoC > 8 deg.
6. The probability of knock combustion with an active pre-chamber is higher in the PC than in the MC. Once the CoC > 5 deg aTDC is exceeded, the probability drops rapidly to minimum values regardless of λ.

Acknowledgements

The work was supported by the 'PhDBoost' Program for doctoral students of the Doctoral School of Poznan University of Technology (in 2024) from the University's subsidy financed from the funds of Ministry of Science and Higher Education; and by statutory work: 0415/SBAD/0351 and 0415/SBAD/0353.

Nomenclature

CoC	center of combustion
CTC	cycle-to-cycle
IMEP	indicated the mean effective pressure
MAPO	maximum amplitude pressure oscillation
MC	main chamber
MFB	mass fraction burned
MFM	mass flow meter
PC	pre-chamber
TDC	top dead center
λ	air excess ratio

Bibliography

[1] Aramburu A, Guido C, Bares P, Pla B, Napolitano P, Beatrice C. Knock detection in spark ignited heavy duty engines: an application of machine learning techniques with various knock sensor locations. Measurement. 2024;224: 113860. https://doi.org/10.1016/j.measurement.2023.113860

[2] Aziz M, Wijayanta AT, Nandiyanto ABD. Ammonia as effective hydrogen storage: a review on production, storage and utilization. Energies. 2020;13(12):3062. https://doi.org/10.3390/en13123062

[3] Brecq G, Bellettre J, Tazerout M. A new indicator for knock detection in gas SI engines. Int J Therm Sci. 2003;42(5): 523-532. https://doi.org/10.1016/S1290-0729(02)00052-2

[4] Chai WS, Bao Y, Jin P, Tang G, Zhou L. A review on ammonia, ammonia-hydrogen and ammonia-methane fuels. Renew Sustain Energy Rev. 2021;147:111254. https://doi.org/10.1016/j.rser.2021.111254

[5] Dimitriou P, Javaid R. A review of ammonia as a compression ignition engine fuel. Int J Hydrog Energy. 2020;45(11): 7098-7118. https://doi.org/10.1016/j.ijhydene.2019.12.209

[6] Górzyńska M, Pielecha I. Numerical investigation of pre-chamber holes diameter geometry on combustion parameters in a hydrogen-powered Turbulent Jet Ignition engine. Combustion Engines. 2024;199(4):126-139. https://doi.org/10.19206/CE-193950

[7] Güdden A, Pischinger S, Geiger J, Heuser B, Müther M. An experimental study on methanol as a fuel in large bore high speed engine applications – port fuel injected spark ignited combustion. Fuel. 2021;303:121292. https://doi.org/10.1016/j.fuel.2021.121292

[8] Guo X, Li T, Huang S, Zhou X, Chen R, Wei W et al. Characteristics of ignition, combustion and emission formation of premixed ammonia-hydrogen blends by hydrogen-fueled pre-chamber turbulent jets. Energy. 2025; 322:135573. https://doi.org/10.1016/j.energy.2025.135573

[9] Gürbüz H, Topalci Ü, Akçay H. Experimental evaluation of the combustion process of H_2-assisted flame jet ignition conditions in a direct injection gasoline SI engine. Appl Therm Eng. 2025;270:126248. https://doi.org/10.1016/j.applthermaleng.2025.126248

[10] Ji F, Meng S, Han Z, Dong G, Reitz RD. Progress in knock combustion modeling of spark ignition engines. Appl Energy. 2025;378:124852. https://doi.org/10.1016/j.apenergy.2024.124852

[11] Liu X, Menaca R, Mohan B, Silva M, AlRamadan AS, Cenker E et al. Assessment of piston and injector cap designs on the performance of a hydrogen direct-injection spark-ignition engine. Appl Therm Eng. 2025;271:126372. https://doi.org/10.1016/j.applthermaleng.2025.126372

[12] Matla J, Kaźmierczak A, Haller P, Trocki M. Hydrogen as a fuel for spark ignition combustion engines – state of knowledge and concept. Combustion Engines. 2024;196(1): 73-79. https://doi.org/10.19206/CE-171541

[13] Menaa A, Amrouche F, Lounici MS, Loubar K. Experimental investigation of hydrogen use in dual fuel and like dual fuel mode. Fuel. 2025;393:135031. https://doi.org/10.1016/j.fuel.2025.135031

[14] Pielecha I, Szwajca F, Skobiej K. Experimental investigation on knock characteristics from pre-chamber gas engine fueled by hydrogen. Energies. 2024;17(4):937. https://doi.org/10.3390/en17040937

[15] Pla B, Bares P, Jimenez I, Guardiola C. Increasing knock detection sensitivity by combining knock sensor signal with a control oriented combustion model. Mech Syst Signal Process. 2022;168:108665. https://doi.org/10.1016/j.ymssp.2021.108665

[16] Puzinauskas PV. Examination of methods used to characterize engine knock. SAE Technical Paper. 920808. 1992. https://doi.org/10.4271/920808

[17] Rimkus A, Kozłowski E, Vipartas T, Pukalskas S, Wiśniowski P, Matijošius J. Emission characteristics of hydrogen-enriched gasoline under dynamic driving conditions. Energies. 2025;18(5):1190. https://doi.org/10.3390/en18051190
[18] Shi H, Tang Q, Uddeen K, Magnotti G, Turner J. Optical diagnostics and multi-point pressure sensing on the knocking combustion with multiple spark ignition. Combust Flame. 2022;236:111802. https://doi.org/10.1016/j.combustflame.2021.111802
[19] Shi W, Li Z, Dong W, Sun P, Yu X, Yang S et al. Effect of pre-combustion chamber hydrogen injection strategy on emissions and fuel economy of jet ignition engines under ultra lean-burn conditions. Int J Hydrog Energy. 2025;113: 147-160. https://doi.org/10.1016/j.ijhydene.2025.02.421
[20] Silva M, Liu X, Hlaing P, Sanal S, Cenker E, Chang J et al. Computational assessment of effects of throat diameter on combustion and turbulence characteristics in a pre-chamber engine. Appl Therm Eng. 2022;212:118595. https://doi.org/10.1016/j.applthermaleng.2022.118595
[21] Sun J, Zhang X, Tang Q, Wang Y, Li Y. Knock recognition of knock sensor signal based on wavelet transform and variational mode decomposition algorithm. Energy Convers Manag. 2023;287:117062. https://doi.org/10.1016/j.enconman.2023.117062
[22] Szwaja S, Naber JD. Dual nature of hydrogen combustion knock. Int J Hydrog Energy. 2013;38(28):12489-12496. https://doi.org/10.1016/j.ijhydene.2013.07.036
[23] Verhelst S, Wallner T. Hydrogen-fueled internal combustion engines. Prog Energy Combust Sci. 2009;35(6):490-527. https://doi.org/10.1016/j.pecs.2009.08.001
[24] Wakasugi T, Tsuru D, Tashima H. Influences of the pre-chamber orifices on the combustion behavior in a constant volume chamber simulating pre-chamber type medium-speed gas engines. Combust Engines. 2022; https://doi.org/10.19206/CE-148171
[25] Wang K-D, Zhang Z-F, Sun B-G, Zhang S-W, Lai F-Y, Ma N et al. Experimental investigation of the working boundary limited by abnormal combustion and the combustion characteristics of a turbocharged direct injection hydrogen engine. Energy Convers Manag. 2024;299:117861. https://doi.org/10.1016/j.enconman.2023.117861
[26] Yang X, Li G, Liang Y, Wang P, Cheng Y, Zhao Y. Effect of auxiliary hydrogen injection in the prechamber on the combustion process of a natural gas engine. ACS Omega. 2025;10(12):11935-11947. https://doi.org/10.1021/acsomega.4c08779
[27] Zhu S, Akehurst S, Lewis A, Yuan H. A review of the pre-chamber ignition system applied on future low-carbon spark ignition engines. Renew Sustain Energy Rev. 2022;154: 111872. https://doi.org/10.1016/j.rser.2021.111872
[28] Zuo Q, Yang D, Shen Z, Chen W, Lu C, Chen L et al. Effect of premixed ratio on combustion and emission characteristics in a spark ignition engine with hydrogen-ammonia direct injection. Fuel. 2025;393:135051. https://doi.org/10.1016/j.fuel.2025.135051

Filip Szwajca, DEng. – Faculty of Civil and Transport Engineering, Poznan University of Technology, Poland.
e-mail: *filip.szwajca@put.poznan.pl*

Prof. Ireneusz Pielecha, DSc., DEng. – Faculty of Civil and Transport Engineering, Poznan University of Technology, Poland.
e-mail: *ireneusz.pielecha@put.poznan.pl*

Dawid Mielcarzewicz, MEng. – Faculty of Civil and Transport Engineering, Poznan University of Technology, Poland.
e-mail:
dawid.mielcarzewicz@doctorate.put.poznan.pl

Article citation info:
Markiewicz M, Kaszkowiak J, Hujo L. The effect of ethanol in gasoline on exhaust gas components emitted by spark ignition engines. Combustion Engines. 2025;203(4):42-49. https://doi.org/10.19206/CE-206029

Marietta MARKIEWICZ
Jerzy KASZKOWIAK
Lubomir HUJO

Combustion Engines
Polish Scientific Society of Combustion Engines

The effect of ethanol in gasoline on exhaust gas components emitted by spark ignition engines

ARTICLE INFO

Received: 25 April 2025
Revised: 27 May 2025
Accepted: 7 June 2025
Available online: 5 August 2025

Fuels of natural origin are the most frequently used source of power for spark ignition engines. Their exhaustibility causes the search for alternative sources, which are plant-derived fuels. The paper presents tests of the amount of exhaust gas components in a spark ignition engine powered by mixtures of gasoline and ethyl alcohol. Pure ethanol and gasoline without biocomponent additives were used as research material. The experiments were performed using an exhaust gas analyzer and a particle analyzer during tests on a chassis dynamometer. The drive unit used for the tests was powered by mixtures with various ethanol content, from 10% to 100%. The analysis of the conducted tests showed a reduction in the amount of the formation of exhaust gas components hazardous to the natural environment.

Key words: *petrol engine, biofuels, engine, environmental protection, noise emission*

1. Introduction

The most commonly used source of power for spark ignition engines are fuels of natural origin. Exhaustibility of these fuels makes it necessary to seek new solutions, such as alternative fuels. Emission of exhaust gas components and soot particles to the natural environment is another important argument in favor of alternative fuel application. The kind of fuel mixture to be used depends on the design of the drive unit. The fuel which is most frequently used for spark ignition engines is ethanol. Application of biofuels in drive units is one of the methods to reduce greenhouse gas emission. This is set out in Directive 2009/28/WE of the EU Parliament and of the Council of 23 April 2009 on the promotion and application of energy from renewable sources. Ecological aspects connected with the application of fuels from different renewable sources are very important for the sustainable development of transport [7, 27]. Constantly growing transport increases the demand for energy, which subsequently leads to an increase in fuel consumption by 3% annually [37]. This, in turn, causes pollution of the natural environment by emission of exhaust gas components such as carbon dioxide, carbon monoxide, hydrocarbons, nitrogen oxides, and solid particles.

Despite the benefits of using ethanol as a fuel additive, its use is also associated with a number of potential risks to the durability and reliability of fuel systems and engine lubrication. Ethanol has hygroscopic properties, meaning it has the ability to absorb moisture from the environment. The presence of water in the fuel system can lead to phase separation in the fuel mixture, corrosion of metal components, and problems with engine starting. Furthermore, ethanol may have a harmful effect on plastics and elastomers commonly used in vehicle fuel systems, such as seals, fuel lines, and membranes. These materials may swell, harden, become brittle, or even cause the fuel system to leak. Additionally, the use of ethanol-gasoline blends can lead to increased dilution of lubricating oil in the engine's crankcase. Fuel entering the oil reduces its viscosity and lubricating properties, leading to faster oil degradation and the need for more frequent oil changes. In extreme cases, this can result in reduced engine durability and increased wear of its components [5, 10, 12, 25, 36].

The most popular blend of ethanol and gasoline is E85 bioethanol, containing 85% ethanol and 15% unleaded gasoline [30, 32, 33]. The components of the above-mentioned blend need to comply with current norms. In the case of ethanol, it is EN 15376 norm, and for unleaded gasoline, EN 228 norm. An important reference when discussing the impact of ethanol in fuels on the operation of internal combustion engines, including exhaust emissions, is the document "Ethanol Guidelines" developed by the Worldwide Fuel Charter Committee. This document provides recommendations regarding the quality of ethanol as a fuel additive (e.g., water, sulfur, metal, and contaminant content), insights into the effects of ethanol on exhaust emissions and engine performance (such as knock resistance and cold start behavior), the durability of materials in the fuel system (e.g., corrosion, elastomer swelling), as well as potential technical issues related to engine fueling [33]. E85 is recommended for flexible fuel vehicle FFV engines whose design is adjusted to this kind of fuelling. Bioethanol E85 is a collarless liquid obtained from the fermentation of plants such as corn, sugar cane, or sugar beets [3, 16, 22, 30, 42]. The most popular plants used for the production of bioethanol in Europe are corn products and sugar beets. As a result of their fermentation, a water solution of ethanol (about 15%) and other alcohols is obtained. Pure ethanol comes from a distillation process whose outcome is a rectified spirit containing 96% ethanol and 4% water [15]. Ethanol for industrial purposes is obtained from synthesis gas as a result of direct synthesis. The substance is a chemically clean ethanol. Results of tests of bioethanol provided by the literature indicate that, compared to gasoline, it is characterized by [2, 17, 29]:

- lower calorific value
- lower need for air during fuel combustion
- higher octane number

Table 1. Selected properties of the fuel blends [12, 40]

Properties	Gasoline	Mixture of 85% ethanol and 15% unleaded gasoline	Ethanol
Density	720–775 km/m^3	785 km/m^3	794 km/m^3
Calorific value	42.3–43.5 MJ/kg	29 MJ/kg	26.8 MJ/kg
Test octane number	95	105	120–135
Motor octane number	85	90	100–106
Air excess coefficient	14.7–14.7	9.7	3.5–17
Vaporation heat	350 kJ/kg	780 kJ/kg	855–870 kJ/kg

– lower ignition energy
– higher susceptibility to corrosion and melting of the engine rubber elements.

The properties of fuel blends determine their suitability to be used as a power source for the drive unit. They are also determinants of optimization for the exhaust gas components, the engine performance and its functional qualities. The fuel is supposed to provide an engine with proper efficiency and performance parameters as well as compliance with emissivity norms in its life cycle. Although the basic fuel for a spark engine has always been gasoline, the environment-friendly approach involves the need to search for alternative fuel sources, for instance, such as ethanol or a mixture of 85% ethanol and 15% unleaded gasoline [13, 22, 35, 41]. The most significant differences between these mixtures are presented in Table 1.

Literature provides results of tests conducted for drive units fueled with gasoline and ethanol blends [9, 20, 21, 23, 26, 32]. Authors of numerous publications claim that because of the design, only mixtures with 10% of ethanol are suitable for spark ignition engines. In order to reduce the risk of damage to the drive unit, it is necessary to modify the computer control system. Modifications of the engine computer control systems are supposed to adjust the engine to a given fuel mixture, and they are applied to the fuel injection system by changing the intake valve opening timing [8, 11, 14]. Tests of drive units fueled with E85 mixtures indicate problems with the engine startup in low temperatures. Literature provides results of tests of the exhaust gas components, which were conducted in real road conditions [4, 7, 8, 31]. Test results concerning vehicles powered with gasoline and ethanol blends show a reduction in emission of the exhaust gas components, including: carbon dioxide, carbon monoxide, nitrogen oxides, and hydrocarbons. Moreover, the tests indicate an increase in the fuel consumption by app. 30% [1, 24, 26, 41].

The idea of using alternative fuels was imposed by pro-ecological strategies introduced by the European Union. The European Parliament and Council directive number 2018/8421 imposes a requirement to comply with the norms regarding exhaust gas emission from transport by the member states. The major goal set out in the directive is to reduce greenhouse gas emission by 40% up to 2030 in reference to 2005. Currently, there are exhaust emission norms that need to be complied with in the territory of the European Union. Recently, a new exhaust emission norm – Euro 6D ISC FCM has been introduced. Each successively introduced exhaust gas emission norm reduces nitrogen oxides and carbon dioxide emissions to the environment by motor vehicles. The current norm allows a spark ignition engine vehicle to emit 60 mg NO_x per kilometer. Whereas, in the case of carbon dioxide emission, the regulations provide for its reduction down to 95 g/km. The European Union legislation on harmful exhaust gas component reduction are being constantly modified. The European Commission announced the introduction of the next Euro 7 norm that would rigorously reduce the emission of carbon monoxide, nitrogen oxides, and solid particles. The norm is also supposed to impose strict requirements for vehicles to be equipped with filters and catalyzers. The changes to be introduced are supposed to reduce the negative impact of transport on the natural environment, which involves taking actions to promote the application of ecological transport forms. [5, 6, 19, 24, 34].

The introduction of exhaust emission standards and the requirement to reduce the emission of harmful substances released from spark-ignition engines during combustion necessitate the design and implementation of new fueling solutions for power units. Regulations introduced by the European Union and its member states are intended to ensure sustainable development in transportation. Research findings reported in the literature indicate a reduction in exhaust gas components and particulate matter emissions from engines fueled with gasoline-ethanol blends [1, 4, 8, 9, 11, 14, 18, 20–23, 26, 28, 31, 32, 37]. The studies were conducted for various computer-controlled engine management systems, aiming to improve engine performance and reduce its environmental impact. Researchers are seeking solutions that would enable the achievement of goals outlined in the European Union's sustainable transport development documents while maintaining high vehicle performance parameters. The use of ethanol as a bio-component in small amounts (up to 10%) has little effect on exhaust composition and does not require engine recalibration. However, for ethanol content above 10%, engine adjustments, particularly of fuel dosage, are recommended due to the adverse effects of an overly lean air-fuel mixture, which can lead, among other things, to an increase in hydrocarbon content in the fuel [38, 39, 43].

This study aims to verify the exhaust gas components emitted to the natural environment by a spark ignition engine fueled with different blends of gasoline and ethanol, and for different adjustments of the engine computer control system.

2. Materials and methods

The conditions of the tests were similar to real road traffic. The tests were carried out for a spark ignition engine with a multipoint ignition fueled with a blend of gasoline and ethanol.

The material used in the tests was ethyl alcohol and unleaded gasoline. The gasoline used in the tests had no bio-

component additives. Proportions of the blends are presented in Table 2.

Table 2. Proportions of mixtures used in tests

No.	Mixture composition	Denotation
1	100% unleaded gasoline	PB100
2	90% gasoline 10% ethanol	BIO10
3	70% gasoline 30% ethanol	BIO30
4	50% gasoline 50% ethanol	BIO50

The material used in the tests was unleaded gasoline and dehydrated ethyl alcohol with maximum 1% water content which is obtained from a biomass. A sample blend is shown in Fig. 1. The properties of the individual tested blends are presented in Table 3.

Fig. 1. Fuel blend used in tests

Table 3. Selected properties of the tested fuel mixtures

Properties	PB100	BIO10	BIO30	BIO50
Density	0.72–0.77 g/cm³	0.81 g/cm³	0.85 g/cm³	0.72 g/cm³
Calorific value	42.3–43.5 MJ/kg	40–42 MJ/kg	36 MJ/kg	34 MJ/kg
Test octane number	95	96	99	99.5
Air excess coefficient	14.7–14.7	13.2	12.2	10.6
Vaporation heat	350–400 kJ /kg	350–400 kJ/kg	350–400 kJ/kg	350–400 kJ/kg

The research object was a vehicle powered with 8 valve engine with spark ignition and multipoint injection, whose cylinder capacity was 1242 cm^3, power 44 kW, and maximum torque 102 Nm. It was a drive unit that met the Euro 4 standard. The tested drive unit is presented in Fig. 2. It was chosen due to its widespread use in motor vehicles (numerous cars make are equipped with this type of drive unit). The unit selected for testing was not equipped with an exhaust gas cleaning system; the authors wanted to obtain the most reliable engine emissions results possible.

The tests were carried out with the use of a gasoline and ethyl alcohol blend. The research subject was to analyze the effect of ethanol content change on the values of exhaust gas components emitted to the natural environment by the drive unit. Technical specifications of the engine are presented in Table 4.

Fig. 2. Drive unit used in the tests

The tests were carried out with the use of a gasoline and ethyl alcohol blend. The research subject was to analyze the effect of ethanol content change on the values of exhaust gas components emitted to the natural environment by the drive unit.

Table 4. Specifications of the investigated engine

Engine type	Inline, Spark ignition
Engine capacity	1242 cm^3
Number of cylinders	4
Number of cylinder valves	2
Timing system	OHV
Engine power	44 kW
Torque	102 Nm for 2500 rpm
Engine placement	Diagonally in the vehicle front
Compression ratio	9.8
Type of fueling system	Multipoint injection

Prior to the experiment, the engine oil, oil filter, air filters, and fuel were changed in the drive unit. The supply system was adjusted so as to allow a noninvasive fuel change. Those adjustments were applied to the fuel supply system. An additional fuel tank was connected. A special 5 dm^3 tank was used. The fuel excess returned to the external fuel tank through a special return pipe. After each fuel change, the engine worked for about 10 minutes in order to remove the remaining fuel from the fuel filter and the supply system. Prior to measurements, the engine had been heated up until the temperature of the liquid coolant reached 75°C. The ambient temperature was 15°C and the pressure was 1004 hPa.

The experiment was supposed to determine the amount of exhaust gases generated by a spark injection engine fueled with a mixture of gasoline and ethyl alcohol in different proportions. The tests were carried out on a chassis dynamometer with an eddy current brake, under conditions reproducing real traffic. Required loads were applied to the vehicle. Exhaust gas and solid particle analyzers were connected to the vehicle to determine the content of exhaust components that were emitted to the environment. Measurements of the exhaust component concentration were carried out by an exhaust gas analyzer to define the amount of exhaust gas components discharged to the environment

in the form of gases. The goal was to determine the values of such compounds as: hydrocarbons (HC), oxygen (O_2), carbon dioxide (CO_2), and carbon monoxide (CO). From the perspective of emissions from spark-ignition engines, nitrogen oxides and nitrogen dioxide are also important components; however, these are the subject of discussion in a separate study. A solid particle analyzer using an optical method was applied to measure particles larger than 100 mm. During its operation, an engine produces particles of carbon and absorbs smaller ones, i.e., soot. The distribution of solid particle dimensions, that is, their number, was determined using an electronic particle counter. All the measurements were performed for a spark ignition engine under the conditions of maximal loads.

The tests were carried out on a single-axle chassis dynamometer equipped with a DynoTech DS04 2WD eddy current brake. The support roller diameter was 323.9 mm, and the dynamometer was electronically controlled. During the measurements, the room temperature was 15°C, with fluctuations of less than 1°C. Atmospheric pressure remained at 1000.4 hPa, with variations of less than 5 hPa throughout the testing period. Measurements were conducted until the tested parameters stabilized.

3. Results

3.1. Statistical analysis

The results obtained from the tests were statistically analyzed and verified for their significance from the point of view of the drive unit functioning.

The test results were statistically analyzed (variance analysis) by means of the Statistica program, with the use of the Tukey test. The content of solid particles in the exhaust gases decreased along with an increase in ethanol to reach a minimum of 30% ethanol content. An increase in the solid particle content was found for an increase in ethanol up to 50%. Differences in the amount of solid particles were statistically significant for all ethanol content levels in the fuel. Such changes of the solid particle amount is probably the effect of lean mixture for higher content of ethanol (the demand for oxygen drops). A drop in the content of solid particles would probably be maintained for an increasing content of ethanol in fuel. The curve of solid particle amount change is presented in Fig. 3.

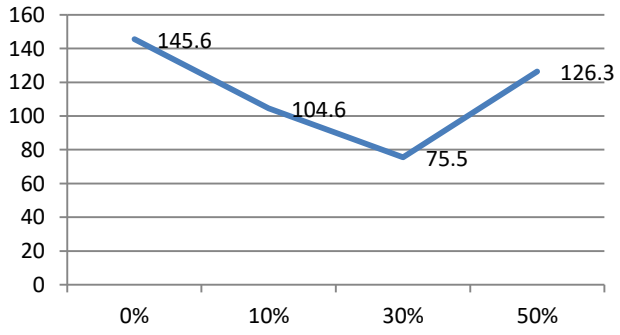

Fig. 3. Amount of solid particles depending on ethanol content in fuel

The content of carbon monoxide was decreasing along with an increase in the content of ethanol in fuel. For 30% and 50% of ethanol content, the differences were found statistically insignificant. This indicates more complete fuel combustion for an increasing content of ethanol. The value changes of carbon monoxide content in exhaust gases is presented in Fig. 4.

CO_2 content in exhaust gases slightly decreased with the increasing ethanol content. Differences occurred only when the level of ethanol content reached 50%. A drop in the percentage share of carbon dioxide in the exhaust gases is probably the effect of air excess in the fuel air mixture (engine setting correction needed). The content of carbon dioxide in exhaust gases is presented in Fig. 5.

The content of oxygen increased with an increase in ethanol content in the fuel. The value differences were statistically significant for all ethanol content levels in the fuel. This is due to a smaller demand for oxygen during combustion of ethanol than combustion of gasoline. The value change curve for oxygen content in exhaust gases is presented in Fig. 6.

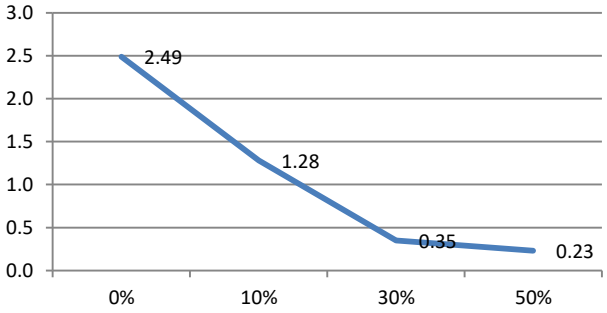

Fig. 4. Dependence of carbon monoxide content change in exhaust gases on the ethanol content in fuel

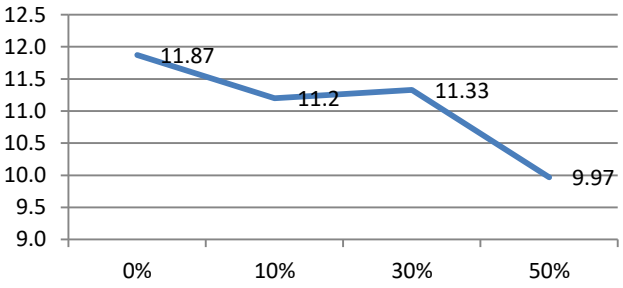

Fig. 5. CO_2 content in exhaust gases depending on the content of ethanol in fuel

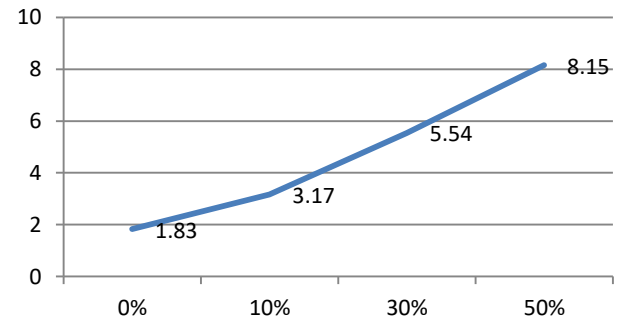

Fig. 6. Value change curve for oxygen content in exhaust gases

The content of hydrocarbons in the fuel changed with the increasing content of ethanol. For fuel without ethanol, the amount of hydrocarbons was 331 ppm. on average, and it decreased down to 254.8 ppm for 10% of ethanol content (statistically significant difference). Next, it increased for ethanol content up to 332.6 ppm averagely and differed significantly statistically from the amount of hydrocarbons in the fuel with no ethanol additive. For 50% of ethanol content, a statistically significant drop in the amount of solid particles was found, though with a value lowest within the analyzed range. The value change curve for hydrocarbon content in exhaust gases is presented in Fig. 7.

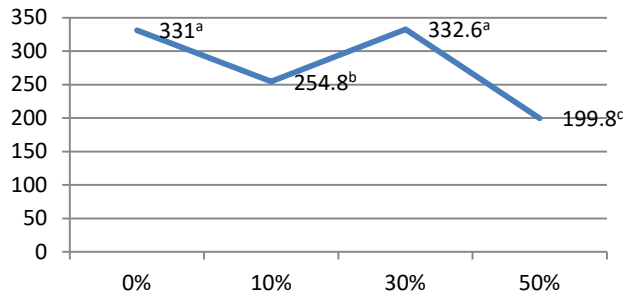

Fig. 7. Value change curve for hydrocarbon content in exhaust gases depending on the ethanol content

3.2. Assessment model for the drive unit quality of functioning

In this study, parameters were identified (concentrations of the exhaust components), to be later evaluated for their impact on the research object functioning quality. In the developed model, X stands for one-dimensional vectors which were accepted to be random variables. The analyzed parameters represent performance of spark ignition engines fueled with gasoline and ethanol blends. Then, the vector assumes the following form:

$$X_i = < X_1, X_2, X_3, X_4, X_5 > \quad (1)$$

where the form vector components are: X_1 – solid particles contained in exhaust gases, X_2 – carbon monoxide, X_3 – carbon dioxide, X_4 – oxygen, X_5 – hydrocarbons.

For the research object used, the random variable is in the form:

$$Z_x = \sum_{i=1}^{p} \alpha_i X_i \quad (2)$$

where: $\boldsymbol{\alpha_i \geq 0, \sum_{i=1}^{p} \alpha_i = 1}$, α_i, i = 1,2,…, p – stand for the values of weights for particular parameters, Z_X – is a random variable, being a finite mixture of variables: X_i, i = 1,2,…,p.

MOA (multi criteria optimizations analysis) was used for the above case. AHP method (Analytic Hierarchy Process) was used for determination of heights for particular parameters. In order to perform measurements of uncountable criteria, the assessment was rendered in a numerical form, according to an accepted grading scale that is presented in Table 5.

Based on the prepared grading scale, a reversed comparison in pairs was made. The grades were presented in the form of a square matrix. First, a matrix was built to define the significance degree for the criteria in reference to the assumed goal, in the following form:

Table 5. Grading scale accepted for the analysis

Grade	Definition	Explanation
1	Equal significance	The effect of compared parameters is the same
3	Slight dominance	One parameter is slightly more important than the other
5	Significant dominance	Significant dominance of one parameter over the other
7	Large dominance	Distinct dominance of one parameter over the other
9	Absolute dominance	Dominance of one parameter over the other is of absolute character
2,4,6,8	Intermediate values	If a compromise between two adjacent grades is needed

$$q = \begin{bmatrix} 1 & q_{1,2} & \dots & q_{1,n} \\ \frac{1}{q_{1,2}} & 1 & \dots & q_{2,n} \\ \vdots & 0 & 1 & \vdots \\ \frac{1}{q_{1,n}} & \frac{1}{q_{2,n}} & \dots & 1 \end{bmatrix} \quad (3)$$

Next, a matrix was created to indicate the significance degree of the accepted decision variants in reference to each subcriterion from the directly higher level, defined as a matrix of normalized grades in the form:

$$q = \begin{bmatrix} 1 & \frac{q_{1,2}}{\sum_{i=1}^{n} q_{i,2}} & \dots & \frac{q_{1,n}}{\sum_{i=1}^{n} q_{i,n}} \\ \frac{q_{2,1}}{\sum_{i=1}^{n} q_{i,2}} & 1 & \dots & \frac{q_{2,n}}{\sum_{i=1}^{n} q_{i,n}} \\ \vdots & 0 & 1 & \vdots \\ \frac{q_{n,1}}{\sum_{i=1}^{n} q_{i,2}} & \frac{q_{n,2}}{\sum_{i=1}^{n} q_{i,2}} & \dots & 1 \end{bmatrix} \quad \mathbf{(4)}$$

Then, a mean value of the priority vectors was calculated for an element of each matrix verse of normalized grades which determined the relative weight (significance). The sum of priorities was equal to 1. Next, measures of the comparison consistence and the value of eigen vector were calculated, and the inconsistence index and coefficient were constructed. The sum of partial priorities for a given decision variant was determined to be its global priority, which means that the variant with the highest priority is considered to be the best. The share of priorities of a given variant in the main goal through implementation of the analysed parameters is presented in Table 6.

Table 6. Determination of significance (weights) for the analyzed parameters

Denotation	Explanation	Weight
α_1	exhaust gas solid particles	0.215
α_2	carbon monoxide	0.143
α_3	carbon dioxide	0.558
α_4	oxygen	0.046
α_5	hydrocarbons	0.038

Tests of the drive unit were carried out in 24 hour time intervals, ten repetitions for each parameter. Based on the tests, the values of each parameter were determined for each time interval, The values determined for the considered parameters were recoded so that the minimal value would reflect the worst level, whereas the maximal value would represent the most desired one. For transparency and

unambiguity of the results, the values on the analyzed set were normalized onto interval <0–10>, using the following dependency:

$$10 \times \frac{(X_i - X_{min})}{(X_{max} - X_{min})} \quad (5)$$

The results were used to determine mean values and variability intervals (minimal and maximal values) from the time intervals for particular measurement groups. The test results for further analyses of each fuel blend are presented in Table 7.

Table 7. The values of the considered parameter set for he analyzed fuel mixtures

Parameter	Mean value	Maximal value	Minimal value
Unleaded gasoline			
Solid particles	145.6	152.0	139.0
Carbon monoxide	2.49	4.71	0.02
Carbon dioxide	11.87	12.90	9.10
oxygen	1.83	5.26	0.20
hydrocarbons	331	464	216
90% unleaded gasoline and 10% ethanol			
Solid particles	104.6	107.0	10.0
Carbon monoxide	1.28	4.04	0.15
Carbon dioxide	11.2	13.6	9.4
oxygen	3.17	6.81	0.43
hydrocarbons	25.8	292.0	209.0
70% unleaded gasoline and 30% ethanol			
Solid particles	75.5	91.0	69.0
Carbon monoxide	0.35	0.44	0.13
Carbon dioxide	11.33	13.90	8.80
oxygen	5.54	9.01	3.30
hydrocarbons	332.6	577.0	194.0
50% unleaded gasoline and 50% ethanol			
Solid particles	126.3	150.0	103.0
Carbon monoxide	0.23	0.99	0.06
Carbon dioxide	9.97	13.00	5.90
oxygen	8.15	11.48	4.18
hydrocarbons	199.8	287.0	110.0

The test results were normalized based on the data included in Table 7, according to dependency 5. The vector components obtained for particular blends from the parameter normalized results are presented in Table 8.

Table 8. Normalized results for particular components of the form vector

Parameters	Fuel blends			
	PB100	BIO10	BIO30	BIO50
Solid particles	5.0769	5.2000	2.9545	4.9574
Carbon monoxide	6.1407	3.1619	7.0968	1.8279
Carbon dioxide	7.2895	4.2857	4.9608	5.7324
Oxygen	3.2213	4.2947	3.9229	5.4384
Hydrocarbons	4.6371	5.5181	3.4621	5.0734

Determination of the vector components enabled to provide a geometric interpretation of the drive unit parameter mean value for blends of gasoline and ethanol. In this case, it was unleaded gasoline with no ethanol additive that was accepted to be the reference point. A comparison of gasoline and ethanol blends with the reference point is presented in Fig. 8. The vector components were marked as X with indexes defining the parameter number. In the case of the compared blends, the vector components were also marked as X with their indexes denoting a given fuel blend, in the following order: X_{A1}–A_5 for BIO10 blend, X_{B1}–B_5 for BIO30 blend, X_{C1}–C_5 for BIO50 blend.

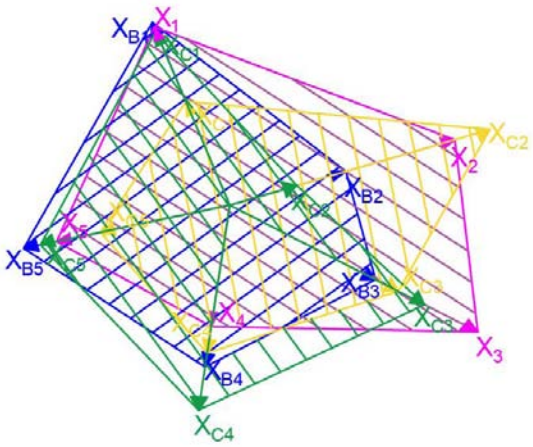

Fig. 8. Comparison of vector components for blends of gasoline and ethanol with the reference point

A random variable was defined for the tested drive unit on the basis of the vector components determined for each fuel blend, in the following form:

$$Z_x = \alpha_1 X_1 + \alpha_2 X_2 + \alpha_3 X_3 + \alpha_4 X_4 + \alpha_5 X_5 \quad (6)$$

The values of a random variable defined for the fuel blends are presented in Fig. 9.

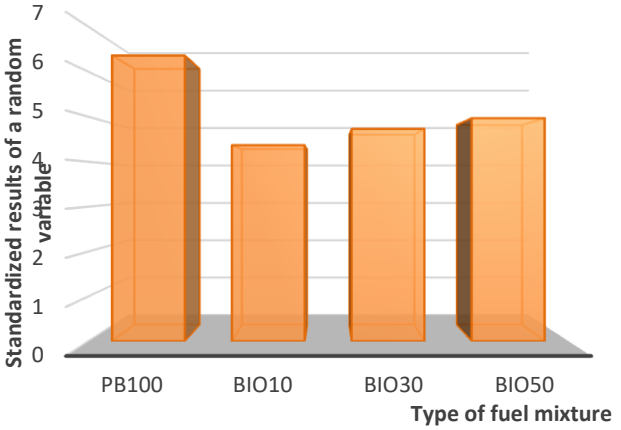

Fig. 9. Standardized random variables defined for the tested fuel blends

A graphic interpretation of a random variable, determined for the analyzed fuel blends, allows to perform a complete analysis of each vector component, consistently with significance defined on the basis of the accepted weights. The diagram presented in Fig. 4 shows that BIO10 blend achieved the lowest results, compared to the reference point, whereas BIO50 blend the highest. It means that application of ethanol in gasoline has a positive effect on the drive unit exhaust gas emission reduction.

5. Conclusions

Based on the tests, it can be said that an additive of ethanol to gasoline does have an impact on the exhaust com-

ponents emitted by the considered spark ignition engine. An analysis of the component values shows that the best blend is that of 70% gasoline and 30% ethanol. According to the analysis, the composition of the blend has the largest impact on the carbon dioxide criterion, whereas the lowest on hydrocarbons. Value changes of the analyzed parameters are presented in the form of vectors which allows their simultaneous analysis. Application of ethanol additive to gasoline reduced the drive unit emission of exhaust gases into the environment. The test results confirm advisability of using alternative fuel for powering drive units of spark ignition engines. From the point of view of natural resources exhaustibility, the use of alternative solutions for fueling spark ignition engines is a good solution. Blends of gasoline with ethanol exhibit similar or better characteristics as compared to pure gasoline which fully justifies their application. The results obtained from the conducted tests indicate the advisability of using ethanol as a bio-component in fuel, both due to its renewable nature and its positive impact on the exhaust composition of spark-ignition engines.

Nomenclature

AHP	analytic hierarchy process	HC	hydrocarbons
CO	carbon monoxide	MOA	multi criteria optimizations analysis
CO_2	carbon dioxide	O_2	oxygen

Bibliography

[1] Almaid L, Sales L, Sodre J. Fuel consumption and emissions from a vehicle operating with ethanol, gasoline and hydrogen produced on board. Int J Hydrogen Energ. 2015; 40(21):6988-6994. https://doi.org/10.1016/j.ijhydene.2015.03.167

[2] Baena L, Gomez M, Calderon J. Aggressiveness of a 20% bioethanol–80% gasoline mixture on autoparts: I behavior of metallic materials and evaluation of their electrochemical properties. Fuel. 2012;95:320-328. https://doi.org/10.1016/j.fuel.2011.12.002

[3] Balat M, Balat H, Cahide O. Progress in bioethanol processing. Prog Energ Combust. 2008;34(5):551-573. https://doi.org/10.1016/j.pecs.2007.11.001

[4] Balki M, Sayin C, Canakci M. The effect of different alcohol fuels on the performance, emission and combustion characteristics of a gasoline engine. Fuel. 2014;115:901-906. https://doi.org/10.1016/j.fuel.2012.09.020

[5] Bielaczyc P, Klimkiewicz D, Szczotka A, Woodburn J. A comparison of the exhaust emission of a vehicle fuelled with different ethanol-petrol blends. Combustion Engines. 2012; 149(2):57-65. https://doi.org/10.19206/CE-117041

[6] Costa R, Filho F, Moreira T, Baeta J, Guzzo M, Souza J. Exploring the lean limit operation and fuel consumption improvement of a homogeneous charge prechamber torch ignition system in an SI engine fueled with a gasoline-bioethanol blend. Energy. 2020;197:114-123. https://doi.org/10.1016/j.energy.2020.117300

[7] Costa R, Sodre J. Hydrous ethanol vs. gasoline-ethanol blend: Engine performance and emissions. Fuel. 2010;89(2): 287-293. https://doi.org/10.1016/j.fuel.2009.06.017

[8] Costagliola M, Iannaccone S, Prati M. Combustion efficiency and engine out emissions of a S.I. engine fueled with alcohol/gasoline blends. Appl Energ. 2013;111:1162-1171. https://doi.org/10.1016/j.apenergy.2012.09.042

[9] Deng X, Chen Z, Wang X, Zhen H, Xie R. Exhaust noise, performance and emission characteristics of spark ignition engine fuelled with pure gasoline and hydrous ethanol gasoline blends. Case Studies in Thermal Engineering. 2018;12: 55-63. https://doi.org/10.1016/j.csite.2018.02.004

[10] Dhaliwal JS, Negi MS, Kapur GS, Kant S. Compatibility studies on elastomers and polymers with ethanol blended gasoline. Journal of Fuels. 2014:1-8. https://doi.org/10.1155/2014/429608

[11] Duc K, Duy V, Dinh L, Viet T, Anh T. Performance and emission characteristics of a port fuel injected, spark ignition engine fueled by compressed natural gas. Sustainable Energy Technologies and Assessments. 2019;31:383-389. https://doi.org/10.1016/j.seta.2018.12.018

[12] Elfasakhany A. Engine performance evaluation and pollutant emissions analysis using ternary bioethanol–isobutanol–gasoline blends in gasoline engines. J Clean Prod. 2016;139:1057-1067. https://doi.org/10.1016/j.jclepro.2016.09.016

[13] Elfasakhany A. Investigations on the effects of ethanol–methanol–gasoline blends in a spark ignition engine: Performance and emissions analysis. Engineering Science and Technology, an International Journal. 2015;18(4):713-719. https://doi.org/10.1016/j.jestch.2015.05.003

[14] Fernandez J, Arnal J, Gomez J, Lacelle N, Dorado M. Performance tests of a diesel engine fueled with pentanol/diesel fuel blends. Fuel. 2013;107:866-872. https://doi.org/10.1016/j.fuel.2013.01.066

[15] Galadima A, Muraza O. Catalytic upgrading of bioethanol to fuel grade biobutanol: a review. Ind Eng Chem Res. 2015; 54(29):7181-7194. https://doi.org/10.1021/acs.iecr.5b01443

[16] Ghobadian B, Rahimi H, Tavakauli T, Khatami M. Production of bioethanol and sunflower methyl ester and investigation of fuel blend properties. J Agric Sci Technol. 2008;10: 225-232.

[17] Grzelak P, Chłopek Z, Szczepański K. Properties of substitute motor fuels produced from ethanol in biorefineries. Combustion Engines. 2024;198(3):41-47. https://doi.org/10.19206/CE-184488

[18] Harbi A, Alabduly A, Alkhedhair A, Alqahtani N, Albishi M. Effect of operation under lean conditions on NO_x emissions and fuel consumption fueling an SI engine with hydrous ethanol–gasoline blends enhanced with synthesis gas. Energy. 2022;238(A):121-129. https://doi.org/10.1016/j.energy.2021.121694

[19] Hassan A, Rawashdeh H, Muhtaseb A, Abu Jrai A, Ahmad R, Zeaiter J. Impact of changing combustion chamber geometry on emissions, and combustion characteristics of a single cylinder SI (spark ignition) engine fueled with ethanol/gasoline blends. Fuel. 2018;231:197-203. https://doi.org/10.1016/j.fuel.2018.05.045

[20] Iliev S. A comparison of ethanol and methanol blending with gasoline using a 1D engine model. Procedia Engineer. 2015;100:1013-1022. https://doi.org/10.1016/j.proeng.2015.01.461

[21] Iodice P, Senatore A, Langella G, Amoresano A. Effect of ethanol–gasoline blends on CO and HC emissions in last generation SI engines within the coldstart transient: an experimental investigation. Appl Energ. 2016;179:182-190. https://doi.org/10.1016/j.apenergy.2016.06.144

[22] Jakliński P, Czarnigowski J, Ścisłowski K. Study of the effect of ignition crank angle and mixture composition on the performance of a spark-ignition engine fueled with ethanol. Combustion Engines. 2024;197(2):56-63. https://doi.org/10.19206/CE-174888

[23] Jamrozik A, Tutak W, Gruca M, Pyrc M. Performance, emission and combustion characteristics of CI dual fuel engine powered by diesel/ethanol and diesel/gasoline fuels. J Mech Sci Technol. 2018;32:2947-2957. https://doi.org/10.1007/s12206-018-0551-8

[24] Jhang S, Lin Y, Chen K, Lin S, Batterman S. Evaluation of fuel consumption, pollutant emissions and well-to-wheel GHGs assessment from a vehicle operation fueled with bioethanol, gasoline and hydrogen. Energy. 2020;209:118436. https://doi.org/10.1016/j.energy.2020.118436

[25] Kass M, Janke C, Connatser RM, Lewis S, Baustian J, Wolf L et al. Performance of vehicle fuel system elastomers and plastics with test fuels representing gasoline blended with 10% ethanol (E10) and 16% isobutanol (iBu16). SAE Int J Fuels Lubr. 2020;13(2):137-150. https://doi.org/10.4271/04-13-02-0008

[26] Lodice P, Senatore A, Langella G, Amoresano A. Ethanol in gasoline fuel blends: effect on fuel consumption and engine out emissions of SI engines in cold operating conditions. Appl Therm Eng. 2018;130:1081-1089. https://doi.org/10.1016/j.applthermaleng.2017.11.090

[27] Masum B, Masjuki HH, Kalam H, Fattah I, Palash S, Abedin M. Effect of ethanol–gasoline blend on NO_x emission in SI engine. Renew Sust Energ Rev. 2013;24:209-222. https://doi.org/10.1016/j.rser.2013.03.046

[28] Mourad M, Mahmoud K. Investigation into SI engine performance characteristics and emissions fuelled with ethanol/butanol-gasoline blends. Renew Energ. 2019;143:762-771. https://doi.org/10.1016/j.renene.2019.05.064

[29] Muhammad M. Comparison of the properties and yield of bioethanol from mango and orange waste. Arid Zone Journal of Engineering, Technology and Environment. 2017; 13(6):779-789.

[30] Nwufo O, Nwafor O, Igbokwe J. Effects of blends on the physical properties of bioethanol produced from selected Nigerian crops. International Journal of Ambient Energy. 2016;37:10-15. https://doi.org/10.1080/01430750.2013.866907

[31] Roso V, Santos N, Alvarez C, Filho F, Pujatti F, Valle R. Effects of mixture enleanment in combustion and emission parameters using a flexfuel engine with ethanol and gasoline, Appl Therm Eng. 2019;153:463-472. https://doi.org/10.1016/j.applthermaleng.2019.03.012

[32] Singh P, Ramadhas A, Mathai R, Sehgal A. Investigation on combustion, performance and emissions of automotive engine fueled with ethanol blended gasoline. SAE Int J Fuels Lubr. 2016;9(1):215-223. https://doi.org/10.4271/2016-01-0886

[33] Szlachetka M, Wendeker M. Model research of injection of gasoline and E85 into the engine intake pipe. Combustion Engines. 2012;151(4):55-63. https://doi.org/10.19206/CE-117021

[34] Turkcan A, Ozsezen A, Canakci M. Experimental investigation of the effects of different injection parameters on a direct injection HCCI engine fueled with alcohol–gasoline fuel blends. Fuel Process Technol. 2014;126:487-496. https://doi.org/10.1016/j.fuproc.2014.05.023

[35] Taghavifar H, Kaleji B, Kheyrollahi J. Application of composite TNA nanoparticle with bi-ethanol blend on gasoline fueled SI engine at different lambda ratios. Fuel. 2020;277: 1-12. https://doi.org/10.1016/j.fuel.2020.118218

[36] Thakur A, Kaviti A, Mehra R, Mer K. Progress in performance analysis of ethanolgasoline blends on SI engine. Renew Sust Energ Rev. 2017;69:324-340. https://doi.org/10.1016/j.rser.2016.11.056

[37] Thangavelu S, Ahmed A, Ani F. Review on bioethanol as alternative fuel for spark ignition engines. Renew Sust Energ Rev. 2016;56:820-835. https://doi.org/10.1016/j.rser.2015.11.089

[38] Tutak W, Jamrozik A, Bereczky A, Lukacs K. Effects of injection timing of diesel fuel on performance and emission of dual fuel diesel engine powered by diesel/E85 fuels. Transport. 2018;33(3):633-646. https://doi.org/10.3846/transport.2018.1572

[39] Tutak W. Bioethanol E85 as a fuel for dual fuel diesel engine. Energ Convers Manage. 2014;86:39-48. https://doi.org/10.1016/j.enconman.2014.05.016

[40] Wang X, Chen Z, Ni J, Liu S, Zhou H. The effects of hydrous ethanol gasoline on combustion and emission characteristics of a port injection gasoline engine. Case Studies in Thermal Engineering. 2015;6:147-154. https://doi.org/10.1016/j.csite.2015.09.007

[41] Yao Y, Tsai J, Wang I. Emissions of gaseous pollutant from motorcycle powered by ethanol–gasoline blend. Appl Energ. 2013;102:93-100. https://doi.org/10.1016/j.apenergy.2012.07.041

[42] Yusuf A, Inambao F. Bioethanol production from different Matooke peels species: a surprising source for alternative fuel. Case Studies in Thermal Engineering. 2019;13:100357. https://doi.org/10.1016/j.csite.2018.11.008

[43] Zhuang Y, Hong G. Primary investigation to leveraging effect of using ethanol fuel on reducing gasoline fuel consumption. Fuel. 2013;105:425-431. https://doi.org/10.1016/j.fuel.2012.09.013

Marietta Markiewicz, DSc. DEng. – Faculty of Mechanical Engineering, Bydgoszcz University of Science and Technology, Poland.
e-mail: *marmar000@pbs.edu.pl*

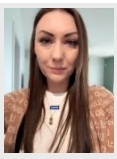

Jerzy Kaszkowiak, DEng. – Faculty of Mechanical Engineering, Bydgoszcz University of Science and Technology, Poland.
e-mail: *jerzy.kaszkowiak@pbs.edu.pl*

Prof. Lubomir Hujo, DEng. – Mechanical Engineering Technologies and Materials, Trenčianska Univerzita Alexandra Dubčeka, Slovakia.
e-mail: *lubomir.hujo@tnuni.sk*

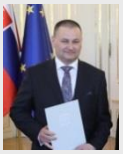

Article citation info:
Zimakowska-Laskowska M, Kozłowski E, Wiśniowski P, Żbik K, Świderski A, Rostek E et al. The influence of ambient temperature on exhaust emissions during cold start in the homologation test. Combustion Engines. 2025;203(4):50-58. https://doi.org/10.19206/CE-207577

Magdalena ZIMAKOWSKA-LASKOWSKA
Edward KOZŁOWSKI
Piotr WIŚNIOWSKI
Ksawery ŻBIK
Andrzej ŚWIDERSKI
Ewa ROSTEK
Radovan MADLEŇÁK

Combustion Engines
Polish Scientific Society of Combustion Engines

The influence of ambient temperature on exhaust emissions during cold start in the homologation test

ARTICLE INFO

Received: 19 May 2025
Revised: 6 June 2025
Accepted: 25 June 2025
Available online: 12 July 2025

The cold start phase in an ICE is susceptible to changing environmental conditions, especially ambient temperature. The work aimed to analyse the influence of different thermal conditions on the concentration of pollutants and operating parameters of the drive unit during a cold start. The tests were conducted on a chassis dynamometer at various ambient temperatures. The same homologation cycle was used in both cases, allowing direct comparison of results. The concentrations of HC, CH_4, CO_2, and NO_x were recorded, as well as the basic operating parameters of the engine: coolant temperature, rotational speed, load, and throttle position. Based on empirical data, mathematical models describing the influence of ambient temperature on the dynamics of emissions and stabilisation of engine operation were developed. Relationships were identified that allow for assessing the time to reach steady-state conditions as a function of starting temperature. The results of the analysis provide the basis for developing a start control strategy in climatically variable conditions. They can support the development of adaptive emission control systems compliant with current and future legal standards.

Key words: *cold start, internal combustion engine, ambient temperature, pollutant concentration, quantile regression*

1. Introduction

Cold starting of a combustion engine is one of the most significant challenges concerning pollutant emissions, especially in light of increasingly stringent environmental standards. The significance of this phase has been recently emphasised in studies focused on emission surges during cold start [19]. In this short but intensive phase of the engine's operation, there are rapid emissions of hydrocarbons (HC), carbon monoxide (CO), nitrogen oxides (NO_x), and methane (CH_4) before the catalytic converter reaches operating temperature. One of the key factors influencing this phenomenon is the ambient temperature and the thermal state of the engine at the time of start-up, reflected, among other things, by the initial coolant temperature.

In emissions research, increasing attention is being paid to analysing the impact of variable thermal conditions on emission dynamics and engine stabilisation. Low starting temperatures result in delayed catalyst warm-up, a richer fuel-air mixture, and higher internal friction, translating into more intense and longer-lasting emissions. Therefore, comparing the cold start process under different initial conditions – especially at different coolant temperatures – allows for a more accurate determination of emission characteristics in real conditions.

The following literature review explores the influence of coolant temperature on emissions, combustion behaviour, and exhaust treatment effectiveness. It highlights findings related to hydrocarbon, carbon monoxide, nitrogen oxide and particulate emissions, as well as the role of fuel type and control strategies.

The influence of coolant temperature on pollutant emissions during cold start has been the subject of numerous studies in both spark-ignition and compression-ignition engines. Similar analyses of low-temperature effects on exhaust composition, including detailed hydrocarbon speciation, were performed by Hunicz and Krzaczek [11] in a gasoline HCCI engine.

Low coolant temperature at start significantly affects combustion processes, fuel-air mixture formation and the efficiency of exhaust gas treatment systems. In their studies on emission dynamics and drive system reliability, Kozłowski et al. [16] emphasised the importance of the technical condition of the system in the context of emissions. Rimkus et al. [29] analysed the influence of hydrogen addition on emissions from combustion engines in dynamic driving conditions, indicating high variability of drive unit operating parameters. Kozłowski et al. [17] also analysed the relationships between vehicle acceleration and energy consumption, which is important in the context of the WLTC start analysis.

He et al. [9] showed that under low coolant temperature conditions, combustion becomes slower and less stable, and HC, CO, and particulate matter (PM) emissions significantly increase. Only with increasing coolant temperature does combustion quality improve and emissions decrease, although NO_x concentration may increase due to higher combustion temperature. Similar relationships were observed by Irimescu et al. [12] in a direct injection engine fueled with gasoline and butanol – the cold coolant promoted the formation of fuel films on the combustion chamber walls, which resulted in slower flame propagation and increased emissions.

Bielaczyc et al. [2] confirmed that the coolant temperature and the low ambient temperature significantly increased the emissions during cold start. In particular, an

increase of up to tenfold in HC emissions was observed compared to steady-state conditions.

In the analyses of Mancarella and Marello [24] and Tauzia et al. [33], it was emphasised that higher coolant temperature improves engine thermal efficiency and reduces CO, HC, and PM emissions, but this is associated with the risk of increasing NO_x emissions. Dynamic modelling of thermal parameters (e.g. oil temperature, combustion chamber walls) was also indicated as a key factor in the realistic representation of emissions during the warm-up phase.

The type of fuel is also important. Farooq et al. [6] showed that engines fueled with methanol or its mixtures are characterised by an apparent sensitivity to low coolant temperature, which makes ignition difficult and leads to increased soot and HC emissions, especially at high fuel evaporation enthalpy. In the context of using modern emission analysis and prediction methods, Kłosowski et al. [14] proposed using LSTM networks to monitor industrial processes, which can also be adapted in the context of exhaust emissions. Pawlik et al. [27] indicated the potential of unsupervised algorithms to identify machine operating states, which is a direction for further development of emission models based on empirical data.

Proposed technical solutions include catalytic heaters [4], intake air preheating systems, and injection strategy optimisation [7, 9]. In recent years, predictive models using machine learning algorithms have also gained much popularity, which allow predicting emissions as a function of coolant temperature and starting conditions [21].

The cold start of an internal combustion engine is particularly problematic in low ambient temperature conditions, as it leads to heat losses, ignition delays and increased emissions due to incomplete combustion [1, 35]. This applies especially to hydrocarbons and carbon monoxide, which reach levels even several times higher in this phase than in the steady state.

In the studies by Andrych-Zalewska et al. [1] it was emphasised that not only the ambient temperature, but also the thermal state of the engine itself at the time of start (i.e. coolant and oil temperature) significantly affects the emission characteristics, which is fully confirmed by thermodynamic analyses [5]. A cold engine, even at moderate outside temperatures, can increase HC and PM emissions due to the delayed activation of exhaust gas combustion systems.

Attention is also drawn to the different engine behaviour depending on the fuel type. For example, fuels with high enthalpy of vaporisation, such as ethanol, methanol, or ammonia, require special ignition and injection management strategies [3, 15], including the use of fuel reformers or mixture preheaters. Koike et al. [15] demonstrated that using on-board ammonia reforming significantly improves the ignition stability during cold start. Recent research increasingly focuses on dynamic thermal management systems, including electrically heated catalysts [4], preheating strategies for intake air or coolant [7], and predictive algorithms for optimizing coldstart emissions using machine learning [21]. These approaches provide practical pathways for reducing pollutant peaks during start-up and improving overall emission control calibration.

An important technical aspect is optimising control strategies – modification of the ignition timing, injection time, and fuel delivery amount [22, 26]. Hybrid systems or auxiliary heat sources are also increasingly used in modern powertrains [15].

This study aims to assess the influence of ambient temperature and initial coolant temperature on pollutant emissions during the cold start of a combustion engine. In the first part, a literature review was conducted on measurement conditions, empirical relationships, and prediction models related to this phenomenon. Then, an experimental analysis of HC, CO, and CO_2 emissions in the WLTC test was conducted for two initial coolant temperature levels: 6°C and 28°C. The study aimed to determine the influence of these thermal differences on emission levels and the rate of their stabilisation during the engine warm-up phase.

In addition to the analysis of instantaneous emission values, a set of quantitative indicators is proposed, such as: total pollution (area under the curve), the relative share of emissions due to cold start, and the sensitivity of emissions to changes in initial temperature. The proposed indicators constitute a new analysis element, enabling a quantitative assessment of the engine's sensitivity to thermal conditions during start-up. In particular, the coefficient $\eta_{T_0^c \cdot T_0^n}$ can be used as a comparative measure of the engine's "ecological sensitivity" and the effectiveness of the applied technical solutions in the context of cold start. This approach allows for a better capture of the relationships between thermal conditions and emission characteristics.

The presented results can be used to develop start strategies in variable climatic conditions and to calibrate emission prediction models in the cold start phase. These conclusions apply to homologation processes and the design of adaptive engine control systems that are compliant with future emission standards.

The main hypothesis of this study is that the initial thermal state of the engine, particularly the coolant temperature, significantly affects both the magnitude and dynamics of pollutant emissions during the cold start phase. The objective is to quantify this impact and propose diagnostic indicators for engine control strategy development.

2. Methodology

The choice of research methodology was based on analyses by previous authors [16, 17, 29], who emphasised the importance of vehicle starting conditions and drive system reliability in the context of pollutant emissions. Particular attention was paid to the influence of driving dynamics and the possibility of reproducing it during laboratory tests. The WLTC cycle was used in the study, following the recommendations for emission measurements in dynamic conditions, which allows for a realistic assessment of the start and initial phase of engine operation.

The tests were performed using a Ford Focus passenger car equipped with a spark-ignition engine with a displacement of 1798 cm³, in the Flexifuel version. The tests were performed on a chassis dynamometer, which reproduced a vehicle's rolling resistance and aerodynamic drag in real conditions. This combined measurement-modelling approach was successfully used in other studies [36]. The WLTC cycle procedure was carried out for the simulated

drive. Figure 2 shows the changes in the coolant temperature during the test, while Fig. 1 shows the vehicle speed profiles in two drives by the WLTC cycle.

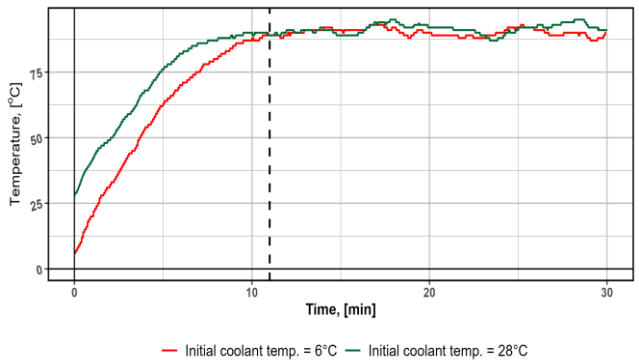

Fig. 1. Coolant temperature changes over time WLTC test

Figure 1 shows the coolant temperature increase during the WLTC test in two starting variants. The higher initial coolant temperature (28°C) resulted in faster achievement of the operating temperature (90°C), which is important for stabilising combustion processes and operating exhaust gas after-treatment systems.

A comparison of emissions was made between CO_2, CO and HC during the start of a passenger car, where in the first case the temperature of the cooling system was 6°C and in the second case 28°C. We consider the sequences $\{(x_i^c, T_i^c, v_i^c)\}_{0\le i\le m}$ and $\{(x_i^n, T_i^n, v_i^n)\}_{0\le i\le m}$, the quantity x_i^a denotes the amount of pollution in [ppm], T_i^a – engine temperature [°C], v_i^a – vehicle speed at the moment of i, $0 \le i \le m$, and $a \in \{c, n\}$, where c- the case where, when the vehicle was started, the temperature of the cooling system was 6°C, i.e. $T_0^c = 6$, n – the case where, when the vehicle was started, the temperature of the cooling system was 28°C, i.e. $T_0^n = 28$.

The contamination was analysed until the moment $\tau = \min\{i: T_i^c = T_i^n, 0 \le i \le m\}$. The moment of reaching identical temperatures $\tau = 656$, i.e. the moment of temperature equalisation (90°C), was obtained after 10 min 56 s. Therefore, the influence of temperature differences on contamination was analysed until the moment τ. When the initial temperature of the cooling system was 28°C, the engine operating temperature reached 90°C after 9 min 31 s.

The use of statistical and predictive methods is based on the approach proposed in [14] and [27], where the usefulness of machine learning algorithms in analysing technical and emission data has been demonstrated. This approach enables future extension of classical analysis methods with predictive components based on neural networks and temporal models as recommended in introductory machine learning frameworks [13]. Such extensions can be supported by cognitive tools and simulation-based frameworks developed for sustainable engine control [25].

Figure 2 shows the vehicle speed dynamics in two runs by the WLTC cycle, conducted at different initial coolant temperatures (6°C and 28°C). The similarity of the curves indicates high repeatability of the driving conditions, enabling a reliable comparison of the effect of the initial temperature on the dynamics of changes in the concentrations of pollutants in the exhaust gases.

Let $\{v_i\}_{0\le i\le\tau}$ be a sequence of speed differences at the appropriate moments of the journey between the two tests until τ (the moment when the engine temperatures equalise), i.e. $v_i = v_i^n - v_i^c$, $0 \le i \le \tau$. The average of speed differences in the tests $\bar{v} = \frac{1}{\tau}\sum_{i=1}^{\tau} v_i$ is – 0.08 km/h. In contrast, the standard deviation of speed differences $S_v = \sqrt{\frac{1}{\tau}\sum_{i=1}^{\tau}(v_i - \bar{v})^2}$ is 1.66 km/h, the average of absolute values of speed differences $\tilde{v} = \frac{1}{\tau}\sum_{i=1}^{\tau}|v_i|$ is equal 1.06 km/h. The statistical convergence of the recorded speeds, confirmed by the low deviation and the average difference, is consistent with the course shown in Fig. 2 and provides a basis for a reliable comparison of emissions under conditions of different initial temperatures.

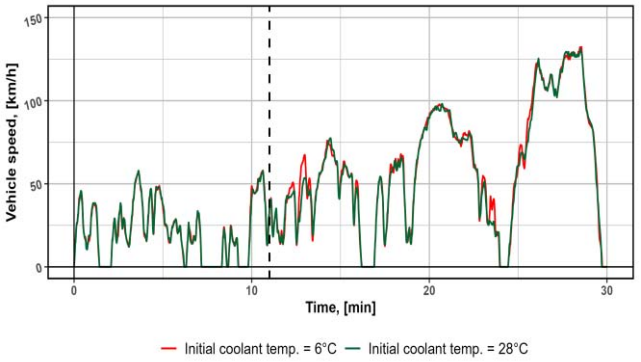

Fig. 2. WLTC cycle course for two tests with different temperatures initial liquid cooling

The graphs below show the differences in pollution (red curve for starting from a temperature of 6°C and green curve for starting from a temperature of 28°C) and vehicle speed (black curve, scale on the right side of the graph).

Starting at a lower initial temperature led to increased CO_2 concentrations in the exhaust gases in the first minutes of the test (see Fig. 3), which reflects the intensification of the combustion process with an enriched mixture. As the coolant warms up, a gradual convergence of the concentration curves for both cases is observed.

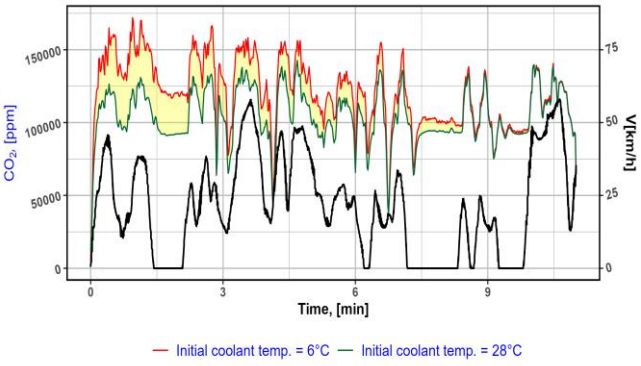

Fig. 3. CO_2 concentration and vehicle speed as a function of time (WLTC)

The concentration of carbon monoxide (CO) remains significantly higher during cold start (Fig. 4), which confirms the lower efficiency of exhaust gas combustion in this operation phase. The differences decrease with the increase in coolant temperature, but complete stabilisation occurs only after reaching operating conditions.

From Fig. 5, we can see that the concentration of unburned hydrocarbons (HC) after a cold start is several times higher than in the case of a start with a higher coolant temperature due to fuel condensation on the cold surfaces of the combustion chamber and delayed activation of emission reduction systems.

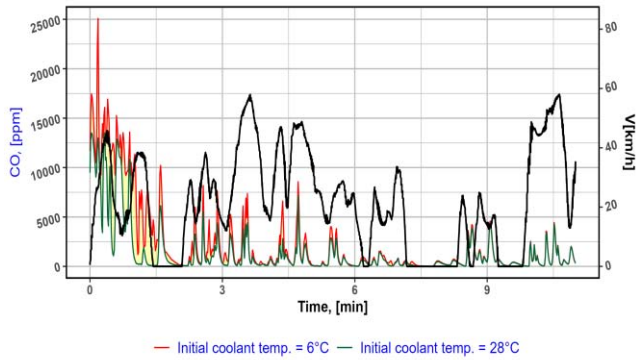

Fig. 4. CO concentration and vehicle speed as a function of time (WLTC)

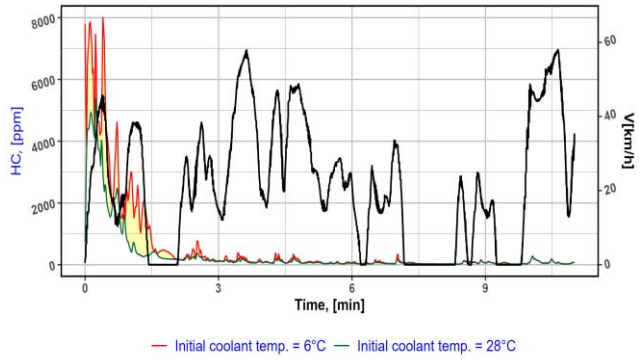

Fig. 5. HC concentration and vehicle speed as a function of time (WLTC)

Quantitative analysis of pollution growth

The value

$$W_{T_0^a} = \int_0^\tau x_t^a \, dt \tag{1}$$

is called the total pollution caused by starting the car for initial temperatures T_0^a, $a \in \{c, n\}$. The quantity $W_{T_0^a}$ means the area under the curve x_t^a for $0 \le t \le \tau$. In the case of measurements taken, for example, every second, the total pollution up to the moment $\tau$is approximated by $W_{T_0^a} \approx \sum_{i=0}^{\tau} x_i^a$. The quantity

$$\kappa_{T_0^c:T_0^n} = \frac{W_{T_0^c} - W_{T_0^n}}{W_{T_0^c}} \tag{2}$$

denotes the share of the increase in pollutants caused by starting the engine from the initial temperature T_0^c compared to the state of temperature T_0^n($T_0^c < T_0^n$) and operating the engine until the engine operating temperature is reached, i.e. $T_\tau^c = T_\tau^n$.

In order to compare the differences caused by different initial temperatures, the coefficient

$$\eta_{T_0^c:T_0^n} = \frac{\int_0^\tau |x_t^c - x_t^n| dt}{\int_0^\tau |T_t^n - T_t^c| dt} \approx \frac{\sum_{i=1}^{\tau} |x_i^c - x_i^n|}{\sum_{i=1}^{\tau} |T_i^n - T_i^c|} \tag{3}$$

was defined, which means the rate of change of pollutant concentration about changes in the initial engine operating temperature (emission sensitivity to changes in initial temperature). The parameters presented in equations (1)–(3) are an extension of the classical emission assessment methods with an approach that considers instantaneous concentrations. The indicator $\kappa_{T_0^c:T_0^n}$ expresses the relative increase in the cumulative pollutant concentration in cold start conditions, compared to a start with a higher initial temperature. In turn, the value $\eta_{T_0^c:T_0^n}$ describes the rate of change of cumulative concentration about the change in initial temperature, constituting a measure of the sensitivity of the drive system to cooling down. On the one hand, these indicators allow for a quantitative assessment of the impact of start conditions on emissions from the perspective of the concentration curve, and on the other hand – especially in the case of CO and HC – they indicate the variability of combustion efficiency and operation of exhaust gas treatment systems in the warm-up phase. A high value η for a given component may indicate limited engine capability for stable fuel energy conversion in low-temperature conditions. The proposed indicators can be used in thermal diagnostics and when comparing emission reduction strategies in different start scenarios.

Analysis of the impact of temperature differences

To analyse the effect of temperature differences on pollutants generated by the combustion engine, we define the sequence $\{(p_t, T_t)\}_{0 \le t \le \tau}$, where $T_t = T_t^n - T_t^c$ denotes the temperature difference and the pollutant difference $p_t = x_t^c - x_t^n$ for the moments $0 \le t \le \tau$, by the definition $T_\tau = 0$ and the largest temperature difference $T_{max} = \max\{T_j^n - T_j^c : 0 \le j \le \tau\}$. The interval $[0, T_{max}]$ has been divided into k −separate intervals, so that $[0, T_{max}] \subset [0, d) \cup [d, 2d) \cup \ldots \cup [(k-1)d, kd)$ and $T_{max} \in [(k-1)d, kd)$. As a representative of the temperature interval $[(j-1)d, jd)$ for $j = 1,2, \ldots, k$ the value $t_j = (j - 0.5)d$ was taken.

For each set $P_j = \{p_i : T_i \in [(j-1)d, jd), 0 \le i \le \tau\}, j = 1,2, \ldots, k$ the quantiles of order $\alpha/2$ and $1 - \alpha/2$ were determined and denoted as $q_j^{\alpha/2}$and $q_j^{1-\alpha/2}$respectively. The sequences $\left\{\left(t_j, q_j^{\alpha/2}\right)\right\}_{1 \le j \le k}$ and $\left\{\left(t_j, q_j^{1-\alpha/2}\right)\right\}_{1 \le j \le k}$ consist of a representative of the temperature difference interval $\left\{\left(t_j, q_j^{\alpha/2}\right)\right\}_{1 \le j \le k}$ and the limits of the pollutant quantiles for these intervals. In order to predict the pollutants concerning the temperature difference for each of the sequences $\left\{\left(t_j, q_j^{\alpha/2}\right)\right\}_{1 \le j \le k}$ and $\left\{\left(t_j, q_j^{1-\alpha/2}\right)\right\}_{1 \le j \le k}$ the dependence

$$\log\left(q_j^s\right) = \theta_0^s + \theta_1^s t_j + \theta_2^s \sqrt{t_j} + \theta_3^s \frac{1}{t_j} + \varepsilon_j \tag{4}$$

was considered, where ε_j denotes a random variable with a normal distribution $N(0, \sigma_s^2)$, $s \in \{\alpha/2, 1 - \alpha/2\}$. The Least Squares Method was used to estimate the structural parame-

ters of the model (4). Additionally the coefficient of determination

$$R^2 = 1 - \frac{\sum_{j=1}^{k} \varepsilon_j^2}{\sum_{j=1}^{k} \left(\log\left(q_j^s\right) - \hat{g}^s\right)^2} \quad (5)$$

was determined, where $\hat{g}^s = \frac{1}{k}\sum_{j=1}^{k} \log\left(q_j^s\right)$. The determination coefficient shows what part of the quantile variability of the order $s \in \{\alpha/2, 1-\alpha/2\}$ due to the temperature difference is explained by the model, Based on the following formula

$$q^s(t) = \exp\left(\hat{\theta}_0^s + \hat{\theta}_1^s t + \hat{\theta}_2^s \sqrt{t} + \hat{\theta}_3^s \frac{1}{t}\right) \quad (6)$$

the values of the quantile of order $s \in \{\alpha/2, 1-\alpha/2\}$ for temperature differences $t \in (0, T_0]$ were estimated.

3. Results

Using formulas (1)–(3), the indicators of the impact of the initial temperature on the pollutants generated by the operation of the combustion engine were estimated.

Table 1: Total pollution for normal start, total pollution from cold start, relative pollution due to starting the engine from low temperature, and the coefficient of change of contaminant concentration relative to changes in initial temperatures

	$W_{T_0^n}$	$W_{T_0^c}$	$\kappa_{T_0^c:T_0^n}$	$\eta_{T_0^c:T_0^n}$
CO_2	68506849	78926888	0.132	1328
CO	929425	1537429	0.3955	77
HC	221151	378723	0.4161	20

Using the quantitative indicators in Table 1, a clear relationship was observed between the initial engine temperature and the cumulative concentration of pollutants in the exhaust gases. The highest relative increase in the total concentration was noted for unburned hydrocarbons (HC), the share of which in emissions attributed to the cold start phase exceeded 40%. It is worth noting that, according to the time graphs (Fig. 5), this increase is concentrated mainly in the initial phase of the test, especially during accelerations, when the combustion chamber remains cooled. The concentration sensitivity indicator to initial temperature differences (η) reached the highest value for CO_2, which indicates a significant dependence of combustion intensity on thermal conditions of start-up, even though the total increase in the concentration of this component was relatively low. High values of the indicators for CO and HC indicate a high susceptibility of these compounds to the effect of delayed activation of after-treatment systems and combustion quality in the initial phase of the cycle.

The temperature difference interval $[0,24]$ was divided into intervals of length $d = 1$. For each type of pollutant, CO_2, CO, and HC, for the appropriate intervals and level, $\alpha = 0.1$ quantiles of order $\alpha/2 = 0.05$ and were estimated, $1 - \alpha/2 = 0.95$ and sequences $\left\{\left(t_j, q_j^{0.05}\right)\right\}_{1\le j\le k}$ and were determined, $\left\{\left(t_j, q_j^{0.95}\right)\right\}_{1\le j\le k}$. Using the least squares method, structural parameters (4) were determined and using formula (6), quantiles for pollutants were predicted concerning the temperature difference at the start. In Fig. 6–8 in the Cartesian coordinate system, the realisation of the sequence $\{(p_t, T_t)\}_{0\le t\le \tau}$, where the temperature difference $T_t = T_t^n - T_t^c$ on the abscissa axis, and the pollutant difference on $p_t = x_t^c - x_t^n$ the ordinate axis for the moments, were marked with black points $0 \le t \le \tau$. Values prediction of quantiles are salmon coloured.

The models describing the behaviour of quantiles for CO_2, CO, and HC concentrations showed high values of the coefficient of determination ($R^2 > 0.86$), confirming the agreement between the difference in initial temperatures and the distribution of the analysed components' concentrations. The differences in the values of structural parameters between quantiles 0.05 and 0.95 reflect the increasing risk of extreme concentrations in conditions of strong cooling of the powertrain. In particular, a larger range of these parameters results in wider confidence intervals for the predicted concentrations, which means that a larger difference in initial temperatures leads to increased prediction uncertainty. The smallest differences in structural parameters and the smallest fitting error were observed for CO_2 (quantile 0.95), which indicates the stable nature of this component's emissions. In turn, for CO, the highest values of standard deviations of predictions and relatively lower R^2 were observed (especially for the 0.05 quantile), which confirms its greater susceptibility to the variability of start conditions and lower accuracy of representation in the model.

Table 2: The values of estimators of structural parameters, the values of coefficient determination and the values of standard deviations for quantitative models

Pollution	s	θ_0^s	θ_1^s	θ_2^s	θ_3^s	R_s^2	σ_s
CO_2	0.05	5.73	–0.17	1.73	–0.62	0.90	0.39
CO_2	0.95	3.82	–0.28	2.57	0.76	0.99	0.11
CO	0.05	64.12	3.79	–29.49	–67.34	0.87	0.96
CO	0.95	6.44	0.44	–1.39	–0.79	0.94	0.430
HC	0.05	26.76	2.56	–16.47	–10.38	0.95	0.65
HC	0.95	5.87	0.79	–3.08	–1.17	0.975	0.42

For each of the pollutants, the values of structural parameters for the model (4), the values of the standard deviation of the residuals, and the values of the coefficient of determination (5) are given in Table 2. The lowest value of the coefficient of determination, equal to 0.8674, was obtained for the CO pollutant when fitting the dependence of the quantile of the order of 0.05 on the temperature differences, while for the remaining pollutants, the value of the coefficient of determination exceeds 0.90.

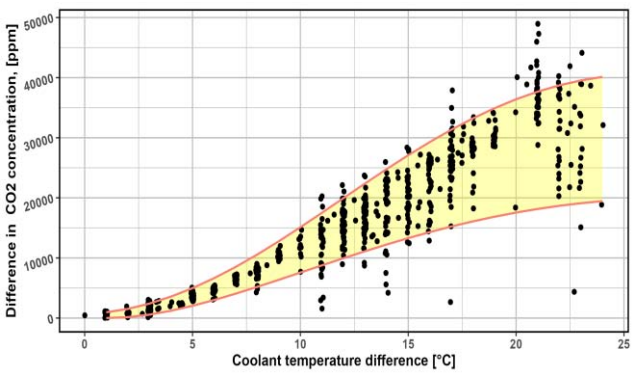

Fig. 6. Fitting models of 0.05 and 0.95 quantiles of CO_2 concentration with respect to the initial temperature difference

The increase in the initial temperature difference results in a moderate increase in CO_2 concentrations within both analysed quantiles. The model shows a perfect fit, especially for the 0.95 quantile ($R^2 = 0.9915$), which indicates the stability of this component's characteristic concerning the start-up's thermal conditions.

In the case of CO, there is a clear dependence of the upper quantile value on the temperature difference, which indicates an increased probability of high concentrations occurring when the system is strongly cooled. However, the data scatter is larger than in the case of CO_2, which translates into a lower quality of the model fit for the quantile of the order of 0.05.

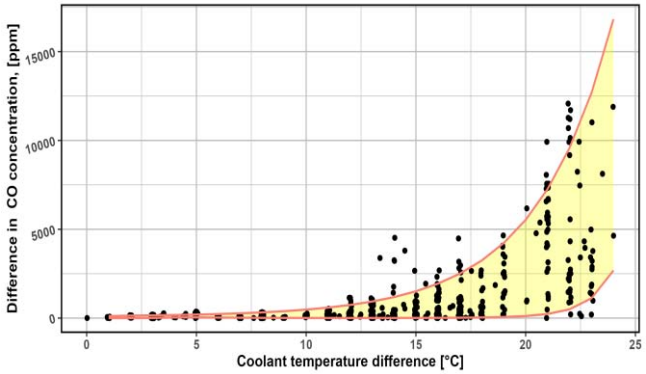

Fig. 7. Fitting models of 0.05 and 0.95 quantiles of CO concentration with respect to the initial temperature difference

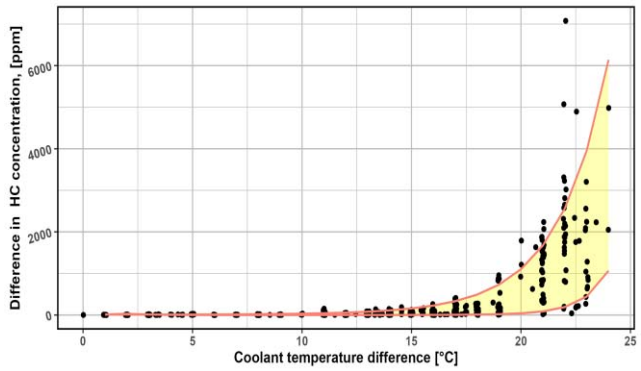

Fig. 8. Fitting models of 0.05 and 0.95 quantiles of HC concentration with respect to the initial temperature difference

HC concentration shows an apparent sensitivity to temperature differences in the cold start phase. At a lower initial engine temperature, significantly higher values of unburned hydrocarbon concentration are observed, which results from worse ignition conditions, fuel condensation on the cold walls of the combustion chamber, and delayed activation of exhaust gas after-treatment systems. With decreasing starting temperature difference, HC concentration values stabilise quickly – the curves of the courses get closer to each other, confirming this component's strong dependence on the thermal conditions of start-up. A high level of fit of regression models for both quantiles ($R^2 = 0.9485$ and $R^2 = 0.9695$ for 0.05 and 0.95) indicates high predictability of this dependence, despite significant dynamics of concentration changes.

4. Discussion of the results

The results of the conducted studies confirm that lowering the initial coolant temperature significantly affects the combustion process and the concentration of pollutant components in the cold start phase. The increases in HC, CO, and CO_2 concentrations observed in the WLTC tests at a lower starting temperature (6°C vs. 28°C) are consistent with the phenomenon of reduced combustion quality and delayed achievement of catalyst activation conditions described in the literature [2, 9, 12]. The formation of a liquid fuel film on the cold surfaces of the combustion chamber, as well as enrichment of the mixture to improve ignition, results in increased emissions of hydrocarbons and carbon monoxide in the initial minutes of engine operation [6, 12].

The time dependencies in Fig. 3–5 show apparent differences in CO_2, CO, and HC concentrations between tests with different initial temperatures. Especially for HC, a several-fold increase in concentration was observed in the first minutes of the test at low temperature conditions, consistent with the results of Andrych-Zalewska et al. [1] and Yusuf and Inambao [35]. At the same time, the CO concentration remained at a higher level throughout the test under cold start conditions, indicating insufficient catalyst activity in the transient phase [34].

The quantitative indicators presented in Table 1 are also of diagnostic value, including the relative share of emissions related to cold start and the sensitivity of emissions to changes in initial temperature. The most significant relative increase in concentration was for HC (over 40%), while for CO it reached almost 40% and for CO_2 slightly above 13%. The high sensitivity index for CO_2 indicates that, despite the relatively stable nature of this component, the combustion process at low temperature may be less efficient, which translates into its increased emission, which is also confirmed by Hossain et al. [10].

The $\eta_{T_0^c:T_0^n}$ [ppm/°C or g/km/°C] indicator describes the sensitivity of pollutant concentrations or emissions generated during engine operation to changes in thermal start-up conditions. It determines the average increase in these values for each 1°C drop in initial temperature. The lower the indicator's value, the smaller the increase in pollutants associated with a decrease in initial temperature, which means greater emission resistance of the system to cold start conditions. Depending on the available measurement data, this indicator can analyse concentrations (e.g. ppm) and emissions (e.g. g/km). In the future, it may be a universal comparative tool for assessing the emission sensitivity of different drive units, control strategies, or exhaust gas treatment technologies to variations in initial temperature.

Quantile regression allowed for better capturing the variability of extreme pollutant concentrations concerning the initial temperature difference in line with advanced statistical learning approaches [8]. The models (Fig. 6–8) showed a perfect fit for CO_2 ($R^2 \approx 0.99$) and HC ($R^2 \approx 0.97$), slightly lower for CO, which is probably due to the greater scatter and temporary increase in emissions in response to the engine operation dynamics. The range of prediction values in the upper quantiles (0.95) was significant, which increased nonlinearly with the initial temperature difference.

This phenomenon indicates an increased risk of extreme concentration levels in severe cooling conditions [21].

Figures 1 and 2, illustrating the WLTC cycle and the change in coolant temperature, confirm that differences in starting conditions did not significantly affect the vehicle speed profile, while the time needed for the cooling system to reach the operating temperature was significantly extended in the case of a lower starting temperature (10:56 min vs. 9:31 min). The extension of the warm-up time is associated with a delayed achievement of the catalyst's light-off temperature, which, according to literature data [23, 28], may result in an even several-fold increase in the total HC and CO emissions in this phase. Similar conclusions were drawn by Slavin et al. [30], who showed that electrically heated catalysts can effectively reduce cold start emissions in LPG-fueled vehicles, highlighting the importance of thermal emission management.

From the perspective of designing emission reduction strategies, the presented results emphasise the validity of using technical solutions such as heated catalysts [4], advanced injection strategies [32], or thermal management systems with heat recovery from exhaust gases [28]. Quantile regression models can also help predict extreme emissions, which is reflected in the growing interest in using machine learning techniques for this purpose [21].

5. Conclusions

The analyses showed that the coolant's initial temperature significantly affects the dynamics of changes in the concentrations of pollutants emitted by the spark-ignition engine during cold start. Lowering the starting temperature to 6°C resulted in a significant increase in CO, HC, and CO_2 concentrations in the first minutes of the WLTC cycle, which can be associated with delayed activation of exhaust gas treatment systems, lower charge temperature, and enrichment of the fuel-air mixture.

CO and HC showed the greatest sensitivity to start conditions among the compounds tested. In the case of HC, the share of concentration assigned to the cold start phase exceeded 40%, which confirms its high susceptibility to the effect of cooling the combustion chamber. Similar HC emission patterns during cold start were reported in previous studies [18, 20]. Conversely, CO showed the greatest scatter of values in the empirical data, which is confirmed by high standard deviations and discrepancies between quantiles, especially at significant differences in initial temperatures.

In order to quantitatively assess the effect of thermal conditions on emissions, a set of indicators was used, such as the total cumulative concentration, the share of emissions attributed to cold start $\kappa_{T_0^c:T_0^n}$ and the sensitivity indicator $\eta_{T_0^c:T_0^n}$. These indicators allowed to capture the relationship's nonlinear nature and distinguish the response of individual exhaust components to engine cooling. The highest thermal sensitivity was demonstrated for CO_2, although its total increase was moderate, which may indicate variable combustion efficiency depending on the initial temperature.

Quantile models allowed the analysis of both average and extreme drive system behaviour. High coefficients of determination ($R^2 > 0.90$) obtained for CO_2, CO, and HC confirm the validity of the approach. The models showed that the upper quantile values (0.95) of HC and CO concentrations increase nonlinearly with the starting temperature difference, indicating an increased risk of extreme emissions in winter conditions.

In addition, it was found that the time to reach the operating coolant temperature at a lower initial temperature is longer by more than 1 minute (10:56 min vs. 9:31 min), directly affecting the length of the period of increased emissions. The extended warm-up phase is associated with limited efficiency of the afterburning systems, which can significantly increase the total environmental load of the vehicle in urban and suburban cycles.

The obtained results have practical applications both in designing start strategies in variable climatic conditions and in the calibration of emission prediction tools used in homologation procedures and systems for assessing the impact of transport on air quality. This approach can also support broader life-cycle and environmental impact assessments [31]. The proposed analytical approach can also be a starting point for further research on optimising injection, ignition, and thermal management systems in modern drive systems.

Furthermore, these indicators may support the development of advanced cold start control strategies, enable dynamic thermal management and improving catalyst activation during homologation cycles and real-world driving.

Bibliography

[1] Andrych-Zalewska M, Chlopek Z, Merkisz J, Pielecha J. Impact of the internal combustion engine thermal state during start-up on the exhaust emissions in the homologation test. Energies. 2023;16(4):1937. https://doi.org/10.3390/en16041937

[2] Bielaczyc P, Szczotka A, Woodburn J. The effect of a low ambient temperature on the cold-start emissions and fuel consumption of passenger cars. P I Mech Eng D-J Aut. 2011;225(9):1253-1264. https://doi.org/10.1177/0954407011406613

[3] Cao Y, Chen D. A cold-start method and analysis for internal combustion engines particularly using a renewable fuel. Int J Energ Res. 2011;35(4):358-364. https://doi.org/10.1002/er.1683

[4] Duan L, Tan P, Liu J, Liu Y, Chen Y, Lou D et al. Emission characteristics of a diesel engine with an electrically heated catalyst under cold start conditions. J Clean Prod. 2022;380: 134965. https://doi.org/10.1016/j.jclepro.2022.134965

[5] E J, Liu G, Zhang Z, Han D, Chen J, Wei K et al. Effect analysis on cold starting performance enhancement of a diesel engine fueled with biodiesel fuel based on an improved thermodynamic model. Appl Energ. 2019;243:321-335. https://doi.org/10.1016/j.apenergy.2019.03.204

[6] Farooq MS, Baig A, Wei Y, Liu H, Ali U. A concise review of developments to overcome the cold start problems by analyzing combustion and emissions of methanol-based-fueled spark ignition engines. Int J Hydrogen Energy. 2025;99:852-871. https://doi.org/10.1016/j.ijhydene.2024.12.263

[7] Galindo J, Dolz V, Monsalve-Serrano J, Bernal Maldonado MA, Odillard L. EGR cylinder deactivation strategy to accelerate the warm-up and restart processes in a diesel engine operating at cold conditions. Int J Engine Res. 2022;23(4): 614-623. https://doi.org/10.1177/14680874211039587

[8] Hastie T, Tibshirani R, Friedman J. The elements of statistical learning. Springer New York 2009. https://doi.org/10.1007/978-0-387-84858-7

[9] He X, Zhou Y, Liu Z, Yang Q, Sjöberg M, Vuilleumier D et al. Impact of coolant temperature on the combustion characteristics and emissions of a stratified-charge direct-injection spark-ignition engine fueled with E30. Fuel. 2022;309: 121913. https://doi.org/10.1016/j.fuel.2021.121913

[10] Hossain A, Smith D, Davies P. Effects of engine cooling water temperature on performance and emission characteristics of a compression ignition engine operated with biofuel blend. J Sustain Dev Energy Water Environ Syst. 2017;5(1): 46-57. https://doi.org/10.13044/j.sdewes.d5.0132

[11] Hunicz J, Krzaczek P. Detailed speciation of emissions from low-temperature combustion in a gasoline HCCI engine. Pol J Environ Stud. 2016;25(1):137-145. https://doi.org/10.15244/pjoes/60082

[12] Irimescu A, Merola SS, Tornatore C, Valentino G. Effect of coolant temperature on air–fuel mixture formation and combustion in an optical direct injection spark ignition engine fueled with gasoline and butanol. J Energy Inst. 2017;90(3): 452-465. https://doi.org/10.1016/j.joei.2016.03.004

[13] James G, Witten D, Hastie T, Tibshirani R. An introduction to statistical learning: with applications in R. Springer New York 2021. https://doi.org/10.1007/978-1-0716-1418-1

[14] Kłosowski G, Rymarczyk T, Niderla K, Kulisz M, Skowron Ł, Soleimani M. Using an LSTM network to monitor industrial reactors using electrical capacitance and impedance tomography – a hybrid approach. Eksploat Niezawodn. 2023; 25(1):11. https://doi.org/10.17531/ein.2023.1.11

[15] Koike M, Suzuoki T, Takeuchi T, Homma T, Hariu S, Takeuchi Y. Cold-start performance of an ammonia-fueled spark ignition engine with an on-board fuel reformer. Int J Hydrogen Energ. 2021;46(50):25689-25698. https://doi.org/10.1016/j.ijhydene.2021.05.052

[16] Kozłowski E, Borucka A, Oleszczuk P, Leszczyński N. Evaluation of readiness of the technical system using the semi-markov model with selected sojourn time distributions. Eksploat Niezawodn. 2024;26(4):191545. https://doi.org/10.17531/ein/191545

[17] Kozłowski E, Wiśniowski P, Gis M, Zimakowska-Laskowska M, Borucka A. Vehicle acceleration and speed as factors determining energy consumption in electric vehicles. Energies. 2024;17(16):4051. https://doi.org/10.3390/en17164051

[18] Laskowski P, Zasina D, Zimakowska-Laskowska M, Orliński P. Modelling hydrocarbons cold-start emission from passenger cars. Adv Sci Technol Res J. 2021;15(3): 117-125. https://doi.org/10.12913/22998624/138764

[19] Laskowski P, Zimakowska-Laskowska M, Jan M, Wiśniowski P. The problem of cold start emissions from vehicles. Combustion Engines. 2024;199(4):43-51. https://doi.org/10.19206/CE-186471

[20] Laskowski P, Zimakowska-Laskowska M, Zasina D. Modelling of the air pollutants' cold-start emissions depending on average vehicles' speed. Combustion Engines. 2022;188(1): 96-103. https://doi.org/10.19206/CE-142171

[21] Liu K, Zhou J, Pei Z, Fu W, Yang H, Jiang Z et al. Research on transient emissions prediction for natural gas engine using the tuna swarm optimization-extreme gradient boosting algorithm under worldwide harmonized transient cycle. Atmos Pollut Res. 2025;16(4):102425. https://doi.org/10.1016/j.apr.2025.102425

[22] Liu R, Wei M, Yang H. Cold start control strategy for a two-stroke spark ignition diesel-fuelled engine with air-assisted direct injection. Appl Therm Eng. 2016;108:414-426. https://doi.org/10.1016/j.applthermaleng.2016.07.148

[23] Lodi F, Zare A, Arora P, Stevanovic S, Jafari M, Ristovski Z et al. Engine performance and emissions analysis in a cold, intermediate and hot start diesel engine. Appl Sci. 2020; 10(11):3839. https://doi.org/10.3390/app10113839

[24] Mancarella A, Marello O. Effect of coolant temperature on performance and emissions of a compression ignition engine running on conventional diesel and hydrotreated vegetable oil (HVO). Energies. 2022;16(1):144. https://doi.org/10.3390/en16010144

[25] Orynycz O, Tucki K, Prystasz M. Implementation of lean management as a tool for decrease of energy consumption and CO_2 emissions in the fast food restaurant. Energies. 2020;13(5):1184. https://doi.org/10.3390/en13051184

[26] Pastor JV, García-Oliver JM, Pastor JM, Ramírez-Hernández JG. Ignition and combustion development for high speed direct injection diesel engines under low temperature cold start conditions. Fuel. 2011;90(4):1556-1566. https://doi.org/10.1016/j.fuel.2011.01.008

[27] Pawlik P, Kania K, Przysucha B. Fault diagnosis of machines operating in variable conditions using artificial neural network not requiring training data from a faulty machine. Eksploat Niezawodn. 2023;25(3):168109. https://doi.org/10.17531/ein/168109

[28] Rakov V, Pikalev O, Bogomolov A, Dymov N. Modeling of engine warm-up with the use of an exhaust gas recuperator at low ambient temperatures. Transp Res Proc. 2021;57:547-552. https://doi.org/10.1016/j.trpro.2021.09.083

[29] Rimkus A, Kozłowski E, Vipartas T, Pukalskas S, Wiśniowski P, Matijošius J. Emission characteristics of hydrogen-enriched gasoline under dynamic driving conditions. Energies. 2025;18(5):1190. https://doi.org/10.3390/en18051190

[30] Slavin V, Shuba Y, Caban J, Matijosius J, Rimkus A, Korpach A et al. The performance of a car with various engine power systems – part I. LOGI – Scientific Journal on Transport and Logistics. 2022;13(1):130-140. https://doi.org/10.2478/logi-2022-0012

[31] Sobaszek Ł, Piasecka I, Flizikowski J, Tomporowski A, Sokolovskij E, Bałdowska-Witos P. Environmentally oriented analysis of benefits and expenditures in the life cycle of a wind power plant. Materials. 2023;16(2):538. https://doi.org/10.3390/ma16020538

[32] Song J, Lee Z, Song J, Park S. Effects of injection strategy and coolant temperature on hydrocarbon and particulate emissions from a gasoline direct injection engine with high pressure injection up to 50 MPa. Energy. 2018;164:512-522. https://doi.org/10.1016/j.energy.2018.09.011

[33] Tauzia X, Karaky H, Maiboom A. Evaluation of a semi-physical model to predict NOx and soot emissions of a CI automotive engine under warm-up like conditions. Appl Therm Eng. 2018;137:521-531. https://doi.org/10.1016/j.applthermaleng.2018.04.005

[34] Tsiuman M, Sadovnyk I. Research on the efficiency of catalytic conversion of exhaust gases from a car engine during warm-up mode. Avtošljachovyk Ukraïny. 2024;2(279): 70-73. https://doi.org/10.33868/0365-8392-2024-2-279-70-73

[35] Yusuf AA, Inambao FL. Effect of cold start emissions from gasoline-fueled engines of light-duty vehicles at low and high ambient temperatures: recent trends. Case Studies in Thermal Engineering. 2019;14:100417. https://doi.org/10.1016/j.csite.2019.100417

[36] Zimakowska-Laskowska M, Kozłowski E, Laskowski P, Wiśniowski P, Świderski A, Orynycz O. Vehicle exhaust emissions in the light of modern research tools: synergy of chassis dynamometers and computational models. Combustion Engines. 2025;200(1):145-154. https://doi.org/10.19206/CE-201224

Magdalena Zimakowska-Laskowska, DEng. – Environment Protection Centre, Motor Transport Institute, Poland.
e-mail: *magdalena.zimakowska-laskowska@its.waw.pl*

Prof. Andrzej Świderski, DSc., DEng. – Motor Transport Institute, Warsaw, Poland.
e-mail: *andrzej.swiderski@its.waw.pl*

Edward Kozłowski, DSc., prof. LUT – Faculty of Management, Lublin University of Technology, Poland.
e-mail: *e.kozlovski@pollub.pl*

Ewa Rostek, MSc. – Centre for Material Testing, Motor Transport Institute, Warsaw, Poland.
e-mail: *ewa.rostek@its.waw.pl*

Piotr Wiśniowski, DEng. – Environment Protection Centre, Motor Transport Institute, Warsaw, Poland.
e-mail: *piotr.wisniowski@its.waw.pl*

Prof. Radovan Madleňák, PhD. – Faculty of Operation and Economics of Transport and Communications, University of Žilina, Slovakia.
e-mail: *radovan.madlenak@uniza.sk*

Ksawery Żbik, MEng. – Environment Protection Centre, Motor Transport Institute, Warsaw, Poland.
e-mail: *ksawery.zbik@its.waw.pl*

Article citation info:
Muszyńska-Pałys J, Orkisz M, Wygonik P. Analysis of the development of energy storage systems in regional aviation. Combustion Engines. 2025;203(4):59-66. https://doi.org/10.19206/CE-205186

Jagoda MUSZYŃSKA-PAŁYS
Marek ORKISZ
Piotr WYGONIK

Combustion Engines
Polish Scientific Society of Combustion Engines

Analysis of the development of energy storage systems in regional aviation

ARTICLE INFO

Received: 3 March 2025
Revised: 12 May 2025
Accepted: 15 May 2025
Available online: 30 September 2025

Regional aviation plays a crucial role in Europe's transportation system, connecting smaller cities and peripheral regions. In the face of growing demands for CO_2 emission reductions and improved energy efficiency, there is an increasing interest in hybrid and electric propulsion systems in this sector. A key component of these systems is rechargeable batteries, which must meet stringent requirements for energy density, weight, safety, and reliability. The article analyzes available rechargeable battery technologies that can power regional aircraft propulsion systems, including lithium-ion, lithium-sulphur, and metal-air rechargeable batteries. It also discusses current trends in energy storage technology development and the challenges of their implementation in aviation.

Key words: *aviation, regional aviation, rechargeable battery*

1. Introduction

Regional flights play a key role in the European transportation system, providing fast and convenient access to smaller cities, peripheral regions, and islands not served by larger airlines. Regional flights are usually shorter routes, usually within one country or between neighbouring countries. While between one and two hours. Regional flight airlines choose, with capacities ranging from 20 to 100 seats. These can be either jet-powered or turboprop aircraft. Turboprop planes, such as the ATR 72 or Bombardier Q400, are especially efficient on routes of approximately 500–700 km due to their fuel economy and ability to operate on shorter runways. As a result, they are ideally suited for serving smaller regional airports, providing transport connectivity in peripheral, island, and remote regions [37, 55]. For example, the flight from Copenhagen to Tórshavn in the Faroe Islands takes just 1.5 hours by plane, while the ferry journey takes a whopping 36 hours.

In 2023, approximately 1.5 million regional flights took place in Europe, accounting for about 30% of all passenger flights on the continent [60]. Although regional aviation is crucial for mobility, it also generates significant environmental challenges. These flights emit approximately 50 million tons of CO_2 annually in Europe, with an average CO_2 emission of 150 grams per passenger per kilometer [1, 57, 59]. Regional airports are also responsible for approximately 20% of the total noise pollution generated by aviation [60].

In light of the need to reduce aviation emissions, optimizing energy consumption in regional aircraft becomes crucial. In addition to the energy required for thrust generation, these aircraft must power numerous onboard systems, such as navigation, communication, flight control, safety, and passenger comfort systems [9]. Some of these systems rely on electrical power, whereas others, such as pneumatic or hydraulic systems, use compressed air from the engine or working fluid pumped by hydraulic pumps. It makes all these systems intrinsically linked to the processes occurring in the internal combustion engine. The More Electric Aircraft (MEA) concept aims to gradually replace traditional mechanical, pneumatic, and hydraulic systems with their electric counterparts [30, 43], which increases energy efficiency, reduces aircraft weight by eliminating complex installations, and improves reliability and system maintenance [43]. In the case of traditionally powered aircraft, even if they are based on the MEA concept, the electrical power required to operate systems other than propulsion, such as avionics, lighting, anti-icing systems, or air conditioning, usually comes from generators driven by the aircraft's main engines [5]. These generators convert mechanical energy from the engine shafts into electrical energy, and additional power sources may include rechargeable batteries, which serve as backup or supplementary power, particularly during system startup.

Hybrid-powered aircraft have been available on the market for some time [27, 64], and new designs of this type continue to emerge; however, their further development requires advanced energy storage technologies. Rechargeable batteries are most commonly used for this purpose [20], although fuel cells and supercapacitors are also being tested [33, 56]. The types of rechargeable batteries used in aviation include: alkaline, lead-acid, nickel-cadmium, nickel-metal hydride, lithium-ion, and lithium-polymer batteries, with the latter two being the most widely available [21] and developing lithium-sulphur batteries. It is important to say that research is also being conducted on the use of graphene and magnesium in rechargeable batteries [58]. However, not all of these are concerned with weight, energy density, reliability, and safety.

To summarize, the rechargeable batteries used in modern aviation are divided into those powering various onboard systems and those responsible for providing energy for thrust generation. The requirements for the chosen technology differ depending on the application.

This article aims to analyze available rechargeable battery technologies that can power aircraft propulsion systems. The authors focus only on those that can be used in regional aviation. This article also aims to highlight current trends in energy storage technologies and point out the

main challenges and opportunities related to applying these solutions in aviation.

2. Battery parameters in the context of aviation applications

2.1. General considerations for aviation batteries

When evaluating rechargeable battery technologies for aviation, certain, performance factors become especially important. These include how much energy a battery can store and deliver, how long it lasts, and how efficiently it operates. Below is a breakdown of the most relevant parameters that engineers consider when determining whether a given battery can actually meet the demands of flight.

2.2. Energy density as a key factor in aircraft design

Energy density (Wh/kg or Wh/dm^3) [29] reflects how much energy a battery stores relative to its weight or volume. In aviation, where every extra kilogram is important, this is a top priority. Simply put, a higher energy density implies lighter systems and a longer range. For fully electric regional aircraft to become practical, experts suggest that they will need batteries with over 500 Wh/kg – something current technologies are still striving to reach [35].

2.3. Specific power and its role during critical flight phases

Specific power [W/kg] is about how fast a rechargeable battery can deliver energy relative to its mass. That matters most during phases like takeoff, where systems need much power in a short time. While there's no official minimum, higher specific power is always better in aviation because it helps reduce weight and improves responsiveness.

2.4. Cycle life and long-term reliability of aviation batteries

This refers to how many charge and discharge cycles the battery can go through before its performance starts to degrade. Aircraft rechargeable batteries are charged and discharged frequently, so a longer cycle life is not just convenient – it is critical. A, good target is around 3000 cycles with minimal capacity loss, though some advanced types can push this even further.

2.5. Energy efficiency and minimization of losses

Efficiency [%] [18, 40] measures how much of the energy used to charge the battery can actually be recovered during discharge. Losses here usually show up as heat. The more efficient the battery, the better it performs overall – especially important for electric aircraft where every watt counts.

2.6. Cost per unit of stored energy

Affordability still matters, even in aviation. The cost of storing each unit of energy [$/kWh] needs to be competitive, especially if electric aircraft are to scale commercially. Lowering this cost could be key to making the switch from fossil fuels.

2.7. Charging current and turnaround time

Charging current [A] [40] defines how quickly a battery can be safely recharged. Faster charging means less downtime between flights, which is particularly useful for short-haul or commuter aircraft that have tight turnarounds.

2.8. Discharging current and high-demand flight phases

Just like with charging, the discharge current [A] defines how much power the battery can release at any given moment. High discharge rates are needed during takeoff and other demanding situations, so this value directly affects aircraft capability and safety.

2.9. Depth of discharge as a compromise between range and durability

Depth of discharge (DoD) [%] [3] shows how much of the batteries total capacity can be used in a single cycle. Deeper discharge gives more energy per flight, but it can also reduce the batteries lifespan if not properly managed. In most aviation applications, staying under 80% DoD is seen as a good compromise between output and durability.

Each of these parameters has a direct impact on the viability of a battery system for flight. Some technologies might excel in one area but fall short in another. Among them all, energy density remains the biggest hurdle. Unless batteries can significantly close the gap with traditional aviation fuels in this regard, their role in long-range commercial aviation will likely stay limited.

3. First rechargeable batteries

The first useful alkaline battery was developed in 1949 by Canadian chemist Lewis Frederick Urry for Eveready (now Energizer). Replacing the acidic electrolyte with an alkaline one significantly improved efficiency and enabled the production of commercially viable batteries. Alkaline batteries are single-use, devices, although rechargeable alkaline, batteries are also available, their performance, however, is lower than, other types of rechargeable batteries [34].

The history, of rechargeable batteries begin in 1800 when Alessandro Volta created the first battery (disposable battery) made, of copper and zinc plates. The first mass-producing battery was created in 1802 by William Cruickshank, and the first rechargeable battery in 1859, when Gaston Planté developed the lead-acid battery, which is still in use today [34, 36].

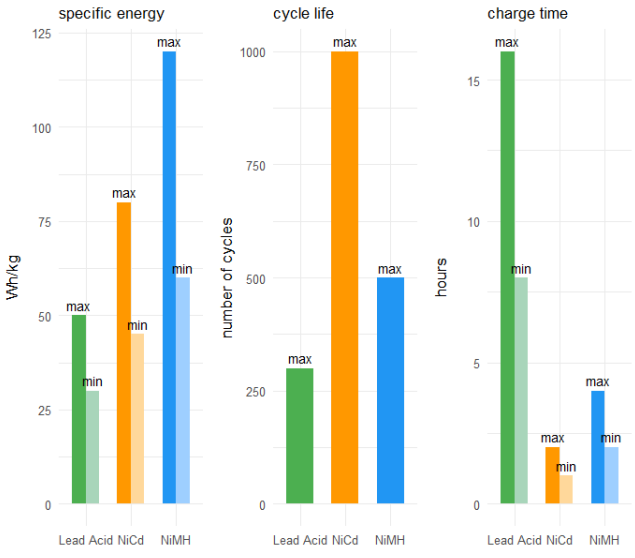

Fig. 1. Comparison of the most important parameters of lead-acid, nickel-cadmium (NiCd), and nickel-metal hydride (NiMH) rechargeable batteries [4]

The early 20th century saw the emergence of nickel-cadmium rechargeable batteries. They were slightly more efficient than lead-acid batteries but provided resistance to temperatures as low as –40°C and higher voltages [46]. However, due to the harmful cadmium content, they were banned throughout the European Union in 2004 [8].

Nickel-metal hydride (NiMH) batteries represent an improved version of nickel-cadmium batteries, offering higher capacity and, eliminating the toxicity issue of cadmium [7]. They, are lighter and exhibit less memory effect compared to NiCd. In aviation, they have been used in some auxiliary systems and portable devices.

Figure 1 shows a comparison of the key parameters of lead-acid, nickel-cadmium (NiCd), and nickel-metal hydride (NiMH), rechargeable batteries.

4. Lithium-ion rechargeable batteries

Initially, lithium batteries used pure metallic lithium as the anode material, providing exceptionally high specific energy and electrochemical potential. However, this design proved problematic because the charging process led to the formation of dendrites – needle-like, lithium structures that could pierce the separator, causing short circuits and a rapid temperature increase [53, 66, 78]. As a result, although lithium-metal rechargeable batteries were highly efficient, they were unsafe and had to be withdrawn from the market.

To address these issues, researchers began searching for a more stable solution. Instead of metallic lithium as the anode, graphite was introduced – a material capable of safely storing lithium ions within its layered structure [2]. In lithium-ion batteries, lithium ions, which are charged particles, move between the graphite anode and the cathode. This ion migration process is the core mechanism of the battery: during charging, lithium ions travel from the cathode to the anode, and during discharging, they return from the anode to the cathode, releasing electrical energy [24]. This structural change made lithium-ion batteries significantly safer and more stable while maintaining high energy density.

The previously mentioned cathodes are a key component affecting the performance, lifespan, and safety of the cells. They are made from various chemical elements, including nickel, manganese, cobalt, aluminum, phosphorus, and iron. These elements, in different combinations, enable an optimal balance between energy density, power density, durability, and safety [31, 75]. The most commonly uses types of lithium-ion rechargeable batteries include:

- Lithium iron phosphate (LFP)
- lithium nickel cobalt aluminum oxide (NCA)
- lithium nickel manganese cobalt oxide (NMC) [48].

Figure 2 presents a comparison of the key parameters of these lithium-ion battery types.

The Boeing 787 Dreamliner was one of the first commercial aircraft to use lithium-ion batteries to power auxiliary systems. In January 2013, two incidents occurred: an APU battery fire on a Japan Airlines aircraft and an emergency landing of an All Nippon Airways flight due to an issue with the main battery. The FAA grounded all Dreamliners, and Boeing introduced additional steel enclosures and ventilation systems to enhance safety [17, 71].

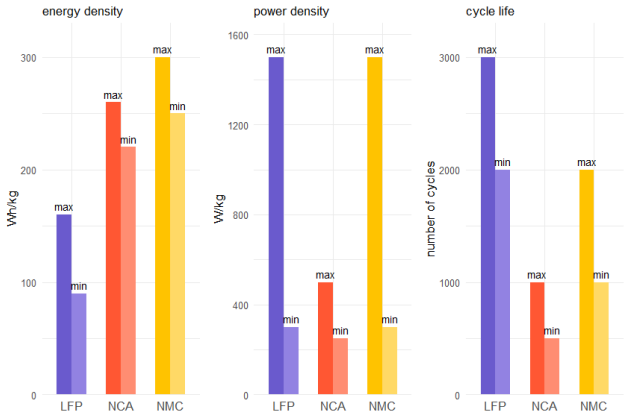

Fig. 2. Comparison of the most important parameters of different types of lithium-ion rechargeable batteries [52]

In December 2019, the first flight of a fully electric commercial aircraft powered by lithium-ion batteries took place. A modified de Haviland Canada DHC-2 Beaver, equipped with a magni500 electric motor producing approximately 552 kW (750 hp), took off for a 15-minute test flight in Richmond, Canada [23, 72].

Hyundai and Uber partnered to develop electric vertical takeoff and landing (eVTOL) aircraft. In 2020, during the CES trade show in Las Vegas, they unveiled the concept of a flying taxi called the S-A1. This vehicle is designed to be fully electric, powered by lithium-ion batteries, capable of reaching speeds of up to 290 km/h, and offering a range of approximately 100 km [68].

5. Lithium-ion polymer rechargeable batteries

Lithium-ion polymer rechargeable batteries (LiPo) are modern variant of lithium-ion batteries that use a polymer electrolyte instead of a liquid one [10]. Thanks to the use of a flexible electrolyte, LiPo batteries, can be shaped into various forms and, sizes, with an additional advantage of improved safety due to the elimination of flammable electrolytes [16, 38]. Their theoretical energy density is estimated to be between 500–800 Wh/kg, but currently achievable values range from 400–500 Wh/kg [52, 65, 77].

Additionally, LiPo batteries can provide better performance at high altitudes due to their lower sensitivity to pressure changes. However, they have a slightly shorter cycle life and greater susceptibility to mechanical, damage compared to lithium-ion batteries [16, 52].

The graph presented in Fig. 3 offers a visual comparison, of the properties of liquid electrolytes, which are standard in, lithium-ion batteries, and polymer electrolytes based on PEO, used in lithium-ion polymer batteries. It can be considered an indirect comparison of lithium-ion and lithium-ion polymer battery technologies through the lens of the type of electrolyte used.

Liquid, electrolytes are characterized by higher ionic conductivity and lower interface resistance, which contribute to better current efficiency. In contrast, PEO-based polymer electrolytes offer increased safety, higher electrochemical stability, and excellent electrode compatibility. Additionally, PEO polymers stand out due to their ease of ,processing, better thermal stability, and more, effective suppression of lithium dendrite formation, minimizing the

risk of short circuits and improving cell, lifespan. The cost, of both materials is comparable.

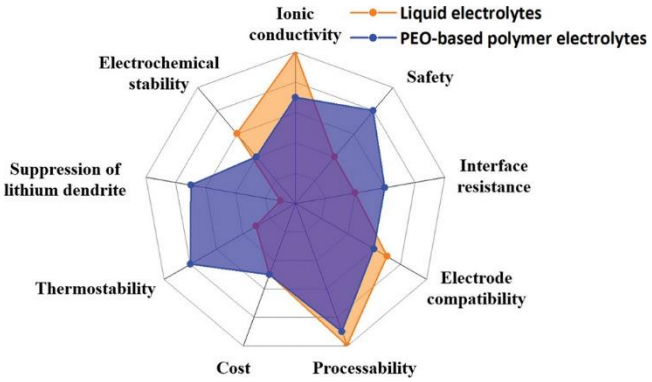

Fig. 3. Comparison of properties of liquid electrolytes and polymer electrolytes based on PEO [38]

6. Metal-air rechargeable batteries

6.1. Fundamentals of metal–air rechargeable batteries

Metal-air, rechargeable batteries are a group of energy storage systems in which metal serves as the anode, while oxygen from the air acts as the oxidizer at the cathode [6]. They are a promising technology due to their high theoretical energy density, making them attractive for transportation, and energy storage. Depending on the metal used, several key types of these batteries exist, each with different electrochemical properties.

6.2. Lithium-air rechargeable batteries

Lithium-air rechargeable batteries offer a very high energy density of 3600 Wh/kg, which is their biggest advantage and main superiority over other energy storage technologies [13, 38, 62]. Due to the use of lithium, a low-mass material, they provide high capacity at a relatively low weight. However, in practice, their performance is significantly lower than theoretical values, mainly due to clogging of the porous cathode by solid oxygen reduction products, which limits the amount of stored energy. Additionally, phase transitions between gaseous oxygen (charging product) and solid Li_xO (discharging product) cause large potential differences between charging and discharging, leading to energy losses [42, 54]. Limited cycle life and electrolyte degradation result in a rapid capacity decline after just a few charge-discharge cycles [12]. Problems also arise under high loads, where the stability of electrochemical reactions is compromised, and system efficiency decreases. The requirement for pure oxygen, supplied from external sources or through air purification systems, further increases complexity and limits the potential commercialization of this technology [22, 32].

6.3. Zinc-air rechargeable batteries

Zinc-air rechargeable batteries achieve a high theoretical energy density of approximately 1200 Wh/kg [51], while their production costs remain low. They are also environmentally friendly, as they do not contain toxic substances [6, 41, 70, 74]. Their ,main drawback is a limited number of charge cycles, leading to faster battery degradation. Cathode reactions are, slow, resulting in low energy efficiency. Additionally, the large voltage difference between charging and discharging reduces battery efficiency. Under high load and humidity conditions, performance decreases, and difficulties in controlling air access can cause operational instability, affecting their long-term functionality [9, 49].

6.4. Aluminum-air rechargeable batteries

Aluminum-air rechargeable batteries offer high energy density and relatively low production costs [19]. Additionally, aluminum, as an ,anode material, is safe, easy to transport, and recyclable without greenhouse gas emissions [67]. The main drawbacks include low reversibility of electrochemical reactions, which limits the number of charge cycles, and anode corrosion in contact with the electrolyte, leading to H_2 gas emissions and reduced battery lifespan [25, 63]. The aluminum, reduction process also requires significant energy input, lowering charging efficiency [61].

6.5. Sodium-air rechargeable batteries

Sodium-air rechargeable batteries have moderate energy density but offer a cheaper alternative to lithium-air batteries due to the wide availability and low cost of sodium [50]. Their development is still in an early stage due to limitations in efficiency, durability, and cycle stability. Nevertheless, these batteries are considered a promising solution for large-scale energy storage, particularly in stationary applications where cost outweighs energy density concerns [14, 73].

6.6. Potassium-air rechargeable batteries

Potassium-air rechargeable, batteries, like sodium-air batteries, have potentially lower production costs due to the broad availability of potassium, as a low-cost anode material. However, their development faces significant challenges, including limited reversibility of electrochemical reactions and cathode stability issues. These technological barriers currently make the commercial application of these batteries highly limited [11, 69].

6.7. Iron-air rechargeable batteries

Iron-air rechargeable batteries attract attention due to their exceptionally low material costs and high chemical stability, making, them a potentially cost-effective solution for large-scale energy storage. Although their theoretical energy density is approximately 1200 Wh/kg, current technological limitations result in significantly lower practical energy density. Ongoing research focuses on improving electrochemical efficiency, cycle stability, and reducing material, losses to bring their parameters closer to their full, theoretical potential and enhance commercialization prospects [15, 47, 76].

Lithium-air rechargeable batteries offer the highest energy density but have limited durability and low efficiency under high loads. Potassium-air batteries are the cheapest but have the lowest energy density and issues with reaction reversibility. Sodium-air, batteries, while cheaper than lithium-based ones, are less efficient. Iron-air batteries have low material costs and high stability, but their practical energy density remains significantly lower than theoretical values. Aluminum, air batteries offer high energy density, but their limitations include anode corrosion and low reaction reversibility.

7. Lithium-sulfur rechargeable batteries

A lithium-sulfur rechargeable battery consists of a cathode with a capacity of 1672 mAh/g, made of sulfur, and an anode made of metallic lithium, with a capacity of 3860 mAh/g. Due to these properties, these rechargeable batteries offer an exceptional theoretical energy density of 2600 Wh/kg [38]. Because sulfur is widely available, lithium-sulfur rechargeable, batteries are inexpensive. Unfortunately, their lifespan is limited due to processes like "stripping" (loss of lithium from the anode) and "shuttling" (migration of lithium polysulfides), which lead to capacity loss and degradation of active materials. Additionally, difficulties in controlling reactions during charge and discharge cycles affect the cell's stability, limiting the number of, cycles in which the rechargeable battery can maintain high performance [26, 39, 40, 44, 45, 79].

8. Summary

The COVID-19 pandemic, caused a significant reduction in air traffic, temporarily slowing the growth of emissions. However, the sector's return to full activity, with forecasts exceeding pre-pandemic emission levels [28], increases the pressure to introduce more environmentally friendly and quieter aircraft. As part of global efforts for sustainable development, progress towards low-emission technologies in aviation has become a key element of strategies aimed at minimizing the sector's impact ,on climate change. The, main challenge in the electrification of aviation is developing batteries that provide sufficient power at a low weight. The chart presented in Fig. 4 compares the energy density of various types of rechargeable batteries discussed in the article. The black horizontal line indicates the minimum energy density that batteries must achieve to provide sufficient energy for aircraft operations during regional flights. Among the currently available types of batteries, only lithium-ion-polymer and lithium-sulfur rechargeable batteries meet this requirement. Unfortunately, both types still face challenges related to production costs, chemical stability, and lifespan. Despite their potential, they are not yet widely used in aviation due to technological and economic limitations.

The chart, presented in Fig. 5 compares the life cycle of selected types of rechargeable batteries. The chart shows that lithium iron phosphate ,rechargeable batteries, despite having nearly, the lowest energy density, have by far the longest life cycle. On the other hand, rechargeable battery types that could potentially compete with aviation fuel in terms of energy density have a significantly shorter life cycle.

The literature, analysis shows that there is no single type of rechargeable battery that meets all the requirements for energy storage systems in aviation. Each mentioned type offers specific, benefits but also faces limitations that determine its application depending on the project's specific requirements.

Aviation rechargeable ,batteries must meet high demands for delivering large amounts of power, especially during the takeoff and climb phases. Lithium-ion rechargeable batteries, despite their good energy efficiency, offer a relatively low, power-to-weight ratio (1–2 kW/kg), making them unable to provide power levels achieved by jet engines (5–10 kW/kg). As a, result, larger and heavier battery packs must be used, which impacts the overall mass and design of the propulsion system.

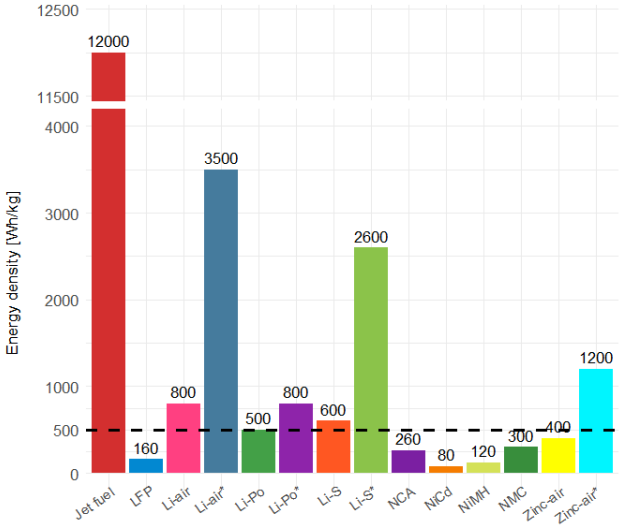

Fig. 4. Comparison of energy densities of different types of rechargeable batteries | * maximum theoretical energy density of a given type of rechargeable battery

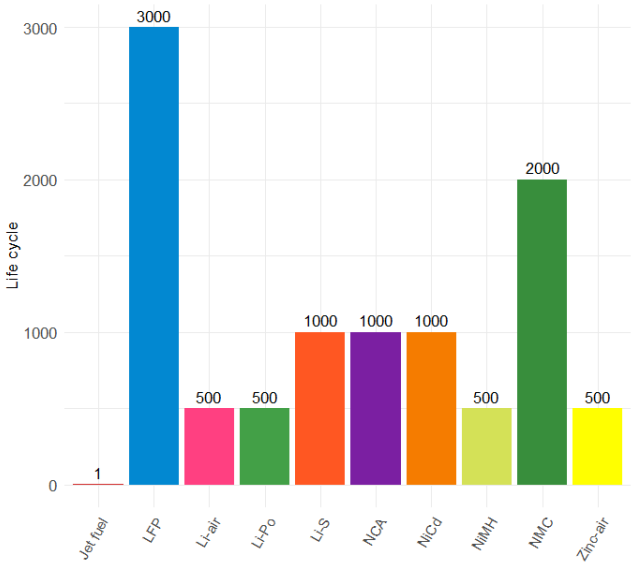

Fig. 5. Comparison of the life cycle of different types of rechargeable batteries

Additionally, frequent changes between high and low power states can accelerate the aging of rechargeable batteries, requiring the use of battery types that are resistant to these fluctuations.

Another challenge ,is the cooling system, which must adapt to changing thermal conditions during different flight phases.

Moreover, the environmental impact of battery technologies, particularly the extraction of raw materials such as lithium, cobalt, and nickel, can lead to significant ecological damage if these processes are not carried out sustainably.

Finally, the certification process for new battery technologies in aviation is complex, time-consuming, and expensive, presenting a significant barrier to the faster deployment of innovative solutions.

Therefore, the further development and implementation of energy storage technologies in aviation requires a balanced approach that considers both operational needs as well as environmental, ecological, and legal challenges facing the aviation industry.

Nomenclature

APU	auxiliary power unit
DoD	depth of discharge
FAA	Federal Aviation Administration
LFP	lithium iron phosphate
LiPo	lithium-ion polymer
MEA	more electric aircraft
NCA	lithium nickel cobalt aluminum oxide
NiCd	nickel-cadmium
NiMH	nickel-metal hydride
NMC	lithium nickel manganese cobalt oxide

Bibliography

[1] Analysis of traffic in Polish airports in the first quarter of the year 2021.

[2] Asenbauer J, Eisenmann T, Kuenzel M, Kazzazi A, Chen Z, Bresser D. The success story of graphite as a lithium-ion anode material – fundamentals, remaining challenges, and recent developments including silicon (oxide) composites. Sustainable Energy Fuels. 2020;4(11):5387-5416. https://doi.org/10.1039/D0SE00175A

[3] Battery charging and discharging parameters. PVEducation. https://www.pveducation.org/pvcdrom/battery-characteristics/battery-charging-and-discharging-parameters?utm_source=chatgpt.com (accessed on 2025.02.04).

[4] Battery University Homepage. https://batteryuniversity.com/ (accessed on 2025.02.13).

[5] Benzaquen J, He JB, Mirafzal B. Toward more electric powertrains in aircraft: technical challenges and advancements. CES Transactions on Electrical Machines and Systems. 2021;5(3):177-193. https://doi.org/10.30941/CESTEMS.2021.00022

[6] Bi X, Jiang Y, Chen R, Du Y, Zheng Y, Yang R et al. Rechargeable zinc–air versus lithium–air battery: from fundamental promises toward technological potentials. Adv Energy Mater. 2024;14(6). https://doi.org/10.1002/aenm.202302388

[7] Bondier JR, Michel G, Propper A, Badot PM. Harmful effects of cadmium on olfactory system in mice. Inhal Toxicol. 2008;20(13):1169-1177. https://doi.org/10.1080/08958370802207292

[8] CELEX_32006L0066_PL_TXT.

[9] Chang H, Shi LN, Chen YH, Wang PF, Yi TF. Advanced MOF-derived carbon-based non-noble metal oxygen electrocatalyst for next-generation rechargeable Zn-air batteries. Coord Chem Rev. 2022;473:214839. https://doi.org/10.1016/J.CCR.2022.214839

[10] Chattopadhyay J, Pathak TS, Santos DMF. Applications of polymer electrolytes in lithium-ion batteries: a review. Polymers. 2023;15:3907. https://doi.org/10.3390/POLYM15193907

[11] Chen J, Zhang H, Yu F, Chen Y. Evaluation of polymetallic phosphide cathodes for sodium-air batteries by distribution of relaxation time. ACS Appl Mater Interfaces. 2024;16(20): 26226-26233. https://doi.org/10.1021/acsami.4C03678

[12] Chen K, Yang DY, Huang G, Zhang XB. Lithium-air batteries: air-electrochemistry and anode stabilization. Acc Chem Res. 2021;54(3):632-641. https://doi.org/10.1021/ACS.ACCOUNTS.0C00772

[13] Chen Y, Xu J, He P, Qiao Y, Guo S, Yang H et al. Metal-air batteries: progress and perspective. Sci Bull (Beijing). 2022; 67(23):2449-2486. https://doi.org/10.1016/J.SCIB.2022.11.027

[14] The Chinese are investing in the world's largest sodium-ion energy storage facility – RES Industry in Poland. https://top-oze.pl/chinczycy-inwestuja-w-najwiekszy-na-swiecie-magazyn-energii-sodowo-jonowej/ (accessed on 2025.02.16).

[15] Deyab MA, Mohsen Q. Improved battery capacity and cycle life in iron-air batteries with ionic liquid. Renew Sust Energ Rev. 2021;139:110729. https://doi.org/10.1016/J.RSER.2021.110729

[16] Domalanta MRB, Castro MT, Ocon JD, del Rosario JAD. An electrochemical-thermal multiphysics model for lithium polymer battery. Chem Eng Trans. 2022;94:145-150. https://doi.org/10.3303/CET2294024

[17] Dreamliner: Boeing 787 planes grounded on safety fears. BBC News. Published online January 17, 2013. https://www.bbc.co.uk/news/business-21054089 (accessed on 2025.02.13).

[18] Eftekhari A. Energy efficiency: a critically important but neglected factor in battery research. Sustain Energy Fuels. 2017;1(10):2053-2060. https://doi.org/10.1039/C7SE00350A

[19] Egan DR, Ponce De León C, Wood RJK, Jones RL, Stokes KR, Walsh FC. Developments in electrode materials and electrolytes for aluminium–air batteries. J Power Sources. 2013;236:293-310. https://doi.org/10.1016/J.JPOWSOUR.2013.01.141

[20] Finger DF. Methodology for multidisciplinary aircraft design under consideration of hybrid-electric propulsion technology. Doctoral Thesis. RMIT University 2020.

[21] Gao XZ, Hou ZX, Guo Z, Chen XQ. Reviews of methods to extract and store energy for solar-powered aircraft. Renew Sust Energ Rev. 2015;44:96-108. https://doi.org/10.1016/j.rser.2014.11.025

[22] Grande L, Paillard E, Hassoun J, Park JB, Lee YJ, Sun YK et al. The lithium/air battery: still an emerging system or a practical reality? Adv Mater. 2015;27(5):784-800. https://doi.org/10.1002/adma.201403064

[23] Harbour air and magniX announce successful flight of world's first commercial electric airplane. https://www.prnewswire.com/il/news-releases/harbour-air-and-magnix-announce-successful-flight-of-worlds-first-commercial-electric-airplane-300972566.html?utm_source=chatgpt.com (accessed on 2025.02.13).

[24] Horiba T. Lithium-ion battery systems. P IEEE. 2014;102(6): 939-950. https://doi.org/10.1109/JPROC.2014.2319832

[25] Hosseini S, Xu TH, Masoudi Soltani S, Ko TE, Lin YJ, Li YY. The efficient acetoxy-group-based additives in protect-

ing of anode in the rechargeable aluminium-air batteries. Int J Hydrogen Energy. 2022;47(1):501-516. https://doi.org/10.1016/j.ijhydene.2021.10.030
[26] Hwang JY, Park H, Kim H, Kansara S, Sun YK. Advanced cathodes for practical lithium-sulfur batteries. Acc Mater Res. 2025;6(2):245-258. https://doi.org/10.1021/accountsmr.4c00368
[27] Hypstair home. http://www.hypstair.eu/ (accessed on 2025. 02.04).
[28] IATA 2023. https://www.iata.org/en/iata-repository/publications/economic-reports/global-outlook-for-air-transport----june-2023/ (accessed on 2024.06.12).
[29] Jha AR. MEMS and nanotechnology-based sensors and devices for communications, medical and aerospace applications. CRC Press 2008.
[30] Jia Y, Rajashekara K. Induction machine for more electric aircraft: enabling new electrical power system architectures. IEEE Electrification Magazine. 2017;5:25-37. https://doi.org/10.1109/MELE.2017.2755267
[31] Johnson CS. Charging up lithium-ion battery cathodes. Joule. 2018;2(3):373-375. https://doi.org/10.1016/j.joule.2018.02.020
[32] Jordan JW, Vailaya G, Holc C, Jenkins M, McNulty RC, Puscalau C et al. A lithium–air battery and gas handling system demonstrator. Faraday Discuss. 2024;248:381-391. https://doi.org/10.1039/D3FD00137G
[33] Khan N, Dilshad S, Khalid R, Kalair AR, Abas N. Review of energy storage and transportation of energy. Energy Storage. 2019;1(3):e49. https://doi.org/10.1002/est2.49
[34] Křepelková M. Evolution of batteries: from experiments to everyday usage. Engineering, Materials Science. 2017. https://api.semanticscholar.org/CorpusID:209515152
[35] Kühnelt H, Beutl A, Mastropierro F, Laurin F, Willrodt S, Bismarck A et al. Structural batteries for aeronautic applications – state of the art, research gaps and technology development needs. Aerospace. 2022;9(1):7. https://doi.org/10.3390/aerospace9010007
[36] Kurzweil P. Gaston Planté and his invention of the lead-acid battery – the genesis of the first practical rechargeable battery. J Power Sources. 2010;195(14):4424-4434. https://doi.org/10.1016/j.jpowsour.2009.12.126
[37] Leveraging our national investments to energize the American travel experience. Regional Air Mobility. https://ntrs.nasa.gov/citations/20210014033.
[38] Li J, Cai Y, Wu H, Yu Z, Yan X, Zhang Q et al. Polymers in lithium-ion and lithium metal batteries. Adv Energy Mater. 2021;11(15). https://doi.org/10.1002/aenm.202003239
[39] Li J, Sun L, Lv G, Liao L. Application of clay minerals in lithium-sulfur batteries: a review. J Energy Storage. 2025; 106:114852. https://doi.org/10.1016/j.est.2024.114852
[40] Li K, Tseng KJ. Energy efficiency of lithium-ion battery used as energy storage devices in micro-grid. IECON 2015 – 41st Annual Conference of the IEEE Industrial Electronics Society. 2015:5235-5240. https://doi.org/10.1109/iecon.2015.7392923
[41] Liu L, Hu Z, Wang M, Ma J, Chen Z, Ning X et al. Ultrathin NiFe-LDH nanosheets strongly coupled with MOFs-derived hybrid carbon nanoflake arrays as a self-supporting bifunctional electrocatalyst for flexible solid Zn-air batteries. J Alloys Compd. 2022;925:166665. https://doi.org/10.1016/j.jallcom.2022.166665
[42] Lu YC, Gallant BM, Kwabi DG, Harding JR, Mitchell RR, Whittngham MS et al. Lithium–oxygen batteries: bridging mechanistic understanding and battery performance. Energy Environ Sci. 2013;6(3):750-768. https://doi.org/10.1039/c3ee23966g
[43] Madonna V, Giangrande P, Galea M. Electrical power generation in aircraft: review, challenges, and opportunities. IEEE Transactions on Transportation Electrification. 2018;4(3): 646-659. https://doi.org/10.1109/tte.2018.2834142
[44] Manthiram A, Chung SH, Zu C. Lithium–sulfur batteries: progress and prospects. Adv Mater. 2015;27(12):1980-2006. https://doi.org/10.1002/adma.201405115
[45] Manthiram A, Fu Y, Su YS. Challenges and prospects of lithium-sulfur batteries. Acc Chem Res. 2013;46(5):1125-1134. https://doi.org/10.1021/ar300179v
[46] McDowall J. Nickel-cadmium batteries for energy storage applications. Fourteenth Annual Battery Conference on Applications and Advances. Proceedings of the Conference (Cat. No.99TH8371). Long Beach 1999:303-308. https://doi.org/10.1109/bcaa.1999.796008
[47] McKerracher RD, Poncedeleon C, Wills RGA, Shah AA, Walsh FC. A review of the iron–air secondary battery for energy storage. Chempluschem. 2015;80(2):323-335. https://doi.org/10.1002/cplu.201402238
[48] Mekonnen Y, Sundararajan A, Sarwat AI. A review of cathode and anode materials for lithium-ion batteries. SoutheastCon 2016, Norfolk 2016:1-6. https://doi.org/10.1109/secon.2016.7506639
[49] Meng L, Liu W, Lu Y, Liang Z, He T, Li J et al. Lamellar-stacked cobalt-based nanopiles integrated with nitrogen/sulfur co-doped graphene as a bifunctional electrocatalyst for ultralong-term zinc-air batteries. J Energy Chem. 2023;81:633-641. https://doi.org/10.1016/j.jechem.2023.02.035
[50] Murugesan C, Senthilkumar B, Barpanda P. Biowaste-derived highly porous n-doped carbon as a low-cost bifunctional electrocatalyst for hybrid sodium-air batteries. ACS Sustain Chem Eng. 2022;10(28):9077-9086. https://doi.org/10.1021/acssuschemeng.2c01300
[51] Nazir G, Rehman A, Lee JH, Kim CH, Gautam J, Heo K et al. A review of rechargeable zinc–air batteries: recent progress and future perspectives. Nano-Micro Letters. 2024; 16(1):1-44. https://doi.org/10.1007/s40820-024-01328-1
[52] Pattanayak T, Mavris D. Battery technology in aviation: current state and future prospects. Enrgxiv. https://doi.org/10.31224/4220
[53] Qian L, Zheng Y, Or T, Park HW, Gao R, Park M et al. Advanced material engineering to tailor nucleation and growth towards uniform deposition for anode-less lithium metal batteries. Small. 2022;18(50):2205233. https://doi.org/10.1002/smll.202205233
[54] Qiao Y, Jiang K, Deng H, Zhou H. A high-energy-density and long-life lithium-ion battery via reversible oxide–peroxide conversion. Nature Catalysis. 2019;2(11):1035-1044. https://doi.org/10.1038/s41929-019-0362-z
[55] Regional air mobility: a short-range flight renaissance? | McKinsey. 2023. https://www.mckinsey.com/industries/aerospace-and-defense/our-insights/short-haul-flying-redefined-the-promise-of-regional-air-mobility#/ (accessed on 2024.08.09).
[56] Rendón MA, Sánchez RCD, Gallo MJ, Anzai AH. Aircraft hybrid-electric propulsion: development trends, challenges and opportunities. Journal of Control, Automation and Electrical Systems. 2021;32(5):1244-1268. https://doi.org/10.1007/S40313-021-00740-X
[57] Skobiej K. A review of hydrogen combustion and its impact on engine performance and emissions. Combustion Engines. 2025;200(1):64-70. https://doi.org/10.19206/CE-195470
[58] Sliwinski J, Gardi A, Marino M, Sabatini R. Hybrid-electric propulsion integration in unmanned aircraft. Energy. 2017; 140:1407-1416. https://doi.org/10.1016/j.energy.2017.05.183

[59] Sroka ZJ, Heda R. Experimental verification of changes in the control map of a diesel engine operation due to fuel consumption. Combustion Engines. 2025;200(1):31-36. https://doi.org/10.19206/CE-194472
[60] Statistics, analyses – ULC. 2024. https://www.ulc.gov.pl/pl/statystyki-analizy (accessed on 2024.08.09).
[61] Suresh T, Kumar SR, Nithyadharseni P. Aluminium air batteries for sustainable environment: a review. Journal of Alloys and Compounds Communications. 2025;6:100048. https://doi.org/10.1016/j.jacomc.2024.100048
[62] Tan P, Jiang HR, Zhu XB, An L, Jung CY, Wu MC et al. Advances and challenges in lithium-air batteries. Appl Energy. 2017;204:780-806. https://doi.org/10.1016/j.apenergy.2017.07.054
[63] Tan WC, Saw LH, Yew MC, Thiam HS, Kuo PY. Characterization of the aluminium-air battery utilizing a polypropylene separator with corrosion inhibition ability. Chem Eng J. 2024;488:151106. https://doi.org/10.1016/j.cej.2024.151106
[64] Tecnam P2010 H3PS Hybrid Private I-EASA – AirTeam-Images.com. https://www.airteamimages.com/tecnam-p2010_i-easa_private_402732 (accessed on 2025.02.04).
[65] Toghyani S, Baakes F, Zhang N, Kühnelt H, Cistjakov W, Krewer U. Model-based design of high energy all-solid-state Li batteries with hybrid electrolytes. J Electrochem Soc. 2022;169(4):040550. https://doi.org/10.1149/1945-7111/ac653b
[66] Tomaszewska A, Chu Z, Feng X, O'Kane S, Liu X, Chen J et al. Lithium-ion battery fast charging: a review. eTransportation. 2019;1:100011. https://doi.org/10.1016/j.etran.2019.100011
[67] Trowell KA, Goroshin S, Frost DL, Bergthorson JM. Aluminum and its role as a recyclable, sustainable carrier of renewable energy. Appl Energy. 2020;275:115112. https://doi.org/10.1016/j.apenergy.2020.115112
[68] Uber and Hyundai Motor announce aerial ridesharing partnership, release new full-scale air taxi model at CES. https://www.hyundai.com/worldwide/en/newsroom/detail/uber-and-hyundai-motor-announce-aerial-ridesharing-partnership%252C-release-new-full-scale-air-taxi-model-at-ces-0000000738?utm_source=chatgpt.com (accessed on 2025.02.13).
[69] Wang W, Lu YC. The potassium-air battery: far from a practical reality? Acc Mater Res. 2021;2(7):515-525. https://doi.org/10.1021/accountsmr.1c00061
[70] Wang Y, Li A, Cheng C. Ultrathin $Co(OH)_2$ nanosheets@ nitrogen-doped carbon nanoflake arrays as efficient air cathodes for rechargeable Zn–air batteries. Small. 2021;17(35): 2101720. https://doi.org/10.1002/smll.202101720
[71] Williard N, He W, Hendricks C, Pecht M. Lessons learned from the 787 Dreamliner issue on lithium-ion battery reliability. Energies. 2013;6(9):4682-4695. https://doi.org/10.3390/en6094682
[72] "World's first" fully-electric commercial flight takes off. https://www.bbc.com/news/business-50738983 (accessed on 2025.02.13).
[73] World's largest sodium-ion BESS starts operation – Batteries International. https://www.batteriesinternational.com/2024/07/12/worlds-largest-sodium-ion-bess-starts-operation/ (accessed on 2025.02.16).
[74] Xue J, Deng S, Wang R, Li Y. Efficient synergistic effect of trimetallic organic frameworks derived as bifunctional catalysis for the rechargeable zinc-air flow battery. Carbon N Y. 2023;205:422-434. https://doi.org/10.1016/j.carbon.2023.01.034
[75] Yoon CS, Ryu HH, Park GT, Kim JH, Kim KH, Sun YK. Extracting maximum capacity from Ni-rich $Li[Ni0.95Co0.025Mn0.025]O_2$ cathodes for high-energy-density lithium-ion batteries. J Mater Chem A Mater. 2018; 6(9):4126-4132. https://doi.org/10.1039/c7ta11346c
[76] Yu X, Manthiram A. A voltage-enhanced, low-cost aqueous iron-air battery enabled with a mediator-ion solid electrolyte. ACS Energy Lett. 2017;2(5):1050-1055. https://doi.org/10.1021/acsenergylett.7b00168
[77] Zeng Y, Wu K, Wang D, Wang Z, Chen L. Overcharge investigation of lithium-ion polymer batteries. J Power Sources. 2006;160(2):1302-1307. https://doi.org/10.1016/j.jpowsour.2006.02.009
[78] Zhang X, Yang Y, Zhou Z. Towards practical lithium-metal anodes. Chem Soc Rev. 2020;49(10):3040-3071. https://doi.org/10.1039/c9cs00838a
[79] Zhao M, Peng HJ, Li BQ, Huang JQ. Kinetic promoters for sulfur cathodes in lithium-sulfur batteries. Acc Chem Res. 2024;57(4):545-557. https://doi.org/10.1021/acs.accounts.3c00698

Jagoda Muszyńska-Pałys, MEng. – Faculty of Mechanical Engineering and Aeronautics, Rzeszow University of Technology, Poland.
e-mail: *j.muszynska@prz.edu.pl*

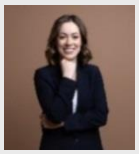

Piotr Wygonik, DEng. – Faculty of Mechanical Engineering and Aeronautics, Rzeszow University of Technology, Poland.
e-mail: *piowyg@prz.edu.pl*

Prof. Marek Orkisz, DSc., DEng. – Faculty of Mechanical Engineering and Aeronautics, Rzeszow University of Technology, Poland.
e-mail: *mareko@prz.edu.pl*

Article citation info:
Vrublevskyi O, Skonieczna D. Optimisation-oriented verification of a plain bearing process model taking into account actual tolerances and measurement accuracy. Combustion Engines. 2025;203(4):67-75. https://doi.org/10.19206/CE-207652

Oleksandr VRUBLEVSKYI
Daria SKONIECZNA

Combustion Engines
Polish Scientific Society of Combustion Engines

Optimisation-oriented verification of a plain bearing process model taking into account actual tolerances and measurement accuracy

ARTICLE INFO

Received: 12 May 2025
Revised: 25 June 2025
Accepted: 27 June 2025
Available online: 16 July 2025

This paper presents a methodology for verifying a numerical model of the plain bearing test process used to evaluate the characteristics of internal combustion engine components, in particular camshaft bearings. The developed approach is based on the use of optimisation methods under parametric uncertainty, which makes it possible to take into account the actual spread of technological and operational parameters.
The study uses a test rig that reflects the operating conditions of a bearing in an internal combustion engine, including a load simulated with an eccentric. SAE 15W40 grade oil, typical for engine lubrication systems, was used as the lubricant. The input parameter space includes geometrical features of the bearing (diameter, width, clearance, eccentricity), initial load force, shaft speed, and rheological properties of the oil.
The proposed approach to verification does not involve a direct comparison of computational and experimental data, but rather a search for the most probable solution within given tolerance limits and taking into account the measurement accuracy of the selected characteristics. The verification criteria are the measured values of oil and bearing surface temperature, load force, and friction torque in the oil film. Measurement uncertainty is also taken into account in the optimisation process.
The developed methodology makes it possible not only to assess the reliability of the numerical model, but also to analyse the sensitivity of the model to parameter variability and to determine the robustness of the friction node under study.

Key words: *camshaft, engine oil, wear, robustness, kinematic node*

1. Introduction

Nowadays, plain bearings are an important component of various technical objects [17], including in vehicle drive systems. The introduction of innovative control concepts with artificial intelligence elements, which are precisely adapted to changing operating conditions, requires the search for new or clarification of known bearing criteria (characteristics). Therefore, it is important to search for criteria that are able to combine tribological, thermodynamic, and hydrodynamic characteristics of the bearing processes. The success of this search is possible through the synergistic use of detailed simulation models describing bearing processes and experimental studies. It is worth noting that a number of research results have been published in recent years that present bearing calculation methods verified using empirical data.

For example, in [3], the authors present a highly effective computational method applied in the context of plain bearings in planetary gearboxes, validated using pressure measurement data in a wind turbine gearbox. The authors use the simulation results to analyse the influence of structural deformation and pressure distribution in the lubricating film. Fernández et al. [5] developed a bearing model using MSC software for multibody dynamics analysis. Adams performed its experimental validation. In addition, the authors use the presented model to minimise frictional losses in the bearing. König et al. [9] presented a method for predicting friction losses in plain bearings in start and stop modes. The paper [9] compared numerical models with experimental data, emphasising the importance of accurate simulation of mixed lubrication conditions. Machado and Cavalca, in their article [11], present an experimental validation of a bearing wear model using rotor frequency characteristics. The authors note good agreement between simulation and experiment. Goto et al. [7] developed a model for diagnosing plain bearing wear using the support vector method (SVM), validated using experimental data. The authors [7] indicate that high accuracy is achieved in wear diagnosis. Li et al. [4] developed a program to calculate friction in plain bearings and conducted experimental tests on a tribological test machine. Panara et al. [13] emphasise the importance of accurate simulation for high-speed and loaded bearings. The authors presented numerical models of fluid dynamics in bearings validated against experimental data.

Despite the fact that many contemporary works have proposed effective methods to validate plain bearing models using experimental data, in most cases a direct comparison of calculated and measured values at fixed parameters is used. This approach, although useful, does not take into account the actual uncertainty of the design parameters and test conditions. This paper proposes an alternative methodology in which the uncertainties in the input parameters and verification criteria are treated as an integral part of the problem, allowing for a more comprehensive and realistic assessment of model reliability.

One of the key challenges associated with the verification of engineering simulation models is the presence of unavoidable uncertainty in both the input parameters and the experimental results. Input data are characterised by fuzziness due to manufacturing tolerances, operational variability and limited parameter accuracy. On the other hand, the experimental verification criteria – temperature, load, and friction torque – are also subject to measurement

errors. As a result, a solution space is created with undefined boundaries in both input and output parameters. Under these conditions, the verification problem should be considered not as a direct comparison of calculated and empirical values, but as a problem of finding such sets of input parameters in which the calculated values fall within an acceptable (fuzzy) experimental space. Such an approach also makes it possible to analyse the sensitivity of the model and assess its robustness (resistance to parametric bias).

In order to solve the described problem, different approaches can be used to explore the fuzzy parameter space. First of all, attention should be paid to optimisation algorithms. These algorithms provide for the generation of sample points [1, 12, 15], parameters located in the space, and the use of the multi-criteria principle [2, 16].

The aim of this paper is to develop and demonstrate a multi-criteria method for the verification of a simulation model of a plain bearing, taking into account parametric uncertainty and tolerances of experimental measurements. The proposed method combines experimental testing with optimisation parameter selection that ensures convergence of calculated and empirical characteristics, thus providing not only verification but also sensitivity and stability analysis of the model.

In order to solve the above problem of verification of the computational model created for an in-depth study of the processes accompanying the operation of a sliding bearing, the paper presents the methodology of experimental testing, basic information about the created model, the method of processing empirical data, the author's verification algorithm with elements of optimisation, as well as a sensitivity study of the tribosystem under study.

2. Subject of the study, features of the experiment, and measurement methods

The processes taking place in a plain bearing, the design of which is used in internal combustion engines, were investigated using a stand (Fig. 1). The set speed of the bearing shaft ω (Table 2) was provided by an electric motor and a manual gearbox. The stand is equipped with a load system and measuring channels for the bearing friction index M, the force acting on the bearing F_N, the oil temperature T_{oil}, and the surface temperature of the bearing bushing $T_{bearing}$. During the experiment, the plain bearing was immersed in SAE class 15W40 engine oil with a volume of 0.3 dm^3. Since one of the objectives of the experiment was to test the bearing from a tribological aspect and also to simulate the operation of the friction assembly under varying load conditions, which is typical for friction assemblies of internal combustion engines, the shaft had an off-centre mounting hole (eccentric ε). This provided a force variation during shaft rotation of ±20% of the nominal value, which will be shown below in the load force measurement results.

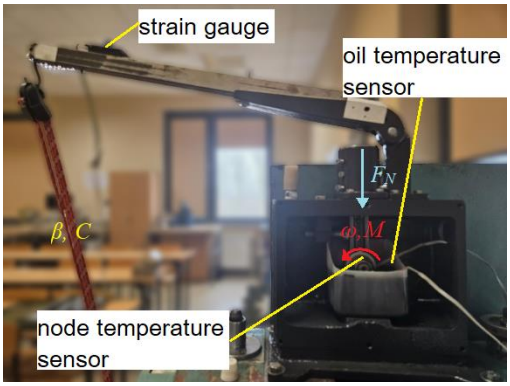

Fig. 1. Photo of the plain bearing and sensors on the test

Direct measurements of geometrical quantities were mainly used to determine the parameters of the plain bearing (Table 1). To determine the radial clearance h in the bearing, digital models of the shaft and sleeve (Fig. 2a, b), obtained by 3D scanning with the GOM® ATOS Core 80 scanner with post-processing in GOM Inspector, were used. For the central section, the clearance profile formed by the friction pair of the shaft-bushings (Fig. 2c) allowed the average value to be determined (Table 1). From the results presented, it can be seen that the bushing used in the test is close to the nominal diameter of 25 mm, with a deviation of no more than –0.02 mm. The bushing has a positive deviation of +0.03 mm. It should also be noted that the scanning accuracy is ±0.02 mm.

The method of conducting the experimental test was to load the bearing rotating at 300 rpm. The final experimental time was determined by reaching a temperature of 120°C on the surface of the bushing. For the tested bearing, the experimental time was approximately 5000 s.

As shown above (Fig. 1), the bench is equipped with channels for measuring load force F_N, friction torque M and temperatures (T_{oil}, $T_{bearing}$). A TorqueSensor Series 2300 from NCTE was used to measure the friction torque. The bearing load force was measured using a BF1K-3EB bridge strain gauge with a measuring base of 8.5×8.5 mm to ensure thermal compensation and linearity of characteristics and the temperature of the bushing surface (sensor position is shown in Fig. 1) using an Omega K-Type thermocouple. The measurement accuracy of the sensors used is shown in Table 2. A Picoscope 3000 series ADC and PicoScope 7 T&M® software were used for data collection and initial analysis.

Table 1. Plain bearing parameters

Parameter	Designation	Unit	Nominal value	Accuracy	Average	Deviation
Radial clearance	h	mm	0.020	±0.002	0.020	0.005
Stiffness of the load elastic element	C	$N \cdot m^{-1}$	100	±10	100	10
Damping coefficient of the load elastic element	β	$N \cdot (m \cdot s^{-1})^{-1}$	14	±1.4	14	1.4
Starting force	F_0	N	60	±6	60	6
Eccentricity	ε	mm	0.70	±0.07	0.70	0.07
Bearing width	B	mm	19	±0.19	19	0.19
Diameter of the sleeve	D	mm	25	±0.25	25	0.25

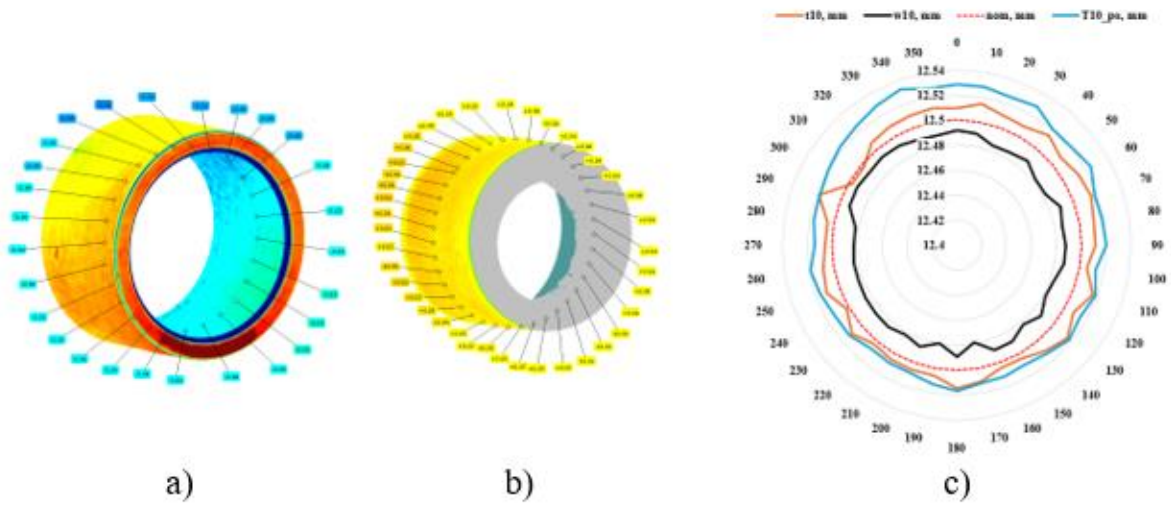

Fig. 2. Results of scanning the surfaces of the bushing (a), shaft (b) and clearance profile at the centre of the plain bearing (c)

Based on the measurements and tolerance analysis, it can therefore be concluded that the model input parameters vary within the ranges described in Table 1, and the measured characteristics vary to an accuracy of ± 7% (Table 2). These ranges were taken into account as part of the multi-criteria verification procedure.

3. Simulation model of a test stand with plain bearing

A simulation model of a sliding bearing test rig has been developed for the verification procedure, taking into account the identified parametric uncertainties. The model is built in the Amesim Simcenter environment and includes physical modules that describe friction, heat transfer and load kinematics.

In this study, the bearing model implemented in the simulation model of the test stand was used to increase the reliability of the modelling processes in the plain bearing and to develop a verification methodology with optimisation elements under fuzzy parameters and criteria. The computational scheme (Fig. 3) and the subsequent simulation were implemented in Amesim Simcenter space [14].

Table 2. Verification criteria and the accuracy of their determination

Name	Designation	Unit	Nominal value in the experiment	Accuracy
Verification criterion				
Oil temperature	T_{oil}	°C	48	±0.5°C
Bearing sleeve temperature	$T_{bearing}$	°C	82	±0.75%
Bearing load force	F_N	N	750	±7%
Friction torque	M	Nm	0.443	±5%
Friction power	P_{fr}	W	14	±3 W
Regulatory parameter				
Shaft speed	n, ω	rpm, $rad \cdot s^{-1}$	300, 31.4	±2.5%

The structural diagram (Fig. 3) is a set of interconnected modules that reflect the kinematic, tribological and thermodynamic processes in the friction unit. The key elements of the model are:

– Electric drive – sets a nominal shaft speed similar to that used in the experiment (300 rpm). Fluctuations in the shaft speed are taken into account in the simulation, which is ±2.5% of the nominal speed.
– Load mechanism – implemented by means of an eccentric, which allows the reproduction of a variable load force with an amplitude of ±20% of the mean value, as in the physical laboratory bench. In the loading mechanism, the stiffness and damping properties, as well as the preload force, are defined using a submodel of the elastic element. These parameters are also vague and are included in the verification process.
– The sliding bearing simulation unit is based on the solution of the Reynolds equation [8], which describes the pressure distribution in the lubricating layer during hydrodynamic lubrication, taking into account the non-stationarity of the loading and rotation conditions. In addition, the Goenki model [6, 10] is used to describe the thermal interaction in the tribosystem, which provides a calculation of heat dissipation depending on local friction parameters and lubricant viscosity.

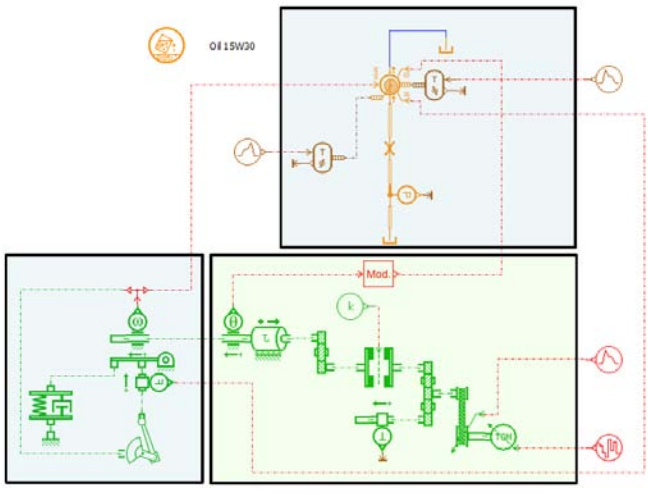

Fig. 3. Construction scheme of plain bearing test stand

– Heat transfer modules – simulate heat flows between bearing, shaft, and oil medium. This allows the change in temperature under load to be monitored, including self-heating and cooling.
– Sensors are virtual measurement units that correspond to the physical sensors (friction torque, temperature, load) used in the experiment. This allows comparison of modelled and empirical data for similar features.

In developing the model, a wizard was used to determine the physical and rheological properties of the oil. Empirical data obtained by the authors in the process of testing the engine oil samples used in the experiment were used to determine these properties.

The use of the Reynolds equation (1) allows the influence of geometric tolerances (for example, radial clearance) and lubricating film dynamics on the behaviour of the system to be taken into account, while the use of the Goenka model (2) allows an adequate assessment of the local thermal effects that occur under varying operating modes.

$$\frac{1}{r^2}\frac{\partial}{\partial\theta}\left(\rho h^3\frac{\partial p}{\partial\theta}\right)+\frac{\partial}{\partial z}\left(\rho h^3\frac{\partial p}{\partial z}\right)= = 6\eta\left(\omega_j+\omega_b\right)\frac{\partial ph}{\partial\theta}+12\eta\frac{\partial ph}{\partial t} \quad (1)$$

$$\frac{d}{dt}=\frac{|F_N|\left(\frac{h}{r}\right)^2}{\eta BD}M\left(\varepsilon,\frac{B}{D}\right)+\omega\times e \quad (2)$$

where is p(z, θ, t) is the oil film pressure, ρ is the lubricant density, r is the bearing radius, h(z, θ, t) is the radial clearance in the bearing, η is the oil film viscosity, Θ is the bearing angle, and ω_j, ω_b are the journal angular velocity and bearing angular velocity.

Therefore, the model structure provides not only physical plausibility, but also high sensitivity to parametric changes, which is essential for multi-criteria verification.

4. Multi-criteria bearing model verification algorithm

A proprietary algorithm for multi-criteria verification of the mathematical model was proposed to account for uncertainties in input parameters and experimental measurement errors. Its structure is shown in the diagram (Fig. 4) and reflects the key steps in the integration of simulation modelling, experimental, and optimisation methods.

The method is based on the assumption that both the model input parameters and the experimentally obtained output characteristics are described not by point values, but by ranges resulting from technological and measurement uncertainties. The task of verification is to determine the parameter vector in which the simulated output values (criteria) are within the acceptable range defined by the experimental data, taking into account errors.

The algorithm involves the following main steps:

1. Creation of the parameter space. Nominal values and acceptable ranges of the model input parameters (for example, clearances, viscosity, eccentricity) are determined taking into account measurement errors, manufacturing tolerances, and operating conditions (Table 1).

2 Generating test points. Experimental design methods (e.g. Sobol nets, Monte Carlo method, Latin Hypercube) generate a set of test vectors of input parameters that uniformly cover the parameter space.

3 Running the simulation. For each test vector, the values of the verification criteria are calculated: oil temperature, friction torque, load, oil film temperature.

4. Definition of the correct range. Based on the experimental data and their errors, tolerance ranges are created for each criterion (Table 2). Together, these form a multidimensional parallelogram of acceptable solutions.

5. Comparison of calculated and experimental criteria. If at least one set of calculated outputs (vector) falls within the range of valid values, the model is considered verified. The parameters corresponding to these simulations form a set of valid solutions.

6. Sensitivity and robustness assessment. The sensitivity of the model to parameter changes is analysed, and the areas of stability of the friction unit, i.e., the parameter ranges at which stable operation of the plain bearing is maintained, are determined.

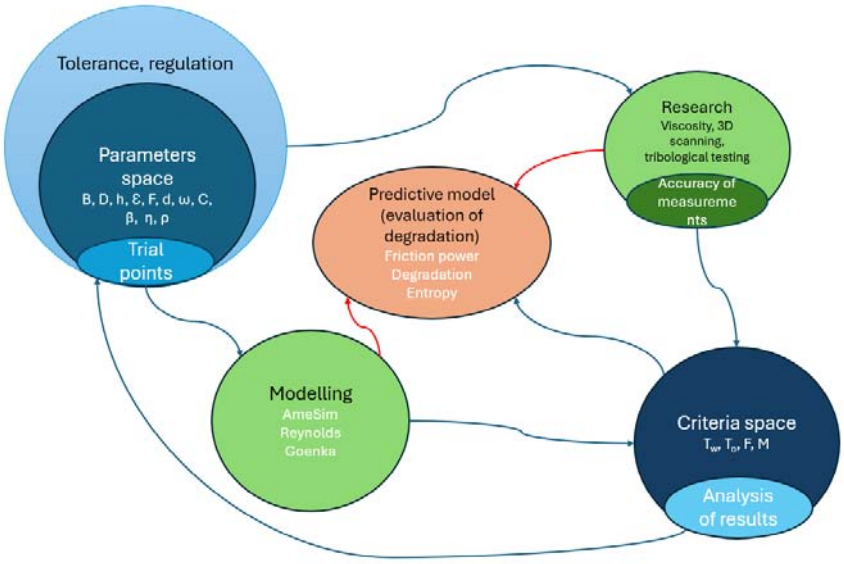

Fig. 4. Structure of the multi-criteria verification algorithm for the bearing model

Consequently, model verification takes the form of a vector parametric identification problem in the presence of fuzzy input and output data. The advantage of the proposed approach is its ability to account for real uncertainty at all levels, which is particularly important in the study of complex tribosystems operating under varying conditions.

5. Measurement results and analysis of verification criteria

5.1. Experimental observations

To verify the plain bearing model, a thermally stabilised mode of operation was used in which the system reached a steady state temperature. In this mode, the friction torque M and the load force F_N varied in time in a near sinusoidal manner due to the eccentricity (Fig. 5). Consequently, the friction power P_{fr}, calculated as the product of M·ω, where ω is the angular velocity of the shaft, also showed regular oscillations.

To ensure the validity of the comparison with model data, synchronisation of the measured signals is crucial. In this study, in order to synchronise the criteria M(t) and F_N(t), an approach based on minimising the variance of the current friction coefficient μ_{fr}, calculated according to the formula: $\mu_{fr} = \frac{M}{F_N \cdot 0.5 \cdot D}$.

The optimum moment shift was ~0.016 s, ensuring the physical behaviour of μ_{fr}(t). After synchronisation, the coefficient of friction stabilised within $\mu_{fr} \approx 0.046 \pm 0.002$, corresponding to known values for mixed and hydrodynamic lubrication modes.

Analysis of the friction power showed stable oscillations between 4 and 22 W, without the presence of drift or instability. This confirms the correct operation of the test rig and sufficient repeatability.

The characteristics presented – friction torque, load force, and power – are used as key verification criteria. Their behaviour over time confirms that the measured data are physically interpretable, stable and suitable for further comparison with simulation results.

Thus, the data preprocessing, including synchronisation, smoothing, and evaluation of the stability of the criteria, provides a reliable basis for implementing the proposed multi-criteria verification algorithm.

5.2. Results of model verification

The stochastic generation of test points in the model parameter space was used to implement the developed multi-criteria verification methodology. For this purpose, a Monte Carlo method was used with a normal distribution of the input variables around nominal values. The use of Gaussian

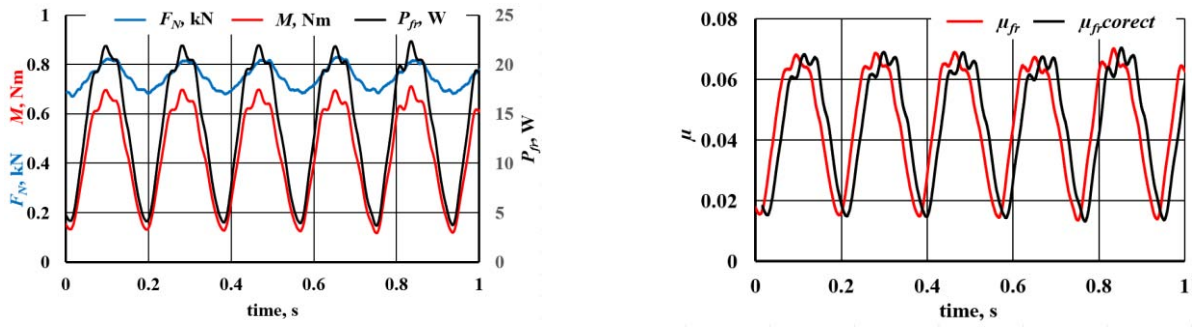

a) b)

Fig. 5. Run area with stabilised plain bearing operation: a) measured load force F_N, bearing friction torque M and friction power P_{fr}, b) result of determining friction coefficient μ_{fr}(t) with correction of torque signal M

Table 3. Acceptable solution vectors

# point	B, mm	β, N·(m·s^{-1})$^{-1}$	C, N·m^{-1}	D, mm	F_0, N	h, mm	ε, mm	F_N, N	P_{fr}, W	T_{oil}, °C	T_{bearin}, °C
1	19.29	13.79	87.16	24.64	52.85	0.03	0.51	843.84	9.87	47.96	81.27
…											
3	18.97	12.26	95.92	25.15	50.59	0.02	0.39	799.49	11.21	47.96	81.33
…											
11	18.87	14.75	103.82	24.65	45.10	0.01	0.44	706.32	16.84	48.08	81.91
…											
24	19.02	10.23	92.50	25.20	44.69	0.02	0.40	702.76	15.52	48.02	81.64
25	18.99	15.93	86.91	25.01	46.83	0.02	0.40	741.29	15.62	48.02	81.64
…											
37	19.18	13.23	98.69	25.07	47.29	0.02	0.41	744.02	15.09	48.01	81.59
…											
40	19.21	14.82	97.16	25.09	47.47	0.02	0.36	746.41	13.82	47.99	81.49
…											
42	19.42	14.15	93.27	24.93	44.75	0.02	0.38	703.22	12.65	47.97	81.43
…											
46	18.97	14.74	108.51	25.19	46.08	0.02	0.49	722.01	15.32	48.01	81.61
…											
48	19.28	16.41	96.53	24.97	48.86	0.02	0.34	769.08	14.60	48.00	81.55
49	19.08	16.58	103.82	24.65	48.65	0.02	0.43	765.02	14.13	47.99	81.54
50	18.78	13.29	111.63	24.83	56.48	0.027	0.35	889.05	10.29	47.96	81.29

dispersion reflects the physical nature of variances such as process tolerances, inconsistent operating conditions and limited measurement accuracy.

5.3. Generation of input data and parameters

The calculations used 50 test points (Table 3), each representing a unique set of parameters: radial clearance h, stiffness C, and load system damping β, initial force F_0, eccentric ε, bushing width B, and shaft diameter D. Mean values and standard deviations are determined for each parameter, as shown in the Table 1.

5.4. Modelling and sampling

A numerical simulation of the plain bearing was carried out for 150 seconds for each test point, which was sufficient to achieve a quasi-stationary temperature regime. The calculations were carried out in the Amesim Simcenter simulation environment. The total execution time per calculation did not exceed 20 minutes. The output included the values of the key verification criteria: oil temperature, bushing surface temperature, load force and power.

5.5. Verification analysis in the criteria space

Test points were analysed in two-dimensional criteria spaces:

– Oil temperature – bushing temperature (Fig. 6)
– Friction force – load force (Fig. 7).

In the first diagram, most of the points were within the tolerance range set by the accuracy of the measurements. This is particularly true for points with smaller radial clearance values (e.g. positions 8, 27, 34, 41, 42, 49), confirming the sensitivity of the thermal behaviour of the model to the geometry.

In the second graph, the proportion of deviation points increases, indicating that the model is more sensitive to changes in loading parameters. Nevertheless, a compact cluster of trial solutions was identified (points 3, 11, 24, 25, 37, 40, 42, 46, 48, 49) that fell within the confidence interval for all criteria.

5.6. Interpretation of results

Analysis of the distribution of sample solutions allows the following conclusions to be drawn:

– The verification is considered successful because there are a number of points that meet all criteria within the experimental accuracy limits.
– A robust range of input parameters is revealed within which the model gives output characteristics consistent with experiment.
– At the same time, the model is found to have limited sensitivity within the current tolerances: most parameters have a weak effect, with the exception of the clearance h and load parameters.
– This provides a basis for using the model in engineering practice as stable or, if necessary, for refining the model structure in sensitive areas.

5.7. Verification

To quantify the effectiveness of the proposed verification methodology, ratios of simulation results falling within experimental tolerances were calculated according to the key criteria. A verified test point is one for which all calculated criterion values were simultaneously placed within the established uncertainty ranges obtained from the accuracy of the measurement systems.

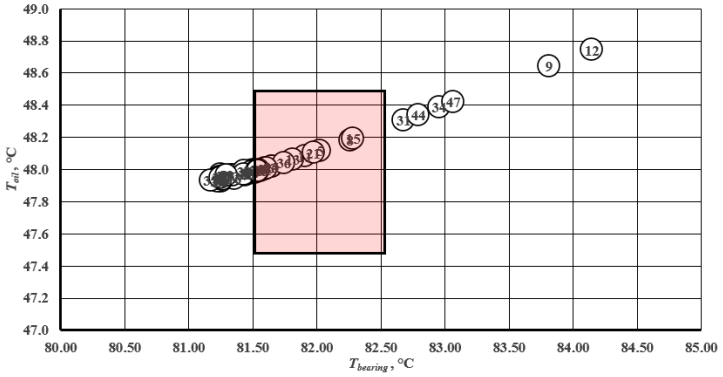

Fig. 6. Location of test points in the plane of the verification criteria oil temperature T_{oil} surface temperature $T_{bearing}$

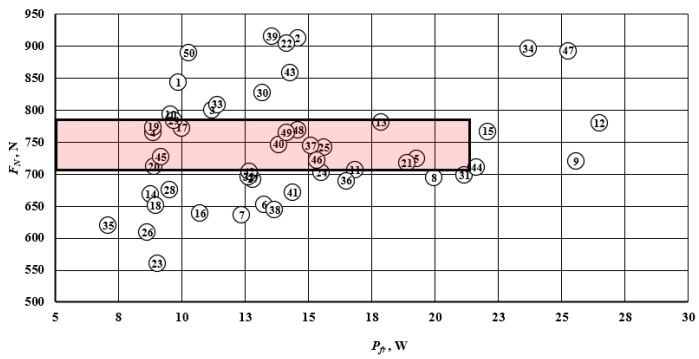

Fig. 7. Location of test points in the plane of the verification criteria, friction power P_{fr} and force F_N

Table 4. Variation of the surface temperature of the bearing sleeve as a function of the input parameters

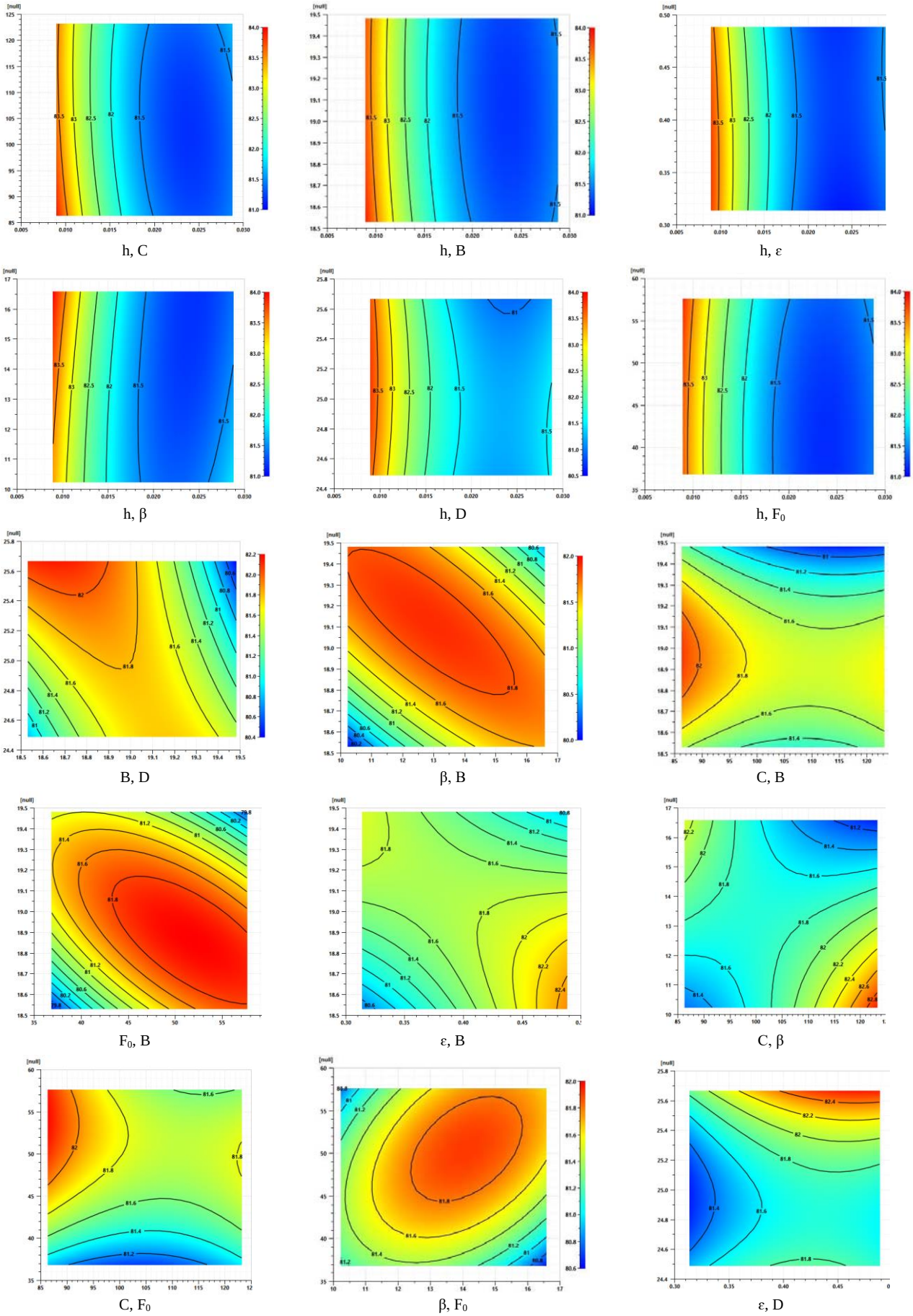

h, C | h, B | h, ε

h, β | h, D | h, F_0

B, D | β, B | C, B

F_0, B | ε, B | C, β

C, F_0 | β, F_0 | ε, D

The following criteria and acceptable deviations were selected for the verification assessment (Table 2).

As part of the verification step, 50 test points (Table 3) generated by the Monte Carlo method based on Gaussian distributions of the model parameters were analysed. Calculations were carried out in steady-state thermodynamic mode. The results obtained allowed the following indicators to be evaluated:

- number of points meeting the two temperature criteria: 37 out of 50
- number of points meeting both power and load criteria: 10 z 50
- number of fully verified points (according to all criteria): 10 out of 50
- total percentage of verification: 20%.

The percentage of verification obtained confirms the realism of the model, as in the case of parametric fuzziness and metrological uncertainty, absolute convergence is not required, but the existence of a domain of acceptable solutions is sufficient.

The identified cluster of verified solutions (10 points) indicates the existence of a parameter domain in which the model shows consistency with the experiment. This confirms the adequacy of the model structure, the physical consistency of the mechanisms for generating output values and the robustness of the model to acceptable parameter dispersion.

At the same time, the percentage of unverified points highlights the limited sensitivity of the model to certain parameter combinations, which may serve as a starting point for further refinement of the model.

6. Sustainability analysis

The final stage of the work was to assess the stability of the investigated plain bearing to changes in its parameters. As mentioned above, such changes are inevitable during the production, adjustment and operation of the bearing. Using the calculation results of the verified model (Fig. 6 and Fig. 7), it is possible to analyse the effect of selected parameter pairs on the surface temperature of the bearing sleeve (Table 4).

In spaces where one of the parameters is the radial clearance in the bearing h, the other parameter does not play a decisive role in the surface temperature level of the bearing bushing in the investigated steady state of operation. This indicates the dominant influence of the clearance on the thermal regime of the bearing and the low sensitivity of the system to other parameters at a constant value of h. The bearing shows local resistance to variations in the parameters C, B, ε, β, D, F_0 if the radial clearance is within tolerance. This also suggests that it is possible to simplify the model or control the system by focusing primarily on the clearance as the main factor affecting thermal behaviour.

In all other combinations (without h), the temperature field shows a clear extreme, i.e. a maximum or minimum temperature in the middle of the tested parameter range. In these zones, the system is sensitive to simultaneous changes in two parameters, which can result in thermal overload or, conversely, a mode with minimal losses. In this way, it is possible to identify unsafe parameter combinations that lead to overheating, and to locate optimal parameter combinations that ensure minimum temperatures (and probably minimum wear).

On the basis of a pairwise analysis, the following can be assumed:

A number of practical conclusions can be drawn from the analysis:

- A key factor is the radial clearance h
- Under variable parameter conditions without backlash control, the model shows local areas of high sensitivity, which can lead to unstable operation or overheating
- This technique allows the identification of zones of stability and instability, which is extremely important for design tasks, tolerances, diagnostics, and monitoring.

Table 5. The importance of the relationship between the parameters

C	It is sensitive in combination with other dynamic parameters (ε, F_0, β), influencing force transmission and thus losses.
β	It participates in several pairs with a clear extreme, influencing the stabilisation mode and amplitude of load fluctuations.
ε	A noticeable effect in combination with F_0, B, and D affects the change in cycle load and pressure distribution.
B	In combination with other geometrical parameters, it determines the contact area, but can both reduce and increase the temperature depending on the combination.
F_0	It affects pre-stress and can significantly alter temperature modes in combination with other power parameters.

7. Conclusions

The following conclusions can be drawn from the study:

1. A method for multi-criteria verification of a simulation model of a sliding bearing operating in a real experiment has been developed. The technique takes into account the parametric fuzziness of the input data and the errors of the measurement systems.

2. The verification was carried out by generating 50 test points using the Monte Carlo method, taking into account the statistical distributions of the parameters. Of these, 37 points met the temperature criteria, 10 met the load-power criteria and 10 met all criteria. This corresponds to an overall verification success rate of 20%, confirming that there is a range of valid design solutions.

3. Sensitivity analysis showed a dominant influence of radial clearance on the temperature behaviour of the system, with eccentricity and load parameters influencing the shape of the power and torque distributions. This highlights the key role of geometric tolerances in ensuring component stability.

4. This technique not only allows verification to be carried out, but also to identify areas of robustness – ranges of parameters at which the model remains within experimental tolerances. This is particularly important for engineering calculations related to tolerance selection and condition control.

5. The developed model and verification algorithm focus on plain bearings, typically used in internal combustion engines (crankshaft supports, camshafts, etc.), where evaluation of heating, friction, and loading is important under conditions of limited access to measurements.

6. The proposed method can be generalised to other types of bearings and contact assemblies where similar sources of uncertainty are observed.

Nomenclature

B	bearing width
C	stiffness of the load elastic element
D	diameter of the sleeve
F_0	starting force
F_N	bearing load force
h	radial clearance
M	friction torque
n	shaft speed
p	oil film pressure
P_{fr}	friction power
r	bearing radius
$T_{bearing}$	bearing sleeve temperature
T_{oil}	oil temperature
β	damping coefficient of the load elastic element
ε	eccentricity
η	oil film viscosity
Θ	bearing angle
μ_{fr}	current friction coefficient
ρ	lubricant density
ω	shaft speed
ω_b	bearing angular velocity
ω_j	journal angular velocity

Bibliography

[1] Asmussen S, Glynn PW. Stochastic simulation: algorithms and analysis. Springer 2007.

[2] Deb K. Multiobjective Optimization Using Evolutionary Algorithms. Wiley. 2001

[3] Ding H, Mermertas Ü, Hagemann T, Schwarze H. Calculation and validation of planet gear sliding bearings for a three-stage wind turbine gearbox. Lubricants. 2024;12(3): 95. https://doi.org/10.3390/lubricants12030095

[4] Du F, Li D, Hao M, Yu Y, Wang W. Simulation and experimental research on the failure of marine sliding bearings. J. Mar. Sci. Eng. 2023;11(1):61. https://doi.org/10.3390/jmse11010061

[5] Fernández MM, Rüth L, Sauer B. Comparative study of a simulative bearing design with an experimentally determined data of a prototype bearing. Forsch Ingenieurwes. 2021;85:1015-1027. https://doi.org/10.1007/s10010-021-00494-7

[6] Goenka PK. Analytical curve fits for solution parameters of dynamically loaded journal bearings. ASME J Tribol. 1984; 106(3):421-427.

[7] Goto M, Inoue T, Heya A, Katayama K, Kimura S, Tomimatsu SE et al. Modeling of journal bearings for wear diagnosis and its verification using SVM. 4th Asia Pac Conf Progn Health Manag. 2023. https://doi.org/10.36001/phmap.2023.v4i1.3640

[8] Hamrock BJ, Schmid SR, Jacobson BO. Fundamentals of fluid film lubrication. Boca Raton 2004. eISBN 9780429215315. https://doi.org/10.1201/9780203021187

[9] König F, Sous C, Jacobs G. Numerical prediction of the frictional losses in sliding bearings during start-stop operation. Friction. 2020;9(12):583-597. https://doi.org/10.1007/s40544-020-0417-9

[10] Kumar A, Goenka PK, Booker JF. Modal analysis of elastohydrodynamic lubrication: a connecting rod application. J Tribol. 1990;112(3):537-544.

[11] Machado T, Cavalca KL. Experimental validation of a bearing wear model using the directional response of the rotor-bearing system. An Acad Bras Ciênc. 2016;88(4). https://doi.org/10.1590/0001-3765201620150414

[12] Montgomery DC. Design and analysis of experiments. Wiley. 2017. ISBN 1119299365, 9781119299363

[13] Panara D, Pivetta V, Shoup T, Baldassarre L. Numerical models and experimental validation of high speed, high load, hydrodynamic bearings. Turbomach Lab Tex A&M Eng Exp Stn. 2019. https://hdl.handle.net/1969.1/188638

[14] Simcenter Amesim Software Quick Access Guide. 2019

[15] Sobol IM, Kucherenko S. Global sensitivity indices for nonlinear mathematical models. Review Wilmott. 2005;1: 56-61. https://doi.org/10.1002/wilm.42820050114

[16] Sobol M, Statnikov RB. Selecting optimal parameters in multicriteria problems. Drofa, Moscow 2006.

[17] Sroka Z, Prakash S, Wlostowski R. Design of the turbocharger bearing arrangement to increase the overall efficiency of the combustion engine. Combustion Engines. 2022;188(1): 83-89. https://doi.org/10.19206/CE-142348

Prof. Oleksandr Vrublevskyi, DSc., DEng. – Faculty of Technical Sciences, University of Warmia and Mazury in Olsztyn, Poland.
e-mail: *aleksander.wroblewski@uwm.edu.pl*

Daria Skonieczna, MEng. – Faculty of Technical Sciences, University of Warmia and Mazury in Olsztyn, Poland.
e-mail: *daria.skonieczna@uwm.edu.pl*

Article citation info:
Bilski M. Alternative energy sources and modern fuel stations for motor yachts. Combustion Engines. 2025;203(4):76-86. https://doi.org/10.19206/CE-211824

Maciej BILSKI

Combustion Engines
Polish Scientific Society of Combustion Engines

Alternative energy sources and modern fuel stations for motor yachts

ARTICLE INFO

Received: 11 August 2025
Revised: 7 October 2025
Accepted: 8 October 2025
Available online: 00 January 0000

The yachting industry is undergoing a dynamic transformation driven by global environmental policies, technological advances, and rising societal awareness of sustainable transport. Conventional motor yachts powered by fossil fuels contribute significantly to greenhouse gas emissions and local pollution, prompting increasing interest in alternative propulsion technologies. This article examines two of the most promising solutions – electric propulsion and hydrogen fuel cells – focusing on their technical characteristics, economic feasibility, and environmental impacts. A methodological framework was developed to assess modern fuel station infrastructure for motor yachts, applying criteria such as availability, safety, energy efficiency, and regulatory compliance. Life-Cycle Costing (LCC), Net Present Value (NPV), and Life Cycle Assessment (LCA) analyses were conducted to compare the long-term economic and ecological performance of electric charging and hydrogen refuelling stations. Case studies from Europe, North America, and Asia illustrate the rapid expansion of alternative fuel infrastructure, ranging from high-power DC charging and wireless inductive systems to containerised hydrogen stations integrated with renewable energy sources. The results demonstrate that electric propulsion is best suited to short-distance recreational navigation, while hydrogen offers advantages for long-range and intensive applications. The study concludes that both technologies will likely coexist as complementary solutions, with investment potential concentrated in tourist-intensive waterfronts and urbanised port areas. Future prospects include innovations in wireless charging, local green hydrogen production, and hybrid infrastructure, reinforcing the role of marinas as active players in the maritime energy transition.

Key words: *alternative energy sources, motor yachts, electric propulsion, hydrogen fuel cells, marina infrastructure*

1. Introduction

The yachting sector, similarly to other branches of transportation, faces challenges stemming from global environmental regulations and a growing societal awareness of ecology. Conventional motor yachts powered by fossil fuels emit considerable amounts of carbon dioxide (CO_2), nitrogen oxides (NO_x), sulphur oxides (SO_x), and particulate matter. These pollutants adversely affect aquatic ecosystems and air quality, while even relatively small spills of fuel or lubricants in marinas accumulate in enclosed waters, causing disproportionate ecological harm. One of the key factors accelerating the transition is the implementation of international regulations limiting greenhouse gas emissions in shipping, such as the International Maritime Organization (IMO) norms and the European Green Deal strategy [12, 24].

Although motor yachts account for a relatively small share of overall maritime traffic, their environmental impact is increasingly scrutinised. Marinas are often located in sensitive coastal areas with high tourism activity, which amplifies the social visibility of environmental issues. The International Maritime Organization's Emission Reduction Strategy [24] sets out a long-term pathway for lowering greenhouse gas emissions in maritime transport. While its direct scope applies primarily to commercial vessels, the resulting regulatory environment exerts pressure on the recreational sector to adopt sustainable solutions. Likewise, the European Green Deal [12] and its associated initiatives emphasise the need to decarbonise all modes of transport, including leisure navigation, as part of broader climate goals.

In response to these challenges, yacht manufacturers and port-infrastructure operators increasingly invest in alternative propulsion solutions such as electricity and hydrogen. This transition is not without hurdles, however. Limited availability of charging and refuelling infrastructure, high implementation costs of new technologies, and the need to adapt current regulations to modern propulsion systems are only some of the aspects that require solutions [28]. Despite these difficulties, the decarbonisation trend in the yachting sector appears inevitable, with alternative energy sources playing a key role.

Contemporary propulsion technologies for motor yachts concentrate on two main approaches: electric energy and hydrogen. Both systems have benefits and challenges that influence their adoption in the yachting sector. Electric propulsion is currently one of the most rapidly developing solutions in recreational navigation. The use of lithium-ion batteries and the growing number of charging stations enable increasingly widespread deployment of electric craft. The key advantages include zero local emissions, quiet operation, and low operating costs as noted in conventional diesel yacht engine literature [54]. Nevertheless, limited range and long charging time are significant barriers, especially for vessels covering longer distances.

Hydrogen propulsion uses proton-exchange membrane fuel cells (PEMFC), which convert hydrogen into electrical energy, producing only water as a by-product. The technology allows for a substantially greater range than batteries, while hydrogen refuelling time is comparable to conventional petrol or diesel refuelling. The main challenges include the high costs of hydrogen production and storage, as well as the underdeveloped refuelling infrastructure in marinas. Both solutions underpin the decarbonisation of waterborne transport and can coexist as complementary technologies in the future – electric propulsion being optimal

for shorter routes, while hydrogen will be used for long-distance voyages. Zaha Hadid Architects proposed the first design attempts into new marinas as NatPower H hydrogen refuelling stations, designed for 25 Italian marinas and ports (Fig. 1).

Fig. 1. Zaha Hadid architects reveals design for hydrogen refueling stations across the Italian marinas [46]

At the same time, the regulatory context is becoming increasingly complex. The IMO's Revised GHG Strategy, adopted in 2023, strengthened the ambition to achieve net-zero emissions from shipping by 2050, with intermediate milestones for 2030 and 2040. Although the strategy does not explicitly cover yachts, it provides an important political signal that all segments of maritime activity should contribute to decarbonisation. In Asia, national hydrogen strategies, particularly in Japan and South Korea, promote large-scale deployment of hydrogen infrastructure that also extends into recreational maritime applications. These policy frameworks create both opportunities and obligations for the yachting sector [35].

The environmental transition is not only a technical or regulatory matter but also an economic and social one. Unlike commercial shipping, motor yachts are luxury goods. Their owners and users are often motivated not only by functionality but also by reputation and lifestyle choices. Ecological awareness is becoming an element of social prestige, with yacht buyers increasingly seeking vessels that combine performance with environmental responsibility. As a result, marina operators who implement visible, sustainable solutions – such as solar canopies, floating photovoltaic platforms, or hydrogen refuelling barges – gain reputational advantages. This dimension is particularly relevant in tourist destinations, where environmental performance can directly influence customer satisfaction and regional image.

Digitalisation and "smart marina" concepts further accelerate the transition. Modern marinas integrate Internet of Things (IoT) devices, intelligent energy-management systems, and predictive maintenance tools. These allow optimisation of charging infrastructure, reduction of downtime, and enhancement of safety. Integration with renewable energy sources, such as solar modules on docks or small-scale wind turbines, supports energy autonomy. The deployment of hybrid solutions combining batteries and hydrogen storage illustrates the direction of innovation (Fig. 2).

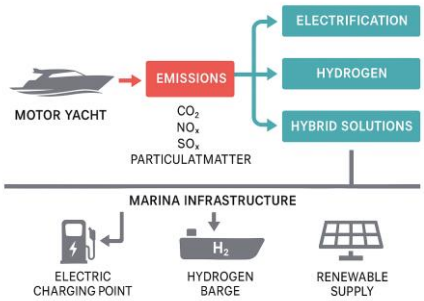

Fig. 2. Main sources of emissions in motor yachts and potential alternative energy pathways

The academic debate highlights that electricity and hydrogen will most likely coexist rather than compete. Electric propulsion is optimal for short-range and urban navigation, while hydrogen offers greater range and faster refuelling. Both require significant infrastructural investments, supportive regulation, and long-term environmental assessment. The gaps that remain include economic viability modelling, standardisation of hydrogen safety procedures in small ports, and behavioural analysis of yacht users.

The aim of this paper is therefore to examine alternative energy sources and modern fuel stations for motor yachts in a holistic manner. Specifically, the objectives are:

1. To provide an overview of the state of the art in electric and hydrogen propulsion for motor yachts, including comparative efficiency analysis
2. To assess the infrastructure requirements of modern fuel stations, with evaluation criteria derived from literature and expert consultations
3. To apply life-cycle cost (LCC), net present value (NPV), and return on investment (ROI) methods to economic feasibility
4. To model the environmental impacts of different station variants using life-cycle assessment (LCA)
5. To examine selected case studies in Europe, North America, and Asia, identifying best practices and architectural integration strategies.

The ultimate goal is to situate the recreational yachting sector within the broader energy transition of maritime transport, highlighting both opportunities and challenges. By emphasising infrastructure, economics, and consumer behaviour, this paper contributes to the ongoing discussion on sustainable mobility and coastal development.

2. Literature review and state of the art

2.1. Previous research on alternative energy sources in yachting

Research on alternative energy sources in waterborne transport has gained prominence in recent years, especially in the context of global climate goals. The literature on electric and hydrogen propulsion focuses primarily on energy efficiency, infrastructure barriers, and the costs of deployment. At the same time, studies on conventional diesel yacht engines remain an important reference point for assessing the transition towards low- and zero-emission systems [54]. While most research has historically focused

on large-scale shipping, there is growing recognition that recreational craft also require sustainable solutions.

Electric propulsion systems today are applied mostly in smaller recreational craft. The main barrier to their wider diffusion in motor yachts remains the limited battery capacity and long charging time. Kolodziejski and Michalska-Pozoga [30] analysed battery energy storage systems in ships' hybrid and electric propulsion, pointing to their growing relevance for smaller vessels. Grey and Hall [17] projected that technological progress in lithium-ion batteries – particularly advances toward solid-state batteries – may significantly increase the range of electric vessels in the next decade (Fig. 3).

Fig. 3. Aqua superPower charging station for small vessels [45]

By contrast, hydrogen technology is currently applied predominantly in larger vessels and demonstration projects. Proton-exchange membrane fuel cells (PEMFC) are considered the most promising solution for marine use, due to their relatively high energy efficiency and compact size. Van Biert et al. [7] reviewed marine fuel-cell systems, highlighting their potential for zero-emission operation but also the high costs of hydrogen production and infrastructure.

Recent comparative analyses of hydrogen production methods confirm that the environmental impact of hydrogen depends strongly on the energy source used in electrolysis. Ji and Wang demonstrated that only hydrogen produced from renewable electricity ("green hydrogen") offers genuine decarbonisation potential. This distinction is critical when evaluating hydrogen's role in yachting.

Several demonstration projects provide empirical evidence. In Norway, fuel-cell ferries and hybrid yachts are part of a broader national hydrogen strategy. In the Netherlands, research programmes combine urban mobility, inland waterways, and recreational boating in pilot projects. In Japan and South Korea, hydrogen and electric yachts are integrated into national "green port" strategies [29].

Table 1. Comparison of the basic parameters of electric and hydrogen propulsion

Parameter	Electric propulsion	Hydrogen propulsion
Range	150–300 km	400–600 km
Charging/refuelling time	60–120 min	5–10 min
CO_2 emissions	0 g/km (with RES)	0 g/km (with RES)
Infrastructure cost	Low	High

These data suggest that electric propulsion will be optimal for coastal and short-range navigation, whereas hydrogen will be preferable in long-range and more commercial applications (Fig. 4).

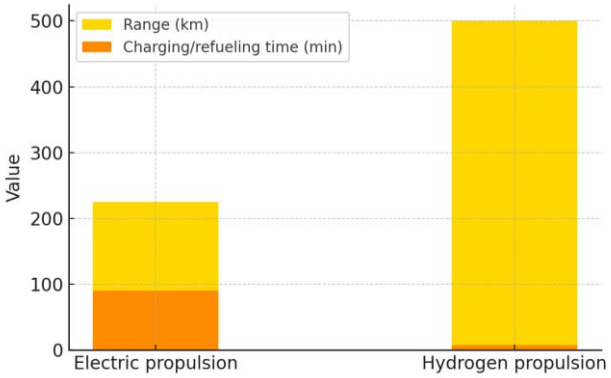

Fig. 4. Comparison of charging/refuelling time for electric and hydrogen propulsion

2.2. Additional comparative research

To complement the existing findings, new studies have introduced multidimensional frameworks for evaluating propulsion technologies. Bouman et al. [38] emphasised the importance of integrating greenhouse gas reduction measures across all shipping sectors, while Balcombe et al. [9] highlighted the role of policy in accelerating adoption of low-carbon fuels.

Table 2. Selected research themes on alternative propulsion in yachting

Author(s)	Technology	Focus	Key Findings
Kolodziejski & Michalska-Pozoga (2023) [30]	Electric batteries	Hybrid/electric propulsion	Batteries feasible for small vessels, limited by range
Grey & Hall (2020) [17]	Lithium-ion, solid-state	Technological outlook	Solid-state batteries may revolutionise vessel range
Van Biert et al. (2016) [7]	Fuel cells	Maritime applications	PEMFC promising, infrastructure costly
Ji & Wang (2021) [28]	Hydrogen	Production methods	Green hydrogen essential for sustainability
Kim et al. (2022) [29]	Hydrogen + electric	Port infrastructure	Hybrid systems feasible, supported by policy
Balcombe et al. (2019) [9]	Multi-fuel	Policy and technology	Electricity + hydrogen will coexist in future transport

This body of literature demonstrates that while both electricity and hydrogen are being developed, research often treats them in isolation. Comparative studies specific to yachting remain relatively scarce, leaving room for further integrated analysis.

2.3. Comparative efficiency of propulsion technologies

When comparing electric and hydrogen propulsion, assessments must include not only range, CO_2 emissions, and refuelling/charging time, but also infrastructure require-

ments, life-cycle costs, and safety considerations [2]. Electric propulsion is generally more cost-effective and better suited to small craft, whereas hydrogen offers longer range and shorter refuelling times but requires significantly higher capital investment. Life-cycle assessments confirm that electric yachts powered by renewable energy have the lowest carbon footprint, but hydrogen offers higher scalability for long-range applications [9].

Table 3. Efficiency of different fuel-cell types in maritime applications

Fuel-cell type	Efficiency (%)	Advantages	Drawbacks
PEMFC	40–60	Compact, quick start	Sensitive to impurities, costly catalysts
SOFC	50–65	High efficiency, fuel flexibility	Slow start-up, high temperature
AFC	50–60	High performance with pure H_2	Sensitive to CO_2 contamination
Abbreviations: PEMFC – Proton Exchange Membrane Fuel Cell; SOFC – Solid Oxide Fuel Cell; AFC – Alkaline Fuel Cell			

Balcombe argues that both electricity and hydrogen will play complementary roles. The efficiency of each depends on vessel size, operational profile, and infrastructure context. DNV's *Maritime Forecast to 2050* [11] projects that both battery-electric and hydrogen-fuelled vessels will gain significant shares of the maritime market. In addition to propulsion efficiency, safety remains a decisive factor. Hydrogen storage at 350–700 bar requires advanced safety systems and regulatory approval, while electric batteries pose risks of thermal runaway [5]. Both technologies demand tailored safety frameworks for marinas. Finally, market projections suggest that battery costs will continue to decline, while green hydrogen costs are expected to decrease significantly by 2030 due to scaling and renewable expansion [23, 43] (Fig. 5).

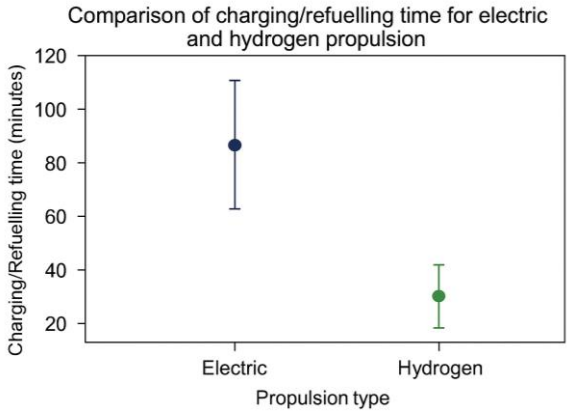

Fig. 5. Comparative efficiency of electric vs hydrogen propulsion

3. Research methodology

3.1. Evaluation criteria for alternative fuel stations infrastructure

The objective of the analysis of modern fuel stations for motor yachts is to determine their suitability within the energy transition of recreational navigation. The infrastructure supporting alternative energy sources – electricity and hydrogen – was assessed. The key criteria included availability, energy efficiency, operational safety, and compliance with environmental regulations. A qualitative indicator method was applied based on a weighted scoring matrix, with weights derived from literature analysis and consultations with industry experts. Port accessibility and technical feasibility of implementing the infrastructure in existing marinas were also considered [10].

Table 5. Weights assigned to the evaluation criteria

Criteria	Description	Weight (%)
Availability	Number of charging/refuelling points on a given waterbody	30
Energy efficiency	Average conversion and transmission losses	25
Operational safety	Risk of failure and compliance with technical standards	20
Regulatory compliance	Compliance with EU and IMO environmental regulations	15
Integration with infrastructure	Applicability in existing marinas without major changes	10

The sum of weights equals 100%, and the final score for a given station was calculated as a weighted average according to the above distribution [10].

Table 6. Extended evaluation criteria with additional socio-economic indicators

Criterion	Description	Weight (%)
Social acceptance	User perceptions and willingness to adopt technology	10
Economic incentives	Availability of subsidies, grants, or tax relief	8
Aesthetic integration	Visual compatibility with marina architecture	7
Life-cycle adaptability	Flexibility to incorporate future technologies	5

These added indicators reflect the importance of social, economic, and architectural dimensions in marina planning.

3.2. Methods for economic efficiency analysis

The economic efficiency of alternative fuel stations was evaluated using the Life-Cycle Costing (LCC) methodology, enabling a comprehensive assessment of capital expenditures, operating costs, and environmental costs over the entire life cycle of the investment. Additionally, Net Present Value (NPV) and Return on Investment (ROI) were used to assess the profitability of modernisation projects and construction of new facilities [19].

Table 7. Example input data for LCC analysis for electric and hydrogen stations

Parameter	Electric station	Hydrogen station
Capital cost [million EUR]	0.45	1.25
Annual operating cost [EUR]	15,000	30,000
Service life [years]	20	20
Residual value [million EUR]	0.05	0.10

NPV and ROI were calculated for three scenarios – conservative, realistic, and optimistic – considering discount rates from 3% to 7% [19].

Table 8. Comparative LCC outcomes for electric vs hydrogen stations under different scenarios (new)

Scenario	Electric station NPV [M€]	Hydrogen station NPV [M€]	ROI (Electric)	ROI (Hydrogen)
Conservative (7%)	0.12	–0.30	6%	–2%
Realistic (5%)	0.25	–0.05	11%	1%
Optimistic (3%)	0.40	0.20	18%	7%

The analysis demonstrates that economic feasibility strongly depends on the discount rate and subsidy availability. Electric stations show higher resilience across scenarios.

3.3. Environmental impact modelling of modern fuel stations

Environmental impacts were analysed using a Life Cycle Assessment (LCA) model that considered greenhouse gas emissions, primary energy consumption, and potential impacts on aquatic ecosystems. Input data originated from real-world analyses of fuel stations in Europe and from peer-reviewed literature. Modelling was conducted for three infrastructure variants: electricity-only, hydrogen-only, and hybrid [6].

Table 9. Comparative LCA outcomes for different station types

Variant	CO_2 emissions [kg CO_2-eq/yr]	Primary energy demand [MWh/yr]	Aquatic impact score (0–100)
Electric (RES supply)	2100	11.5	10
Hydrogen (grey)	8700	32.0	40
Hydrogen (green)	3000	14.2	12
Hybrid	3500	16.0	15

Results confirm that green electricity is the lowest-impact pathway, but hydrogen from renewables also offers competitive reductions compared to fossil-fuel baselines [34].

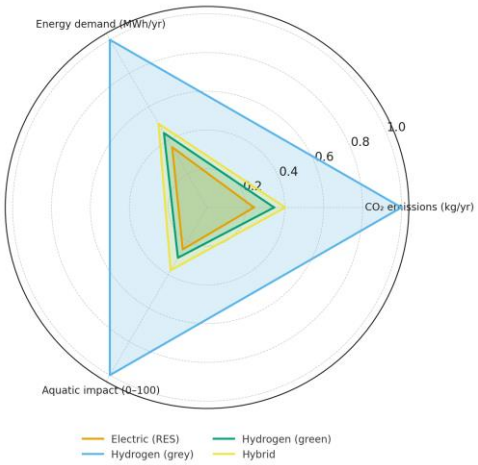

Fig. 6. Comparative LCA impact of electric, hydrogen, and hybrid stations (new)

In addition to environmental indicators, modelling also took into account compliance with international safety and design standards. The ISO 19880-1:2020 guidelines for hydrogen fuelling stations provide the fundamental framework for assessing risks and ensuring the safe integration of hydrogen technology in marina environments [22].

Radar chart showing three categories (CO_2 emissions, energy demand, aquatic impact), with four variants compared in proportional scales.

4. Characteristics of alternative energy sources

4.1. Electrical energy: batteries and charging systems

The application of electricity in motor-yacht propulsion depends primarily on advances in energy storage and charging infrastructure. The key component is the lithium-ion (Li-ion) battery, which provides favourable energy density and a relatively long lifetime. Lithium-iron-phosphate ($LiFePO_4$) batteries are increasingly popular due to their high chemical stability and operational safety.

Table 10. Comparison of battery technologies

Battery type	Energy density [Wh/kg]	Cycle life [cycles]	Charging time	Advantages
Lithium-ion	150–250	1000–3000	4–8 h	Good availability; high energy density
$LiFePO_4$	90–140	2000–7000	4–6 h	High durability; safer chemistry
Solid-state (SSB)	300–500 (forecast)	> 5000 (forecast)	< 2 h (forecast)	High-efficiency potential

Recent technological progress includes:

- Solid-state batteries (SSBs), which are expected to improve energy density, lifespan, and safety significantly [26]
- Second-life battery use, where automotive Li-ion batteries are repurposed for marine storage applications, reducing costs and environmental impact [8]
- High-power DC fast charging, already piloted in Norway and the Netherlands, reduces charging times below one hour [33].

Charging infrastructure is developing in parallel, from standard marina AC chargers to high-power DC systems and wireless solutions. Ports increasingly implement fast-charge stations that can reduce charging times to one hour or less [32]. “We are thrilled to lead the charge in embracing Aqua SuperPower’s revolutionary marine fast charge network, positioning Marina di Stabia as a vanguard of sustainable boating practices in the Gulf of Naples,” said Salvatore La Mura, Marina Manager at Marina di Stabia.

Fig. 7. Example of a modern marina with integrated electric charging systems [51]

Table 11. Classification of charging systems for yachts

System type	Power range [kW]	Typical location	Pros	Cons
AC standard	11–22	Small marinas	Low cost, easy installation	Slow charging
DC fast	50–350	Commercial ports	Very fast charging	Requires advanced cooling, grid impact
Inductive wireless	10–50	Premium marinas	High convenience	Lower efficiency, higher cost
Mobile charging barges	100–200	Urban waterfronts	Flexible deployment	Logistics complexity

4.2. Hydrogen: storage and applications in a yacht propulsion

Hydrogen as an alternative fuel is primarily used in proton-exchange membrane (PEM) fuel cells, characterised by high energy efficiency and zero local emissions. The main challenge for hydrogen remains its storage and distribution [1].

Table 12. Hydrogen storage forms and characteristics

Storage form	Pressure/ temperature	Typical application	Advantages	Drawbacks
Compressed (gaseous)	350–700 bar	Mobile tanks	Mature technology	High pressure; safety systems required
Liquefied (cryogenic)	−253°C	Stationary applications	Higher volumetric energy density	High cooling costs; boil-off losses
Chemical (e.g., hydrides)	Depends on the compound	Experimental	Potential for long-term storage	Complex recovery; mass penalties

Several innovations are being tested:

- On-site hydrogen generation using electrolysers integrated with marina PV systems [15]
- Liquid organic hydrogen carriers (LOHCs) that allow for safer transport of hydrogen at ambient conditions [39]
- Mobile hydrogen refuelling barges, considered in the Netherlands, offer flexibility in seasonal yachting destinations [44].

5. Modern fuel stations for motor yachts

5.1. Electric charging stations: challenges and prospects

The development of charging infrastructure for electric recreational craft is a key element of decarbonising the yachting sector. Current solutions vary in power, charging method, and integration with existing port infrastructure. The most common are AC chargers rated 11–22 kW, but in commercial ports and larger marinas, DC stations of 50–150 kW are increasingly installed. Inductive (wireless) charging systems also offer high operational convenience, eliminating the need to connect cables. Implementing such technologies requires adapting quay infrastructure and equipping vessels to receive power from wireless platforms [36].

Table 6. Types of electric charging stations

Station type	Power [kW]	Supply	Average charging time	Notes
AC standard	11–22	AC	4–8 h	Common, slow charging
DC fast	50–150	DC	1–2 h	Requires cooling and supervision
Inductive	10–50	Wireless	1.5–3 h	High convenience; lower power

From an infrastructural perspective, the most significant challenges include:

- Grid capacity limits, particularly in tourist-heavy coastal areas
- Investment costs, especially when installing DC or wireless stations
- Standardisation issues arise as different manufacturers propose non-harmonised connectors and charging protocols [21].

Future developments point to megawatt charging systems (MCS), which could allow fast charging even for large passenger vessels, and hybrid marina systems, where charging is supported by on-site energy storage to stabilise local grids [18].

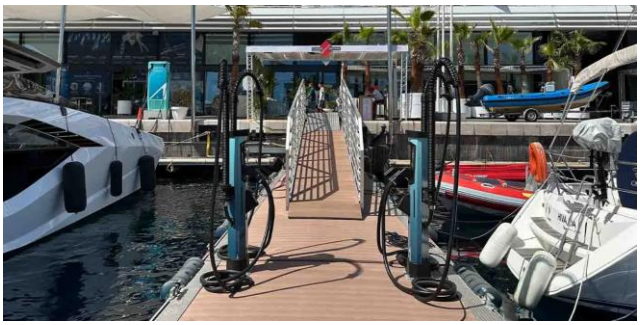

Fig. 8. Example of a modern marina integrating fast DC charging for yachts at the Yacht Club de Monaco [50]

5.2. Hydrogen refuelling stations: technical requirements and safety

Hydrogen stations for recreational navigation pose new challenges for design and operations. They require specialist tanks and compressors as well as adherence to stringent safety standards and regulations governing pressure systems. A typical hydrogen refuelling station comprises a storage tank, compression system, and dispensing module. In marinas, mobile solutions are most frequently considered – barges or trailer-mounted units that can be moved between locations depending on demand [3].

Table 7. Technical requirements for hydrogen stations

Infrastructure element	Characteristic
Refuelling pressure	350–700 bar
Safety systems	Leak detection, ventilation, relief, and shut-off valves
Location requirements	Setbacks from buildings, signage, and monitoring
Mobile variants	Barges or containerised trailer solutions

Although the capital cost of hydrogen stations remains high, pilot projects in Norway, Germany, and the Netherlands have demonstrated technical feasibility and growing user acceptance. Their implementation in marinas requires environmental permits, risk assessments, and routine inspections to ensure compliance with ISO and IMO regulations [25].

6. Results analysis and case studies

6.1. Modern fuel stations in Europe

Europe is at the forefront of implementing alternative-fuel infrastructure for navigation, not only due to technological capabilities but also thanks to a robust political framework that encourages sustainable development. EU directives, Green Deal policies, and IMO requirements have pushed many countries to test solutions that integrate energy transition with marina architecture.

The Ulsteinvik marina (Norway) stands as a milestone in hydrogen refuelling for recreational yachts. Its architectural concept is particularly innovative because the design deliberately reduces the perception of industrial infrastructure. The use of glulam timber beams creates a natural and regionally contextual character, while expansive glass façades provide both natural light and a visual connection with the fjord. From a technical perspective, the station includes mobile hydrogen tanks and modular compressors, which allow for scalability depending on seasonal demand. Socially, the station has been widely accepted by the local community, partly because it has been presented as both a functional facility and a public meeting place with educational content about renewable energy (Fig. 9).

Fig. 9. Ulsteinvik marina with integrated hydrogen refuelling station [47]

The Port of Bergen (Norway) is another leading example, but here the focus lies on electricity rather than hydrogen. The hybrid station combines AC slow chargers for smaller yachts with DC fast chargers for larger vessels. A distinctive element is the use of hydropower, which makes the energy cycle almost completely carbon neutral. The architecture of the technical enclosures has been deliberately minimised; small modular pavilions with green roofs integrate visually with the waterfront and even serve ecological functions, such as providing habitats for insects and retaining rainwater. From an operational perspective, the port authority emphasises that the modularity of the infrastructure allows for quick replacement and future upgrades, reducing life-cycle costs [37] (Fig. 10).

Fig. 10. A ship using Zinus Cruiser charger in the Port of Bergen [47]

In Amsterdam (Netherlands), space constraints in the densely built waterfront have inspired highly flexible solutions. The city has introduced several DC fast-charging points that can be accessed by both commercial and recreational craft. However, the most innovative element is the mobile hydrogen-barge concept, a floating refuelling unit that can move between districts depending on seasonal demand. This model not only reduces the need for permanent onshore facilities but also offers a scalable and transferable solution that could be replicated in other urban ports worldwide. Amsterdam's approach demonstrates how limited urban space can be optimised through mobile, modular energy infrastructure, which reduces environmental impact while supporting economic activity in water tourism [14] (Fig. 11).

Fig. 11. Amsterdam marina with DC charging points and mobile hydrogen barge concept [53]

6.2. Development of alternative fuel infrastructure in North America

In North America, the transition towards alternative energy in marinas is driven by both environmental policies and the private sector's interest in branding marinas as sustainable tourism hubs. Particularly in the United States and Canada, public–private partnerships have proven crucial in financing and scaling projects.

Marina del Rey (California, USA) illustrates how energy infrastructure can serve as a symbol of innovation. The installation of solar PV canopies with integrated DC fast chargers has not only decarbonised local yachting but also created a new architectural landmark. The wave-inspired design of the canopies echoes the maritime identity of the marina, blending aesthetics with function. From a techno-

logical perspective, the integration of a 500 kWh energy storage system ensures grid stability, which is crucial given the high power demand of simultaneous yacht charging. The marina has become a tourist attraction in its own right, often featured in media as an example of green port design [42] (Fig. 12).

Fig. 12. Marina del Rey with PV-integrated fast-charging canopies [52]

In the Great Lakes region, the *Clean Ports Project* has implemented stations in Chicago and Cleveland that are technologically simpler but socially significant. Floating pontoons with charging units represent a climate-resilient solution, able to adapt to fluctuating water levels caused by seasonal variations and climate change. Construction materials such as wood, composite panels, and anodised aluminium combine resilience with modern aesthetics. Importantly, local stakeholders – including yacht clubs and municipalities – have expressed support because the stations enable new eco-tourism initiatives, including "green regattas" and sustainable water sports [16].

In British Columbia (Canada), the flagship Vancouver project focuses on hydrogen. What makes it exceptional is the integration of local electrolysis units powered by hydropower. This enables full autonomy, avoiding the logistical challenges of hydrogen delivery. The design also includes public walkways and observation decks, allowing visitors to observe the hydrogen production process. This educational component is intended to build trust and social acceptance, countering scepticism often associated with hydrogen storage. By combining infrastructure with public outreach, the project is reshaping perceptions of hydrogen as a safe and sustainable fuel (Fig. 13).

Fig. 13. Vancouver marina project with on-site hydrogen electrolysis station [48]

6.3. Asian innovations in sustainable yachting

In Asia, rapid urbanisation and high population density create unique challenges, but also foster bold experiments with compact, multifunctional infrastructure. Japan and South Korea are currently at the forefront of marina innovation.

In Yokohama (Japan), the automated electric charging station combines AC slow charging for overnight berthing with DC fast charging for day users. Its defining feature is the digital reservation system, integrated into a mobile application that manages marina traffic and energy use. Architecturally, the use of translucent PV roofs allows the structures to blend into the urban waterfront while providing shading and energy generation. The facility is also connected to a district energy management system, ensuring that surplus electricity can be redistributed within the city grid. Yokohama thus demonstrates how a marina can function not only as a transport hub but also as an active node in a smart city energy network [27] (Fig. 14).

Fig. 14. Yokohama marina with translucent PV-integrated charging canopy [49]

The Busan EcoPort (South Korea) pilots hydrogen refuelling in combination with automated berthing systems, where digital sensors guide yachts to align precisely with refuelling arms. This reduces human error and enhances safety. Architecturally, the project features a glazed hydrogen pavilion with educational and exhibition spaces, as well as a public viewing terrace overlooking the bay. By combining infrastructure with cultural and social functions, Busan EcoPort transforms a purely technical facility into a civic attraction.

Moreover, South Korea's Blue Marina initiative envisions ten hybrid marinas, each equipped with both hydrogen and electric charging facilities. This program is directly supported by the Korea Energy Agency, reflecting the country's strategic commitment to marine decarbonisation. Importantly, the program also includes training for marina personnel and awareness campaigns for yacht owners, ensuring that the technological transformation is matched by social readiness [229].

6.4. Comparative global overview

The case studies analysed above highlight distinct regional approaches to marina decarbonisation:

– Europe focuses on contextual design and hybridisation, ensuring that energy infrastructure blends with cultural landscapes while offering flexibility (Ulsteinvik, Bergen, Amsterdam)
– North America prioritises large-scale integration and resilience, with emphasis on grid stability, floating solutions, and hydrogen autonomy (Marina del Rey, Great Lakes, Vancouver)

– Asia pushes towards automation, multifunctionality, and urban integration, embedding marinas into wider smart-city systems (Yokohama, Busan).

The comparative analysis suggests that while all regions share the common goal of decarbonisation, their approaches differ depending on geography, cultural context, and economic structure.

7. Conclusions and future directions

7.1. Potential innovations in refuelling technology

The analysis of alternative energy infrastructure for motor yachts highlights a range of innovations that are likely to reshape the yachting sector in the near and medium term. Both electricity-based systems and hydrogen-based technologies are developing rapidly, but future advancements are expected to move beyond current limitations [41].

One of the most promising directions is the development of high-power wireless inductive charging systems. Unlike conventional plug-in technologies, inductive charging eliminates the need for manual connection of cables, which is often cumbersome and poses safety risks in humid marina environments. Pilot projects in Norway and Japan demonstrate that inductive pads embedded in pontoons or quay walls can enable automatic power transfer at capacities exceeding 100 kW. Once commercialised, such systems could support short-term docking, where vessels recharge opportunistically during passenger embarkation or provisioning.

Another significant innovation is the emergence of containerised hydrogen stations. These are modular units integrating storage tanks, compressors, and dispensing modules in compact, relocatable containers [31]. Some prototypes include on-board electrolysers, allowing local production of green hydrogen from renewable sources such as photovoltaic panels or small-scale wind turbines. The decentralisation of hydrogen production would reduce reliance on large-scale logistics chains, which remain a bottleneck for maritime decarbonisation. Containerised stations could be deployed seasonally or in response to tourism intensity, ensuring both flexibility and cost-effectiveness [4].

Fig. 15. Conceptual rendering of a hybrid marina integrating electric, hydrogen, and renewable energy systems

Hybridisation of energy sources is another direction. Combining batteries, hydrogen, and renewable generation (PV, wind, wave energy) in a single marina could increase resilience and reduce operating costs. Smart microgrids capable of balancing supply and demand in real time are being tested in ports in Germany and South Korea. Such systems may evolve into autonomous energy hubs, serving not only yachts but also adjacent urban districts.

Architecturally, marina infrastructure will increasingly integrate energy technologies into landscape and design concepts. Green roofs, façade-integrated photovoltaics, and floating structures are no longer optional but essential in reconciling environmental performance with aesthetic quality. Future marinas will likely be conceived not just as refuelling points but as multifunctional civic spaces – combining leisure, education, and sustainability.

7.2. Development prospects and possible investment directions

From an investment perspective, the development of alternative-fuel marinas presents both opportunities and challenges.

Regulatory and policy context

The EU's Fit for 55 package, IMO emission strategies, and North American clean port initiatives provide a strong regulatory framework. Public subsidies, green transition funds, and private venture capital are already supporting pilot projects. However, a lack of standardised technical norms remains a barrier. International harmonisation of pressure standards for hydrogen refuelling (350 vs 700 bar), as well as universal charging protocols for electric vessels, will be critical for scaling infrastructure globally [20].

Economic efficiency and return on investment

Life-cycle cost analyses indicate that while electric charging stations offer lower capital costs and shorter payback periods, hydrogen infrastructure may deliver higher long-term returns in marinas with heavy traffic and larger vessels. For investors, the most promising business models combine user fees, public subsidies, and ancillary services such as renewable energy sales to adjacent urban grids [13].

Strategic locations for investments

The analysis of global case studies suggests that the most promising investment locations include:

– Tourist-intensive coastal regions (Mediterranean, Caribbean), where demand is seasonal but concentrated
– Urban waterfronts (Amsterdam, Vancouver, Yokohama), where marinas form part of broader smart-city strategies
– Climate-sensitive inland waterways (Great Lakes, Danube), where floating modular infrastructure provides resilience.

Social and cultural dimensions

The success of alternative fuel marinas depends not only on technology but also on user acceptance. Hydrogen, in particular, faces public scepticism linked to perceived safety risks. Educational pavilions, transparent design, and public outreach programmes – as demonstrated in Busan and Vancouver – are crucial in building trust. Future marinas will likely serve as demonstration spaces for sustainable living, influencing not only yacht owners but also local communities and tourists.

Long-term perspectives

In the longer term, the integration of marinas into blue economy strategies will be vital. Alternative energy marinas can become nodes of broader coastal development policies, supporting renewable energy production, ecotourism, and urban resilience. By 2050, it is plausible that zero-emission marinas will form part of international environmental certifications, similar to today's Blue Flag programme but focused on energy sustainability [13, 40].

7.3. Achieved goals and original contribution

This article achieved its goals by:

1. Systematically reviewing alternative propulsion technologies for yachts and their infrastructural requirements
2. Proposing an original evaluation framework (weighted indicators)
3. Applying LCC and LCA methodologies to assess economic and environmental feasibility
4. Conducting comparative case studies from three continents
5. Developing conceptual diagrams and visualisations integrating engineering and architectural perspectives.

The originality of this study lies in its integrative perspective. For the first time, the technical–economic assessment of alternative fuel stations for motor yachts has been systematically combined with architectural and social dimensions of marina development. While most existing studies address engineering feasibility or environmental performance in isolation, this article introduces a holistic evaluation framework that incorporates weighted indicators, life-cycle costing (LCC), and life-cycle assessment (LCA), alongside aesthetic, spatial, and user-related criteria.

Another innovative contribution is the use of conceptual diagrams and visual renderings as part of the methodological approach. These visualisations are not only illustrative but also serve as tools for design integration and stakeholder communication, enabling decision-makers, architects, and engineers to align technical requirements with urban and landscape contexts. In this sense, the paper moves beyond a descriptive review of state-of-the-art technologies and proposes an original model for assessing and planning sustainable marina infrastructure.

By bridging technical, economic, and architectural perspectives, the study highlights the potential for marinas to act not only as energy nodes but also as civic and cultural spaces. This dual function reflects a novel paradigm for the decarbonisation of recreational navigation, positioning marina design at the intersection of engineering innovation and socio-spatial development.

Bibliography

[1] Ahluwalia RK, Hua TQ, Peng JK. On-board and Off-board performance of hydrogen storage options for light-duty vehicles. Int J Hydrogen Energy. 2012;37(3):2891-2910. https://doi.org/10.1016/j.ijhydene.2011.05.040

[2] Balcombe P, Brierley J, Lewis C, Skatvedt L, Speirs J, Hawkes A et al. How to decarbonise international shipping: Options for fuels, technologies and policies. Energy Convers Manage. 2019;182;72-88. https://doi.org/10.1016/j.enconman.2018.12.080

[3] Ball M, Weeda M. The hydrogen economy – vision or reality? Int J Hydrogen Energy. 2015;40(25):7903-7919. https://doi.org/10.1016/j.ijhydene.2015.04.032

[4] Ball M, Wietschel M. (eds). The hydrogen economy: opportunities and challenges. Cambridge University Press. Cambridge: 2009. https://doi.org/10.1017/CBO9780511635359

[5] Bicer Y, Dincer I. Life cycle environmental impact assessments and comparisons of alternative fuels for clean vehicles. Resour Conserv Recycl. 2018;132:141-157. https://doi.org/10.1016/j.resconrec.2018.01.036

[6] Bicer Y, Dincer I. Comparative life cycle assessment of hydrogen, methanol and electric vehicles from well to wheel. Int J Hydrogen Energy. 2017;42(6):3767-3777. https://doi.org/10.1016/j.ijhydene.2016.07.252

[7] van Biert L, Godjevac M, Visser K, Aravind PV. A review of fuel cell systems for maritime applications. J Power Sources. 2016;327:345-364. https://doi.org/10.1016/j.jpowsour.2016.07.007

[8] Bobba S, Mathieux F, Ardente F. Life cycle assessment of repurposed electric vehicle batteries: an adapted method based on modelling energy flows. Publications Office of the European Union. Luxembourg 2018;19;213-225 https://doi.org/10.1016/j.est.2018.07.008

[9] Bouman EA, Lindstad E, Rialland AI, Strømman AH. State-of-the-art technologies, measures, and potential for reducing GHG emissions from shipping – a review. Transp Res D Trans Environ. 2017;52:408-421. https://doi.org/10.1016/j.trd.2017.03.022

[10] DNV. Maritime Forecast to 2050: Energy Transition Outlook 2024. Høvik: Det Norske Veritas; 2024. Available from: https://www.isesassociation.com/wpcontent/uploads/2024/08/DNV_Maritime_Forecast_2050_2024-final-3.pdf

[11] DNV. Maritime Forecast to 2050 – Energy Transition Outlook. Det Norske Veritas 2022.

[12] European Commission. Communication: The European Green Deal. Brussels: European Commission; 2019. COM(2019) 640 final. Available from: https://eur-lex.europa.eu/legal-content/EN/TXT/?uri=CELEX:52019DC0640

[13] European Commission (2021). Fit for 55: Delivering the EU's 2030 Climate Target on the Way to Climate Neutrality. EU Publications.

[14] European Commission. Hydrogen Valleys in Europe: 2022 Status Report. Brussels: EU Publications Office; 2022. Available from: https://data.europa.eu/doi/10.2830/315310

[15] Glenk G, Reichelstein S. Economics of converting renewable power to hydrogen. Nat Energy. 2019;4:216-222. https://doi.org/10.1038/s41560-019-0326-1

[16] Great Lakes Commission. Great Lakes Clean Ports and Waterways Program Report. GLC Publications 2021.

[17] Grey CP, Hall DS. Prospects for lithium-ion batteries and beyond – a 2030 view. Nat Commun. 2020;11:6279. https://doi.org/10.1038/s41467-020-19991-4

[18] Hovi IB, Figenbaum E, Pinchasik DR, Thorne RJ. Experiences from battery-electric truck users in Norway. World Electr Veh J. 2020;11(1):5. https://doi.org/10.3390/wevj11010005

[19] IEA. Net Zero by 2050: A Roadmap for the Global Energy Sector. Paris: International Energy Agency 2021.

[20] IEA. Global Hydrogen Review 2022. International Energy Agency 2022.

[21] IEC. Technical Report on Standardisation of Electric Charging Interfaces for Small Vessels. International Electrotechnical Commission 2022.

[22] International Energy Agency (IEA). Hydrogen in Ports and Shipping – Pathways to Decarbonisation. Paris: IEA; 2022. Available from: https://iea.blob.core.windows.net/assets/44d8d12f-58ac-46b8-9b36-43ac8a7e1c44/Hydrogen_in_Ports_and_Shipping.pdf
[23] International Energy Agency (IEA). The future of hydrogen – seizing today's opportunities. Paris 2021.
[24] International Maritime Organization. IMO Emission Reduction Strategy. IMO Reports 2021.
[25] International Organization for Standardization (ISO). ISO 19880-1:2020. Gaseous hydrogen – Fuelling stations – Part 1: General requirements. Geneva: ISO; 2020.
[26] Janek J, Zeier WG. A solid future for battery development. Nat Energy. 2016;1:16141. https://doi.org/10.1038/nenergy.2016.141
[27] Japan Ministry of Land, Infrastructure, Transport and Tourism (MLIT). Roadmap to Zero Emission in International Shipping. Tokyo: MLIT; 2021. Available from: https://www.mlit.go.jp/en/report/press/PortMarineBureau.html
[28] Ji M, Wang J. Review and comparison of various hydrogen production methods based on costs and life cycle impact assessment indicators. Int J Hydrogen Energy. 2021;46(100):38612-38635. https://doi.org/10.1016/j.ijhydene.2021.09.142
[29] Kwon JW, Lee JH, Kim JY, Park JW. Assessment of shipping emissions on Busan Port of South Korea. J Mar Sci Engineer. 2023;11(4):716. https://doi.org/10.3390/jmse11040716
[30] Kolodziejski M, Michalska-Pozoga I. Battery energy storage systems in ships' hybrid/electric propulsion systems. Energies. 2023;16(3):1122. https://doi.org/10.3390/en16031122
[31] Pielecha I, Cieślik W, Szałek A. The use of electric drive in urban driving conditions using a hydrogen-powered vehicle – Toyota Mirai. Combustion Engines. 2018;172(1):51-58. https://doi.org/10.19206/CE-2018-106
[32] Polak F. Energy balance comparison of small unmanned vehicle equipped with electric and hybrid propulsion. Combustion Engines. 2020;182(3):23-27. https://doi.org/10.19206/CE-2020-304
[33] Roy RB, Alahakoon S, Van Rensburg PJ. Impact analysis on distribution network due to coordinated electric ferry charging. IET Energy Systems Integration. 2024;6(4);638-663 https://doi.org/10.1049/esi2.12165
[34] Rehmatulla N, Smith T, Tibbles L. The relationship between EU's public procurement policies and energy efficiency of ferries in the EU. Mar Policy. 2017;75:278-289. https://doi.org/10.1016/j.marpol.2015.12.018
[35] Roslan SB, Konovessis D, Tay ZY. Sustainable hybrid marine power systems for power management optimisation: a review. Energies. 2022;15(23):9622. https://doi.org/10.3390/en15249622
[36] Seddiek IS, Ammar NR,. Evaluation of the environmental and economic impacts of electric propulsion systems onboard ships: case study passenger vessel. Environ Sci Pollut Res. 2021;28:37851-37866. https://doi.org/10.1007/s11356-021-13271-4
[37] Smit R, van der Veen A, Verbeek R. Hydrogen infrastructure development in the Netherlands: modelling and simulation study. The Hague: TNO 2020. Available from: https://publications.tno.nl/publication/34633253/1faP29/w07026.pdf
[38] Szałek A. Energy conversion in motor vehicles. Combustion Engines. 2020;183(4):50-57. https://doi.org/10.19206/CE-2020-408
[39] Teichmann D, Arlt W, Wasserscheid P, Freymann R. A future energy supply based on liquid organic hydrogen carriers (LOHC). Energy Environ Sci. 2021;4(8):2767-2773. https://doi.org/10.1039/C1EE01454D
[40] UN Environment Programme. Blue Economy and Sustainable Coastal Development. UNEP Reports 2022.
[41] UNCTAD. Review of Maritime Transport 2021. United Nations Conference on Trade and Development 2021.
[42] U.S. Department of Energy. Hydrogen Program Record & Clean Energy Marine Infrastructure. DOE, Office of Energy Efficiency & Renewable Energy 2022.
[43] Wang Q, Mao B, Stoliarov SI, Sun J. A review of lithium ion battery failure mechanisms and fire prevention strategies. Prog Energy Combust Sci. 2019;73:95-131. https://doi.org/10.1016/j.pecs.2019.03.002
[44] Weeda M, Smit R, de Groot A. Hydrogen infrastructure development in the Netherlands. Int J Hydrogen Energy. 2007;32(10-11):1387-1395. https://doi.org/10.1016/j.ijhydene.2006.10.044
[45] www.aqua-superpower.com
[46] www.archdaily.com
[47] www.businessnorway.com
[48] www.dnv.org
[49] www.marine-project.com
[50] www.monacolife.net/yacht-club-de-monaco-installs-two-super-fast-marine-e-charging-stations/
[51] www.oceanindependence.com/berths/80m-berth-in-marina-di-stabia/
[52] www.planetizen.com
[53] www.sustainable-ships.org
[54] Zbierski K. Jachtowe napędy silnikowe w pigułce (in Polish). Gdańsk 2021.

Maciej Bilski, DEng. – Faculty of Architecture, Poznan University of Technology, Poland.
e-mail: *maciej.bilski@put.poznan.pl*

Article citation info:
Dziubak T. Analysis of the filtration process of inlet air to an internal combustion engine in a two-stage filter. Combustion Engines. 2025;203(4):87-102. https://doi.org/10.19206/CE-207838

Tadeusz DZIUBAK

Combustion Engines
Polish Scientific Society of Combustion Engines

Analysis of the filtration process of inlet air to an internal combustion engine in a two-stage filter

ARTICLE INFO

Received: 2 June 2025
Revised: 1 July 2025
Accepted: 2 July 2025
Available online: 16 July 2025

The destructive effect of mineral dust grains (SiO_2 and Al_2O_3) on the accelerated abrasive wear of engine connections was demonstrated. It was shown that the use of two-stage (multi-cyclone-baffle) air intake filters for motor vehicle engines used in conditions of high air dustiness is necessary. The aim of the work was a theoretical and experimental analysis of the properties of paper filters operating in series behind a cyclone and without a cyclone. An original research methodology was used, which consisted of the simultaneous testing of a single cyclone and a paper filter with an appropriately selected surface area. The system tests (cyclone-paper filter) were carried out using conditions that corresponded to the actual filtration conditions in a two-stage air filter, including the filtration speed in the paper bed, the dust concentration in the air sucked into the engine, and the average cyclone inlet speed. The basic filtration characteristics of filtration efficiency, accuracy, and pressure drop of two paper filters were determined as a function of the dust mass fed to the system (cyclone-paper filter) or directly to the characteristic filter. It was found that the paper filter operating in series behind the cyclone achieves four times longer operating time, limited by a specific value of permissible resistance. In the initial (short) filtration period, lower filtration efficiency values were obtained than the required value of 99.5%. On the other hand, dust grains with a maximum size of 13.5 µm were found in the air behind the paper filter. The required filtration accuracy of the engine intake air is in the range of 2–5 µm. For this reason, the initial air filtration period is an undesirable phenomenon and may cause accelerated engine wear.

Key words: *internal combustion engine, air filter, multicyclone, paper filter, air filtration efficiency and pressure drop*

1. Introduction

The basic component of the working medium of an internal combustion engine is air taken from the atmosphere, and its quantity is proportional to the power output of the engine.

The mass of air supplied to an internal combustion engine depends on the displacement V_{ss} of its rotational speed n and the filling of the cylinder with a fresh charge, and this depends on the type of engine intake system, in which there may be a supercharging device.

For passenger car engines, the intake air flow (theoretically calculated) can be in the range of 150–400 m^3/h. Truck engines, due to their significantly larger V_{ss} displacement, achieve higher values (900-2000 m^3/h) of the intake air flow. However, the highest values of air demand (3500–6000 m^3/h) are achieved by CI engines, which are the drive unit of special vehicles, and these are tanks, armoured personnel carriers, and special units built on the chassis of these vehicles.

Various pollutants in the atmospheric air are sucked into the engine along with the intake air. The main component of engine intake air pollution is mineral dust. Its source is sandy and deserted areas and off-road areas, where trucks, special vehicles, including tracked military vehicles and work machines are used. Dust is lifted from dry ground by moving vehicles or by the wind, but after some time it falls by gravity. The concentration of dust in the air specified in the conditions of vehicle use is particularly high, often exceeding the value of 1 g/m^3 and can reach the value of 10 g/m^3.

Mineral dust has a specific chemical and granulometric origin that varies with the type of surrounding soils and location. Regardless, silicon oxide (SiO_2) and aluminum oxide (alumina), Al_2O_3 (about 10–15%), account for the largest share of dust (about 60–90%). The various oxides found in dust (Fe_2O_3, MgO, CaO, K_2O, Na_2O, SO_3) reach trace values [32]. Silicon oxide, known as silica, is a very common compound in nature. It makes up 12% of the earth's crust and is also found in minerals where it is in bound form (silicates, aluminosilicates). Then its content reaches 52% of the earth's crust. Silica is therefore a major component of sand, rocks, and soil. The most common varieties of crystalline silica in the world are quartz and cristobalite.

The chemical composition of dust depends strictly on the type and condition of the substrate (dry sandy substrate), altitude above the ground, climatic factors, as well as the type of dust fallout from fires, landfills, forests, peat bogs, and fallout from industrial dust and dust from volcanic eruptions [62].

The measure of dust content in the air is the concentration defined as the mass of dust (in grams or milligrams) contained in 1 m^3 of atmospheric air. The concentration of dust in the air is a variable quantity and depends on many factors: the type of ground (sandy, loess, grassy), vehicle movement dynamics (speed, single vehicle or convoy), the presence of other vehicles in the vicinity, weather conditions (rain, drought, wind direction), and the type of chassis (wheeled, tracked).

The dustiness of the air during vehicle operation varies with the concentration of dust in the ambient air and depends on the type of soil on the ground, vehicle movement conditions such as speed, the position of the vehicle in the convoy, and the type of running gear, as well as the type and intensity of precipitation. For this reason, the concentration of dust around a moving vehicle varies greatly.

Airborne dust concentrations can vary from 0.01 mg/m^3 in rural environments to approximately 20 g/m^3 during the movement of tracked vehicles in desert conditions on dry ground [54]. The author of [36] states that dust concentrations in the air can range from 0.001 to 10 g/m^3. According to research presented in [49], the maximum concentration of dust in the air varies widely, from 0.05 to 10 g/m^3. When vehicles are traveling on highways, the dust concentration can vary within a fairly wide range of 0.0004–0.1 g/m^3, and when a convoy of vehicles is traveling on sandy terrain, the concentration reaches 0.03–8 g/m^3 [6]. The author's research [20] shows that the dust concentration in the air measured behind a column of tracked vehicles reached a maximum value of 1.17 g/m^3. The dust concentration determined during measurements at a distance of 80 mm from the surface of the armour of a tracked vehicle used in sandy terrain at a speed of 14–18 km/h has values in the range of 2.1–3.8 g/m^3 [14]. The dust concentration increases with increasing driving speed. During the landing of a CH-53 helicopter on a landing site with sandy terrain, the dust concentration in the air at a height of about 0.5 m above the ground can reach the value of s = 3.33 g/m^3 [11]. The intake system's combustion engine intake system draws in air where the dust concentration usually does not exceed 2.5 g/m^3 [36, 49] when the vehicle travels on sandy ground.

Dust in the atmospheric air limits visibility. Dust content in the air of 0.6–0.7 g/m^3 causes a significant reduction in visibility, while if the dust content of the air exceeds 1.5 g/m^3 there is a complete lack of visibility, which is very dangerous for moving vehicles [56]. Examples of air dust concentration for various terrain conditions are shown in Fig. 1.

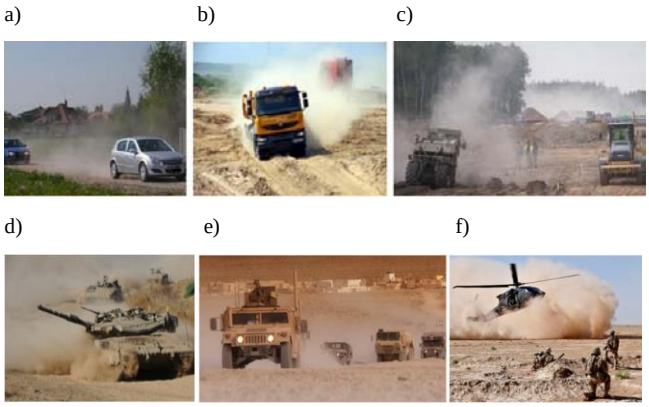

Fig. 1. Use of vehicles in high air dust levels: a) passenger cars on dirt roads, b) trucks on construction sites, c) working machines during road construction, d) tanks in desert terrain, e) military vehicles in a column in sandy terrain, f) helicopter landing in a desert [21]

The density of dust in the air depends on the type of roads and the conditions of vehicles (Fig. 2).

The highest air dust concentration (over 1,000 times higher than during vehicle traffic on city streets, highways, and paved roads) occurs during the use of tracked vehicles on dry, sandy training grounds. Dust levels are significantly higher behind a column of tracked vehicles than behind a column of wheeled vehicles, which is mainly due to the type of vehicle drive system.

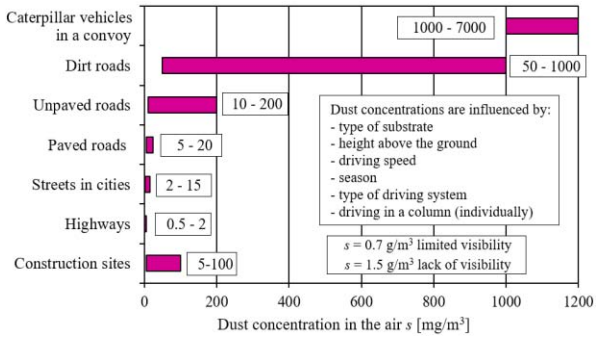

Fig. 2. Dust concentration in the air depends on the type of substrate [22]

2. The impact of dust on the wear of internal combustion engine components and its operation

The thickness of the oil film depends proportionally on the temperature of the oil and the relative velocity of the mating surfaces, and inversely proportionally on the thrust force, and therefore on the operating conditions of the engine (speed, load) and on the position of the piston between BDC and TDC and takes variable values in the range h_{min} = 0–50 μm [17]. When the piston with its rings is at the top of the cylinder (compression or work stroke) the oil film reaches its smallest values.

The high temperature of the connection elements causes a decrease in viscosity and the thickness of the oil film. In addition, the low relative speed of the piston and rings (at TDC it has the value of "0"), as well as the high load, reduce the thickness of the oil film, which leads to contact of dust grains (even those of small size) with the surfaces and their wear. This causes the highest wear of the upper part of the cylinder and the upper piston rings. Numerous literature data indicate that dust grains in the range of 1–40 μm are the main cause of excessive abrasive wear of engine parts surfaces. However, dust grains in the size range of 5–20 μm are the most dangerous for two cooperating surfaces and therefore should be removed from the intake air of engines [7, 47, 55].

The authors of [42] state that more than 30% of the pollutant mass delivered with the engine intake air stream does not participate in abrasive wear, but gets into the engine exhaust system, which causes increased emission of particulate matter (PM). On the other hand, very small dust grains can be burned at high temperatures in the cylinder. Other processes are subject to mineral dust grains, whose melting point is much lower than the temperature in the cylinder during combustion (2000–2500°C). The melting point of polymorphic varieties of SiO_2 quartz is: tridymite 1470–1710°C, and cristobalite about 1722°C. Grains of these minerals are melted and, in the form of droplets, enter the exhaust system, where they are deposited on its components. The glassy surface formed on the catalytic layer weakens the performance of the catalytic reactor [10].

Excessive wear of the P-PR-C assembly causes increased leakage in the supercharged space, which is the cause of increased blow-by of fresh charge into the crankcase during the compression stroke. This results in a drop in compression pressure and thus a drop in engine power. Leakage of the P-PR-C joint increases blow-by of exhaust gases into the crankcase, which raises the oil temperature

and increases the content of contaminants, mainly soot, accelerating oil aging [39, 64]. Excessive leakage between the P-PR-C components means a greater flux of oil above the piston, where it becomes coked up at the high temperatures found in the combustion chamber, which in turn increases particulate emissions [2, 8, 31, 41].

Dust grains contained in the air entering the engine cylinders and, in the oil, have a destructive effect on engine components, and their effects are varied and consist of (Fig. 3):

- abrasive wear of P-PR-C components
- abrasive wear of friction-operated components supplied with lubricating oil: main and connecting rod bearings (journal-bearing) of the engine crankshaft and camshaft, valve guide, camshaft cam-valve disc, pin-piston connecting rod, and valve seat
- erosive wear of the compressor and turbine
- reduction of heat exchange on the measuring element of the air flow meter by forming an insulating layer of dust and other contaminants
- reduction in the effectiveness of catalytic reactors as a result of molten dust particles settling on the catalytic surface.

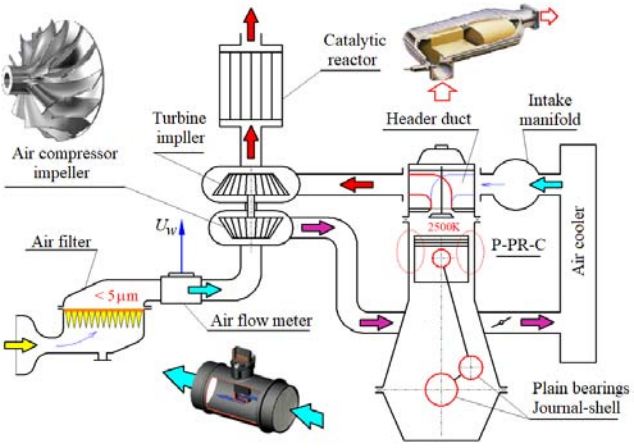

Fig. 3. Functional diagram of the intake system of a motor vehicle combustion engine and components affected by mineral dust

3. Air filtration systems in internal combustion engines

In order to ensure the required purity of the inlet air to the engine (removal of grains above the 2-5 µm range), and thus minimize excessive abrasive wear of engine components, air filters are used as part of the air supply system.

Air filters made of standard fibrous media are selective in terms of the size of the particles they retain, since not all particles are retained and collected in the filter bed with the same efficiency. For example, the authors of papers [60, 51] found a lack of penetration for particles larger than 4 µm during testing, even with new, unloaded filters.

The author of the paper [7] concludes that for all practical purposes, typical heavy-duty, high-efficiency air filters are 100% effective for particles larger than 4 to 5 µm when operating properly. These figures, combined with the information given earlier that particles smaller than 2 µm do not contribute significantly to wear of the engine's P-PR-C association, constitute the critical particle size range assumed hereafter as 2–5 µm. Particles smaller than this size range penetrate the filter but do not contribute to wear. Particles larger than the 2 to 5 µm range can be major contributors to wear, but do not penetrate high efficiency filters. The author's study of the paper [7] shows that only 14% of the particle mass according to ISO 12103-1, A1 Ultrafine Test Dust is smaller than 2 µm.

Depending on the conditions in which vehicles are used, and in particular on the value of dust concentration in the air, their engines are equipped with a single-stage (passenger cars) or two-stage (trucks and special vehicles) air filtration system. The filter element of a single-stage filter is a rectangular panel made of paper or composite materials (polyester + glass microfiber + cellulose). The pleating of the paper provides a large (about 2 m^2) filter area in a small filter body, which allows passenger cars to be used at low dust concentrations for about 30,000–50,000 km of mileage. Filter papers that are less than 1 mm thick have low dust absorption in the range (200–240 g/m^2). Therefore, they cannot be used as stand-alone air filters for a vehicle engine operating at high dust concentration in the air.

For example, the air intake of the engine of a tracked vehicle with a power of 700 kW and a displacement of V_{ss} = 38.8 dm^3, which is operated at an average speed of v = 20 km/h on sandy roads at a dust concentration of s = 1 g/m^3, sucks in about 170 kg of mineral dust with the air after 1,000 km. A passenger car engine with a much smaller displacement (V_{ss} = 1.5 dm^3) is capable of sucking in more than 0.6 kg of dust with the air if it is used over a 40,000 km mileage on paved roads, where the dust concentration in the air is only s = 5 mg/m^3.

Therefore, air-supply systems for the propulsion engines of motor vehicles, mainly military vehicles (tanks, wheeled and tracked transporters) and engineering machinery, are equipped with filters that can retain significant masses of dust from the intake air and at the same time ensuring high filtration efficiency and accuracy. These are filters with a two-stage filtration system (Fig. 4). The function of the first stage of filtration is performed by an inert filter, usually a multicyclone, although monocyclones are popularly used in truck filters. In series behind the multicyclone, forming an integral unit, is the second filtration stage for engine inlet air. This is a cylindrical filter cartridge (baffle filter) constructed of pleated paper or a component of filter materials and a surface area so selected that the velocity of flow through the bed (filtration speed) does not exceed 0.06 m/s. Constructed and operated in this way, the device primarily provides the required 99.9% efficiency and accuracy of filtration of dust grains above the range of 2–5 µm, and a slow increase in pressure drop, resulting in a long service life.

A multicyclone is a device built of individual cyclones, the internal diameters of which do not exceed D = 40 mm. The cyclones are arranged in parallel next to each other for short distances. The cyclones are arranged vertically next to each other at short distances. The cyclone's dust discharge openings are fixed to a sealed settling tank, and the purified air outlet tubes are fixed tightly to a plate that is the base of a rectangular tank, where the second-stage filter cartridge is located [23, 27, 45, 48].

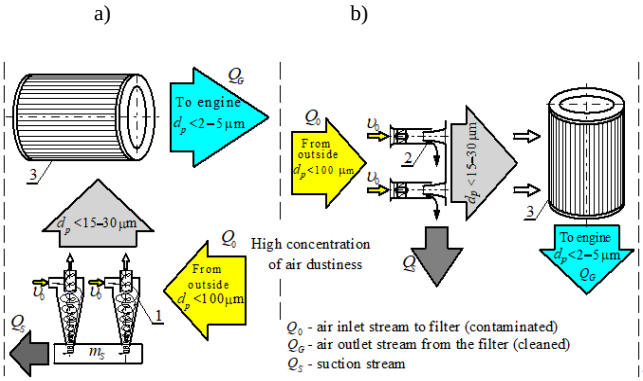

Fig. 4. Air filtration systems in a two-stage filter: a) multicyclone built of return cyclones with tangential inlet – porous baffle), b) multicyclone built of through cyclones – porous baffle

The number of cyclones in a multicyclone is from several dozen to several hundred. The multicyclone of the PT-91 tank air filter contains 108 return cyclones with a tangential inlet, and the multicyclone of the Leopard tank filter contains 288 through-flow cyclones with an axial inlet. The types of cyclones used for filtering the intake air of motor vehicle engines are shown in Fig. 5.

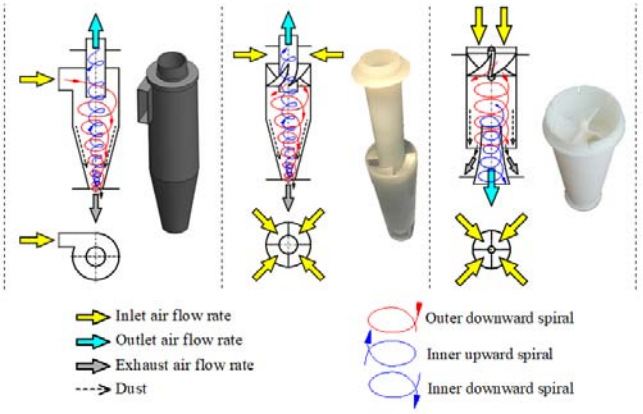

Fig. 5. Types of cyclones used for intake air filtration in motor vehicles: a) reverse cyclone with tangential inlet, b) reverse cyclone with axial inlet, c) axial flow cyclone

The second stage of filtration is a cylindrical filter cartridge made of pleated filter paper, a cheap and easy-to-process material, which is arranged in series behind the multicyclone.

The disadvantage of paper filter beds is their low initial filtration efficiency and high pressure drop, with a small mass of dust retained by the filter bed. For this reason, filter media manufacturers use composite beds made of synthetic layers and a layer of nanofibers.

A layer of nanofibers with a thickness of 1–5 μm and fibre diameters of 300–800 nm [15, 29, 33] is applied to a standard filter bed made of fibres with diameters of 10–15 μm, which improves the filtration efficiency of dust particles smaller than 5 μm in the air sucked into the engine. Examples of the design of pleated paper filter cartridges shaped into cylinders having an elliptical or circular cross-section suitable as a second filtration stage behind a multicyclone are shown in Fig. 6.

Fig. 6. Examples of designs of filter cartridges of two-stage filter

4. Air filtration process in a two-stage filter

4.1. Introduction

The essence of a two-stage filter (multicyclone-paper cartridge) is to combine the operation of two devices, where different air filtration processes take place. A multicyclone is a device that uses centrifugal force to separate solids or liquids from gas. Therefore, in a multicyclone, at a specific flow rate, only large particles (above 15–35 μm) and heavy particles will be separated from the air. Multicyclones are characterized by the ability to remove large air streams for an unlimited time without the need to handle significant amounts of dust, with an efficiency of 85–90%. As a result, only a small portion of the dust mass that was in the air sucked in from the environment flows into the filter cartridge located behind the multicyclone.

The return cyclone with tangential inlet is made of a body consisting of a cylindrical part with a diameter D and a part in the shape of an inverted cone, the smaller diameter of which is tightly connected to the dust settling chamber, where the pollutants separated in the cyclone are stored (Fig. 7). The upper part of the cylindrical body is the place of the tangentially attached inlet nozzle, which usually has a rectangular cross-section with sides “a” and “b”.

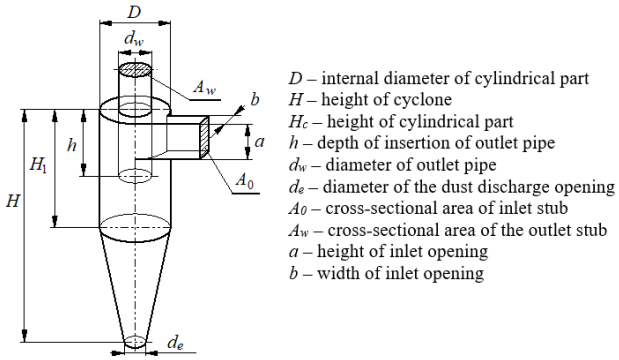

Fig. 7. Typical dimensions of a reverse cyclone with tangential inlet

The inlet pipe is positioned in relation to the cylindrical part of the cyclone so that its axis is usually perpendicular to the main axis of the cyclone, although there are cyclones with an inclined inlet pipe. The cylindrical part of the cyclone is covered tightly from the top with a circular cover, in the center of which, centrally in the vertical axis of the cyclone, is fixed tightly a cylindrical outlet tube usually with a diameter of 0.5D.

4.2. Air filtration in a multicyclone

The process of cleaning gases from solid particles carried out in a cyclone consists in introducing a stream of

contaminated gas into a rotating motion, followed by a change in the direction of the flow of the stream of contaminated air, which causes that solid particles of larger size and mass, due to their inertia, tend to follow the original direction of movement and are separated from the air, and then collect in a special settling tank, while the cleaned air together with particles of lower density or smaller size pass further. The idea of cleaning gases in a cyclone was patented by Knickerbocker Co. Jackson, USA in 1886 [61]. The design of the cyclone is very simple, but the process of aerosol filtration in the cyclone is very complicated, difficult to describe mathematically, which is mainly due to the complex vortex motion of the aerosol stream, first the screw motion of the gas (external vortex) together with the dust downwards (Fig. 8), and then the screw motion of the gas upwards (internal vortex), to the cyclone outlet [17].

Considering the movement of a dust grain in a cyclone in a plane perpendicular to the cyclone axis, it can be seen (Fig. 8) that two opposing forces act on the grain: the inertial force F_B and the aerodynamic force F_R. After several rotations, the particle meets the cyclone wall, which significantly reduces its speed. Then the particle, driven mainly by the spiral air flow, rotates along the cyclone wall and moves into the collection chamber. The effect of gravity on the particle is of little importance.

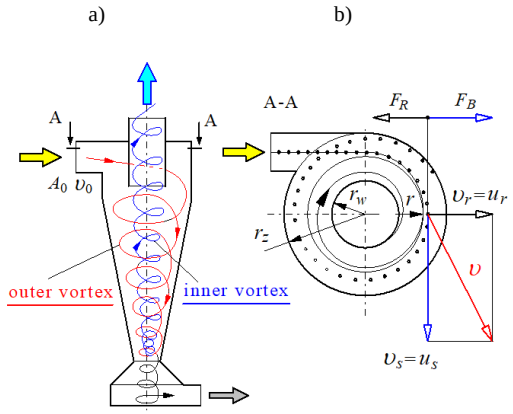

Fig. 8. Simplified model of aerosol flow in a reverse cyclone: a) vortex system, b) force system: a) vortex system, b) force system: A_0 – cross-sectional area of inlet tube, r_w – radius of outlet pipe, r_z – radius of cylindrical part, υ_0 – cyclone inlet velocity, υ_r – radial component of gas velocity in the cyclone, υ_s – tangential component of gas velocity. u_s – tangential component of grain velocity, u_r – radial component of grain velocity

The air stream is set in rotational motion in a reverse flow cyclone by feeding it tangentially into the cylindrical part of the cyclone through a special nozzle (Fig. 3a) or by flowing through stationary, obliquely positioned deflectors mounted between the inner wall of the cylindrical part and the outlet pipe (Fig. 8b). The dust separated in the cyclone is directed to the settling tank, which is tightly attached to the dust removal opening located in the lower part of the cyclone.

Excessive dust accumulation in the cyclone settling chamber is not recommended, as it may be re-sucked through the opening in the cyclone bottom. This situation may occur during vehicle shocks or sudden changes in the air flow through the cyclones, which result from rapid changes in engine speed when used on uneven terrain. Entrainment of dust from the settling chamber by the air flow rotating towards the outlet pipe results in a decrease in the cyclone filtration efficiency. To prevent this phenomenon, continuous dust removal from the settling chamber is used, using an additional air flow (Q_S suction flow), which is part of the cyclone inlet flow.

The main air stream, after being freed from dust particles of larger size and mass and flowing to the lowest zone of the cyclone, abruptly changes the direction of flow by 180 degrees, followed by a helical motion (internal vortex) flow back upward. The air stream moves upward along the cyclone's central axis and then leaves the cyclone through the outlet pipe while still performing a helical motion and lifting smaller dust particles with it. During the outflow of the air stream through the outlet tube, there are significant pressure losses, which, according to the authors of works [44, 50], reach up to 50–80% of the total pressure drop in the cyclone. Tangential inlet returns cyclones achieve a pressure drop in the range of 2–3 kPa, which is their main disadvantage. In comparison, the pressure drop of axial cyclones is much lower, reaching values of 0.5–0.7 kPa. The high pressure drop in the air supply system caused by the air filter has an adverse effect on filling the engine with fresh air, resulting in a decrease in torque and power. It can also cause excessive emissions of toxic components in the exhaust gas.

The movement of dust particles in a cyclone is usually considered only in the plane perpendicular to the cyclone axis. In this case, two forces act on the dust particle: the inertial force F_B and the aerodynamic drag force F_R (Fig. 8). Other forces also act on the dust particle in the cyclone, but their influence on the trajectory is negligible. Dust particles move along a trajectory whose shape depends on the mutual relationship between the values of F_B and F_R. In turn, the value of both forces depends on the size, shape, and material of the dust particle, as well as the type of gas flowing through the cyclone. Dust particles that have been given a spinning motion obtain the centrifugal force described by the relation:

$$F_B = \frac{m_z \cdot u_s^2}{r} \cdot \rho_g \qquad (1)$$

where: m_z – mass of the dust particle, u_s – tangential component of the particle velocity approximately equal to the tangential component of the gas velocity υ_S at this point, r – distance of the dust particle from the axis of rotation.

This force causes the particle to move towards the cyclone wall at a speed u_r. This movement is counteracted by the medium resistance force F_R, determined by the relationship:

$$F_R = \lambda \cdot A_p \cdot \frac{u_r^2}{2} \cdot \rho_g \qquad (2)$$

where: A_p – projection area of the grain (area of the grain projected onto a plane) in the direction of its movement, u_r – component of the radial movement of the grain, ρ_g – gas density, λ – friction coefficient depending on the shape of the grain and the Reynolds number

It is assumed that dust particles with diameters smaller than a certain dimension dpg, defined as the limiting particle diameter, for which the condition $F_B < F_R$ applies, will

enter the cyclone and be carried by the internal air vortex towards the cyclone outlet pipe. On the other hand, dust particles with diameters greater than the dpg dimension, for which $F_B > F_R$, will move along a spiral line and be directed towards the cyclone wall, and thus be separated. The balance equation of forces acting on single dust grains is expressed by the relationship [16].

$$m_p \frac{du_p}{dt} = F_R + F_B + F_G + F_M + F_C \quad (3)$$

F_M – Magnus force (created by the rotation of particles in the flow field), F_C – force created between dust particles and the inner wall of the cyclone, as well as the force generated as a result of collisions between dust particles, F_G – gravitational force.

It follows from the relationship (1) that the smaller the distance of the dust grain from the axis of rotation r (smaller diameter D of the cylindrical part of the cyclone), the greater the inertia force at the same cyclone inlet velocity υ_0 and the same dust particle mass. This results in increased efficiency and accuracy of air filtration in the cyclone. For this reason, in practice, sets of cyclones with small diameters (multicyclones) are used instead of one cyclone with a large diameter. In the air-supply systems of internal combustion engines of motor vehicles, for air pre-filtration, are used assemblies of 100–300 return or through cyclones, the internal diameter of which does not usually exceed D = 40 mm. The ends of the cyclones are mounted in common lower and upper plates, which allows for the supply of aerosol through a common pipe from the place with the lowest dust concentration. Aerosol suction by individual cyclones can also be carried out directly from the environment. Figure 9 shows a two-stage air filter for a tracked vehicle engine, where the multicyclone is constructed of return cyclones with a tangential inlet.

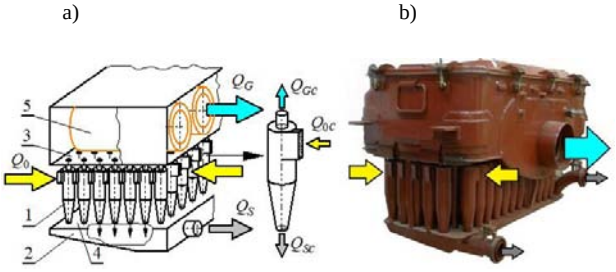

Fig. 9. Two-stage air filtration system for a tracked vehicle engine: 1 – multicyclone (return cyclones with tangential inlet), 2 – dust tank, 3, 4 – top and bottom plate fixing cyclones, 5 – paper filters of the second stage of filtration

4.3. Air filtration in a porous partition

In a porous partition, where the filter bed is made of densely packed fibres, dust particles are retained by individual fibres as a result of the simultaneous action of several filtration mechanisms: interception, inertial, diffusion, gravitational settling, and sieving [38, 70] (Fig. 10).

The interception mechanism occurs when a dust particle moving along the air stream line, flowing around the bed fibre, approaches the fibre to a distance equal to its radius and comes into physical contact with it. The inertial mechanism occurs when a heavy particle cannot adapt to sudden changes in the direction of the air stream near the fibre and, due to inertia, continues to move along its original path and then comes into contact with the fibre, where it is retained. The inertial mechanism is more effective at high particle inflow velocities [70]. The diffusion mechanism exists in laminar flow when particles do not move near the fibre along the streamline, but perform random Brownian motion, moving in directions transverse to the direction of aerosol flow, colliding with fibres and settling there. The smaller the particle size (< 0.1 μm) and their velocity, the more intensely they fall out of the stream line and the greater the likelihood of their deposition on the fibre surface.

The gravitational mechanism exists as a result of the retention of large and heavy particles with a free fall velocity. It is particularly important in vertical flow through the filter bed. The gravitational mechanism is significant for particles with a diameter greater than 1 μm flowing through the filter bed at a velocity greater than 0.05 m/s. The effect of gravity is negligible for particles smaller than 0.5 μm [5].

The total separation efficiency of the bed results from the combined effect of all filtration mechanisms. Figure 10 shows that the efficiency of the capture mechanism and the inertial mechanism increases with the size of dust grains above 0.1 μm [5]. A similar nature of the increase in filtration efficiency, but dust grains above 1 μm is presented by the sieve mechanism. In contrast, the efficiency of the diffusion mechanism has the opposite effect to the previous mechanisms. Its value decreases with increasing dust grains. For small dust grains (less than 0.1 μm), the efficiency resulting from the inertial mechanism is the highest. Therefore, the total filtration efficiency assumes a characteristic minimum in the graph (Fig. 10), from which it follows that dust particles in the range of 0.08–0.3 μm are retained by the filtration mechanisms with lower efficiency [3, 70].

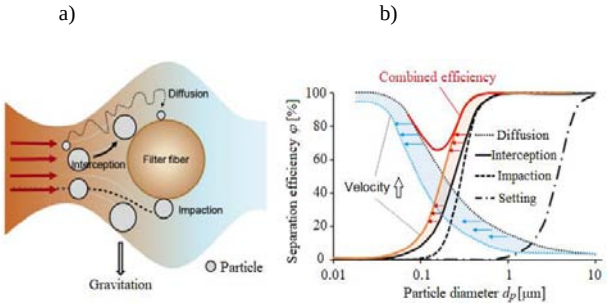

Fig. 10. Model of particle retention in a porous partition. (a) operation of filtration mechanisms on a single fibre: (b) total efficiency of filtration mechanisms [38]

The result of the filtration mechanisms in the filter bed is the retention of dust particles on the surface of the fibres of the porous structure and on previously deposited particles. This creates complex dendritic structures (agglomerates) that slowly grow and fill the free spaces between the fibres (Fig. 11). The filter cartridge made of pleated paper is characterized by high filtration efficiency (99.5–99.9%) and accuracy above 2–5 μm. The disadvantage of filter papers is their low dust absorption capacity (in the range of 220–250 g/m^2). This is due to the structure of the filter bed and its small thickness, which does not exceed g_m = 0.6–0.9 mm. The accumulation of dust on the fibres of the porous

partition causes the free spaces between the fibres to fill up (Fig. 11), which reduces the space for air flow and results in a continuous increase in pressure drop Δp_f, which, after some time, can reach significant values.

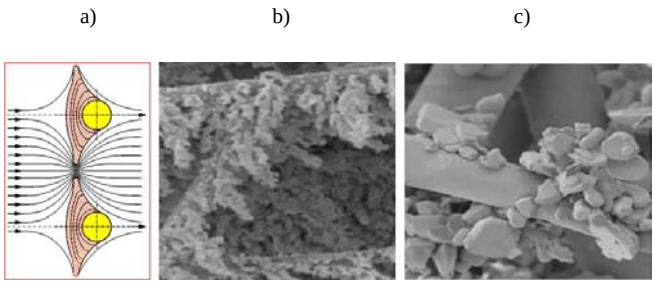

Fig. 11. View of accumulated dust particles (agglomerates) on the fibers of the filter bed: a) scheme of layer formation, b) SEM image of agglomerates formed on the fiber, c) SEM image of the bed of micron-sized aluminum oxide aerosol agglomerates [3]

This is a characteristic feature of partition filters. An increase in the pressure drop Δp_f of the filter above a specified permissible resistance value Δp_{fdop} is not recommended. This causes a decrease in the engine's fresh charge and power, and an increase in the emission of harmful exhaust components [59]. The criterion determining the permissible resistance value Δp_{fdop} of air filters is based on a 3% decrease in engine power. The experimentally determined permissible resistance values for passenger car engines are in the range of Δp_{fdop} = 2.5–4.0 kPa. For truck engines and special vehicles, these values are Δp_{fdop} = 4–7 kPa [13, 25]. In order for the filter to achieve the Δp_{fdop} value, the filter cartridge must be replaced with a new one.

Multicyclones have the fundamental advantage of being able to separate significant amounts of dust from a large air stream in a short time without affecting the pressure drop. A multicyclone does not require maintenance, and the dust collected in the sedimentation tank is systematically removed by an ejection suction system.

The combination of a multicyclone and a partition filter as a two-stage filter extends the service life of the air filtration system several times (until the value of Δp_{fdop} is reached) compared to a single-stage filter, which results in a longer vehicle mileage (Fig. 12).

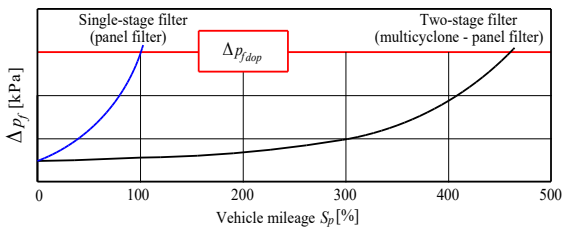

Fig. 12. Change of pressure drop of the air filter (porous membrane) and the filter with a two-stage filtration system ("multicyclone – porous membrane") as a function of vehicle mileage

In the available literature, the results of numerical and experimental studies of single return cyclones with a tangential inlet [9, 40, 66, 67] and through cyclones with an axial inlet [4, 24, 34, 69] aimed at selecting the optimal dimensions of the cyclone and its components are presented in quite large numbers. In the literature, there are, but not very many, studies of an ensemble of several or dozens of cyclones in terms of the uniformity of airflow through individual cyclones and its effect on filtration efficiency [18, 46, 68].

Computational fluid dynamics simulations coupled with experimental validation of fibre beds are being conducted to determine recommended parameter combinations for their optimal design in terms of minimizing flow resistance characteristics or increasing the filtration efficiency of filter media [28, 43]. Studies are being conducted on the effects of dust particle size distribution and filter air velocity on dust layer structure. Experimental results showed that layers containing smaller particles of equivalent mass showed increased pressure drop [65].

A considerable amount of work deals with the study of filter beds with a layer of nanofibers, which is applied to a standard filter bed (cellulose). The nanofiber layer has a thickness of 1–5 μm and fiber diameters in the range of 300–800 nm [12, 33, 57]. This improves the filtration efficiency of dust grains with a diameter of less than 5 μm in the inlet air of the engine, resulting in less wear on its components and increased durability. The results of original scale testing of internal combustion engine air filters are few [35, 42, 63], which is mainly due to the high cost of testing, as well as the availability of a test bench to produce the air flow resulting from engine operation, especially a special vehicle engine at full load.

From the above analysis, it can be seen that the performance and flow resistance characteristics of a single cyclone or cyclone unit are studied, and fibre beds are separately studied in terms of performance and flow resistance. The problem of aerosol filtration in a cyclone is quite different from that in a filter with a porous baffle, where dust accumulation causes an increase in flow resistance, which is a limitation of its further use. This problem does not exist in cyclone filters, which is a maintenance-free filter if extraction of the separated dust is used.

The combination of these two units into a single device, if a number of conditions are met, functions as a two-stage filter. However, the available literature lacks a quantitative and qualitative description of the phenomena occurring in the process of air filtration in a two-stage filter operating in a "multicyclone-baffle filter" system. The present work aims to partially fill this gap, and these are the conducted experimental studies of the two-stage air filtration system "single cyclone-paper filter". This is a novel test method, which consists of testing an assembly: a single cyclone and a paper filter set in series behind it, which has an appropriately sized filter surface to maintain the required ($\upsilon_{Fdop} \leq$ 0.06 m/s) filtration speed.

In addition, other important test conditions that characterize the actual filtration process in the original two-stage air filter were maintained. These are the filtration velocity of the original paper filter bed and the cyclone inlet velocity derived from the number of cyclones in the multicyclone and the engine inlet air flow. The test results of the paper filter bed operating directly downstream of the single cyclone can be used in the design work of two-stage filters in terms of evaluating its filtration capacity and estimating the

mileage of the vehicle limited by the achievement of acceptable pressure drop.

5. Methodology and conditions of experimental research on the "cyclone-research filter" unit

5.1. Purpose and scope of the study

Experimental tests were aimed at evaluating the properties of two filter papers covering the characteristics of filtration efficiency and accuracy, dust absorption, and pressure drop. The filter papers were pleated and then shaped into a cylindrical filter cartridge, which was placed in a housing, and the whole was named the A1 and A2 research filters (Fig. 13a).

The scope of the study was to examine the filter characteristics of the two research filters, which operated in two filtration systems (variants). The two-stage filtration system was a return cyclone and an integrally connected (arranged in series) research filter (A1 or A2). The single-stage system was a research filter without a cyclone. The filtration characteristics of the research filters (A1 and A2) were determined according to the mass of dust m_D dosed uniformly and with a specified concentration (s = 1 g/m^3) into the cyclone of the "cyclone-test filter" research unit, and in the case of single-stage operation directly into the research filter (s = 0.5 g/m^3).The other test conditions themselves were the same for both variants.

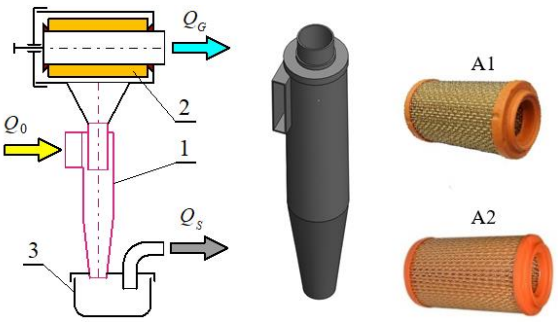

Fig. 13. Filter assembly "return cyclone - research filter": 1 – cyclone, 2 – paper filter cartridge, 3 – tank of separated dust

The reverse cyclone with a tangential inlet was the first stage of filtration in the "cyclone–test filter" filtration unit. The basic parameters of the cyclone are shown in Fig. 14a. The second stage of filtration consisted of test filters, A1 and A2, with the parameters given in Fig. 14b.

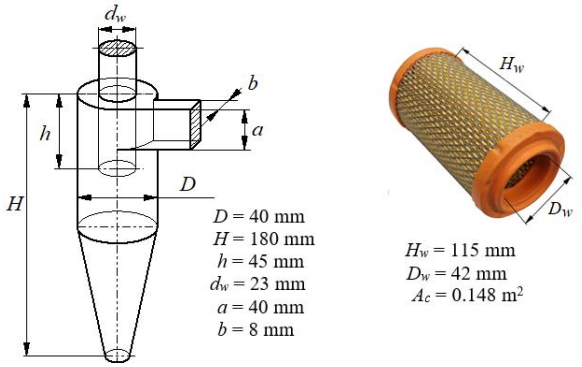

Fig. 14. Basic dimensions of a) return cyclone with tangential inlet, b) research filter

The value of the air flow rate Q_G flowing through a single cyclone was determined as the quotient of the air flow rate Q_{Silmax} flowing into the engine for speed n_N and the number of return cyclones with tangential inlet in the multicyclone for which the baffle filter is selected. In the case of the cyclone under study, this value is Q_G = 34 m^3/h. The Ac surface area of the filter paper of the test filter was selected from the condition of the permissible (maximum) filtration velocity, which for filter papers used for the second stage of filtration should not exceed the value $\upsilon_{Fdop} \leq 0.06$ m/s. A cylindrical test filter was made from the calculated A_c surface of the paper (Fig. 14b). Two test filters were made, each from a different filter paper (made by J.C. BINZER), which were named A1 and A2, respectively. The parameters of the cartridges are given in Fig. 14. The papers differed in the values of the structure parameters (Table 1). The A1 filter paper has six times higher pressure drop than the A2 paper, due to its higher grammage (204 g/m^2) and smaller (42 μm) diameter. Filters made in this way were the subject of research in the "reverse cyclone-filter research" team.

Table 1. Basic parameters of filter paper manufactured by J.C. BINZER Papierfabrik, used to make filter cartridges for testing

Parameters	Units	Paper identification	
		A1	A2
Grammage	g/m^2	204	108
Thickness - load 2 N/cm^2	mm	0.9	0.67
Pressure drop at 400 cm^3/s, A = 10 cm^2	mbar	6.7	1.04
Tearing strength	kPa	385	212
Resin content	%	18.8	17
Maximum value of pore diameter	μm	51	89
Average value of pore diameter	μm	42	76

Experimental tests were performed on the characteristics of A1 and A2 test filters operating as a second stage of filtration in a "cyclone-test filter" unit and without a cyclone. The tests were carried out using PTC-D test dust while maintaining a constant flux value of Q_G = 34 m^3/h, which corresponds to the actual filtration velocity $\upsilon_F \leq 0.0638$ m/s. The following characteristics were studied:

– filtration efficiency $\varphi_w = f(m_D)$
– pressure drop $\Delta p_w = f(m_D)$

where: m_D – dust mass dosed uniformly to the "cyclone-test filter" unit or directly to the test filter.

– filtration accuracy $d_{pmax} = f(m_D)$.

Since dust grains are retained in the filter bed selectively in terms of particle size, in the air downstream of the filter, their size also varies from d_{pmin} to d_{pmax}, with dust grains of the smallest size being the largest. Therefore, in this study, the criterion for filtration accuracy is the dust grain with the largest size found in the air behind the filter and is designated d_{pmax}. The number of dust grains in the air behind the filter under study and their sizes, including the size of the dust grain d_{pmax}, were determined in each measurement cycle using a particle counter.

5.2. Experimental research methodology

The tests were carried out on a test stand (Fig. 15), the main components of which are a return cyclone with

a tangential inlet and a test filter (A1 or A2) located behind it in series.

The suction fan forces the air stream Q_G flowing in the "cyclone-test filter" unit. To measure the Q_G flow rate, and mass flow meter with a measuring range of 10–150 m^3/h and an accuracy of 1.2% was used. A dust extraction system pipe is connected to the dust settling tank, together with a safety filter and a rotameter, which is used to measure the Q_S extraction flux. A rotameter with a measuring range of 1–7 m^3/h and an accuracy of 0.01 m^3/h was used. To determine the pressure drop Δp_w of the test filter, a water pressure gauge U-tube connected after the test filter at a distance of $6d_w$ (d_w – filter outlet diameter), where the values of pressure drop Δh_m after the filter were recorded. To protect the flow meter sensor from dust, there is an absolute filter in the measuring line, which is also a filter for measuring the mass of dust passed through the filter.

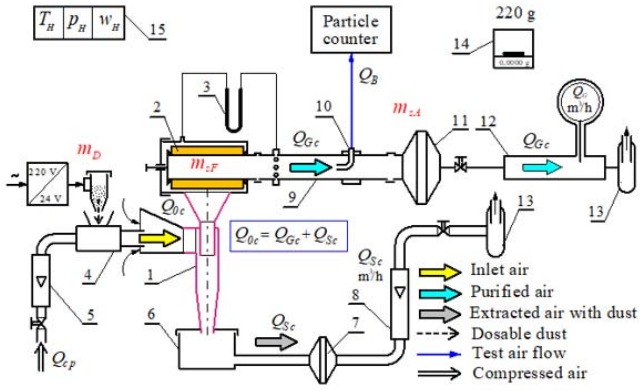

1 – cyclone, 2 – measuring filter, 3 – U-tube manometer, 4 – dust dispenser, 5 – compressed air rotameter, 6 – dust settling tank, 7 – absolute filter, 8 – suction flow rotameter, 9 – measuring tube, 10 – dust measuring probe, 11 – measuring (safety) filter, 12 – air mass flow meter, 13 – suction fans, 14 – analytical balance, 15 – device for measuring air humidity, temperature and ambient pressure

Fig. 15. Diagram of the test stand for the "cyclone-filter test" assembly

The experimental tests were performed using polydisperse PTC-D test dust, which is suitable in Poland for testing air filters in motor vehicle engines as a substitute for AC fine test dust. The chemical and granulometric composition of PTC-D dust is consistent with AC fine dust in terms of particle sizes below 80 µm. The mass content of particles smaller than 10 µm in the total dust mass is over 50%. These are particles that are very difficult to retain by filtration systems. The chemical and fractional composition of PTC-D dust is given in Table 2 and Table 3.

Table 2. Chemical composition of PTC-D dust

Dust component	SiO_2	Al_2O_3	Fe_2O_3	Na_2O	K_2O	CaO	MgO	moisture
Mass content in dust [%]	67.15	15.25	4.9	4.5	4.5	2.35	1.15	3

Table 3. fractional composition of PTC-D dust

Dust grain size d_p [µm]	0÷5	5÷10	10÷20	20÷40	40÷80
Mass share of dust fraction U_m [%]	38.55	15.97	16.48	19.46	9.54

Of note is the high (more than 50%) content in the dust of grains below 10 µm and the fact that more than 67% of the dust by weight is SiO_2, which is a mineral of high hardness.

During the testing of the characteristics of filters A1 and A2 operating in a single-stage and two-stage filtration system, the following conditions were applied:

– outlet air flow from the test filter Q_G = 34 m^3/h
– suction flow Q_S is defined as 10% of the outlet air flow from the Q_G filter
– dust concentration for the inlet stream to the cyclone s = 1 g/m^3
– dust concentration for the inlet stream (single-stage filtration) to the test filter s = 0.5 g/m^3
– mass filtration efficiency of the cyclone used for testing φ_c = 92%.

Filtration characteristics: efficiency $\varphi_w = f(m_D)$ and filtration accuracy $d_{pmax} = f(m_D)$ as well as pressure drop $\Delta p_f = f(m_D)$ were determined for a constant air flow rate Q_G. The same measurement cycles j of a fixed duration were performed sequentially, during which dust was evenly dosed into the test system. The measurement duration was set to τ_p = 120 s in the initial period. During the main operating period of the filters, the duration was extended to τ_p = 240–480 s. The number and size of dust particles in the air behind the filter were recorded by a particle counter.

After each test cycle, j, measurements were made of the quantities that were necessary to determine the characteristics: efficiency and filtration accuracy, pressure drop, and actual dust concentration in the inlet air stream.

The filtration efficiency of the test filters was determined by the gravimetric method as the quotient of the mass of dust m_{zFj} retained by the filter and the mass of dust m_{DFj} dosed uniformly over a specified time to the test unit (measurement cycle j) using the relation:

$$\varphi_j = \frac{m_{zFj}}{m_{DFj}} = \frac{m_{zFj}}{m_{zFj}+m_{zAj}} 100\% \quad (4)$$

where: m_{zAj} – mass of dust retained on the absolute filter during the next "j" measurement cycle.

The mass of dust retained on the test filter cartridge during the next "j" measurement cycle was determined from the relation:

$$m_{zFj} = m''_{zFj} - m'_{zFj}, \quad (5)$$

where: m''_{zFj}, m'_{zFj} – the mass of the test filter after (before) the measurement.

The mass of dust retained on the absolute filter during the next "j" measurement cycle was determined from the relation:

$$m_{zFj} = m''_{zAj} - m'_{zAj}, \quad (6)$$

where: m''_{zAj}, m'_{zAj} – the mass of the absolute filter, after the measurement and before the measurement, respectively.

The dust mass retained on the research filter m_{zFj} and the absolute filter m_{zAj} and the mass dosed to the m_D unit were determined using an analytical balance with a measuring range of 220 g and an accuracy of 0.0001 g.

2. Filtration accuracy was determined as the largest dust grain size $d_{pj} = d_{pmax}$ in the air stream behind the filter.

3. The pressure drops Δp_{fj} of the research filter was determined as the static pressure drop before and after the filter based on the measured height Δh_{mj} on a U-tube water manometer according to the relationship:

$$\Delta p_{wj} = \frac{\Delta h_{mj}}{1000} \cdot (\rho_m - \rho_H) \cdot g \text{ [Pa]} \quad (7)$$

where: Δh_{mj} – height measured on a U-tube water manometer after the end of dust dosing, ρ_m – density of the manometric liquid [kg/m^3], ρ_H – air density [kg/m^3], g – gravity [m/s^2].
4. The amount of N_{zi} dust particles in the purified air downstream of the filter was measured within established size ranges (d_{pimin}-d_{pimax}).
5. For a given test cycle, the percentage fraction (d_{pimin} – d_{pimax}) of dust grains in the air stream was calculated from the following relationship:

$$U_{zi} = \frac{N_{zi}}{N_z} = \frac{N_{zi}}{\sum_{i=1}^{32} N_{zi}} 100\%, \quad (8)$$

where: $N_z = \sum_{i=1}^{32} N_{zi}$ – total amount of dust particles in the air cleaned after the filter during one measurement cycle
6. The actual dust concentration in the cyclone inlet air was determined after the test using the quantities measured during the test and applying the relation:

$$s = \frac{3600 \cdot m_D}{(Q_G + Q_S) \cdot \tau_p} \text{ [g/m}^3\text{]} \quad (9)$$

According to the above methodology, the filtration characteristics were determined: efficiency $\varphi_w = f(m_D)$ and filtration accuracy $d_{pmax} = f(m_D)$ and pressure drop $\Delta p_w = f(m_D)$ of the A1, A2 research filters operating in a single- and two-stage system. The criterion for completing the tests was that the test filter (A1, A2) achieved the established set value of acceptable resistance Δp_{fdop}.

6. Results of experimental studies and their analysis

The results of the filtration efficiency $\varphi_w = f(m_D)$, filtration accuracy $d_{pmax} = f(m_D)$, and pressure drop $\Delta p_w = f(m_D)$ tests of test filters A1 and A2, which operated as a single-stage filter (without a cyclone) and as a second stage of filtration (after a reverse cyclone), are presented in Fig. 16–18. The filtration characteristics were determined as a function of the dust mass m_D supplied to the "cyclone-test filter" test unit or directly to the test filter. The filtration efficiency characteristics $\varphi_w = f(m_D)$ and pressure drop characteristics $\Delta p_w = f(m_D)$ of test filters A1 and A2, which were the second stage of filtration after the reverse cyclone, are shown in Figure 16. Despite the same test conditions, the characteristics of both tested filters differ across the entire range in terms of values and performance, which is mainly due to the different parameters of the filter paper structure (Table 1) used to make the test filters.

The main difference in the course of the characteristics can be seen in the first (initial) period of filtration, which is designated conventionally (F_{A1}, F_{A2}). This period is called the transient filtration period in the literature. Its characteristic feature is small values of filtration efficiency. Filters A1 and A2 achieve an initial filtration efficiency of φ_{wA1} = 71.1% and φ_{wA2} = 50.6%, respectively. However, with the amount of dust mass retained by the filter paper, the filtration efficiency increases steadily, with the intensity of the increase for the two filters studied being different.

It was assumed for the purposes of this study that the criterion for the end of the initial filtration period (the transient filtration period) is that the paper achieves a filtration efficiency of φ_w = 99.5%. Within the framework of this study, it was assumed that the criterion for the end of the initial (interim) filtration period is that the paper reaches the filtration efficiency φ_w = 99.5%. The above conventional value was adopted based on the work of [7, 30, 36, 54], where the presented test results indicate that an increase in filtration efficiency above the range φ_w = 99.5–99.9% clearly reduces engine wear. Figure 16 shows the dependence of the filtration efficiency of a typical air filter over its full-service life fed with AC fine dust and the resulting engine wear in the form of a normalized wear index. As the filter's operating time increases, the efficiency increases, resulting in a decrease in the abrasive wear of the engine and thus an increase in its service life. From the course of both curves, it can be seen that reaching a filtration efficiency of φ_w = 99.9%, the intensity of engine wear decreases significantly. If the filter is serviced at 100% of its design life, engine wear is minimized (the normalized wear rate is 1.0), and the filtration efficiency reaches the design level of ~99.97% (Fig. 16). The graph indicates the increasing rate of engine wear resulting from servicing the air filter more often than necessary.

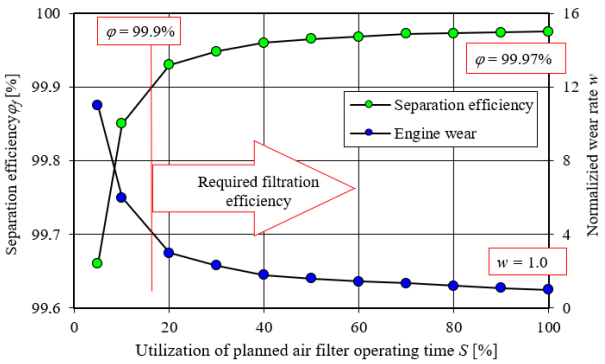

Fig. 16. Filtration efficiency and relative value of engine wear as a function of air filter operating time [7, 30]

Figure 17 shows the rate of abrasive wear of the cylinder liner and piston ring when three air filters with different filtration efficiency are used compared to when no air filter is installed in the engine.

Any air filter with higher efficiency reduces the wear of both engine components dramatically, with the wear rate of the piston ring being several times higher than that of the cylinder liner. Taking the abrasive wear of both the cylinder liner and piston ring without an air filter as 100% (Fig. 17), using an air filter with 97.8% efficiency reduces the wear of both components to 1.89%. After using an air filter with a higher efficiency of 99.45% and 99.42%, the wear of the cylinder liner and piston ring is only 0.41% and 0.43%, respectively, compared to the wear when there was no air filter in the engine. Hence, the reasonableness of taking the

filtration efficiency of 99.5% as the required minimum value for the cleanliness of the engine's inlet air.

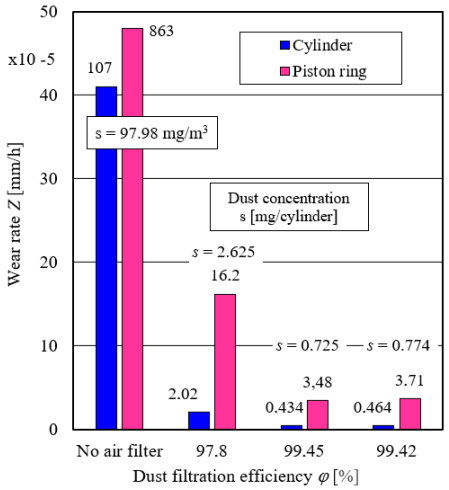

Fig. 17. Effect of air filter efficiency on the wear rate of cylinder liner and piston rings compared to no air filter [1]

The test results shown in Fig. 18 prove that the initial filtration period for the A1 filter is much shorter than that of the A2 filter. This is due to the different values of the parameters of the filter paper structure and the filtration process that takes place in it. The paper of the A1 filter has twice the grammage, which is due to the greater packing of the fibers, and thus the pore diameters obtain smaller values. For this reason, the A1 filter's conventional filtration efficiency (φ_w = 99.5%) is achieved after retaining m_{DA1} = 16.82 g of dust, while the mass of dust retained by the A2 filter until it achieves (φ_w = 99.5%) has a value of m_{DA2} = 35.78 g, twice as much.

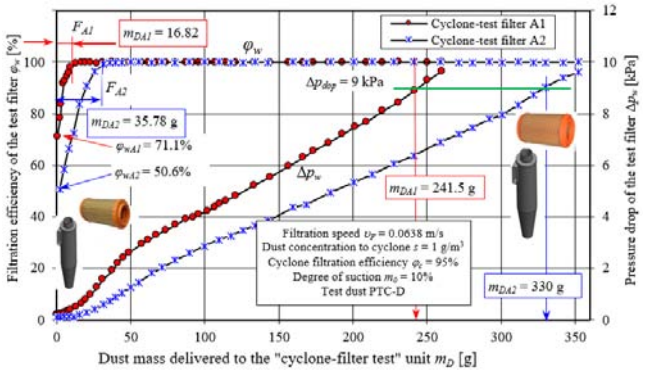

Fig. 18. Characteristics $\varphi_w = f(m_D)$, $d_{pmax} = f(m_D)$ and $\Delta p_w = f(m_D)$ of test filters A1 and A2 depending on the mass of dust mD delivered to the "return cyclone-test filter A1 (A2)" unit

The operation of the filtration mechanisms in A1 paper is more efficient. Dust particles retained by the direct hooking and inertial mechanism more intensively form tree-like dendritic clusters on the fibers, which fill the free spaces (pores) between the fibers. The consequence of this phenomenon is the impeded aerosol flow between fibers, an increase in flow velocity, and an increase in pressure drop, which is a function of velocity to the second power. The inherent phenomenon of dust mass retention by the filter bed is an increase in pressure drop. On the other hand, the dendrites growing on the fibers reduce the distance between adjacent fibers, resulting in the retention of smaller and smaller dust grains. This phenomenon should be explained by the continuous increase in filtration efficiency and accuracy. In the initial period of filtration, dust grains with a maximum size of d_{pmax} = 13.3 µm were recorded in the air behind the A1 filter, after which the size of these grains decreases and for a dust mass of m_{DA1} = 16.82 g has a value of only d_{pmax} = 2.3 µm (Fig. 19). On the other hand, for the A2 filter, the maximum size of dust grains in the purified air has a value of d_{pmax} = 13.5 µm, but dust grains with a size of d_{pmax} = 2.7 µm were recorded only after m_{DA2} = 64.17 g of dust was delivered to the system.

Dust filtration phenomena occurring in the filter bed cause changes in filtration efficiency and accuracy and are closely related to changes in pressure drop. Therefore, the pressure drop of filter A1 increases more intensively than that of filter A2. The different intensity of the increase in pressure drop causes the A1 filter to achieve a pressure drop value of Δp_w = 9 kPa, when a mass of dust (m_{DA1} = 241.5 g) is delivered to the test assembly. Filter A2, due to a less intense increase in pressure drop, the value of Δp_w = 9 kPa was obtained much later than filter A1, which is related to the dust mass m_{DA2} = 330 g delivered to the "cyclone-filter test" assembly.

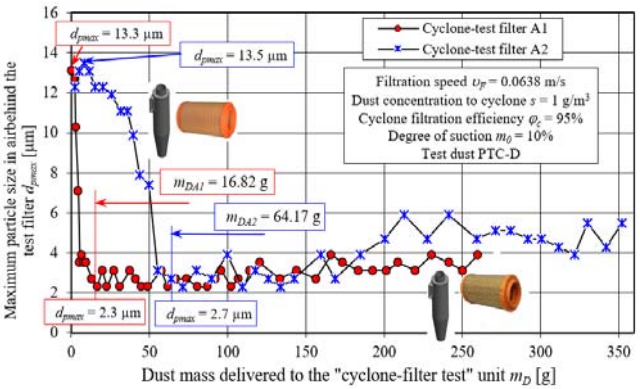

Fig. 19. Characteristics $d_{pmax} = f(m_D)$ of test filters A1 and A2 depending on the mass of dust m_D delivered to the "return cyclone-test filter A1 (A2)" unit

For this reason, in the air stream flowing out of the test filter, the number of N_{zp} dust grains was recorded during each measurement, starting with measurement No. 1, in a dozen fixed same measurement channels, which were limited by fixed $d_{pmin} - d_{pmax}$ grain sizes (Fig. 20) ranging from 0.7 µm to 80 µm. It was found that for a given measurement, the number of dust grains in the air behind the filter with increasingly larger diameters decreased until they were completely absent (Figure 20). The dust grain located in the last dimension channel has the largest size $d_p = d_{pmax}$ and is an indication of filtration accuracy.

During the tests, it was assumed that the air filtration accuracy is determined in each measurement cycle and is expressed by the diameter of the largest dust grain d_{pmax} found in the stream of cleaned air leaving the filter.

Figure 20 shows the change in the number of dust grains depending on their size, d_{pmax}, for subsequent test cycles distinguished by the dust mass m_D retained on the filter during the preliminary (unsteady) filtration period of the A1 test filter. Measurement cycle No. 1 showed that the air behind the A1 test filter contained dust grains with a maximum size d_{pmax} = 13.3 μm.

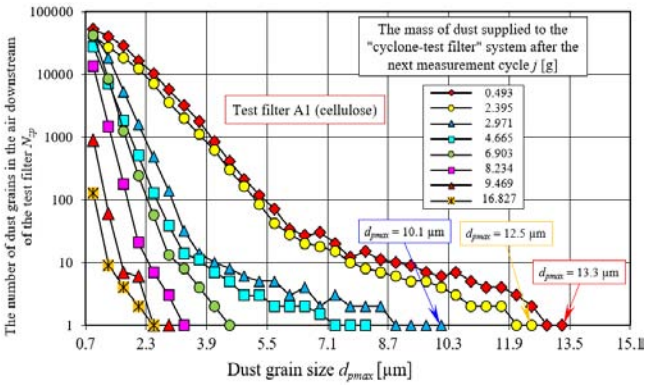

Fig. 20. Number of dust grains Nzp in the air behind the A1 filter insert depending on their size for subsequent test cycles (dust mass m_D) during unsteady filtration

Each subsequent measurement cycle showed that the total number of dust grains N_{zp} decreases, and the diameters of dust grains with a maximum size d_{pmax} are smaller and smaller. This phenomenon should be explained by the formation of dendrites on the fibres, which reduces the space for free flow and causes the retention of dust grains of smaller and smaller sizes. In the second test cycle, this is a grain size d_{pmax} = 12.3 μm, and after the third d_{pmax} = 10.1 μm (Fig. 20).

The diameter d_{pmax} = 2.3 μm, which is the smallest value of the dust grain behind the filter, was found after 16.82 g of dust was supplied to the system together with the air. This is also the moment when the filter achieved a filtration efficiency of 99.9%, which is the condition for ending the initial filtration period for the A1 filter.

The main filtration period following the initial filtration period is characterized by stabilization of filtration efficiency at the level of 99.95–99.99% and stabilization of maximum diameter sizes in the range of d_{pmax} = 2.3–3.9 μm for both filters (Fig. 20). In the final stage of the A2 filter operation, dust grains of increasingly larger sizes appear in the exhaust air but not exceeding 5.9 μm.

The above phenomenon is due to the fact that the deposit of dust grains on the fibers causes the growth of dendrites, which reduces the free flow of air and results in an increase in flow velocity. Exposed and susceptible to greater flow, the tops of the dendrites are destroyed, and detached dust grains, and sometimes significant parts of dust agglomerates, move deeper and deeper in the filter bed with the direction of air flow until they completely leave the bed. Signs of such a phenomenon were recorded during the study.

The resistance to flow of the tested research filters (A1, A2) increases all the time, which is due to the accumulation of dust and the filling of the free spaces between the fibres, resulting in a smaller airflow space, and thus a higher speed. Larger values of pressure drop Δp_w and higher intensity of growth were obtained for A1 paper. This should be explained by smaller (42 μm) pore diameters than in A2 paper (76 μm), which is associated with lower dust absorption and much lower paper permeability.

The filtration characteristics that were experimentally determined for the A1 test filter, which was the second filtration stage in the "cyclone-test filter" unit, and the characteristics of the A1 filter without a cyclone (single-stage filtration) are shown in Fig. 21.

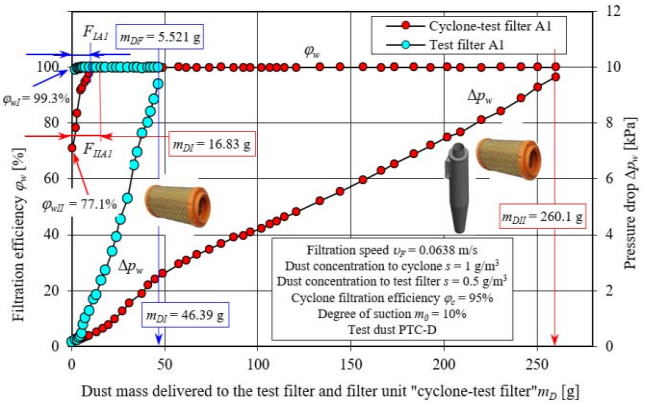

Fig. 21. Characteristics of filtration efficiency $\varphi_w = f(m_D)$ and pressure drop $\Delta p_w = f(m_D)$ of the research filter A1 as a function of the dust mass m_D supplied to the "reverse cyclone-research filter A1" assembly and to the research filter A1 without a cyclone

Significant differences can be observed as to the value and course of the characteristics $\varphi_w = f(m_D)$ and $\Delta p_w = f(m_D)$ of the A1 filter tested in different configurations.

If the test filter is operated individually (without a cyclone) it achieves high (φ_{wI} = 99.3%) initial filtration efficiency. This is due to the fact that dust grains of large size, in this case less than 80 μm, flow onto the bed. Large grains are retained mainly by the inertia mechanism and direct hooking more quickly forms dendrites on the fibres, which restrict the flow between the fibres.

The above phenomenon simultaneously increases the filtration efficiency of the tested filter, resulting in a shorter initial filtration period. Achieving an efficiency of φ_w = 99.5% ends when dust with a mass of m_{DF} = 5.521 g is delivered to Filter A1. In contrast, when Filter A1 operated as a second stage of filtration, the initial efficiency was much lower at φ_{wII} = 71.1%, and during the initial period, m_{DII} = 16.83 g of dust was delivered to the filter.

Regardless of whether the A1 filter operates without a cyclone or in a "cyclone-paper filter" unit, the pressure drop increases steadily with the amount of dust mass delivered with the air. However, the intensity of the increase in both cases is different, and therefore, the A1 filter operating without a cyclone achieves a pressure drop of Δp_{wI} = 9.6 kPa after delivering m_{DF} = 46.39 g of dust. The same value of pressure drop is obtained by filter A1 operating in a "cyclone-test filter" unit after delivering m_{DF} = 260.1 g of dust to its filter bed. This value is five times higher than that of the A2 filter. The results presented and the phenomenon described (Fig. 19) clearly explain the idea of air filtration in a two-stage filter (multicyclone-paper filter). This

makes the mileage of the vehicle until the execution of obtaining an acceptable value of pressure drop and the associated servicing of the air filter (replacement of the filter element) significantly increased.

In the case of single-stage filtration (filter operation without a cyclone), dust flows directly from the environment along with the air onto the filter bed.

When testing the characteristics of a test filter operating without a cyclone (single-stage filtration), test dust is dosed directly onto the filter bed, which corresponds to drawing air with dust directly from the environment. The inlet air contained dust grains with maximum sizes not exceeding d_{pmax} = 80 μm. On the other hand, in a two-stage filter (multi-cyclone-paper filter), the air with dust from the environment first reaches the cyclone, where the separation of dust grains of higher density and size takes place as a result of turbulence, as a result of which the dust at the outlet of the cyclone has a completely different granulometric composition than at the inlet to the cyclone (Fig. 22).

Depending on the filtration conditions, dust grains with sizes above d_p = 15–35 μm are retained in cyclones. The largest share of U_p = 16.2% in the total number of grains in the inlet air stream Q_0 to the cyclone was for dust grains with a size of 4 μm (Fig. 22). The filtration of the air in the cyclone resulted in the largest share of U_p = 36.1% in the cyclone exhaust air for dust grains with a size of 0.7 μm. As the size of the dust grains increases, their shares decrease sharply, and the share of d_p = 4 μm grains was reduced to 7% (Fig. 22).

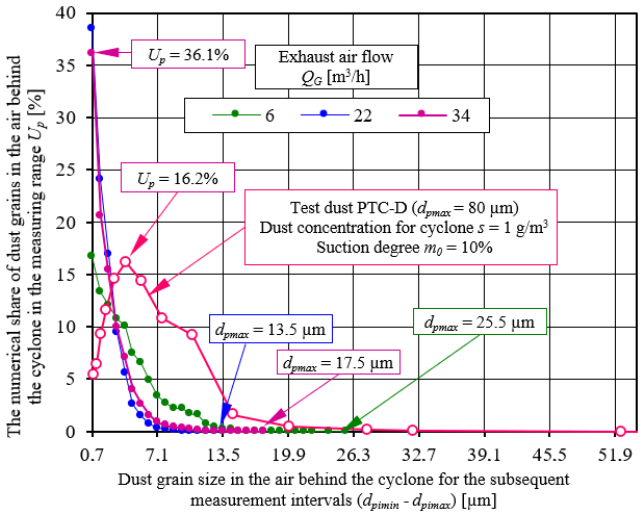

Fig. 22. Fractional composition of dust $U_{pi} = f(d_p)$ in the inlet air stream Q_0 and outlet air stream Q_0 of a reverse cyclone with a tangential inlet

This causes dust grains of smaller size and mass to be directed to the second filtration stage (paper filter), which are slower to form dendrites on the fibres and fill the space between the fibres [19, 26, 37, 52, 53, 58].

Measurements were made once, which is due to the specifics of the air filter testing methodology, so calculation of standard deviations and related standard uncertainties determined by the type A method is impossible. As for the standard uncertainties determined by the B-type method, they were due to the accuracy of the dust mass measurement assumed on the basis of the technical documentation of the balance as 0.0001 g.

Comparing the ranges of permissible variability of the obtained values of the weighted mass (±0.0001 g) with the values of the mass assumed for determining the value of filtration efficiency, it was found that the resulting uncertainties of the obtained results are at least several orders of magnitude smaller than these results (for relative uncertainties at the level of 0.012–0.021%). In view of the above, it can be concluded that the uncertainty values are small enough not to affect the obtained results.

7. Conclusions

The aim of the work was a theoretical and experimental analysis of the air filtration process in a two-stage filter, which was performed using an original research methodology consisting in testing a single cyclone and a research filter placed in series behind it, with an appropriately selected filter paper surface. The filtration characteristics were tested as a function of the dust mass fed to the system (cyclone-paper filter) or directly to the research filter. Two filters, A1 and A2, differing in paper structure, were used. During the tests, the same filtration conditions were maintained, including filtration speed, dust concentration, and cyclone inlet speed, as during filtration in a real two-stage air filter. The tests of the "single cyclone-barrier filter" assembly showed that the use of an inertial filter (multicyclone) as the first stage of filtration is beneficial due to the removal of a significant mass (85–95%) of dust from the engine intake air.

Studies of the “single cyclone-baffle filter” assembly have shown that the use of an inertia filter (multi-cyclone) as the first stage of filtration is advantageous, due to the fact that the removal of a significant mass (85-95%) of dust from the engine's inlet air extends the time of efficient operation of the two-stage filter several times.

The analysis and experimental research carried out led to the following conclusions:

1. Filter materials operating in the "cyclone-research filter" system are characterized by a less intensive increase in pressure drop and reach the permissible pressure drop 2–4 times slower than the same materials operating in a single-stage filtration system, despite the same mass m_D supplied to the system.
2. The first (initial) stage of operation of the tested filters has low (φ_w = 50–70%) filtration efficiency and low filtration accuracy, as evidenced by large (d_{pmax} = 13.5 μm) dust grains in the cleaned air. This phenomenon occurs regardless of whether the filter operates in a two-stage system (after the cyclone) or a single-stage system.
3. Lower filtration efficiency values during the initial filtration period and lower intensity of its growth occur for the filter operating in a two-stage system. Therefore, the operating time of this filter until the efficiency value (φ_w = 99.5%) is reached, which was established as the end of the initial period, lasts much longer. This is due to the fact that dust of smaller size is directed from the cyclone to the partition filter operating in the two-stage system. Dust of such granulation is difficult to retain by filtration mechanisms.

4. The initial period phenomenon is characteristic of each partition filter that starts working with dust. Such a period occurs after replacing the filter element with a new one. During this time, the air exhausted from the filter (air intake to the engine) contains dust grains whose sizes are significantly above the required filtration accuracy d_{pmax} = 2–5 μm. For this reason, this phenomenon is particularly dangerous, as it can cause accelerated wear of the piston-cylinder ring (P-PR-C) connection elements and other friction pairs lubricated with oil, which reduces the durability of the engine. It is advisable to replace the engine intake air filter element with a low frequency.
5. The developed research methodology allows for the experimental determination of basic characteristics of filter materials intended for the second stage of air filtration with any structural parameters and in a wide range of changes in filtration conditions corresponding to the operation of the air filter in conditions of high dust concentration in the air.
6. The originality of the research methodology lies in the fact that the filter material constituting the second stage of filtration is contaminated with dust whose chemical and granulometric composition has been changed and shaped as a result of the actual air filtration process in the cyclone.

Acknowledgements

This work was financed/co-financed by Military University of Technology under research project UGBWIM_22012025_15.

Nomenclature

BDC	bottom dead center
d_{pmax}	filtration accuracy
F_B	centrifugal force
F_R	air resistance force
P-PR-C	piston-piston ring-cylinder
TDC	top dead center
φ_w	filtration efficiency
Δp_f	pressure drop
Q_G	extraction flow
Q_S	exhaust air stream

Bibliography

[1] Alfadhli A, Alazemi A, Khorshid, E. Numerical minimisation of abrasive-dust wear in internal combustion engines. Int J Surf Sci Eng. 2020;14;68-88. https://doi.org/10.1504/IJSURFSE.2020.10027562

[2] Andrych-Zalewska M, Chłopek Z, Merkisz J, Pielecha J. Determination of characteristics of pollutant emission from a vehicle engine under traffic conditions in the engine. Combustion Engines. 2022;191(4):58-65. https://doi.org/10.19206/CE-147327

[3] Ardkapan SR, Johnson MS, Yazdi S, Afshari A, Bergsøe NC. Filtration efficiency of an electrostatic fibrous filter: studying filtration dependency on ultrafine particle exposure and composition. J Aerosol Sci. 2014;72;14-20. https://doi.org/10.1016/j.jaerosci.2014.02.002

[4] Babaoğlu NU, Hosseini SH, Ahmadi G, Elsayed K. The effect of axial cyclone inlet velocity and geometrical dimensions on the flow pattern, performance, and acoustic noise. Powder Technol. 2022;407:117692. https://doi.org/10.1016/j.powtec.2022.117692

[5] Bai H, Qian X, Fan J, Shi Y, Duo Y, Guo C et al. Theoretical model of single fiber efficiency and the effect of microstructure on fibrous filtration performance: a review. Ind Eng Chem Res. 2021;60(1):3-36. https://doi.org/10.1021/acs.iecr.0c04400

[6] Barbolini M, Di Pauli F, Traina M. Simulation der Luftfiltration zur Auslegung von Filterelementen. MTZ – Motortechnische Zeitschrift. 2014;5(11):52-57. https://doi.org/10.1007/s35146-014-0556-5

[7] Barris MA. Total Filtration™. The influence of filter selection on engine wear. Emissions and performance. SAE Technical Paper 952557. 1995. https://doi.org/10.4271/952557

[8] Bastuck T, Böhnke F, Hoppe S, Mittler R. Systemische Kolbenringauslegung zur Reduzierung von Partikelrohemissionen. MTZ – Motortechnische Zeitschrift. 2020;81(10): 50-55. https://doi.org/10.1007/s35146-020-0283-z

[9] Bayareh M. A review of the experimental analysis of gas–solid cyclone separators. ChemBioEng Rev. 2024;11(6). https://doi.org/10.1002/cben.202400036

[10] Bojdo N, Filippone A. a simple model to assess the role of dust composition and size on deposition in rotorcraft engines. Aerospace. 2019;6(4),44:1-26. https://doi.org/10.3390/aerospace6040044

[11] Bojdo N. Rotorcraft engine air particle separation. A thesis submitted to the for the degree of Doctor of Philosophy. Faculty of Engineering and Physical Sciences, University of Manchester. 2012. https://pure.manchester.ac.uk/ws/portalfiles/portal/38538381/FULL_TEXT.pdf (accessed 01 June 2025).

[12] Borojeni IA, Gajewski G, Riahi RA. Application of electrospun nonwoven fibers in air filters. Fibers. 2022;10:15. https://doi.org/10.3390/fib10020015

[13] Bugli NJ, Green GS. Performance and benefits of zero maintenance air induction systems. SAE Trans. 2005;114: 1015-1028. https://doi.org/10.4271/2005-01-1139

[14] Burda S, Chodnikiewicz Z. Konstrukcja i badania pyłowe filtrów powietrza silnika czołgowego(in Polish). Biuletyn WAT. 1962;3(115):12-34.

[15] Cai RR, Li SZ, Zhang LZ, Lei Y. Fabrication and performance of a stable micro/nano composite electret filter for effective PM2.5 capture. Sci Total Environ. 2020;7225: 138297. https://doi.org/10.1016/j.scitotenv.2020.138297

[16] Chen X, Yu J, Zhang Y. The use of axial cyclone separator in the separation of wax from natural gas: a theoretical approach. Energy Rep. 2021;7:2615-2624. https://doi.org/10.1016/j.egyr.2021.05.006

[17] Dehdarinejad E, Bayareh M. An overview of numerical simulations on gas-solid cyclone separators with tangential inlet. ChemBioEng Rev. 2021;8(4):1118. https://doi.org/10.1002/cben.202000034

[18] Dziubak T. Experimental studies of dust suction irregularity from multi-cyclone dust collector of two-stage air filter. Energies. 2021;14:3577. https://doi.org/10.3390/en14123577

[19] Dziubak T. Experimental dust absorption study in automotive engine inlet air filter materials. Materials. 2024;17: 3249. https://doi.org/10.3390/ma17133249
[20] Dziubak T. Zapylenie powietrza wokół pojazdu terenowego (in Polish). Wojskowy Przegląd Techniczny. 1990;3(257): 154-157.
[21] Dziubak T, Ślęzak M. Characteristics of pollutants emitted by motor vehicles and their impact on the environment and engine operation. Combustion Engines. 2025;200(1):37-55. https://doi.org/10.19206/CE-194628
[22] Dziubak T. Analysis of the influence of air pollution in the intake air of the combustion engine on the wear of its components and operation. Motor Transport. 2024;70(2):3-21. https://doi.org/10.5604/01.3001.0054.8182
[23] Dziubak T. Theoretical and experimental studies of uneven dust suction from a multi-cyclone settling tank in a two-stage air filter. Energies. 2021;14:8396. https://doi.org/10.3390/en14248396. 13.12.2021
[24] Dziubak S, Małachowski J, Dziubak T, Tomaszewski M. Numerical studies of an axial flow cyclone with ongoing removal of separated dust by suction from the settling tank. Chem Eng Res Des. 2024;208:29-51. https://doi.org/10.1016/j.cherd.2024.05.044
[25] Dziubak T, Boruta G. Experimental and theoretical research on pressure drop changes in a two-stage air filter used in tracked vehicle engine. Separations. 2021;8(71). https://doi.org/10.3390/separations8060071
[26] Fotovati S, Tafreshi HV, Pourdeyhimi B. A macroscale model for simulating pressure drop and collection efficiency of pleated filters over time. Sep Purif Technol. 2012;98:344-355. https://doi.org/10.1016/j.seppur.2012.07.009
[27] Fushimi C, Yato K, Sakai M, Kawano T, Kita T. Recent progress in efficient gas–solid cyclone separators with a high solids loading for large-scale fluidized beds. KONA Powder Part J. 2021;38;94-109. https://doi.org/10.14356/kona.2021001
[28] Gao J, Wang W, Cao Ch, Huang L, Hou Y, Xu Y et al. The relationship between the resistance characteristics and structural parameters of the elongated filter cartridge in the dust collector. Energy and Built Environment. 2024 https://doi.org/10.1016/j.enbenv.2024.03.008
[29] Grafe T, Gogins M, Barris M, Schaefer J, Canepa R. Nanofibers in filtration applications in transportation. Filtration 2001 International Conference and Exposition, Chicago. December 3-5, 2001.
[30] Graham K, Ouyang M, Raether T, Grafe T, Mc Donald B, Knauf P. Polymeric nanofibers in air filtration applications. Proceedings of the 5th Annual Technical Conference & Expo of the American Filtration & Separations Society, Galveston, 9–12 April 2002.
[31] Gunkel M, Frensch M, Robota A, Gelhausen R. Innermotorische Emissionsreduzierung Zusammenhang zwischen Partikelemissionen und Ölverbrauch. MTZ – Motortechnische Zeitschrift. 2018;79(7-8):46-51. https://doi.org/10.1007/s35146-018-0044-4
[32] Haig CW, Hursthouse A, Mc Ilwaina S, Sykes D. The effect of particle agglomeration and attrition on the separation efficiency of a Stairmand cyclone. Powder Technol. 2014;258; 110-124. https://doi.org/10.1016/j.powtec.2014.03.008
[33] Heikkilä P, Sipilä A, Peltola M, Harlin A. Electrospun PA-66 coating on textile surfaces. Text Res J. 2007;77(11):864-870. https://doi.org/10.1177/0040517507078241
[34] Huang L, Deng S, Chen Z, Guan J, Chen M. Numerical analysis of a novel gas-liquid pre-separation cyclone. Sep Purif Technol. 2018;194:470-479. https://doi.org/10.1016/j.seppur.2017.11.066
[35] Jaroszczyk T, Fallon SL, Dorgan JE, Moy JJ, Sonsalla TP, Henke B. Development of high dust capacity multi-media engine air filters. Fluid/Particle Separation Journal. 2003; 15(2):57-65.
[36] Jaroszczyk T, Pardue BA, Heckel SP, Kallsen KJ. Engine air cleaner filtration performance – theoretical and experimental background of testing. AFS Fourteenth Annual Technical Conference and Exposition, May 1, 2001, Tampa, Florida.
[37] Jeon W, Lee BH, Yun H, Kim J, Kang S, Seo Y. Characterization of pressure drop through two-stage particulate air filters. Sci Technol Built Environ. 2020;26:835-843. https://doi.org/10.1080/23744731.2020.1738870
[38] Jung S, Kim J. Advanced design of fiber-based particulate filters: materials, morphology, and construction of fibrous assembly. Polymers. 2020;12(8):1714. https://doi.org/10.3390/polym12081714
[39] Koszałka G, Suchecki A. Changes in blow-by and compression pressure of a diesel engine during a bench durability test. Combustion Engines. 2013;154(3):34-39. https://doi.org/10.19206/CE-116983
[40] Kumar M, Prakasa O, Brar LS. Analyzing the impact of inclined single and multi-inlet configurations on the turbulent flow field in cyclone separators using large-eddy simulation. Sep Purif Technol. 2025;376:134111. https://doi.org/10.1016/j.seppur.2025.134111
[41] Lensch-Franzen Ch, Gohl M, Scholl P, Paoloni F. Einfluss der Flüchtigkeit von Schmierölen auf die Öl- und Partikelemissionen. MTZ – Motortechnische Zeitschrift. 2019;80(9):46-55. https://doi.org/10.1007/s35146-019-0090-6
[42] Long J, Tang M, Sun Z, Liang Y, Hu J. Dust loading performance of a novel submicro-fiber composite filter medium for engine. Materials. 2018;11(10):2038. https://doi.org/10.3390/ma11102038
[43] Mercier Ch, Kirsch R, Antonyuk S. Analytical model for the initial efficiency of compressed nonwoven electret media for air filtration. Chem Eng Res Des. 2025l;216:549-563. https://doi.org/10.1016/j.cherd.2025.01.032
[44] Misiulia D, Elsayed K, Andersson AG. Geometry optimization of a deswirler for cyclone separator in terms of pressure drop using CFD and artificial neural network. Sep Purif Technol. 2017;185:10-23. https://doi.org/10.1016/j.seppur.2017.05.025
[45] Muschelknautz U. Comparing efficiency per volume of uniflow cyclones and standard cyclones. Chemie Ingenieur Technik. 2020;93(1-2):91-107. https://doi.org/10.1002/cite.202000149
[46] Muschelknautz U. Design criteria for multicyclones in a limited space. Powder Technol. 2019;357: https://doi.org/10.1016/j.powtec.2019.08.057
[47] Nagy J. Filtrowanie a żywotność silnika. Silniki Spalinowe 1973;3:43-47 (in Polish).
[48] Nejad JVN, Kheradmand S. The effect of arrangement in multi-cyclone filters on performance and the uniformity of fluid and particle flow distribution. Powder Technol. 2022; 399:117191. https://doi.org/10.1016/j.powtec.2022.117191
[49] Pinnick RG, Fernandez G, Hinds BD, Bruce CW, Schaefer KW, Pendelton JD. Dust generated by vehicular traffic on unpaved roadways: sizes and infrared extinction characteristics. Aerosol Sci Technol. 1985;4:99-121. https://doi.org/10.1080/02786828508959042
[50] Raoufi A, Shams M, Farzaneh M, Ebrahimi R. Numerical simulation and optimization of fluid flow in cyclone vortex finder. Chem Eng Process Process Intensif. 2008;47:128-137. https://doi.org/10.1016/j.cep.2007.08.004

[51] Reinhart C, Weisert L, Measurement of engine air cleaner efficiency using airborne particle size analysis. SAE Technical Paper 831262, 1983. https://doi.org/10.4271/831262
[52] Saleh AM, Tafreshi HV. Semi-numerical model for predicting the service life of pleated filters. Sep Purif Technol. 2014;137:94-108. https://doi.org/10.1016/j.seppur.2014.09.029
[53] Saleh AM, Fotovati S, Tafreshi HV, Pourdeyhimi B. Modeling service life of pleated filters exposed to poly-dispersed aerosols. Powder Technol. 2014;266:79-89. https://doi.org/10.1016/j.powtec.2014.06.011
[54] Schaeffer JW, Olson LM. Air filtration media for transportation applications. Filtr Separat. 1998;35(2):124-129. https://doi.org/10.1016/S0015-1882(97)80292-3
[55] Smialek JL, Archer FA, Garlick RG. Turbine airfoil degradation in the Persian Gulf War. The Journal of The Minerals Metals & Materials Society (TMS). 1994;46(12):39-41. https://doi.org/10.1007/BF03222663
[56] Szczepankowski A, Szymczak J, Przysowa R. The effect of a dusty environment upon performance and operating parameters of aircraft gas turbine engines. Conference: Specialists' Meeting – Impact of Volcanic Ash Clouds on Military Operations NATO AVT-272-RSM-047 Vilnius. May 2017. https://doi.org/10.14339/STO-MP-AVT-272-06-PDF
[57] Tian X, Ou Q, Liu J, Liang Y, Pui DY. Particle loading characteristics of a two-stage filtration system. Sep Purif Technol. 2019;215,351-359. https://doi.org/10.1016/j.seppur.2019.01.033
[58] Thomas D, Penicot P, Contal P, Leclerc D, Vendel J. Clogging of fibrous filters by solid aerosol particles Experimental and modelling study. Chem Eng Sci. 2001;56:3549-3561. https://doi.org/10.1016/S0009-2509(01)00041-0
[59] Trautmann P, Durst M, Pelz A, Moser N. High performance nanofibre coated filter media for engine intake air filtration. Proceedings of the AFS 2005 Conference and Expo, Rosemont. 10–13 April 2005.
[60] Treuhaft M, The use of radioactive tracer technology to measure engine ring wear in response to dust ingestion. SAE Technical Paper 930019, 1993. https://doi.org/10.4271/930019
[61] van Benthum R. Investigation towards the efficiency of a multi-cyclone dust separator in biomass combustion. Eindhoven, August 2007. Available online: https://www.scribd.com/document/537185062/8394 (accessed on 01 June 2025).
[62] Vogel A, Durant AJ, Cassiani M, Clarkson RJ, Slaby M, Diplas S et al. Simulation of volcanic ash ingestion into a large aero engine: particle–fan interactions. ASME J Turbomach. 2019;141(1):011010. https://doi.org/10.1115/1.4041464
[63] Wang Q, Lin X, Chen DR. Effect of dust loading rate on the loading characteristics of high efficiency filter media. Powder Technol. 2016;287:20-28. https://doi.org/10.1016/j.powtec.2015.09.032
[64] Wróblewski P. Technology for obtaining asymmetries of stereometric shapes of the sealing rings sliding surfaces for selected anti-wear coatings. SAE Technical Paper 2020-01-2229, 2020. https://doi.org/10.4271/2020-01-2229
[65] Yu W, Chen F, Li M, Cao H, Wu X, Ji Z. Experimental study on dynamic evolution characteristics of dust layer structure based on curing method. Ind Eng Chem Res. 2025; 64:4568-4580. https://doi.org/10.1021/acs.iecr.4c04727
[66] Zhang Y, Li K, Zhang K, Zhu G, Sun Z, Shi J. Research on the flow field characteristics of the industrial elliptical cyclone separator. Separations. 2025;12(50): https://doi.org/10.3390/separations12020050
[67] Zhang W, Zhang L, Yang J, Hao X, Guan G, Gao Z. An experimental modeling of cyclone separator efficiency with PCA-PSO-SVR algorithm. Powder Technol. 2019;347:114-124. https://doi.org/10.1016/j.powtec.2019.01.070
[68] Zhou X, Cheng L, Wang Q, Luo Z, Cen K. Non-uniform distribution of gas–solid flow through six parallel cyclones in a CFB system: an experimental study. Particuology. 2012; 10:170-175. https://doi.org/10.1016/j.partic.2011.10.006
[69] Zhu DZ, Han D, He WF, Chen JJ, Ji YY, Peng T et al. Optimization and assessment of the comprehensive performance of an axial separator by response surface methodology. J Appl Fluid Mech. 2023;16(1):61-73. https://doi.org/10.47176/jafm.16.01.1367
[70] Zhu M, Han J, Wang F, Shao W, Xiong R, Zhang Q et al. Electrospun nanofibers membranes for effective air filtration. Macromol Mater Eng. 2017;302:1600353. https://doi.org/10.1002/mame.201600353

Prof. Tadeusz Dziubak, DSc., DEng. – Faculty of Mechanical Engineering, Military University of Technology, Warsaw, Poland.
e-mail: *tadeusz.dziubak@wat.edu.pl*

Article citation info:
Pielecha J, Skobiej K, Sieroń M. Evaluation of RDE exhaust emission indicators of Euro 6 passenger cars using classical and window averaging methods. Combustion Engines. 2025;203(4):103-113. https://doi.org/10.19206/CE-211320

Jacek PIELECHA
Kinga SKOBIEJ
Marek SIEROŃ

Combustion Engines
Polish Scientific Society of Combustion Engines

Evaluation of RDE exhaust emission indicators of Euro 6 passenger cars using classical and window averaging methods

ARTICLE INFO

Received: 19 June 2025
Revised: 20 September 2025
Accepted: 25 September 2025
Available online: 28 September 2025

The article presents a comparison of exhaust emission results obtained in on-road tests using the latest legislative proposals relating to passenger cars. The results were analyzed with reference to the classical method (considering all measurement data) and the measurement window averaging method, also referred to in the literature as the EMROAD method. In this approach, measurement windows are defined (based on carbon dioxide emission data from the WLTC test), and the corresponding on-road emissions are determined for the RDE test. The study included Euro 6c vehicles equipped with gasoline engines and diesel engines. The gasoline engines featured direct fuel injection, while the diesel vehicle was equipped with a particulate filter and a selective catalytic reduction system to reduce nitrogen oxide emissions. In on-road tests, the correction factors depended on the applied technical solutions. For direct-injection gasoline engines in the Euro 6 class, the values remained below 1. A characteristic feature was that the correction factors were higher in the urban part of the test and lower for the entire RDE cycle. A different pattern was observed for diesel vehicles: in on-road tests, the correction factors were higher for the entire test than for the urban part of the RDE test. The conducted research and the determined emission indices made it possible to evaluate the environmental performance of vehicles from different emission classes and, at the same time, to provide a basis for proactive measures aimed at reducing selected pollutants from passenger cars.

Key words: *exhaust emissions, conventional vehicle, combustion engines, Euro 6*

1. Introduction

The need to determine real-world vehicle emissions arose from efforts to reduce the gap between laboratory test results and those obtained under actual driving conditions [2, 33]. Numerous scientific studies indicate that laboratory procedures, particularly type approval tests, are not the most reliable solution for assessing emissions and fuel consumption [22]. Laboratory results are often significantly lower compared to those measured during real-world vehicle operation [21]. Portable emission measurement systems are already widely available, and their use will soon become a legal requirement in the EU [34]. However, many open issues remain regarding the correlation between real-world emissions and those determined in laboratory conditions. In addition, despite recent legislative changes, several legal and technical aspects of RDE testing still remain, at least to some extent, unresolved [9].

These factors guide research and development towards the design of low-emission vehicles, the use of alternative fuels [10, 29], the introduction of new and more environmentally friendly engine types, as well as the improvement of the efficiency of existing engines. Consequently, emission tests involving gravimetric particle measurements, particle number counting, the determination of carbon dioxide mass, the assessment of fuel consumption, and the evaluation of the effectiveness of emission control systems have become more important than ever from both an industrial and scientific perspective. Advanced methods of emission measurement can provide valuable insights into the processes of pollutant formation and transport originating from exhaust gases.

The determination of exhaust gas emissions from any vehicle can be carried out using several methods:

- based on chassis dynamometer tests [27], where exhaust emissions are determined under a defined driving cycle. In accordance with standards and regulatory frameworks, it is also possible to determine the road emissions of a given exhaust component [g/km; g/test]
- based on on-road tests [23–26], where the concentrations of gaseous components as well as the mass and number of particles are determined. When the exhaust flow rate is taken into account, the road emissions of these components can also be calculated.

The emission values of exhaust gases from vehicles (mopeds [15, 31], tractors [28], or rail machinery [12]), determined on the basis of the methods presented above, cannot be directly compared. The procedures and conditions under which the tests are carried out differ, which results in a lack of standardisation among these methods. In this article, it is assumed that exhaust gas emission and fuel consumption measurements will be conducted both on a chassis dynamometer and using a mobile system for measuring exhaust gases, PEMS (Portable Emission Measurement System). Such a system enables the measurement of all engine and vehicle operating parameters. To determine load values (torque) and engine speed, vehicle speed, fuel flow rate, and coolant temperature, data from the vehicle's control unit are used. Regulations require that these data be provided by the control unit and read and recorded by PEMS-type systems. It should be noted that exhaust gas emission results obtained during on-road tests represent real values for a given type of vehicle and reflect specific road conditions [30]. Such conditions make it possible to estimate the environmental performance of the tested vehicles and their engines during typical operation (eg. temperature [1]).

2. Literature review

Exhaust gas emission standards are established to control the pollutants emitted by vehicles worldwide. In most regions, limits on carbon dioxide emissions have also been set, as they are directly related to fuel consumption [32]. Exhaust gas values are measured under laboratory conditions (for passenger cars on a chassis dynamometer) in a defined type-approval test [14]. This part of the vehicle certification process determines its "environmental performance" and is identical for all passenger cars. The driving cycle is designed to represent the "most probable" road conditions, and the uniform testing procedure for all vehicles allows direct comparison of exhaust gas results [4]. However, increasing emphasis is now placed on on-road testing (already reflected in proposed European Union regulations), referred to as RDE, which is carried out using mobile measurement equipment of the PEMS type [3].

The latest studies on exhaust gas emissions from vehicles under real-world driving conditions, conducted using mobile measurement systems, reflect the actual environmental performance of vehicles [5]. The primary focus is on the potential use of such tests for powertrain calibration, in order to reduce exhaust gas emissions not only during the certification test but also across the entire operating range of engines. The authors of publication [16] indicated that future on-road testing, currently simulated in various research procedures, may lead to increased on-road emissions of nitrogen oxides from vehicles. To mitigate this, they proposed essential modifications in vehicle control unit software, noting that these changes are likely to be effective only for vehicles equipped with gasoline engines. Vehicles with diesel engines [11], on the other hand, will require additional financial investments in improving the effectiveness of exhaust aftertreatment by applying new methods for reducing nitrogen oxide concentrations.

Similar conclusions were reached by the authors of the article [13], in which road exhaust gas emissions under real driving conditions were compared using PEMS-type analyzers and the COPERT program [17]. It was found that, within the speed range of 20–120 km/h, calculations performed with the COPERT program were approximately 10% higher for parameters such as fuel consumption and on-road hydrocarbon emissions. In contrast, with respect to on-road nitrogen oxide emissions, the values obtained from the COPERT program were underestimated by about 30%.

Comparative studies of exhaust gas emissions from Euro 5 class vehicles, carried out in a laboratory on a chassis dynamometer [8] using various driving cycles, also confirmed the results described earlier. The authors applied tests in which the characteristics of speed variation reflected real driving conditions. It was found that, for vehicles with gasoline engines, on-road carbon monoxide emissions did not exceed 1 g/km (the permissible Euro 5 limit is also 1 g/km). On-road hydrocarbon emissions did not exceed 10% of the limit value (0.1 g/km), while on-road nitrogen oxide emissions corresponded to approximately 20% of the limit value (0.06 g/km). The authors indicated, however, that vehicles equipped with diesel engines significantly exceeded the permissible nitrogen oxide emission limits – the values obtained were approximately four times higher than the standard (the permissible Euro 5 nitrogen oxide emission value is 0.18 g/km).

In on-road studies, significant particulate emissions have been observed, particularly in the range of nanoparticles from combustion engines powered also by alternative fuels (eg. natural gas) [19]. The authors highlighted the high mileage of vehicles powered by alternative fuels, which consequently results in up to an eightfold increase in particulate number emissions for vehicles with a mileage of around 500,000 km compared to those with a mileage of 75,000 km. The article further confirmed, based on RDE tests under different traffic intensity conditions, that vehicles fueled with compressed natural gas emit higher amounts of nitrogen oxides compared to vehicles equipped with gasoline engines.

With regard to the accuracy of measurements during real-world driving, the final result depends on the operating conditions of the vehicle and the engine (including vehicle speed, road surface, driver characteristics and driving style, as well as other factors determining traffic conditions). These conditions are unpredictable and can significantly affect the outcome of exhaust gas emission measurements. Data presented in publications [7, 35] indicate that the most influential factors on the measured exhaust gas emissions are: the thermal state of the vehicle (engine), the average driving speed and dynamics, and the road gradient.

The impact of road conditions on exhaust gas emission results was the main subject of the article [20], in which sport utility vehicles (SUVs) with both gasoline and diesel engines were tested under varying road gradients. The authors attempted to estimate the change in on-road exhaust gas emission values of individual components as a function of road slope angle. They demonstrated that a 10% change in road gradient caused a twofold change in on-road emissions for vehicles with gasoline engines and a 1.5-fold change for vehicles with diesel engines.

The review of the current state of research highlights both the limitations of laboratory-based procedures and the importance of on-road testing supported by mobile measurement systems. It also demonstrates the significant influence of vehicle technology, driving conditions, and road gradients on the measured values of exhaust gas emissions. Against this background, the aim of the present article is to compare the results of on-road exhaust gas emission tests for passenger cars with the latest legislative proposals. The analysis includes both the classical method, which accounts for all measurement data, and the measurement window averaging method (EMROAD). This approach makes it possible to assess the environmental performance of Euro 6 vehicles with different powertrain technologies and to provide guidance for further reduction of selected exhaust components in real driving conditions.

3. Research methodology

3.1. Research objects

The objects of the study were passenger cars, the characteristics of whose powertrains are presented in Table 1. The vehicles were equipped with gasoline and diesel engines, all meeting the Euro 6 emission standard. Despite differences in engine displacement and type, a common

feature was their comparable curb weight. The aim of the study was to determine the relationship between on-road exhaust gas emissions of specific compounds for both gasoline and diesel engines separately.

Table 1. Technical characteristics of the engines and vehicles used in the study

Parameter	Gasoline	Diesel
Engine		
Number and arrangement of cylinders	4, in-line	4, in-line
Engine displacement [cm3]	1984	1968
Emission standard	Euro 6	Euro 6
Maximum engine power [kW] at [rpm]	169/4700-6200	135/4000
Maximum engine torque [Nm] at [rpm]	350/1500–4400	380/1750–3000
Fuel supply	TSI	Common Rail
Drive		
Drive type	front-wheel drive	front-wheel drive
Gearbox type and number of gears	automatic, 6	automatic, 6
Weight		
Curb weight [kg]	1349	1354
Performance		
Top speed [km/h]	250	230
Acceleration 0–100 km/h [s]	6.4	7.1
Fuel consumption		
Combined cycle fuel consumption [dm³/100 km]	6.4	4.2
CO_2 emissions [g/km]	139	109

3.2. Research equipment

Exhaust gas emission measurements were carried out under real driving conditions, in accordance with the methodology presented, among others, in studies [1, 18, 20]. This approach required the installation of an exhaust sampling system on the vehicle in a manner that allowed its normal operation. For this purpose, an exhaust sampling line was constructed, which, when connected to the exhaust flow measurement system, formed a complete exhaust sampling setup for the measurement analyzers.

For the measurement of harmful compound concentrations in exhaust gases, a Semtech DS mobile analyzer from Sensors Inc. was used. It enabled the measurement of harmful components such as CO, NO_x, and CO_2. Additional data were supplied to the central unit of the analyzer directly from the vehicle's onboard diagnostic system, along with a GPS location signal. Information presented in publications concerning the use of mobile exhaust analyzers combined with data recorded from onboard diagnostic systems confirms the validity of assessing exhaust gas emissions under real driving conditions using the described measurement configuration.

3.3. Research route

On-road emission measurements were carried out under real traffic conditions (detailed characteristics – Table 2). The test route included urban, highway, and rural sections (Figures 1 and 2) and was performed for vehicles with different powertrain configurations (gasoline and diesel engines). Each test was repeated three times; the partial results presented are given as examples, while the final results represent the average of all measurements obtained.

Table 2. Test route characteristics

Test conditions	Vehicle A (gasoline engine)	Vehicle B (diesel engine)	Relative difference $\frac{(A-B)\times 100\%}{\frac{1}{2}(A+B)}$
Total time [s]	5349	5209	2.65
Maximum speed [km/h]	147.9	133.3	11.36
Average speed [km/h]	33.73	34.51	–2.28
Distance [km]	50.11	49.93	0.43
Share of vehicle operating conditions			
V = 0 [%]	34.71	33.02	4.99
V = const [%]	9.24	9.58	–3.61
a > 0 [%]	29.51	30.20	–2.31

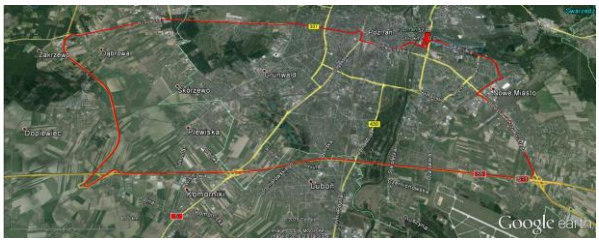

Fig. 1. Test route

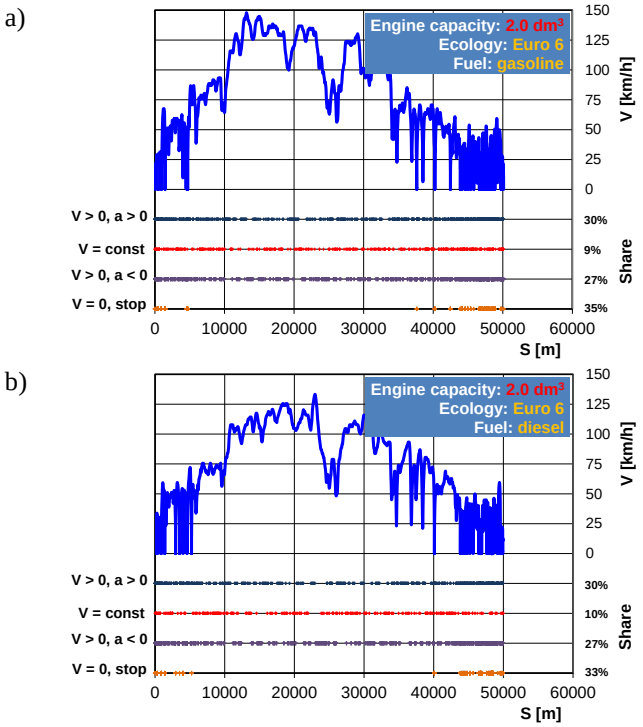

Fig. 2. Characteristics of the test drive: vehicle with gasoline engine (a) and diesel engine (b)

The test route was selected to cover diverse driving conditions, taking into account different topographies: urban, rural, and highway, in order to assess their impact on the exhaust gas emission values of gaseous components.

On-road studies are characterized by an inherent non-repeatability, which should be regarded not as a limitation but as a source of valuable information. In the analysis of exhaust gas emissions, the objective was not to perform a precise comparison of individual vehicles, but rather to select measures that are objective and independent of test

variability. Therefore, non-repeatability should be considered an essential attribute of studies conducted under real operating conditions.

4. Measurement results

4.1. Gasoline engine vehicle

During the tests of the vehicle with a gasoline engine, measurements were taken of CO, NO_x, and CO_2 concentrations in the exhaust gases, as well as engine speed and load, which were recorded from the vehicle's diagnostic system. The figures present the time traces of the recorded harmful compounds. The carbon monoxide concentration along the analyzed section of the route was mostly below 0.05%, which consequently resulted in a carbon monoxide emission rate not exceeding a few mg/s (Fig. 3).

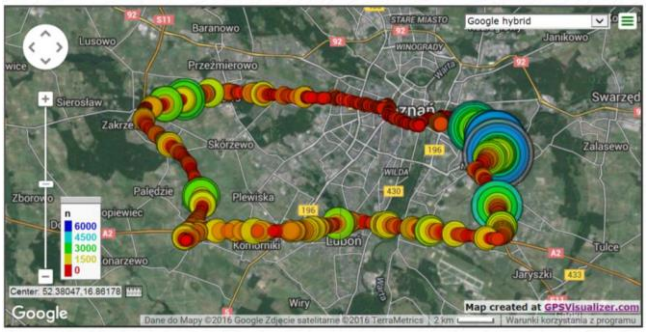

Fig. 3. CO concentration recorded during tests for the gasoline engine vehicle (visualized along the test route)

The concentration of the next gaseous component – nitrogen oxides – remained at a very similar level throughout the entire test. The concentration values, within the range up to 100 ppm, were the result of exhaust aftertreatment devices applied to reduce this compound. The nitrogen oxides emission rate did not exceed 1 mg/s for most of the test (Fig. 4). The observed variability of the results reflected normal engine operation, while the recorded increases in emission rate occurred during acceleration and highway driving conditions, where the emission rate significantly exceeded the previously reported values.

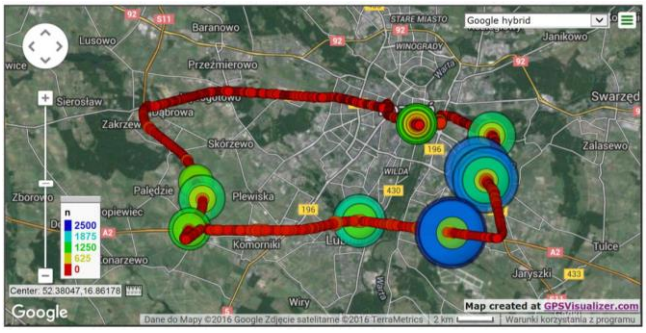

Fig. 4. NO_x concentration recorded during tests for the gasoline engine vehicle (visualized along the test route)

The carbon dioxide concentration presented in Fig. 5 reached a maximum of 13%. This is the peak value corresponding to an air-fuel equivalence ratio equal to one. For values of the equivalence ratio greater than one, lower concentrations of this compound were recorded (only during engine braking). During the tests, the carbon dioxide emission rate did not exceed 7000 mg/s (highway conditions), while the average value was approximately 1000 mg/s. Larger fluctuations were observed in the middle phase of the test under highway driving conditions.

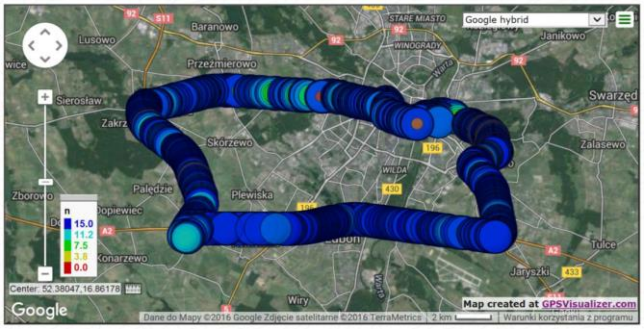

Fig. 5. CO_2 concentration recorded during tests for the gasoline engine vehicle (visualized along the test route)

The recorded variations in engine speed and load are presented in Fig. 6, where the largest operating range of the engine corresponds to medium loads and medium rotational speeds. The concentration profiles of exhaust constituents obtained during the tests made it possible to identify relationships that characterize the influence of the engine's dynamic properties on exhaust emissions, taking into account the results from the entire measurement route. The dynamic properties of the engine were considered indirectly by dividing the full range of engine speed and load under real driving conditions to generate concentration maps of selected exhaust constituents. These data were then presented on engine characteristics plotted in the coordinates of engine speed and load.

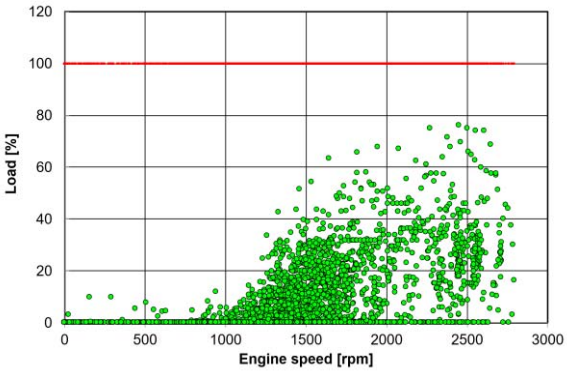

Fig. 6. Engine operating conditions in engine speed–load coordinates (gasoline engine)

The recorded emission rates of exhaust constituents, when related to engine speed and load, allowed the identification of characteristic dependencies for the tested engine, which are defined by the following values:

- the maximum emission rate of carbon monoxide (Fig. 7a) is approximately 20 mg/s and occurs at an engine speed of around 2800 rpm and a load in the range of 40–50%

– the maximum emission rate of nitrogen oxides (Fig. 7b) is approximately 70 mg/s and occurs at an engine speed of 2200 rpm and a load in the range of 60–70%
– the maximum particle number emission rate (Fig. 7c) reaches approximately 15–20·10^{13} 1/s, occurring at an engine speed in the range of 1200–1300 rpm and a load of 20–30%.

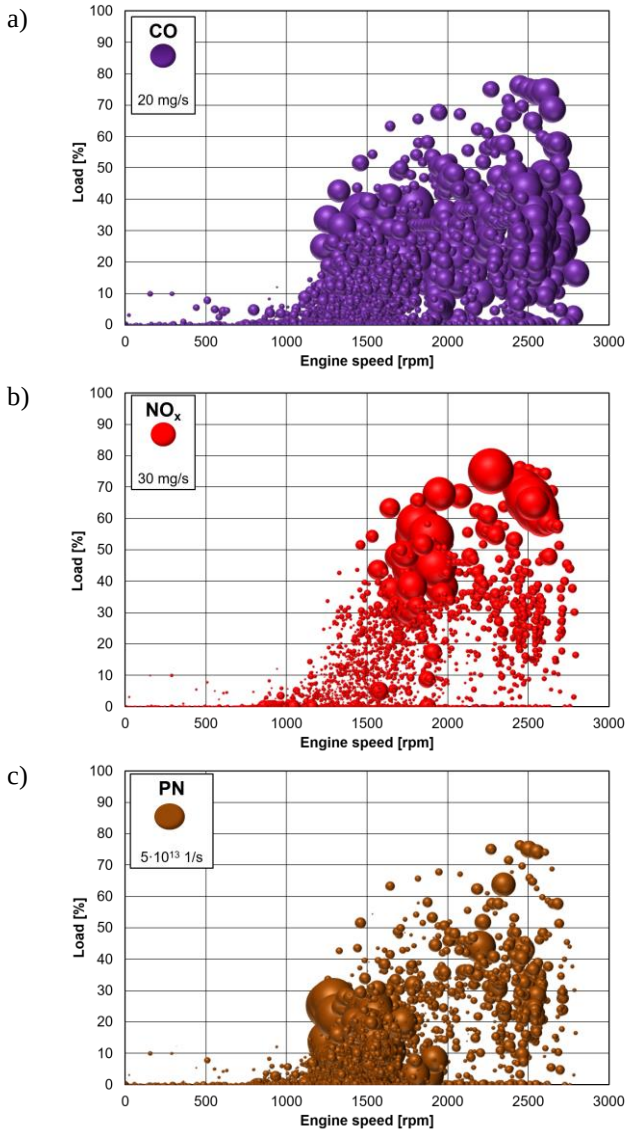

Fig. 7. Emission rates of CO (a), NO_x (b), and PN (c) related to engine operating parameters in vehicle speed–acceleration coordinates during tests for the gasoline engine vehicle

The analysis of the gasoline engine vehicle confirmed generally low levels of CO and NO_x emissions under real driving conditions, with emission peaks observed mainly during acceleration and highway operation. The highest variability was recorded for CO_2 and PN, reflecting the influence of engine dynamics on emission characteristics. These results highlight the importance of considering both transient conditions and engine load when evaluating the real-world environmental performance of gasoline engines.

4.2. Diesel engine vehicle

Figure 8 presents the recorded variations in engine speed and load, with the largest operating area corresponding to medium loads and medium rotational speeds. Based on the recorded concentration profiles of exhaust constituents, it was possible to develop relationships describing the influence of the engine's dynamic properties on exhaust emissions, considering the results from the entire measurement route. To account for engine dynamics indirectly, the full range of engine speed and load under real driving conditions was divided into intervals to generate concentration maps of selected exhaust constituents. These data are shown on the engine characteristics plotted in engine speed–load coordinates.

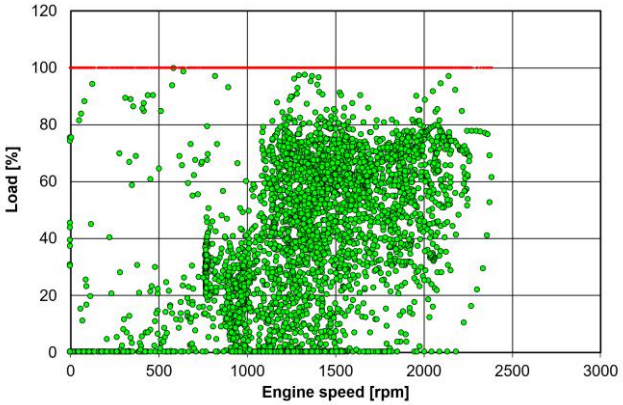

Fig. 8. Engine operating conditions in engine speed–load coordinates (diesel engine)

Relating the emission rates of exhaust constituents to engine speed and load made it possible to determine characteristic patterns for the tested engine, which are defined by the following values:
– the maximum emission rate of carbon monoxide (Fig. 9a) is approximately 70 mg/s and occurs at an engine speed in the range of 1500–2000 rpm and a load in the range of 20–40%
– the maximum emission rate of nitrogen oxides (Fig. 9b) is approximately 120 mg/s and occurs at an engine speed in the range of 2000–2500 rpm and a load in the range of 60–70%
– the maximum particle number emission rate (Fig. 9c) is approximately 2.5·10^{13} 1/s and occurs at an engine speed in the range of 1500–2000 rpm and a load in the range of 30–50%.

The analysis of the diesel engine vehicle revealed considerably higher emission levels compared to the gasoline case, particularly for NO_x and particulate matter. The highest CO and PN emission rates were observed at medium engine speeds and loads, while NO_x reached peak values at higher loads and engine speeds. These results confirm the strong influence of engine operating conditions on real-world exhaust emissions and underline the challenges of meeting stringent emission limits for diesel engines.

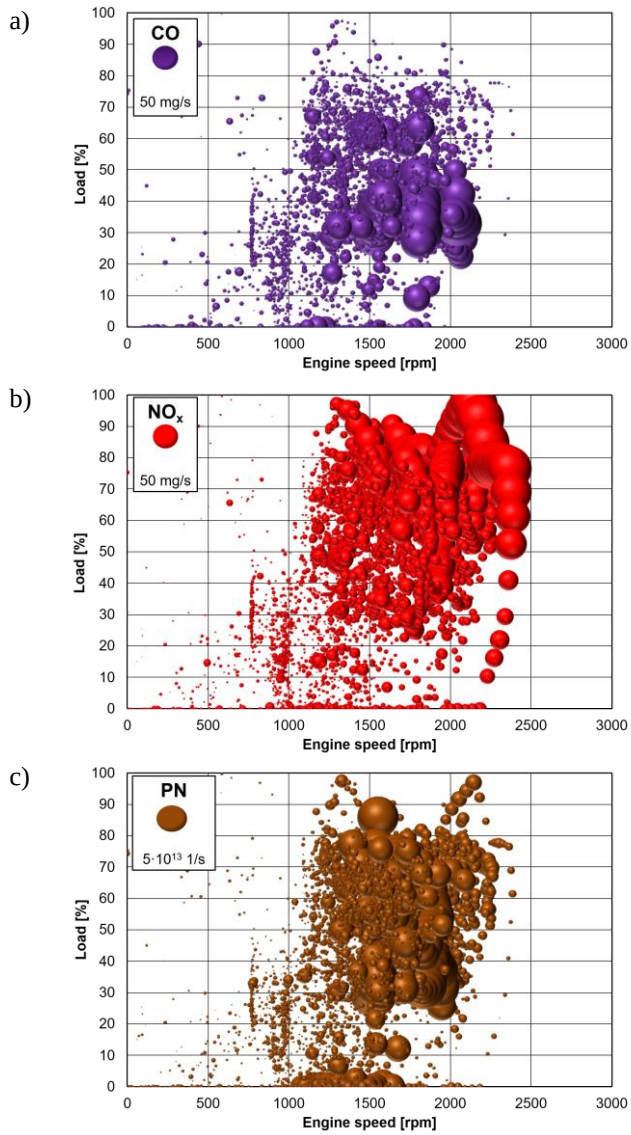

Fig. 9. Emission rates of CO (a), NO_x (b), and PM (c) recorded for the diesel engine vehicle during tests

5. On-road emission factors of exhaust constituents in RDE tests

5.2. Gasoline engine vehicle

Based on the previously obtained emission rate values and the known distance traveled by the vehicle, instantaneous emission indicators, CF (Conformity Factor), were determined. They are defined as the ratio of the on-road emission of a given constituent to the corresponding on-road emission limit specified by the standard ($CF = b_{RDE}/b_{norm}$).

The following values were obtained for the respective exhaust constituents:

– the emission index value for carbon monoxide (Fig. 10a) does not exceed 1, with the final value being less than 0.2
– the initial emission index value for nitrogen oxides (Fig. 10b) exceeds 2, while the final value is also around 1
– the instantaneous emission index value for particle number (Fig. 10c) exceeds 1, whereas the final value remains below 1.

The on-road emission values for the gasoline engine vehicle obtained during the test route are as follows:

– on-road carbon monoxide emission: 216 mg/km
– on-road nitrogen oxides emission: 56 mg/km
– on-road particle number emission: $5.8 \cdot 10^{11}$ 1/km
– on-road carbon dioxide emission: 117 g/km.

Compliance of on-road emissions with the Euro 6 limit values was observed for all analyzed constituents (Fig. 11):

– the emission index for carbon monoxide was 0.22
– the emission index for nitrogen oxides was 0.89
– the emission index for particle number was 0.68.

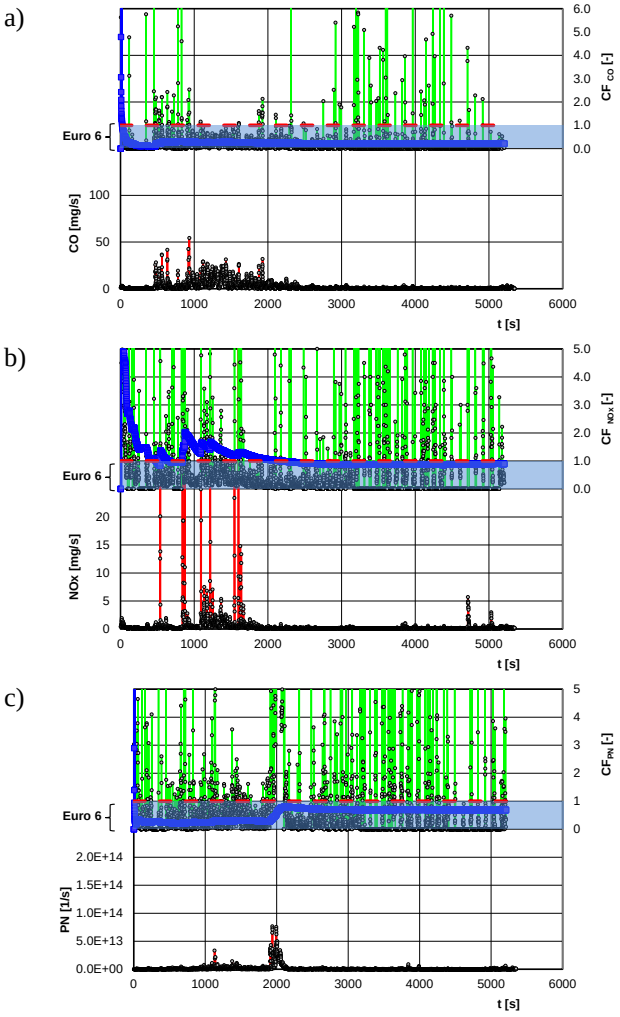

Fig. 10. Emission index of CO (a), NO_x (b), and PN (c) – instantaneous and cumulative values during the test for the gasoline engine vehicle

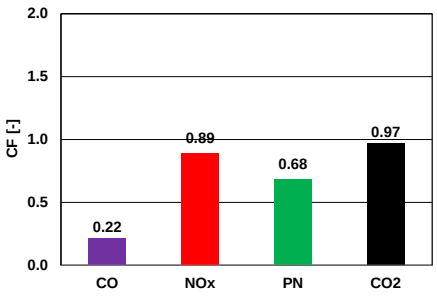

Fig. 11. Emission index determined during on-road tests for the gasoline engine vehicle

The data analysis shows that the on-road emission values obtained under real operating conditions do not exceed the permissible limits for vehicles with gasoline engines.

5.2. Diesel engine vehicle

For the individual exhaust constituents, the following values were obtained:

– the emission index value for carbon monoxide (Fig. 12a) does not exceed 1, with the final value being less than 0.5
– the instantaneous emission index value for nitrogen oxides (Fig. 12b) exceeds 1, while the final value is also around 1
– the emission index value for particle number (Fig. 12c) does not exceed 1 in the first part of the test.

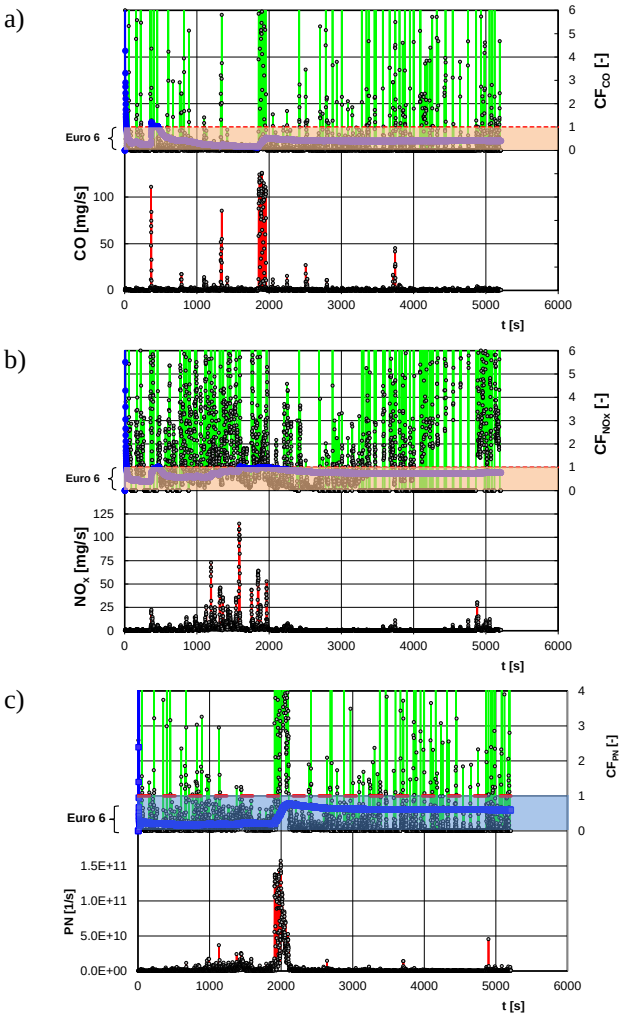

Fig. 12. Emission index of CO (a), NO_x (b), and PN (c) – instantaneous and cumulative values during the test for the diesel engine vehicle

The on-road emission values determined for the diesel engine vehicle during the test route are as follows:

– on-road carbon monoxide emission: 204 mg/km
– on-road nitrogen oxides emission: 66 mg/km
– on-road particle number emission: $3.6 \cdot 10^{11}$ 1/km
– on-road carbon dioxide emission: 148 g/km.

The emission indices determined for the diesel engine vehicle show a similar pattern to those of the gasoline engine. No exceedances were recorded with respect to the Euro 6 limit values. The indices were as follows (Fig. 13):

– carbon monoxide emission index: 0.41
– nitrogen oxides emission index: 0.82
– particle number emission index: 0.60.

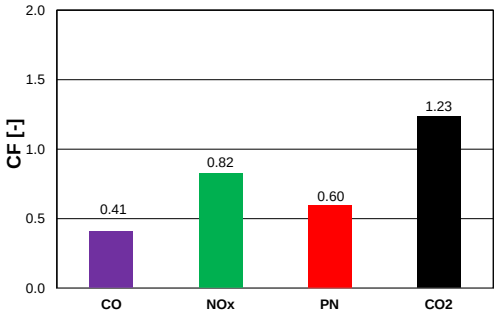

Fig. 13. On-road emissions of exhaust gas constituents determined during tests for the diesel engine vehicle

6. On-road exhaust emission indices in RDE tests – measurement window averaging

The first stage in determining on-road emission values according to the RDE testing procedure is the verification of the test validity. The following data were taken into account for the gasoline engine:

– test distance, which must be at least 48 km (divided into three parts of 16 km each); in the conducted test, the obtained values were 16.58, 11.54, and 23.18 km, giving a total distance of 51.30 km (one value does not meet the test requirement)
– test duration, which must range from 90 to 120 minutes; in the study, the duration was 90 minutes
– test duration during which the engine is not warmed up to its normal operating temperature; in the study, the value obtained was 5 minutes (requirement met)
– share of individual phases of the test in the total emission test: urban driving must account for 29–44% of the total test time (value obtained: 32.33%), rural driving must account for 23–43% (value obtained: 22.49%), highway driving must account for 23–43% (value obtained: 45.18%); all obtained values meet the test requirements (differences are very small)
– average speed in urban driving must be between 15 and 40 km/h; in the study, the value obtained was 14.69 km/h (requirement met – very small difference)
– share of driving at speeds exceeding 145 km/h on the highway section; in the study, this speed was not exceeded (requirement met)
– duration of driving at speeds above 100 km/h during the highway section must be at least 5 minutes; in the study, the value obtained was 9.5 minutes (requirement met)
– share of stop time in the urban part must range from 6% to 30%; in the study, the value obtained was 28.7% (requirement met)
– altitude difference between the start and end of the test must be less than 100 m; in the study, the result obtained was 7.1 m (requirement met).

With all test requirements fulfilled, it was considered justified to perform a comparison of emissions determined

by two methods, since the obtained measurements were derived from the same test drive. The plot of on-road carbon dioxide emissions as a function of the average speed in the measurement windows shows that the on-road emissions of this constituent were lower in the test than in the type-approval test (Fig. 14).

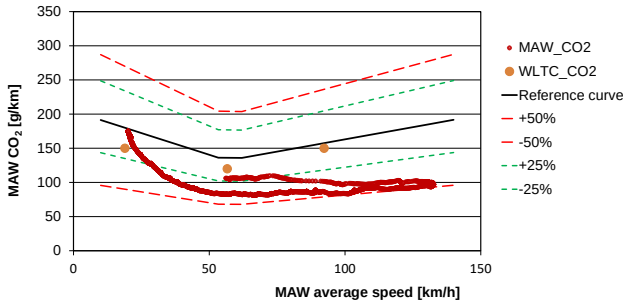

Fig. 14. Relationship between on-road carbon dioxide emissions and average speed in the measurement windows (gasoline engine vehicle)

The on-road emission results for carbon monoxide, nitrogen oxides, and particle number were determined in accordance with the procedure presented in [26, 27]. The following values were obtained:

- on-road carbon monoxide emission: 430 mg/km in the urban section, 150 mg/km in the rural section, and 110 mg/km in the highway section; the total value for the entire test was 230 mg/km (Fig. 15a)
- on-road nitrogen oxides emission: 22.4 mg/km in the urban section, 43.6 mg/km in the rural section, and 71.9 mg/km in the highway section; the total value for the entire test was 45.7 mg/km (Fig. 15b)
- on-road particle number emission: $4.9 \cdot 10^{11}$ 1/km in the urban section, $4.3 \cdot 10^{11}$ 1/km in the rural section, and $5.8 \cdot 10^{11}$ 1/km in the highway section; the total value for the entire test was $5.0 \cdot 10^{11}$ 1/km (Fig. 15c).

As in the previous case, the validity of the test procedure was also verified for the diesel engine vehicle. The following data were obtained:

- test distance; in the conducted test, the values were 17.16, 16.69, and 20.83 km, giving a total distance of 51.68 km (values meet the test requirements)
- test duration, which must range from 90 to 120 minutes; in the study, the duration was 92 minutes (requirement met)
- test duration during which the engine was not warmed up to normal operating temperature; in the study, the value obtained was 5 minutes (requirement met)
- share of individual phases of the emission test: urban driving – 33.20%, rural driving – 26.49%, highway driving – 40.31% (all values meet the test requirements)
- average speed in urban driving must be between 15 and 40 km/h; in the study, the value obtained was 16.09 km/h (requirement met)
- share of driving at speeds exceeding 145 km/h on the highway section; in the study, this speed was not exceeded (requirement met)
- duration of driving at speeds above 100 km/h during the highway section must be at least 5 minutes; in the study, the value obtained was 9.28 minutes (requirement met)
- share of stop time in the urban part must range from 6% to 30%; in the study, the value obtained was 28.32% (requirement met)
- altitude difference between the start and end of the test must be less than 100 m; in the study, the result obtained was 7.6 m (requirement met).

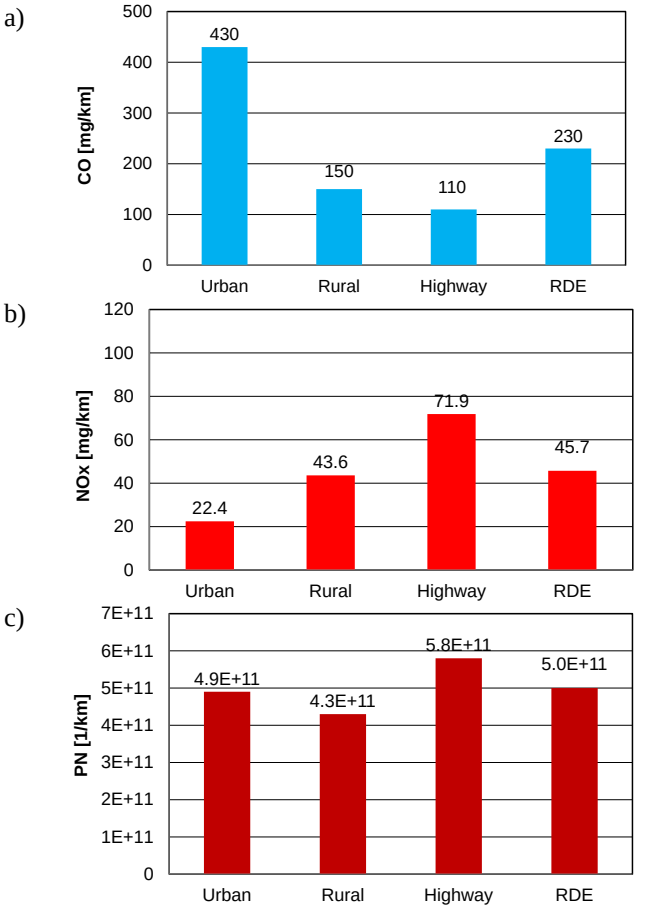

Fig. 15. On-road emissions of CO (a), NO_x (b), and PN (c) obtained in individual parts of the test and the average value for the entire test (values determined using measurement window averaging) for the spark-ignition engine vehicle

The plot of on-road carbon dioxide emissions as a function of average speed in the measurement windows shows that the on-road emissions of this constituent were lower in the test than in the type-approval test (Fig. 16).

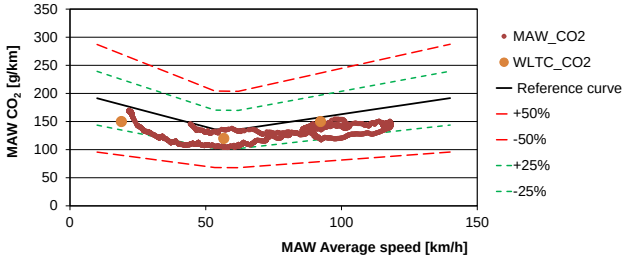

Fig. 16. Relationship between on-road carbon dioxide emissions and average speed in the measurement windows (diesel engine vehicle)

The on-road emission results for carbon monoxide, nitrogen oxides, and particle number were determined in

accordance with the RDE procedure. The following values were obtained:

– on-road carbon monoxide emission: 100 mg/km in the urban section, 87.1 mg/km in the rural section, and 328 mg/km in the highway section; the total value for the entire test was 171 mg/km (Fig. 17a)
– on-road nitrogen oxides emission: 31.1 mg/km in the urban section, 35 mg/km in the rural section, and 117.1 mg/km in the highway section; the total value for the entire test was 61.1 mg/km (Fig. 17b)
– on-road particle number emission: $4.2 \cdot 10^{11}$ 1/km in the urban section, $4.6 \cdot 10^{11}$ 1/km in the rural section, and $6.3 \cdot 10^{11}$ 1/km in the highway section; the total value for the entire test was $5.0 \cdot 10^{11}$ 1/km (Fig. 17c).

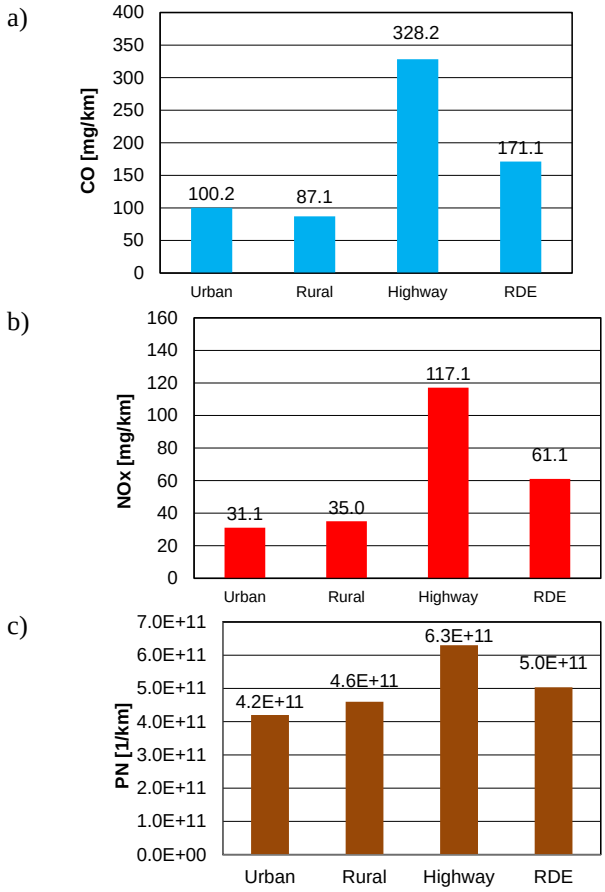

Fig. 17. On-road emissions of CO (a), NO_x (b), and PN (c) obtained in individual parts of the test and the average value for the entire test (values determined using measurement window averaging) for the diesel vehicle

7. Summary

The obtained on-road emission results for the tested vehicles are presented for carbon monoxide, nitrogen oxides, and particle number. When comparing the procedures for determining on-road emissions in RDE tests, it can be concluded that using all measurement data from the entire test drive provides comparable exhaust emission results:

– for the gasoline engine vehicle: for on-road carbon monoxide emissions, the difference is approximately 5% (with values of 216 mg/km and 227 mg/km, respectively); for on-road nitrogen oxides emissions, the difference is approximately 20% (values of 56 mg/km and 46 mg/km, respectively); for on-road particle number emissions, the difference is approximately 16% (values of $5.8 \cdot 10^{11}$ 1/km and $5.0 \cdot 10^{11}$ 1/km, respectively)
– for the diesel engine vehicle: for on-road carbon monoxide emissions, the difference is approximately 17% (values of 204 mg/km and 171 mg/km, respectively); for on-road nitrogen oxides emissions, the difference is approximately 27% (values of 66 mg/km and 182 mg/km, respectively); and for on-road particle number emissions, the difference is approximately 35% (values of $3.6 \cdot 10^{11}$ 1/km and $5.0 \cdot 10^{11}$ 1/km, respectively).

The comparison of emission index (CF) values in RDE tests provided the following results:

– for the gasoline vehicle: the on-road carbon monoxide emission index values were 0.23 and 0.43 (for the entire RDE test and the urban section, respectively); the nitrogen oxides emission index values were 0.76 and 0.90 (for the entire RDE test and the urban section, respectively); and the particle number emission index values were 0.67 and 0.87 (for the entire RDE test and the urban section, respectively) – Fig. 18a
– for the diesel vehicle: the on-road carbon monoxide emission index values were 0.34 and 0.20 (for the entire RDE test and the urban section, respectively); the nitrogen oxides emission index values were 0.76 and 0.39 (for the entire RDE test and the urban section, respectively); and the particle number emission index values were 0.84 and 0.70 (for the entire RDE test and the urban section, respectively) – Fig. 18b.

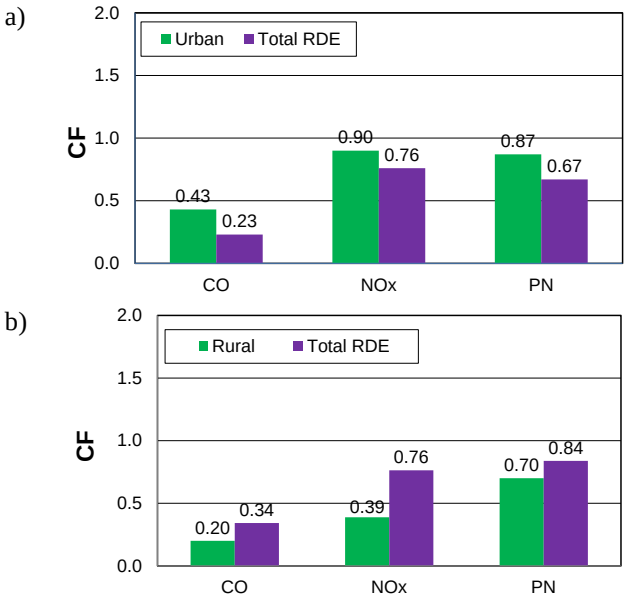

Fig. 18. Comparison of on-road emission indices of carbon monoxide, nitrogen oxides, and particle number in road tests: a) gasoline engine vehicle, b) diesel engine vehicle

Based on the obtained on-road emission results and emission indices, it can be concluded that the emission indices of CO, NO_x, and PN do not exceed the permissible limits for conventional Euro 6 passenger cars equipped with gasoline and diesel engines. Future work is expected to focus on testing hybrid vehicles of the latest emission class,

as well as on durability studies, in which exhaust gas emissions will be monitored during several years of vehicle operation. The comparison of the classical and EMROAD methods demonstrated their mutual consistency, which confirms their suitability for assessing the environmental performance of Euro 6 passenger cars. The observed differences between gasoline and diesel vehicles highlight the greater challenges associated with diesel powertrains, particularly regarding NOx and PN control. These insights provide valuable input for both legislative development and the design of more effective emission reduction strategies.

Nomenclature

CF	conformity factor
CI	compression ignition
CO	carbon monoxide
CO_2	carbon dioxide
EU	European Union
FC	fuel consumption
NO_x	nitrogen oxides
PEMS	portable emission measurement system
PN	particle number
RDE	real driving emissions
SI	spark ignition
SUV	sport utility vehicle
WLTC	Worldwide Harmonized Light-duty Vehicles Test Cycles

Bibliography

[1] Bielaczyc P, Merkisz J, Pielecha J, Woodburn J. RDE-compliant PEMS testing of a gasoline Euro 6d-TEMP passenger car at two ambient temperatures with a focus on the cold start effect. SAE Technical Paper. 2020-01-0379. 2020. https://doi.org/10.4271/2020-01-0379

[2] Czerwiński J, Comte P, Zimmerli Y, Reutimann F. Testing emissions of passenger cars in laboratory and on-road (PEMS, RDE). Combustion Engines. 2016;166(3):17-23. https://doi.org/10.19206/CE-2016-326

[3] Dollinger M, Fischerauer G. Physics-based prediction for the consumption and emissions of passenger vehicles and light trucks up to 2050. Energies. 2023;16(8):3591. https://doi.org/10.3390/en16083591

[4] Donateo T, Giovinazzi M. Building a cycle for real driving emissions. Energy Procedia. 2017;126:891-898. https://doi.org/10.1016/j.egypro.2017.08.307

[5] Engelmann D, Hüssy A, Comte P, Czerwinski J, Bonsack P. Influences of special driving situations on emissions of passenger cars. Combustion Engines. 2021;184(1):41-51. https://doi.org/10.19206/CE-134828

[6] European Environmental Agency. Emissions of air pollutants from transport in Europe. 2024. https://www.eea.europa.eu/en/analysis/indicators/emissions-of-air-pollutants-from (accessed on 22.08.2025).

[7] Feist MD, Sharp CA, Spears MW. Determination of PEMS measurement allowances for gaseous emissions regulated under the heavy-duty diesel engine in-use testing program Part 1-project overview and PEMS evaluation procedures. SAE International Journal of Fuels and Lubricants. 2029;2(1):435-454. https://doi.org/10.4271/2009-01-0940

[8] Fontaras G, Franco V, Dilara P, Martini G, Manfredi U. Development and review of Euro 5 passenger car emission factors based on experimental results over various driving cycles. Sci Total Environ. 2014;468-469:1034-1042. https://doi.org/10.1016/ j.scitotenv.2013.09.043

[9] Gebisa A, Gebresenbet G, Gopal R, Nallamothu RB. Driving cycles for estimating vehicle emission levels and energy consumption. Future Transp. 2021;1(3):615-638. https://doi.org/10.3390/futuretransp1030033

[10] Gis W, Pielecha J, Waśkiewicz J, Gis M, Menes M. Use of certain alternative fuels in road transport in Poland. IOP Conf Ser: Mater Sci Eng. 2016;148(1):012040. https://doi.org/10.1088/1757-899X/148/1/012040

[14] Hussein Hassan Q, Al-Abboodi H. Experimental investigation of the impact of methanol-diesel blends on diesel engine emissions and performance. Combustion Engines 2025; 201(2):150-157. https://doi.org/10.19206/CE-204494

[12] Kamińska M, Rymaniak Ł, Lijewski P, Szymlet N, Daszkiewicz P, Grzeszczyk R. Investigations of exhaust emissions from rail machinery during track maintenance operations. Energies. 2021;14(11):31-41. https://doi.org/10.3390/en14113141

[13] Kousoulidou M, Fontaras G, Ntziachristos L, Bonnel P, Samaras Z, Dilara P. Use of portable emissions measurement system (PEMS) for the development and validation of passenger car emission factors. Atmos Environ. 2013;64:329-338. https://doi.org/10.1016/j.atmosenv.2012.09.062

[14] Krysmon S, Dorscheidt F, Claßen J, Düzgün M, Pischinger S. Real Driving Emissions – conception of a data-driven calibration methodology for hybrid powertrains combining statistical analysis and virtual calibration platforms. Energies. 2021;14(16):4747. https://doi.org/10.3390/en14164747

[15] Lijewski P, Szymlet N, Fuć P, Domowicz A, Rymaniak Ł. The effect of start-stop systems on scooter exhaust emissions. Transp Res Part D Transp Environ. 2021:91. https://doi.org/10.1016/j.trd.2020.102684

[16] May J, Favre C, Bosteels D, Emissions from Euro 3 to Euro 6 light-duty vehicles equipped with a range of emissions control technologies. Association for Emissions Control by Catalyst. London 2013.

[17] Official Site of the COPERT 4 Model (2024). http://lat.eng.auth.gr/copert (accessed on 12.09.2025).

[18] Pielecha I, Cieślik W, Szałek A. Energy recovery potential through regenerative braking for a hybrid electric vehicle in a urban conditions. IOP Conf Ser: Earth Environ Sci. 2019; 214(1):012013. https://doi.org/10.1088/1755-1315/214/1/012013

[19] Pielecha J, Merkisz J, Jasiński R, Gis W. Real driving emissions testing of vehicles powered by compressed natural gas. SAE Technical Paper. 2015-01-2022. 2015. https://doi.org/10.4271/2015-01-2022

[20] Pielecha J, Skobiej K. Evaluation of ecological extremes of vehicles in road emission tests. Archives of Transport. 2020; 56(4):33-46. https://doi.org/10.5604/01.3001.0014.5516

[21] Previti U, Brusca S, Galvagno A. Passenger car energy demand assessment: A new approach based on road traffic data. E3S Web of Conferences, EDP Sciences: Les Ulis, France. 2020;197:05006. https://doi.org/10.1051/e3sconf/202019705006

[22] Pryciński P. Selected emissivity assessment issues for electric and hybrid vehicles. Combustion Engines. 2025;202(3): 27-35. https://doi.org/10.19206/CE-205274
[23] RDE Act 1. Commission Regulation (EU) 2016/427 of 10 march 2016 amending Regulation (EC) No 692/2008 as regards emissions from light passenger and commercial vehicles (Euro 6). Official Journal of the European Union L 82/1. 31 March 2016. http://data.europa.eu/eli/reg/2016/427/oj (accessed on 2.09.2025).
[24] RDE Act 2. Commission Regulation (EU) 2016/646 of 20 april 2016 amending Regulation (EC) No 692/2008 as regards emissions from light passenger and commercial vehicles (Euro 6). Official Journal of the European Union L 109/1. 26 April 2016. http://data.europa.eu/eli/reg/2016/646/oj (accessed on 2.09.2025).
[25] RDE Act 3. Commission Regulation (EU) 2017/1154 of 7 june 2017 amending Regulation (EU) 2017/1151 supplementing regulation (EC) No 715/2007 of the European Parliament and of the Council on type-approval of motor vehicles with respect to emissions from light passenger and commercial vehicles (Euro 5 and Euro 6) and on access to vehicle repair and maintenance information, amending Directive 2007/46/EC of the European Parliament and of the Council, Commission Regulation (EC) No 692/2008 and Commission Regulation (EU) No 1230/2012 and repealing Regulation (EC) No 692/2008 and Directive 2007/46/EC of the European Parliament and of the Council as regards real-driving emissions from light passenger and commercial vehicles (Euro 6). Official Journal of the European Union L 175/70. 7 July 2017. http://data.europa.eu/eli/reg/2017/1154/oj (accessed on 3.09. 2025).
[26] RDE Act 4. Commission Regulation (EU) 2018/1832 of 5 november 2018 amending Directive 2007/46/EC of the European Parliament and of the Council, Commission Regulation (EC) No 692/2008 and Commission Regulation (EU) 2017/1151 for the purpose of improving the emission type approval tests and procedures for light passenger and commercial vehicles, including those for in-service conformity and real-driving emissions and introducing devices for monitoring the consumption of fuel and electric energy. Official Journal of the European Union L 301/1. 27 December 2018. http://data.europa.eu/eli/reg/2018/1832/oj (accessed on 2.09. 2025).
[27] Regulation (EU) 2024/1257 of the European Parliament and of the Council of 24 april 2024 on type-approval of motor vehicles and engines and of systems, components and separate technical units intended for such vehicles, with respect to their emissions and battery durability (Euro 7), amending Regulation (EU) 2018/858 of the European Parliament and of the Council and Repealing Regulations (EC) No 715/2007 and (EC) No 595/2009 of the European Parliament and of the Council, Commission Regulation (EU) No 582/2011, Commission Regulation (EU) 2017/1151, Commission Regulation (EU) 2017/2400 and Commission Implementing Regulation (EU) 2022/1362. http://data.europa.eu/eli/reg/2024/1257/oj (accessed on 7.08.2025).
[28] Rymaniak Ł, Merkisz J, Szymlet N, Kamińska M, Weymann S. Use of emission indicators related to CO_2 emissions in the ecological assessment of an agricultural tractor. Eksploat Niezawodn. 2021;23(4):605-611. https://doi.org/10.17531/ein.2021.4.2
[29] Skobiej K. A review of hydrogen combustion and its impact on engine performance and emissions. Combustion Engines. 2025;200(1):64-70. https://doi.org/10.19206/CE-195470
[30] Szałek A, Pielecha I. The influence of engine downsizing in hybrid powertrains on the energy flow indicators under actual traffic conditions. Energies. 2021;14(10):2872. https://doi.org/10.3390/en14102872
[31] Szymlet N, Lijewski P, Kurc B. Road tests of a two-wheeled vehicle with the use of various urban road infrastructure solutions. Journal of Ecological Engineering. 2020;21(7):152-159. https://doi.org/10.12911/22998993/125503
[32] UN Regulation No 168 – Uniform provisions concerning the approval of light duty passenger and commercial vehicles with regards to real driving emissions (RDE) [2024/211]. http://data.europa.eu/eli/reg/2024/211/oj (accessed on 5.08. 2025).
[33] Valentini S, Trikka M, Cotogno G, Canevari P, Otura M, Giechaskiel B et al. Assessment of a real driving emissions inter-laboratory correlation circuit. Joint Research Centre, Publications Office of the European Union. Luxembourg, 2025. https://doi.org/10.2760/3632769 (accessed on 2.09. 2025).
[34] Valverde-Morales V. Overview of the light-duty vehicles tailpipe emissions regulations in the European Union: status and upcoming type-approval and market surveillance schema. Combustion Engines. 2020;180(1):3-7. https://doi.org/10.19206/CE-2020-101
[35] Weiss M, Bonnel P, Hummel R, Provenza A, Manfredi U. On-road emissions of light-duty vehicles in Europe. Environ Sci Technol. 2011;45:8575-8581. https://doi.org/10.1021/es2008424

Prof. Jacek Pielecha, DSc., DEng. – Faculty of Civil and Transport Engineering, Poznan University of Technology, Poland.
e-mail: *jacek.pielecha@put.poznan.pl*

Kinga Skobiej, DEng. – Faculty of Civil and Transport Engineering, Poznan University of Technology, Poland.
e-mail: *kinga.skobiej@put.poznan.pl*

Marek Sieroń, MEng. – Volkswagen Rzepecki Mroczkowski, Poland.
e-mail: *marek.sieron@rzepeckimroczkowski.pl*

Article citation info:
Kamińska M, Urbański P. Impact of transportation on air quality: modern emission measurement methods and reduction perspectives. Combustion Engines. 2025;203(4):114-125. https://doi.org/10.19206/CE-207823

Michalina KAMIŃSKA
Patryk URBAŃSKI

Combustion Engines
Polish Scientific Society of Combustion Engines

Impact of transportation on air quality: modern emission measurement methods and reduction perspectives

ARTICLE INFO

Received: 24 February 2025
Revised: 26 June 2025
Accepted: 2 July 2025
Available online: 24 July 2025

Air pollution, one of the most critical environmental and health challenges, causes millions of premature deaths annually. Transportation, especially internal combustion vehicles, is a significant source of pollutants such as particulate matter, nitrogen oxides, carbon monoxide, and hydrocarbons. This article analyzes methods for measuring exhaust emissions in laboratories and real-world operating conditions, discussing their advantages and limitations. Traditional dynamometer tests conducted on test benches enable detailed analyses but do not fully reflect real-world operating conditions. These tests fail to account for factors such as driving style or variable weather conditions. Modern methods, such as Real Driving Emissions (RDE) tests using Portable Emissions Measurement Systems (PEMS), allow for emission measurements in real traffic conditions, although they are costly and time-consuming. Alternative approaches for measuring emissions during transit, such as remote sensing (tunnel, extractive, or open-path methods), enable quick and efficient studies on large vehicle samples, though they come with certain limitations, such as result precision or the influence of external conditions. The article also highlights research on rail vehicle emissions, which remain limited to laboratory engine tests. This underscores the need for further development of measurement technologies and the implementation of more advanced methods for better emission monitoring. Measurements play a crucial role in designing policies aimed at reducing pollution, such as low-emission zones or stricter exhaust emission standards. This is of critical importance for achieving climate goals, such as carbon neutrality.

Key words: *exhaust emission, RDE, PEMS, remote sensing, tunnel studies, extractive method, open-path system*

1. Introduction

The 2019 "State of Global Air" report, developed by U.S. research organizations – Health Effects Institute and the Institute for Health Metrics and Evaluation – states that air pollution was the fourth leading risk factor for premature death worldwide. It is estimated to have contributed to 6.67 million deaths within a year, accounting for nearly 12% of the global total (Fig. 1). It is the primary environmental risk factor for premature death, with its combined impact surpassed only by high blood pressure (10.8 million), smoking (8.71 million), and dietary risks (7.94 million). Each year, significantly more people worldwide die from exposure to air pollution than from road collisions, which are estimated to cause 1.28 million deaths annually. Additionally, air pollution contributes to a higher number of deaths than factors such as malnutrition, alcohol consumption, or lack of physical activity [44, 46].

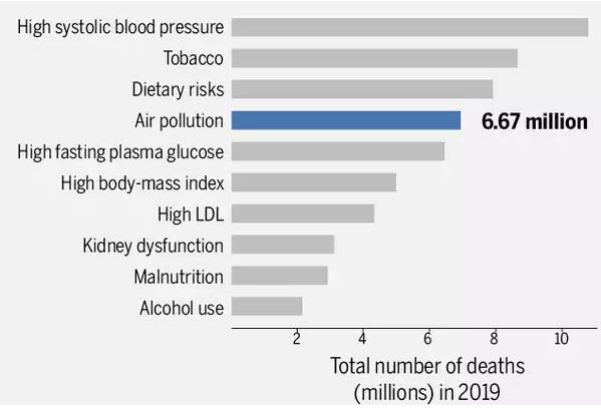

Fig. 1. Total number of deaths from all causes in 2019 [46]

Air pollution is a problem that negatively affects health and the environment in all countries worldwide, differing only in its severity (Fig. 2) [47]. The most vulnerable groups to the adverse effects of poor air quality include children, pregnant women, the elderly, and individuals with heart or lung diseases. Over 90% of the population still lives in areas where PM2.5 concentrations exceed the air quality standards set by the World Health Organization (WHO). Numerous current studies [44, 46] have unequivocally demonstrated that both short-term and long-term exposure to polluted air can contribute to serious health effects. These effects can include temporary or chronic diseases, mild or debilitating conditions, and even fatal outcomes.

Short-term exposure, lasting from several hours to a few days, can cause irritation of the ears, nose, and throat. These symptoms usually subside when pollution levels decrease. However, short-term exposure can also worsen the condition of the lower respiratory tract and lead to chronic illnesses such as allergies, asthma, chronic obstructive pulmonary disease (COPD), and bronchitis. For individuals with heart diseases, short-term exposure to PM2.5 can lead to arrhythmias, heart attacks, or even death. On the other hand, long-term exposure to air pollution, lasting from several months to several years, increases the risk of premature death due to chronic heart diseases, respiratory diseases, lung infections, lung cancer, diabetes, and other health problems. Additionally, growing scientific evidence indicates that exposure to polluted air during pregnancy can contribute to premature births, putting newborns at high risk of severe illnesses and mortality [44, 46, 66]. Numerous studies also suggest that air pollution may have neuro-

logical effects on children and cause neurodegenerative diseases in adulthood [44, 46, 66]. Considering these impacts, exposure to air pollution can significantly reduce life expectancy.

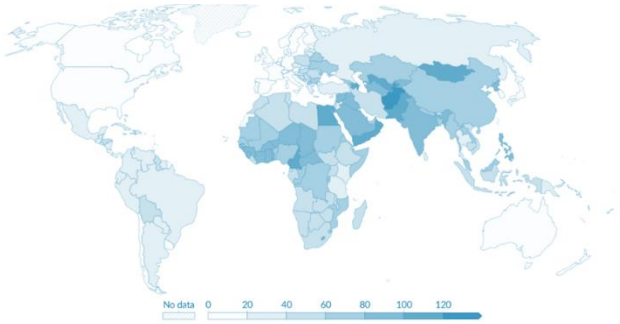

Fig. 2. Death rate attributed to ambient air pollution, 2019. Estimated annual number of deaths attributed to ambient air pollution per 100,000 people [66]

Reports on the state of global air also highlight the effects of pollution, which are the focus of the Global Burden of Disease Study (GBD) [45]. The GBD analysis estimates the societal burden in terms of years lived with illness and the number of deaths, most of which result from long-term exposure to air pollution. The study primarily examines mortality caused by five chronic non-communicable diseases, for which the strongest scientific evidence currently exists: diabetes, stroke, COPD, lung cancer, and ischemic heart disease, as well as one communicable disease – lower respiratory tract infections. Additionally, the estimates of particulate matter exposure include infant mortality caused by complications related to premature birth. The burden of diseases associated with air pollution is substantial, contributing significantly to the global percentage of deaths (Fig. 3) [45].

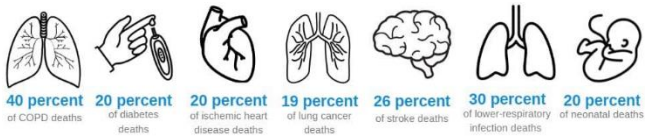

Fig. 3. Percentage of global deaths (by cause) attributed to air pollution in 2019 [45]

The impact of transport emissions on human health is not the only negative phenomenon. Significant amounts of emitted greenhouse gases (GHG) also have a strong impact on the environment. One of the results is global warming. Especially in the last 100 years, an enormous increase in the average global temperature was noted [52]. In this case, GHG emissions rose dramatically and were mainly caused by human activity. Faster warming process of the planet is causing weather anomalies and increasingly frequent, unpredictable, and dangerous phenomena such as hurricanes, tornadoes, droughts, and fires. Thus, paying attention to the growing negative trends in the environment and counteracting them is a key element in stopping the process of environmental destruction and degradation [1].

2. European legal regulations concerning exhaust emissions

2.1. Regulations concerning passenger cars

The European Union regulations on pollutant emissions from passenger cars and light commercial vehicles are described in Directive 70/220/EEC [27], which underwent a series of amendments up to the year 2004. In 2007, it was repealed and replaced by Regulation (EC) No. 715/2007 of the European Parliament and of the Council [74]. The most important legal documents include:

- Euro 1 standard: Directive 91/441/EEC [28], Directive 93/59/EEC [29]
- Euro 2 standard: Directive 94/12/EEC [32], Directive 96/69/EEC [33]
- Euro 3/4 standard: Directive 98/69/EC [35] Directive 2002/80/EC [15]
- Euro 5/6 standard: Regulation (EC) No. 715/2007 [74], Regulation (EC) No. 692/2008 [19]
- WLTP/WLTC tests: Regulation (EU) 2017/1151 [22], Regulation (EU) 2017/1247 [24]
- RDE tests: Regulation (EU) 2016/427 [20], Regulation (EU) 2016/646 [21], Regulation (EU) 2017/1154 [23], Regulation (EU) 2018/1832 [25].

The above-mentioned documents, starting with Directive 91/441/EEC, apply to exhaust emissions, fuel vapor emissions, crankcase emissions, and the durability of emission control systems in all motor vehicles equipped with spark-ignition engines, as well as to exhaust emissions and the durability of emission control systems in category M1 and N1 vehicles (Table 1) equipped with compression-ignition engines.

Table 1. Vehicle categories [30]

<table>
<tr><th>Cat.</th><th>Description</th><th colspan="2">Subcat.</th><th>Number of People</th><th colspan="2">Weight Limit</th></tr>
<tr><td rowspan="3">M</td><td rowspan="3">Passenger transport, minimum 4 wheels, passenger vehicles</td><td colspan="2">M1</td><td>up to 9</td><td colspan="2">–</td></tr>
<tr><td colspan="2">M2</td><td rowspan="2">> 9</td><td colspan="2">GVW ≤ 5 t[1)]</td></tr>
<tr><td colspan="2">M3</td><td colspan="2">GVW > 5 t</td></tr>
<tr><td rowspan="5">N</td><td rowspan="5">Goods transport, minimum 4 wheels, light and heavy commercial vehicles</td><td rowspan="3">N1</td><td>CL1</td><td rowspan="5">not applicable</td><td rowspan="3">GVW ≤ 3.5 T</td><td>RM ≤ 1.305 t</td></tr>
<tr><td>CL2</td><td>1.305 t < RM ≤ 1.76 t</td></tr>
<tr><td>CL3</td><td>1.76 t < RM ≤ 3.5 T</td></tr>
<tr><td colspan="2">N2</td><td colspan="2">3.5 t < GVW ≤ 12 t</td></tr>
<tr><td colspan="2">N3</td><td colspan="2">GVW > 12 t</td></tr>
<tr><td colspan="7">[1)] Until Euro 4: two subgroups: M1 DMC ≤ 2.5 t and M1 DMC 2.5 t < DMC ≤ 3.5 t
RM – Reference Mass
GVW – Gross Vehicle Weight</td></tr>
</table>

With the introduction of Directive 98/69/EC [35], the scope was expanded to include testing of exhaust emissions at normal and low ambient temperatures for spark-ignition engines, as well as verification of the proper functioning of onboard diagnostic (OBD) systems for both spark-ignition and compression-ignition engines (for categories M1 and

N2). Regulation (EU) 630/2012 [26] introduced additional requirements for mono- and bi-fuel gas vehicles and for flex-fuel vehicles running on a mixture of hydrogen and natural gas. At the manufacturer's request, type approval granted under these directives for category M1 and N1 vehicles equipped with compression-ignition engines may be extended to category M2 and N2 vehicles with a reference mass not exceeding 2840 kg, provided they meet the conditions for EEC type approval extension described in Directive 91/441/EEC [28].

Emission standards for passenger cars and light commercial vehicles apply to all vehicles in categories M1, M2, N1, and N2 with a reference mass not exceeding 2610 kg (or up to 2840 kg in the case of extended type approval), equipped with either spark-ignition or compression-ignition engines. Petrol-fueled engines must meet requirements for total hydrocarbons and methane (THC), non-methane hydrocarbons (NMHC), nitrogen oxides (NO_x), and carbon monoxide (CO). Compression-ignition engines, on the other hand, must meet standards for nitrogen oxides (NO_x), the sum of hydrocarbons and nitrogen oxides (HC + NO_x), and carbon monoxide (CO). Additionally, starting with Euro 5b for CI (compression-ignition) engines and with Euro 6 for SI (spark-ignition) engines with direct fuel injection (DI), vehicles are also required to undergo testing for particulate mass (PM) and particle number (PN) [56]. Table 2 presents the limit values for Euro 5–6 standards for passenger vehicles approved under category M1.

In order to obtain type approval, all internal combustion vehicles covered by the latest legal regulations must meet specific requirements and undergo the following tests:

Table 2. Euro 5–6 emission standards for M1 vehicles [30]

Standard		Euro 5a	Euro 5b/b+	Euro 6b, 6c	Euro 6d-Temp, 6d
		(WE) 715/2007 (WE) 692/2008			
Date		TA[1] 9/2009, FR[2] 1/2011	TA[1] 9/2011, FR[2] 1/2013	TA[1] 9/2014,(6b) FR[2] 9/2015(6b) FR[2]09/2018 (6c)	TA[1] 9/2017 (6d-Temp) TA[1] 1/220, (6d) FR[2] 1/2021 (6d)
Test type		Modified ECE + EUDC			WLTC + RDE
Engine type		Spark ignition			
THC	g/km	0.1	0.1	0.1	0.1
NMHC	g/km	0.068	0.068	0.068	0.068
NO_x	g/km	0.06	0.06	0.06	0.06
CO	g/km	1.0	1.0	1.0	1.0
PM[3)4)]	g/km	0.005[6]	0.005[6]	0.005	0.005
PN[3)4)]	1/km	–	–	6×10^{11} [5]	6×10^{11} [5]
Engine type		Compression ignition			
NO_x	g/km	0.18	0.18	0.08	0.08
HC+NO_x	g/km	0.23	0.23	0.17	0.17
CO	g/km	0.5	0.5	0.5	0.5
PM	g/km	0.005[6]	0.005[6]	0.005[6]	0.005[6]
PN	1/km	–	6×10^{11}	6×10^{11}	6×10^{11}

[1] TA – Type Approval
[2] FR – First Registration (approval for use)
[3] Test procedure defined in Regulation No. 83 (UNECE)
[4] Applies only to vehicles with direct injection gasoline engines (DI)
[5] 6,0×1012 1/km during the first three years after the Euro 6 standard comes into force
[6] 0,0045 g/km using the PMP (Particulate Measuring Protocol) measurement procedure

- Type 1 test – measurement of the average emission of gaseous compounds and particulate matter (PM and PN) from the vehicle's exhaust system
- Type 1A test – measurement of the average emission of gaseous compounds and particulate matter from the vehicle's exhaust system under real-world driving conditions
- Type 2 test – measurement of CO emissions at idle
- Type 3 test – measurement of crankcase gas emissions
- Type 4 test – measurement of fuel vapor emissions
- Type 5 test – verification of the durability of emission control systems
- Type 6 test – measurement of exhaust emissions at low ambient temperatures
- In-use compliance check
- Verification of the proper functioning of the OBD system
- Measurement of CO_2 emissions and fuel consumption
- Measurement of exhaust smoke opacity.

The values of emitted pollutants are primarily measured under laboratory conditions (for passenger cars, on a chassis dynamometer) using a strictly defined type-approval test designed to reflect normal driving conditions. However, with the adoption of Commission Regulation (EU) 2016/427 [20] of 10 March 2016, amending Regulation (EC) No 692/2008 [19] with regard to pollutant emissions from passenger cars and light commercial vehicles (Euro 6), provisions concerning emissions testing under real driving conditions were introduced – RDE (Real Driving Emission).

These guidelines were further supplemented by Regulations (EU) 2016/646 [21], 2017/1151 [23], and 2018/1832 [25]. Pollutants emitted during RDE tests must be recorded at a frequency of one second and calculated using strictly defined methods. Additionally, final values must be corrected using appropriate conformity factors (CF) in accordance with the guidelines set out in the above-mentioned regulations.

The emission of toxic pollutants during any real driving emissions test conducted in compliance with the requirements of the aforementioned legal acts, throughout the entire lifetime of vehicles approved under Regulation (EC) No 715/2007 [74], must not exceed the following Not-To-Exceed (NTE) values for individual exhaust compounds, which are dependent on the CF defined as:

$$\mathrm{NTE_j} = \mathrm{CF_j} \cdot \mathrm{EURO\ 6} \tag{1}$$

where: j – the pollutant for which the emission index is defined, NTE – Not-To-Exceed emission limit, CFj – Conformity Factor – operational conformity factor for a given pollutant, EURO 6 – limit value for a given toxic compound defined by the Euro 6 standard.

The vehicle operational CF for pollutant emissions is determined across all measurement windows for each exhaust gas component. It represents the multiplier by which pollutant emissions under real driving conditions may increase (or decrease) relative to the type-approval test, and is expressed by the following formula:

$$\mathrm{CF} = \frac{\mathrm{M_{RDE,j}}}{\mathrm{M_{test,j}}} \tag{2}$$

where: j – pollutant for which the CF index is defined, MRDE,j – on-road emission of the harmful exhaust compound obtained under real driving conditions during the RDE test [g/km], Mtest,j – on-road emission of the harmful exhaust compound obtained during the type-approval test [g/km].

The values of the vehicle operational CF for the respective pollutants are presented in Table 3. These values are subject to periodic review and are updated as PEMS (Portable Emission Measurement Systems) procedures or technologies improve. With the introduction of the temporary Euro 6d-TEMP standard, a CF value of 2.1 for NO_x and 1.5 for PN was adopted (1 + a margin for PN = 0.5). In the subsequent stage (Euro 6d), the CF for NO_x was reduced to 1.43 (1 + a margin for NO_x = 0.43), while the CF for PN remained unchanged. The margin is a parameter that accounts for the additional measurement uncertainty of equipment used to measure harmful exhaust compounds under real driving conditions. This parameter is reviewed annually.

Table 3. Conformity factors for emissions [30]

	NO_x CF	PN CF	CO
Euro 6d-TEMPT	2.1	1.5 (1 + margin = 0.5)	Must be measured and recorded
Euro 6d	1.43 (1 + margin = 0.43)	1.5 (1 + margin = 0.5)	Must be measured and recorded

In the absence of information regarding pollutant emissions from a vehicle recorded during the type-approval test, it is possible to adopt the permissible values specified in the Euro emission standards applicable to the given vehicle. Emission indices (for individual pollutants) can be defined as the following types:

- Instantaneous – characterized by high variability, calculated for each second of the test
- Cumulative during the test – calculated as the running on-road emission of specific harmful exhaust compounds (from the start of the test to the current moment) relative to the normative value
- Overall, for the entire test, calculated as the ratio of on-road emissions in the RDE test to the normative value.

The validity of a completed run within an RDE test must be verified through a three-stage procedure as follows:

- STAGE A – verification of general requirements, boundary conditions, trip and operational requirements, as well as specifications for operational fluids, as defined in Regulation (EU) 2016/427 [20]
- STAGE B – verification of general driving dynamics requirements and the procedure for determining the cumulative positive altitude gain, as defined in Regulation (EU) 2016/427 [20]
- STAGE C – verification of dynamic driving conditions and calculation of the final emission value under real driving conditions using the moving averaging window method based on CO_2 mass, as defined in Regulation (EU) 2016/427 [20].

2.2. Regulations concerning rail vehicles

The regulations in force in Europe regarding the permissible emissions of harmful exhaust compounds from combustion engines used in vehicles of the NRMM category (Non-Road Mobile Machinery Emissions) are defined by the requirements set out in the Stage I–V standards. These regulations are specified in Directive 97/68/EC of the European Parliament and of the Council [37] and in subsequent amendments:

- Stage I/II standard: Directive 97/68/EC [34], Directive 2002/88/EC [36]
- Stage III/IV standard: Directive 2010/26/EU [17], Directive 2010/26/EC [16]
- Stage V standard: Regulation (EU) 2016/1628 [75], Regulation (EU) 2017/654 [127], Regulation (EU) 2018/989 [14], Regulation (EU) 2017/655 [12], Regulation (EU) 2018/987 [13].

In the European Union regulation, the following categories of engines used in traction vehicles have been defined:

a) Category NRE (Engines For Non-Road Mobile Machinery)
   - Engines for mobile machinery not intended for use on roads
   - Engines with a rated power of less than 560 kW
b) Category NRS (Spark Ignition Engines For Non-Road Mobile Machinery) – SI engines
   - Engines with a rated power below 56 kW
c) Category RLL (Railway Locomotives)
   - Engines used in locomotives
d) Category RLR (Railway Railcars)
   - Engines used in railcars
   - Engines used instead of RLL category engines under Stage V [38].

The first emission limits with the force of European Union law for the non-road vehicle group were introduced in the 1990s. The Stage standards were gradually implemented as increasingly strict regulations based on engine power (Tables 4–7). Type approval is granted when the power unit meets the requirements set out in the relevant directives and when the emission of toxic compounds in the exhaust gases complies with the limits defined by the applicable standard.

Table 4. Stage IIIA/B emission standards for locomotives and railcars [10]

Cat.	Power [kW]	Date	CO	HC	NO_x	PM
			g/kWh			
Stage III A						
RC A	P > 130	2006	3.5	HC+NO_x = 4.0		0.2
RL A	130 ≤ P ≤ 560	2007	3.5	HC+NO_x = 4.0		0.2
RH A	P > 560	2009	3.5	0.5[1]	6.0[1]	0.2
Stage III B						
RC B	P > 130	2012	3.5	0.19	2.0	0.025
R B	P > 130	2012	3.5	HC+NO_x = 4.0		0.025

The emission of harmful exhaust compounds from NRMM vehicles in the European Union is assessed using two test cycles:

- NRSC (Non-Road Stationary Cycle) – a stationary test cycle used to measure toxic exhaust compounds (CO, HC, NO_x, PM) from non-road vehicles. It is applied under Stage I–V standards for CI engines operating at constant or variable speed with a net power output in the range of 19 kW ≤ P ≤ 560 kW. The NRSC test is also used to measure emissions from engines intended for use in locomotives and railcars (Stage IIIA/B).

– NRTC (Non-Road Transient Cycle) – a transient test cycle used to measure toxic exhaust compounds (CO, HC, NO_x, PM) from non-road vehicles. It is applied under Stage III B–V standards for compression ignition engines with a net power output in the range of 19 kW ≤ P ≤ 560 kW operating under variable speed conditions [17, 18, 37].

Table 5. Stage IIIA/B and Stage IV emission standards for rail vehicles [10]

Cat.	Power [kW]	Date	CO	HC	NO_x	PM
			g/kWh			
Stage III A						
H	130 ≤ P ≤ 560	2006	3.5	HC+NOx = 4.0		0.2
I	75 ≤ P < 130	2007	5.0	HC+NOx = 4.0		0.3
J	37 ≤ P < 75	2008	5.0	HC+NOx = 4.7		0.4
K	19 ≤ P < 37	2007	5.5	HC+NOx = 7.5		0.6
Stage III B						
L	130 ≤ P ≤ 560	2011	3.5	0.19	2.0	0.025
M	75 ≤ P < 130	2012	5.0	0.19	3.3	0.025
N	56 ≤ P < 75	2012	5.0	0.19	3.3	0.025
P	37 ≤ P < 56	2013	5.0	HC+NOx = 4.7		0.025
Stage IV						
Q	130 ≤ P ≤ 560	2014	3.5	0.19	0.4	0.025
R	56 ≤ P < 130	2014	5.0	0.19	0.4	0.025
[1] HC = 0.4 g/kWh, NO_x = 7.4 g/kWh for engines with power P > 2000 kW and displacement D > 5 dm^3/cylinder						

Table 6. Stage V emission standards for engines of category NRE [10]

Cat.	Power [kW]	Date	CO	HC	NO_x	PM	PN
			g/kWh				1/kWh
NRE-v/c-1	P < 8[1)]	2019	8.0	HC+NO_x = 7.5		0.4	–
NRE-v/c-2	8 ≤ P < 19[1)]	2019	6.6	HC+NO_x = 7.5		0.4	–
NRE-v/c-3	19 ≤ P < 37[1)]	2019	5.0	HC+NO_x = 4.7		0.015	1×10^{12}
NRE-v/c-4	37 ≤ P < 56[1)]	2019	5.0	HC+NO_x = 4.7		0.015	1×10^{12}
NRE-v/c-5	56 ≤ P < 130[2)]	2019	5.0	0.19	0.4	0.015	1×10^{12}
NRE-v/c-6	130 ≤ P ≤ 560[2)]	2019	3.5	0.19	0.4	0.015	1×10^{12}
NRE-v/c-7	P > 560[2)]	2019	3.5	0.19	3.5	0.045	–
[1)] Ignition – CI [2)] Ignition – CI, SI							

Table 7. Stage V emission standards for locomotive and railcar propulsion systems [10]

Cat.	Power [kW]	Date	CO	HC	NO_x	PM	PN
			g/kWh				1/kWh
RC A	P > 0[1)]	2021	3.5	HC+NO_x = 4.0		0.025	–
RL A	P > 0[1)]	2021	3.5	0.19	2.0	0.025	1×10^{12}
[1)] Ignition – CI, SI							

In emission tests of exhaust systems, measurements are performed for gaseous compounds (CO, HC, NO_x) as well as PM. CO_2 is often used as a reference gas to determine the dilution level in both full-flow and partial-flow dilution systems. Additionally, it is recommended to monitor CO_2 concentrations due to their usefulness in detecting measurement issues during the test based on their readings. The stationary test cycle consists of a strictly defined number of engine speed and load phases, designed to represent the typical operating ranges of non-road mobile machinery engines. In all test phases, the concentrations of harmful exhaust compounds, exhaust gas flow rate, engine power, and the weighted average of measured values are determined. Pollutants from the vehicle's exhaust system are measured continuously by sampling undiluted exhaust gas under precisely defined operating conditions with a warmed-up engine. PM is measured by collecting the sample on a suitable filter, which is then diluted using conditioned ambient air. The PM sample can either be collected as a single sample for the entire test or as individual samples on separate filters for each test phase, with a weighted average then calculated for the whole test. The method for calculating the specific emission of pollutants (g/kWh), i.e., the number of grams of all measured harmful compounds per unit of work performed, is strictly defined. The NRSC includes various profiles that define how the measurement test is conducted for different types of equipment as specified in Directive 2004/26/EC [17, 18, 37].

3. Measurement of harmful exhaust emissions in laboratory tests

The primary tests for measuring exhaust emissions are dynamometer tests conducted under laboratory conditions. These measurements aim to simulate real-world vehicle operating conditions, with the resulting emission data often serving as input for models assessing the impact of road traffic on air quality. Laboratory measurements are divided into two groups. The first group consists of engine dynamometer tests, where the engine is mounted directly on a test bench and equipped with only the components necessary for its proper functioning. The second group involves chassis dynamometer tests, where vehicles are tested on rollers that simulate road conditions. The main advantage of laboratory tests is their ability to perform multiple measurement cycles at relatively low costs. However, the results are only approximate, as the tests do not account for factors such as road conditions, driver behaviour, or the quality of ambient air. Consequently, most test cycles conducted on dynamometers do not accurately reflect the actual operating conditions of vehicles in urban traffic [55]. Literature analyses confirm significant differences between parameters measured in laboratory and real-world conditions [3, 51, 88]. Additionally, most tests are conducted on new or minimally used engines, which are in much better technical condition than the majority of vehicles on the road. This highlights the need to consider the degree of wear and tear of tested vehicles, as it significantly impacts exhaust emissions. Numerous studies [6, 9, 62, 90–92] have demonstrated that old and worn-out vehicles pose the greatest threat to the environment and human health. As a result, several alternative methods have been developed in recent years to obtain more reliable results. One of the first approaches involved the creation of dynamic test cycles that simulate specific driving conditions [2, 83]. Another approach involved conducting tests under real-world operating conditions.

4. Measurement of harmful exhaust emissions in real-world operating conditions

Homologation regulations currently mandate that emissions measurements for passenger cars must be conducted on the road, using specially designed RDE tests with PEMS [95]. The program for the RDE test is a development of the stationary World Wide Harmonised Light Vehicle Test

Procedure (WLTP). The WLTP test is performed on a car dynamometer and consists of four phases, which are different due to speed and driving dynamics. Phases in WLTP test are: low, medium, high, and extra-high. The test applies to passenger cars and delivery vans.

The driving test in the RDE procedure consists of a sequence of three driving stages: urban, rural, and motorway, which are classified based on instantaneous speed, with their proportions expressed as a percentage of the total driving distance (tab. 8). The test covers approximately (±10%) 34% urban driving with vehicle speeds not exceeding 60 km/h, 33% rural driving with speeds between 60 km/h and 90 km/h, and 33% motorway driving with vehicle speeds above 90 km/h. The total duration of the test is between 90 and 120 minutes, and the minimum distance covered in urban, rural, and motorway segments must be 16 km for each stage. Due to these requirements, such measurements are very time-consuming and require substantial financial resources.

Table 8. RDE test driving conditions [67]

Parameter	Requirements		
Segment	urban	rural	motorway
Duration of test	90–120 min		
Proportion of test time	29–44%	23–43%	23–43%
Minimum distance	16 km	16 km	16 km
Vehicle speed	v ≥ 60 km/h	60km/h < v ≤ 90 km/h	v > 90 km/h
Average vehicle speed	15–40 km/h	–	–
v > 100 km/h	–	–	≥ 5 min
v > 140 km/h	–	–	< 3% of motorway driving time
Stops during urban driving	6–30% of the urban segment time	–	–
Cumulative positive altitude gain	< 1200 m/100 km		
Difference in altitude (start vs. end)	≤ 100 m		

Real-world testing aims to verify the ecological performance of vehicles across a wide spectrum of operating conditions [96]. These measurements primarily focus on assessing the impact of applied powertrain systems and vehicle parameters on emissions of harmful substances and identifying differences between homologation procedures and real-world usage. Numerous global tests have demonstrated significant discrepancies between dynamometer-based laboratory tests and real-world road tests, particularly concerning nitrogen oxides [5, 42, 65]. Advancements in measurement equipment miniaturization have enabled increasingly precise studies in real-world operating conditions.

Moreover, the application potential of such devices continues to expand, allowing the inclusion of specific movement patterns for different vehicle types (road, off-road, including rail). However, there are certain limitations to using PEMS equipment. Primarily, the measurement analyzers must be installed on the test vehicle, and the measurement probes must be directly integrated into the exhaust system [64, 78, 87]. The installation process is often time-consuming, and it is not always feasible to use exhaust gas flow meters, which streamline the testing process. Consequently, flow characteristics often must be determined using data on intake manifold pressure, post-turbocharger temperature, and crankshaft rotational speed.

RDE procedures, however, cover only passenger cars and delivery vans, and there are no specific regulations yet for testing NRMM under real-world conditions. These vehicles, or more specifically their combustion engines, are only tested in laboratory conditions using engine dynamometers. The operational characteristics of engines for Stage standards are predetermined. For static tests, NRSC is tailored for specific engine groups, while the dynamic NRTC serves as a common test for all vehicle types. Both tests are mandatory, but they often fail to replicate real-world operating conditions. The latest regulations regarding NRMM emissions include provisions for real-world testing [31], but they lack defined research procedures or specific emission limits for harmful exhaust gases in such tests.

Real-world operating condition tests are a very modern solution designed to accurately reproduce the conditions prevailing during normal vehicle operations. However, such tests are primarily conducted on new vehicles that are being approved for road use, as mandated by homologation regulations. Older and more heavily used vehicles, which pose the greatest risk to the environment and human health, are typically only tested in research centres for scientific purposes or, more commonly, during inspections at Vehicle Inspection Stations. These inspections rely on basic and often imprecise equipment, which often yields unreliable results. As a result, there is ongoing development of measurement methods that do not require interference with the vehicle's structure and involve significantly lower financial costs [62, 90–92].

5. Remote sensing measurements

5.1. Tunnel studies

An alternative to PEMS-based testing is remote sensing measurements, which allow for the evaluation of vehicle emissions without the need to install equipment on the tested vehicles. These systems record instantaneous measurements of exhaust concentrations from passing vehicles, enabling the testing of a large number of vehicles in a short period and at low unit costs. Three main remote sensing systems can be distinguished: tunnel studies, the extractive method, and the open-path system. A comprehensive literature review revealed numerous solutions for measuring emissions from passenger cars and heavy vehicles, but there is a lack of research regarding such measurements for rail vehicles. Tunnel studies (Fig. 4) [48, 49, 81] are conducted for groups of vehicles, and harmful exhaust emissions are measured for the studied area.

In this type of research, a ventilation system is commonly used to collect samples. A reference gas sample is introduced prior to measurement. Air samples are collected at several measurement points, enabling the determination of average concentrations across a cross-section. These samples are stored in special bags or are sent directly to measurement devices at a defined flow rate. The collected pollutants are then analyzed using specific analyzers for measur-

ing harmful exhaust gases. For CO_2 and CO measurements, NDIR (Non-Dispersive Infrared) analyzers or related technologies are commonly used [48, 57, 63]. NO_x measurements employ chemiluminescent detectors [48, 57, 63, 81], while HC is measured using a Flame Ionization Detector (FID) [57, 63, 85]. PM is analyzed using gravimetric methods [57, 58, 60]. Tunnel-based emission studies were first implemented in the late 1970s [68], and over time, these measurements have been widely adopted in the United States [40, 77, 79] and other countries [48, 58, 80, 86].

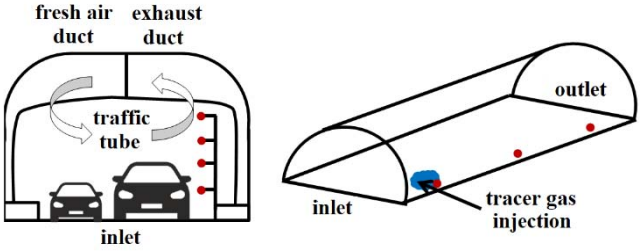

Fig. 4. Tunnel test method for exhaust gas sampling, where red dots (●) indicate the locations of measurement points [48, 49, 80]

The main advantage of tunnel studies is the location where the measurements are conducted. Tunnel walls and the use of air filtration systems act as barriers against external factors, such as pollution from vehicles outside the tunnel or from local stationary sources. Additionally, the tunnel's ventilation system facilitates the measurement of airflows. Another advantage of tunnel studies is the ease of setting up measurement equipment. However, research [50, 69] has shown that local emission models often significantly differ from real-world values, particularly for CO and HC results, which were found to be approximately half the actual values. This discrepancy raises concerns about the accuracy of the obtained measurement results.

5.2. Extractive method

Another type of remote sensing study is the extractive method (Fig. 4) [71, 72, 93]. This approach utilizes the principle of extractive remote sensing, where a sample of exhaust gas is collected and analysed by a specialized system. A test setup for this method can be mounted on a mobile research unit equipped with devices that capture exhaust gases. In this case, the test vehicle follows the analysed vehicle, capturing a portion of the emitted exhaust gases. The collected gases are then directed to specialized analysers for identification and measurement. Alternatively, stationary measurement points can be used, which continuously sample air, with the samples being taken near the vehicle's exhaust outlet. The extractive remote sensing technique is characterized by high precision due to the advanced technology of the analysers used.

However, a limitation of this method is the relatively small number of vehicles that can be tested simultaneously [8]. In most cases, extractive studies rely on specially adapted air monitoring systems that are modified by researchers [4, 41, 43]. The equipment used in these studies typically includes NDIR analysers for CO measurements [4, 11, 53], chemiluminescent analysers for NO [4, 11], and NDUV (Non-Dispersive Ultraviolet) analysers for O_3 [11], as well as optical particle counters for PM [11, 41, 89]. A review of the literature indicates that extractive studies have yet to define specific emission or concentration thresholds for the tested vehicles.

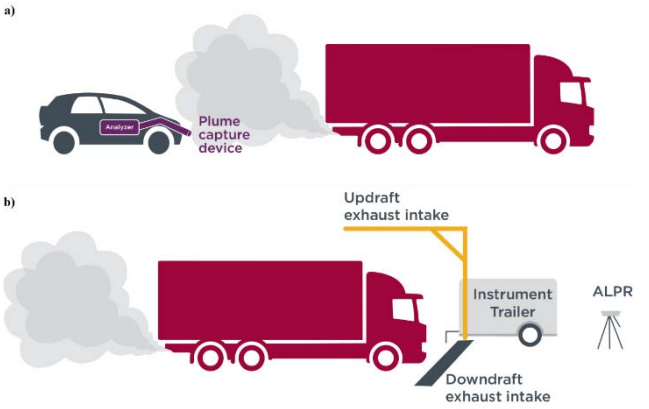

Fig. 5. Method of sampling exhaust gases using extraction remote sensing using a) mobile measuring point, b) stationary measuring point [8]

5.3. Open-path system

Another type of remote sensing system is the open-path method, which utilizes a light source and a detector placed either at the roadside or above the roadway (Fig. 5) [59, 94]. The light source, operating in the infrared or ultraviolet spectrum, is reflected by a mirror located on the opposite side of the road. Exhaust gases passing through the light beam absorb part of the radiation, allowing the concentrations of specific pollutants to be determined. This measurement occurs as the vehicle passes through the beam. The monitoring equipment also records environmental conditions, enabling the registration and control of surrounding air quality, which allows for the separation of background pollutants from those emitted by the analysed vehicle. This type of remote sensing station also facilitates the measurement of vehicle speed, acceleration, and the identification of license plates using cameras [8].

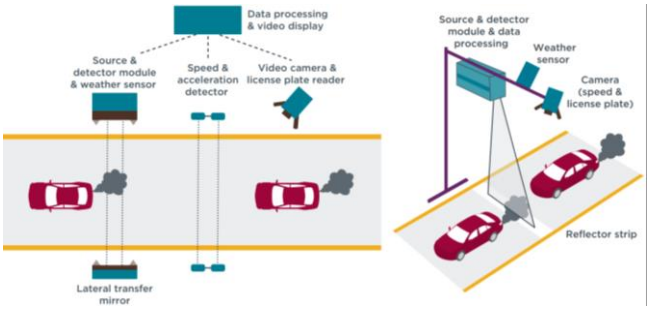

Fig. 6. Open path measurement scheme: a) configuration used at intersections, b) top-down detection system [8]

However, the open-path method has some limitations, such as differences in scanning time due to gaps between vehicles or variability in the composition of background air. Another issue is the significant uncertainty of results caused by the length of the measurement path, which often necessitates normalizing the data relative to CO_2 emissions [70, 73, 84]. Remote sensing studies of this type typically last several weeks or months, allowing data to be collected for

a very large fleet of vehicles. Remote sensing devices are most commonly used to measure concentrations of CO, HC, NO, and PM. The scientific literature reports typical values for these pollutants as follows: CO ranging from 0.2% to 3.5% [54, 76, 82], HC ranging from 0.004% to 0.22% [54, 76, 82], and NO ranging from 35 ppm to 1000 ppm [54, 76, 82].

A review of the literature shows that for over a decade, researchers from various scientific institutions worldwide have been working on developing devices to assess emissions under both real-world and laboratory conditions [2, 3, 61, 65, 67]. However, the technologies developed so far remain insufficient. Given the persistent issue of harmful emissions from combustion vehicles, further research utilizing more advanced measurement technologies is necessary [7].

6. Summary

Due to the significant impact of transportation on air pollution, new regulations are being implemented to reduce harmful exhaust emissions. The European Union's primary goal is to introduce regulations for zero CO_2 emissions from vehicles by 2035. Intermediate emission reduction targets for 2030 have been set at 55% for passenger cars and 50% for commercial vehicles [39]. The final version of these regulations was approved by the European Parliament in February 2023. The overarching objective of these actions is to achieve a 90% reduction in greenhouse gas emissions from transportation by 2050 compared to 1990 levels, supporting the attainment of climate neutrality under the European Green Deal. However, transportation is the only sector where greenhouse gas emissions increased over the past three decades, rising by 33.5% between 1990 and 2019. Significant reductions in CO_2 emissions will therefore not be easy, as the rate of reduction has slowed.

Current forecasts indicate that emissions from the transportation sector will decrease by only 22% by 2050, far below the established goals [39]. Achieving the desired targets and addressing the health crisis caused by air pollution will require swift and comprehensive actions. In highly developed economies, various solutions are being implemented to improve air quality, such as establishing low-emission zones in city centres. The effectiveness of such zones can be assessed through remote sensing devices that measure harmful exhaust emissions from vehicles operating in these areas. The main advantage of such measurements is obtaining real-world data on the state of vehicles operating within a specific area, including compliance with legislative standards and the level of wear and tear of the vehicles. Remote sensing enables the determination of pollutant concentrations emitted by vehicles within and outside low-emission zones. This provides valuable insights into the actual impact of these zones in reducing automotive-related environmental pollution.

Additionally, this type of research can identify and exclude vehicles that excessively emit harmful substances, reducing their negative impact on the environment and public health. High-emission vehicles can then undergo diagnostics to identify the source of the issue. This approach encourages faster action from vehicle owners to repair or replace damaged components. In cases where repairs are not economically viable, the vehicles should be retired and replaced with modern, more environmentally friendly models. This strategy effectively reduces emissions and promotes more sustainable vehicle use. It is also essential to conduct similar studies in the non-road transport sector. Rail vehicles, especially older and heavily used units, are significant sources of harmful emissions, and research on their emissions remains limited and insufficient. Applying remote sensing systems to railways would, as with road vehicles, allow for the identification of units emitting excessive pollutants and enable corrective actions. A lack of action in the non-road vehicle sector risks the continued operation of vehicles that significantly exceed homologation limits, posing threats to human health and contributing to environmental degradation. Introducing remote sensing studies for rail vehicles is, therefore, not only necessary but also a critical step toward sustainable railway transport.

Acknowledgements

The research was funded by European Union from European Regional Development Fund through the National Centre for Research and Development (Narodowe Centrum Badań i Rozwoju) – research project within the Smart Growth Programme (contract No. POIR.04.01.02-00-0002/18).

Nomenclature

CF	conformity factors
CI	compression-ignition
CO	carbon monoxide
CO_2	carbon dioxide
COPD	chronic obstructive pulmonary disease
DI	direct fuel injection
FID	flame ionization detector
GBD	global burden of disease study
GHG	green house gases
HC	hydrocarbons
NDIR	non-dispersive infrared
NDUV	non-dispersive ultraviolet
NMHC	non-methane hydrocarbons
NO_x	nitrogen oxides
NRE	engines for non-road mobile machinery
NRMM	non-road mobile machinery
NRS	spark ignition engines for non-road mobile machinery
NRSC	non-road steady cycle
NRTC	non-road transient cycle
NTE	Not-To-Exceed emission limit
O_3	ozone
OBD	onboard diagnostic
PEMS	portable emissions measurement systems
PM	particulate mass
PN	particle number

RDE	real driving emission	WHO	World Health Organization
SI	spark-ignition	WLTP	World Wide Harmonised Light Vehicle Test Procedure
THC	total hydrocarbons		

Bibliography

[1] Aminzadegan S, Shahriari M, Mehranfar F, Abramović B. Factors affecting the emission of pollutants in different types of transportation: a literature review. Energy Rep. 2022;8:2508-2529. https://doi.org/10.1016/j.egyr.2022.01.161

[2] André M. The ARTEMIS European driving cycles for measuring car pollutant emissions. Sci Total Environ. 2004; 334-335:73-84. https://doi.org/10.1016/j.scitotenv.2004.04.070

[3] Andrews GE, Li H, Wylie JA, Zhu G, Bell M, Tate J. Influence of ambient temperature on cold-start emissions for a Euro 1 SI car using in-vehicle emissions measurement in an urban traffic jam test cycle. SAE Technical Paper 2005-01-1617. 2005. https://doi.org/10.4271/2005-01-1617

[4] Ayala A, Olson B, Cantrell B, Drayton M, Barsic N. Estimation of diffusion losses when sampling diesel aerosol: a quality assurance measure. SAE Technical Paper 2003-01-1896. 2003. https://doi.org/10.4271/2003-01-1896

[5] Bajerlein M, Daszkiewicz P, Dobrzyński M, Rymaniak Ł, Siedlecki M. ENThe analysis of emission from CNG city bus in terms of procedures NTE and the EU 582/2011. Combustion Engines. 2015;54(3):800-804. bwmeta1.element.baztech-806cdf63-3538-4787-88dd-4385aab68911

[6] Bajerlein M, Karpiuk W, Kurc B, Smolec R, Waligórski M. Refining combustion dynamics: dissolved hydrogen in diesel fuel within turbulent-flow environments. Energies. 2024; 17(11):2446. https://doi.org/10.3390/en17112446

[7] Bajerlein M, Karpiuk W, Smolec R. Application of gas dissolved in fuel in the aspect of a hypocycloidal pump design. Energies. 2022;15(23):9163. https://doi.org/10.3390/en15239163

[8] Bernard Y, German J, Muncrief R. Worldwide use of remote sensing to measure motor vehicle emissions. Int Counc Clean Transp ICCT. April 2019.

[9] Bin O. A logit analysis of vehicle emissions using inspection and maintenance testing data. Transp Res Part Transp Environ. 2003;8(3):215-227. https://doi.org/10.1016/S1361-9209(03)00004-X

[10] Borg Warner. On and Off-Highway Commercial Vehicles Emissions Standards Booklet 2021-2022.

[11] Bukowiecki N, Dommen J, Prévôt ASH, Richter R, Weingartner E, Baltensperger U. A mobile pollutant measurement laboratory – measuring gas phase and aerosol ambient concentrations with high spatial and temporal resolution. Atmos Environ. 2002;36(36):5569-5579. https://doi.org/10.1016/S1352-2310(02)00694-5

[12] Commission Delegated Regulation (EU) 2017/655 of 19 December 2016 supplementing Regulation (EU) 2016/1628 of the European Parliament and of the Council with regard to monitoring of gaseous pollutant emissions from in-service internal combustion engines installed in non-road mobile machinery.

[13] Commission Delegated Regulation (EU) 2018/987 of 27 April 2018 amending and correcting Delegated Regulation (EU) 2017/655 supplementing Regulation (EU) 2016/1628 of the European Parliament and of the Council with regard to monitoring of gaseous pollutant emissions from in-service internal combustion engines installed in non-road mobile machinery.

[14] Commission Delegated Regulation (EU) 2018/989 of 18 May 2018 amending and correcting Delegated Regulation (EU) 2017/654 supplementing Regulation (EU) 2016/1628 of the European Parliament and of the Council with regard to technical and general requirements relating to emission limits and type-approval for internal combustion engines for non-road mobile machinery.

[15] Commission Directive 2002/80/EC of 3 October 2002 adapting to technical progress Council Directive 70/220/EEC relating to measures to be taken against air pollution by emissions from motor vehicles.

[16] Commission Directive 2010/22/EU of 15 March 2010 amending, for the purposes of their adaptation to technical progress, Council Directives 80/720/EEC, 86/298/EEC, 86/415/EEC and 87/402/EEC and Directives 2000/25/EC and 2003/37/EC of the European Parliament and of the Council relating to the type-approval of agricultural or forestry tractors.

[17] Commission Directive 2010/26/EU of 31 March 2010 amending Directive 97/68/EC of the European Parliament and of the Council on the approximation of the laws of the Member States relating to measures against the emission of gaseous and particulate pollutants from internal combustion engines to be installed in non-road mobile machinery.

[18] Commission Directive 2012/46/EU of 6 December 2012 amending Directive 97/68/EC of the European Parliament and of the Council on the approximation of the laws of the Member States relating to measures against the emission of gaseous and particulate pollutants from internal combustion engines to be installed in non-road mobile machinery Text with EEA relevance.

[19] Commission Regulation (EC) No 692/2008 of 18 July 2008 implementing and amending Regulation (EC) No 715/2007 of the European Parliament and of the Council on type-approval of motor vehicles with respect to emissions from light passenger and commercial vehicles (Euro 5 and Euro 6) and on access to vehicle repair and maintenance information.

[20] Commission Regulation (EU) 2016/427 of 10 March 2016 amending Regulation (EC) No 692/2008 as regards emissions from light passenger and commercial vehicles (Euro 6).

[21] Commission Regulation (EU) 2016/646 of 20 April 2016 amending Regulation (EC) No 692/2008 as regards emissions from light passenger and commercial vehicles (Euro 6).

[22] Commission Regulation (EU) 2017/1151 of 1 June 2017 supplementing Regulation (EC) No 715/2007 of the European Parliament and of the Council on type-approval of motor vehicles with respect to emissions from light passenger and commercial vehicles (Euro 5 and Euro 6) and on access to vehicle repair and maintenance information, amending Directive 2007/46/EC of the European Parliament and of the Council, Commission Regulation (EC) No 692/2008 and Commission Regulation (EU) No 1230/2012 and repealing Commission Regulation (EC) No 692/2008.

[23] Commission Regulation (EU) 2017/1154 of 7 June 2017 amending Regulation (EU) 2017/1151 supplementing Regulation (EC) No 715/2007 of the European Parliament and of the Council on type-approval of motor vehicles with respect to emissions from light passenger and commercial vehicles

(Euro 5 and Euro 6) and on access to vehicle repair and maintenance information, amending Directive 2007/46/EC of the European Parliament and of the Council, Commission Regulation (EC) No 692/2008 and Commission Regulation (EU) No 1230/2012 and repealing Regulation (EC) No 692/2008 and Directive 2007/46/EC of the European Parliament and of the Council as regards real-driving emissions from light passenger and commercial vehicles (Euro 6).

[24] Commission Regulation (EU) 2017/1347 of 13 July 2017 correcting Directive 2007/46/EC of the European Parliament and of the Council, Commission Regulation (EU) No 582/2011 and Commission Regulation (EU) 2017/1151 supplementing Regulation (EC) No 715/2007 of the European Parliament and of the Council on type-approval of motor vehicles with respect to emissions from light passenger and commercial vehicles (Euro 5 and Euro 6) and on access to vehicle repair and maintenance information, amending Directive 2007/46/EC of the European Parliament and of the Council, Commission Regulation (EC) No 692/2008 and Commission Regulation (EU) No 1230/2012 and repealing Regulation (EC) No 692/2008.

[25] Commission Regulation (EU) 2018/1832 of 5 November 2018 amending Directive 2007/46/EC of the European Parliament and of the Council, Commission Regulation (EC) No 692/2008 and Commission Regulation (EU) 2017/1151 for the purpose of improving the emission type approval tests and procedures for light passenger and commercial vehicles, including those for in-service conformity and real-driving emissions and introducing devices for monitoring the consumption of fuel and electric energy.

[26] Commission Regulation (EU) No 630/2012 of 12 July 2012 amending Regulation (EC) No 692/2008, as regards type-approval requirements for motor vehicles fuelled by hydrogen and mixtures of hydrogen and natural gas with respect to emissions, and the inclusion of specific information regarding vehicles fitted with an electric power train in the information document for the purpose of EC type-approval.

[27] Council Directive 70/220/EEC of 20 March 1970 on the approximation of the laws of the Member States relating to measures to be taken against air pollution by gases from positive-ignition engines of motor vehicles.

[28] Council Directive 91/441/EEC of 26 June 1991 amending Directive 70/220/EEC on the approximation of the laws of the Member States relating to measures to be taken against air pollution by emissions from motor vehicles.

[29] Council Directive 93/59/EEC of 28 June 1993 amending Directive 70/220/EEC on the approximation of the laws of the Member States relating to measures to be taken against air pollution by emissions from motor vehicles.

[30] Delphi Technologies, Worldwide emissions standards, Passenger cars and light duty vihicles 2020/2021.

[31] Delphi Technology. On and Off-Highway Commercial Vehicles. Worldwide emissions standards. 2018 | 2019.

[32] Directive 94/12/EC of the European Parliament and the Council of 23 March 1994 relating to measures to be taken against air pollution by emissions from motor vehicles and amending Directive 70/220/EEC.

[33] Directive 96/69/EC of the European Parliament and of the Council of 8 October 1996 amending Directive 70/220/EEC on the approximation of the laws of the Member States relating to measures to be taken against air pollution by emissions from motor vehicles.

[34] Directive 97/68/EC of the European Parliament and of the Council of 16 December 1997 on the approximation of the laws of the Member States relating to measures against the emission of gaseous and particulate pollutants from internal combustion engines to be installed in non-road mobile machinery.

[35] Directive 98/69/EC of the European Parliament and of the Council of 13 October 1998 relating to measures to be taken against air pollution by emissions from motor vehicles and amending Council Directive 70/220/EEC.

[36] DIRECTIVE 2002/88/EC of the European Parliament and of the Council of 9 December 2002 amending Directive 97/68/EC on the approximation of the laws of the Member States relating to measures against the emission of gaseous and particulate pollutants from internal combustion engines to be installed in non-road mobile machinery.

[37] Directive 2004/26/EC of the European Parliament and of the Council of 21 April 2004 amending Directive 97/68/EC on the approximation of the laws of the Member States relating to measures against the emission of gaseous and particulate pollutants from internal combustion engines to be installed in non-road mobile machinery.

[38] Duffy BL, Nelson PF. Non-methane exhaust composition in the sydney harbour tunnel: A focus on benzene and 1,3-butadiene. Atmos Environ. 1996;30(15):2759-2768. https://doi.org/10.1016/1352-2310(95)00372-X

[39] European Parliament. https://www.europarl.europa.eu/portal

[40] Fraser MP, Buzcu B, Yue ZW, McGaughey GR, Desai NR, Allen DT et al. Validation of source attribution using organic molecular markers for emissions of fine particles from mobile sources. Environ Sci Technol. 2003;37:3904-3909.

[41] Fruin SA, Winer AM, Rodes CE. Black carbon concentrations in California vehicles and estimation of in-vehicle diesel exhaust particulate matter exposures. Atmos Environ. 2004;38(25):4123-4133. https://doi.org/10.1016/j.atmosenv.2004.04.026

[42] Fuć P, Lijewski P, Ziółkowski A, Siedlecki M. Tendencje zmian przepisów homologacyjnych w aspekcie emisji gazów wylotowych dla pojazdów kategorii PC i LDV. Combustion Engines. 2015;54(3)417-424. https://bibliotekanauki.pl/articles/133307

[43] Gouriou F, Morin JP, Weill ME. On-road measurements of particle number concentrations and size distributions in urban and tunnel environments. Atmos Environ. 2004;38(18): 2831-2840. https://doi.org/10.1016/j.atmosenv.2004.02.039

[44] Health Effects Institute. State of Global Air 2019: Air pollution a significant risk factor worldwide. Health Effects Institute. June 7, 2019. https://www.healtheffects.org

[45] Health Effects Institute. State of Global Air Annual Report 2022. Health Effects Institute. January 30, 2023. https://www.healtheffects.org

[46] Health Effects Institute. State of Global Air Report 2020. https://www.stateofglobalair.org

[47] Huang Y, Organ B, Zhou JL, Surawski NC, Hong G, Chan EFC et al. Remote sensing of on-road vehicle emissions: Mechanism, applications and a case study from Hong Kong. Atmos Environ. 2018;182:58-74. https://doi.org/10.1016/j.atmosenv.2018.03.035

[48] Hwa MY, Hsieh CC, Wu TC, Chang LFW. Real-world vehicle emissions and VOCs profile in the Taipei tunnel located at Taiwan Taipei area. Atmos Environ. 2002;36(12): 1993-2002. https://doi.org/10.1016/S1352-2310(02)00148-6

[49] Imhof D, Weingartner E, Prévôt ASH, Ordóñez C, Kurtenbach R, Wiesen P et al. Aerosol and NO_x emission factors and submicron particle number size distributions in two road tunnels with different traffic regimes. Atmospheric Chem Phys. 2006;6(8):2215-2230. https://doi.org/10.5194/acp-6-2215-2006

[50] Ingalls MN. On-road vehicle emission factors from measurements in a Los Angeles area tunnel. Vol Paper 89-1373.

[51] Joumard R, André M, Vidon R, Tassel P, Pruvost C. Influence of driving cycles on unit emissions from passenger cars. Atmos Environ. 2000;34(27):4621-4628.

https://doi.org/10.1016/S1352-2310(00)00118-7
[52] Kazancoglu Y, Ozbiltekin-Pala M, Ozkan-Ozen YD. Prediction and evaluation of greenhouse gas emissions for sustainable road transport within Europe. Sustain Cities Soc. 2021; 70:102924. https://doi.org/10.1016/j.scs.2021.102924
[53] Kittelson D, Watts W, Johnson JP. Diesel aerosol sampling methodology–CRC E-43. Final Report. Coordinating Research Council; 2002.
[54] Ko YW, Cho CH. Characterization of large fleets of vehicle exhaust emissions in middle Taiwan by remote sensing. Sci Total Environ. 2006;354(1):75-82. https://doi.org/10.1016/j.scitotenv.2005.05.040
[55] Kozak M, Merkisz J. Oxygenated diesel fuels and their effect on PM emissions. Appl Sci. 2022;12(15):7709. https://doi.org/10.3390/app12157709
[56] Kozak M, Waligórski M, Wcisło G, Wierzbicki S, Duda K. Exhaust emissions from a direct injection spark-ignition engine fueled with high-ethanol gasoline. Energies. 2025; 18(3):454. https://doi.org/10.3390/en18030454
[57] Kristensson A, Johansson C, Westerholm R, Swietlicki E, Gidhagen L, Wideqvist U et al. Real-world traffic emission factors of gases and particles measured in a road tunnel in Stockholm, Sweden. Atmos Environ. 2004;38(5):657-673. https://doi.org/10.1016/j.atmosenv.2003.10.030
[58] Laschober C, Limbeck A, Rendl J, Puxbaum H. Particulate emissions from on-road vehicles in the Kaisermühlen-tunnel (Vienna, Austria). Atmos Environ. 2004;38(14):2187-2195. https://doi.org/10.1016/j.atmosenv.2004.01.017
[59] Lawson DR, Groblicki PJ, Stedman DH, Bishop GA, Guenther PL. Emissions from lit-use motor vehicles in Los Angeles: a pilot study of remote sensing and the inspection and maintenance program. J Air Waste Manag Assoc. 1990; 40(8):1096-1105. https://doi.org/10.1080/10473289.1990.10466754
[60] Ma CJ, Tohno S, Kasahara M. A case study of the single and size-resolved particles in roadway tunnel in Seoul, Korea. Atmos Environ. 2004;38(38):6673-6677. https://doi.org/10.1016/j.atmosenv.2004.09.006
[61] May J, Bosteels D, Favre C. An Assessment of Emissions from Light-Duty Vehicles using PEMS and chassis dynamometer testing. SAE Int J Engines. 2014;7(3):1326-1335. https://doi.org/10.4271/2014-01-1581
[62] Mazzoleni C, Moosmüller H, Kuhns HD, Keislar RE, Barber PW, Nikolic D et al. Correlation between automotive CO, HC, NO, and PM emission factors from on-road remote sensing: implications for inspection and maintenance programs. Transp Res Part Transp Environ. 2004;9(6):477-496. https://doi.org/10.1016/j.trd.2004.08.006
[63] McGaughey GR, Desai NR, Allen DT, Seila RL, Lonneman WA, Fraser MP et al. Analysis of motor vehicle emissions in a Houston tunnel during the Texas Air Quality Study 2000. Atmos Environ. 2004;38(20):3363-3372. https://doi.org/10.1016/j.atmosenv.2004.03.006
[64] Merkisz J, Gallas D, Siedlecki M, Szymlet N, Sokolnicka B. Exhaust emissions of an LPG powered vehicle in real operating conditions. E3S Web Conf. 2019;100:00053. https://doi.org/10.1051/e3sconf/201910000053
[65] Merkisz J, Rymaniak Ł. Tests of urban bus specific emissions in terms of currently applicable heavy vehicles operating emission regulations. Combustion Engines. 2017;168(1): 21-26. https://doi.org/10.19206/CE-2017-103
[66] Our World in Data OW. Our World Data. Published online February 28, 2024. https://ourworldindata.org
[67] Pielecha J. Badania emisji zanieczyszczeń silników spalinowych (in Polish). Poznan University of Technology Publishing House 2017.
[68] Pierson WR, Brachaczek WW, Hammerle RH, McKee DE, Butler JW. Sulfate emissions from vehicles on the road. J Air Pollut Control Assoc. 1978;28(2):123-132. https://doi.org/10.1080/00022470.1978.10470579
[69] Pierson WR, Gertler AW, Bradow RL. Comparison of the SCAQS tunnel study with other on road vehicle emission data. J Air Waste Manag Assoc. 1990;40(11):1495-1504. https://doi.org/10.1080/10473289.1990.10466799
[70] Pokharel S, Bishop G, Stedman D. On-road remote sensing of automobile emissions in the Denver area: year 2. Fuel Effic Automob Test Publ. Published online 2001. https://digitalcommons.du.edu
[71] Pokharel S, Bishop G, Stedman D. On-road remote sensing of automobile emissions in the Los Angeles area: year 3 (Riverside). Fuel Effic Automob Test Publ. Published online 2002. https://digitalcommons.du.edu
[72] Pokharel S, Bishop G, Stedman D. On-road remote sensing of automobile emissions in the Phoenix area: year 3. Fuel Effic Automob Test Publ. Published online 2002. https://digitalcommons.du.edu
[73] Popp P, Bishop G, Stedman D. On-road remote sensing of automobile emissions in the Chicago area: year 2. Fuel Effic Automob Test Publ. Published online January 1, 1999. https://digitalcommons.du.edu
[74] Regulation (EC) No 715/2007 of the European Parliament and of the Council of 20 June 2007 on type approval of motor vehicles with respect to emissions from light passenger and commercial vehicles (Euro 5 and Euro 6) and on access to vehicle repair and maintenance information.
[75] Regulation (EU) 2016/1628 of the European Parliament and of the Council of 14 September 2016 on Requirements Relating to Gaseous and Particulate Pollutant Emission Limits and Type-Approval for Internal Combustion Engines for Non-Road Mobile Machinery, Amending Regulations (EU) No 1024/2012 and (EU) No 167/2013, and Amending and Repealing Directive 97/68/EC. Vol 252.; 2016.
[76] Revitt DM, Muncaster GM, Hamilton RS. Trends in hydrocarbon fleet emissions at four UK highway sites. Sci Total Environ. 1999;235(1):91-99. https://doi.org/10.1016/S0048-9697(99)00195-3
[77] Rogak SN, Pott U, Dann T, Wang D. Gaseous emissions from vehicles in a traffic tunnel in Vancouver, British Columbia. J Air Waste Manag Assoc. 1998;48(7):604-615. https://doi.org/10.1080/10473289.1998.10463713
[78] Rymaniak Ł, Merkisz J, Szymlet N, Kamińska M, Weymann S. Use of emission indicators related to CO_2 emissions in the ecological assessment of an agricultural tractor. Eksploat Niezawodn. 2021;23(4):605-611. https://doi.org/10.17531/ein.2021.4.2
[79] Sagebiel JC, Zielinska B, Pierson WR, Gertler AW. Real-world emissions and calculated reactivities of organic species from motor vehicles. Atmos Environ. 1996;30(12): 2287-2296. https://doi.org/10.1016/1352-2310(95)00117-4
[80] Schmid H, Pucher E, Ellinger R, Biebl P, Puxbaum H. Decadal reductions of traffic emissions on a transit route in Austria – results of the Tauerntunnel experiment 1997. Atmos Environ. 2001;35(21):3585-3593. https://doi.org/10.1016/S1352-2310(00)00568-9
[81] Schürmann D, Staab J. On-the-road measurements of automotive emissions. Sci Total Environ. 1990;93:147-157. https://doi.org/10.1016/0048-9697(90)90103-2
[82] Sjödin Å, Lenner M. On-road measurements of single vehicle pollutant emissions, speed and acceleration for large fleets of vehicles in different traffic environments. Sci Total Environ. 1995;169(1):157-165. https://doi.org/10.1016/0048-9697(95)04644-G

[83] Smolec R, Karpiuk W, Bajerlein M, Waligórski M, Kril P. The use of dimethyl ether (DME) solution in compression ignition engine. Combustion Engines. 2024;198(3):123-128. https://doi.org/10.19206/CE-188832

[84] Stedman D, Bishop G. An analysis of on-road remote sensing as a tool for automobile emissions control. Fuel Effic Automob Test Publ. Published online February 1, 1990. https://digitalcommons.du.edu

[85] Stemmler K, Bugmann S, Buchmann B, Reimann S, Staehelin J. Large decrease of VOC emissions of Switzerland's car fleet during the past decade: results from a highway tunnel study. Atmos Environ. 2005;39(6):1009-1018. https://doi.org/10.1016/j.atmosenv.2004.10.010

[86] Sturm PJ, Baltensperger U, Bacher M, Lechner B, Hausberger S, Heiden B et al. Roadside measurements of particulate matter size distribution. Atmos Environ. 2003;37(37): 5273-5281. https://doi.org/10.1016/j.atmosenv.2003.05.006

[87] Szymlet N, Lijewski P, Kurc B. Road tests of a two-wheeled vehicle with the use of various urban road infrastructure solutions. J Ecol Eng. 2020;21(7):152-159. https://doi.org/10.12911/22998993/125503

[88] Takada Y, Miyazaki T, Iida N, Takada Y, Miyazaki T, Iida N. Study on local air pollution caused by NOx from diesel freight vehicle. SAE Technical Paper 2002-01-0651. 2002. https://doi.org/10.4271/2002-01-0651

[89] Weijers EP, Khlystov AY, Kos GPA, Erisman JW. Variability of particulate matter concentrations along roads and motorways determined by a moving measurement unit. Atmos Environ. 2004;38(19):2993-3002. https://doi.org/10.1016/j.atmosenv.2004.02.045

[90] Wenzel T. Reducing emissions from in-use vehicles: an evaluation of the Phoenix inspection and maintenance program using test results and independent emissions measurements. Environ Sci Policy. 2001;4(6):359-376. https://doi.org/10.1016/S1462-9011(01)00032-6

[91] Wenzel T. Use of remote sensing measurements to evaluate vehicle emission monitoring programs: results from Phoenix, Arizona. Environ Sci Policy. 2003;6(2):153-166. https://doi.org/10.1016/S1462-9011(03)00004-2

[92] Wenzel TP, Singer BC, Slott RR, Stedman DH. Short-term emissions deterioration in the California and Phoenix I/M programs. Transp Res Part Transp Environ. 2004;9(2):107-124. https://doi.org/10.1016/j.trd.2003.09.001

[93] Williams M, Bishop G, Stedman D. On-road remote sensing of automobile emissions in the LaBrea area: year 2. Fuel Effic Automob Test Publ. Published online 2003. https://digitalcommons.du.edu

[94] Zhang Y, Stedman DH, Bishop GA, Beaton SP, Guenther PL. On-road evaluation of inspection/maintenance effectiveness. Environ Sci Technol. 1996;30(5):1445-1450. https://doi.org/10.1021/es950191j

[95] Ziolkowski A, Daszkiewicz P, Rymaniak L, Fuc P, Ukleja P. Analysis of the exhaust emissions from hybrid vehicle during RDE test. MATEC Web Conf. 2019;294:02002. https://doi.org/10.1051/matecconf/201929402002

[96] Ziółkowski A, Fuć P, Jagielski A, Bednarek M, Konieczka S. Comparison of the energy consumption and exhaust emissions between hybrid and conventional vehicles, as well as electric vehicles fitted with a range extender. Energies. 2023;16(12):4669. https://doi.org/10.3390/en16124669

Michalina Kamińska, DEng. – Faculty of Civil and Transport Engineering, Poznan University of Technology, Poland.
e-mail: *michalina.kaminska@put.poznan.pl*

Patryk Urbański, MEng. – Centre for Modern Mobility, Łukasiewicz Research Network – Poznan Institute of Technology, Poland.
e-mail: *patryk.urbanski@pit.lukasiewicz.gov.pl*

Article citation info:
Kurzydym D. Comparative study of aftermarket and OEM DPFs for Periodic Technical Inspections (PTI) compliance with new PN emission limits. Combustion Engines. 2025;203(4):126-137. https://doi.org/10.19206/CE-208400

Damian KURZYDYM

Combustion Engines
Polish Scientific Society of Combustion Engines

Comparative study of aftermarket and OEM DPFs for Periodic Technical Inspections (PTI) compliance with new PN emission limits

ARTICLE INFO

Received: 9 June 2025
Revised: 10 July 2025
Accepted: 18 July 2025
Available online: 2 August 2025

This study evaluates the performance of aftermarket and OEM diesel particulate filters (DPFs) using a particle number counter (PNC) during stationary Periodic Technical Inspection (PN-PTI) tests. Several European countries have already implemented regulations requiring this test to ensure that vehicles equipped with DPFs meet the stringent particle number (PN) emission limits. In this work, measurements were conducted on various vehicles with new and conditioned DPFs. The results revealed significant variability in PN emissions, with some filters failing to meet the required limits. Key contributors to elevated PN levels were identified, including filter aging and inadequate conditioning procedures. Based on the findings, the paper proposes practical recommendations and diagnostic approaches to support compliance with PN-PTI test requirements.

Key words: *Periodic Technical Inspections, particle number counter, PN-PTI test, DPF*

1. Introduction

1.1. Aftertreatment technologies for particulate matter emission control

Stringent global emission regulations have necessitated the integration of advanced aftertreatment technologies in diesel vehicles. Among these technologies, Diesel Particulate Filters (DPF) have become essential for effectively reducing particulate matter emissions. DPFs are now standard in all new passenger and diesel vehicles due to European regulations [9]. The introduction of limits on particle number (PN), along with existing particulate matter (PM) standards, demonstrates the growing concern about the health effects of very fine particles [4]. These regulations have encouraged the development of DPF technology, creating a market with both original equipment and aftermarket alternatives. Periodic Technical Inspections (PTI) are essential to ensure that vehicles continue to comply with environmental and safety standards throughout their service life [14]. Emission tests during Periodic Technical Inspections help identify vehicles that release too many particles, confirming the proper operation of Diesel Particulate Filters. PTI procedures are created to find cars that don't have DPFs or DPFs that aren't working properly [9].

The effectiveness of a DPF is determined by a variety of parameters, including the design of the filter substrate, the materials used, and the regeneration process. Original Equipment Manufacturer (OEM) and aftermarket DPFs have different designs, materials, and production processes, which affect their performance and durability. A typical DPF consists of a metallic shell and a substrate made of cordierite or silicon carbide (SiC). The filter has a honeycomb structure with alternating plugged channels, forcing exhaust gas to flow through the porous walls [4, 16].

Diesel particulate filters (Fig. 1) are critical to reducing emissions of particulate matter from diesel engines, improving air quality, and public health. These filters trap particulate matter, or soot, and later burn it off in a process called regeneration, which significantly reduces the number of harmful particles released into the atmosphere. As exhaust gas flows through the DPF channels, particulate matter (mainly soot and ash) is trapped on the walls of the filter. The accumulated soot needs to be removed periodically to prevent excessive pressure drop and maintain filter efficiency. This is done through a process called regeneration, where the soot is oxidized at high temperatures [1, 4]. There are two main types of regeneration [1, 16]:

- passive regeneration: this occurs continuously during normal engine operation when exhaust gas temperatures are high enough (300–400°C) to oxidize the soot
- active regeneration: this is triggered when exhaust temperatures are not high enough for passive regeneration. It involves injecting extra fuel to raise the exhaust temperature and burn off the collected soot.

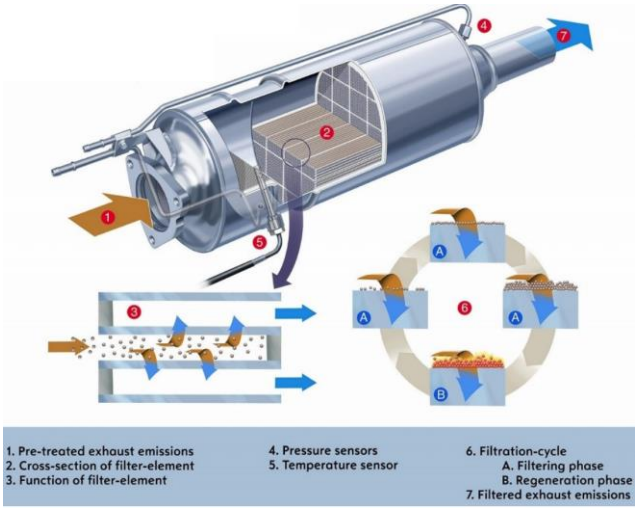

Fig. 1. Construction and operation of the DPF filter [1]

Even slight damage, such as small cracks on the DPF's substrate, whether from physical impact, thermal stress, erosion, or manipulation, can greatly impair its particle

filtration performance. The presence of cracks enables exhaust gases to bypass the intended filtration channels, resulting in a rapid reduction in the DPF's ability to capture particles [4].

The porosity of the DPF substrate is a critical parameter influencing filtration efficiency and backpressure. Higher porosity can reduce backpressure, which may compromise filtration efficiency, while lower porosity can increase filtration efficiency, which raises backpressure. The optimal porosity is a balance between these competing effects. The introduction of particle number emission limits in addition to particulate matter mass limits has further necessitated the use of highly efficient DPFs capable of capturing even the smallest particles [14]. Typically, silicon carbide filter walls have a porosity of 40% to 50%. Cordierite DPFs, however, generally exhibit a porosity between 50% and 60%.

Diesel engine particle sizes (Fig. 2) typically range from 5 nm to 1000 nm (1 μm). Ultrafine particles (< 100 nm) can penetrate deep into the lungs and subsequently enter the bloodstream, primarily depending on their size. Insoluble particles, such as soot and metal oxides, are transported via the circulatory system throughout the body, crossing both the blood–brain barrier and the placenta [17]. Particle size distributions from diesel engines are often lognormal, with mean diameters ranging from 60 to 120 nm [7]. However, it's important to note that particle formation and size are affected by combustion conditions, engine operating conditions, and fuel composition [1, 2]. Particulate matter in diesel exhaust is a complex mixture of carbon soot, unburned fuel and lubricating oil, and products of fuel pyrolysis reactions. Typically, PM consists of four components: solid soot, soluble organic fraction, sulfur compounds, and ash. In modern engines, the sulfur content of the fuel significantly impacts particulate formation [2].

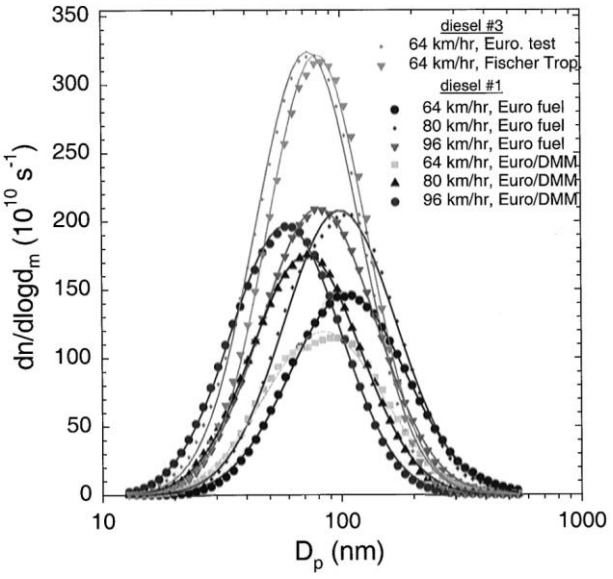

Fig. 2. Particle size distributions measured for a diesel vehicle under various engine speeds [7]

1.2. Current and planned particulate matter emission limits

The old opacimeter method measures smoke emissions from diesel vehicles during a free acceleration test. An opacimeter measures the absorption of light through the exhaust gas, providing a reading in m^{-1}. However, this method has limitations in assessing the performance of modern DPF equipped vehicles. Traditional opacimeters are not very effective in detecting DPF malfunctions. Even vehicles with damaged or removed DPFs can pass the opacity limits (< 0.5 1/m). The opacity limits in place are often too high to identify vehicles with malfunctioning DPFs. The accuracy of opacimeters can be limited, especially at low smoke emission levels [5, 9]. Several European member states are considering the introduction of SPN (solid particle number) concentration measurement in PTI [14].

Dynamometer testing, conducted within a controlled laboratory environment, serves to assess particulate matter and particle number emissions. Exhaust gases are then collected and analyzed using various instruments. Particulate matter can be measured using a filter method, while the solid particle number is measured using a particle counter. The emission is measured during a specific driving cycle, such as the New European Driving Cycle or the Worldwide Harmonized Light Vehicle Test Cycle [9, 18]. Comprehensive vehicle emissions assessments under controlled conditions offer several advantages, like the ability to measure multiple pollutants at once. However, they can be expensive and time-consuming and may not be suitable for large-scale fleet monitoring. The limitations of traditional opacity measurements in accurately evaluating DPF performance are prompting a shift towards particle number measurements. Measuring particle number at idle appears to be a promising way to detect DPF malfunctions [15].

The PN-PTI test is a method used during Periodic Technical Inspections to check the presence and proper functioning of diesel particulate filters in vehicles. It measures the concentration of solid particles in the exhaust gas [13]. Particle number concentration quantifies the number of particles within a specified volume of exhaust gas. The goal of PN-PTI is to identify vehicles that emit excessive particulate number due to DPF damage or removal. It is essential to guarantee compliance with emission standards and safeguard air quality [14]. PN-PTI utilizes specialized equipment to sample and measure the particle number concentration in the exhaust. The test is performed with the engine at idle speed. The procedure involves inserting a probe into the exhaust pipe to extract a sample of the exhaust gas. The gas sample is then processed to remove any volatile components, ensuring that only solid particles are measured. The concentration of solid particles is quantified using a particle counter. The result is compared with a set limit value [13, 14].

Table 1 presents an overview of PN-PTI measurement procedures and limits. The engine conditions, test duration, repetitions, and limit values exhibit variability across different countries.

Several issues and damages can affect DPF filters, leading to increased PN emissions and potential environmental concerns. Damage or malfunction of the DPF directly leads to a significant increase in PN emissions (Fig. 3). Even minor damage can cause emissions to exceed regulatory limits, and the PN-PTI test is designed to identify vehicles with such issues.

Table 1. PN measurement procedure during PTI in different countries [14]

Country	NL / BE	DE	CH
Effective date	07.2022	01.2023	01.2023
Engine conditions	Cold (only in case of "pass" result) or Hot	Hot (engine coolant > 60°C)	Hot
Sampling	15 s	30 s	5 s
Repetitions	1	3	3
Limit (#/cm^3)	1 000 000	250 000	100 000 * 250 000 **
Application	Euro 5 Euro 6	Euro 6	DPF equipped
* at low idling, ** at high idling (2000 rpm)			

The On-Board Diagnostics system may not always detect DPF failures, even when PM emissions are significantly higher than the regulation limit [18]. Because current EOBD systems lack PM or PN sensors, they cannot detect DPF failures and are easily manipulated when DPFs are removed. Also, engine behavior can strongly influence the PN emission. For example, the application of EGR can have a substantial effect on the PN emission of an engine at low idle speed. Therefore, the engine's condition should be taken into account during a PN-PTI test. Cracks or leaks in the DPF can result in significantly increased PN emissions. For instance, a DPF with a crack can lead to a PN emission of 2,000,000 #/cm^3 at low idle speed and over 6,000,000 #/cm^3 at high idle speed [9]. As mileage increases, DPF performance may degrade, leading to higher PN emissions, especially in retrofitted DPFs [3]. Furthermore, high sulfur content in fuel can negatively impact DPF regeneration [12]. Therefore, regular and appropriate maintenance practices are crucial to ensure continued optimal DPF functionality. The implementation of PN-PTI is expected to enhance the detection of malfunctioning or removed DPFs, contributing to improved air quality and environmental protection.

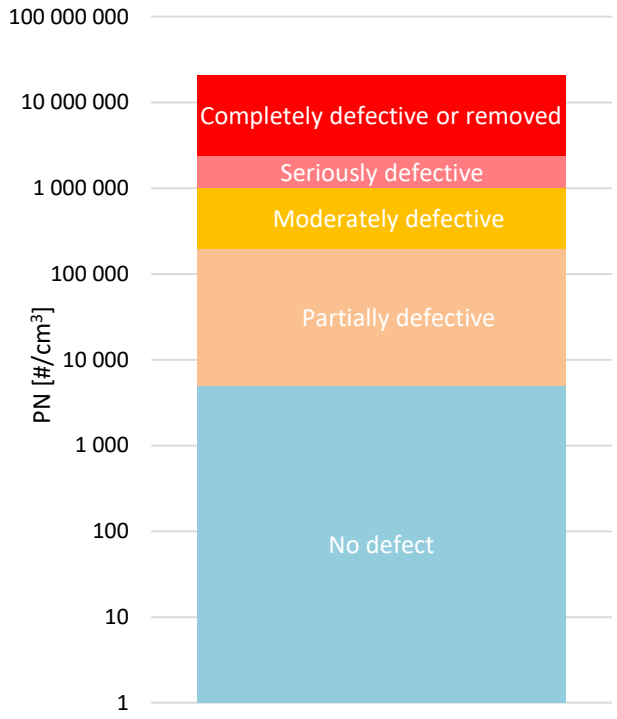

Fig. 3. DPF filter assessment depending on PN emissions [10]

2. Research methodology

2.1. Research objectives

The research aimed to evaluate the effectiveness of diesel particulate filters in meeting new periodic technical inspection (PTI) requirements based on particle number emissions. To achieve this, a series of emission tests were conducted using certified particle number counters (PNC).

The study was carried out in several stages. In the initial phase, PN emissions were measured from a variety of passenger vehicles equipped with diesel engines compliant with Euro 3, Euro 4, Euro 5, and Euro 6 standards. All vehicles were fitted with original (OEM) exhaust aftertreatment systems (Table 2). To provide a comparative baseline with legacy testing methods, an additional tester was used to assess particulate matter emissions based on smoke opacity, in accordance with the older methodology. The measurements were conducted at the beginning of the year on an outdoor parking area, with an ambient temperature of approximately 5°C. All tested vehicles had cold engines, and the measurements were taken 30 seconds after engine start, under idling conditions at low engine speed.

Table 2. Cars tested for different emission standards

Vehicle	Emission standard	Mileage ×10^3 [km]	Aftertreatment system
BMW X3 E83 3.0d 204 HP	Euro 3 (2004 year)	255	DOC without DPF
Toyota Auris 1.4 D4D 90 HP	Euro 4 (2007 year)	205	DOC without DPF
BMW 325d E91 3.0d 197 HP	Euro 4 (2007 year)	340	DOC with DPF but without filter inside
Peugeot 308 1.6 HDi 92 HP	Euro 5 (2012 year)	136	DOC with DPF
Skoda Octavia III 1.6 TDI 105 HP	Euro 5 (2014 year)	189	DOC with DPF
VW Passat B8 2.0 TDI 150 HP	Euro 6 (2019 year)	78	DOC with DPF and SCR

In the next stage of the research, a controlled test was performed on a Peugeot 308 passenger vehicle to investigate the impact of mechanical interference with the DPF on PN emissions (Fig. 4). The particle number measurements for the Peugeot 308 were conducted at an authorized service facility. The ambient temperature during testing was approximately 20°C. The vehicle arrived with a fully warmed-up engine, and the measurements were carried out 30 seconds after restarting the engine, under idling conditions at low engine speed. Three holes, each with a diameter of 10 mm, were drilled into the original diesel particulate filter to simulate unauthorized physical modifications made by the vehicle owner. Emission measurements were then taken to assess the effect of partial filter damage. Subsequently, the entire DPF core was removed from the housing, effectively disabling the particulate filtration system. Additional emission tests were conducted to evaluate particle number levels in the absence of any particulate control device. Finally, a new DPF unit was installed in the vehicle, and further tests were carried out to verify the performance of the fresh system in reducing particulate emissions.

In the following stage, new aftermarket diesel particulate filters were purchased from eight different suppliers operating in the secondary market.

Fig. 4. Tested DPF filters with 3 holes and empty

The selection included both silicon carbide (SiC) and cordierite DPFs. For comparison, original filters were also acquired, one OE filter (Eurorepar) and one OEM filter, to evaluate differences in performance between aftermarket and original equipment products. PN measurements were also performed at an authorized service center. The engine was already warmed up upon arrival, and the measurements were conducted 30 seconds after engine start, under idling conditions at low engine speed. All filters were tested for particle number emissions immediately after installation in the Peugeot 308 test vehicle, using a particle number counter. This allowed for a direct comparison of filtration efficiency among new and unused DPFs from different sources.

Additionally, two selected aftermarket DPFs were installed in the vehicle for real-world driving over defined distances (200 km and 1000 km, respectively), to evaluate how conditioning and initial soot loading affect filtration efficiency and PN emissions. These results provided insight into how aftermarket filters perform not only when new, but also after a short period of use under typical operating conditions.

In the final stage of the study, an additional test was conducted on a new aftermarket DPF. A forced regeneration procedure was carried out at an authorized service center (in the outdoor parking) for the Peugeot 308 vehicle. The regeneration was performed in stationary conditions according to the official guidelines provided by the vehicle manufacturer (Peugeot). Immediately after the forced regeneration (i.e., after conditioning the filter DPF), particle number emissions were measured using a particle number counter. This test aimed to evaluate the effect of the conditioning procedure on the initial filtration efficiency of a new aftermarket DPF.

An additional investigation was conducted on a used DPF that had been previously operated in a vehicle and exhibited particle number emissions exceeding the regulatory limits. To determine the possible cause of the poor filtration performance, the filter was sent to a specialized laboratory for a computed tomography (CT) scan. The CT analysis was performed to examine the internal structure of the DPF and verify whether the filter core had been damaged or degraded during use. This non-destructive diagnostic method allowed for a detailed internal inspection to identify potential structural defects or signs of mechanical interference that could explain the excessive PN emissions.

2.2. PTI-PN measurement devices

An opacimeter measures the opacity of smoke, indicating the concentration of particulate matter in the exhaust gas. It assesses how much light is blocked by the exhaust. During operation, a light beam is directed through a section of the exhaust gas stream. A sensor positioned on the opposite side of the exhaust gas stream measures the amount of light that passes through. The instrument then calculates the opacity based on the amount of light blocked, where higher opacity signifies more smoke [9, 18]. However, it's crucial to recognize that opacity tests possess a limited capacity to detect malfunctioning DPFs, in contrast to the heightened sensitivity of the PN-PTI method [14].

Particle Number measurement employs two primary technological approaches: condensation particle counters (CPC) and diffusion charging (DC) counters. Both types of particle number counters are utilized in PN-PTI tests to assess the performance of diesel particulate filters. Condensation particle counters (Fig. 5) are utilized to measure particle number during vehicle type approval, both in controlled laboratory settings and during on-road testing. Within a CPC, the process involves mixing the aerosol flow with a working fluid, often isopropanol, within a saturator, facilitating the fluid's evaporation. Subsequently, the saturated flow enters a condenser, where the isopropanol vapor condenses onto the particles, causing them to enlarge into detectable droplets. The instrument then counts these droplets by using light scattering to determine the number of particles [13].

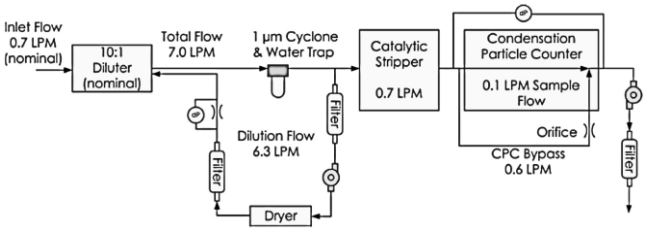

Fig. 5. Schematic of a CPC type counter [8]

DC-based PN counters (Fig. 6) are another type of instrument used in PN-PTI tests [6]. These counters work by first passing particles through a corona discharge, which transfers an electrical charge to them. The charged particles then enter an electric field. This electric field is used to collect the charged particles, and the instrument measures the electrical current produced. The measured current is proportional to the number of particles present in the sample [13].

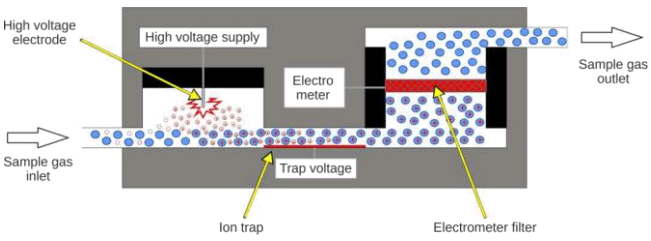

Fig. 6. Schematic of a DC type counter [20]

In summary, while opacity meters offer a simple check for excessive smoke, PN counters provide a more precise assessment of DPF performance by directly measuring the number of particles emitted, and different types of PN counters are available based on different measurement technologies. PN-PTI instruments should be robust, reliable, and easy to use. They also need to operate in a wide range of ambient conditions. The instruments determine the solid particle number concentration down to 23 nm [13].

3. Results

3.1. Overview of emission results for DPF filters

Using the Continental DX280 DC particle number counter, measurements of PN were conducted on vehicles compliant with Euro 3 to Euro 6 emission standards. The PNC used for testing was equipped with software calibrated for the Dutch market, where the limit is set at 1 000 000 #/cm^3. The device was borrowed courtesy of the director of Wijs-Air. Prior to testing, the PNC underwent a standardized warm-up procedure. Once ready, idle PN emissions were measured for all tested vehicles (Fig. 7). The result of each measurement was displayed on a wireless monitor approximately 15 seconds after the sampling began (Fig. 8).

Fig. 7. Measurement of PN and PM from the exhaust pipe

Fig. 8. PN measurement result on the Continental PNC display for the Peugeot 308 and for old OEM DPF

In addition, the same vehicles were also assessed for particulate matter emissions by measuring the exhaust smoke opacity using a DPF100 PM tester, which was also borrowed. For this device, results were categorized as follows: good (0–500 µg/m^3), marginal (500–1000 µg/m^3), and poor (above 1000 µg/m^3). Measurement results were visually indicated both by a corresponding LED on the tester's housing and on a wireless display (Fig. 9), which presented a real-time graph with horizontal limit lines for easy interpretation.

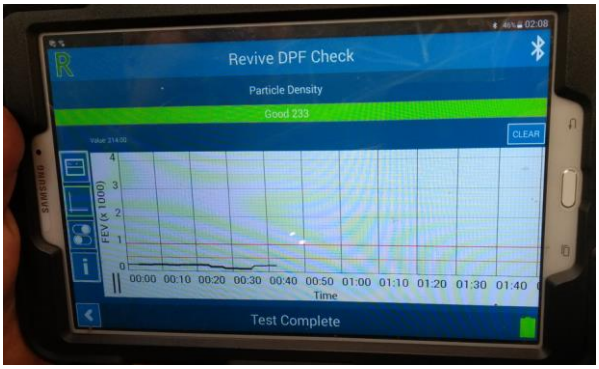

Fig. 9. PM measurement result (density) on the DPF100 tester display for the Peugeot 308 and for the old OEM DPF

As shown in Fig. 10, vehicles that were not originally equipped with a diesel particulate filter (BMW X3, BMW 325d, and Toyota Auris) exhibited PN emissions that exceeded the measurement range of the particle number counter, with values exceeding 20 million #/cm^3. In terms of PM emissions, the BMW vehicles recorded "poor" results, according to the DPF100 tester. Interestingly, the Toyota Auris, despite also lacking a DPF, showed a "good" PM result, with a value below 500 µg/m^3. This unexpected outcome for the Toyota may be attributed to the engine being fully warmed up at the time of testing. This suggests that the DPF100 PM tester may not be reliable as a standalone tool for verifying the presence or functionality of a DPF part, as thermal conditions can significantly influence the readings. For the Peugeot 308, the PN measurement exceeded 2 million #/cm^3, which clearly indicates a malfunction of the DPF. However, the PM tester reported a "good" result of 233 µg/m^3, again highlighting the limited diagnostic reliability of the DPF100 PM tester. Only the Skoda and Volkswagen vehicles produced PN results within the acceptable range, indicating that their DPF parts were functioning properly.

Figure 11 presents the results obtained from a series of controlled modifications performed on the DPF of a Peugeot 308. Initially, three 10 mm diameter holes were drilled into the existing DPF. In this configuration, the PNC immediately detected abnormally high PN emissions exceeding 10 million #/cm^3, indicating severe filter damage. However, the DPF100 PM tester reported a "marginal" result of 653 µg/m^3, suggesting that the filter was not in optimal condition.

In the next stage, the DPF core was completely removed. This resulted in an even higher PN reading from the PNC (over 20 million #/cm^3) and notably higher PM emis-

sions measured by the DPF100 to 1154 µg/m^3, classified as a "poor" result. At this point, both devices correctly indicated the lack of DPF functionality.

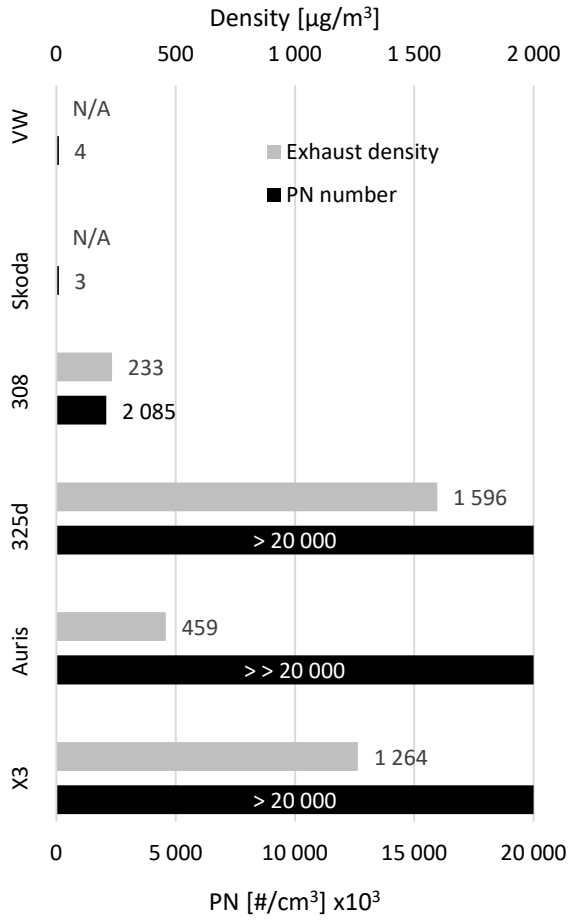

Fig. 10. DPFs assessment depending on PN emissions for different cars

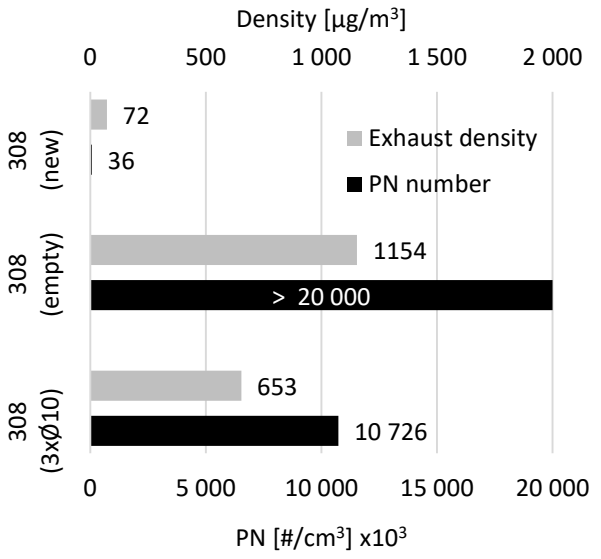

Fig. 11. PN emission results for damaged and new DPF in a Peugeot 308

Finally, after installing a new aftermarket DPF, both instruments recorded values consistent with proper filter operation. The PN count dropped dramatically to 36,000 #/cm^3, and the PM tester showed a "good" result of 72 µg/m^3. These results confirm that while both devices can detect a fully removed or replaced filter, only the PNC counter reliably identifies partial damage (e.g., drilled holes), highlighting its superior sensitivity to even minimal damage to the DPF.

The next stage of the study involved evaluating the performance of newly purchased diesel particulate filters, both original equipment manufacturer parts and aftermarket alternatives supplied by major secondary market producers. The tested DPFs included filters based on both silicon carbide (SiC) and cordierite substrates. Particle number measurements were carried out using a newly acquired Bartec nEC particle number counter (Fig. 12). Each measurement was conducted immediately after the installation of the respective DPF, under idle conditions. The vehicle used for all tests was the previously examined Peugeot 308 1.6 HDi.

The software of the Bartec nEC particle number counter was configured for the Swiss market and validated with the homologation certificate number CH-K4-23008-00. In accordance with current Swiss regulatory requirements, the measurement consists of three exhaust samples, from which the software calculates a final averaged PN emission result (an example is shown in Fig. 13 – test failed). The first stage of the measurement is performed at idle, with a strict limit of 100,000 #/cm^3 for the final result. If this maximum allowable value is exceeded, the procedure moves on to the second stage, where the software prompts the user to increase engine speed to 2000 rpm while remaining at idle. In this second stage, the emission limit is raised to 250,000 #/cm^3. All tested DPFs were evaluated during the first measurement stage only, at idle and under the 100,000 #/cm^3 limit. The emission levels observed were high, and proceeding to the second stage would likely have led to even higher emission values.

Fig. 12. Purchased Bartec nEC PNC for measurements

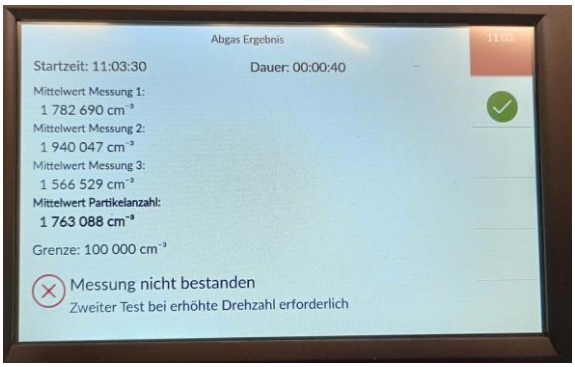

Fig. 13. PN measurement result on the Bartec nEC PNC display for the Peugeot 308 and for the cordierite DPF of competitor 8

Referring to the results shown in Fig. 14, none of the aftermarket DPFs tested (representing eight different competitors) passed the particle number emission tests, regardless of substrate type (SiC or cordierite). The average particle number for these aftermarket parts was significantly high, reaching approximately 1.6 million #/cm^3. Only the OEM DPF remained within the acceptable upper limit, achieving a value of 137,280 #/cm^3.

Interestingly, the OE Eurorepar filter ("OE_ER._SiC") also failed the test, clearly exceeding the regulatory limits. Although labeled as OE, this filter had been sourced through an aftermarket supplier, which was evident from its physical construction and manufacturer markings.

Additionally, after the initial testing, the OE Eurorepar part remained installed in the vehicle and was driven for approximately 1,000 km. A follow-up measurement then showed a dramatic improvement in performance, with a result of just 563 #/cm^3. Subsequently, a competitor 8 cordierite DPF ("Comp.8_Cord.") was installed, driven for about 200 km, and also delivered very good results (1854 #/cm^3). These road test results clearly indicate that aftermarket DPFs may require a period of conditioning before reaching their optimal filtration efficiency.

The final test conducted on the Peugeot 308 involved a forced regeneration of the DPF. After installing one of the aftermarket cordierite DPF filters, the particle number emissions were measured using the PNC device, resulting in a high value of 2 205 387 #/cm^3.

Subsequently, a forced regeneration procedure was performed at an authorized service. According to the manufacturer's diagnostic software, the regeneration process (Fig. 15) lasted approximately 1.5 hours and consisted of three identical cycles:

– 1st cycle: 35 min (7 min at 3000 rpm, remaining time at idle)
– 2nd cycle: 35 min (7 min at 3000 rpm, remaining time at idle)
– 3rd cycle: 35 min (7 min at 3000 rpm, remaining time at idle).

Immediately after the regeneration process, a follow-up PNC measurement showed that PN emissions had dropped below the 250,000 #/cm^3 limit, with a result of 173,172 #/cm^3. This demonstrates that forced regeneration has a measurable positive effect on the functional performance of the DPF.

3.2. CT scan analysis of filter structure and internal damage in DPF

An OEM diesel particulate filter removed from a Peugeot 308, provided by one of our customers, was found to exhibit elevated particle number emissions despite being a genuine component. The filter had a mileage of approximately 139,000 km at the time of inspection. This unit had previously been inspected and diagnosed by an authorized service center, after which it was replaced due to performance degradation. The filter featured a cylindrical geometry with a diameter of 5.66 inches, a length of 6 inches, and a cell density of 200 CPSI (cells per square inch), resulting in an approximate volume of 2.5 liters. According to the service report, the total soot load (i.e., particulate matter that can be removed through thermal regeneration) was measured at 1.65 g/l. In contrast, the ash content, which accumulates over time and cannot be removed by standard regeneration processes, represented about 82% of the total solid deposits within the DPF. Further inspection revealed that the filter was also physically damaged, with a visible crack in the ceramic structure. This combination of high ash loading and mechanical failure indicates an advanced stage of filter degradation and a significant reduction in soot storage capacity, ultimately justifying the need for replacement.

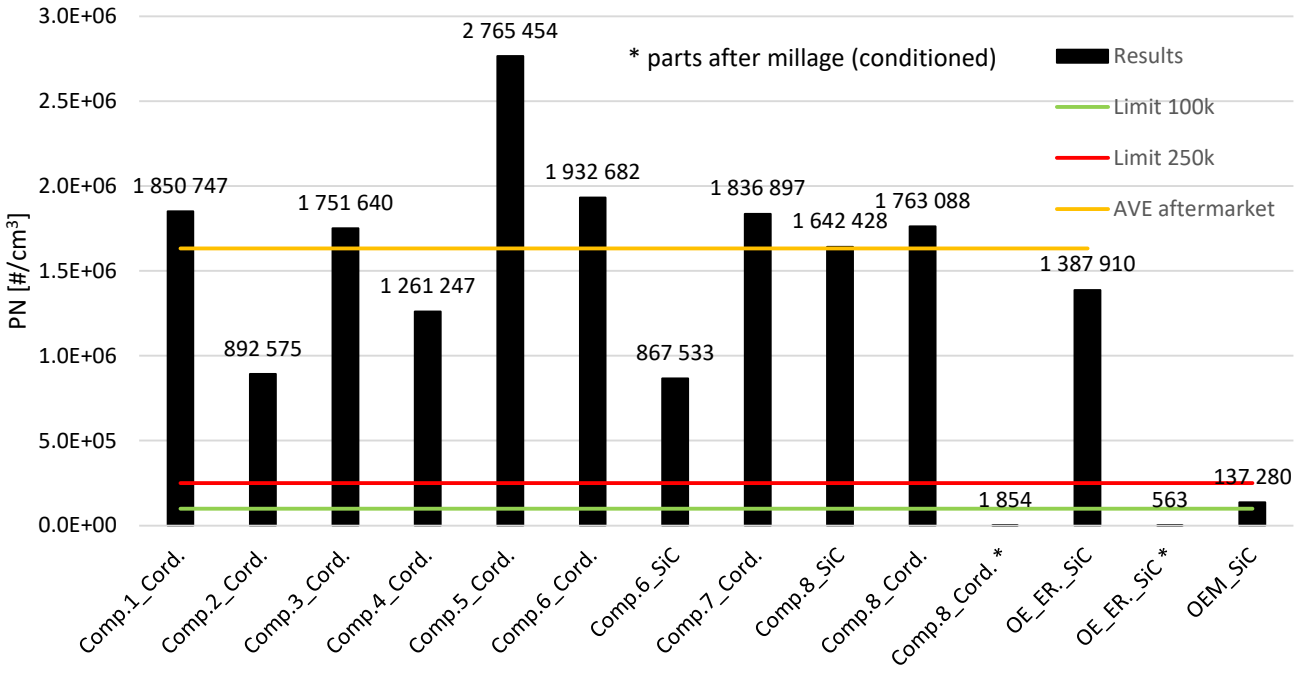

Fig. 14. PN emission results in a Peugeot 308 for different DPF filters from the aftermarket and original equipment

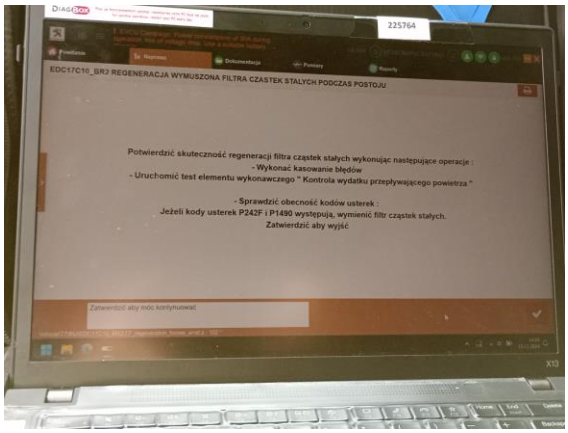

Fig. 15. Forced and stationary DPF filter regeneration by an authorized service

Following the installation of a new aftermarket DPF in the Peugeot 308, and after approximately two years of vehicle operation (covering a total distance of 33,000 km), the particle number emissions were remeasured using the PNC device. The recorded value reached 1 850 747 #/cm^3, indicating a significant deterioration in filtration performance.

To investigate the internal condition of the filter's core, the DPF was sent for X-ray computed tomography scanning at the CTLAB X-ray Computed Tomography laboratory, part of the Central European Institute of Technology. The CT scan was carried out using a GE Phoenix v|tome|x L240 tomograph, allowing for a non-destructive, high-resolution analysis of the filter's internal structure.

Computed tomography of the DPF revealed multiple transverse cracks in the lower part of the DPF filter (Fig. 16), a characteristic sign of "ring-off cracks", which commonly occur in diesel particulate filters [11, 19].

This type of damage usually happens when the DPF regeneration process doesn't occur properly. If the filter is clogged and the exhaust gases aren't hot enough, regeneration starts only at the front (inlet) of the filter. A heat wave then slowly moves toward the outlet. Because the rear part of the filter is still blocked with soot, it gets very hot. After some time, the high temperature at the outlet can also trigger regeneration from the rear side. Now, two heat waves travel toward each other – one from the front and one from the outlet. Meanwhile, the front of the filter stays relatively cool due to the incoming exhaust gases. This creates a strong temperature difference inside the filter. When the two heat zones meet (approximately one-third of the filter length from the rear), the thermal stress is so high that it causes the ceramic filter to crack – a failure known as "ring-off cracks".

The primary cause appears to be thermal stress generated during uncontrolled or interrupted regeneration processes. This typically occurs when the filter is heavily loaded with soot and regeneration initiates irregularly, creating intense localized heating. The resulting thermal gradients induce mechanical stress within the ceramic structure, leading to transverse cracks (ring-off cracks). Additional contributing factors may include:

– unplanned interruption of the regeneration process, such as turning off the engine while it's operating at high rpm
– the end-of-life condition of the DPF, where the filter becomes filled with non-burnable ash. This reduces flow and regeneration efficiency, leading to overheating
– poor engine condition or improper usage, such as excessive oil consumption or frequent short-distance driving, can contribute to excessive soot loading and regeneration difficulties.

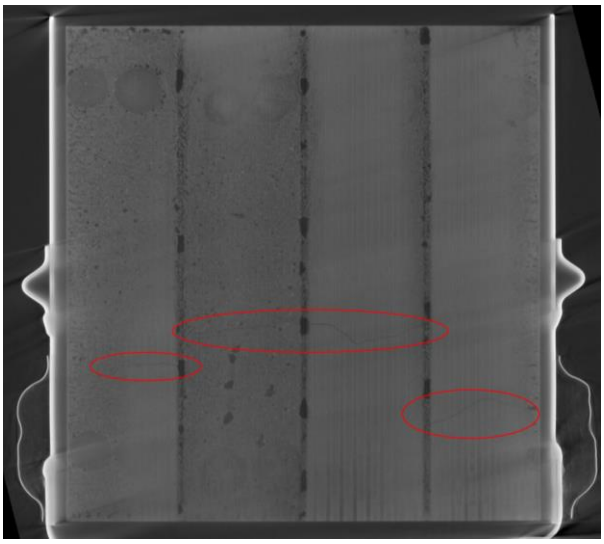

Fig. 16. Computer tomography of the DPF filter in the housing

The cracks likely resulted from a combination of excessive soot accumulation, irregular regeneration, and extended thermal gradients, all of which contributed to structural damage of the ceramic DPF filter.

After performing the CT scan of the DPF, the filter housing was cut for visual inspection of the internal damage. As shown in Fig. 17, a full circumferential crack was

Fig. 17. The filter after removing it from the housing

confirmed, and the filter unexpectedly split into two separate parts upon removal from the surrounding support mat.

The vehicle owner reported that the car was mainly driven on very short trips, typically around 3 km and occasionally up to 10 km. Additionally, the driver was unaware of when DPF regeneration cycles occurred. This strongly suggests that regeneration processes were either unsuccessful or early interrupted, which is a known cause of ring-off cracks.

In this case, the increased particulate number emissions recorded by the PNC device were caused by structural cracks in the DPF, which were confirmed both through computed tomography scanning and after cutting the filter housing. In addition to the high emissions, visual inspection showed significant smoke, a dirty exhaust outlet, and a noticeable unpleasant odor coming from the tailpipe.

In addition to the DPF filter that exhibited high PN emissions, a small cubic sample from both an OEM (SiC) filter (Fig. 18) and an aftermarket (cordierite) filter (Fig. 19) was sent to the CTLAB X-ray Computed Tomography facility at the Central European Institute of Technology. The purpose of this supplementary analysis was to examine the internal structure of the filters (wall thickness and porosity). This investigation aimed to explain why the OEM filter exhibited compliant PN emission levels immediately after installation in the vehicle, whereas the aftermarket DPF required initial conditioning to reach acceptable emission levels.

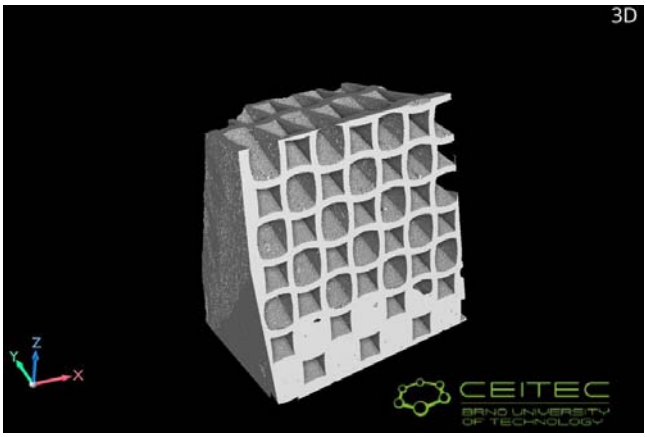

Fig. 18. 3D scan of a section of an OEM filter

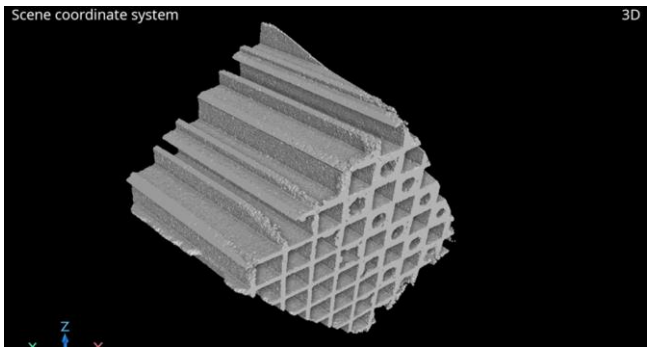

Fig. 19. 3D scan of a section of an aftermarket filter

Figure 20 shows the honeycomb structure of the OEM SiC filter, which features a relatively uncommon channel geometry. In contrast, Fig. 21 presents the more typical honeycomb structure of an aftermarket cordierite filter. A comparison of both structures indicates that the wall thickness of the OEM filter is 0.38 mm, while the aftermarket filter has a thinner wall of 0.31 mm – approximately 18% thinner. This reduced wall thickness likely contributes to lower particle filtration efficiency.

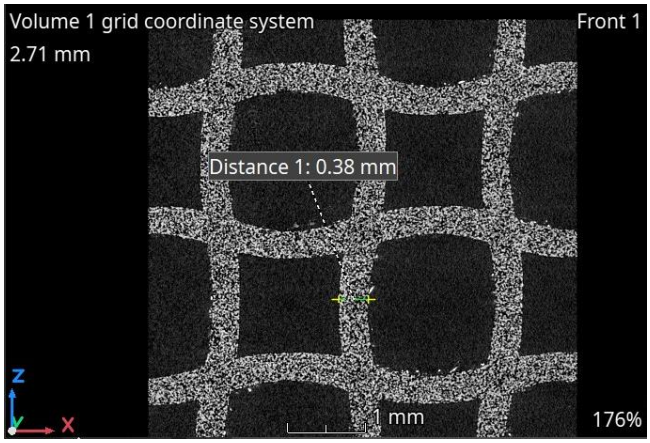

Fig. 20. Structure and wall thickness for OEM DPF SiC filter

Additionally, the OEM filter walls appear denser, with smaller pore sizes, whereas the aftermarket filter shows greater porosity (higher percentage of open space within the porous wall structure). This increased porosity improves the flow of exhaust gases and, consequently, allows more solid particles to pass through the filter wall.

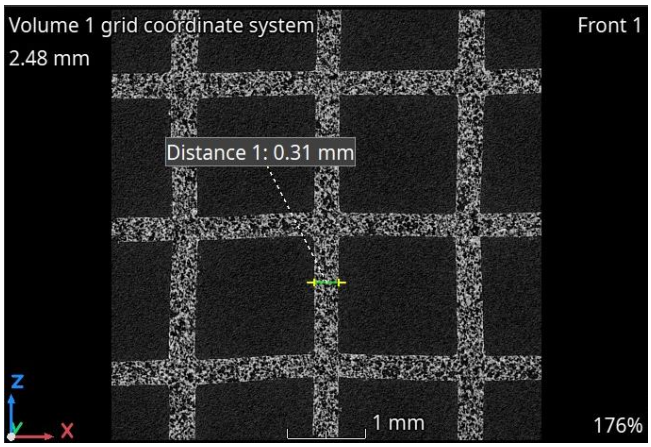

Fig. 21. Structure and wall thickness for Aftermarket DPF Cordierite filter

Figure 22 (OEM filter) and Fig. 23 (aftermarket filter) show magnified CT scan images of the filter walls and their pores. Several representative pore diameters are indicated, ranging from small pores of approximately 0.01 mm to larger ones around 0.06 mm. A visual comparison shows that the OEM filter contains a greater number of smaller pores, whereas the aftermarket filter exhibits larger pores.

Figures 24 and 25 present the pore diameter distributions for the OEM and aftermarket filters, respectively. Each histogram illustrates the frequency of pore sizes observed in the samples. The red solid line represents the fitted normal distribution, while the green dashed line cor-

responds to the log-normal distribution. These plots were generated using MATLAB, based on measurements extracted from CT scan image data.

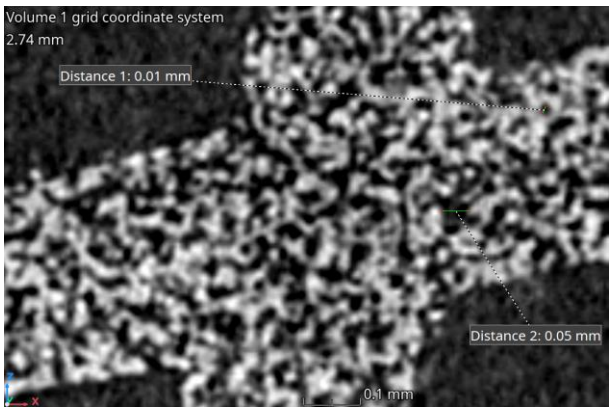

Fig. 22. OEM filter wall – magnified pore structure

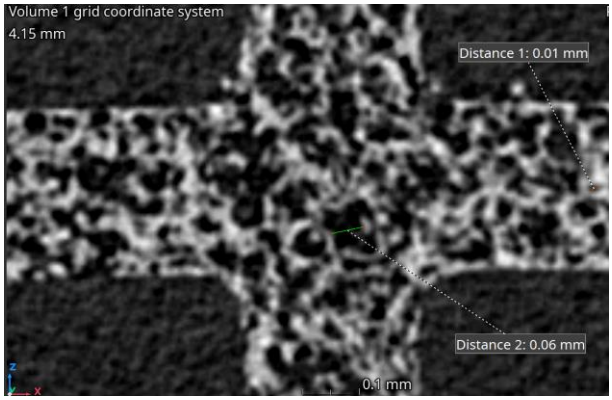

Fig. 23. Aftermarket filter wall – magnified pore structure

The OEM filter exhibits a more homogeneous pore structure, characterized by a narrower pore size distribution and reduced variability in pore diameters. In contrast, the aftermarket filter shows a broader pore size distribution, including a noticeable presence of larger pores. Such characteristics may suggest reduced efficiency in capturing fine particulate matter, although they could also result in lower flow resistance (i.e., lower pressure drop) across the filter.

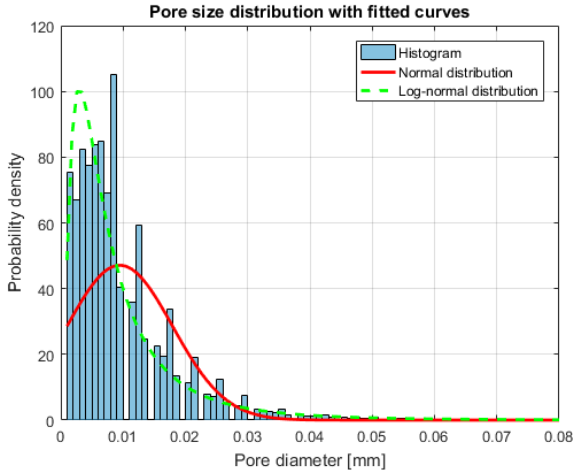

Fig. 24. Pore size distribution – OEM filter section

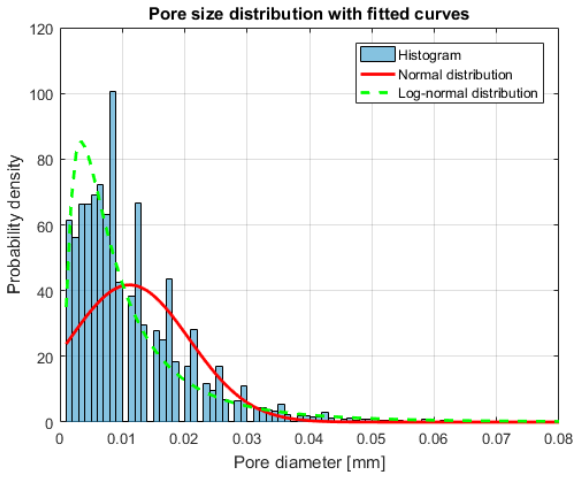

Fig. 25. Pore size distribution – aftermarket filter section

Based on this analysis, the mean pore diameter was calculated to be 9.5 µm for the OEM filter and 11.1 µm for the aftermarket filter. The porosity of each filter was determined by calculating the ratio of total pore volume to total sample volume, expressed as a percentage. According to this approach, the OEM filter exhibited a porosity of 39.5%, while the aftermarket filter showed a higher porosity of 45.5%.

As a result, the new aftermarket filter shows higher PN emissions during the initial phase. However, after a short conditioning period, the larger pores begin to fill with particulate matter, which enhances the filter's ability to trap particles and reduces emissions to levels compliant with regulatory limits.

4. Summary and conclusion

The conducted tests on vehicles with different emission standards demonstrated that particle number counters (PNC) are highly effective tools for determining the presence and proper functioning of diesel particulate filters, as well as for identifying their failure. In contrast, traditional opacity meters used to assess particulate matter (PM) emissions in the past often failed to accurately detect faulty or missing DPFs. Vehicles not equipped with DPFs – typically those compliant with emission standards lower than Euro 5, were unable to meet the new, stricter particle number (PN) limits during inspections when tested using PNC devices.

Further testing with the Peugeot 308 confirmed that aftermarket DPFs do not appropriately reduce PN emissions immediately after installation. Only vehicles equipped with original DPFs (OEM) consistently met the regulatory PN limits. One of the key factors influencing this outcome is the structural difference between filters, particularly wall thickness and porosity, which significantly affect filtration efficiency. However, the present study provides an initial comparison between OEM and aftermarket diesel particulate filters based on a limited number of samples. While the structural differences observed, such as variations in porosity and wall thickness, may suggest potential factors influencing filtration efficiency and PN emissions, the conclusions drawn should be considered preliminary.

To strengthen these findings and minimize overinterpretation, further comparative analyses are planned, including

a larger sample size encompassing both OEM and aftermarket DPFs made of cordierite and SiC. This will include expanded CT imaging for evaluating structural and performance related differences between filter types and manufacturers.

New aftermarket DPFs require initial conditioning before they can reliably meet the PN limits during MOT testing using PNC devices. PN measurements should not be conducted immediately after DPF installation, as unconditioned filters may not yet be effective in trapping particulate matter.

Conditioning of aftermarket DPF filters can be achieved through a forced regeneration process, which is time-consuming, or through a relatively short driving period. Internal tests showed that after just a few kilometers of driving, the filters began functioning correctly and complied with the regulatory PN limits. Nevertheless, to ensure reliable performance and reduce variability caused by factors such as vehicle age, engine size, load, and fuel consumption, a minimum recommended distance of 60–100 kilometers should be covered before performing periodic technical inspections (PTI) using PNC devices.

Acknowledgements

The author gratefully acknowledges Tenneco for funding the research and supporting participation in the 11th International Congress on Internal Combustion Engines.

Nomenclature

CPC	condensation particle counter
CT	computed tomography
DC	diffusion charging
DPF	diesel particulate filters
OEM	original equipment manufacturer
PM	particulate matter
PN	particle number
PNC	particle number counter
PTI	Periodic Technical Inspections
SiC	silicon carbide
SPN	solid particle number

Bibliography

[1] Bari S, Marian R. Evolution of risk of diesel engine emissions on health during last 4 decades and comparison with other engine cycles – an innovative survey. Proceedings of the ASME 2015 International Mechanical Engineering Congress & Exposition. IMECE2015-51887. 2015. https://doi.org/10.1115/IMECE2015-51887

[2] Bielaczyc P, Szczotka A, Woodburn J. An overview of particulate matter emissions from modern light duty vehicles. Combustion Engines. 2013;153(2):101-108. https://doi.org/10.19206/ce-117007

[3] Botero ML, Londoño J, Agudelo AF, Agudelo JR. Particle number emission for periodic technical inspection in a bus rapid transit system. Emission Control Science and Technology. 2023;9:128-139. https://doi.org/10.1007/s40825-023-00222-3

[4] Ge Z, Zhao W, Lyu L, Zhu Z. Fast identification of the failure of heavy-duty diesel particulate filters using a low-cost condensation particle counter (CPC) based system. Atmosphere. 2022;13(2):268. https://doi.org/10.3390/atmos13020268

[5] Giechaskiel B, Lähde T, Suarez-Bertoa R, Valverde V, Clairotte M. Comparisons of laboratory and on-road type-approval cycles with idling emissions. Implications for periodical technical inspection (PTI) sensors. Sensors. 2020; 20(20):5790. https://doi.org/10.3390/s20205790

[6] Hammer T, Roos D, Giechaskiel B, Melas A, Vasilatou K. Influence of soot aerosol properties on the counting efficiency of instruments used for the periodic technical inspection of diesel vehicles. Aerosol Research. 2024;2(2):261-270. https://doi.org/10.5194/ar-2-261-2024

[7] Harris SJ, Maricq MM. Signature size distributions for diesel and gasoline engine exhaust particulate matter. J Aerosol Sci. 2001;32(6):749-764. https://doi.org/10.1016/s0021-8502(00)00111-7

[8] Jarosiński W, Wiśniowski P. Verifying the efficiency of a diesel particulate filter using particle counters with two different measurements in periodic technical inspection of vehicles. Energies. 2021;14(16):5128. https://doi.org/10.3390/en14165128

[9] Kadijk G, Elstgeest M, Ligterink NE, Van Der Mark PJ. Investigation into a periodic technical inspection (PTI) test method to check for presence and proper functioning of diesel particulate filters in light-duty diesel vehicles – part 2. TNO Report R10530. 2017. https://doi.org/10.13140/RG.2.2.14297.06241

[10] Kadijk G. Particles Matter: Getting a grip on Diesel Particulate Filters with an effective particle number test. Emission Training Services. 2021.

[11] Kim J, Lee J, Seo J, Bauman J, Hornback L, Joo H, Lindeman D. Test method development and understanding of filter ring-off-cracks in a Catalyzed Silicon Carbide (SiC) Diesel Particulate Filter system design. SAE Technical Paper 2008-01-0765. 2008. https://doi.org/10.4271/2008-01-0765

[12] Mayer A, Czerwiński J, Bonsack P, Karvonen L. DPF regeneration with high sulfur fuel. Combustion Engines. 2012; 148(1):71-81. https://doi.org/10.19206/ce-117054

[13] Melas A, Franzetti J, Suárez-Bertoa R, Giechaskiel B. Evaluation of two particle number (PN) counters with different test protocols for the periodic technical inspection (PTI) of gasoline vehicles. Sensors. 2024;24(20):6509. https://doi.org/10.3390/s24206509

[14] Melas A, Selleri T, Suárez-Bertoa R, Giechaskiel B. Evaluation of measurement procedures for solid particle number (SPN) measurements during the periodic technical inspection (PTI) of vehicles. Int J Environ Res Public Health. 2022;19(13):7602. https://doi.org/10.3390/ijerph19137602

[15] Melas A, Selleri T, Suárez-Bertoa R, Giechaskiel B. Evaluation of solid particle number sensors for periodic technical inspection of passenger cars. Sensors. 2021;21(24):8325. https://doi.org/10.3390/s21248325

[16] Sala R, Kołek K, Konior W. Methodology of diesel particulate filter testing on test bed for non-road engine application. Combustion Engines. 2022;190(3):72-79. https://doi.org/10.19206/ce-142168

[17] Ulrich A, Mayer A, Kasper M, Wichser A, Czerwiński J. Emission of metal-oxide particles from IC-engines. Combustion Engines. 2011;144(1):72-78. https://doi.org/10.19206/CE-117125

[18] Yamada H. Improving methodology of particulate measurement in periodic technical inspection with high-sensitivity techniques: laser light scattering photometry and particle number method. Emission Control Science and Technology. 2019;5:37-44. https://doi.org/10.1007/s40825-019-0108-z

[19] Zhang D, Li M, Li L, Deng J, Li Y, Zhou R et al. Failure analysis and reliability optimization approaches for particulate filter of diesel engine after-treatment system. International Journal of Automotive Manufacturing and Materials. 2025;4(1):2. https://doi.org/10.53941/ijamm.2025.100002

[20] Website: DieselNet. (accessed on 08.06.2025). https://dieselnet.com/news/2020/08ten.php

Damian Kurzydym, DEng. – Institute of Technology, University of Applied Sciences in Racibórz and Senior Engineer at Tenneco Automotive Eastern Europe Sp. z o. o., Gliwice, Poland.
e-mail: *damian.kurzydym@akademiarac.edu.pl*

Article citation info:
Piasecka I, Tomporowski A, Piotrowska K. Environmental life cycle assessment of selected SUV passenger cars. Combustion Engines. 2025;203(4):138-145. https://doi.org/10.19206/CE-208505

Izabela PIASECKA
Andrzej TOMPOROWSKI
Katarzyna PIOTROWSKA

Combustion Engines
Polish Scientific Society of Combustion Engines

Environmental life cycle assessment of selected SUV passenger cars

ARTICLE INFO

Received: 18 May 2025
Revised: 5 July 2025
Accepted: 22 July 2025
Available online: 19 August 2025

This paper primarily aimed to conduct an environmental life cycle assessment of selected SUV passenger cars. The study focused on vehicles supplied with three dissimilar drive systems: BEV, petrol-powered PHEV, and ICEV. Two time ranges were considered: one for vehicles currently in use and another for those anticipated to be registered by 2050. The research employed the LCA method. Among the life cycle stages related to production and post-use management, the highest environmental repercussions were observed for currently used BEV vehicles, while the lowest impact was associated with ICEVs projected for 2050. During the operational phase, the ICEVs from 2020 exhibited the greatest level of environmental harm, whereas the BEVs from 2050 showed the least impact.

Key words: *life cycle assessment, SUV, ICEV, PHEV, BEV*

1. Introduction

The new passenger automotive market in Europe enlarges by 0.9% in 2024, representing 12,909,741 registrations. Same year, SUVs accounted for 54% of all passenger car registrations in the European market, setting a historic record for the segment's share. The total number of SUVs sold amounted to 6.92 million vehicles, representing a 4% increase compared to 2023. The most popular models in this category were compact SUVs (C-SUVs), accounting for 42% of the total number of registrations in the segment. In second place were superminis, also known as small hatchbacks, versions (B-SUVs), along with a market share of 36%. Then again, the uppermost surge was recorded in the luxury SUV segment, where registrations increased by 13%, reaching 56,300 units (Fig. 1) [23].

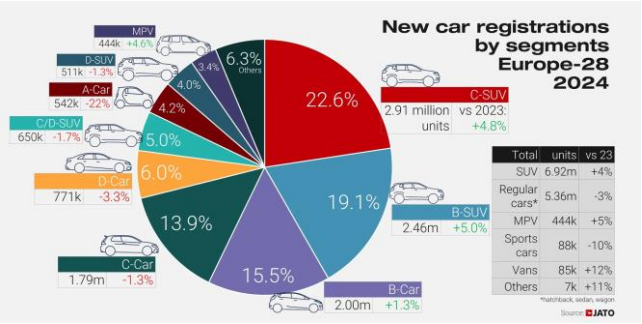

Fig. 1. New car registrations by segments (Europe-28, data for 2024) [23]

In connection with the above, the fundamental purpose of this paper was to conduct an environmental life cycle assessment of selected SUV passenger cars.

2. Materials and methods

2.1. Object and plan of the analysis

In this paper, materials and structural elements of SUV-class passenger vehicles rigged with three diverse drive systems: ICEV and PHEV as a petrol-powered representative, plus BEV. The LCA practice was chosen to assess the environmental impact. In accordance with ISO 14040 and ISO 14044 standards, it was decided that the life cycle analysis in this research shall divide the subject into the following: determination of goals and scope, life-cycle inventory, life-cycle impact assessment, and interpretation [16, 17, 25, 26, 33].

In the primary part of this paper, the purpose and spectrum of the analysis work was outlined (specifics are presented in part 2.2). During the ongoing research, the fundamental task was to assemble as much unquestionable and complete data as possible concerning the examined passenger vehicles. This task was carried out thanks to cooperation with manufacturers and recycling companies (specifics are presented in part 2.3). The following step aimed at conducting a life cycle analysis of the weighed SUV passenger vehicles. For this inquiry, calculations were created based on Sima-Pro 9.5 (with the Ecoinvent 3.9.1 database), based on the ReCiPe 2016 and IPCC 2021 models (specifics are presented in part 2.4). Acquired outcome, including thorough clarification, is given in parts 3 and 4.

2.2. Determination of goals and scope

The initial part of the life cycle analysis (LCA) consists of precisely defining its purpose and scope. The LCA was conducted to distinguish probable divergence in the environmental impact between three types of SUVs equipped with three different drive systems (ICEV, PHEV, BEV).

The systems of vehicles under study were designed to enable comparability in conditions of both the range and the detail of the performed research. In geographical terms, the area of the analysis aims to be a territory of Europe. The time horizon of this paper is 2020, up to 2050 (forecast). Transport processes were omitted from the analyses due to the significant variability of the potential locations of production plants and places of operation of the research objects, which could significantly disrupt the reliability of the results. A cut-off level of 0.1% was adopted in all assessments.

The studies conducted were categorized as bottom-up analyses, and that served to describe the existing reality (retrospective analysis), but also constituted a basis for modeling more sustainable solutions (prospective analysis).

Due to the high level of advancement, the conducted studies can be classified as detailed analyses. The data used was obtained directly from manufacturers and recycling companies, and when this was not possible, from SimaPro software databases. For the purposes of the conducted analyses, it was assumed that the cars would be used for an average period of 18 years. For an average annual mileage of approximately. 15,000 km/year, the range of their use was estimated at 270,000 km [3, 13, 22, 35].

2.3. Life-cycle inventory (LCI)

In the next phase of the appraisal, data collection and initial analysis take place. During this phase, assessable data is gathered to identify both the input and output data related to the object being tested. This is a crucial step in reaching the analysis goal and creating a life cycle model for the evaluated passenger vehicles. In this phase, input data such as energy and materials, as well as output streams such as waste and emissions, are identified and quantified [7, 28, 30, 37].

This study examined the life cycles of SUVs, focusing on the materials, energy consumption, and emissions involved in their production, operation, and end-of-life management (the so-called cradle to grave approach). In Europe, the average weight of SUVs registered in 2020 was 1537 kg. In the next 25 years, a reduction in vehicle weight by about 20% is expected. Currently, steel, polymers, and iron play a dominant role in the mass structure. Forecasts indicate that the share of high-strength steel, aluminum, and carbon fiber reinforced polymers will increase in the case of cars registered in 2050. At the same time, a decrease in the share of iron, other types of polymers, and other types of steel is expected (Fig. 2) [6, 14].

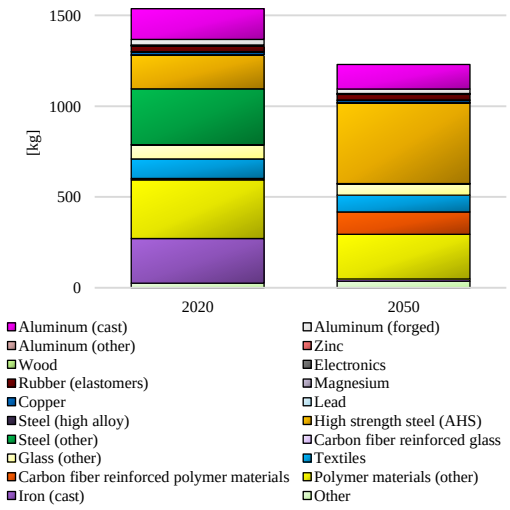

Fig. 2. Simplified material composition of SUV passenger cars registered in 2020 and 2050 (forecast) [personal study conducted through literature analysis and data gathered from manufacturers]

In the case of vehicles registered in 2020, a higher percentage of steel and iron in the total weight of the car is noticeable. Forecasts indicate that for cars to be registered in 2050, the dominant percentage will be characterized by high-strength steel and polymer materials (Fig. 3).

For battery electric vehicles (BEVs) and plug-in hybrid electric vehicles (PHEVs) registered in 2020, the emission factors stemming from battery production were determined by the prevalent chemical composition, specifically NMC622 type batteries with graphite, along with the European battery market mix relevant for that period. For cars with forecast registration in 2050, the emission factors included NMC811-type graphite batteries manufactured in Europe [11].

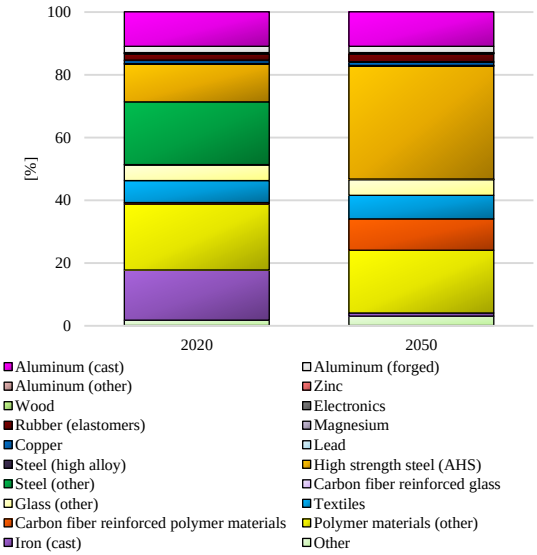

Fig. 3. Share of key materials in the construction of SUV passenger cars registered in 2020 and 2050 (forecast) [personal study conducted through literature analysis and data gathered from manufacturers]

2.4. Life-cycle impact assessment (LCIA)

The third phase of life cycle analysis encompasses the evaluation of the potential environmental impact associated with the subjects studied. This phase, known as life cycle impact assessment (LCIA), comprises both mandatory and optional components. The mandatory components involve the selection of impact categories, category indicators, characterization models, as well as the processes of classification and characterization. In contrast, the optional components consist of normalization, grouping, and weighting. In this research, both mandatory and optional elements were incorporated to provide a comprehensive analysis. The assessment was conducted utilizing SimaPro 9.5, supported by the Ecoinvent 3.9.1 database and the ReCiPe 2016 and IPCC 2021 models [1, 8–10].

Classification involves the process of assigning life cycle inventory (LCI) results to their corresponding impact categories. Characterization constitutes a process wherein LCI results are analyzed and converted by applying specific characterization parameters. These transformed results are subsequently expressed as relative contributions to each impact category. For this study, the ReCiPe and IPCC models were utilized to facilitate the characterization process. The normalization stage consists of relating the results of impact category indicators to established reference values. Grouping and weighting, on the other hand, are processes involving the assignment of weighting factors for each impact category and then multiplying them by the normalized values of the indicators [2, 12, 18, 32].

ReCiPe serves as one of the key models in life cycle impact assessment (LCIA), streamlining the transformation

of life cycle inventory results into environmental impact indicators. These indicators quantify the potential magnitude of environmental impact across various impact categories. The model operates on two clearly delineated levels: 22 midpoint impact categories and 3 endpoint areas of influence. The midpoint categories focus on specific environmental issues, while the endpoint areas of influence represent a broader perspective of environmental effects, aggregated into three overarching dimensions: human health, ecosystem quality, and resource depletion. The ReCiPe 2016 model expresses grouping and weighting outcomes in environmental points (Pt). A total of 1000 points represents the average environmental repercussions attributed to a single individual over the span of one year [5, 15, 19, 31].

The analysis also used the IPCC 2021 GWP model, which allowed for the estimation of the greenhouse potential (GWP). This model is based on carbon dioxide as a reference compound, against which the greenhouse potential of other gases is determined. The findings from the analyses were expressed in terms of kilograms of carbon dioxide equivalent (kg CO_2 eq), as referenced in prior studies [21, 24, 27].

2.5. Interpretation

Interpretation serves not merely as the concluding phase of life cycle assessment but constitutes a fundamental component embedded within each preceding step of the process. The primary objective of this stage is to critically assess the derived results and ensure their alignment with the initially established objectives and scope of the study. Within this framework, the analysis underwent scrutiny for completeness, culminating in a favorable outcome. The results of the assessment, together with their interpretation, are presented in detail in sections 3 and 4 [4, 20, 36].

3. Results

3.1. Life cycles of materials, components, and work units

The analysis assessed the potential impact of SUV vehicles on the environment, considering three different drive systems: petrol-powered ICEV, petrol-powered PHEV, and BEV. Two distinct scenarios for managing post-consumer materials were thoroughly evaluated, focusing on two key approaches: the option of storage and the alternative strategy of recycling. Each scenario was carefully examined to understand its implications, benefits, and potential challenges in addressing waste management effectively. Two-time horizon scenarios were also adopted, covering cars registered in 2020 and a forecast referring to cars to be registered in 2050. Section 3.1 presents an assessment performed exclusively of the life cycles of materials, components and working assemblies of the vehicles considered. The results obtained for fuel and energy cycles are presented in Section 3.2.

3.1.1. ReCiPe 2016

The key findings of the research, analyzed using the The ReCiPe 2016 model is expressed in units of environmental points (Pt). Figure 4 illustrates a comprehensive analysis of grouping and assigning weight to the anticipated environmental impacts associated with each stage of the life cycle for materials, components, and functional assemblies used in the production of the evaluated passenger vehicles within the SUV class. This assessment specifically excludes any environmental consequences arising from fuel consumption and energy generation processes, focusing solely on the broader materials and manufacturing systems. Passenger vehicles registered in 2020 are expected to have a more harmful effect on the environment over their lifespan than those set to be registered three decades later. When evaluating the life cycles of these vehicles, assuming they are disposed of through storage after use, their environmental impact is significantly more severe than if they were managed through recycling. The highest level of harmful impacts is noted for BEV vehicles, whose materials, components, and working assemblies would be designated for landfill ($6.21 \cdot 10^3$ Pt for those registered in 2020 and $5.22 \cdot 10^3$ Pt – in 2050). Implementing recycling practices can substantially minimize the overall negative repercussions throughout their entire lifecycle ($-5.23 \cdot 10^3$ Pt for cars from 2020 and $-4.34 \cdot 10^3$ Pt for those from 2050). The main reason for this situation was the impact on the environment of the production and post-consumer management of their batteries.

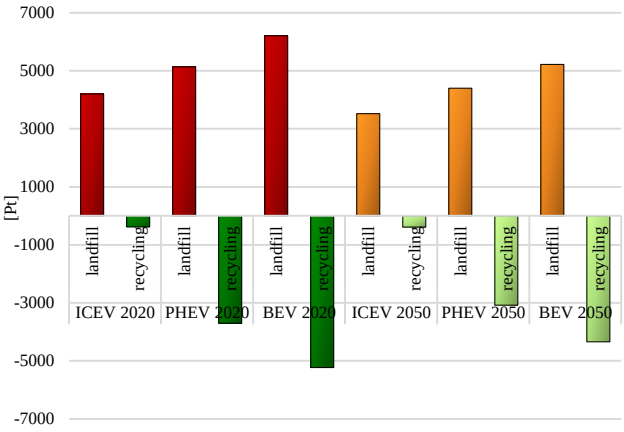

Fig. 4. The outcomes of categorizing and assigning weight to the anticipated environmental impacts throughout the life cycle of the analyzed SUV passenger vehicles, which vary based on their drive systems, while considering various post-consumer management scenarios, have been assessed using the ReCiPe 2016 model

Table 1 and Fig. 5 illustrate the outcomes of categorizing and evaluating the predicted environmental repercussions occurring throughout the life cycle of materials, components, and functional units associated with the analyzed passenger vehicles. Particular attention is given to three key impact areas: human health, ecosystems, and raw material depletion. Among these, the most significant adverse effects were identified in the areas of human health, while the least impact was observed in relation to raw material resource depletion. Notably, the life cycle of battery electric vehicles (BEVs) exhibited the highest number of negative effects, particularly when considering their storage requirements ($6.21 \cdot 10^3$ Pt for those registered in 2020 and $5.22 \cdot 10^3$ Pt – in 2050, within the realm of effects on human health, $5.81 \cdot 10^3$ Pt for cars from 2020 and $4.88 \cdot 10^3$ Pt for those from 2050). Recycling would reduce the destructive

environmental consequences over their entire life cycle ($–5.23·10^3$ Pt for those registered in 2020 and $–4.34·10^3$ Pt in 2050, within the realm of effects on human health $–4.62·10^3$ Pt for cars from 2020 and $–3.84·10^3$ Pt for those from 2050). The least negative impacts were recorded in the case of ICEV life cycles.

Table 1. The outcomes of categorizing and assigning weight to the anticipated environmental impacts throughout the life cycle of the analyzed SUV passenger vehicles, which vary based on their drive systems and three areas of repercussions while considering various post-consumer management scenarios, have been assessed using the ReCiPe 2016 model [unit: Pt]

Areas of influence			Human health	Ecosystems	Resources
2020	ICEV	landfill	$3.88·10^3$	$3.12·10^2$	$9.86·10^0$
		recycling	$–3.02·10^2$	$–9.04·10^1$	$7.66·10^0$
	PHEV	landfill	$4.77·10^3$	$3.39·10^2$	$1.61·10^1$
		recycling	$–3.28·10^3$	$–4.34·10^2$	$1.21·10^1$
	BEV	landfill	$5.81·10^3$	$3.68·10^2$	$2.46·10^1$
		recycling	$–4.62·10^3$	$–6.33·10^2$	$1.91·10^1$
2050	ICEV	landfill	$3.24·10^3$	$2.64·10^2$	$8.48·10^0$
		recycling	$–3.16·10^2$	$–7.90·10^1$	$6.58·10^0$
	PHEV	landfill	$4.08·10^3$	$2.94·10^2$	$1.38·10^1$
		recycling	$–2.74·10^3$	$–3.60·10^2$	$1.04·10^1$
	BEV	landfill	$4.88·10^3$	$3.19·10^2$	$2.12·10^1$
		recycling	$–3.84·10^3$	v$5.22·10^2$	$1.66·10^1$

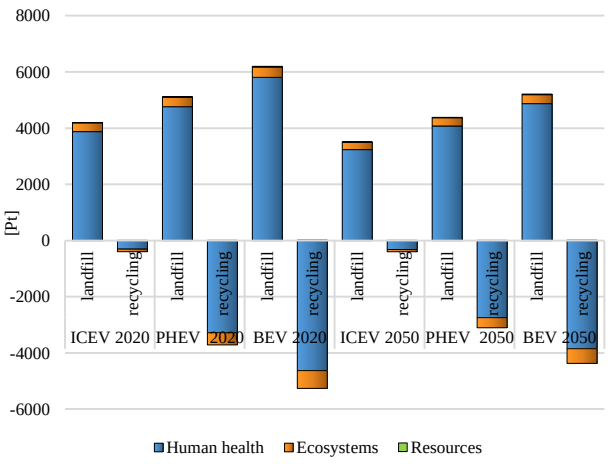

Fig. 5. Summarized outcomes of categorizing and assigning weight to the anticipated environmental impacts throughout the life cycle of the analyzed SUV passenger vehicles, which vary based on their drive systems and three areas of repercussions, while considering various post-consumer management scenarios, have been assessed using the ReCiPe 2016 model

3.1.2. IPCC 2021

During the second phase of the research, the IPCC 2021 model served as the foundation for analysis, with the results expressed in kilograms of CO_2 equivalent. Figure 6 provides a concise overview of the GHG emissions generated across the life cycles of materials, components, and operational assemblies for the examined SUV passenger vehicles. The findings highlight that the most significant environmental impacts occur when post-use waste is managed through landfill disposal, whereas the smallest impacts are observed in cases where recycling is implemented. Life cycles of vehicles to be registered in 2050 would cause lower greenhouse gas emissions compared to those in 2020. The maximum level of destructive impacts again characterized the life cycle of BEV cars, including their storage (2.00104 kg CO_2 eq for those registered in 2020 and 1.68104 kg CO_2 eq in 2050). The life cycles of all assessed vehicles, which include landfilling instead of recycling, result in higher GHG emissions. In this case, the life cycles of ICEVs also had the lowest level of hazardous environmental impact.

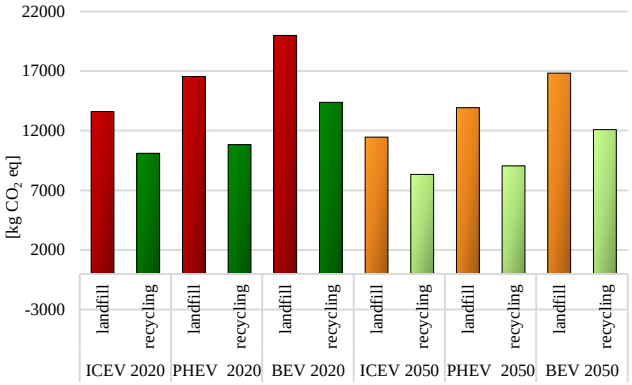

Fig. 6. Characterization results of greenhouse gas emissions throughout the life cycle of the analyzed SUV passenger vehicles, differentiated by their drive system types and considering various post-consumer management possibilities, have been evaluated based on the IPCC 2021 model

3.2. Fuel and energy cycles

During the next phase of the research, a comprehensive analysis was conducted on the fuel and energy life cycles for all the vehicles assessed in the study. This analysis was carefully framed within the context of two separate future time scenarios: one set in the year 2020 and the other projected for 2050. Within this timeframe, the GHG emissions associated with these fuel and energy cycles were systematically divided into two primary stages, allowing for a more structured and detailed examination of their environmental repercussions. The initial phase, known as well-to-tank (WTT), involves the comprehensive process of producing fuel and generating electricity, covering a wide range of activities from start to finish. This stage begins with the creation or extraction of the primary energy source, whether it be petroleum-based fuels like petrol and diesel or other forms of energy such as electricity. It extends through various intermediate steps, culminating in the efficient delivery of the fuel to its intended destination. This destination could range from an electric vehicle charging station to a fuel distributor or supplier, ensuring the necessary resources are made available for subsequent use. The second stage in the process, commonly referred to as tank-to-wheel (TTW), specifically addresses the emissions generated directly from the combustion of fuel. This phase begins at the moment when the energy, in its usable form, is accessed, whether sourced from a charging station supplying electricity or a fuel distributor providing gasoline or diesel, and concludes with the energy being expended during vehicle operation. At its core, this stage encapsulates the quantity of fuel consumed by the vehicle and

the resulting emissions released as a consequence of driving. The analytical framework for this study was structured using the IPCC 2021 model. Within this framework, the outcomes of the analysis were quantified and presented in terms of kilograms of carbon dioxide equivalent (kg CO_2 eq), providing a standardized metric for assessing environmental impact.

Vehicles registered during the year 2020 are notable for exhibiting significantly higher levels of greenhouse gas emissions throughout their fuel production and energy consumption cycles when compared to the anticipated emissions of vehicles that are expected to be registered by the year 2050. This difference underscores the gradual shift toward more sustainable and environmentally friendly transportation technologies and practices projected to evolve over the coming decades. The maximum total level of greenhouse gas emissions was recorded for ICEVs, while the minimum – for BEVs. For example, cars with an internal combustion engine, the TTW stage covering emissions from fuel combustion causes more destructive environmental consequences compared to the WTT stage, taking into account the production of the above types of fuels. PHEVs registered in 2020 generate more GHG as part of the WTT stage, and those to be registered in 2050 – during the TTW stage. Changes in the European energy mix would reduce the level of greenhouse gas emissions over the next 30 years for BEVs (Fig. 7).

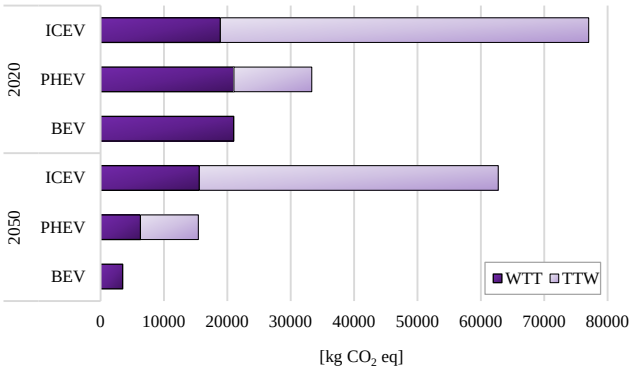

Fig. 7. Analysis of greenhouse gas emissions across the fuel and energy life cycles for SUV passenger vehicles with varying drive systems under different time horizon possibilities has been conducted, including assessments of emissions from the fuel and electricity production phase (WTT) as well as those resulting from fuel combustion during vehicle operation (TTW), based on the IPCC 2021 model

Balancing environmental priorities, it is crucial to address the levels of harmful emissions generated during both the production and consumption phases of fuel and electricity, commonly categorized as well-to-tank (WTT) and tank-to-wheel (TTW) emissions. Equally significant, however, is the need to mitigate destructive environmental impacts stemming from other key lifecycle stages, namely production (P), maintenance (M), and end-of-life (EoL) processes. Recognizing this dual importance, further in-depth analyses of greenhouse gas emissions across all these stages were undertaken to ensure a more comprehensive understanding and targeted approach to emission reduction.

The life cycle analysis reveals that internal combustion engine vehicles (ICEVs) exhibit the highest total greenhouse gas (GHG) emission levels, reflecting significant environmental drawbacks. For vehicles registered in both 2020 and 2050, the tank-to-wheel (TTW) phase emerges as the primary contributor to these harmful emissions, underscoring its critical environmental impact. Conversely, battery electric vehicles (BEVs) achieve the lowest cumulative GHG emission levels across their life cycle, demonstrating their relative advantage in reducing emissions. For BEVs registered in 2020, the emission levels during both the production and operation phases show a roughly comparable contribution to the overall carbon footprint. However, for vehicles set to be registered three decades later in 2050, a notable shift is expected. By this time, advances in technology and cleaner energy sources will likely result in significantly reduced emissions during the operation phase, while production remains the dominant source of GHG releases within the BEV life cycle. Overall, SUVs registered in 2050 are projected to produce lower total greenhouse gas emissions than those registered in 2020. However, for SUVs from 2020, the operation phase contributes substantially more to the intensification of the greenhouse effect compared to their production phase. This distinction clearly illustrates the evolving dynamics in vehicle lifecycle emissions and the environmental benefits of transitioning to more sustainable vehicular technologies (Fig. 8).

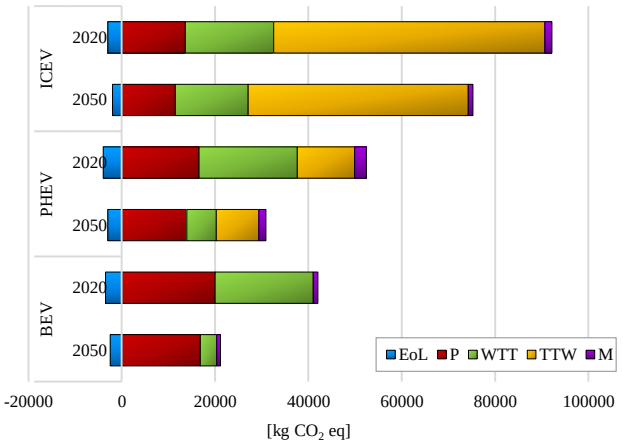

Fig. 8. Life cycle greenhouse gas emissions for analyzed SUV passenger vehicles, varying by drive system, were assessed across different time horizon scenarios, while key stages considered include: end-of-life (EoL), production (P), fuel/electricity production (WTT), fuel combustion emissions (TTW), and maintenance (M), using the IPCC 2021 model

4. Summary and conclusions

SUVs are the most frequently purchased cars on the European market. Depending on the drive system used, their life cycle has a different level of impact on the environment. Transport is the only sector of the economy where greenhouse gas emissions are increasing rather than decreasing. In particular, light vehicles, including passenger cars, represent a large part (approx. 50%) of energy demand in the transport sector [29, 34].

The study successfully accomplished its primary goal by performing an environmental life cycle assessment of selected SUV passenger cars. This assessment focused on

internal combustion engine vehicles (ICEV) and plug-in hybrid electric vehicles (PHEV) using gasoline, as well as battery electric vehicles (BEV). It considered two scenarios for post-use management: storage and recycling, alongside two different temporal contexts: one for vehicles currently in use and another for those expected to be registered by 2050. The analyses were conducted using the life cycle assessment (LCA) method, including the ReCiPe 2016 model and IPCC 2021 guidelines.

Based on the obtained results, the following relationships were noted:

- all SUVs registered in the year 2020 contribute notably more to environmental degradation when compared to the SUVs anticipated to be registered by 2050. This significant disparity is primarily evident in their higher greenhouse gas emissions. The data highlights the environmental progress anticipated in vehicle technology and regulatory standards over these three decades, reflecting efforts to minimize the ecological footprint of future SUV models (Table 1, Fig. 4–6)
- Life cycles that rely on post-use management strategies, such as landfilling rather than adopting recycling methods, contribute to significantly more harmful environmental impacts. This approach leads to higher levels of GHG emissions, exacerbating climate change and putting additional strain on ecological systems. By depositing waste into landfills instead of processing materials for reuse, valuable resources are squandered, and the potential for reducing energy consumption and pollution through recycling is lost. Furthermore, the long-term effects of landfill accumulation, including soil and water contamination, further amplify ecological degradation, making this practice an unsustainable option for waste management (Table 1, Fig. 4–6)
- The maximum level of total destructive impacts was recorded for the BEV life cycle, assuming their storage after the end of their use. Recycling would enable a significant reduction of hazardous repercussions in the perspective of their whole life cycle (Fig. 4)
- The most significant number of adverse effects was observed regarding the influence of all tested SUVs on human health, highlighting a critical area of concern. In contrast, the smallest impact was identified in relation to the depletion of raw material resources, indicating a comparatively minor issue in this particular domain (Table 1, Fig. 5)
- Across all examined time horizons and end-of-life scenarios, internal combustion engine vehicles (ICEVs) powered by gasoline consistently result in higher greenhouse gas emissions when compared to vehicles with alternative drive systems. This holds true particularly when assessing their impact based on fuel production and energy consumption cycles (Fig. 7–8)
- The lowest total GHG emissions are noted for the life cycle of BEVs due to be registered in 2050 (Fig. 7–8)
- In the case of ICEV, the TTW stage causes more greenhouse gas emissions compared to the WTT stage (Fig. 7–8)
- BEVs do not cause GHG emissions in the TTW area because they are powered by electricity. From the perspective of the next 30 years, the level of GHG emissions in the scope of their WTT will decrease if the assumed changes in the European energy mix are implemented, among others, by expanding the share of renewable sources in energy production.

Based on the foregoing considerations, it becomes evident that for all evaluated SUV class vehicles, it is essential to implement targeted strategies designed to mitigate their adverse effects while enhancing their beneficial contributions to the environment. For internal combustion engine vehicles (ICEVs), these efforts should predominantly focus on reducing environmental impact during their operational phase. Meanwhile, for battery electric vehicles (BEVs), the primary emphasis should be placed on addressing environmental concerns arising during their production process.

In today's rapidly evolving automotive industry, it is becoming increasingly imperative to address the significant challenges related to reducing both material and energy consumption alongside minimizing harmful emissions throughout every stage of the life cycle of SUV class vehicles. This includes the design, manufacturing, usage, and eventual disposal phases. To accomplish this, there is a pressing need to significantly enhance the proportion of renewable energy sources integrated into these life cycles, particularly during the stages where battery electric vehicles (BEVs) and plug-in hybrid electric vehicles (PHEVs) are in operation. Moreover, continuous efforts are required in researching and developing materials and vehicle components that are not only environmentally sustainable but also economically feasible. These materials must meet rigorous standards of quality while maintaining desirable mechanical and technical parameters essential for their specific roles within various operational systems. Additionally, advancing battery technology remains a cornerstone of this sustainability drive. It is crucial to focus on creating batteries that are not only more efficient in terms of energy storage and usage but also possess an extended service life. These batteries should ideally be constructed from materials that allow for easy recycling, thereby supporting a circular economy and reducing environmental repercussions.

BEVs have the potential to significantly diminish GHG emissions in the coming years if powered by renewable energy sources. In this case, they have around 80% lower life-cycle greenhouse gas emissions than their combustion-powered counterparts.

The relationship between cars and their impact on the surrounding environment is intricately multifaceted, presenting a challenging task in evaluating the full extent of their environmental consequences. Addressing these challenges in search of an optimal solution requires a multi-pronged approach. This process involves designing vehicles with features and structural elements that harmonize with the goal of producing a high-quality product while simultaneously focusing on refining operational and production processes. These refinements must aim to minimize energy consumption and material usage throughout every phase of the vehicle's life cycle, from initial manufacturing through its ultimate disposal or recycling.

Nomenclature

BEV	battery electric vehicles
EoL	end-of-life
GHG	greenhouse gas
GWP	global warming potential
ICEV	internal combustion engine vehicles
LCA	life cycle assessment
LCI	life cycle inventory
LCIA	life cycle impact assessment
M	maintenance
P	production
PHEV	plug-in hybrid electric vehicles
SUV	sport utility vehicle
TTW	tank-to-wheel
WTT	well-to-tank

Bibliography

[1] Bałdowska-Witos P, Piasecka I., Flizikowski J, Tomporowski A, Idzikowski A, Zawada M. Life cycle assessment of two alternative plastics for bottle production. Materials. 2021;14:4552. https://doi.org/10.3390/ma14164552

[2] Bare JC, Hofstetter P, Pennington DW, Udo de Haes HA. Midpoints versus endpoints: the sacrifices and benefits. Int J Life Cycle Assess. 2000;5:319-326. https://doi.org/10.1007/BF02978665

[3] Bäumer M, Hautzinger H, Pfeiffer M, Stock W, Lenz B, Kuhnimhof T et al. Driving performance survey – domestic mileage. Document of the Federal Road Research Institute (Bundesanstalt für Straßenwesen). Brema 2017. https://www.bast.de/DE/Publikationen/Berichte/unterreihe-v/2018-2017/v290.html

[4] Curran MA. Interpretation, critical review and reporting in life cycle assessment. Springer. Cham 2023. https://doi.org/10.1007/978-3-031-35727-5

[5] Dekker E, Zijp MC, van de Kamp ME, Temme EHM, van Zelm R. A taste of the new ReCiPe for life cycle assessment: consequences of the updated impact assessment method on food product LCAs. Int J Life Cycle Assess. 2020;25:2315-2324. https://doi.org/10.1007/s11367-019-01653-3

[6] Díaz S, Mock P, Bernard Y, Bieker G, Pniewska I, Ragon PL et al. European vehicle market statistics 2020/21. International Council on Clean Transportation Document. Beijing – Berlin – Brussels – San Francisco – Washington 2020. https://theicct.org/publication/european-vehicle-market-statistics-2020-21/

[7] Finkbeiner M, Inaba A, Tan R, Christiansen K, Klüppel HJ. The New International Standards for Life Cycle Assessment: ISO 14040 and ISO 14044. Int. J. Life Cycle Assess. 2006;11:80-85. https://doi.org/10.1065/lca2006.02.002

[8] Finnveden G, Hauschild MZ, Ekvall T, Guinée J, Heijungs R, Hellweg S et al. Recent developments in life cycle assessment. J. Environ. Manag. 2009;91(1):1-21. https://doi.org/10.1016/j.jenvman.2009.06.018

[9] Fukushige S, Kobayashi H, Yamasue E, Hara K. Ecodesign for sustainable products, services and social systems II. Springer. Singapore 2024. https://doi.org/10.1007/978-981-99-3897-1

[10] Guinée J. Handbook on life cycle assessment: operational guide to the ISO standards. Springer. Dordrecht 2002. https://doi.org/10.1007/0-306-48055-7

[11] Harlow JE, Ma X, Li J, Logan E, Liu Y, Zhang N et al. A wide range of testing results on an excellent lithium-ion cell chemistry to be used as benchmarks for new battery technologies. J Electrochem Soc. 2019;166(13):3031-3044. https://doi.org/10.1149/2.0981913jes

[12] Hauschild MZ, Goedkoop M, Guinée J, Heijungs R, Huijbregts M, Jolliet O et al. Identifying best existing practice for characterization modeling in life cycle impact assessment. Int J Life Cycle Assess. 2013;18:683-697. https://doi.org/10.1007/s11367-012-0489-5

[13] Hesser F, Kral I, Obersteiner G, Hörtenhuber S, Kühmaier M, Zeller V et al. Progress in life cycle assessment. Springer. Cham 2021. https://doi.org/10.1007/978-3-031-29294-1

[14] Hill N, Amaral S, Morgan-Price S, Nokes T, Bates J, Helms H et al. Determining the environmental impacts of conventional and alternatively fuelled vehicles through LCA. Ricardo-AEA, IFEU and E4tech document for the European Commission. Brussels 2020. https://op.europa.eu/en/publication-detail/-/publication/1f494180-bc0e-11ea-811c-01aa75ed71a1

[15] Huijbregts MAJ, Steinmann ZJN, Elshout PMF, Stam G, Verones F, Vieira M et al. ReCiPe2016: a harmonised life cycle impact assessment method at midpoint and endpoint level. Int J Life Cycle Assess. 2017;22:138-147. https://doi.org/10.1007/s11367-016-1246-y

[16] ISO 14040:2006. Environmental Management – Life Cycle Assessment – Principles and Framework. International Organization for Standardization. Geneva. Switzerland. 2006.

[17] ISO 14044:2006. Environmental management – Life Cycle Assessment – Requirements and Guidelines. International Organization for Standardization. Switzerland. Geneva 2006.

[18] Jolliet O, Müller-Wenk R, Bare J, Brent A, Goedkoop M, Heijungs R et al. The LCIA midpoint-damage framework of the UNEP/SETAC life cycle initiative. Int J Life Cycle Assess. 2004;9:394-404. https://doi.org/10.1007/BF02979083

[19] Kjaer LL, Pigosso DCA, McAloone TC, Birkved M. Guidelines for evaluating the environmental performance of product/service-systems through life cycle assessment. J Clean Prod. 2018;190:666-678. https://doi.org/10.1016/j.jclepro.2018.04.108

[20] Kłos Z. Ecobalancial assessment of chosen packaging processes in food industry. Int J Life Cycle Assess. 2002;7:309. https://doi.org/10.1007/BF02978894

[21] Masson-Delmotte V, Zhai P, Pirani A, Connors SL, Péan C, Berger S et al. IPCC, 2021: Climate Change 2021: The Physical Science Basis. Contribution of Working Group I to the Sixth Assessment Report of the Intergovernmental Panel on Climate Change Cambridge. Cambridge University Press 2021. https://doi.org/10.1017/9781009157896

[22] Mehlhart G, Möck A, Goldman D. Effects on ELV waste management as a consequence of the decisions from the Stockholm Convention on decaBDE. Öko-Institut Document. Fryburg 2018. https://www.oeko.de/fileadmin/oekodoc/ACEA-DecaBDE-final-report.pdf

[23] Munoz F. European new car market growth in 2024 driven by hybrids and Chinese brands. https://www.jato.com/resources/media-and-press-releases/european-new-car-market-growth-in-2024-driven-by-hybrids-and-chinese-brands?utm_content=324341353&utm_medium=social&utm_source=facebook&hss_channel=fbp-141752974736982 (accessed on April 15, 2025).

[24] Muñoz I, Schmidt JH. Methane oxidation, biogenic carbon, and the IPCC's emission metrics. Proposal for a consistent greenhouse-gas accounting. Int J Life Cycle Assess. 2016; 21:1069-1075. https://doi.org/10.1007/s11367-016-1091-z
[25] Muthu SS. Life cycle sustainability assessment (LCSA). Springer. Singapore 2021. https://doi.org./10.1007/978-981-16-4562-4
[26] Nakamura S. A practical guide to industrial ecology by input-output analysis. Springer. Cham 2023. https://doi.org/10.1007/978-3-031-43684-0
[27] Nalau J, Gilmore E, Howden M. Improving adaptation assessment in the IPCC. NJP Clim Action. 2024;3:76. https://doi.org/10.1038/s44168-024-00155-9
[28] Palousis N, Luong L, Abhary K. An integrated LCA/LCC framework for assessing product sustainability risk. WIT Press. Southampton 2008. https://doi.org/10.2495/RISK080131
[29] Piasecka I, Tomporowski A, Piotrowska K. Environmental analysis of post-use management of car tires. Przem Chem. 2018;97(10):1649-1653. https://doi.org/10.15199/62.2018.10.4
[30] Proske M, Finkbeiner M. Obsolescence in LCA–methodological challenges and solution approaches. Int J Life Cycle Assess. 2020;25:495-507. https://doi.org/10.1007/s11367-019-01710-x
[31] Rashedi A, Khanam T. Life cycle assessment of most widely adopted solar photovoltaic energy technologies by mid-point and end-point indicators of ReCiPe method. Environ Sci Pollut Res Int. 2020;27:29075-29090. https://doi.org/10.1007/s11356-020-09194-1
[32] Reap J, Roma F, Duncan S, Bras B. A survey of unresolved problems in life cycle assessment. Int J Life Cycle Assess. 2008;13:290-300. https://doi.org/10.1007/s11367-008-0008-x
[33] Schmidt WP. Solutions for sustainability challenges. technical sustainability management and life cycle thinking. Springer. Cham 2024. https://doi.org/10.1007/978-3-031-63624-0
[34] Sikora A. European Green Deal – legal and financial challenges of the climate change. ERA Forum. 2021;21:681-697. https://doi.org/10.1007/s12027-020-00637-3
[35] Stoffels P, Kaspar J, Baehre D, Vielhaber M. Holistic material selection approach for more sustainable products. Procedia Manuf. 2017;8:401-408. https://doi.org/10.1016/j.promfg.2017.02.051
[36] Suppipat S, Chotiratanapinun T, Teachavorasinskun K, Hu AH. Design for enhancing eco-efficiency of energy-related products. The integration of simplified LCA tools in industrial design education. Springer. Cham 2023. https://doi.org/10.1007/978-3-031-15060-9
[37] Wang S, Su D. Sustainable product innovation and consumer communication. Sustainability. 2022;14:8395. https://doi.org/10.3390/su14148395

Prof. Izabela Piasecka, DSc, DEng. – Faculty of Mechanical Engineering, Bydgoszcz University of Science and Technology, Poland.
e-mail: *izabela.piasecka@pbs.edu.pl*

Prof. Andrzej Tomporowski, DSc., DEng. – Faculty of Mechanical Engineering, Bydgoszcz University of Science and Technology, Poland.
e-mail: *a.tomporowski@pbs.edu.pl*

Prof. Katarzyna Piotrowska, DSc, DEng. – Faculty of Mechanical Engineering, Lublin University of Technology, Poland.
e-mail: *k.piotrowska@pollub.pl*

Article citation info:
Snarska-Bień G, Lasocki J. Enhancing driving cycle development using artificial intelligence. Combustion Engines. 2025;203(4):146-154. https://doi.org/10.19206/CE-209909

Gabriela SNARSKA-BIEŃ
Jakub LASOCKI

Combustion Engines
Polish Scientific Society of Combustion Engines

Enhancing driving cycle development using artificial intelligence

ARTICLE INFO

Received: 15 June 2025
Revised: 25 July 2025
Accepted: 25 August 2025
Available online: 14 September 2025

In recent years, artificial intelligence (AI) has found application in numerous technical areas, including the automotive research and development sector. This paper considers the use of AI tools for the development of driving cycles for testing vehicles on a chassis dynamometer. The above idea was investigated on the example of a driving cycle simulating the use of a passenger car in urban conditions. The empirical data were collected during vehicle road tests in real traffic and then processed statistically by determining the values of selected driving pattern characteristics. Sections of vehicle velocity courses ('micro-trips') were selected and combined into a driving cycle representative of the road conditions prevailing during road tests. Processing of empirical data and combining velocity sections into a driving cycle was performed using AI-enhanced software utilizing large language models that convert user commands in natural language into Python code. The developed driving cycle was compared with selected standard urban driving cycles in terms of the values of driving pattern characteristics.

Key words: *driving cycle, artificial intelligence, AI, urban traffic, passenger car*

1. Introduction

The most significant negative impacts of combustion engines on the environment include exhaust emissions, which contain substances that are toxic to living organisms and contribute to climate change [13]. Additionally, the combustion of fossil fuels leads to the depletion of non-renewable natural resources [16]. Growing awareness of these threats has sparked actions against environmental degradation. They were first undertaken in the field of combustion engine applications in motor vehicles, both light- and heavy-duty, primarily due to their widespread use. Over the past few decades, significant progress has been made in this area, thanks in part to the development and validation of effective methods for testing pollutant emissions [22].

To ensure consistent testing conditions for vehicles, standardized test procedures are necessary. In the case of light vehicles, such as passenger cars and delivery vans (which are categorized according to relevant regulations), these tests are conducted under conditions that simulate traction operation. For metrological reasons, testing is carried out in laboratories using chassis dynamometers [1, 9, 24]. A crucial element of the dynamometer testing methodology, which connects the testing conditions with real driving performance, is the driving cycle [9, 11].

A 'Driving cycle' refers to a predefined sequence of vehicle velocity as a dependence of time, designed to replicate real-world driving patterns for testing purposes, typically related to emissions or fuel efficiency [3, 9, 11, 20]. Driving cycles can be divided into two categories [11]:

1. Standard cycles, which are recognized by international homologation regulations (e.g. WLTC, FTP-75, UDDS (FTP-72), HWFET, SFTP US06, SFTP SC03, NEDC, JC08, 10-15 Mode and CLTC)
2. Special cycles, which are created for specific scientific, research, and development purposes (e.g. CADC (Artemis), Autobahn, ADAC Highway Cycle, PIMOT CT, UT, RT, HT).

To date, several hundred driving cycles have been developed globally [3, 11]. The vast number of cycles can be attributed to the diverse traffic conditions they simulate, such as urban, rural, motorway, and expressway driving, as well as traffic congestion. Additionally, the development of cycles that are representative of specific geographical areas, such as countries, regions, or even cities, has contributed to the increasing number of driving cycles. This growth is further driven by advancements in the scientific foundations and methodologies used to create these cycles.

The representativeness of driving cycles relative to the actual traffic conditions they aim to simulate is influenced by four main factors [5]:

1. Quality and quantity of empirical data obtained from the vehicle road test
2. Methodology used to develop the driving cycle
3. Selection of driving pattern parameters that serve as criteria for the driving cycle's compliance with actual empirical data
4. Duration of the driving cycle.

As for the stage of collecting empirical data, currently most researchers utilize information from the vehicle's On-Board Diagnostics (OBD) system [19], and devices based on Global Positioning System (GPS) technology [28]. These tools allow for conducting low-cost, large-scale road tests, with multiple vehicles and/or drivers, providing an extensive dataset for further analysis. Additionally, the scope of these road tests can be expanded to include pollutant emission measurement using Portable Emission Measurement Systems (PEMS) [25] and visual recordings of driver behavior or the vehicle's surroundings.

Regarding the second factor, methods for developing driving cycles can be categorized into two main groups: deterministic and stochastic [8, 27], with further subdivisions according to minor methodological nuances.

The most commonly utilized deterministic approach is the trip-based method, where each vehicle trip recorded during data collection can be selected as a representative driving cycle using criteria based on the similarity of driv-

ing pattern parameters, such as average velocity or average acceleration. This method is repeatable, generating the same driving cycle each time for the same input data and similarity criteria.

The primary stochastic methods include the Markov chain-Monte Carlo method and the micro trip method [30]. In the first one, the velocity course of the driving cycle is generated artificially through a detailed analysis of road test data. Velocity and acceleration matrices are created along with the probabilities of specific states defined by velocity and acceleration. The order of these states is then selected using a pseudo-random Monte Carlo method [15, 30]. In the micro trip method, all recorded velocity courses from road tests are divided into micro trips by isolating from each velocity course individual sections that cover the vehicle's movement: starting from a complete stop, traveling at a non-zero velocity, braking to a stop, and the subsequent period of time when the vehicle remains stationary. Then, the sections are selected and connected in a quasi-random manner until the assumed total cycle time is reached [8]. Additionally, microtrips can be grouped into clusters based on common features, typically utilizing two or three selected parameters [31]. The main advantage of these stochastic methods is that the generated driving cycle is not identical to any samples recorded during empirical tests. Consequently, a different driving cycle can be obtained each time, even with the same input data.

Since pollutant emissions and fuel consumption of vehicle engines are exclusively tied to the conditions under which the vehicle is tested, meaning a specific driving cycle with a defined velocity course, it becomes essential to establish criteria for assessing these velocity courses. In principle, the basis for quantitative assessment should be numerical estimates [33]. For a specific time course of velocity, these numerical estimates are referred to as 'driving pattern parameters' or ‘zero-dimensional characteristics’ [2, 7, 20]. The quality of these parameters is determined by their effectiveness for a particular application.

While some driving pattern parameters, such as average and maximum velocity, average positive and negative acceleration, and the share of driving and standing time, are widely recognized, there is no consensus on the best set of parameters to describe vehicle velocity patterns effectively. Numerous examples of driving pattern parameters can be found in the extensive literature on the topic [3, 4, 27]. To ensure that the developed driving cycle accurately represents the simulated road conditions, driving pattern parameters must be determined and compared for the driving cycle’s velocity course and the entire set of velocity samples from road tests [7, 27]. The above criterion is considered to be fulfilled if the values of the driving pattern parameters in both scenarios are similar and if the fuel/energy consumption and pollutant emissions of a given vehicle during normal use align with those observed in the driving cycle on a chassis dynamometer.

The duration of the driving cycle is also an important factor [12]. Long cycles can be costly to conduct and may exceed the capabilities of laboratory equipment, such as the capacity of exhaust gas bags, while shorter cycles may increase the measurement uncertainty. In practice, the duration of the driving cycle depends on the developer, as there is no consistent, recognized methodology in this field. Many of the common driving cycles are typically around 20 minutes long [27].

In recent years, artificial intelligence (AI) has found application in numerous technical fields, including automotive research and development. AI is a general term that encompasses several specific domains, such as machine learning, fuzzy logic, computer vision, evolutionary computing, and neural networks. The scientific literature highlights the application of certain AI features in the context of developing driving cycles. For example, Jia et al. [17] proposed a new method for generating driving cycles for heavy-duty vehicles using the Markov Chain method together with an average velocity-based matching algorithm. Mostasharshahidi et al. [23] examined the impact of learning-based AI algorithms on constructing driving cycles for off-road vehicles, namely agricultural tractors. Sankar et al. [29] employed a constrained genetic algorithm to optimize the vehicle velocity when creating a driving cycle oriented towards fuel consumption and driver comfort. Qiu et al. [26] demonstrated a data-driven, recurrent neural network-based method to develop driving cycles for light-duty vehicles in Beijing that simulate actual driving patterns. Gebisa et al. [10] utilized a neural network and principal component analysis to create a driving cycle for passenger cars using real-time data from Addis Abeba. Londoño et al. [21] proposed a methodology to identify the most representative motorcycle driving patterns across various topographies, taking into account factors like elevation above sea level and slope variations, using AI techniques such as support vector machines and clustering.

The purpose of this paper is to demonstrate the feasibility of using AI tools based on natural language processing to develop driving cycles. A case study of a driving cycle designed to simulate urban traffic conditions for a passenger car is presented. The cycle was generated based on empirical data collected from road tests of a vehicle in real traffic. The velocity course constituting the driving cycle was generated using the micro-trip method, where individual velocity sections were selected and compiled by AI. Finally, the developed driving cycle was compared with selected standard urban driving cycles in terms of the values of driving pattern characteristics.

2. Materials and methods

2.1. Research framework

The subsequent section outlines the research framework of this study. Section 2.2 provides an overview of the collection of road traffic data, including the technical specifications of the vehicle and the test equipment used. Section 2.3 introduces the main methodological assumptions regarding the procedures adopted for processing empirical data to construct the driving cycle, the selection of driving pattern characteristics as criteria for the representativeness of the developed driving cycle, and the duration of the cycle. Finally, section 2.4 describes the AI-based software that supports the development of the driving cycle.

2.2. Experimental data collection

Road tests were conducted to gather statistical data on vehicle driving under the urban conditions considered, which later served as the foundation for developing a representative driving cycle. The tests were conducted in Warsaw. To account for the random nature of the vehicle driving conditions, no specific route or time of day was designated. The same driver operated the vehicle throughout the tests. The methodology involved having the driver follow another randomly selected road user, thereby replicating their driving style.

The object of the road tests was a city passenger car – a hatchback from segment B, equipped with a spark-ignition combustion engine. Figure 1 shows the test vehicle, while its technical specifications are presented in Table 1.

Fig. 1. Vehicle used for the road tests

Table 1. Technical specifications of the tested vehicle

Parameter	Unit	Value
Engine type		Spark-ignition
Fuel		Gasoline
Engine displacement volume	cm^3	1596
Arrangement and number of cylinders		Inline, 4
Fuel supply system		Indirect, multi-point injection
Engine maximum power /at rotational speed	kW/rpm	88/6000
Engine maximum torque /at rotational speed	Nm/rpm	152/4050
Axle driven		Front
Vehicle curb mass	kg	1045
Transmission type		Manual, 5-speed
Production year		2011
Emission class		Euro 5

During road tests, the following driving parameters were recorded:

– vehicle velocity [km/h]
– engine rotational speed [rpm]
– accelerator pedal relative position [%]
– coolant temperature [°C]
– engine relative load [%]
– air mass flow rate [g/s]
– air temperature in the intake manifold [°C]
– air pressure in the intake manifold [kPa]
– fuel pressure in the supply system [kPa]
– voltage at the battery terminals [V].

These driving parameters were recorded directly from the vehicle's OBD system using the TEXA OBD Log (Fig. 2). The technical specifications of the device can be found in Table 2.

Fig. 2. TEXA OBD Log used to collect data in road tests

Table 2. Technical specifications of TEXA OBD Log

Parameter	Unit	Value
Processor		ARM 32-bit Contex-M3
RAM	kB	256
Internal memory	kB	2048
Maximum data recording time	h	90
Maximum sampling frequency	Hz	1
Operating temperature range	°C	–40 to +85
Software		IDC3 PC Suite
PC interface		USB 1.0 cable
Power supply in the vehicle		OBD 12 V connector

A total of 250 samples, which contain data from individual 'journeys', that is, periods of vehicle use from engine startup to shut down, were collected through road tests. The samples underwent preliminary screening, and those with a travel time exceeding 180 s and an average velocity of no less than 10 km/h were arbitrarily accepted for further analysis [19]. Such a selection criterion aimed to eliminate the few samples recorded during heavy traffic jams, treating such conditions as a distinct category of road traffic [6]. Ultimately, 242 vehicle velocity course samples that met the above-mentioned requirements were utilized as the basis for developing the driving cycle.

The statistical parameters of the vehicle velocity courses for 242 qualified measurements were as follows:

– total duration of all journeys – 214,067 s (almost 60 h)
– average duration of a single journey – 885 s (almost 15 min)
– average driving velocity – 24.82 km/h
– average maximum velocity – 74.61 km/h
– average time share of stops – 28.84%
– average number of stops – 15
– average duration of a single stop – 16 s
– average number of changes in the sign of the velocity derivative (in 100 s) – 2
– average number of accelerations and decelerations in a single journey – 153.

2.3. Main methodological assumptions

In this study, the driving cycle was developed using the micro-trip method. Each recorded trip was divided into sections that begin and end with the vehicle stopped, i.e. when the vehicle's velocity is zero and the engine is idling. The idling time at the end of the micro trip was included. These sections were then randomly combined using the AI tool. The goal was for the values of the selected driving pattern parameters to closely match those of the entire data set from the empirical studies (section 2.2).

The driving pattern parameters adopted as criteria for evaluating the driving cycle included:
– average vehicle velocity
– maximum vehicle velocity
– time share of vehicle stops (with the engine idling).
The number of criteria parameters was intentionally kept limited to avoid complicating the optimization task assigned to the AI software. Thus, no parameters related to acceleration and deceleration were introduced, assuming compliance of their values, as they were derived from actual fragments of velocity courses from the road tests.

The duration of the driving cycle was arbitrarily set at 1200 s, which is similar to the timeframes of typical urban cycles, such as JC08, NEDC, or FTP-72 [3, 11]. The WLTC, currently in force in the European Union and some other countries, lasts 1800 s, but accounts for urban, rural, and highway driving conditions. In addition, it was assumed that the driving cycle would begin and end with a short phase (5 s) of the vehicle being stopped with the engine idling.

The work on the driving cycle proceeded gradually. Initially, an attempt was made to create a driving cycle for 15 velocity samples. Once this procedure was mastered, the same process was repeated for all 242 samples from the empirical studies. Input commands were formulated for the AI software, and the resulting outputs were analyzed. This process provided the authors with valuable experience in working with the program, and the resulting observations and recommendations are included in the discussion section of this paper.

The following order of commands was ultimately established for the AI software:
1. Load a CSV file containing empirical data
2. Calculate driving pattern parameter values for the empirical data (target values)
3. Split the empirical data (velocity courses) into micro-trips
4. Compile micro-trips into a driving cycle, aiming to obtain driving pattern parameter values as closely aligned with the target as possible
5. Analyze the developed driving cycle
6. Iteratively improve the cycle until the new version achieves driving pattern parameter values closer to the target.

Exemplary prompts entered into the program are included in section 3.5 of the paper.

In this study, the authors adopted a guiding principle that allowed the AI to find its own method for generating a synthetic driving cycle. Therefore, a specific data processing algorithm was not imposed, and a degree of randomness in the selection of micro-trips was intentionally allowed, with the only restrictions being those mentioned above.

2.4. AI software

The processing of empirical data and the compilation of velocity sections into a driving cycle were performed using the AI software Julius. This software is designed for analytical statistics, data science, and computations. It operates on the principle of leveraging large language models (LLMs), such as OpenAI's ChatGPT and Google Gemini, which convert user commands entered in natural language into Python code. For more information about Julius, please refer to [18].

The program features a straightforward interface that facilitates a dialogue with the user. Commands were entered sequentially in a logical order (as outlined in section 2.3), rather than as a single command that would generate a driving cycle instantly.

3. Results and discussion

3.1. The developed driving cycle

Figure 3 illustrates the final version of the driving cycle that simulates urban traffic conditions, developed using the Julius AI software based on a complete set of 242 velocity samples recorded during empirical tests.

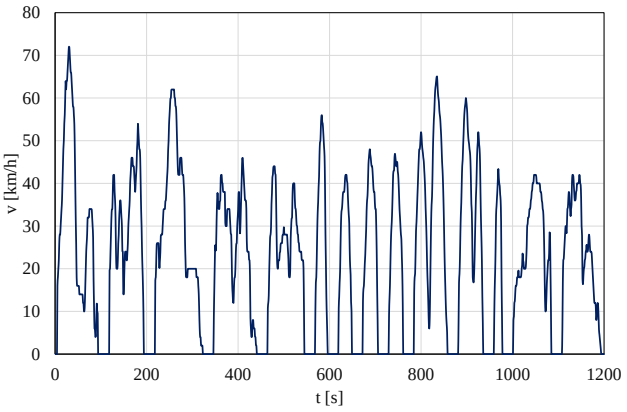

Fig. 3. Vehicle velocity course in the developed driving cycle (AI Cycle)

As can be seen in the graph, the vehicle velocity course reflects typical urban driving patterns. In urban areas, vehicle velocity fluctuates, incorporating phases of acceleration, deceleration, and idling, which capture the stop-and-go nature of city driving. This variability is attributed to various factors, including intersections controlled by traffic lights, traffic calming measures, high traffic volume, reduced velocity limits etc. Traffic lights not only cause vehicles to stop, but also slow them down as drivers anticipate stopping. Similar effects arise from traffic calming measures such as speed bumps, raised intersections, and others, leading to deceleration before and acceleration following these obstacles. Furthermore, rapid changes in vehicle speed are often influenced by the presence of numerous other road users. Finally, the peak velocities observed in the developed driving cycle are typical for urban conditions. In Polish cities, the velocity limit is 50 km/h in built-up areas, though this limit may vary based on road signs. Certain

road sections within cities also allow higher velocities, such as 70 km/h.

The above-mentioned characteristic features of the developed velocity course distinguish it from the relatively smoother velocity patterns typical in rural areas and especially on highways (motorways/express roads) [6], which exhibit fewer sharp peaks and less frequent stops – often none at all.

3.2. Comparison of the developed AI driving cycle with experimental data

The selected driving pattern parameters were chosen to serve as the criteria of representativeness of the created AI driving cycle for the modeled traffic conditions. The values of these parameters were calculated and compared between the developed driving cycle and the complete set of velocity samples from the experimental data. The results are presented in Table 3.

Table 3. Comparison of driving pattern parameters determined for the developed driving cycle and all samples collected during road tests

Parameter	Unit	AI driving cycle	All velocity samples	Relative difference
Time/average time	s	1200	885	35.59%
Average velocity	km/h	22.85	24.82	–7.94%
Maximum velocity	km/h	72.00	74.61	–3.50%
Time share of stop	%	27.08	28.84	–6.10%

The driving pattern parameters determined for the developed driving cycle and the experimental data showed no significant differences. The average vehicle velocity in the driving cycle was 1.97 km/h lower than in road tests, translating to a relative change of –7.94%. The share of idling time was 1.76% lower (–6.10%), and the maximum velocity was 2.61 km/h lower (–3.50%). In terms of the duration of the developed cycle compared to the average time of a single trip during road tests, the difference is not significant, as the cycle time was chosen arbitrarily.

3.3. Comparison of the developed AI driving cycle with selected standard driving cycles

Table 4 presents a comparison of selected parameters of the driving cycle obtained using AI with those of selected standard driving cycles: the Japanese JC08, American UDDS (FTP-72), European NEDC, and the global WLTC. Additionally, Figure 4 graphically compares the velocity courses of the developed driving cycle with those of the aforementioned standard cycles.

Table 4. Comparison of selected parameters of the developed driving cycle and selected standard driving cycles [11]

Parameter	Unit	AI driving cycle	JC08	UDDS (FTP-72)	NEDC	WLTC Class 3-2
Time/average time	s	1200	1204	1372	1180	1800
Distance traveled	m	7616	8171	11997	11017	23250
Average velocity	km/h	22.85	24.40	31.60	33.60	46.50
Maximum velocity	km/h	72.00	81.60	91.25	120.00	131.30
Time share of stop	%	27.08	28.7	17.8	23.7	12.6

The comparison indicates that the AI-generated driving cycle is the closest to the Japanese JC08. Both cycles exhibit a similar overall character of the velocity course (Fig. 4a), nearly the same duration (1200 s vs. 1204 s), and a comparable idling time (27.08% vs. 28.70%). However, the AI cycle has a slightly lower average velocity (22.85 km/h

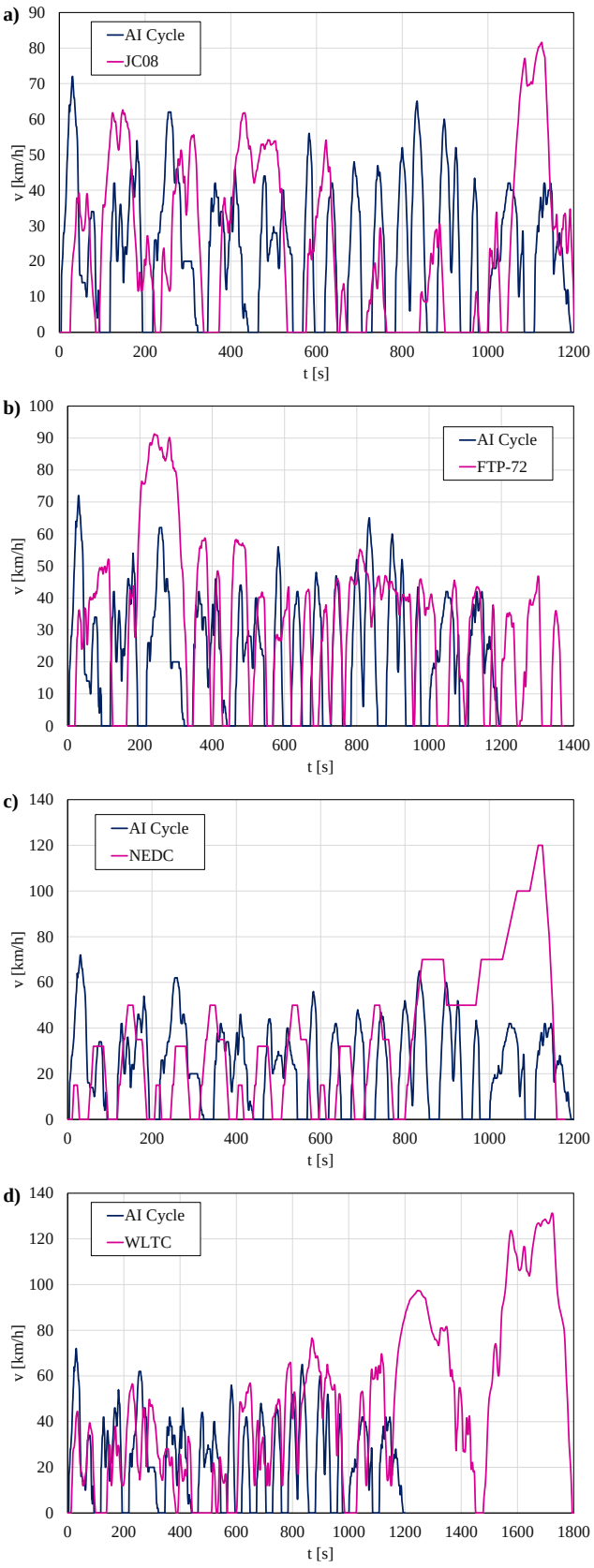

Fig. 4. Comparison of vehicle velocity courses in the developed driving cycle (AI Cycle) with those of selected standard driving cycles: a) JC08, b) FTP-72, c) NEDC, d) WLTC

vs. 24.40 km/h) and a lower maximum velocity (72.00 km/h vs. 81.60 km/h). Consequently, the lower average velocity and cycle time result in a theoretically shorter distance traveled (7616 m vs. 8171 m).

The sharp velocity peaks observed in the AI-generated driving cycle closely resemble those of the UDDS (Figure 4b). However, the American cycle includes a section where the vehicle reaches a velocity exceeding 90 km/h. When comparing the parameters of the driving patterns, the AI-generated cycle falls short of the UDDS in several areas: duration (1200 s vs. 1372 s), distance driven (7616 m vs. 11997 m), average velocity (22.85 km/h vs. 31.60 km/h), and maximum velocity (72.00 km/h vs. 91.25 km/h). Notably, the AI-generated cycle has a higher share of time spent at a stop (27.08% vs. 17.80%).

The AI driving cycle and the NEDC have a similar duration (1200 s vs. 1180 s) and a relatively close share of idling (27.08% vs. 23.70%). However, the other parameters are lower in the AI cycle compared to the NEDC: average velocity (22.85 km/h vs. 33.60 km/h), maximum velocity (72.00 km/h vs. 120 km/h), and distance driven (7616 m vs. 11017 m). This is primarily due to the NEDC's purpose of simulating both urban and extra-urban driving conditions. Additionally, the velocity courses differ, as the NEDC is a synthetic cycle composed of straight lines that correspond to the vehicle traveling at a constant velocity or with constant acceleration and deceleration.

The comparison between the AI-generated cycle and the WLTC is relevant, considering the widespread use of the latter in vehicle homologation. The AI-generated cycle exhibits significantly lower velocities, with average (22.85 km/h vs. 46.50 km/h) and maximum (72.00 km/h vs. 131.30 km/h). Similarly, the total time and distance traveled are shorter (1200 s vs. 1800 s and 7616 m vs. 23,250 m). On the other hand, the time share of the vehicle stop is higher in the AI-generated cycle than in the WLTC cycle (27.08% vs. 12.6%). It should be emphasized, however, that the WLTC simulates various driving conditions, not only urban, but also extra-urban and highway scenarios.

The similarities between the AI-generated driving cycle and standard cycles, particularly those that represent typical urban conditions (such as JC08 and UDDS), indicate that the AI-generated cycle effectively simulates real-world driving scenarios. Furthermore, these similarities reduce the risk that the developed driving cycle would be incompatible with testing equipment used for standard cycles.

From a broader perspective, the observed similarities and differences between the AI-generated cycle and the considered standard cycles could have significant practical implications. The similarities support the validity of existing standard cycles, despite evolving traffic conditions and advancements in automotive technology. However, even though standard cycles are benchmarks for policy frameworks and vehicle development, they may fall short in being responsive to some driving habits. AI applications can, in this regard, help in the development of driving cycles appropriate for given areas, conditions, or types of vehicles, thereby improving the relevance of the testing outcomes. Driving cycles based on local empirical data can capture the dynamics of vehicle performance, emissions, and fuel consumption during actual driving conditions much better than the existing standardized cycles. The adaptation of AI methodologies to generate custom cycles for various driving environments, such as rural, mountainous or congested traffic, is a promising future direction. Insights gained from these cycles, which accurately reflect actual traffic conditions, can complement the general data obtained from standardized driving cycles.

3.4. Study limitations

The resulting driving cycle can be considered a sufficient representation of the modeled vehicle motion conditions. It should be noted that this study aimed to investigate the practical aspects of using AI in developing drive cycles, rather than creating an ideal drive cycle for certain applications, such as emissions testing. Having said that, the authors of this paper identified several areas for improvement.

Firstly, the data collection stage could be expanded in quantitative terms, which would positively impact the quality of the resulting drive cycle. Further, the conditions for collecting empirical data could be specified more precisely: for instance, by designating a single route, selecting specific times of the day, involving various drivers and vehicles, etc. Moreover, the equipment used in the road tests was basic, allowing only the recording of fundamental parameters from the OBD system at a fairly low frequency (1 Hz). With current technical advancement, it is possible to carry out tests that include emission measurements using PEMS, although probably large-scale studies of this type would not be economically justified.

Secondly, at the stage of generating the driving cycle, it would have been beneficial to further refine the velocity profile to obtain driving pattern values even closer to those characterizing all samples from the road tests. In this respect, the authors decided that the obtained results were acceptable and decided not to pursue further enhancements. Additionally, more driving pattern parameters could be included, along with those related to acceleration.

Thirdly, the developed driving cycle should be verified on a chassis dynamometer in terms of its feasibility and subsequently validated on the basis of pollutant emission and fuel consumption results in road tests, i.e. RDE, as well as in standard cycles.

3.5. Precision of commands given to AI

While working on the driving cycle, the authors gained experience in cooperation with AI software. The key issue that determined the efficiency of the process and the quality of the results was the precision of the formulated commands. All user intentions had to be articulated clearly and precisely, e.g. *"Create a new combined speed profile using different speed sections with adjacent idle time sections in between. Take into account the following target parameters: total duration 1200 s, average speed 24.82 km/h, maximum speed 74.61 km/h, percentage idle time 28.84%"*.

In the initial iterations of developing the driving cycle, some inconsistencies appeared. For example, one version of the cycle began and ended with a vehicle velocity different from zero, which is rarely used from the point of view of practical implementation of the cycle on a chassis dynamometer (e.g. the non-standard Autobahn cycle). For this

reason, the program received an additional line of command to ensure the cycle started and ended with a few seconds of engine idling with zero velocity: *"Add 5 seconds idling at the beginning and at the end of the cycle"*.

As with natural language processing used for creating images or videos, a single prompt may provide a completely different driving cycle, even when based on the same set of empirical data. Therefore, it is difficult to discuss the repeatability of the results in a strict sense. However, the proposed procedure allows for reproducibility of the results, understood as obtaining a set of similar driving cycles with driving pattern parameters close to the target values.

3.6. Uncertainty of AI-derived results

An important aspect of working with AI is the concern about the uncertainty of the results obtained using uncontrolled 'hidden' internal algorithms of such tools. This phenomenon is called the 'AI black box problem' [14], which refers to the lack of transparency or the limited transparency in how machine learning systems process the inputs through complex algorithms and generate outputs. As a result, it may be difficult or impossible to understand how the AI tool reached its conclusions. This issue is becoming increasingly important, not only in technology but also in fields such as healthcare, safety, and security [32].

However, the AI black box problem is of lesser concern in this study for two reasons. Firstly, the AI tool used translates natural language commands into explicit Python code, which is fully visible and can be independently inspected and verified by the user. This allows for rigorous checking of the code correctness before execution, mitigating concerns related to hidden algorithmic processes. Additionally, the primary criteria for the driving cycle validity are its empirical representativeness and practical applicability in dynamometer testing, rather than the internal workings of the AI. To safeguard accuracy, the AI-generated driving cycle was compared with real traffic data and standard driving cycles. This confirmed that – theoretically – the cycle reliably reflects urban driving conditions. The final proof of the cycle adequacy will be the empirical testing of pollutant emissions and fuel consumption, which is planned (see section 3.7). Thus, the combination of code transparency and empirical verification addresses the 'black box' concerns in this study context.

3.7. Future perspectives

The approach outlined in this paper, along with the case study example, does not comprehensively cover this broad subject. There are many directions for further research in this field, the prospects of which have opened up with the rapid development of AI in recent years.

First and foremost, the presented AI-enhanced approach for driving cycle development requires empirical validation. The authors plan to utilize the developed cycle to conduct tests on pollutant emissions and fuel consumption on a chassis dynamometer. This will involve comparing the results with those obtained using standard urban driving cycles. Such testing would provide evidence for the practical applicability and accuracy of the AI-enhanced development approach – a critical validation step to confirm the cycle's suitability for regulatory and research purposes.

The authors believe that the optimal way for AI to assist in creating driving cycles would be to produce entirely artificial velocity courses that fully meet the criteria and requirements set by researchers. According to the experimental data from road tests, the primary goal would be to ensure that every driving pattern parameter selected has the same value for the developed cycle and the set of experimental data. Furthermore, the ability to generate these kinds of driving cycles within a short timeframe would make it possible to introduce the idea of testing a vehicle's fuel consumption and pollutant emissions on a chassis dynamometer under random or pseudo-random conditions. This is in line with the stochastic approach to evaluating vehicle performance.

4. Summary and conclusions

This study explored the potential application of AI tools to generate driving cycles, which are essential for assessing pollutant emissions and fuel consumption in passenger vehicles on a chassis dynamometer. This theoretical concept was illustrated through a case study focused on an urban driving cycle. The AI tool employed was based on software that utilizes natural language processing to convert user commands into programming code. The resulting driving cycle was generated according to similarity criteria of several driving pattern characteristics, namely: average vehicle velocity, maximum vehicle velocity, and the time share of vehicle stop with the engine idling.

In summary, the following conclusions and observations can be drawn from this study:

- The developed driving cycle demonstrated the feasibility of using AI tools in developing driving cycles
- AI-driven natural language processing tools are efficient and convenient for driving cycle development, though they do have certain constraints and challenges for beginners
- Data processing using AI tools significantly speeds up the development of driving cycles
- Precise command formulation is essential when using AI tools, as vague instructions may result in inaccurate outcomes
- The proposed method allows for the creation of a wide variety of driving cycles for light vehicles, motorcycles, and heavy vehicles, while accommodating different traffic scenarios, including urban, extra-urban, and motorway conditions
- Further development work on the proposed general approach is needed, mainly for the empirical verification of pollutant emissions and fuel consumption based on these driving cycles.

While the full potential and operational rules of AI have yet to be thoroughly explored, it is reasonable to assume that driving cycle development will benefit greatly from its application in the future. It can significantly enhance the processing of large volumes of road test data, allowing for the generation of driving cycles that accurately reflect specific road conditions. Additionally, it supports the idea of conducting chassis dynamometer tests with randomly selected driving cycles following a stochastic approach.

Nomenclature

ADAC	Allgemeiner Deutscher Automobil-Club
AI	artificial intelligence
CADC	Common Artemis Driving Cycles
CLTC	China Light-duty Vehicle Test Cycle
FTP	Federal Test Procedure
GPS	global positioning system
HWFET	Highway Fuel Economy Test
JC	Japan Cycle
LLM	large language model
NEDC	New European Driving Cycle
OBD	on-board diagnostics
PEMS	portable emission measurement systems
RDE	real driving emissions
SFTP	Supplemental Federal Test Procedure
UDDS	Urban Dynamometer Driving Schedule
WLTC	Worldwide Harmonized Light Vehicle Test Cycle

Bibliography

[1] Adamiak B, Andrych-Zalewska M, Merkisz J, Chłopek Z. The uniqueness of pollutant emission and fuel consumption test results for road vehicles tested on a chassis dynamometer. Eksploat Niezawodn. 2025;27(1):195747. https://doi.org/10.17531/ein/195747

[2] Andrych-Zalewska M, Chłopek Z, Merkisz J, Pielecha J. Determination of characteristics of pollutant emission from a vehicle engine under traffic conditions in the engine test. Combustion Engines. 2022;191(4):58-65. https://doi.org/10.19206/CE-147327

[3] Barlow T, Latham S, McCrae I, Boulter P. A reference book of driving cycles for use in the measurement of road vehicle emissions. Wokingham (UK): Transport Research Laboratory; 2009. (TRL Published Project Report). https://assets.publishing.service.gov.uk/media/5a7984f440f0b642860d8c2d/ppr-354.pdf

[4] Boulter PG, Barlow TJ, McCrae IS, Latham S, Parkin C. Emission factors 2009: report 1 – a review of methods for determining hot exhaust emission factors for road vehicles. Crowthorne (UK): Transport Research Laboratory 2009. PPR353. https://assets.publishing.service.gov.uk/media/5a789a65ed915d0422063e7f/report-1.pdf

[5] Brady J, O'Mahony M. Development of a driving cycle to evaluate the energy economy of electric vehicles in urban areas. Appl Energy. 2016;177:165-178. https://doi.org/10.1016/j.apenergy.2016.05.094

[6] Chłopek Z, Biedrzycki J, Lasocki J, Wójcik P. Correlational analysis of pollutant emission intensity in various conditions of operation of the automotive internal combustion engine. Transport. 2019;34:490-498. https://doi.org/10.3846/transport.2019.11294

[7] Chłopek Z, Lasocki J. Zerowymiarowe charakterystyki testów jezdnych do celów modelowania emisji zanieczyszczeń z samochodowych silników spalinowych (in Polish). Przem Chem. 2024;103:1465-1468. https://doi.org/10.15199/62.2024.12.13

[8] Galgamuwa U, Perera L, Bandara S. Developing a general methodology for driving cycle construction: comparison of various established driving cycles in the world to propose a general approach. J Transp Technol. 2015;5:191-203. https://un.uobasrah.edu.iq/download_paper.php?id=6546

[9] Gebisa A, Gebresenbet G, Gopal R, Nallamothu RB. Driving cycles for estimating vehicle emission levels and energy consumption. Future Transp. 2021;1(3):615-638. https://doi.org/10.3390/futuretransp1030033

[10] Gebisa A, Gebresenbet G, Gopal R, Nallamothu RB. A neural network and principal component analysis approach to develop a real-time driving cycle in an urban environment: the case of Addis Ababa, Ethiopia. Sustainability. 2022;14(21):13772. https://doi.org/10.3390/su142113772

[11] Giakoumis EG. Driving and engine cycles. Athens: Springer; 2017. https://doi.org/doi:10.1007/978-3-319-49034-2

[12] Giraldo M, Quirama LF, Huertas JI, Tibaquirá JE. The effect of driving cycle duration on its representativeness. World Electr Veh J. 2021;12(4):212. https://doi.org/10.3390/wevj12040212

[13] Gnap J, Šarkan B, Konečný V, Skrúcaný T. The impact of road transport on the environment. In: Sładkowski A (ed.). Ecology in transport: problems and solutions. Springer, Cham 2020. https://doi.org/10.1007/978-3-030-42323-0_5

[14] Hassija V, Chamola V, Mahapatra A, Singal A, Goel D, Huang K et al. Interpreting black-box models: a review on explainable artificial intelligence. Cogn Comput. 2024;16:45-74. https://doi.org/10.1007/s12559-023-10179-8

[15] Hung WT, Tong HY, Lee CP, Ha K, Pao LY. Development of a practical driving cycle construction methodology: a case study in Hong Kong. Transp Res D Transp Environ. 2007;12:115-128. https://doi.org/10.1016/j.trd.2007.01.002

[16] Huo J, Peng C. Depletion of natural resources and environmental quality: prospects of energy use, energy imports, and economic growth hindrances. Resour Policy. 2023;86:104049. https://doi.org/10.1016/j.resourpol.2023.104049

[17] Jia X, Wang H, Xu L, Wang Q, Li H, Hu Z et al. Constructing representative driving cycle for heavy duty vehicle based on Markov chain method considering road slope. Energy AI. 2022;7:100123. https://doi.org/10.1016/j.egyai.2021.100115

[18] Julius. The AI data analyst that works for you [Internet]. San Francisco: Caesar Labs Inc; 2025. https://julius.ai/ (accessed on 2025.08.08).

[19] Lasocki J, Chłopek Z, Godlewski T. Driving style analysis based on information from the vehicle's OBD system. Combust Engines. 2019;178(3):173-181. https://doi.org/doi:10.19206/CE-2019-330

[20] Lasocki J. The WLTC vs NEDC: a case study on the impacts of driving cycle on engine performance and fuel consumption. Int J Automot Mech Eng. 2021;18:9071-9081. https://journal.ump.edu.my/ijame/article/view/2508

[21] Londoño J, Serna Cartagena JF, Gomez Miranda IN, Ruiz Holguin FA, Agudelo AF. Methodology for determining motorcycle driving cycles applying computational intelligence tools: case study of Medellín, Colombia. SSRN. https://doi.org/10.2139/ssrn.5062525

[22] Lyu P, Wang P, Liu Y, Wang Y. Review of the studies on emission evaluation approaches for operating vehicles. J Traffic Transp Eng. 2021;8:493-509. https://doi.org/10.1016/j.jtte.2021.07.004

[23] Mostasharshahidi S, Salamat MK, Ghobadian B, Masih-Tehrani M. Agricultural tractor driving cycle extraction using artificial intelligence. J Eng Res. 2024;70(4):14-26. https://doi.org/10.22034/er.2024.2024942.1028

[24] Orliński P, Gis M, Bednarski M, Novak N, Samoilenko D, Prokhorenko A. The legitimacy of using hybrid vehicles in

urban conditions in relation to empirical studies in the WLTC cycle. Probl Ekspl. 2019;112:25-30. http://www.jmcm.itee.radom.pl/images/jmcm_2019/jmcm_1_2019/JMCM_1_2019_s_025_030.pdf
[25] Pielecha J, Kurtyka K. Exhaust emissions from Euro 6 vehicles in WLTC and RDE – part 1: methodology and similarity conditions studies. Energies. 2023;16:7465. https://doi.org/10.3390/en16227465
[26] Qiu D, Li Y, Qiao D. Recurrent neural network based driving cycle development for light duty vehicles in Beijing. Transp Res Procedia. 2018;34:147-154. https://doi.org/10.1016/j.trpro.2018.11.026
[27] Quirama LF, Giraldo M, Huertas JI, Tibaquirá JE, Cordero-Moreno D. Main characteristic parameters to describe driving patterns and construct driving cycles. Transp Res D Transp Environ. 2021;97:102959. https://doi.org/10.1016/j.trd.2021.102959
[28] Rivera-Campoverde ND, Arenas-Ramírez B, Muñoz Sanz JL, Jiménez E. GPS data and machine learning tools, a practical and cost-effective combination for estimating light vehicle emissions. Sensors. 2024;24(7):2304. https://doi.org/10.3390/s24072304
[29] Sankar SS, Xia Y, Carmai J, Koetniyom S. Optimal eco-driving cycles for conventional vehicles using a genetic algorithm. Energies. 2020;13(17):4362. https://doi.org/10.3390/en13174362
[30] Shi S, Lin N, Zhang Y, Cheng J, Huang C, Liu L et al. Research on Markov property analysis of driving cycles and its application. Transp Res D Transp Environ. 2016;47:171-181. https://doi.org/10.1016/j.trd.2016.05.013
[31] Tong HY, Hung WT. A framework for developing driving cycles with on-road driving data. Transp Rev. 2010;30(5): 589-615. https://doi.org/10.1080/01441640903286134
[32] von Eschenbach WJ. Transparency and the black box problem: why we do not trust AI. Philos Technol. 2021;34:1607-1622. https://doi.org/10.1007/s13347-021-00477-0
[33] Zimakowska-Laskowska M, Kozłowski E, Laskowski P, Wiśniowski P, Świderski A, Orynycz O. Vehicle exhaust emissions in the light of modern research tools: synergy of chassis dynamometers and computational models. Combustion Engines. 2025;200(1):145-54. https://doi.org/10.19206/CE-201224

Gabriela Snarska-Bień, MEng. – Faculty of Automotive and Construction Machinery Engineering, Warsaw University of Technology, Poland.
e-mail: *gabriela.snarska.knss@gmail.com*

Jakub Lasocki, DEng. – Faculty of Automotive and Construction Machinery Engineering, Warsaw University of Technology, Poland.
e-mail: *jakub.lasocki@pw.edu.pl*

Article citation info:
Babuchowska P, Pielecha I. Camera systems – key technology for ADAS in autonomous vehicles. Combustion Engines. 2025;203(4):155-163. https://doi.org/10.19206/CE-209703

Paulina BABUCHOWSKA
Ireneusz PIELECHA

Combustion Engines
Polish Scientific Society of Combustion Engines

Camera systems – key technology for ADAS in autonomous vehicles

ARTICLE INFO

Received: 30 November 2024
Revised: 20 May 2025
Accepted: 19 August 2025
Available online: 29 August 2025

Advanced Driver Assistance Systems (ADAS) have become an integral part of modern vehicles, with the potential to significantly enhance safety on the road. ADAS technology involves the use of sensors, algorithms, and software to assist drivers and provide them with real-time information about their surroundings, traffic conditions, and potential hazards. Sensors utilized for object tracking and environmental detection, particularly those based on laser, radar, and camera technologies, are fundamental to the functional performance of ADAS. Within automotive applications, the majority of camera systems are equipped with wide-angle or fish-eye lenses, both of which are known to introduce substantial optical distortion. To ensure accurate environmental perception, particularly in the context of geometric feature recognition and distance estimation, such cameras require meticulous calibration. Therefore, this paper describes a case study concerning cameras used in vision-based ADAS, as well as the most frequently used calibrating techniques. It describes the fundamentals of camera calibration and implementation, with results given for different lenses and distortion models. By engaging with this article, readers will gain a comprehensive understanding of the technological foundations, functional principles, and practical challenges associated with camera-based ADAS that need to be addressed to ensure its safe and effective operation on the road. The article serves as a technical reference that not only enhances the reader's theoretical knowledge but also informs practical decision-making in the development of safe and effective driver assistance systems.

Key words: *automotive camera, ADAS, advanced driver assistance systems, autonomous vehicles, camera systems*

1. Introduction

In the context of the development of autonomous driving, an automated and connected vehicle is nowadays taken as the basis. With the advancement of the Internet and wireless communication connections, the possibilities for networking vehicles are also increasing. The range of infotainment systems is growing through the use of Bluetooth connections, navigation systems receive immediate traffic jam and closure information, and smartphone apps can be operated directly via the multifunction display. In the near future, mobile online services are to be expanded so that the customer can purchase additional functions and assistance systems similar to an app store after buying the vehicle [6].

The first assistance systems in vehicles were introduced to increase the stability of the vehicle: an electronic stability program (ESP) and an anti-lock braking system (ABS). To date, a large number of informative, supportive, and warning systems have been added. The primary goal is to make traffic safer and to avoid accidents or reduce the severity of accidents through the widespread installation of ADAS.

The five levels of driving automation serve as a basic classification of ADAS. The differentiation is made by evaluating the shares that the driver and the system take on the driving task [22].

The driving task is divided according to the three-level hierarchy of Edmund Donges into navigation, lane guidance, and stabilization. The navigation task includes choosing a suitable route with an estimate of the required time, while the driver draws conclusions from the upcoming traffic situation for adjusting, for example, the target lane and target speed during lane guidance. In the context of the stabilization level, the driver performs corrective interventions so that the control deviation is stabilized and reduced to an acceptable level [8].

Level 0, Driver only, is understood as driving without assistance systems. This means that the driver takes on the entire driving task themselves. They perform longitudinal and lateral control continuously. The lowest degree of automation is level one. Within limits, it is possible for the system to take over either longitudinal or lateral control, while the driver performs the other task. The second level, also called partial automation, includes systems that can take over both lateral and longitudinal guidance. The driver must monitor the traffic and their vehicle at all times to take over vehicle control in case of danger. This also includes a system failure. The current state of technology can largely be classified into these two categories. In the case of the third level, the driver no longer has to monitor the traffic and their vehicle continuously, but must be able to follow a takeover request. This is because the system recognizes its limits but is not able to return to a risk-minimal state in every situation. The driver can also decide to take over control again at any time. Systems of the fourth and fifth level, fully autonomous, should be able to return to a risk-minimal state without any driver intervention. Problems for implementation arise not only from immature technology but also from the driver's behavioural obligations, which they must fulfil when driving [10].

As perception and vision is key for ADAS operation to be successful, this work covers details on specific applications of camera-based driver assistance systems and the resulting technical needs for the camera system. Use cases covering the outside of the vehicle are shown. The basis of every camera system is the camera module with its main parts – the lens system and the image sensor. The underlying technology is described, and the formation of the camera image is discussed. Moving to the system level,

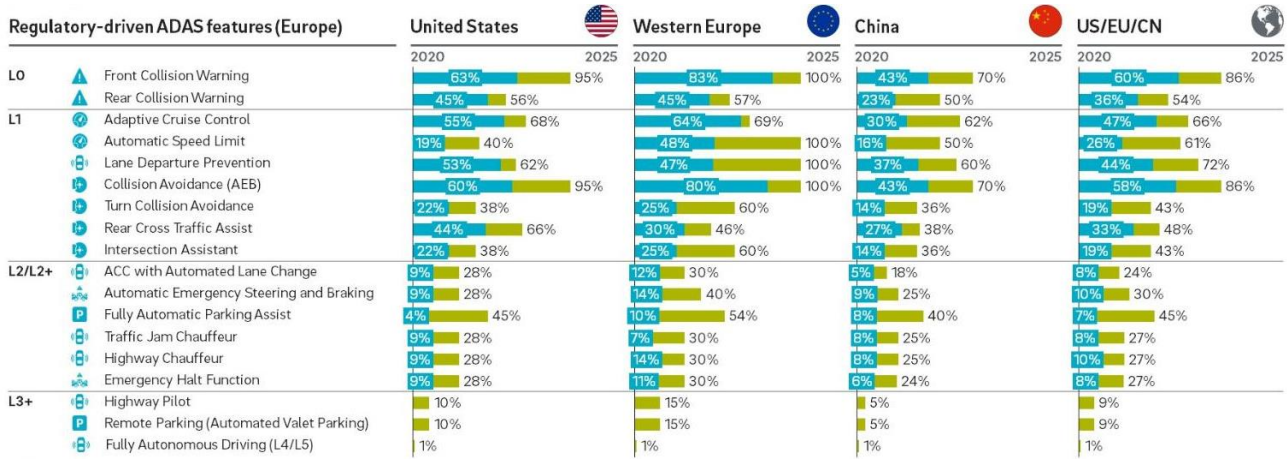

Fig. 1. Percentage of features installed on vehicles by region [17]

basic camera architectures, including mono and stereo systems, are analysed.

ADAS capabilities are classified according to six distinct feature levels, ranging from Level 0 to Level 5:

Level 0: Basic level encompasses fundamental warning systems, including front and rear collision alerts, blind spot detection, and lane departure warnings. These features are increasingly incorporated into modern vehicles either as standard equipment or available as optional add-ons.

Level 1: Driver assistance level offers support functionalities such as automatic emergency braking, adaptive cruise control, lane-keeping assistance, distance control, automated speed regulation, driver interaction aids, and collision avoidance technologies.

Level 2: Partial automation involves the concurrent deployment of adaptive cruise control and lane-keeping capabilities. It also includes advanced cruise features, automated emergency steering and braking, as well as fully autonomous parking functionalities.

Level 3: Conditional automation enables vehicles to manage highway driving autonomously, including executing automatic lane changes and remote parking manoeuvres. These systems offer comprehensive environmental sensing and do not require driver input during specified operational scenarios, such as travel from the highway entrance to the exit.

Level 4: A High automation level represents highly autonomous driving capabilities, enabling vehicles to operate without human oversight in certain defined scenarios. Currently, no production vehicles offer Level 4 automation, nor have any such systems been officially announced for commercial release.

Level 5: Full automation enables vehicles to operate entirely autonomously under all conditions, eliminating the need for any human driver intervention. As of now, no Level 5 systems are commercially available, and their market readiness is not anticipated before 2030 or 2035 at the earliest [22].

Due to regulatory requirements, Europe grows and leads overall ADAS features. Notably, European Union legislation has stipulated that as of 2024, all newly manufactured vehicles must be equipped with both front-facing cameras and radar sensors as standard components. For instance, the integration rate of collision warning systems increased from 83% in 2020 to a projected 100% by 2025. Similarly, the adoption of automated speed limiters rose from 48% to complete implementation over the same period. Lane departure prevention systems also saw significant growth, with usage doubling to 100% by 2025.

On a global scale, forecasts for 2025 indicate that 14% of the world's vehicles will lack any ADAS features, while 40% are expected to support Level 1 functions, 36% will incorporate Level 2 capabilities, and approximately 10% will be outfitted with Level 3 or more advanced systems. Overall, these figures represent a substantial increase in ADAS deployment compared to current levels, as illustrated in Fig. 1.

The objective of this article is to provide a structured review of automotive camera systems as a fundamental technology in ADAS, with a focus on their architecture, calibration techniques, and sensor performance. Emphasis is placed on both monocular and stereo camera configurations, as well as static, dynamic, and learning-based calibration methods essential for accurate perception.

The significance of this work lies in its relevance to current challenges in ADAS development, where precise sensor operation and reliable environmental interpretation are critical for vehicle safety. By synthesizing technical knowledge and recent advancements, the article offers valuable insights for researchers and engineers working on vision-based autonomous systems.

2. Advanced driver assistance systems in vehicles

2.1 Methodology

The study is based on a qualitative engineering analysis of camera systems used in ADAS. The authors conducted a comprehensive literature review using various databases. Based on the gathered data, the authors analysed the technological components of mono and stereo camera systems, focusing on architecture, image quality factors (resolution, colour, dynamic range), and calibration needs. The paper presents a synthesis of calibration models with a practical emphasis on their applicability in ADAS platforms. Furthermore, the authors discuss emerging trends in real-time and deep learning-based calibration, highlighting their significance for future development.

2.2. Overview and function

Advanced Driver Assistance Systems technology is designed to assist drivers and enhance safety on the road. It does this by using sensors, algorithms, and software to collect data about the vehicle's surroundings and provide real-time information to the driver.

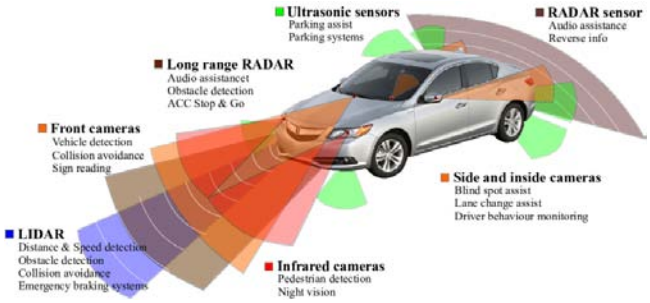

Fig. 2. Sensors used in ADAS – including camera, radar, LiDAR, and ultrasonic components [16]

ADAS technology relies on various sensors (Fig. 2) to collect data about the vehicle's environment. These sensors include cameras, radar, LiDAR, and ultrasonic sensors. Cameras are used to capture visual data, such as lane markings, traffic signs, and other vehicles. Radar sensors use radio waves to detect the position and speed of objects in the vehicle's path, while LiDAR sensors use laser beams to create a detailed 3D map of the surroundings. Ultrasonic sensors use sound waves to detect the distance between the vehicle and nearby objects.

The data collected by the sensors is used and analysed by algorithms of ADAS to make real-time decisions. These algorithms can detect potential hazards, such as a vehicle in the driver's blind spot, and alert the driver with visual or auditory cues [9].

ADAS technology relies heavily on software to control the various components of the vehicle. This software is responsible for processing the data collected by the sensors and executing the algorithms that control the brakes, steering, and other systems. The software must be designed to be reliable, secure, and easy to update as new features are added or improved [10].

2.3. Calibration of ADAS

ADAS calibration and recalibration is the precise physical alignment, testing, and electronic aiming of sensors. In newly manufactured vehicles, ADAS sensors are accurately installed and configured according to predefined factory specifications, ensuring that each sensor is precisely oriented as intended. However, over the operational lifespan of a vehicle, various incidents such as collisions, minor accidents, or repairs involving adjacent components, can result in the misalignment of these sensors. When such misalignments occur, it becomes essential to recalibrate the affected systems to restore them to their original, pre-incident condition, thereby ensuring that the sensors continue to perform in accordance with their intended design specifications. Depending on the configuration of the vehicle's ADAS platform and the guidelines established by the original equipment manufacturer (OEM), calibration may involve static procedures, dynamic procedures, or a combination of both [12].

The calibration of ADAS components, particularly camera systems, is a critical process that directly affects the accuracy and reliability of environmental perception. Calibration refers to the precise determination and adjustment of sensor parameters to ensure correct spatial interpretation of the environment and accurate data fusion in multi-sensor systems. In the context of camera-based ADAS, two primary categories of calibration are typically distinguished: intrinsic and extrinsic.

Intrinsic calibration involves the estimation of internal camera parameters, such as focal length, principal point, skew coefficient, and lens distortion coefficients. These parameters describe how the camera projects three-dimensional world points onto the two-dimensional image plane. Since most automotive camera systems employ wide-angle or fisheye lenses to maximize field of view, they are subject to substantial optical distortions. Therefore, the accurate modeling and correction of radial and tangential distortions is essential to enable reliable image interpretation and subsequent object detection and tracking [7].

Extrinsic calibration, on the other hand, refers to determining the position and orientation of the camera with respect to a known reference frame, typically the vehicle coordinate system or another sensor in a multi-modal configuration (e.g. radar, LiDAR). This step is fundamental for accurate sensor fusion, allowing the combination of data streams from different modalities into a coherent representation of the environment. Errors in extrinsic calibration can result in significant misalignment of perceived objects and deterioration of system performance.

Depending on the ADAS platform and the manufacturer's specifications, calibration procedures are generally divided into static and dynamic approaches, each with distinct methodologies, requirements, and operational contexts [22].

Static calibration is performed in a controlled environment, typically within a workshop or service center, and involves the use of predefined reference targets and precise positioning of the vehicle. This method relies on physical calibration patterns, such as checkerboards, dot matrices, or specific 2D/3D markers, which are placed at exact distances and orientations relative to the vehicle. The calibration system then captures images of these patterns using the onboard camera sensors and computes the intrinsic and extrinsic parameters through mathematical optimization techniques, such as Zhang's method [24] or bundle adjustment algorithms. Static calibration provides high repeatability and accuracy, making it the preferred choice during manufacturing, sensor replacement, or major maintenance procedures. However, it requires dedicated equipment, ample workspace, and trained personnel, which may limit its applicability in field conditions.

Dynamic calibration, in contrast, is performed during actual vehicle operation and does not depend on dedicated calibration targets. Instead, it uses environmental features such as lane markings, traffic signs, curbs, or roadside infrastructure, which are detected and analyzed by the vehicle's sensors in real time. Advanced computer vision and

machine learning algorithms are employed to identify these features and estimate sensor parameters by observing their geometric consistency over time and motion. Dynamic calibration is particularly advantageous in post-service scenarios or when minor sensor misalignments occur during regular use, as it eliminates the need for workshop visits and minimizes vehicle downtime. However, it may be influenced by variable lighting conditions, road quality, or temporary occlusions.

3. Cameras for ADAS

3.1. Mono camera architecture

Cameras represent the most widely utilized type of vision sensor in automotive applications. In vision-based ADAS, one or more cameras are employed to capture visual data, which is subsequently processed by an embedded computing system to identify, analyse, and track various objects within the scene. Cameras provide critical information, including colour, contrast, and texture, granting them a distinct advantage over alternative sensor technologies. They are capable of delivering high-resolution outputs across spectral, spatial, and temporal dimensions, thereby enabling comprehensive environmental perception. Moreover, certain specialized systems offer extended functionalities, such as night vision capabilities or distance estimation. The following sections present a systematic overview of automotive camera systems, including their underlying technology and structural configurations.

In vision-based ADAS, two principal types of cameras are commonly employed: monocular and stereo systems. An illustrative example of a standard monocular camera architecture for a front-facing application is provided in Fig. 3. In this configuration, the camera module is interfaced through a communication bus, and the image data is transmitted via a parallel connection to a dedicated image processing unit. In the described setup, a digital signal processor (DSP) is implemented to perform real-time video processing. Alternatively, some systems may incorporate field-programmable gate arrays (FPGA) or application-specific integrated circuits (ASIC) to fulfil similar processing requirements [24]. The image processing unit is supported by high-speed memory modules, which serve not only to temporarily store processed image data but also to retain multiple image frames – particularly useful for implementing object tracking algorithms. A microcontroller oversees various support functions, including exposure regulation, control of the windshield heating element, communication via the in-vehicle bus system, and additional system monitoring and management tasks. Interaction between the microcontroller and the digital signal processor is facilitated through an interprocess communication (IPC) interface.

Monocular cameras are characterized by the presence of a single optical lens. Due to the production of only one image stream at any given time, these systems demand relatively modest computational resources for image processing when compared to other, more complex camera configurations. Such cameras are versatile and can be employed in a range of applications, including the detection of obstacles, lane markings, and traffic signs [4]. In addition to external monitoring, monocular cameras can also be used within the vehicle cabin for driver observation tasks, such as facial recognition, eye tracking, and head pose estimation [14]. However, a notable limitation of monocular imaging systems is their inability to capture depth information directly, rendering them less suitable for tasks that require precise distance measurement. Nevertheless, certain algorithmic approaches [4] have been developed to approximate depth by identifying key features in the captured image and tracking their position, particularly when the camera is in motion.

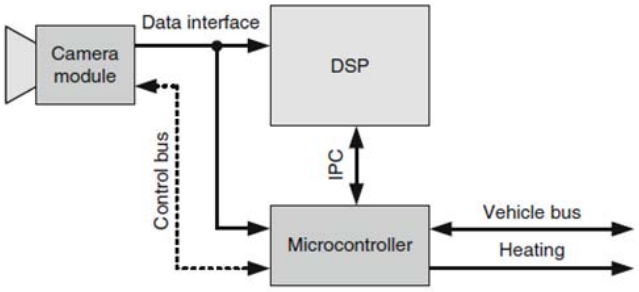

Fig. 3. Architecture of a mono camera system [23]

3.2. Stereo camera

3.2.1. Stereo camera architecture

The basic structure of a stereo camera system is illustrated in Fig. 4. In this architecture, both image sensors are governed by a single microcontroller, which manages the acquisition and coordination of visual data. The captured image signals are subsequently transmitted to the DSP and a FPGA for preliminary processing.

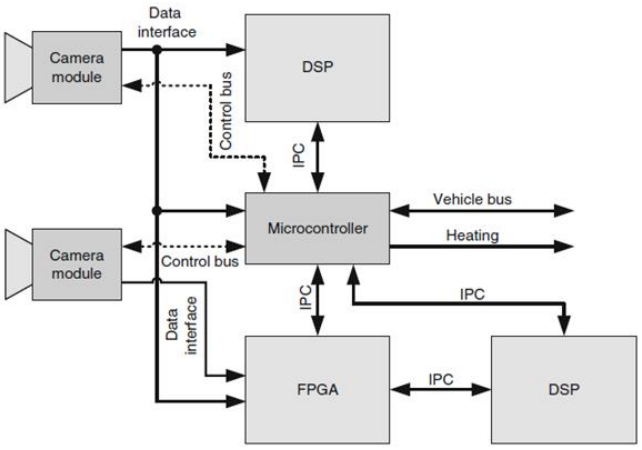

Fig. 4. Architecture of a stereo camera system [23]

The FPGA is responsible for executing critical preprocessing tasks, including image rectification, the generation of disparity maps, and the calculation of optical flow. The DSP then performs object recognition functions, such as identifying pedestrians, vehicles, and other relevant features within the visual scene. A second DSP is often dedicated to performing specific ADAS functionalities, such as lane departure warning and traffic sign recognition. Communication between the stereo vision system and the vehicle's internal network is facilitated by a microcontroller inter-

face. Each of the image processing units is linked to high-speed memory modules, which are used to support rapid data access and temporary storage during computation [19].

Stereo camera systems are composed of two or more camera modules, each containing its own image sensor, and positioned at a fixed distance from one another – a parameter referred to as the stereo base.

These systems are particularly effective in generating three-dimensional (3D) spatial information by comparing pairs of two-dimensional images acquired from the left and right sensors and constructing a disparity map to calculate relative depth within the scene. Stereo vision systems can be applied across a wide range of use cases, including the detection of traffic signs, lane boundaries, pedestrians, and obstacles, as well as accurate estimation of object distances, achieving significantly higher precision than monocular camera systems [23]. To ensure accurate 3D perception, the alignment of the two camera modules must be precisely calibrated across all spatial axes, including pitch, yaw, and roll, prior to their integration into the housing. Even minor deviations in the alignment of the optical axes can lead to miscalibration, ultimately impairing the functionality of the entire stereo vision system.

Image-based techniques provide a rapid and cost-effective approach for acquiring high-quality 3D representations, especially when compared to more expensive alternatives such as radar and LiDAR systems. Continual advancements in image resolution and sensor quality have transformed digital cameras into affordable, highly reliable tools capable of generating detailed 3D data. As a result, stereo cameras have become indispensable components in autonomous vehicle systems, offering a practical solution for real-time depth estimation, as illustrated in Fig. 5. The accurate reconstruction of dense depth maps is a fundamental requirement for numerous ADAS tasks, including obstacle detection, free-space identification, vehicle localization, environmental mapping, path planning, and lane boundary recognition [11].

Fig. 5. Comparison between monocular and stereo vision systems for depth estimation [18]

3.2.2. Structure of a camera system

A basic camera architecture is shown in Fig. 6. In this arrangement, an object or scene is projected through an imaging lens, which focuses the optical information onto an image sensor. The sensor is composed of an array of pixels, each of which converts incident photons into electrical signals, which are then transmitted to a processing unit for analysis. If the processed output is intended for immediate user interpretation, it is subsequently rendered on a display screen.

In the development of a camera system, it is essential to conduct a thorough evaluation of both its individual components and the integrated system as a whole. The optical lens is a critical element that significantly influences the overall performance of the camera. It directly impacts a range of imaging parameters, including achievable resolution, the extent of the field of view, depth of field, colour fidelity, and the system's light sensitivity. Given that optical assemblies inherently introduce imperfections, such as image distortion, appropriate correction mechanisms must be applied to ensure accurate image reproduction. The optical image captured by the lens is subsequently converted into digital signals by the image sensor. Consequently, careful coordination and design optimization between the optical system and the image sensor are vital to achieving high image quality. The sensor itself plays a central role in defining several critical attributes of the final image, including resolution (determined by pixel count), field of view (influenced by pixel count and arrangement), dynamic range, colour accuracy, and, most notably, the sensitivity to light [15].

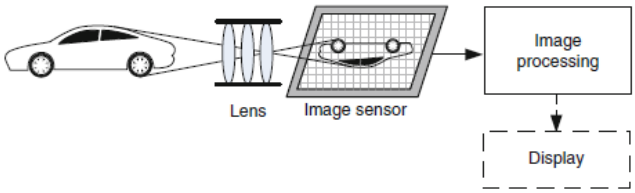

Fig. 6. Basic camera architecture [23]

Field of view

The field of view (FOV) of a camera plays an important role in the application and is essentially defined by the lens and the image sensor (Fig. 7). One distinguishes the field of view in horizontal and vertical direction (HFOV, VFOV).

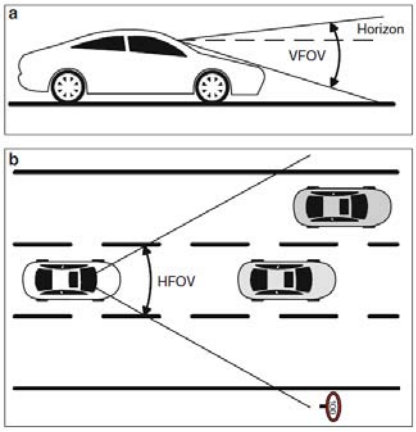

Fig. 7. Vertical (a) and horizontal (b) field of view of a front view camera [23]

Depending on the requirements of the camera, the maximum field of view that the system can monitor is important [6]. A distinction is made here between horizontal and vertical fields of vision. Front view camera systems, such as the multifunctional camera considered in this work, require relatively large HFOV values in case of lane detection (in tight curve scenarios) and object detection. The vertical field of view is determined primarily by the mounting height and the minimum detection distance at close range [7].

Resolution

Optimal image resolution results from the coordinated interaction between the optical system, the image sensor, and the image processing unit. The resolution capacity of the sensor is primarily determined by both the physical size and the total number of pixels it contains. Under low-light conditions, sensors with smaller pixel dimensions tend to produce images with increased noise levels when compared to those with larger pixels, thereby diminishing the system's dynamic response capability. To effectively utilize small pixel architectures, high-precision optical components, specifically lenses with high resolving power, are required to maintain image sharpness. Without such high-quality optics, the system may produce images with a high pixel count but lacking in meaningful structural detail due to blurring. Additionally, the use of small pixel sensors necessitates extremely accurate mechanical alignment of the sensor within the optical path, as such configurations inherently exhibit a significantly reduced depth of field.

On the other hand, as the light-sensitive surface area of an image sensor increases, the system's ability to distinguish finer image details also improves. However, increasing the sensor size also leads to higher production costs and greater physical dimensions, both of which pose limitations in the context of ADAS applications where compactness and cost-efficiency are critical considerations [23].

For driver assistance systems involved in environmental perception, a typical specification entails a resolution greater than 15 pixels per degree of field of view. Among these applications, traffic sign recognition imposes particularly stringent requirements on image resolution, especially when the accurate interpretation of additional characters or symbols is necessary. This concept is illustrated in Fig. 8, which demonstrates how varying resolution levels affect the legibility of traffic signs. While the general shape and warning symbols remain discernible at lower resolutions, the identification of supplementary pictograms or textual information becomes increasingly difficult or impossible. In the context of driver monitoring applications, even higher image resolutions may be required, particularly for functions such as eye tracking that rely on the precise detection of subtle facial features [13].

Fig. 8. Effect of decreasing resolution using the example of a traffic sign (480 × 650/72 × 96/36 × 48/24 × 32/18 × 24/12 × 16) [23]

Colour

In the area of advanced driver assistance systems, complementary metal-oxide-semiconductor (CMOS) image sensors, commonly employed in automotive imaging, are primarily responsive to the visible (VIS) and near infrared (NIR) regions of the electromagnetic spectrum. To enable differentiation across colour channels, these sensors incorporate colour filters that segment incoming light into its constituent spectral components.

Colour fidelity offers substantial advantages in both front-view and surround-view camera applications. In surround-view systems, a lifelike visual representation on the driver's display is essential for intuitive scene interpretation.

Conversely, in front-view systems, the capacity to accurately distinguish between discrete colour channels plays a critical role, particularly in the detection of features such as lane markings, as illustrated in Fig. 9.

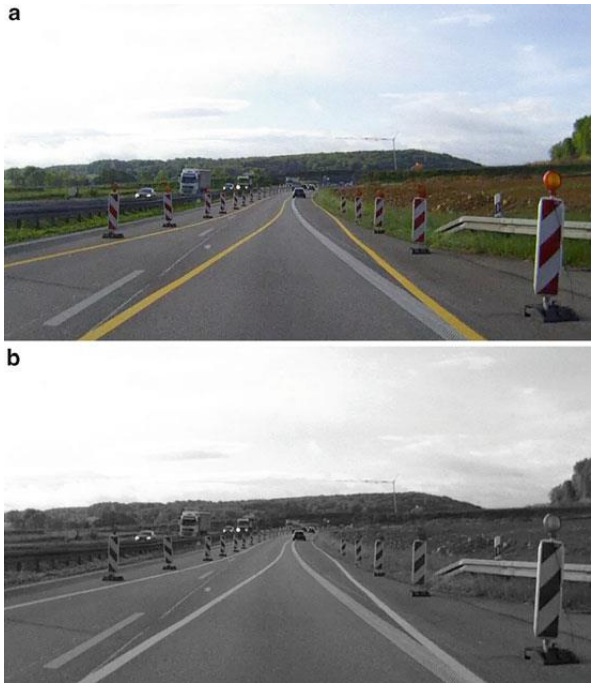

Fig. 9. Importance of colour separation for the detection of lane markers without filtering (a) and with filtering (b) [23]

Dynamic range

The dynamic range (DR) of a camera system defines its ability to simultaneously capture details in both low-light and high-intensity regions within the same image frame. More specifically, it is quantified as the ratio between the luminance of the darkest and the brightest pixels that the sensor can accurately record.

In dark areas, the dynamic range is limited by the noise limit of the image sensor, and in bright areas by the saturation limit of the image sensor. In addition to the image sensor, the dynamic range of the camera lens and the optical path define the overall system dynamic range [1].

The dynamic range of the lens is adversely affected by stray light. In addition, effects such as ghosting and flare can occur, which reduce the image quality, especially in strong front light situations. For stationary objects, the dynamic range can be increased using a so-called high dynamic range (HDR) function (Fig. 10). To do this, sever-

al images of the object with different exposures are taken and put together in a very short time. Since the series of images is taken at a different time, this function is not appropriate for moving objects. The same applies to images taken while a vehicle is moving [3].

Fig. 10. Illustration of a traffic scene with a high dynamic range [23]

Noise

A camera's dynamic range and sensitivity are affected by the "noise" of the sensor. The most common cause of the noise is the so-called dark current. In this case, electrons are triggered and read out incorrectly, for example, due to thermal processes in the pixel. The magnitude of this current increases with temperature and exposure time. For this reason, it is often necessary to cool camera systems or provide sufficient ventilation. Another source of noise is the readout noise, which occurs when electrons are converted into voltage [21].

3.2.3. Image sensor technology

There are two fundamental architectures of digital image sensors for image processing: charge-coupled device (CCD) and complementary metal oxide semiconductor (CMOS). Image sensors are able to convert incident photons into electrical charges. The technology is based on the photoelectric effect, which generally refers to the release of electrons from metallic surfaces through the incidence of light. A distinction is made here between the interior and the exterior photo effect.

The external photo effect describes the phenomenon where electrons are released from a metal when photons hit it. The frequency of the electromagnetic radiation must exceed the characteristic limit frequency of each metal. Above this frequency, electron emission occurs even at very low light intensity [20].

In the case of the internal photo effect, the electrons only detach from their molecular structure, but not from the material. If the energy of the photons is greater than the energy difference between the valence and conduction bands of the photodiode material, the electrons are raised into the conduction band. Free electrons and positively charged holes are created. The change in electrical conductivity can be recorded [2].

A CCD sensor consists of a large number of light-sensitive semiconductor elements arranged over a surface. These semiconductor elements are pixels, individual photodetectors that capture the incident photons of light and convert them into an electrical signal. During the exposure time, the released electrons are collected in a potential well. The accumulated amount of charge is proportional to the intensity of the incident light and the exposure time [21]. To do this, the released charges must be transported to an A/D converter through many small steps, vertical and horizontal shift registers.

Charge-coupled device (CCD) sensors are available in several distinct architectural configurations, including interline transfer CCDs, full-frame CCDs, and frame transfer CCDs. Among these, the interline transfer CCD offers a notable advantage through its use of an "electronic shutter" mechanism, which enables the rapid acquisition of multiple images per second as well as extremely short exposure times. To facilitate this function, each light-sensitive pixel is paired with an adjacent non-photosensitive unit, which serves as a temporary memory cell. This memory cell is equipped with a cover and a light-blocking shield to prevent any additional light exposure, thereby preserving the integrity of the stored charge. Once the exposure phase concludes, the accumulated charges are swiftly transferred from the active pixels into the shielded memory cells. Subsequently, these charges are sequentially read out through vertical and then horizontal shift registers. At the end of this readout chain, the signal is amplified and converted into a voltage for further image processing purposes [21].

Similar to charge-coupled device (CCD) sensors, complementary metal-oxide-semiconductor (CMOS) sensors operate on the principle of the photoelectric effect, whereby incident photons are converted into electrical charges. The primary distinction between CMOS and CCD technologies lies in the method by which the captured electrical signals are transmitted and processed. In CMOS architecture, each photodiode is paired with a parallel capacitor that accumulates charge generated by the incoming photocurrent. The resulting voltage across this capacitor is directly proportional to the intensity of the incident light and the duration of exposure. Unlike CCD sensors, where collected charges are sequentially transferred to a centralized readout amplifier, CMOS sensors assign an individual amplifier to each pixel. which directly provides the analogue signal processor with this capacitor voltage. In the case of CMOS sensors, several transistors are associated with the light-sensitive diodes, which convert the accumulated charges into measurable voltages. As a result, pixels can be read independently without the need for serial charge transfer, as is required in CCD-based systems. The advantage of this architecture is a reduction in blooming effects, which can occur under conditions of overexposure. However, a notable drawback is that the inclusion of additional transistors within each pixel reduces the effective light-sensitive area, thereby diminishing the sensor's overall light collection efficiency. Consequently, CMOS sensors may exhibit inferior performance in low-light environments, as less image information is captured [5]. Nonetheless, like their CCD counterparts, advanced CMOS sensors are capable of discharging all pixels simultaneously, capturing an image, and proceeding with synchronous readout. To implement global shutter functionality, additional transistors must be integrated into each pixel, which further reduces the available photosensitive surface area and may negatively impact image quality.

A CMOS sensor, like many others, can only distinguish between black and white. To enable colour recognition, colour filters are needed that divide the light into the primary colours red, green and blue. Ultimately, only one of the colours is supplied to each pixel.

4. Future directions

Since camera sensors have their advantages and shortcomings, the integration of multiple heterogeneous sensors has emerged as a fundamental strategy for achieving robust and precise environmental perception and spatial localization. However, because these sensors are not inherently co-located within a common spatial framework, accurate calibration is required to establish their relative coordinate relationships and to effectively combine their sensing capabilities.

With the rapid advancements in deep learning technologies, online camera calibration has become increasingly feasible and operationally efficient. This calibration approach entails dynamically updating sensor parameters during operation, thereby allowing the system to adapt to changes in the camera's position or the surrounding environment. Such adaptability can be realized through the application of deep learning algorithms, which are capable of modeling the complex, nonlinear relationships between intrinsic and extrinsic camera parameters and the corresponding image data. Learning-based calibration frameworks hold significant promise for transforming practices within the automotive sector. By enhancing the precision of camera-based vision, online calibration plays a crucial role in improving the reliability of tasks such as object detection [13].

The integration of deep learning-based calibration techniques within multi-sensor platforms may substantially improve the effectiveness of sensor fusion by aligning and harmonizing data from different sources. This enhancement is particularly advantageous in complex operating conditions, including low-light environments, visual occlusions, and adverse weather scenarios. Moreover, leveraging deep learning for the calibration of multiple sensors is likely to yield more stable and accurate outcomes than those typically achieved with conventional calibration methods. These developments outline several promising directions for future research in the domain of deep learning-based camera calibration.

As this field continues to evolve, it is anticipated that numerous additional opportunities for advancement and innovation will emerge. Furthermore, the broader application of these technologies is expected to exert a transformative influence across various sectors in the years to come.

5. Conclusions

Camera systems constitute a foundational element in the architecture of ADAS and are instrumental in enabling the gradual transition toward higher levels of vehicle autonomy. Owing to their capacity to acquire high-resolution visual data, automotive cameras are employed extensively for a wide range of perception tasks, including lane detection, traffic sign recognition, object classification, and distance estimation.

This study has presented a comprehensive overview of the technical configurations and operating principles of monocular and stereo camera systems within ADAS platforms. Particular attention has been devoted to the requirements for camera calibration, which plays a pivotal role in ensuring the geometric and functional accuracy of vision-based systems. Both intrinsic and extrinsic calibration procedures are necessary to mitigate distortions and to maintain reliable environmental perception under real-world operating conditions.

The integration of camera systems into multi-sensor platforms, while offering enhanced perception capabilities, introduces additional challenges related to sensor alignment and data fusion. In this context, recent advances in deep learning have facilitated the development of online calibration methods capable of dynamically adjusting sensor parameters in response to operational or environmental variations. These approaches show considerable potential in improving the robustness and precision of vision-based ADAS functions, particularly in adverse scenarios such as low-visibility or rapidly changing lighting conditions.

Given the increasing regulatory emphasis on safety and the anticipated proliferation of ADAS features in the global vehicle fleet, further research into calibration methodologies, image processing algorithms, and sensor integration strategies is essential. Continued progress in these domains will be critical to support the deployment of reliable, scalable, and cost-effective autonomous driving technologies in the near future.

Acknowledgements

This work was supported by Volkswagen Poznan sp. z o.o. The investigations were carried out within the Implementation Doctorate Program of the Ministry of Education and Science, realized in the years 2021–2025, and were supported by the Research Subsidy SBAD: 0415/SBAD/0353.

Nomenclature

ABS	anti-lock braking system
ADAS	advanced driver assistance system
ASIC	application-specific-integrated circuits
CCD	charge-couple device
CMOS	complementary metal oxide semiconductor
DR	dynamic range
DSP	digital signal processor
ESP	electronic stability program
FOV	field of view
FPGA	field programmable gate arrays
HDR	high dynamic range
HFOV	horizontal field of view
IPC	interprocess communication
LiDAR	light detection and ranging
NIR	near-infrared
OEM	original equipment manufacturers
VFOV	vertical field of view
VIS	visible

Bibliography

[1] Brzozowski M, Parczewski K. Problems related to the operation of autonomous vehicles in adverse weather conditions. Combustion Engines. 2023;194(3):109-115. https://doi.org/10.19206/CE-168805

[2] Chodavarapu VP, Titus AH, Cheung M. CMOS photodetectors. Photodiodes – World Activities in 2011. InTechOpen; 2011. https://doi.org/10.5772/20194

[3] De Locht C. Dynamikerweiterung bei CMOS Bildsensoren. Elektroniknet. 2009. Available from: https://www.elektroniknet.de/elektronik/halbleiter/dynamikerweiterung-bei-cmos-bildsensoren-1612.html

[4] Gat I, Benady M, Shashua A. A monocular vision advance warning system for the automotive aftermarket. SAE Technical Paper. 2005-01-1470. 2005. https://doi.org/10.4271/2005-01-1470

[5] Gouveia LCP, Choubey B. Advances on CMOS image sensors. Sensor Rev. 2016;36(3):231-239. https://doi.org/10.1108/SR-11-2015-0189

[6] Jiménez F, Naranjo JE, Anaya JJ, García F, Ponz A, Armingol JM. Advanced driver assistance system for road environments to improve safety and efficiency. Transp Res Procedia. 2016;14:2245-2250. https://doi.org/10.1016/j.trpro.2016.05.240

[7] Jin CB, Kakani V, Kim H, Kumbham M, Park D, Nguyen VH. Feasible self-calibration of larger field-of-view (FOV) camera sensors for the advanced driver-assistance system (ADAS). Sensors. 2019;19(15):3369. https://doi.org/10.3390/s19153369

[8] Jumaa BA, Abdulhassan AM, Abdulhassan AM. Advanced driver assistance system (ADAS): a review of systems and technologies. Int J Adv Res Comput Eng Technol. 2019; 8(6):231-234. www.ijarcet.org

[9] Kelkar A, Jondhale D, Borade R, Juneja I, Haran Y, Pawar RG. Revolutionizing the driving experience: enhancing safety and comfort using ADAS. 7th Int Conf on Computing, Communication, Control and Automation (ICCUBEA). 2023:1-4. https://doi.org/10.1109/ICCUBEA58933.2023.10392267

[10] Khan MA, El Sayed H, Malik S, Zia MT, Alkaabi N, Khan J. A journey towards fully autonomous driving – fueled by a smart communication system. Veh Commun. 2022;36: 100476. https://doi.org/10.1016/j.vehcom.2022.100476

[11] Kotur M, Lukić N, Krunić M, Lukač Ž. Camera and LiDAR sensor fusion for 3D object tracking in a collision avoidance system. 2021 Zooming Innovation in Consumer Technologies Conference (ZINC); 2021:198-202. https://doi.org/10.1109/ZINC52049.2021.9499281

[12] Kukkala VK, Tunnell J, Pasricha S, Bradley T. Advanced driver-assistance systems: a path toward autonomous vehicles. IEEE Consum Electron Mag. 2018;7(5):18-25. https://doi.org/10.1109/MCE.2018.2828440

[13] Lai Z. Cameras in advanced driver-assistance systems and autonomous driving vehicles. Li Y, Shi H (eds). Advanced driver assistance systems and autonomous vehicles. Springer. Singapore 2022. https://doi.org/10.1007/978-981-19-5053-7_7

[14] Morignot J, Rastelli P, Nashashibi F. Arbitration for balancing control between the driver and ADAS systems in an automated vehicle: survey and approach. Proc IEEE Intell Vehicles Symp. 2014:575-580. https://doi.org/10.1109/IVS.2014.6856577

[15] Radičević V, Vranješ M, Samardžija D, Kovačević J. Moving objects tracking using motion vectors with implementation on a real ADAS platform. 2022 Int Symp ELMAR. 2022:61-66. https://doi.org/10.1109/ELMAR55880.2022.9899803

[16] Rezaei M. Computer vision for road safety: a system for simultaneous monitoring of driver behaviour and road hazards [PhD thesis]. University of Auckland. Auckland 2014.

[17] Roland Berger. Advanced driver assistance systems: a ubiquitous technology for the future of vehicles. Available from: https://www.rolandberger.com/en/Insights/Publications/Advanced-Driver-Assistance-Systems-A-ubiquitous-technology-for-the-future-of.html

[18] Singh S. Understanding technology behind self-driving cars: stereo vision. Labellerr 2022. Available from: https://www.labellerr.com/blog/understanding-technology-behind-self-driving-cars-stereo-vision/

[19] Śmieja M, Wierzbicki S, Mamala J. CAN network in real time on board systems. Combustion Engines. 2017;171(4): 211-214. https://doi.org/10.19206/CE-2017-436

[20] Stefanov KD. CMOS image sensors. IOP Publishing Ltd; United Kingdom 2022. https://doi.org/10.1088/978-0-7503-3235-4

[21] Stemmer Imaging. Available from: https://www.stemmer-imaging.com/s/?language=en_US

[22] Volkswagen internal documentation. ADAS sensors. [Internal source]

[23] Winner H, Hakuli S, Lotz F, Singer C. Handbook of driver assistance systems. Springer International Publishing. Cham 2015. https://doi.org/10.1007/978-3-319-12352-3

[24] Zhang Z. A flexible new technique for camera calibration. IEEE Trans Pattern Anal Mach Intell. 2000;22(11):1330-1334. https://doi.org/10.1109/34.888718

Paulina Babuchowska, MEng. – Doctoral Student in Faculty of Civil and Transport Engineering, Poznan University of Technology, Poland.
e-mail: *paulina.babuchowska@doctorate.put.poznan.pl*

Prof. Ireneusz Pielecha, DSc., DEng. – Faculty of Civil and Transport Engineering, Poznan University of Technology, Poland.
e-mail: *ireneusz.pielecha@put.poznan.pl*

Article citation info:
Ludwiczak A, Kozakiewicz A, Chachurski R, Karczewski M. Measurements of exhaust emissions from the GTM-120 UAV turbine engine using atmosFIR measuring equipment. Combustion Engines. 2025;203(4):164-169. https://doi.org/10.19206/CE-208515

Aleksandra LUDWICZAK
Adam KOZAKIEWICZ
Ryszard CHACHURSKI
Mirosław KARCZEWSKI

Combustion Engines
Polish Scientific Society of Combustion Engines

Measurements of exhaust emissions from the GTM-120 UAV turbine engine using atmosFIR measuring equipment

ARTICLE INFO

Received: 8 May 2025
Revised: 8 July 2025
Accepted: 22 July 2025
Available online: 22 August 2025

The article provides a detailed description of the design and key parameters of the GTM-120 turbine engine, along with flow calculations for this power unit at a selected operating point. These calculations were performed using GasTurb software, which is also capable of assessing nitrogen oxide emissions. Additionally, the article outlines the test stand and the methodology used to determine toxic compounds emitted by the engine. It analyzes the measured results of various exhaust components produced during the engine's operation, specifically focusing on the levels of nitrogen oxides and carbon oxides as influenced by rotational speed and temperature. Conducted studies have established a testing methodology for aviation turbine engines, based on the type of analyzer used. This methodology will facilitate the evaluation of other aviation turbine engines on stationary test stands.

Key words: *miniature aircraft turbine engine, emissions of toxic compounds, exhaust gas measurements*

1. Introduction

UAV turbine engines are becoming increasingly popular as power units for testing toxic emissions and exploring the use of sustainable aviation fuels. They serve as a cost-effective alternative in the initial stages of research, facilitating the transfer of knowledge to full-size power units that power large aircraft. Analyzing the composition of exhaust gases in UAV engines is essential for evaluating their efficiency, environmental impact, and the potential for optimizing the combustion process. These engines are utilized both as power sources in experimental aircrafts and as units for scientific research. Through this, researchers can examine the exhaust gas composition, which helps assess the quality of the combustion process, identify issues related to incomplete combustion, and evaluate harmful emissions such as nitrogen oxides, carbon monoxide, and unburned hydrocarbons. This analysis not only enables improvements in engine efficiency but also reduces the engine's negative environmental impact.

Increasing numbers of authors are addressing the issue of exhaust emissions in their works. Measurements are conducted using portable exhaust analyzers, such as the SEMTECH DS, and the results obtained are analyzed [7, 19].

Research has also been conducted on the GTM 120 engine mentioned in this article. The authors have previously analyzed particle emissions [15], studied noise identification [4], and performed numerical analyses of cold flow in the GTM-120 engine [8]. This article focuses on measurements of toxic combustion compounds emissions, which will enhance the existing literature on this engine and facilitate future numerical analyses of the combustion process, along with comparisons of the results obtained. As a result, upcoming studies will be able to explore possibilities, such as modifying the combustion chamber design.

2. Research object

The tests were conducted using a test bench manufactured by TomSerwis, along with a specially modified version of the GTM 120 engine based on the WML WAT (Faculty of Mechatronics, Armament and Aerospace – Military University of Technology) design. This engine was equipped with measuring probes, which allowed for pressure and temperature measurements. These tubes were installed in the combustion chamber casing, located behind the compressor and in front of the turbine (Fig. 1).

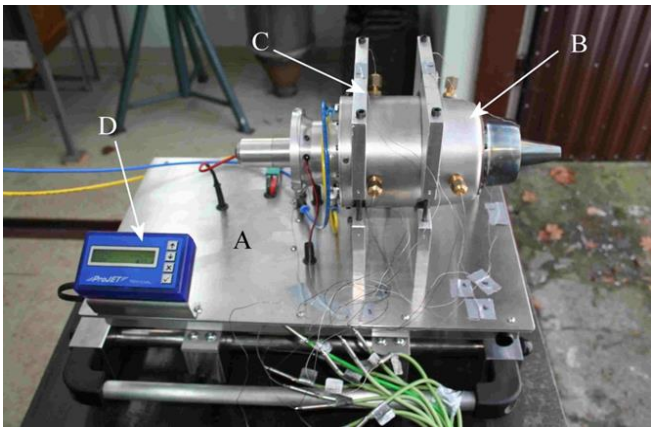

Fig. 1. Test bench of the GTM 120 engine: A – test bench; B – GTM 120 engine; C – engine bed; D – GSU panel of the engine control system

The engine for the GTM 120 is designed similarly to miniature turbine engines, offering a thrust of up to 500 N (see Fig. 2). Its design is based on the KJ 66 engine and is produced by several companies, including JETPOL [12], JetCat [11], AMT Netherlands [2], Turbine Solutions [23], PBS Aerospace [21], King Tech Turbines [14], Frank Turbine Engine Systems [5], ALM-Meca Engineering [1], JetBeetle [10], and others [13].

The engine features an axially symmetrical subsonic inlet, with an electric starter mounted on three supports in front of it. It utilizes a single-stage radial compressor and an annular combustion chamber that incorporates jet injectors and evaporators located in the rear section. The compressor rotor is driven by a single-stage axial turbine. Although this engine model underwent further modifications by the man-

ufacturer to meet current research needs, which did not affect its performance, the original exhaust system – featuring a central cone that extends beyond the nozzle outlet cross-section was retained.

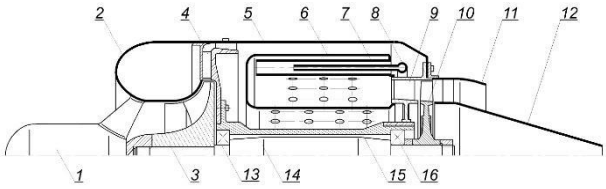

Fig. 2. Cross section of the GTM 120 engine and its basic elements: 1 – electric starter, 2 – inlet, 3 – compressor rotor, 4 – diffuser, 5 – combustion chamber case, 6 – combustion liner, 7 – evaporators, 8 – fuel manifold, 9 – turbine nozzle ring, 10 – turbine rotor, 11 – outlet nozzle, 12 – central cone of the exhaust system, 13, 16 – bearings, 14 – shaft, 15 – shaft sleeve (own elaboration)

The engine is controlled by the Hornet III [9] ProJet electronic system, which generates and sends a signal in the form of the desired voltage value for the electric motor supplying the fuel pump located at the bottom of the mobile test bench platform. The electronic and electrical systems of the engine are powered by a 12 V battery.

Operating parameters of the engine are displayed on the Ground Support Unit (GSU) panel, which works in conjunction with the Hornet III system. The GSU panel allows for starting and stopping the engine, as well as adjusting its operational range. The display shows current values for the exhaust gas temperature (EGT), engine rotor speed, fuel pump supply voltage, and the set engine operating range.

Unlike most engines, this one does not have a typical lubrication system. Instead of oil, a small amount of fuel mixed with 5% oil is supplied to the bearings. The engine typically uses aviation fuel (aviation kerosene), but can also operate on other fuels such as diesel oil, biofuels, etc. During testing, JET A-1 fuel mixed with Aeroshell 500 synthetic oil, commonly used in turbine engine lubrication systems, was utilized.

Table 1 presents the basic technical data for the engine in its original version [3].

Table 1. Basic technical data of the GTM 120 engine parameters in the basic version and the actual [3]

Parameter	Unit	Value
Dry engine weight	kg	1.5
Maximum diameter	mm	110
Length	mm	265
Maximum thrust	N	120
Maximum RPM	rpm	110 000
Air mass flow	kg/s	0.3
Compression	–	2.1
Max temperature after the turbine	K	898

2. Determination of flow parameters of the GTM 120 engine

The necessary data for modeling the performance of turbine engines can be found in various literature sources, such as "Propulsion and Power. An Exploration of Gas Turbine Performance Modeling" by Kurzke et al. [16]. Kurzke is also the author of GasTurb, a software program developed for the MTU company that calculates flow parameters in full-size engines. GasTurb is specifically designed for gas turbine performance calculation and optimization. In this work, the GasTurb 14 software was utilized for calculations, which enables the modeling of various basic types of aircraft turbine engines.

The calculations were based on actual engine operating parameters determined from previous tests, specifically a thrust of 127.3 N and a maximum temperature of 950 K behind the turbine. The results of the calculations are shown in Table 2. Additionally, the distribution of the working medium's flow velocity, pressure, and static temperature in key engine cross-sections during operation at maximum range under static conditions (V = 0 m/s, H = 0 m) is illustrated in Fig. 3. Localization of stations at which parameters were calculated is presented in Fig. 4.

Table 2. Results of calculations of the GTM 120 engine operating parameters performed in the GasTurb 14 program

Parameter	Unit	Value
FN	kN	0.13
TSFC	g/kNs	44.1384
WF	kg/s	0.00595
S NOx	g/kg	0.04059
where: FN – thrust, TSFC – specific fuel consumption, WF – mass flow rate of fuel, S NO_x – NO_x content in exhaust gases.		

The S_{NOx} value is determined from the equation:

$$S_{NO_x} = \left(\frac{P_3}{2965\ \text{kPa}}\right)^{0.4} \cdot e^{\left(\frac{T_3 - 826\ \text{K}}{194\ \text{K}} + \frac{6.29 - 100\ war}{53.2}\right)} \quad (1)$$

where: war – water-air-ratio.

The higher nitrogen oxide values observed in the GasTurb 14 may be due to the positioning of the measuring probe, which captures data from a single point. Additionally, the intake of air can affect the readings.

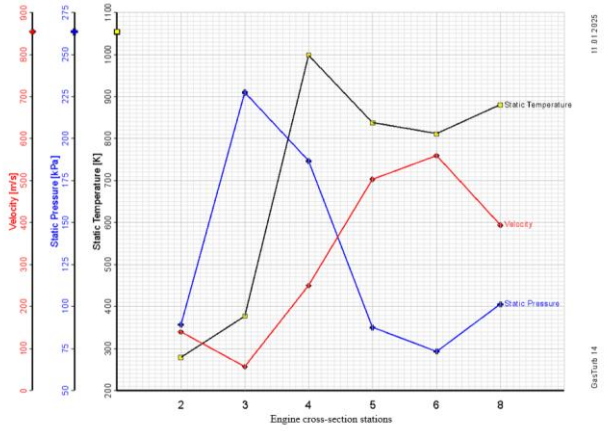

Fig. 3. Distribution of the flow velocity of the working medium and its static pressure and static temperature in characteristic stations of the GTM 120 engine (graph generated by the GasTurb 14 program)

Developing an accurate model of the GTM 120 engine in the GasTurb 14 program proved challenging due to the engine's unique design of the combustion chamber and exhaust system. This complexity made it difficult to select the appropriate input parameters. Nevertheless, the thrust value obtained from the model is within 2.08% of the measured value, and the difference between the measured

and calculated exhaust gas temperatures does not exceed 0.29%.

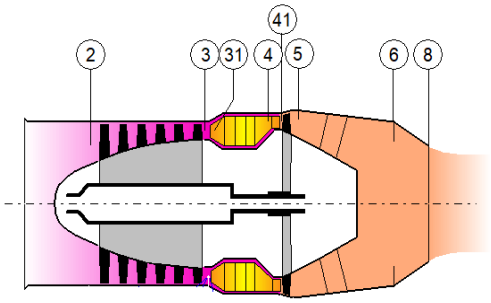

Fig. 4. Engine cross-section with stations, at which parameters were calculated, used in the GasTurb 14 (diagram taken from the GasTurb 14)

3. Research methodology

To measure the exhaust emissions from the GTM-120 the atmosFIR mobile exhaust gas analyzer was utilized. Both the engine and the measuring probe were positioned on a stable base. The measuring station is depicted in Fig. 5.

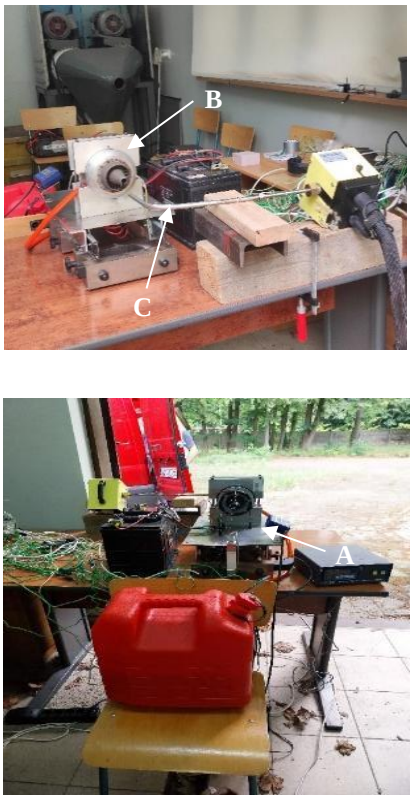

Fig. 5. Measuring station: A –test bench; B – GTM 120 engine; C – measuring probe

The AtmosFIR exhaust gas analyzer is a device made by Protea. It is a multi-component and multi-range analyzer capable of measuring up to 100 different components. This device connects to the PAS-Pro control and data processing program. During the tests, measurements were taken for components such as carbon dioxide, carbon oxides, nitrogen oxides, and sulfur oxides. The specifications and applications of the analyzer are detailed in Table 3. For clarification, the resolution in wavenumbers (cm^{-1}) refers to the instrument's ability to distinguish between closely spaced spectral lines.

Table 3. Protea AtmosFIR analyzer applications and specifications [20]

Typical measurement ranges	0–10 ppm, 0–100 ppm, 0–1000 ppm
Typical detection limit	< 0.2 ppm
Typical spectral resolutions	1 cm^{-1}, 2 cm^{-1}, 4 cm^{-1}, 8 cm^{-1}
Spectral range	485–8500 cm^{-1}
Weight	18–20 kg
Dimensions	440 × 450 × 222 mm

Figure 6 shows an element of the measurement station, which is the central unit of atmosFIR equipment.

Fig. 6. Exhaust gas analyzer atmosFIR

During the measurements, a thermal analysis of the power unit was conducted using a thermal imaging camera. The image captured after completing the measurements is shown in Fig. 7.

Fig. 7. View from the thermal imaging camera after completing the measurements

The measurements of exhaust gas components concentration were conducted over the full engine operation cycle. After starting, the engine automatically increased the rotor speed to approximately 48,000 rpm to assess the parameters of the fuel supply system. It then decreased the speed to 33,000 rpm, which corresponded to idle speed. Following

this, the rotational speed was increased in increments of 20,000 rpm, ranging from 40,000 to 100,000 rpm. The operating range was then expanded to achieve a maximum rotational speed of 110,000 rpm. The rotor speed was subsequently reduced to the idle speed range before the engine was turned off. Each measurement was taken over a period of 2 minutes for every speed range, as shown in Fig. 8.

Fig. 8. Profile of engine test idea

4. Research results

During measurements conducted with the atmosFIR analyzer, we obtained results for a wide range of combustion components from the test object. Due to their predominance and harmful effects, we decided to focus our analysis on carbon dioxide, carbon monoxide, and nitrogen oxides. The concentrations of these components are presented as a function of time, considering the rotational speed [18, 22], and as a function of temperature – Fig. 8 and Fig. 9. To better illustrate the relationship between the amount of nitrogen oxides produced and temperature, we derived a separate characteristic.

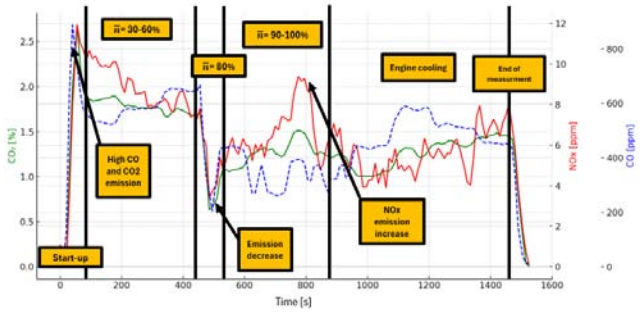

Fig. 9. Measurement results of toxic compounds produced during the operation of the GTM-120 engine as a function of time, considering the ranges of rotational speeds, where: n = 30–60% of maximum rotational speed – engine warm-up, n = 80% of maximum rotational speed – cruise range, n = 90–100% – maximum rotational speed

Figure 8 illustrates the measured data over time, covering a duration of approximately 25 minutes. To enhance clarity, vertical lines indicating the different phases of engine operation have been plotted on the graph.

During the initial phase of engine operation, which is the start-up phase, a high concentration of carbon oxides and carbon dioxide is observed. This phenomenon is typical for turbine engines and results from incomplete combustion shortly after the fuel is injected into the combustion chamber. This observation is further supported by the results shown in Fig. 9, which indicates a low exhaust gas temperature during the engine start-up phase.

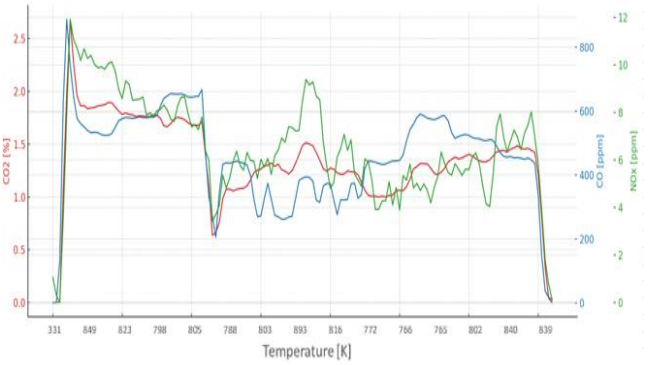

Fig. 10. Results of measurements of harmful compounds produced during the operation of the GTM-120 engine as a function of the measured engine temperature

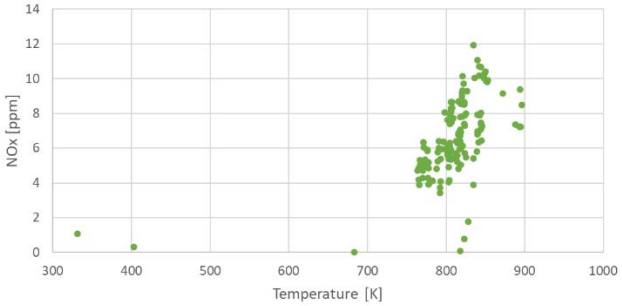

Fig. 11. Measurement results of nitrogen oxides produced during the operation of the GTM-120 engine as a function of the measured engine temperature in front of the turbine

Conversely, Fig. 10 demonstrates that the concentration of nitrogen oxides during this phase remains below 2 parts per million (ppm). In the subsequent phase, which ranges from 30% to 60% of maximum engine speed, the exhaust gas temperature begins to rise, reaching approximately 800 K. This increase in temperature leads to a decrease in the concentrations of CO_2 and CO. As the combustion chamber temperature rises, the concentration of nitrogen oxides in the exhaust gas also increases, peaking at around 11 ppm. During the next phase of engine operation, which corresponds to the cruise range, the engine rotor speed stabilizes at about 80% of the maximum value. In this phase, a notable decrease in the concentration of all analyzed exhaust gas components is observed, indicating that this range represents the optimal operating conditions for maximum combustion chamber efficiency. As the engine reaches its maximum rotational speed, the exhaust gas temperature also escalates, peaking at approximately 896 K. Compared to the cruise phase, the concentrations of CO and CO_2 rise due to the increased fuel supply to the combustion chamber. It is important to note that nitrogen oxides reach their highest concentration during this phase, peaking at around 12 ppm. This relationship aligns with existing literature [17], which indicates that nitrogen oxides typically achieve peak concentrations at elevated exhaust gas temperatures. In the final cooling phase of the engine, there is another increase in the concentrations of carbon oxides and carbon dioxide,

which correlates with a drop in temperature and a decline in combustion efficiency. As the measurements conclude, a reduction in the concentration of all combustion components is recorded. The accompanying Table 4 presents the maximum concentration values of harmful combustion components across the various phases of engine operation.

Table 4. Maximum concentrations of combustion components during individual engine operation phases

Engine operating phase	CO_2 [%] max rpm	CO [ppm]	NO_x [ppm]
1. Start-up	2.7	887.1	1.1
2. Warm-up	1.9	667.3	11.0
3. Cruising range	0.6	204.7	3.4
4. Maximum range	1.5	439.6	11.9
5. Cooling	1.0	585.0	8.0
6. End of operation	0.0	0.4	1.8

The data from Table 4 are also presented in the form of approximation graphs.

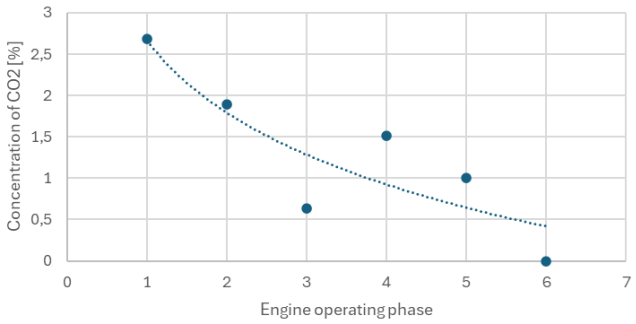

Fig. 12. Concentration of CO_2 during individual engine operation phases – approximation graphs

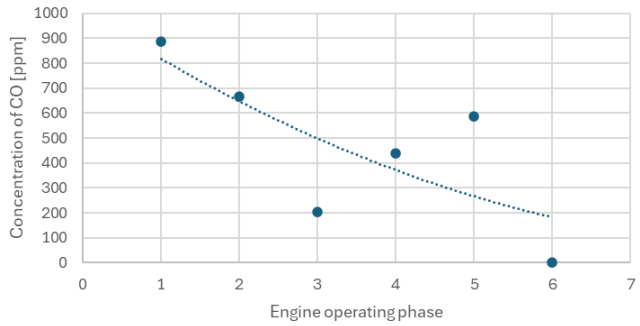

Fig. 13. Concentration of CO during individual engine operation phases – approximation graphs

Calculations performed using the GasTurb 14 program indicated a NO_x concentration of 0.04059 g/kg at maximum rotational speed. However, actual tests revealed this value to be significantly lower, at 11 ppm, or 0.011 g/kg. This discrepancy amounts to about 73%. By employing an exhaust gas analyzer, we can accurately determine the range of nitrogen oxide emissions and use the results to adjust the parameters in the GasTurb 14 software. The team is working to reduce discrepancies between results. Recently, retests were conducted using a modified system and a new engine. The results are still in development.

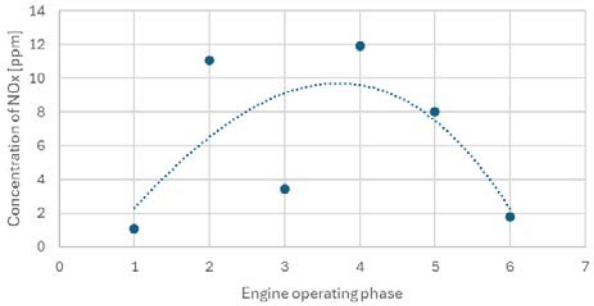

Fig. 14. Concentration of NO_x during individual engine operation phases – approximation graphs

5. Conclusions

The research conducted has determined the influence of the range of work of a UAV turbine engine on the formation of toxic combustion components. The presence of nitrogen oxides at low rotational speeds results from the combustion of nitrogen contained in the fuel, while at high rotational speeds it is associated with a high combustion temperature. At the same time, comparing the results of calculations carried from GasTurb 14 with the results of actual tests allowed analyses of selection of parameters in the software. It may be the direction of further work to obtain greater data compatibility. UAV turbine engines can, with the adoption of appropriate ranges of coefficients, be a reference for full-size power units. Carrying out analyses on small-sized engines allows us to develop measurement methodologies, thanks to which it is possible to make tests carried out on full-size engines more economical. Thanks to the research on UAV engines, it is also possible to test the use of sustainable aviation fuels [6, 24] in further work, which will allow us to compare the amount of exhaust gases in relation to standard aviation fuel.

Acknowledgements

This work was supported by UGB Nr 531-000039-W200-22.

Nomenclature

CO_2 carbon dioxide
CO carbon monoxide
EGT exhaust gas temperature
GSU ground support unit
NO_x nitrogen oxides

Bibliography

[1] ALM Meca Engineering. www.alm-meca.com (accessed on 2025 Jun 22).

[2] AMT Netherlands. www.amtjets.com (accessed on 2025 Jun 22).

[3] Chmielewski M, Gieras M. Small gas turbine GTM-120 bench testing with emission measurements. J KONES Powertrain and Transport. 2015;22(1). https://doi.org/10.5604/12314005.1161610
[4] Czarnecki ML, Lech A. GTM-120 micro gas turbine engine noise identification. Combustion Engines. 2024;199(4):52-59. https://doi.org/10.19206/CE-189743
[5] Frank Turbine Engine Systems. www.frankturbine.com (accessed on 2025 Jun 22).
[6] Gawron B, Białecki T, Dzięgielewski W, Kaźmierczak U. Performance and emission characteristic of miniature turbojet engine fed Jet A-1/alcohol blend. Journal of KONES. 2016;23(1):123-130. https://doi.org/10.5604/12314005.1213540
[7] Gawron B, Białecki T. Measurement of exhaust gas emissions from miniature turbojet engine. Combustion Engines. 2016;167(4):58-63. https://doi.org/10.19206/CE-2016-406
[8] Gieras M, Stańkowski T, Computational study of an aerodynamic flow through a micro-turbine engine combustor. Journal of Power Technologies. 2012;92(2):68-79. https://papers.itc.pw.edu.pl/index.php/JPT/article/download/317/483/0
[9] Hornet III V2.0. Instructions manual. ProJET electronic components.
[10] JetBeetle. www.jetbeetle.com (accessed on 2025 Jun 22).
[11] JetCat. www.jetcat.de (accessed on 2025 Jun 22).
[12] JETPOL. www.jetpol.tech (accessed on 2025 Jun 22).
[13] Kamps T. Model jet engines. World Modeller's Series. Traplet Publication 2005.
[14] KingTech Turbines. www.kingtechturbines.com (accessed on 2025 Jun 22).
[15] Kurzawska-Pietrowicz P. Comprehensive analysis of particle emissions from miniature turbojet engine. Combustion Engines. 2025;200(1):12-18. https://doi.org/10.19206/CE-192421
[16] Kurzke J, Halliwell I, Hill R. Propulsion and power. An exploration of gas turbine performance modeling, Springer. Cham 2025. https://doi.org/10.1007/978-3-031-65026-0
[17] Łapucha R. Komory spalania silników turbinowo-odrzutowych. Procesy, obliczenia, badania (in Polish). Biblioteka Naukowa Instytutu Lotnictwa. Warszawa 2004.
[18] Merkisz J, Cwojdziński L. Badania emisji związków szkodliwych spalin turbinowego silnika odrzutowego podczas przedstartowej próby samolotu Su-22 (in Polish). Autobusy. 2013;159(3).
[19] Merkisz J, Markowski J, Pielecha J. Emission tests of the F100-PW-229 turbine jet engine during pre-flight verification of the F-16 aircraft. Conference: Air Pollution 2013; 174. https://doi.org/10.2495/AIR130191
[20] Młu.pl. https://mlu.pl/produkty/protea-atmosfir/ (accessed on 2025 Jun 22).
[21] PBS Aerospace. www.pbsaerospace.com (accessed on 2025 Jun 22).
[22] Rogers F, Arnott P, Zielinska B, Sagebiel J, Kelly KE, Wagner D et al. Real-time measurements of jet aircraft engine exhaust. J Air Waste Manage. 2005;55(5):583-593. https://doi.org/10.1080/10473289.2005.10464651
[23] Turbine Solutions. www.turbinesolutions.co.uk (accessed on 2025 Jun 22).
[24] Turizo-Donado A, López-Zapata S, Arias S, Agudelo JR. Methodologies for alternative jet fuels testing on small-scale reaction engines. Revista Facultad deIngeniería Universidad deAntioquia. 2025;114:95-111. https://doi.org/10.17533/udea.redin.20240836

Aleksandra Ludwiczak, MEng. – Faculty of Mechatronics, Armament and Aerospace, Military University of Technology, Warsaw, Poland.
email: *aleksandra.ludwiczak@wat.edu.pl*

Prof. Ryszard Chachurski, DSc., DEng. – Faculty of Mechatronics, Armament and Aerospace, Military University of Technology, Warsaw, Poland.
email: *ryszard.chachurski@wat.edu.pl*

Prof. Adam Kozakiewicz, DSc., DEng. – Faculty of Mechatronics, Armament and Aerospace, Military University of Technology, Warsaw, Poland.
email: *adam.kozakiewicz@wat.edu.pl*

Mirosław Karczewski, DEng. – Faculty of Mechanical Engineering, Military University of Technology, Poland.
email: *miroslaw.karczewski@wat.edu.pl*

Article citation info:
Lageweg S, Kubica G. Comparison of traction properties of an N3 category vehicle with a conventional and electric drivetrain. Combustion Engines. 2025;203(4):170-177. https://doi.org/10.19206/CE-208514

Stefan LAGEWEG
Grzegorz KUBICA

Combustion Engines
Polish Scientific Society of Combustion Engines

Comparison of traction properties of an N3 category vehicle with a conventional and electric drivetrain

ARTICLE INFO

Received: 25 November 2024
Revised: 23 May 2025
Accepted: 22 July 2025
Available online: 27 August 2025

The article presents the traction properties of the drive systems installed in a DAF LF vehicle belonging to the N3 category. Based on technical data of the drive systems – both the compression ignition engine (CI) and electric motor specifications – external characteristics containing the power and torque curves of the engines were developed. On their basis, the traction characteristics of the vehicles were determined, showing graphs of movement resistance and driving force. Graphs of the obtained accelerations, dynamic indicators, and vehicle acceleration simulations were also developed. The calculations considered the case in which the vehicle weight corresponds to the gross vehicle mass (GVM), which allowed for obtaining results close to real conditions.
Based on the comparison of the traction properties of both vehicles, it was observed that electric vehicles have much better dynamic parameters. These differences may be very important when moving in mountain conditions. The excessive propelling force in the system generated by the electric motor allows overcoming hills at a much higher speed, reducing the speed difference between trucks and passenger vehicles. It was found that increasing speed on mountainous roads can lead to significant road safety improvements. The simulation of vehicle acceleration allowed for the determination of the time after which the maximum vehicle speed was achieved.

Key words: *heavy-duty, electric, characteristics, traction, acceleration*

1. Introduction

The continuous development of drivetrain systems contributes to the improvement of the driving characteristics of vehicles. This is especially noticeable in heavy-duty vehicles. This type of vehicle is characterized by a high torque demand in connection with carrying heavy loads [1]. An important aspect occurring while configuring trucks is their drive system, which can differ a lot depending on the purpose of the vehicle [24]. Changes in the configuration of the propelling system have an influence on the traction properties as well as on the energy consumption [12, 21].

Thanks to constant developments of energy storage technology using battery cells and technologies based on the use of energy stored in the form of hydrogen, the range of electric trucks has noticed a marked increase compared to vehicles introduced to the market in the previous decade. Vehicles using energy stored in batteries are nowadays capable of covering an operational range of 400–500 km without the need to recharge their energy reserves. The development of cell production technology has also made it possible to increase their ability to fast charge and superfast charge [5, 22, 23]. Currently produced battery cells are characterized by much higher energy density values and lower initial costs [5, 7].

In the past, battery charging was a very problematic issue, especially for heavy-duty vehicles. The infrastructure did not enable trouble-free operation of electric vehicles due to the insufficient number of charging points or network problems during charging related to exceeding peak network power values. High-power stations designed for fast charging using direct current were one of the causes of network disruptions. Thanks to the introduction of charging stations equipped with BESS technology (battery energy storage system), it is possible to reduce the demand for peak power in the electrical network [2, 14, 17].

Due to the fact that the limitations related to the range and lack of charging possibilities or the duration of the process are becoming much less oppressive, the use of vehicles with an electric drive system is being increasingly considered [20].

This is confirmed by the fact that the number of registrations of delivery vehicles and trucks increased by 66% in the period January–December 2023 compared to the same period in 2022 [10]. It is also worth mentioning the significant development that has been made in terms of the efficiency and flexibility of combustion engines and the significant reduction in exhaust emissions. Modern CI heavy-duty (HV) engines stand out due to the wide range in which the maximum torque is achieved. These are often rotational speeds slightly higher than the idle speed. Work related to the development of combustion engines also focuses on developing new alternative fuels and methods of obtaining them [3, 13, 18, 19].

Despite many advantages modern CI combustion engines offer, these are still not able to match the parameters of electric motors made using permanent magnet synchronous motors (PMSM) technology, with which HDVs are mainly fitted. The configuration of the gearbox drive systems (number of gear ratios, their values), and the value of the final drive ratio make these vehicles stand out with above-average traction properties [11].

The article focuses on the comparison of traction characteristics, allowing to determine, among others, the ability to overcome hills and the time it takes for the vehicle to reach maximum speed. For this purpose, an example vehicle belonging to the N3 vehicle category was taken into account – a representative of the urban and local distribution sector – the field in which electric trucks are currently most commonly used.

2. Research object

The test object is an HDV belonging to the N3 category with a total permissible weight exceeding 19 tons. The DAF LF vehicle (Fig. 1) was first offered with a conventional propulsion system and from 2021 to 2023 with an electric driveline. The truck had been sold as a chassis intended for further body build development. The container built on the vehicle frame was recreated using a computer design program – a CAD program. The installation height and external dimensions were determined based on photo documentation and engineering graphics provided by the chassis manufacturer. Vehicle versions equipped with combustion engines can develop different power and torque values, depending on specifications. For comparison purposes, the variant with the most powerful PX-7 series engine was considered. This engine stands out due to its high torque available in a wide range of rotational speeds. A conventional vehicle has been equipped standardly with a six-speed gearbox with a manual shifting mechanism.

Fig. 1. DAF LF Electric [6]

The electric vehicle (EV) is powered by the SUMO HD HV3500 electric motor and has no gearbox. The vehicle's engine is connected directly via a cardan shaft to the drive axle equipped with a final drive.

Detailed technical data of the vehicle are presented in Table 1.

Table 1. Basic technical data of the researched vehicles

	DAF LF	DAF LF Electric
Engine	PX-7	SUMO HD HV3500
Maximum power [kW]	172	370
Rotational speed of max power [rpm]	2000–2300	3400
Maximum torque [Nm]	900	3445
Rotational speed of max torque [rpm]	1000–1700	150–1050
Main gear ratio	5.13	5.57
Number of gears	6	–
1st gear ratio	6.75	–
2nd gear ratio	3.6	–
3rd gear ratio	2.13	–
4th gear ratio	1.39	–
5th gear ratio	1	–
6th gear ratio	0.78	–
Tire size	R22.5 315/70	
Payload [kg]	11,310	11,700
GVM [kg]	19,000	

According to the information provided by the vehicle manufacturer, both versions of the vehicle have a GVM of exactly 19 tons. The aerodynamic properties of the vehicles are the same.

This selection of the research facility allowed for the elimination of variables unrelated to the drive system itself.

3. Methodology

To prepare the traction characteristics of the vehicle, it was necessary to determine the external characteristics of the engines. For this purpose, technical data provided by the vehicle manufacturer and manufacturers of drive system components were used.

Determining the operating characteristics of the electric motor required reproducing the torque waveform, and, on this basis, the engine power was determined. That enabled the creation of the power and torque charts for both engines. The comparison of the vehicle's traction characteristics consisted of determining the external characteristics of the engines and the vehicle's movement resistance.

In the following, the forces acting on the vehicle during its movement were determined. Due to the small impact of some resistances, they were not taken into account in the calculations. The most important resistances to the movement of vehicles were taken into account. In the research, the following forces were taken into consideration:

- rolling resistance
- aerodynamic resistance
- hill resistance.

The calculated aerodynamic drag forces can differ from the real forces as a result of the needed assumptions. Due to the lack of a defined air resistance coefficient in the longitudinal direction from the vehicle axis (C_x factor), it was necessary to determine the value used in the calculations. The value was selected based on the table [4] and on the author's knowledge about the development of aerodynamic properties in trucks and buses.

The frontal surface area for the vehicle under consideration was determined by plotting the outline of the body on the cabin design. The contours of the vehicle's front obtained in this way were printed on graph paper, and its area was calculated.

In the calculations, in order to make the results more realistic, the vehicle weight value resulting from the maximum permissible total vehicle weight was assumed.

As part of the study, a simulation of vehicle acceleration was also carried out in the speed range from 0 km/h to 90 km/h. It was decided to set a maximum speed equal to the speed at which the vehicles can move due to the electronic speed limiter, which is obligatory for every HDV. The simulation is based on the use of maximum instantaneous accelerations and a simple algorithm that allows for the simulation of gear changes. When the previously defined maximum engine speed is reached, a gear change takes place, which lasts a certain time; in the case of a manual gearbox, this time is set at 1.5 seconds [14]. The gear change time is understood as the time from the moment of disengaging the clutch to the moment of engaging it after the next gear is selected.

4. Engine characteristics

4.1. Paccar PX-7

In the case of the Paccar PX-7 engine, creating a graph of the engine's external characteristics involved reflecting the power and torque curves. In this case, the manufacturer provided full external characteristics of the engine. The developed power and torque values are presented in Table 2. The characteristic curve is shown in Fig. 2.

Table 2. Power and torque values for the propulsion engines

n [rpm]	Power [kW]		Torque [Nm]	
	SUMO HD HV3500	PX-7	SUMO HD HV3500	PX-7
0	0	–	2800	–
100	34	–	3230	–
200	72	–	3445	–
300	108	–	3445	–
400	144	–	3445	–
500	180	–	3445	–
600	216	–	3445	–
700	252	–	3445	–
800	288	–	3445	–
900	325	–	3445	–
1000	361	94	3445	900
1100	370	104	3214	900
1200	370	113	2946	900
1300	370	122	2719	900
1400	370	132	2525	900
1500	370	141	2357	900
1600	370	151	2209	900
1700	370	160	2079	900
1800	370	165	1964	874
1900	370	169	1861	848
2000	370	172	1768	822
2100	370	172	1683	783
2200	370	172	1607	747
2300	370	172	1537	714
2400	370	163	1473	650
2500	370	153	1414	586
2600	370	–	1360	–
2700	370	–	1309	–
2800	370	–	1263	–
2900	370	–	1219	–
3000	370	–	1178	–
3100	370	–	1140	–
3200	370	–	1105	–
3300	370	–	1071	–
3400	370	–	1040	–

4.2. Sumo HD HV3500

On the basis of catalogue data, engine calibration instructions, and the torque curve (Fig. 2), the external operating characteristics of the electric motor were determined. For this purpose, the following patterns were used:

For the rotational speed range of 0–1000 rpm, the power was determined using the power dependence on the torque and engine speed (1). Torque for rotational speeds 1026–3400 rpm had been determined by using the same formula.

$$P = \frac{T\,[Nm] \cdot n[rpm]}{9554.14}\,[kW] \tag{1}$$

where: P – power, T – torque, n – rotational engine speed

In order to recreate the linear torque waveform in the rotational speed range from 0 till 1026 rpm, the directional equation of a straight line passing through two points (equation 2) plotted on the torque waveform was used (Fig. 2).

Points coordinates:

- A (0 rpm; 2800 Nm)
- B (150 rpm; 3445 Nm).

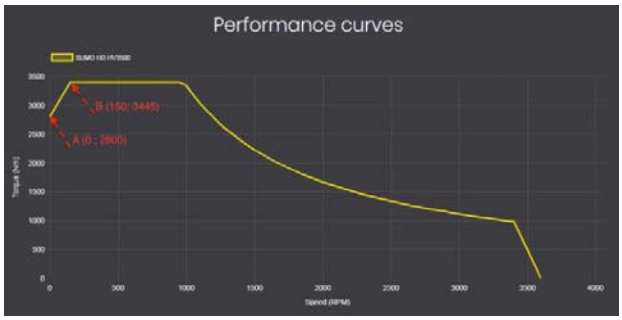

Fig. 2. Torque curve of the SUMO HD HV3500 engine [1]

$$y - y_A = \frac{y_B - y_A}{x_B - x_A} \cdot (x - x_A) \tag{2}$$

where: XA, Y_A – coordinates of point A, X_B, Y_B – coordinates of point B.

The calculated power and torque values depending on the engine speed are presented in Table 2. The operating characteristic curve of the drive unit is shown in Fig. 3.

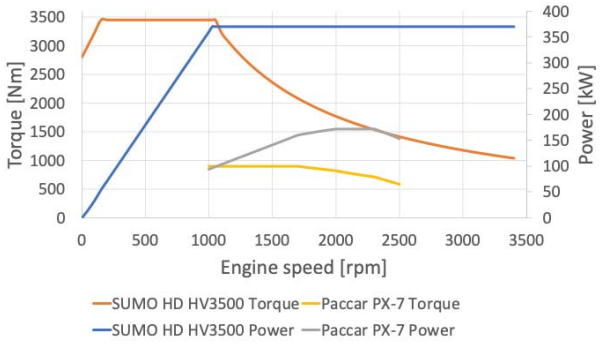

Fig. 3. Engine characteristics

5. Forces acting on the vehicle

Both versions of the vehicle – conventional and electric are characterized by identical movement resistance, which results from the previously made assumptions and technical data of the bodywork. Identical values were maintained for all coefficients during the calculation.

Due to the small share of specific types of resistance in the total resistance force of all vehicle movement resistances acting on it, it was decided to ignore their influence. Forces not included in the simulation include resistances such as:

- resistance of wet surface
- friction resistance of bearings
- resistances related to the tires and resulting from the operation of the suspension and steering system, i.e. wheel turning resistance, toe-in resistance, tire deformation
- resistance resulting from turning – driving in a straight direction was assumed.

Rolling resistance

In the case of HDVs, rolling resistance has a much greater impact on the vehicle's energy consumption than in the case of passenger vehicles, which results directly from

the large weight of the vehicles. The rolling resistance (3) coefficient f_t depends, among other things, on the square of the vehicle's speed and the surface resistance coefficient. For the calculations, an approximate value corresponding to dry asphalt $f_0 = 0.01$ was assumed. To calculate the force the formula (3) was used.

$$F_t = G \cdot f_t = mgf_o(1 + kv^2)\ [N] \tag{3}$$

where: G – vehicle weight, f_t – rolling resistance coefficient, m – mass, g – acceleration of gravity, f_0 – surface rolling resistance coefficient, k – surface coefficient, v – speed.

5.1. Aerodynamic forces

Due to the assumptions made, the simplified formula was used to calculate aerodynamic resistance. The formula uses a conversion factor of 0.047, which replaces the speed converter, allowing the use of speed expressed in kilometres per hour instead of meters per second, and is the result of using the average air density. The formula (4) was used to calculate the aerodynamic drag force.

$$F_a = 0.047 \cdot A \cdot c_x \cdot v^2\ [N] \tag{4}$$

where: Fa – aerodynamic resistance force, A – frontal vehicle surface, c_x – aerodynamic coefficient, v – speed.

The approximate frontal area of the vehicle assumed in the calculations was determined of 8.59 m^2 [9].

5.2. Hill resistance force

The hill's resistant forces are a major obstacle for HDVs when trying to maintain a constant speed or accelerate. The significant weight of the vehicle means that even small slopes can generate very high resistance values, which the vehicle must additionally overcome. In many cases, a significant difference in the vehicle's speed is observed when entering a slope.

The values of the slope angle of driveways are regulated by law and depend on the class the road fulfills and its function. In case of local and access roads with a maximum speed of 30 km/h or 40 km/h, the gradient can be up to 12%. However, heavy goods vehicles mostly travel on highways and urban roads. The permissible slope angle of two-lane roads in the city area is in the range of 4–5% [16].

In order to determine the slope resistance value, a slope of 4% was assumed, and the equation underneath (5) was used.

$$F_w = G \cdot \frac{h_w}{100\%}\ [N] \tag{5}$$

where: F_w – hill resistance force, G – vehicle weight, h_w – slope.

5.3. Propelling force

The formula (6) was used to calculate the driving force in the drive system. The calculations required the assumption that the efficiency of the drive system was 0.9. During the calculations of driving forces for the electric vehicle that was not equipped with a gearbox, the gear ratio was omitted from the calculations

$$F_n = \frac{T \cdot i_{SB} \cdot i_o \cdot \eta_m}{r_d}\ [N] \tag{6}$$

where: F_n – propelling force, T – torque, i_{SB} – gear ratio, i_o – main gear ratio, η_m – mechanical efficiency, r_d – dynamic radius of rolling tyre.

5.4. Vehicle speed

Determining the vehicle speed for each gear was necessary to create graphs of driving force, dynamic index and acceleration. These values change depending on the instantaneous speeds (7) at which the vehicle is moving.

$$v = 0.377 \frac{r_d \cdot n}{i_{sb} \cdot i_o} \left[\frac{km}{h}\right] \tag{7}$$

where: v – speed, r_d – dynamic radius of rolling tyre, n – rotational engine speed [rpm], i_{SB} – gear ratio, i_0 – main gear ratio.

5.5. Vehicle acceleration

Calculating the vehicle acceleration (8) allowed to determine the maximum acceleration values the vehicle can achieve in a given gear and at given driving speeds. This value depends on the value of the vehicle dynamic index and rotating masses for a given gear. These two values will mainly determine the increase in acceleration.

$$a = \frac{(D - f_t) \cdot g}{\delta} \left[\frac{m}{s^2}\right] \tag{8}$$

where: a – acceleration, D – dynamic index, f_t – rolling resistance coefficient, g – acceleration of gravity, δ – rotating mass coefficient.

5.6. The condition of maintaining adhesion

The condition of maintaining adhesion is particularly important from the point of view of vehicle movement safety. It expresses the maximum value of the driving force on the vehicle wheels, at which wheel slippage does not occur. The condition is expressed by the equation (9).

$$F_n = F_p \tag{9}$$

$$\frac{M_r \cdot i_{SB} \cdot i_0 \cdot \eta_m}{r_d} = G_T \cdot m_t \cdot \mu \tag{10}$$

where: F_n – propelling force, F_p – Wheel adhesion force, M_r – Torque used by setting the vehicle into motion, i_{SB} – gear ratio, i_0 – main gear ratio, η_m – mechanical efficiency, r_d – dynamic radius of rolling tire, G_T – drive axle load, m_t – mass displacement factor, μ – rolling resistance coefficient for dry asphalt.

The maximum engine torque that can be used to start the vehicle without losing traction of the drive wheels on a dry asphalt surface was determined based on equation (10). The maximum torque is determined by formula (11). The drive axle load was assumed to be 11.5 tons. The displacement coefficient m_t was assumed to be 1.15, and the gear ratio values for both vehicles were used. The results for the first three gears are presented in table 3.

$$M_r = \frac{G_T \cdot m_t \cdot \mu \cdot r_d}{i_{SB} \cdot i_0 \cdot \eta_m} \tag{11}$$

where: M_r – torque used by setting the vehicle into motion, G_T – drive axle load, m_t – mass displacement factor, μ – rolling resistance coefficient for dry asphalt, r_d – dynamic radius of rolling tire, i_{SB} – gear ratio, i_0 – main gear ratio, η_m – mechanical efficiency.

The maximum torque values that can be used when starting vehicles with no risk of skid are higher than the maximum torque values generated by vehicle engines. There is no risk of wheel slippage during acceleration using the maximum torque on a dry asphalt surface.

Table 3. Adhesion force of the drive axle and the maximum torque values for each gear of the vehicles

	DAF LF Electric	DAF LF
Gt [N]	112815.0	112815.0
Fp [N]	116763.5	116763.5
Mr (i_1) [Nm]	11319.9	1820.8
Mr (i_2) [Nm]	–	3414.1
Mr (i_3) [Nm]	–	5770.3

Using equation (12), the maximum values of the gear ratios of the gearbox had been determined. Depending on the torque used to bring the vehicle into motion, the ratio value changes. The results are presented in Table 4.

$$i_{SB} = \frac{G_T \cdot m_t \cdot \mu \cdot r_d}{M_r \cdot i_0 \cdot \eta_m} \quad (12)$$

where: G_T – drive axle load, m_t – mass displacement factor, μ – rolling resistance coefficient for dry asphalt, r_d – dynamic radius of rolling tire, M_r – torque used by setting the vehicle into motion, i_0 – main gear ratio, η_m – mechanical efficiency.

Table 4. Calculated ratio values depend of the torque used by setting the vehicle into motion

DAF LF Electric		DAF LF	
M_r [Nm]	i_{SB}	M_r [Nm]	i_{SB}
900	12.6	400	30.7
1300	8.7	500	24.6
1700	6.7	600	20.5
2100	5.4	700	17.6
2500	4.5	800	15.4
2900	3.9	900	13.7
3300	3.4	–	–
3500	3.23	–	–

The i_{SB} ratios presented in Table 4 are the maximum values, depending on the starting torque, at which traction of the drive wheels is maintained. All the ratios determined are greater than those available to both vehicles.

6. Discussion of results

6.1. Introduction

The calculated values of the resistance forces were approximated to decimal digits. Due to the lack of knowledge of the maximum design speed of the vehicles, calculations were made for speeds up to 120 km/h. In EU member states, heavy goods vehicles must be equipped with an electronic speed limiter limiting the speed to a maximum of 90 km/h. However, the manufacturer could have provided a different maximum speed for the vehicle in order to create excess driving force.

In order to maintain the accuracy of the calculations, they were carried out starting from a speed of 0 km/h and increasing it by 1 km/h until the speed of 120 km/h was reached.

The forces of resistance and the driving force of the vehicles are presented in the graph in Fig. 4. It shows the values of the driving force for both drive systems.

6.2. Acceleration ability

The driving and resistance force graph (Fig. 4) shows the change in driving force for each gear and movement resistances for vehicles as a function of vehicle speed.

Analyzing the graph, it can be seen that the driving force curve for an electric vehicle is characterized by a lower maximum value of the driving force in comparison with the first gear. In addition to a combustion engine vehicle, it is continuous and flattened in the speed range from 5 km/h to about 40 km/h.

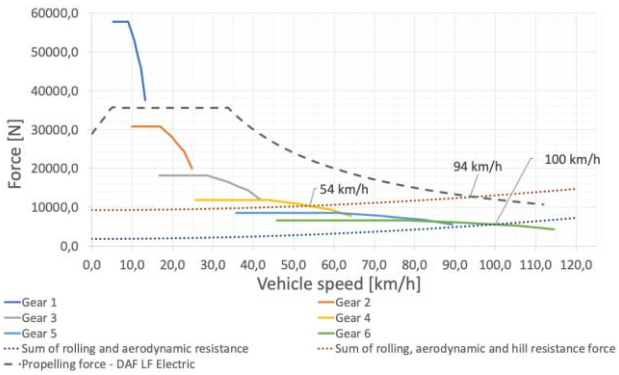

Fig. 4. Forces acting on the vehicles

The continuity of the driving torque is caused by the lack of a gearbox and the ability to reach high rpm values by the electric motor.

This enables accelerating without momentarily losing the driving force on the vehicle's wheels. It is crucial not to lose momentum when overcoming steep slopes. A gear change causes a lack of driving force. In extreme cases, this may cause the vehicle to stop and then roll down the slope or damage components such as the clutch by overheating it while trying to move the vehicle from a still stand. A vehicle powered by a drive system based on an electric motor allows for continuous acceleration without fear of losing driving torque.

The excess driving force of the electric vehicle allows it to overcome a 4% gradient at a maximum speed of 94 km/h. Knowing that the vehicle must be equipped with a system limiting the maximum speed to 90 km/h, it can be stated that the vehicle is capable of overcoming hills with the same or slightly bigger slopes without losing speed while driving at maximum speed. The DAF LF is capable of overcoming the same gradient at a maximum speed of around 54 km/h and requires shifting down from sixth to the fourth gear. This causes significant inconvenience in driving the vehicle because overcoming a four percent gradient with a conventional vehicle requires much more attention from the driver and is less economical due to the change in driving speed and the need to accelerate again after overcoming the hill. Losing speed by 36 km/h can also lead to dangerous situations, e.g., when driving on a motorway. The difference in speed of vehicles moving on a gradient on expressways can be even 86 km/h in this case. A passenger car hitting the back of a truck is comparable to a collision with a stationary obstacle at a speed resulting from the speed difference between the vehicles. The dynamic characteristics graph (Fig. 5) for the vehicles illustrates the excess driving force. Comparing both drive systems, it can be noticed that the conventional drive is characterized by a driving force surplus greater than the electric system only in first gear. The electric vehicle is character-

ized by a generally greater driving force surplus at speeds higher than the minimum driving speed in the second gear for the traditional drive.

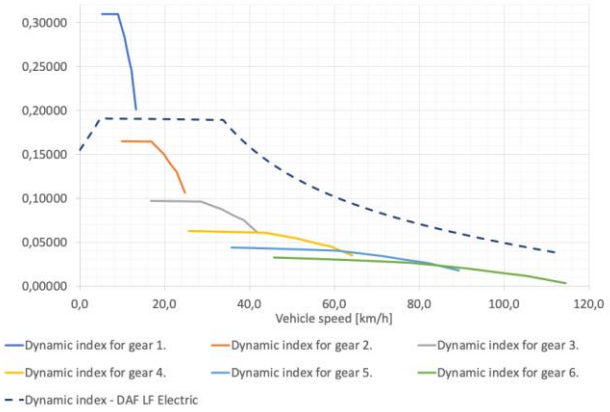

Fig. 5. Dynamic indexes for the vehicles

Comparing the dynamic index graph (Fig. 5) with the acceleration graph (Fig. 6), it can be seen that the acceleration values for the second gear in the DAF LF are higher than for the first gear. This is due to the much higher value of the rotating mass coefficient for the first two gears, which are $\delta_1 = 4.19$ and $\delta_2 = 1.9$. The lower mass of the rotating elements in the drive system and gearbox affects the vehicle acceleration values and its energy consumption [23].

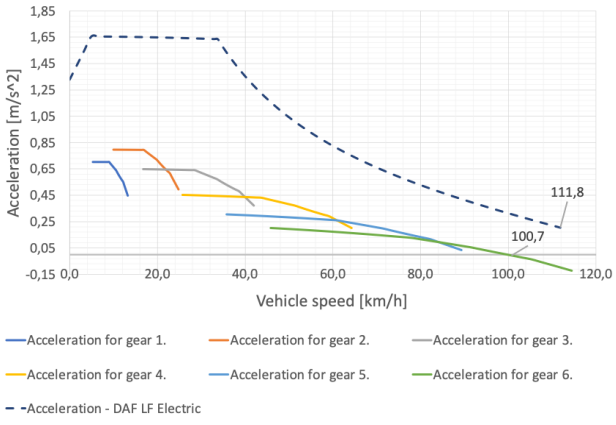

Fig. 6. Vehicle accelerations

The small number of rotating elements in the electric vehicle drive contributes to the improvement of the dynamic qualities of this vehicle. Analyzing the above placed graphs, it can also be seen that the truck is capable of reaching a higher maximum speed, which is approximately 110 km/h, only due to reaching the maximum rpm of the electric engine. Higher maximum speeds that these vehicles are able to reach may result in an increase in the speed limit for trucks in the future, if, together with the capabilities of the drive system, the braking system, and suspension are improved. Increasing the maximum speed at which trucks can move may result in improved safety as a result of the reduced speed difference between vehicles. To precisely determine the effects of changing the speed limit for trucks, research should be carried out by road safety specialists. Currently, these statements are only assumptions.

The simulation of vehicle acceleration was made for the speed range of 0–90 km/h. Figure 7 shows how the speed of the vehicles changed over time. It can be seen that the need to change gears increased the time needed to reach the speed limited by the electronic speed limiter. During the gear change in the vehicle, no torque is supplied. This causes the vehicle to move with a negative acceleration value due to the resistance of movement; as a result, its speed decreases. The simulation was carried out for an even surface. The simulation shows that the electric vehicle is able to reach 90km/h in just 26 seconds, while the conventional HDV needs 83 seconds more.

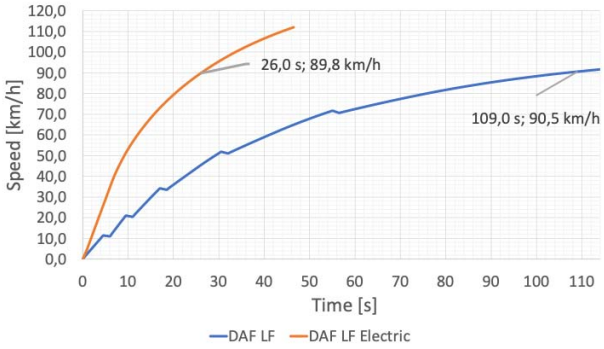

Fig. 7. Acceleration simulation

The time it takes for the vehicle to reach a given speed is important because it will affect the fluidity of vehicle traffic, especially in urban areas where many intersections are placed. This will lead to an increase in the number of vehicles passing intersections. Similarly to the overall higher speed of driving on an incline by an electric vehicle, reaching a given speed faster can contribute to road safety improvements. Currently, it can be very often noticed that passenger cars starting at an intersection firstly accelerate more than they can and then decelerate due to the slower HDV in front of them. That phenomenon results in a wave effect, which in radical conditions can lead to a complete stop of the vehicles far behind the truck. It is possible that with the participation of electric vehicles, this phenomenon will disappear due to the reduction of the difference in acceleration between passenger cars and trucks.

6.3. Speeds at slopes

When analyzing the maximum speeds of climbing hillsides with different degrees of inclination, it can be seen that a vehicle equipped with an electric drive is able to overcome them at higher speeds (Fig. 8) however, it should be noted that the maximum possible slope on which the vehicle can drive equals 18%, while for a vehicle with a conventional drive system it is 30%. The largest speed difference between the vehicles is 41.4 km/h for a hillside of 4%, and the smallest for 18% and equals 6.8 km/h.

The speed curve of overcoming slopes with increasing inclination in the case of a vehicle with a traditional drive system takes the form of an exponentially decreasing function. In the case of a vehicle with an electric drive, the speed in the initial phase decreases proportionally to the value of about 10% of the grade. Then the line of the maximum speed of overcoming hills becomes gentler, and be-

tween the slope value of 16% and the maximum, it drops significantly.

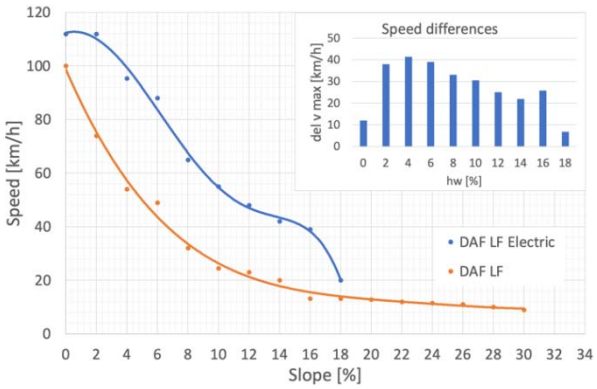

Fig. 8. Vehicle speed and the differences between their maximum values

In connection with the above advantages of electric drives, it can be assumed that in the future, further development of manufacturing techniques will enable the construction of lighter vehicle structures. Changes to Regulation 96/53/EC consist of changes to Article 9a related to the maximum vehicle length, allowing registration of 90cm longer vehicles after 1 September 2020, under the condition that this does not increase the vehicle's load capacity, and these changes will improve the aerodynamic properties and safety of the vehicle. With the development of electromobility and the popularization of electric heavy goods vehicles, proposals have appeared to introduce changes to the regulations that would allow for an increase in the permissible total masses for electric vehicles by four tons. The above study of the traction properties of an electric vehicle confirms the validity of the desire to introduce changes. However, it is necessary to bear in mind issues related to decelerating and bringing to a stillstand vehicles with a greater mass. Simulation studies should be carried out and verified in real conditions in order to determine to what extent an increase in vehicle mass by four tons will affect the vehicle's braking distance, which directly relates to road safety.

7. Conclusions

The traction properties of the drive system of a vehicle equipped with an electric motor causes a significant improvement in vehicle movement properties thanks to the use of these engines for propulsion. The different properties of electric vehicles compared to combustion-powered vehicles suggest that these vehicles may be used in specific conditions. The use of electric motors to support the drive by creating a hybrid vehicle is a good solution to improve the vehicle's traction properties and maintain a large operational range of the vehicle. In addition, the following conclusions can be specified:

1. The maximum acceleration of an electric vehicle is double the maximum of a vehicle with a conventional drivetrain. No need for gear changes increases the acceleration ability and makes it continuous – not interrupted.
2. The electric vehicle characterizes a short time needed to reach the maximum speed (26 seconds), which is possible due to high acceleration values and continuous drive torque.
3. A conventional vehicle can drive on slopes up to 30% while the electric vehicle has the ability to overcome hills up to 18%, but it drives on them at higher speeds.
4. The biggest difference in speed while driving on terrain elevations is 41.4 km/h for a 4% slope.
5. Higher speeds while overcoming slopes by the electric vehicle can cause a smaller risk of rear-end collisions with cars.
6. Carrying out research in the field of road safety is essential to determine the influence of electric trucks and their traction properties on safety, and to determine the ability of increasing speed limits and GVM by 4 tons.

To reach a higher speed on slopes, a very high torque is needed. Using the highest torque of the engine for a long time can cause a rapid increase in energy consumption and affect the maximum 280 km operational range. Due to the ability of regenerative braking, it is possible to partly reduce the declining rate of the vehicle range depending on the mass of the truck [6].

Nomenclature

a	acceleration
A	frontal vehicle surface
BESS	battery energy storage system
CAD	computer aided design
CI	compression ignition
C_x	aerodynamic coefficient
D	dynamic index
EV	electric vehicle
f_0	surface rolling resistance coefficient
f_t	rolling resistance coefficient
F_a	aerodynamic resistance force
F_n	propelling force
F_t	rolling resistance force
F_w	hill resistance force
g	acceleration of gravity
G	vehicle weight
GVM	gross vehicle mass
h_w	slope
HV	heavy-duty
HDV	heavy-duty vehicle
i_0	main gear ratio
i_{SB}	gear ratio
k	surface coefficient
m	mass
n	rotational engine speed [rpm]
P	power [kW]
PMSM	permanent magnet synchronous motor
r_d	dynamic radius of rolling tyre
T	torque [Nm]
v	speed
X_A, Y_A	coordinates of point A
X_B, Y_B	coordinates of point B
δ	rotating mass coefficient
η_m	mechanical efficiency

Bibliography

[1] Bernatchez O. 4 new powertrain options available with increased performances. https://www.danatm4.com/4-new-powertrain-options-available-with-increased-performances/

[2] Bertucci JP, Hofman T, Salazar M. Joint optimization of charging infrastructure placement and operational schedules for a fleet of battery electric trucks. 2024 American Control Conference, ACC 2024. Institute of Electrical and Electronics Engineers. 2024:2995-3000. 10644339 https://doi.org/10.23919/ACC60939.2024.10644339

[3] Bielaczyc P, Woodburn J, Joshi A. World-wide trends in powertrain system development in light of emissions legislation, fuels, lubricants, and test methods. Combustion Engines. 2021;184(1):57-71. https://doi.org/10.19206/CE-134785

[4] Biliński J, Błażejewski M, Malczewska M, Szczepiórkowska M, Drag resistance of electric buses and trolleybuses - empirical formulae. TTS Technika Transportu Szynowego 2020;9:48-52. http://yadda.icm.edu.pl/baztech/element/bwmeta1.element.baztech-28e29698-6f1e-4c3f-8bf1-9943f41aceb7/c/BilinskiTTS9.pdf

[5] Campillo J, Dahlquist E, Danilov DL, Ghaviha N, Notten PHL, Zimmerman N. Battery technologies for transportation applications. in: technologies and applications for smart charging of electric and plug-in hybrid vehicles. Springer International Publishing. Cham 2017:151-206. https://doi.org/10.1007/978-3-319-43651-7_5

[6] DAF LF Electric — pojazd ciężarowy o zerowym poziomie emisji spalin przeznaczony do dystrybucji miejskiej. DAF Trucks Polska SP. z o. o. https://www.daftrucks.pl/pl-pl/wiadomosci-oraz-media/news-articles/global/2021/q1/27-01-2021-daf-lf-electric-for-zero-emission-urban-distribution

[7] Hemlecki P, Fabiś P. Formula Student class electric vehicle energy storage – study and design assumptions. Combustion Engines. 2024;198(3):54-61. https://doi.org/10.19206/CE-186164

[8] Karakas O, Seker U, Solmaz H. Modeling of an electric bus using MATLAB/Simulink and determining cost saving for a realistic city bus line driving cycle. Engineering Perspective. 2021;1(2):52-62. https://doi.org/10.29228/eng.pers.51422

[9] Lageweg S. Electric drive development in heavy-duty vehicles and buses [Master's thesis]. Silesian University of Technology. Katowice 2024.

[10] Licznik Elektromobilności: Podsumowanie 2023 r. w sektorze zeroemisyjnego transportu. PSNM – Polskie Stowarzyszenie Nowej Mobilności. 2024. https://psnm.org/2024/informacja/licznik-elektromobilnosci-podsumowanie-2023-r-w-sektorze-zeroemisyjnego-transportu/

[11] Łebkowski A. Electric vehicles trucks – overview of technology and research selected vehicle. Scientific Journal of Gdynia Maritime University. 2017;98:157-166. https://sj.umg.edu.pl/sites/default/files/ZN506.pdf

[12] Mayet C, Welles J, Bouscayrol A, Hofman T, Lemaire-Semail B. Influence of a CVT on the fuel consumption of a parallel medium-duty electric hybrid truck. Math Comput Simulat. 2019;158:120-129. https://doi.org/10.1016/j.matcom.2018.07.002

[13] Orliński P, Sikora M, Bednarski M, Laskowski PP, Gis M, Wiśniowski PK. Evaluation of selected combustion parameters in a compression-ignition engine powered by hydrogenated vegetable oil (HVO). Combustion Engines. 2024; 198(3):34-40. https://doi.org/10.19206/CE-184222

[14] Polat H, Hosseinabadi F, Hasan MM, Chakraborty S, Geury T, El Baghdadi M et al. A review of DC fast chargers with BESS for electric vehicles: topology, battery, reliability oriented control and cooling perspectives. Batteries. 2023;9(2): 121. https://doi.org/10.3390/batteries9020121

[15] Prażnowski K, Drabik D. Analysis of composition of linear acceleration body structure of vehicle during the gear changing. Autobusy – Technika Eksploatacja Systemy Transportowe. 2018;19(6):678-681. http://doi.org/10.24136/atest.2018.155

[16] Rozporządzenie Ministra Transportu i Gospodarki Morskiej z dnia 2 marca 1999 r. w sprawie warunków technicznych, jakim powinny odpowiadać drogi publiczne i ich usytuowanie (in Polish).

[17] Saldanha JJA, Nied A, Trentini R, Kutzner R. AI-based optimal allocation of BESS, EV charging station and DG in distribution network for losses reduction and peak load shaving. Electr Pow Syst Res. 2024;234:110554. http://doi.org/10.1016/j.epsr.2024.110554

[18] Skobiej K. A review of hydrogen combustion and its impact on engine performance and emissions. Combustion Engines. 2025;200(1):64-70. https://doi.org/10.19206/CE-195470

[19] Smolec R, Karpiuk W, Bajerlein M, Waligórski M, Kril P. The use of dimethyl ether (DME) solution in compression ignition engine. Combustion Engines. 2024;198(3):123-128. https://doi.org/10.19206/CE-188832

[20] Verbruggen FJR, Hoekstra A, Hofman T. Evaluation of the state-of-the-art of full-electric medium and heavy-duty trucks. 31st International Electric Vehicle Symposium and Exhibition, EVS 2018 and International Electric Vehicle Technology Conference 2018, EVTeC 2018. B4-5.

[21] Verbruggen FJR, Silvas E, Hofman T. Electric powertrain topology analysis and design for heavy-duty trucks. Energies. 2020;13(10):2434. http://doi.org/10.3390/en13102434

[22] Yamada T, Akisawa A. Effectiveness of high-power chargers at a quick-charging station for electric vehicles. Appl Energ. 2025;377:124623. http://doi.org/10.1016/j.apenergy.2024.124623

[23] Yao C, Chen S, Salazar M, Yang Z. Joint routing and charging problem of electric vehicles with incentive-aware customers considering spatio-temporal charging prices. IEEE T Intell Transp. 2023;24(11):12215-12226. http://doi.org/10.1109/tits.2023.3286952

[24] Zielińska E, Skalski B. Characteristics of traction properties of selected car models. Autobusy: technika, eksploatacja, systemy transportowe. 2016;17(12):1524-1527 http://yadda.icm.edu.pl/baztech/element/bwmeta1.element.baztech-4ce58b40-a854-42b6-b375-32b2d2dce3a8

Stefan Lageweg, MEng. – Faculty of Transport and Aviation Engineering, Silesian University of Technology, Katowice, Poland.
e-mail: *lagewegstefan@gmail.com*

Grzegorz Kubica, DSc., DEng. – Faculty of Transport and Aviation Engineering, Silesian University of Technology, Katowice, Poland.
e-mail: *grzegorz.kubica@polsl.pl*

Article citation info:
Dębowski K, Karczewski M. Evaluation of the repeatability of fuel dosing by the common rail fuel supply system. Combustion Engines. 2025;203(4):178-190. https://doi.org/10.19206/CE-208508

Karol DĘBOWSKI
Mirosław KARCZEWSKI

Combustion Engines
Polish Scientific Society of Combustion Engines

Evaluation of the repeatability of fuel dosing by the common rail fuel supply system

ARTICLE INFO

Received: 6 June 2025
Revised: 12 July 2025
Accepted: 22 July 2025
Available online: 4 September 2025

This study examined the repeatability of fuel dosage in a Common Rail injection system under five operating conditions: idling, full engine load, micro-dosing, full injector load, and high-frequency operation. Using an injection waveform indicator, researchers analyzed the dynamic behaviour of the injection process, including solenoid valve function and signal waveforms, which were compared to injection pressure buildup. Integral and differential injection characteristics were developed for each condition. Results showed the greatest dosing variability during micro-dosing, with a 6.24% variation in injection volume and 7.81% in pressure. In contrast, full engine load showed minimal variation (0.43% and 1.45%). The study concluded that injector component inertia notably impacts dosing consistency, especially at low pressures or short opening times.

Key words: *common rail system, dosage repeatability, single fuel dose, unit dose, IMA code*

1. Introduction

Compression ignition engines continue to be widely used in various types of machinery and vehicles, including construction equipment, agricultural machines, heavy duty trucks, military vehicles, and passenger cars [5]. A key factor contributing to their broad application is the relatively flat torque curve and the generally higher torque output compared to spark ignition engines [11]. The continuous introduction of increasingly stringent exhaust emission standards compels fuel system manufacturers to constantly improve fuel injection systems to meet these regulatory requirements [7]. The implementation of Common Rail systems was a milestone in the development of compression ignition engines. It enabled modern engines to operate more quietly, emit fewer toxic exhaust components, and achieve higher thermal efficiency (with typical compression ignition engines reaching efficiencies around 0.5 compared to 0.4 in spark ignition engines) [1].

The fuel supply system in compression ignition engines is one of the key components affecting exhaust emissions, thermal efficiency, as well as the noise and vibration levels. To meet emission standards and address the demand for reduced fuel consumption and improved engine performance, precise control over the fuel injection process (timing and fuel volume) has become a primary direction in the development of accumulator type fuel systems [13].

Accumulator type fuel systems for compression ignition engines allow for adjustment of multiple injection parameters, including injection pressure, injection timing, duration (and thus the injected dose), and the number of injection phases. The introduction of these systems represented a major technological advancement, which significantly contributed to the reduction of toxic exhaust emissions [23]. The capability of implementing multi-phase injection at pressure levels tailored to engine operating conditions, along with the use of IMA codes allowing the engine control unit to compensate for manufacturing tolerances of individual injectors, has made these systems the standard in modern compression ignition (CI) engines [10].

Despite their relatively high fuel metering precision compared to other fuel systems, discrepancies still exist between the injection parameters intended by the engine control unit and those actually realized. These discrepancies result from various physical phenomena such as pressure wave reflection, fuel compressibility, or changes in fuel properties due to temperature [4]. Fuel temperature increases, among other reasons, as a result of compression in the high-pressure pump. Additionally, due to the arrangement of injectors in the cylinder head and the proximity of high-pressure lines and fuel rail to the heated engine components, the fuel within these elements undergoes heating by absorbing thermal energy from the cylinder head and from compression effects [9].

Given these factors, engineers around the world are conducting studies aimed at understanding the physical phenomena occurring within the fuel system during operation. These investigations are essential for improving compression ignition engines, as a thorough understanding of fuel injection dynamics enables the development of algorithms for improved spray quality control and operating parameter correction. Ultimately, this leads to the design of more fuel efficient engines with reduced emissions of toxic exhaust components and more stable operation.

Ustrzycki et al. presented research on the influence of high-pressure line length on injection process parameters, including fuel dose, injector leakage, and pressure waveform in the injection line upstream of the solenoid injector. The study demonstrated that greater line length leads to greater deviation in injection parameters. This effect is primarily caused by pressure wave oscillations within the high-pressure lines, which depend on fuel pressure, density, and temperature [22].

Tan et al. investigated the influence of injection pressure and injection timing on the combustion characteristics of a high power six cylinder compression ignition engine equipped with a common rail system. The study concluded that increasing the fuel injection pressure reduces exhaust smoke emissions, although it is accompanied by a rise in NO_x emissions. However, combining increased injection

pressure with retarded injection timing during low and medium load conditions resulted in simultaneous reductions in both NO_x emissions and smoke levels due to lower combustion temperatures [25].

Slavinskas and Bendziunas [20] focused their research on the impact of biofuels on injection characteristics. The results showed that injection occurs with the lowest velocity when using biodiesel. Furthermore, the greatest injection delay was also observed with biodiesel, which is attributed to its high density – the highest among all the tested fuels.

Xu et al. [24] examined the effects of the shapes and volumes of individual components in the high-pressure circuit of a Common Rail system on the fuel injection process. Their findings indicated that increasing the volume of the fuel rail up to a certain point can effectively reduce the amplitude of fuel pressure fluctuations within the rail. A similar relationship was observed with the diameter of high-pressure lines: increasing the internal diameter of these lines resulted in reduced pressure fluctuations. However, this improvement was only effective up to a certain threshold, beyond which further increases in diameter led to a deterioration in performance.

Rothrock [19] addressed the issue of pressure wave phenomena and pressure fluctuations in common rail systems. His study demonstrated that pressure wave dynamics in the high-pressure circuit can be controlled to improve the quality of fuel injection. Additionally, the research provided insights into how fuel injection systems should be designed to ensure consistent fuel release rates, regardless of engine speed.

Krogerus and Huthala [12] undertook research aimed at identifying the actual injection timing during pilot injection events in Common Rail systems. They developed a method for identifying the relative duration of injection, which was validated through experimental results. This approach allows for the detection and quantification of injection duration drift. Such data can be used for adaptive injection control, enabling the adjustment of injection duration for each cylinder to ensure uniform fuel delivery.

In their study, Chau et al. [4] investigated fuel injection rate, which plays a crucial role in the design and optimization of processes aimed at improving engine efficiency and reducing emissions. Experimental results showed that the injection delay decreases as the injection pressure increases. Additionally, it was observed that the actual injection duration exceeds the duration of the electrical control signal applied to the injector.

Bai et al. [2] conducted experiments to evaluate the effectiveness of a control strategy for mitigating injection dose fluctuations during multiple injection events. The researchers proposed a correction based control strategy in which the input parameters included the relative damping coefficient of the fuel, rail pressure, time interval between injections, and the duration of the injector control signal. Experimental results demonstrated that the proposed correction strategy effectively reduced injection dose fluctuations, with the average fluctuation in individual injection volume decreasing by as much as 44.66%.

The issue of injection dose variability was addressed by Ma et al. [14], who focused on the uneven fuel delivery caused by differences in fuel temperature. Specifically, they investigated the cold start behaviour of a common rail equipped engine at low ambient temperatures. Based on their findings, the volume of fuel injected during a single injection event decreases with a drop in fuel temperature. Additionally, it was observed that the penetration depth of the spray also diminishes as the fuel temperature decreases.

Cavicchi et al. [3] investigated the deviations in injection parameters caused by short intervals between consecutive injections. Their study demonstrated that the properties of biodiesel influence pressure wave oscillations, injection variability, and overall injection rate. Furthermore, the time delay between successive injections significantly affects the parameters of the second injection [15].

Nguen et al. [16] conducted an experimental study to evaluate the accuracy of fuel injection using an injection system mounted on a test bench equipped with a Zeuch type injection analyser. The results showed that for single injection events replicating individual phases of injection, the standard deviation of both injection rate and volume was low. However, in split injection mode, these deviations were significantly larger. Moreover, these parameters were found to depend on injection pressure, the time interval between the parts of the split injection, and pressure wave phenomena occurring in the rail, fuel lines, and the injector itself.

The aforementioned studies illustrate the diversity and complexity of the challenges engineers must address to develop engines that are both fuel efficient and environmentally friendly. A review of the available literature indicates that most injection related studies focus on the influence of various factors – such as fuel type, fuel temperature, geometrical characteristics of common rail system components, and physical phenomena within the system – on the injection process. Some researchers have analyzed injection quality under different injection strategies. Notably, there is a lack of studies addressing the repeatability of consecutive single injection events, which would allow the assessment of an injector's ability to deliver consistent fuel doses.

This study is motivated by the aforementioned research gap and focuses on evaluating the ability of a solenoid injector to perform repeatable injections under five representative engine load states. The limited attention given to this issue may be attributed to the use of Injector Quantity Compensation (IMA – *Injektor Mengen Abgleich*) codes by injector manufacturers. Despite the application of IMA codes, the engine control unit (ECU) cannot precisely predict the injector's behaviour. By applying a control signal of a given voltage and current for a defined duration, the ECU expects the injected fuel quantity to match the injector’s flow characteristics associated with a specific IMA code [6].

The ECU can modify the parameters of the control signal supplied to the injector solenoid based on engine operating data, such as crankshaft speed or even angular acceleration during the power stroke in each cylinder [2]. However, for very small variations in the operating parameters of individual cylinders, the ECU may not apply any correction to the injector control signal. Theoretically, the engine operates according to nominal parameters, but in practice, the individual fuel injection events may differ slightly, potentially affecting the emission of toxic exhaust components – particularly particulate matter. For this reason, the

present study investigates the injection dose repeatability of a solenoid injector used in a Common Rail system [16].

Due to the introduction of increasingly stringent exhaust emission standards for internal combustion engines, research on fuel injection systems has largely focused on spray quality and the combustion process of the air-fuel mixture within the engine's combustion chamber. When studies regarding the fuel injection process are published, they are primarily concerned with the main injection dose. At present, as the main fuel injection process has been extensively optimized and the injection of large doses is precisely controlled by the engine control unit, small fuel doses remain problematic in terms of injection precision, accuracy, and repeatability. These small doses play a significant role in determining the emission levels of toxic exhaust components.

It should also be noted that during one full engine cycle, the injector performs a single main injection event, characterized by high injection pressure and a relatively long injector opening time. In contrast, small volume injections, often referred to as micro injections (e.g., pilot or post injections), are executed multiple times within a single engine cycle. Therefore, it is essential to investigate the stability and repeatability of small-volume injections.

The objective of the present study was to assess the injection dose repeatability of a solenoid injector used in common rail fuel systems by employing indirect measurement methods. These methods involved injecting fuel into a long measurement line.

The test conditions proposed in this study are representative of the operating conditions of a compression ignition engine. In such engines, fuel injection occurs at the end of the compression stroke – when the pressure in the combustion chamber is at its highest. This pressure acts upon the nozzle surface, the nozzle holes, and the fuel spray itself. During the experimental investigation, similar pressure conditions were replicated, exerting force on the nozzle tip and the injected fuel stream. In the test setup, the combustion chamber was simulated by a dedicated measurement section consisting of a pipe with a defined cross section, in which pressure was regulated using a control valve. This allowed the injection process to take place under conditions closely resembling those found in real engine operation.

2. Object and research methodology

The tests were carried out based on a brand new BOSCH electromagnetic injector, marked with code 0445110038, from a Renault Espace III car equipped with a 2.2 DCI engine. This engine is characterized by the following parameters: power – 96 kW, torque – 290 Nm, compression ratio – 18.3. The common rail system of this engine is powered by a high-pressure pump marked CP1H3 with the following parameters: maximum working pressure – 135 MPa, number of pistons – 3, maximum capacity – 85 mm^3 per cycle, absorbed power – approx. 3.5 kW, pressure control – regulation on the suction side using a high-pressure regulator.

It is impossible to directly measure the volume of fuel supplied by the injector during a single injection, because the volume of fuel injected during a single injection is too small to be measured directly [17]. For this reason, an injection progress indicator was used to carry out the test, which allows injection into a chamber of constant volume.

In this method, a liquid replacing diesel fuel is injected into a chamber filled with the same substance under low pressure [20]. The chamber with a constant volume will be referred to as the combustion chamber in the rest of the article. The substance used for the tests was the Kalibrol test fluid due to safety conditions (requirement of non-flammability of the fluid used for testing). This is a fluid with a precisely defined viscosity (3 cSt at 40°C) by the ISO 4113 standard. It is characterized by low compressibility and good rheological properties. Meeting the ISO 4406 cleanliness standard, it is a fluid free from impurities that may damage the moving elements of the injector. In addition, it is chemically neutral to materials commonly used in fuel systems. It is also adapted to work in a wide temperature range to simulate various operating conditions of the injector. In the rest of the article, this liquid will be referred to as fuel. This is a substance dedicated to the measuring system used in the Pump and Injector Testing Station (STPiW-2, *Stanowisko Testowania Pomp i Wtryskiwaczy)* test bench. This testing station allows for configurable control of the Common Rail injector operation – adjustment of opening time, frequency, and fuel pressure.

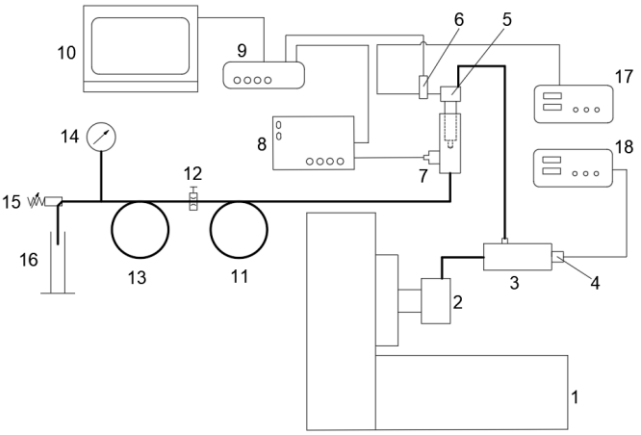

Fig. 1. Schematic diagram of the test stand (thick line – hydraulic lines, thin line – electrical lines): 1 – STPiW-2 test bench, 2 – high-pressure pump, 3 – common rail, 4 – pressure control valve, 5 – injector, 6 – current clamp, 7 – pressure sensor, 8 – current amplifier, 9 – oscilloscope, 10 – portable computer, 11 – measuring tube, 12 – throttle valve, 13 – discharge tube, 14 – pressure gauge, 15 – relief valve, 16 – measuring vessel, 17 – injector controller, 18 – high-pressure pump controller

The schematic of the stand is presented in Fig. 1. The AVL QL61D pressure sensor ensured precise pressure measurements, while the FLUKE 80i-110s current clamps measured the injector control current. During the experimental tests, a Handyscope HS5 digital recorder with a resolution of 16 bits and a sampling rate of up to 500 MHz was employed to record the waveforms of the individual signals. The use of such a high resolution enabled more accurate sampling of the original signal, significantly reducing the quantization error compared to standard A/D converter systems with 12-bit resolution. For direct measurements, multi-channel software, dedicated to the Handyscope HS5, was used. This software facilitated the

recording, archiving, and preprocessing of waveforms - for example, extracting individual injector cycles. Final processing and graphical presentation of the results were performed in MS Excel.

The measurement ranges and accuracies of the equipment used for the tests are listed in Table 1.

Table 1. Summary of measurement ranges and accuracy of measuring devices

Device	Task	Measurement range	Accuracy
FLUKE 80i-110s Current Clamps	Injector control current measurement	0.1–100 A DC/ 0.1–70 A AC	±4%
AVL QL61D pressure sensor	Measurement of instantaneous pressure values in the injection indicator	0–200 MPa	0.249 pC/MPa
KFM digital manometer	Measuring the liquid pressure in the discharge pipe	0–10 MPa	0.01 MPa

The study and development of results involved measuring the voltage and electric current characteristics of the pressure sensor and recording the voltage signal using a portable computer. Subsequently, the voltage value of each sample was converted to the appropriate value (pressure or electric current), and the fuel injection runs were derived from the recorded data. From the recorded signals, the characteristics of the fuel injection process were determined in two forms:

- differential form: illustrating how the fuel flow rate through the injector nozzle changed during the entire injection time
- integral form: showing how the total volume of fuel in the indicator chamber changed over time.

The assessment of fuel dosing repeatability was based on:

- graphic interpretation of the obtained characteristics
- calculated injection doses
- comparative analysis of the peak pressure and current values in each waveform
- statistical parameter lists of the current intensity and injected fuel pressure at selected characteristic operating points of the injector.

During the repeatability testing of fuel dosing, the injector opening time was varied depending on the simulated engine load. Parameters such as the rail pressure and fuel injection frequency were also adjusted. During the test, the rotational speed of the high-pressure pump shaft remained constant – the pressure in the fuel rail was regulated by changing the duty cycle of the current signal in the pressure regulator (PWM regulation). The system pressure was set to 3.8 MPa using the indicator discharge valve [18]. During the tests, the injector operated under conditions corresponding to its characteristic points.

The tests were conducted for the following engine load conditions, corresponding to the operating parameters of the injector:

- idle: standard injector operating conditions at low engine speed
- full engine load: the longest injector opening time
- full injector load: the highest fuel pressure
- injector distribution capacity: the highest injector operating frequency
- minimum fuel doses (hereinafter referred to as "microdoses"), the shortest injector opening time.

Testing the injector operation in these characteristic operating conditions allows for precise analysis and evaluation of the phenomena occurring inside it during various load states of the injector [21].

The injector operating parameters are presented in Table 2.

Table 2. Injector operating parameters for individual engine load conditions

No.	Load status	Injector opening time	Fuel pressure in the fuel tank	Injection frequency
1.	Engine idle	600 μs	40 MPa	10 Hz
2.	Full engine load	1000 μs	100 MPa	20 Hz
3.	Full load on injectors	600 μs	140 MPa	10 Hz
4.	Injector division capacity	500 μs	100 MPa	40 Hz
5.	Microdoses of fuel	300 μs	30 MPa	20 Hz

When the engine is idling, the crankshaft rotates at a low speed. At this operating condition, the engine generates low torque, which is sufficient to overcome the engine's resistance and ensure stable operation. To achieve such engine operating conditions, the injectors introduce a small dose of fuel into the combustion chamber. As a result, the injectors remain open for a short duration (approximately 600 μs), and the pressure in the accumulator is maintained at a low level (approximately 40 MPa). The injector opening frequency is also low – 10 Hz.

During full engine load, the engine must generate maximum torque. An increase in the injected fuel dose leads to an increase in the torque exerted on the crankshaft. To achieve this, the injectors must remain open for a sufficiently long duration (1000 μs), and the fuel pressure in the accumulator is relatively high (100 MPa). Greater torque is generated at higher engine speeds; hence, the injection frequency is already higher (20 Hz).

One of the measurement series in the tests focused on the injector's performance during full load operation. In this state, the injector opening time was shorter than during full engine load (600 μs), although the liquid pressure in the fuel tank was the highest (140 MPa). The injection frequency was 10 Hz. The main objective of this measurement series was to analyse the injector's behaviour when its components were subjected to high liquid pressure.

To evaluate the injector's ability to perform injections in rapid succession, another series of measurements was conducted with a short injector opening time (500 μs). The liquid pressure in the fuel tank was set to 100 MPa, and the injection frequency was 40 Hz.

The common rail system enables the implementation of multi-phase injection, where, in addition to the main injection dose, smaller doses are also injected. To test the injector's ability to implement small injection doses, a dedicated measurement series was carried out, measuring the injection dose volume for a very short injector opening time

(300 μs) and low liquid pressure in the fuel tank (30 MPa). Because small pre-injection doses follow one another in short time intervals, the injection frequency in this measurement series was set to 20 Hz.

3. Calculation method and adopted simplifications

Placing the injector outlet in a pipe filled with fuel allows pressure changes to be observed at any cross-section of the pipe. These changes are proportional to the fuel flow rate from the nozzle outlet of the injector being tested. By throttling the fuel flow from the measuring pipe, it is possible to maintain a pressure level within the pipe that corresponds to the pressure in the cylinder at the end of the compression stroke.

Figure 2 presents the current control curve of the solenoid valve coil and the pressure increase curve in the indicator measuring section. The visible shift in pressure results from the delay introduced by the time required for the injector to open after the control current is applied, as well as the time required to close the injector after the control voltage is cut off.

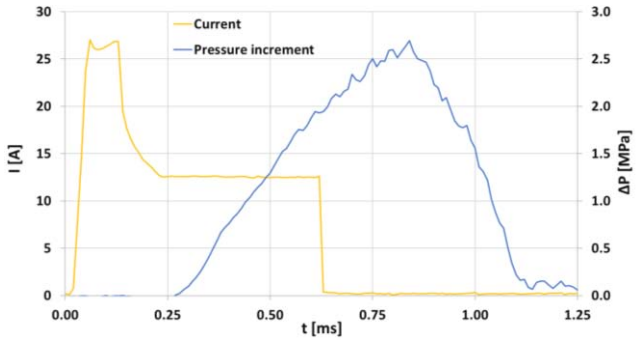

Fig. 2. Shift of the pressure waveform relative to the control current wave form

By using appropriately scaled data, it was possible to create a plot of the electric current intensity profile controlling the solenoid valve coil of the injector, as shown in Fig. 3a. In addition, a plot of the pressure increase in the measuring section of the injection course indicator was also created, as shown in Fig. 3b.

The fuel injection characteristic illustrates the relationship between the amount of fuel injected into the cylinder during a single injection and the engine crankshaft rotation angle or time. The amount of fuel is usually expressed in units of volume. The injection characteristic is presented in two forms: differential and integral.

The differential form depicts the instantaneous fuel flow rate from the injector nozzle during a single injection cycle as a function of time. This relationship is described by eq. 1.

$$\frac{dq}{dt} = f(t) \tag{1}$$

where: q – fuel dose value in cm^3 per injection, t – time in ms.

The surface area bounded by the ordinate, the abscissa, and any section of the characteristic curve described in this form is directly proportional to the amount of fuel delivered to the cylinder during the considered time period.

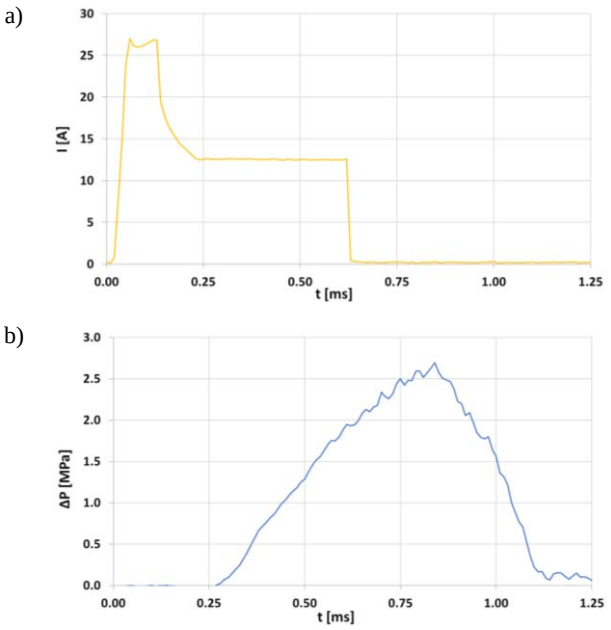

Fig. 3. Example results of direct measurements: a) course of the current controlling the solenoid valve coil of the injector, b) course of changes in the fuel pressure in the injection indicator

The integral form depicts the total variation of fuel supplied to the cylinder from the start of injection to the moment under consideration, expressed as a function of time.

The integral characteristic is represented by eq. 2:

$$\int_{t_0}^{t_x} \frac{dq}{dt}\, dt = F(t) \text{ , that is } q = F(t) \tag{2}$$

where: t_0 – time corresponding to the start of injection, t_x – the time corresponding to the moment under consideration.

The injection characteristic is more commonly defined in the differential form, as it illustrates the intensity of fuel saturation in the air contained within the engine combustion chamber. This characteristic affects the process of fuel evaporation, its mixing with air, and consequently the course of combustion. The shape of the characteristic significantly impacts the length of the preparatory period for combustion, the rate of combustion pressure increase, the peak pressure during combustion, and the indicated efficiency of the cycle.

According to one of the fundamental fluid dynamics relationships, an increase in the velocity of a fluid within a pipe is proportional to the amplitude of the pressure wave caused by this velocity change, as expressed by eq. 3:

$$a \cdot \rho \cdot dw = dp \tag{3}$$

where: a – speed of sound in the considered liquid in m/s, ρ – density of the liquid under consideration in kg/m^3, w – liquid flow velocity in m/s, p – liquid pressure in Pa.

When a liquid flows through a pipe with a cross-sectional area F [m^2], the stream continuity equation, assuming small pressure changes and negligible effects from liquid elasticity and pipe wall deformation, takes the form of equation 4:

$$\frac{dq}{dt} = F \cdot w \tag{4}$$

where: q – the dose of liquid flowing through a given cross-section, F – cross-sectional area through which the fluid flows.

Since the density of hydrocarbon fuels and the speed of sound in the pressure range typical of fuel injection are only slightly dependent on pressure, the equation can be simplified as shown in equation 5:

$$a \cdot \rho \cdot w = p \tag{5}$$

Knowing the speed of sound in the liquid, its density, and pressure, the flow velocity of the liquid stream can be calculated using equation 6:

$$w = \frac{p}{a \cdot \rho} \tag{6}$$

Using equation 4 and knowing the flow velocity of the liquid stream, the fuel flow rate can be calculated. This value determines the fuel flow rate in [m^3/s]. In engineering practice, the flow rate is typically expressed in [mm^3/s]. The relationship is shown in equation 7:

$$\frac{dq}{dt} = 10^9 \cdot F \cdot w \tag{7}$$

To obtain a differential fuel injection characteristic, the flow rate was differentiated with respect to time, where the time interval equalled the pressure sensor sampling period (0.01 ms). The resulting run is shown in Fig. 4a.

By integrating the flow rate from the start of fuel injection to the injector closing time, the fuel injection characteristics in integral form were derived, as shown in Fig. 4b.

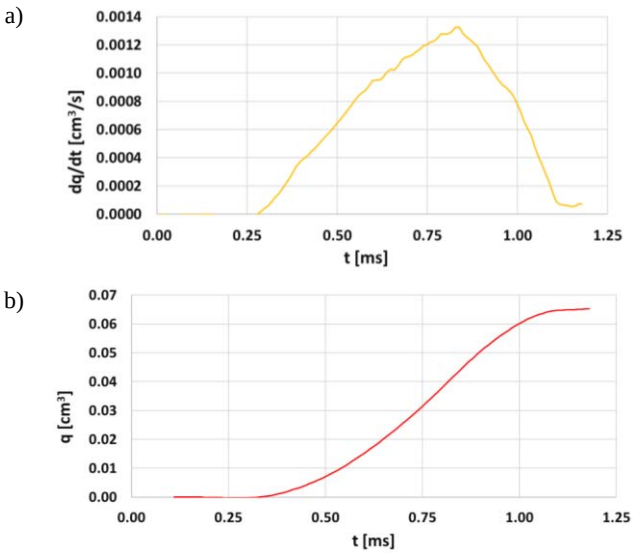

Fig. 4. Fuel injection characteristics determined based on tests in a) differential, b) integral form

In the discussed method, measuring the fuel flow rate is simplified to measuring the instantaneous pressure at a given cross-section of the pipe filled with fuel. For the calculations, the following assumptions were made:

a = 1400 m/s (speed of sound in the liquid under consideration)

p = 832.9 kg/m^3 (density of the liquid under consideration)

F = 0.00001512 m^2 (cross-sectional area through which the liquid flows in the measuring section).

4. Analysis of research results

4.1. Introduction

After completing the site tests, the following were analyzed:

- the maximum liquid pressure during the injection process to assess the correlation between the injection dose variation coefficient and the injection pressure variation coefficient
- the determined volume of each injected dose to evaluate the repeatability of dosing, which impacts the emission of toxic exhaust components and the uniformity of engine operation
- the shape of the injection characteristic in both differential and integral forms to assess the nature of the liquid injection process
- the relationship between the injector solenoid valve actuation time and its opening time to evaluate the effect of the inertia of injector components on the speed of its opening and closing.

The coefficient of variation (CV), used in this study to evaluate the test results, is a standardized measure of the variation in the distributions of a given characteristic. It is defined as the ratio (σ) of the standard deviation to the mean (μ):

$$CV = \frac{\sigma}{\mu} \tag{8}$$

4.2. Engine idle

In this state of engine operation, the injector introduces small volumes of fuel into the combustion chamber to maintain a low and constant engine speed under no load. The solenoid valve coil actuation time of the injector was brief (600 μs in this case), and the injection pressure remained relatively low (40 MPa). At idle speed, due to the low engine speed, the injector operated at an injection frequency of 10 Hz.

In the electric current intensity profile controlling the injector, as shown in Fig. 5a, a short period can be observed during which the solenoid valve coil is supplied with an attraction current exceeding 25 A, which is maintained for approximately 0.15 ms. For the remainder of the period, the holding current is roughly half the magnitude of the attraction current.

In the initial stage of the attraction current waveform, a disturbance is visible, where, after reaching the peak current intensity, the value drops rapidly before stabilizing. This phenomenon results from the impact of the solenoid valve anchor on the front surface of the coil. The change in current intensity in the valve coil circuit does not occur abruptly; a gradual increase in the electric current intensity is noticeable. This behaviour is a direct consequence of the properties of the induction coil, where the current intensity cannot change instantaneously, as dictated by the first law of commutation [8].

The volume of fuel dosed during injection did not change rapidly; instead, the fuel supply was smooth, as

confirmed by the smooth course of the differential fuel injection characteristic shown in Fig. 5b. This characteristic takes the shape of a run, which results from the injector's opening and closing process.

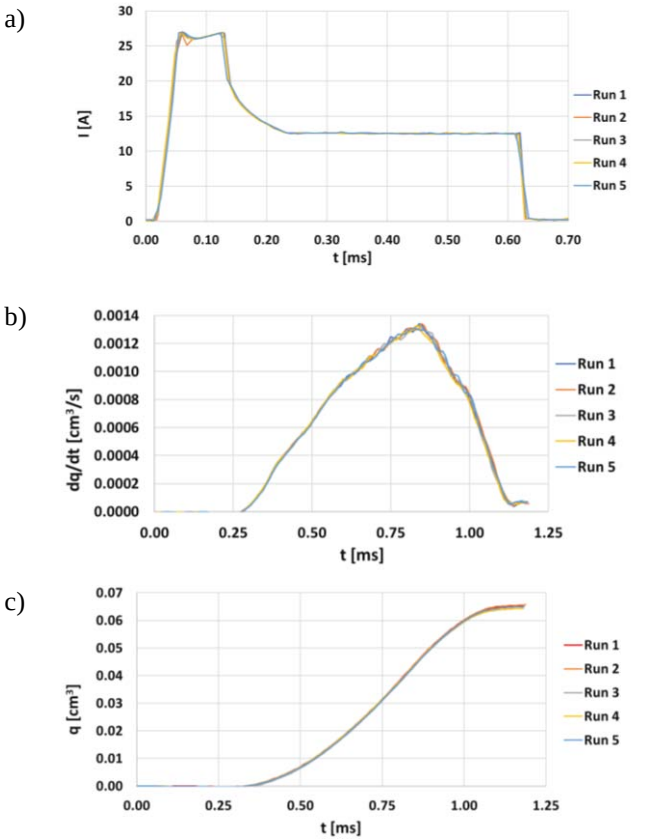

Fig. 5 Injection runs and characteristics obtained from a series of measurements under idle running conditions: a) run and intensity of the current supplying the injector solenoid valve coil, b) fuel injection runs and characteristics in differential form, c) fuel injection runs and characteristics in integral form

The gentle pressure build-up is attributed to the relatively long time it takes for the injector needle to rise, a delay caused by the inertia of the valve anchor and the injector needle. Additionally, the control chamber contributes to the extension of the injector opening time, as fuel must flow out through the outlet choke after the valve anchor has risen. Similarly, the gentle pressure drop can be explained by the need to fill the control chamber through the intake choke, where the fuel pressure exerts a force on the needle plunger, thereby closing the injector.

The integral characteristic is shown in Fig. 5c. In its central part, a linear increase in the fuel dose is evident, indicating that the fuel flow rate through a given cross section is directly proportional to the pressure generated in that cross section.

Characteristic values and statistical parameters of the injections are presented in Table 3.

4.3. Full engine load conditions

This test was carried out using injection parameters corresponding to full engine load conditions. The injector opening time was the longest, at 1000 μs, to achieve a large injection dose. The injection pressure was high (100 MPa). This is necessary because the engine must generate sufficient torque on the crankshaft to exceed the torque loading on the engine.

Table 3. Summary of injection process parameters for engine idle speed

Injection	The volume of fuel injected during individual injections [mm^3]	Maximum pressure for each injection [MPa]
Run 1	0.01672	2.694
Run 2	0.01682	2.682
Run 3	0.01656	2.678
Run 4	0.01650	2.667
Run 5	0.01666	2.615
The highest value	0.01682	2.694
Minimum value	0.01650	2.615
Statistical parameters		
Average value	0.01665	2.667
Standard deviation	0.00011	0.027
The difference between the highest and lowest value	0.00032	0.078
Coefficient of variation [%]	0.69	1.024
Injector control time [ms]	0.620	
Pressure rise time [ms]	0.860	
Control time/pressure duration*100%	72	

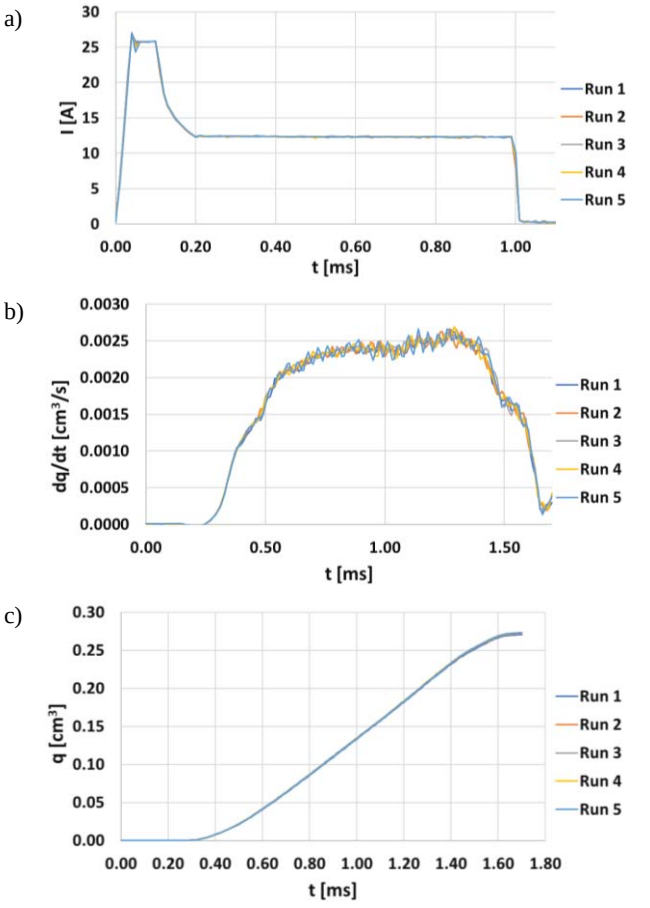

Fig. 6. Injection runs and characteristics obtained from a series of measurements under full engine load conditions: a) run and intensity of the current supplying the injector solenoid valve coil, b) fuel injection runs and characteristics in differential form, c) fuel injection runs and characteristics in integral form

For the injector operating under full engine load conditions, attention is drawn to the significantly longer holding current, with no change in the duration of the period during which the attraction current flows through the coil winding, as shown in Fig. 6a.

Based on the observed fluctuations in flow rate after the injector was fully open, it can be concluded that the fuel pressure at the nozzle outlet was not constant during this period. This inconsistency may be attributed to the turbulent nature of fuel flow through the injector channels.

The integral characteristics of individual injections, as shown in Fig. 6c, "overlap." Based on the graphical evaluation of these characteristics, it can be concluded that the repeatability of fuel dosing at a relatively long opening time and high fuel pressure is high. This conclusion is further supported by numerical values, particularly the coefficient of variation, included in Table 4, which presents characteristic values and statistical parameters for the discussed engine load condition.

The characteristic values and statistical parameters of the injections for this engine load condition are presented in Table 4.

Table 4. Summary of injection process parameters for full engine load

Injection	The volume of fuel injected during individual injections [mm^3]	Maximum pressure for each injection [MPa]
Run 1	0.0693	5.341
Run 2	0.0698	5.343
Run 3	0.0699	5.287
Run 4	0.0698	5.393
Run 5	0.0703	5.517
The highest value	0.0703	5.517
Minimum value	0.0693	5.287
Statistical parameters		
Average value	0.0698	5.76
Standard deviation	0.0003	0.078
The difference between the highest and lowest value	0.0009	0.230
Coefficient of variation [%]	0.43	1.451
Injector control time [ms]	1.010	
Pressure rise time [ms]	1.400	
Control time/pressure duration*100%	72	

4.4. Full load on injectors

During the tests of the injector under full load conditions, the fuel pressure was the highest among all the measurement series (140 MPa), as the greatest forces were exerted on the components inside the injector.

When the injector operates under full load conditions, a nonlinear increase in the fuel flow rate within the measuring section of the indicator is observed, similar to the behaviour observed under full engine load conditions.

For fuel injection characteristics in integral form, the courses of individual injections are also similar in shape and nearly overlap. This indicates a high level of dosing repeatability for these fuel injection parameters, consistent with the results observed under full engine load conditions. In both cases, the injector opening time and fuel pressure were high compared to those observed under other engine load conditions.

The characteristic values and statistical parameters of the injections for this engine load condition are presented in Table 5.

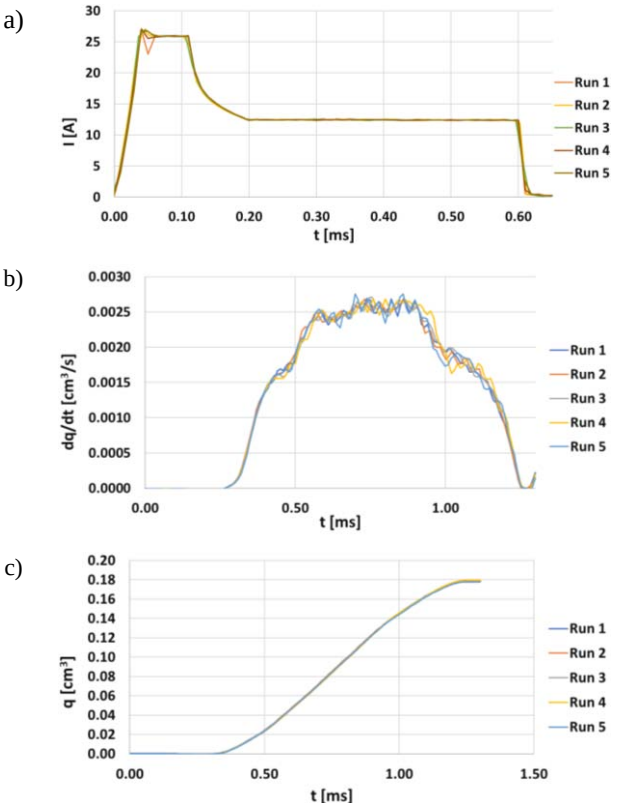

Fig. 7. Injection runs and characteristics obtained from a series of measurements under full load conditions of the injector: a) run and intensity of the current supplying the injector solenoid valve coil, b) fuel injection characteristics in differential form, c) fuel injection characteristics in integral form

Table 5. Summary of injection process parameters for full injector load

Injection	The volume of fuel injected during individual injections [mm^3]	Maximum pressure for each injection [MPa]
Run 1	0.0457	5.478
Run 2	0.0459	5.344
Run 3	0.0461	5.446
Run 4	0.0462	5.388
Run 5	0.0457	5.683
The highest value	0.0462	5.683
Minimum value	0.0457	5.344
Statistical parameters		
Average value	0.0456	5.468
Standard deviation	0.0002	0.117
The difference between the highest and lowest value	0.0005	0.339
Coefficient of variation [%]	0.42	2.143
Injector control time [ms]	0.61	
Pressure rise time [ms]	0.98	
Control time/pressure duration*100%	62	

4.5. Injector division capacity

During this measurement series, the distinguishing parameter, compared to other series, was the high injection frequency of 40 Hz. This part of the study aimed to evaluate how the injection proceeds when the injector operates at such a high frequency. The ability to perform repeatable injections under these conditions is important, as the initial injection phases during engine operation occur within short time intervals, resulting in a high frequency of pre-injections.

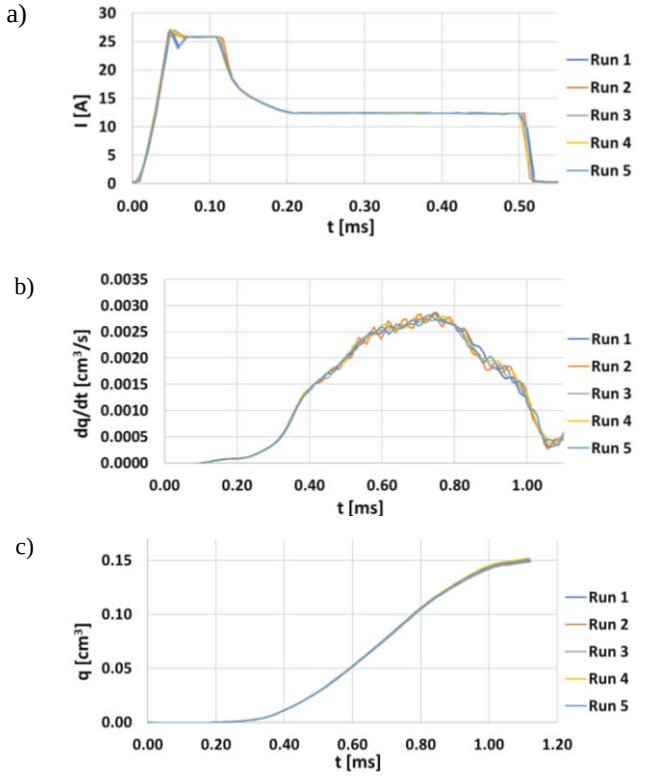

Fig. 8. Injection runs and characteristics obtained from a series of measurements under the conditions of testing the division ability of the injectors: a) run and intensity of the current supplying the solenoid valve coil of the injector, b) fuel injection characteristics in differential form, c) fuel injection characteristics in integral form

In the discussed case, the fuel injection characteristic in the differential form exhibits a disturbance characterized by a nonlinear increase in the volume of injected fuel. After exceeding a flow rate of 0.0015 mm³/s, the rate of increase in fuel flow through the nozzle becomes smaller. The next inflection point in the runs occurs at a flow rate of approximately 0.0025 mm³/s. These inflection points are mirrored on the falling edge for the same flow rate values.

The integral fuel injection characteristic runs reach their peak values almost simultaneously. This indicates that the total volume of fuel injected during each injection was practically the same, suggesting that the higher injection frequency does not significantly affect the repeatability of fuel dosing. This conclusion is further supported by statistical parameters, as the coefficient of variation for the volume of fuel injected during individual injections is 0.72. For the measurement series corresponding to full engine load and full injector load conditions, this coefficient was 0.43 and 0.42, respectively.

The characteristic values and statistical parameters of the injections are presented in Table 6.

Table 6. Summary of injection process parameters for the injector's division capacity

Injection	The volume of fuel injected during individual injections [mm³]	Maximum pressure for each injection [MPa]
Run 1	0.0384	5.754
Run 2	0.0386	5.841
Run 3	0.0382	5.488
Run 4	0.0391	5.633
Run 5	0.0388	5.637
The highest value	0.0391	5.841
Minimum value	0.0382	5.488
Statistical parameters		
Average value	0.0386	5.671
Standard deviation	0.0003	0.120
The difference between the highest and lowest value	0.0008	0.353
Coefficient of variation [%]	0.72	2.116
Injector control time [ms]	0.51	
Pressure rise time [ms]	0.85	
Control time/pressure duration*100%	60	

4.6. Microdoses

During the measurement series corresponding to microdoses, parameters such as fuel pressure and injector opening time were the lowest among all measurement series conducted so far. Microdoses represent the initial injection phases, such as pre-injection, during which a small volume

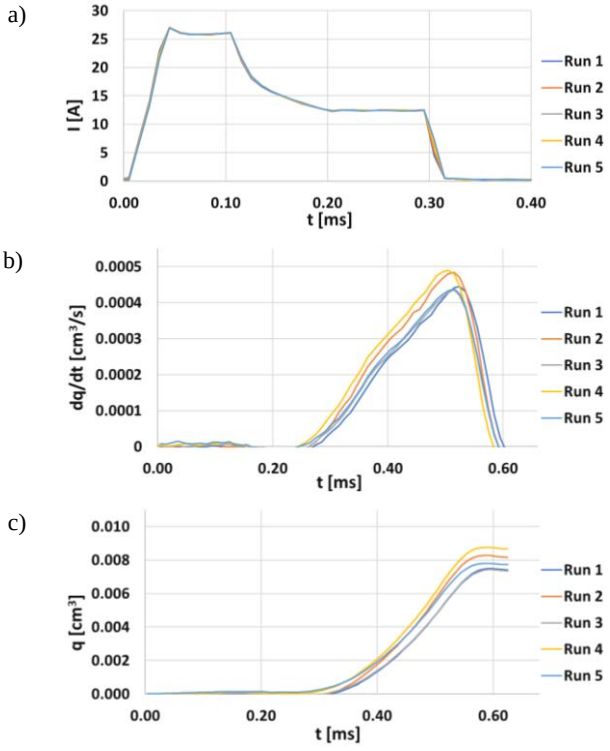

Fig. 9. Injection runs and characteristics obtained from a measurement series under conditions of micro doses: a) run and intensity of the current supplying the solenoid valve coil of the injector, b) fuel injection characteristics in differential form, c) fuel injection characteristics in integral form

of fuel is introduced into the combustion chamber to initiate the combustion process. In this series, the fuel pressure in the rail was 30 MPa, and the injector opening time was 300 µs.

The shapes of the fuel injection characteristics in the differential form clearly indicate that the fuel was injected into the measuring section of the indicator in a largely consistent manner, albeit not entirely uniform. The rising edges of the runs show minimal deviation from straight lines, which may suggest laminar fuel flow through the injector.

The injection courses during the implementation of microdoses differ significantly from those observed in other tests. The fuel doses injected during each course vary considerably, as evidenced by the differing peak values of the injected fuel volumes – the runs do not converge at a single peak value. Additionally, the coefficient of variation for the fuel volume injected during individual injections is the highest recorded so far, at 6.25. This value is more than 11 times greater than the average coefficient of variation observed in all previous measurement series, which was 0.565.

The characteristic values and statistical parameters of the injections for this measurement series are presented in Table 7.

Table 7. Summary of injection process parameters for microdoses

Injection	The volume of fuel injected during individual injections [mm^3]	Maximum pressure for each injection [MPa]
Run 1	0.0019	0.884
Run 2	0.0021	0.962
Run 3	0.0019	0.783
Run 4	0.0022	0.893
Run 5	0.0020	0.791
The highest value	0.0022	0.962
Minimum value	0.0019	0.783
Statistical parameters		
Average value	0.0020	0.863
Standard deviation	0.0001	0.067
The difference between the highest and lowest value	0.0003	0.179
Coefficient of variation [%]	6.25	7.806
Injector control time [ms]	0.31	
Pressure rise time [ms]	0.35	
Control time/pressure duration*100%	89	

5. Discussion and results

Figure 10 compares the injection dose variation coefficients and pressure variation coefficients across the characteristic injector operating conditions. Greater discrepancies were observed for the injected fuel pressure, which, for all operating conditions, showed higher values than the injection dose variation coefficient. These discrepancies may have been influenced by pressure wave phenomena occurring in the measuring section of the injection course indicator. It is important to note that similar phenomena occur in the fuel tank, high-pressure pipe, and inside the injector itself.

For microdoses, both coefficients differ significantly in value from those observed under other conditions. Based on this comparison, it can be concluded that as pressure and injector opening time increase, the repeatability of fuel dosing improves.

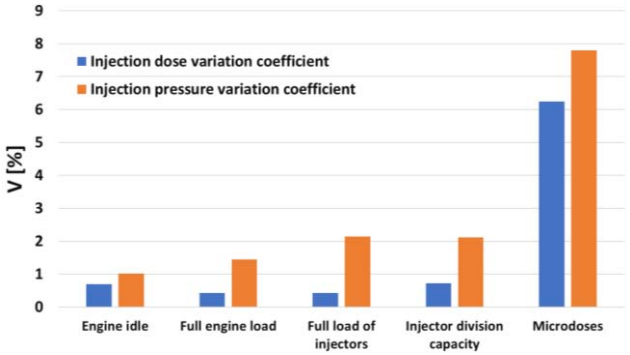

Fig. 10. Summary of the injection dose variation coefficients and injection pressure values depending on the engine load

Table 8 presents the following parameters:

- average value
- standard deviation
- the difference between the smallest and largest value
- coefficient of variation, for the volume of injected liquid and the pressure value.

Additionally, the table compares the ratio of the solenoid valve coil control time to the duration of the pressure in the indicator chamber.

Table 8. Summary of injection process parameters for individual injector operating states

Parameter	Quantity	Engine idle	Full engine load	Full load of injectors	Injector division capacity	Micro-doses
Average value	Volume [mm^3]	0.0647	0.2715	0.1786	0.1502	0.008
	Pressure [MPa]	2.667	5.376	5.468	5.671	0.863
Standard deviation	Volume [mm^3]	0.0004	0.0012	0.0007	0.0011	0.0012
	Pressure [MPa]	0.027	0.078	0.117	0.12	0.067
Difference between the highest and lowest value	Volume [mm^3]	0.0013	0.0036	0.0018	0.0032	0.0031
	Pressure [MPa]	0.078	0.23	0.339	0.353	0.179
Coefficient of variation	Volume [mm^3]	0.69	0.43	0.42	0.72	6.24
	Pressure [MPa]	1.02	1.451	2.143	2.116	7.806
Control time/pressure duration * 100%		72	72	62	60	89

Analyzing Table 8, it is evident that under full engine load conditions, the fuel pressure in the rail was 40% higher than the pressure observed during the injector division test. Despite this, the fuel pressure in the indicator measuring section during the full injector load measurement series was lower than during the injector division test.

For both fuel volume and pressure, the standard deviation was smallest at engine idle speed. For the volume of injected fuel, this parameter was similar across the full engine load, injector division capacity, and microdose measurement series. These three measurement series were also characterized by the largest difference between the maximum and minimum values of the injected fuel volume.

The ratio of the injector solenoid coil power supply time to the pressure duration in the indicator measuring section was highest for microdoses and lowest during the injector division test. This indicates that at a high injector operating frequency, a significant portion of the solenoid coil power supply time (in this case, 40 %) was not used for fuel injection into the indicator measuring section but was instead consumed by the injector opening process itself.

The present study was conducted using a completely new fuel injector. Based on the results obtained under these initial conditions, it is reasonable to hypothesize that, with continued operation and progressive wear of the injector, the repeatability of fuel delivery may deteriorate. This phenomenon merits further investigation in subsequent research efforts.

The ratio of the injector's actual opening time to the solenoid valve coil feed time significantly impacts the precision of fuel dosage. The actual opening duration of the injector is always shorter than the solenoid valve coil feed time, primarily due to the inertia of the injector's moving components. The greater the inertia of these components, the greater the discrepancy between these two durations. Inertia forces acting on the moving parts inside the injector cause delays in both opening and closing the injector. As a result, the fuel injection process ends later than the engine controller assumes. For small injection rates, this time discrepancy becomes critical, as such deviations can lead to undesirable variations in fuel dosage.

For short injector opening times, the time required to open and close the injector accounts for a large proportion of the total opening duration, leading to high dosing variability. This issue becomes less significant as injector opening times increase. The inertia of the injector's moving parts can affect dosing repeatability differently depending on engine load. For example, low injection pressure can extend the injector opening time due to reduced force acting on the injector needle, which influences the proportion of the aforementioned durations.

The high inertia of the moving components inside the injector is one of the most significant factors affecting the emission of toxic exhaust components in compression ignition engines. Uncontrolled injector dosing during low injection rates, when dosing variability is highest, can increase the concentration of toxic exhaust components such as nitrogen oxides and particulates. Addressing the issue of fuel dosing variability is therefore crucial for developing more precise injection control algorithms and improving injector design. These improvements will help engines comply with increasingly stringent emission standards.

To mitigate issues related to dosing variability under conditions of low injection pressure and short injector opening times, the use of more efficient engine control electronics with higher sampling frequencies should be considered. This enhancement would reduce the control system's response delay to signals from engine sensors. Specifically, it would enable a faster response of the engine controller to uneven angular accelerations of the crankshaft during the operating stroke of each cylinder. Such improvements would allow for quicker and more accurate corrections to the solenoid injector coil's control signal, ensuring high fuel dosing repeatability under all operating conditions.

An effective way to improve the repeatability of fuel dosage by electromagnetic injectors is to optimize the injector design. This can be achieved by using lighter materials for the injector's moving parts. As is well known, one of the challenges with electromagnetic injectors is the high inertia of the moving parts, which causes delays in the injector's opening and closing phases. The use of titanium can help mitigate this issue due to its low density and high strength, as titanium is approximately 40% lighter than metal alloys with similar properties.

Another approach to enhancing injector performance in terms of dosing repeatability is to improve the solenoid valve itself. This involves increasing the solenoid's strength to accelerate the solenoid anchor's movement, allowing the control chamber valve of the injector to open more quickly. Additionally, it would be necessary to develop algorithms to adapt the waveform of the solenoid valve control signal to the engine's operating conditions, tailoring the signal to the current engine load. These improvements would enable better control of the injector's opening and closing phases.

Further advancements in electromagnetic injectors remain justified. While piezoelectric injectors have largely replaced electromagnetic injectors in some applications (e.g., passenger cars), electromagnetic injectors continue to be widely used in the automotive industry. For example, HADI (Hydraulically Amplified Diesel Injector) systems, based on electromagnetic injectors, have been utilized in trucks since 2011. Given the extensive use of trucks in transportation and their larger engine displacements compared to passenger cars, further development of electromagnetic injectors aimed at increasing dosage repeat ability is worthwhile. These injectors continue to play a critical role in the automotive sector.

The study provided valuable insights into the relationship between the injector's actual opening time and the timing of the solenoid valve coil supply. The findings illuminate the mechanisms influencing fuel dosage variability, particularly for short injector opening times and low injection pressures. This knowledge can inform the design of new, more precise injectors and enhance injection control algorithms. Understanding how the proportions of actual injector opening time and solenoid valve coil supply time vary with engine load conditions could be incorporated into control algorithms, reducing fuel dos age variability. Moreover, the study identifies the specific conditions under which dosage non-repeatability is most pronounced, offering practical guidance for future research and development.

Continued research into fuel dosing variability is essential to expand knowledge in this area. One promising avenue of research is to analyze the impact of injector design changes – for instance, examining how the diameter or

number of nozzle holes affects dosing repeatability under different conditions. Additionally, studying the effects of materials used for the injector's moving parts could help determine how their masses influence the injector's opening and closing dynamics, and thus fuel dosage repeatability. Computational Fluid Dynamics (CFD) simulations could also be employed to investigate fuel flow dynamics, providing a deeper understanding of how fluid flow characteristics within the injector relate to the repeatability of small injection doses. Another area worth exploring is the effect of alternative fuels and their blends on the injection process, addressing whether fuel type can enhance dosage repeatability and improve combustion quality.

6. Conclusion

It should be noted that the results of this research and the conclusions drawn below apply exclusively to electromagnetic injectors of the Common Rail system.

1. The use of the above-mentioned test stand to achieve the study's objectives did not compromise the validity of the conclusions, as the study was analytical and comparative in nature. Any numerically determined fuel injection parameters differing from actual values would differ consistently, i.e., they would be overstated or understated by the same amount. This consistency ensures that parameters such as the coefficient of variation remain unaffected, preserving the scientific value of this research.
2. The repeatability of the electric current intensity run controlling the solenoid valve coil is very high. Deviations observed on the falling edges of the current run are negligible and do not significantly affect injector operation or fuel dosing repeatability. This insight can be valuable for system diagnostics. Considering that each signal path supplying the solenoid valve coil under steady state conditions is identical, an increase in signal non repeatability would indicate damage to the engine control system rather than a fault in the injector.
3. The fuel injection time exceeds the solenoid valve coil control time due to the emptying and refilling of the control chamber during the injector's opening and closing processes. These actions require a specific amount of time, independent of the ECU (Electronic Control Unit) system. To compare the durations of the solenoid valve coil control period and the pressure maintenance period, the ratio of injector control time to pressure maintenance time was calculated and expressed as a percentage. The largest differences (60%) between these times occurred during high frequency injector operation (injector division capacity), while the smallest differences (89%) were observed during microdose implementation. This indicates that at higher injection frequencies, a significant portion of the control time is devoted to the injector's opening and closing processes. Knowledge of the dynamics of fluid flow in the injector control chamber and its impact on injector processes can be applied to optimize common rail systems using alternative fuels. The flow dynamics depend on fuel properties, which vary significantly for alternative fuels.
4. The lowest repeatability was observed in the pressure run during microdose implementation. Significant differences were noted in both the maximum pressure values and the injected fuel dose volumes. The coefficient of variation reached its highest values in this context: 6.24% for the injected fuel dose volume and 7.80% for the configurable control of the maximum pressure value. Such variability underscores the advantages of piezoelectric injectors, which enable more precise fuel dosing over shorter intervals. Based on the results, it can be concluded that the tested electromagnetic injector would not meet the requirements of current exhaust emission standards.
5. Across all characteristic operating points of the injector, the coefficient of variation for maximum pressure values was consistently higher than that for injected fuel volume. This discrepancy arises due to pressure wave phenomena in the fuel rail, high-pressure pipe, and injector itself. This study highlights the scale of wave phenomena issues within the high-pressure circuit and may encourage injection system designers to consider incorporating pressure wave damping devices into more advanced fuel rail designs.
6. Further work on improving fuel dosing repeatability is highly recommended. Greater dosing repeatability enables more precise control of injection volumes, offering the potential to increase the number of injection phases or divide existing phases, such as splitting a pilot dose into two smaller doses.
7. The developed methodology facilitates research into various aspects of fuel injection, including the effects of different injection strategies on dosing repeatability or the influence of alternative fuel properties. Research using this methodology could contribute to the development of fuel supply systems and injection control algorithms optimized for specific alternative fuels.
8. Shorter injector opening times amplify the impact of the inertia of the injector's moving components on fuel dosing consistency. Similarly, lower injection pressure reduces the forces acting on these components, further diminishing dosing consistency. These factors highlight the importance of addressing injector design and operating conditions to improve fuel dosing precision.

Acknowledgements

This work was financed by the Military University of Technology under research project UGBWIM_22012025_15.

Nomenclature

CFD	computational fluid dynamics
CI	compression ignition
ECU	engine control unit
HADI	hydraulically amplified diesel injector
IMA	Injektor Mengen Abgeleich
NO_x	nitrogen oxides
PWM	pulse width modulation
STPiW	stanowisko testowania pomp i wtryskiwaczy

Bibliography

[1] Balawender K, Kuszewski H, Lejda K, Ustrzycki A. The effect of multi-phase injection on selected parameters of the common rail fuel system. Combustion Engines. 2008; 135(4):22-28. https://doi.org/10.19206/CE-117228

[2] Bai Y, Gu Y, Lan Q, Fan L, Ma X. Correction strategy of fuel injection quantity during pilot main injection for common rail system. J Mech Sci Technol. 2020;34(2):2647-2656. https://doi.org/10.1007/s12206-020-0538-0

[3] Cavicchi A, Postrioti L, Scarponi E. Hydraulic analysis of a GDI injector operation with close multi-injection strategies. Fuel. 2019;235:1114-1122. https://doi.org/10.1016/j.fuel.2018.08.089

[4] Chau VT, Long TD, Vang HB, Hoang NM, Phuc NH, Sy NQ. A study on the injection rate characteristics of the solenoid common-rail injector under using a high-pressure fuel system. Jurnal Teknologi. 2023;85(3):25-33. https://doi.org/10.11113/jurnalteknologi.v85.19106

[5] Chojnowski J, Karczewski M, Szamrej GA. Dual-fuel engines using hydrogen-enriched fuels as an ecological source of energy for transport, industry and power engineering. Combustion Engines. 2024;198(3):3-12. https://doi.org/10.19206/CE-176800

[6] Common Rail Injection Systems. Bosch Technical Bulletin. Warsaw 2005.

[7] Durczak T, Sander P, Lotko W. Development trends of fuel injection systems used in truck engines. Autobusy. 2017; 18(12).

[8] Glinka T. Commutation properties of a series DC motor with a bifilar excitation winding. Scientific Papers of the Silesian University of Technology. Series: Electricity. 1972;38.

[9] Han D, Duan Y, Wang C, Lin H, Huang Z, Wooldridge MS. Experimental study of the two-stage injection process of fatty acid esters on a common rail injection system. Fuel. 2016; 163:214-222. https://doi.org/10.1016/j.fuel.2015.09.066

[10] Karpiuk W, Bor M, Smolec R. Possibilities of analysis of conditions and repair of common rail system injectors. Journal of KONES. 2016;23(4):209-216. https://doi.org/10.5604/12314005.1217208

[11] Kowalski D, Graba M, Lechowicz A, Bieniek A. The influence of the application of multiphase injection on firing pressure flow in the engine cylinder of a farm tractor (in Polish). Agricultural Engineering. 2011;5(130).

[12] Krogerus T, Huhtala K. Diagnostics and identification of injection duration of common rail diesel injectors. Open Engineering. 2018;8(1):1-6. https://doi.org/10.1515/eng-2018-0001

[13] Lejda K. Injection systems of high-speed diesel engines and development trends. Combustion Engines. 2005;123(4):19-30. https://doi.org/10.19206/CE-117366

[14] Ma F, Xu R, Liu X. Fuel injection performance and spray characteristics of high-pressure common rail systems at low temperatures. Energy Sci Eng. 2024;12(3):1233-1241. https://doi.org/10.1002/ese3.1713

[15] Nguyen D, Andrea C, Nguyen KT, Nguyen VH, Postrioti L, Pham PX. Shot-to-shot deviation of a common rail injection system operating with cooking-oil-residue biodiesel. SAE Int J Engines. 2023;16(8):1093-1101. https://doi.org/10.4271/03-16-08-0062

[16] Nguyen VH, Cavicchi A, Nguyen DX, Nguyen KT, Pham PX, Postrioti L. Hydraulic characterization of a second-generation common rail injector operating under solo and split injection strategies. Flow Meas Instrum. 2022;85: 102170. https://doi.org/10.1016/j.flowmeasinst.2022.102170

[17] Postroti L, Buitoni G, Pesce FC, Ciaravino C. Zeuch method-based injection rate analysis of a common-rail system operated with advanced injection strategies. Fuel. 2014;128: 188-198. https://doi.org/10.1016/j.fuel.2014.03.006

[18] Rajewski M, Walentynowicz J. Determination of fuel injection characteristics using an indicator. Bulletin of the Military University of Technology. 1998;47;31-43. bwmeta1.element.baztech-article-BWA2-0001-0003

[19] Rothrock AM, Pressure fluctuations in a common-rail fuel-injection system. J Fluid Eng. 2023;52(9):109-117. https://doi.org/10.1115/1.4057854

[20] Slavinskas S, Bendziunas P. Experimental study on influence of biofuels on injection characteristics of diesel engine common rail system. 23rd International Scientific Conference Engineering for Rural Development. 2024. https://doi.org/10.22616/ERDev.2024.23.TF067

[21] Stoeck T. Enhanced diagnostics of common rail piezoelectric injectors using the box method. Combustion Engines. https://doi.org/10.19206/CE-205812

[22] Ustrzycki A, Kuszewski H, Woś P. The effect of length of high-pressure pipes on injection process in common rail system of diesel engine. Journal of KONES Powertrain and Transport. 2010;17(3).

[23] Wierzbicki S, Śmieja M. Visualization of the parameters and changes of signals controlling the operation of common rail injectors. Sol St Phen. 2013;210:136-141. https://doi.org/10.4028/www.scientific.net/ SSP.210.136

[24] Xu R, Ma F, Li L, Yang W, Zhang Y. Research on fuel injection characteristics of common rail system based on high-pressure pipeline integration and matching. Energy Sci Eng. 2024;12(4):1446-1461. https://doi.org/10.1002/ese3.1672

[25] Xu-Guang T, Hai-Lang S, Tao Q, Zhi-Qiang F, Wen-Hui Y. The impact of common rail system's control parameters on the performance of high-power diesel. Energy Procedia. 2012;16:2067-2072. https://doi.org/10.1016/j.egypro.2012.01.314

Karol Dębowski, MEng. – Faculty of Mechanical Engineering, Military University of Technology, Poland.
e-mail: *karol.debowski@student.wat.edu.pl*

Mirosław Karczewski, DEng. – Faculty of Mechanical Engineering, Military University of Technology, Poland.
e-mail: *miroslaw.karczewski@wat.edu.pl*

Article citation info:
Szumska E, Skuza A. Enhancing regenerative braking efficiency in electric vehicles through urban driving pattern analysis. Combustion Engines. 2025;203(4):191-200. https://doi.org/10.19206/CE-207871

Emilia SZUMSKA
Adriana SKUZA

Combustion Engines
Polish Scientific Society of Combustion Engines

Enhancing regenerative braking efficiency in electric vehicles through urban driving pattern analysis

ARTICLE INFO

Received: 6 June 2025
Revised: 3 July 2025
Accepted: 3 July 2025
Available online: 23 September 2025

Electric vehicles offer a sustainable alternative to internal combustion engine vehicles, significantly reducing emissions and improving energy efficiency. A key feature is the regenerative braking system, which recovers kinetic energy during braking. This study examines how braking parameters affect energy recovery in EVs under urban conditions, combining real-world data with simulation. The research involved two stages: data collection from 60 urban trips using a Hyundai Kona Electric, followed by AVL Cruise simulations. Statistical analysis (correlation and K-Means clustering) assessed the relationship between braking parameters (number of events, average braking speed, deceleration, maximum braking force) and recovered energy. Results showed a strong correlation (r = 0.9) between the number of braking events and recovered energy, highlighting the importance of frequent urban braking. Clustering identified four driving patterns. Cluster C4, with the highest number of braking events (84–158) and moderate intensity, achieved the greatest energy recovery efficiency (23.16%). Cluster C1, with fewer events (26–76) and smoother driving, showed the lowest efficiency (18.45%). The average efficiency across all trips was 21.47%, consistent with the literature. Findings suggest that frequent, moderate braking in dense urban traffic optimizes energy recovery. The study offers practical insights for designing more efficient regenerative systems and promoting driving techniques that enhance EV range.

Key words: *electric vehicle, regenerative braking, energy recovery, K-Means clustering, braking parameters*

1. Introduction

Vehicles with electric powertrains, encompassing both fully electric vehicles (EVs) and hybrid electric vehicles (HEVs), play a pivotal role in transforming the transportation sector towards sustainable and environmentally friendly solutions. The increasing availability of public charging stations, enhanced amenities for electric vehicle owners, and financial incentives such as purchase subsidies serve as powerful motivators for choosing an electric vehicle and offer additional encouragement to undecided potential buyers [2, 4, 13]. EVs contribute to the reduction of greenhouse gas emissions and the improvement of energy efficiency. All vehicles equipped with an electric powertrain possess the capability to recover kinetic energy during braking. The Regenerative Braking System (RBS) converts kinetic energy into electrical energy via an electric motor operating in generator mode. This energy is then transferred to the battery and can be subsequently reused to propel the vehicle or power onboard systems. For purely electric vehicles, regeneration directly extends range and enhances energy efficiency, forming an integral part of their propulsion system. Conversely, in hybrid vehicles, where the electric drive interacts with an internal combustion engine, the energy regeneration system improves overall energy efficiency by reducing fuel consumption and exhaust emissions. With growing interest in electromobility, research into optimizing regeneration processes is becoming increasingly vital, particularly in the context of urban driving, where frequent stops and speed changes create unique opportunities for energy recovery.

Research on energy recuperation in electric vehicles encompasses a wide range of theoretical and experimental approaches, from integrating regenerative braking systems with friction brakes to designing advanced strategies for managing and controlling recovered energy. Control strategies for kinetic energy recovery are developed to maximize the efficiency of regenerative braking in vehicles with electric powertrains [3]. Previously published studies primarily focus on developing and presenting optimization or predictive algorithms, all based on specific braking process parameters. Optimization algorithms are used to maximize energy recovery through mathematical models. For example, in [25], a fuzzy logic-based control strategy with genetic algorithms was presented. The developed algorithm was projected to increase braking energy recovery efficiency by 10% and extend EV range by 8% in the urban cycle. Similarly, torque optimization, as described in [7], improved the recovery coefficient by 3.35% in WLTC tests by minimizing energy losses. Neural networks, applied in [14], enhanced the adaptability of RBS to varying road conditions, increasing recovered energy by 7% compared to classic PID controllers. However, studies [12, 21] indicate that the computational complexity of these methods limits their practical application in vehicles.

Predictive algorithms are used to forecast braking demand and optimize regenerative force. These algorithms draw on both real-time driving data (such as route topography from GPS, speed, acceleration, and brake pedal position) and historical data. This enables the recuperation system to adapt its operation to current road conditions, thereby optimizing energy recovery across various scenarios. For instance, as demonstrated in [23], an energy management strategy based on Model Predictive Control (MPC) boosted energy recovery by 5% in urban environments by precisely adapting to speed profiles. Study [16] utilized Artificial Neural Networks (ANNs) and fuzzy controllers to calculate recovered braking energy based on battery state of charge and braking demand. Linear programming was then

applied to optimize the regenerative force, leading to a 25.7% increase in vehicle range. Due to their ability to better account for variable conditions and uncertainties (such as driver behaviour and route topography), predictive algorithms in EV regenerative braking systems surpass classical optimization algorithms in effectiveness. This advantage enables continuous, real-time recalibration of recuperation control, resulting in more accurate estimations of energy recovery efficiency and, consequently, improved range and reduced energy consumption.

The efficiency of recuperation systems in electric vehicles is highly dependent on operating conditions. In urban environments, characterized by dynamic driving with frequent acceleration and braking cycles, the effectiveness of the kinetic energy recovery system can be substantial. It is estimated that under such conditions, energy recovered during braking can account for 20% to 40% of the energy consumed for vehicle propulsion [19]. Similar conclusions were presented in [9]. Furthermore, [11] demonstrated that in urban settings, recuperation can be responsible for 15–25% of the vehicle's total energy demand, depending on driving dynamics and road infrastructure.

In studies [5, 18, 24], the authors emphasize the significance of frequent braking in urban traffic, which results from the high number of intersections and traffic lights, thus favouring greater energy recovery. Within the context of HEVs, studies such as those presented in [15, 22] indicate that recuperation in urban driving can significantly reduce fuel consumption by increasing the electric powertrain's contribution to the overall driving cycle. However, the majority of existing research relies on standard driving cycles, such as WLTP or NEDC, which do not fully reflect the variability of real-world urban conditions. This limitation restricts their practical application in powertrain system design. This applies to both electric vehicles and those equipped with internal combustion engines [26, 27, 28].

Despite extensive research on energy recuperation in electric vehicles, a notable gap persists in the literature concerning a detailed analysis of how specific braking parameters – such as the number of braking events, average braking speed, deceleration, or maximum braking force – influence energy recovery under real-world urban driving conditions. Most prior studies focus on standardized driving cycles, which fail to account for the complexities of urban traffic, including varying congestion levels, the number of intersections, or changes in terrain elevation. Furthermore, attempts to integrate data from real-world drives with advanced simulations are infrequent, yet such an approach could yield more realistic and applicable conclusions for designing recuperation systems in both EVs and HEVs. This study addresses this gap by analysing the impact of braking parameters on energy recovery across 60 real-world urban driving events, utilizing simulations in AVL Cruise software.

Based on the literature review and the identified research gap, the following hypotheses have been formulated:

– Hypothesis 1: The number of braking events (n_{ham}) is positively correlated with the amount of recovered energy (E_{reg}) in urban driving conditions for both EVs and HEVs.
– Hypothesis 2: Braking parameters, such as average braking velocity (v_{h_sr}), average deceleration (d_{sr}), and maximum braking force (F_{h_max}), have a varied impact on energy recovery, with their significance depending on the specific driving pattern.
– Hypothesis 3: Driving patterns characterized by frequent, moderate braking (e.g., in heavy urban traffic) exhibit higher energy recovery efficiency compared to patterns with less frequent but more intense braking. This is particularly relevant for HEVs in the context of fuel consumption reduction.

The study's methodology employs a two-stage approach: (1) data acquisition from real-world urban driving and (2) simulations conducted in AVL Cruise software. This dual approach allows for capturing authentic driving patterns that are challenging to replicate in standardized laboratory cycles, while simultaneously enabling a precise analysis of braking parameter impact on energy recovery under controlled simulation conditions. A single driver was used to eliminate driving style variability, thereby isolating the influence of the studied parameters. The application of correlation analysis and K-Means clustering then aids in identifying key relationships and patterns, which are vital for developing more effective recuperation systems for both EVs and HEVs.

2. Methods

2.1. Real-world data acquisition

Research into energy recovered during braking was conducted in two stages. First, the kinematic parameters of an electric vehicle were recorded under real-world urban traffic conditions. The resulting speed profiles then served as input data for the simulation software. In the second stage, simulation studies were performed using AVL Cruise software, where a vehicle model corresponding to the real one was developed. The data from these simulations were then subjected to statistical analysis.

Real-world tests were conducted on five selected urban road sections, each approximately 5 km long, characterized by varying traffic densities and road conditions. A total of 60 drives were completed, encompassing both city outbound roads and urban routes with different levels of congestion. Some routes were outbound roads, where traffic was relatively light, and the vehicle moved smoothly with few stops. The remaining routes involved driving through the city center, where traffic density was higher, necessitating more frequent stops and speed changes. Drives were carried out at two times of day: around midday, between the morning and afternoon rush hours, and during the afternoon rush hour itself.

The routes varied in the number of signalized intersections, pedestrian crossings, and permissible speeds. The investigated routes included:

− city outbound road (70 km/h speed limit) featured 3 signalized intersections, 4 marked pedestrian crossings, and one roundabout
− city outbound road (50 km/h speed limit) characterized by a varied elevation profile with an altitude change exceeding 60 m between its highest and lowest points.

This route included 8 intersections (5 signalized) and 4 marked pedestrian crossings

– city center routes:
  1) the first city center route, known for heavy traffic and a varied elevation profile, comprised 9 signalized intersections, 5 marked pedestrian crossings, and 3 roundabouts
  2) the second city center route included 15 intersections (12 signalized) and 3 marked pedestrian crossings;
– residential area route encompassed 29 intersections (4 signalized) and 9 marked pedestrian crossings. It featured significant speed restrictions (in places down to 20 km/h) typical of residential roads, along with speed reductions enforced by speed bumps.

The selection of five routes ensures that the study reflects typical urban driving scenarios. This prevents the results from being limited to specific, atypical situations, allowing them to be generalized to the real-world usage of electric vehicles in urban environments.

The test vehicle used was a Hyundai Kona electric. A Kistler™ type GPS Data Logger was employed to measure vehicle motion parameters, recording data such as travel time, instantaneous velocity, instantaneous longitudinal acceleration, distance traveled, and instantaneous position (10 Hz sampling frequency, GPS position accuracy < 2.5 m). The collected data were used to create velocity profiles characteristic of each route. All drives were performed by a single driver. Examples of the recorded velocity profiles as a function of time are presented in Fig. 1.

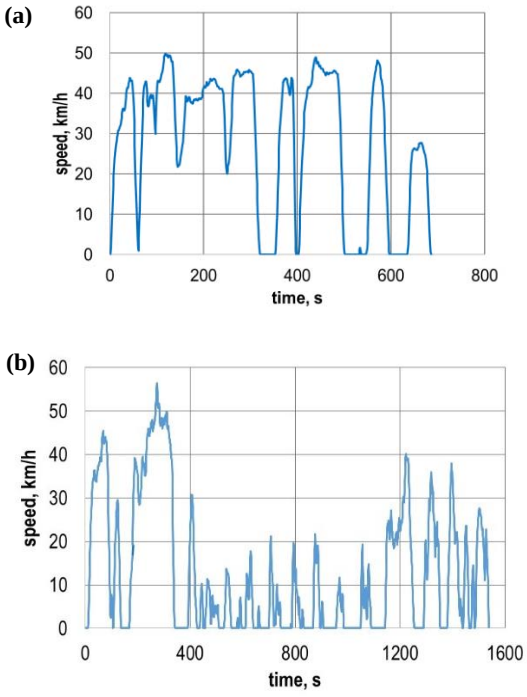

Fig. 1. Representative speed profiles from the investigated routes (a) midday, (b) peak hours

2.2. AVL Cruise modeling and simulation

AVL CRUISE is an advanced analytical tool designed for detailed modeling of both mechanical and regenerative systems. This capability allows for the optimization of braking strategies concerning energy efficiency, safety, and driving comfort. The software serves as a sophisticated instrument for analyzing vehicle dynamics and optimizing its powertrain and braking systems, with particular emphasis on the energy recuperation system. The developed vehicle model facilitates advanced analyses of the kinetic energy recovery process via the recuperation system, while simultaneously accounting for the mechanical and thermal aspects of the braking system's operation. A schematic representation of the electric vehicle model is provided in Fig. 2.

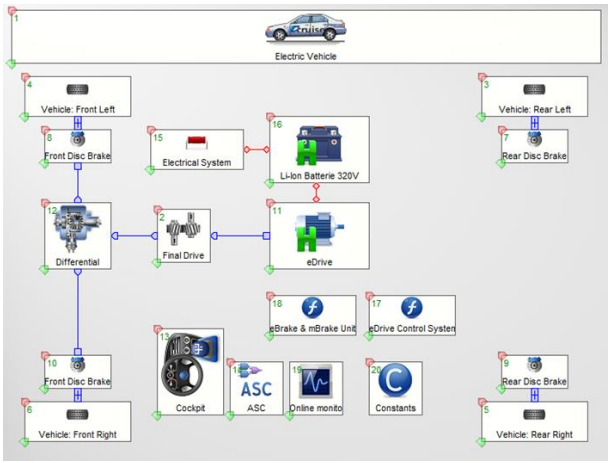

Fig. 2. Electric vehicle model in AVL Cruise

Table 1. Selected technical parameters of the electric vehicle

Electric motor	Motor type	Permanent Magnet Synchronous Motor (PMSM)
	Maximum motor power	100 kW
	Maximum torque	395 Nm
Battery	Type	Lithium-ion
	Energy capacity	39.2 kWh
Vehicle dimensions and mass	Length	4180 mm
	Width	1800 mm
	Height	1570 mm
	Wheelbase	2600 mm
	Curb weight	1535 kg
	Payload capacity	150 kg

The electric vehicle braking system in AVL Cruise comprises two primary components:

– mechanical braking system, which consists of disc brakes actuated by a hydraulic system, which includes a pump, pressure lines, and wheel cylinders located at each wheel;
– kinetic energy recuperation system, that incorporates an electric machine operating in generator mode, converting the vehicle's kinetic energy into electrical energy, which is then directed via an inverter to the battery.

These two systems operate concurrently, with their interaction dictated by braking torque control algorithms.

The electric vehicle model used in the simulation studies replicated the parameters of the actual Hyundai Kona electric. Table 1 presents selected technical parameters of

this electric vehicle. For each simulation performed, the initial battery state of charge was set to 75%.

2.3. Data analysis

The data collected were analysed using Statistica software. Pearson correlation analysis was applied to assess the relationships between braking parameters – such as the number of braking events (n_{ham}), average braking speed (v_{hsr}), average braking deceleration (d_{sr}), and maximum braking force (F_{h_max}), and the amount of recovered energy (E_{reg}). Additionally, the K-Means clustering method was used to group drives into four distinct clusters. This allowed for the identification of driving patterns that influence recuperation efficiency. The results were validated using ANOVA and 10-fold cross-validation, ensuring the robustness and reliability of the obtained data.

3. Results

3.1. Analysis of energy recovered in selected test routes

The analysis is based on data obtained from 60 real-world trips and their corresponding AVL Cruise simulations. The influence of key braking parameters – such as the number of braking events, average braking speed, deceleration, and maximum braking force – on the amount of energy recovered (E_{reg}) is examined. The results are organized into two subsections: Subsection 3.1 details the energy recovery characteristics across the test routes, including statistical correlations between braking parameters and recovered energy. Subsection 3.2 applies K-Means clustering to identify distinct driving patterns and their impact on recuperation efficiency, highlighting optimal conditions for maximizing energy recovery. These findings provide insights into the effectiveness of regenerative braking systems in diverse urban traffic scenarios.

Energy recuperation in electric vehicles is most effective in urban traffic conditions, where the number of braking events is highest. Optimizing recuperation in such environments can significantly boost vehicle energy efficiency. Increasing the initial braking velocity and braking force within moderate limits can favorably impact the amount of energy recovered. Therefore, the goal should be to design recuperation systems that enable maximum energy recovery across a wide range of traffic conditions. Urban driving, while leading to higher energy consumption due to frequent speed changes, also offers the greatest potential for energy recovery during braking.

Simulation studies utilized velocity profiles from 60 urban driving trips, each approximately 5 km in length. The routes were diverse, and data collection took place on weekdays. Figure 3 and Fig. 4 present the number of braking events recorded on the test routes.

An average of 77 braking events was logged per trip. The highest recorded instance was 158 braking events in a single trip, translating to 31 braking events per kilometre. Figure 5 presents the distribution of total energy consumption (E_c) across the analysed trips.

The analysed trips showed an average energy consumption of 2772.6 kJ (0.77 kWh), with values ranging from 1292.28 kJ (0.36 kWh). On a per-kilometre basis, the vehicle consumed an average of 554.52 kJ (0.15 kWh). The peak energy consumption, approximately 3597.24 kJ (1 kWh), occurred during a rush-hour trip through the city centre. This particular instance was characterized by heavy traffic and an average driving speed of 16.36 km/h. Figure 6 presents the distribution of recovered energy values (E_{reg}) for all trips.

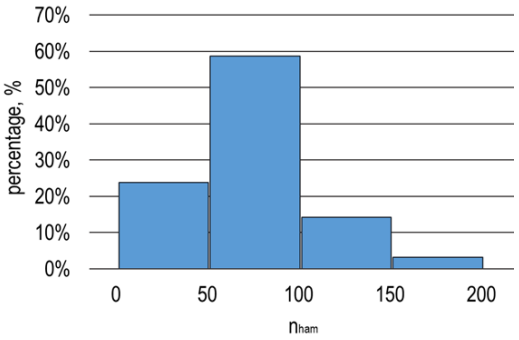

Fig. 3. Distribution of braking events (n_{ham}) in test routes

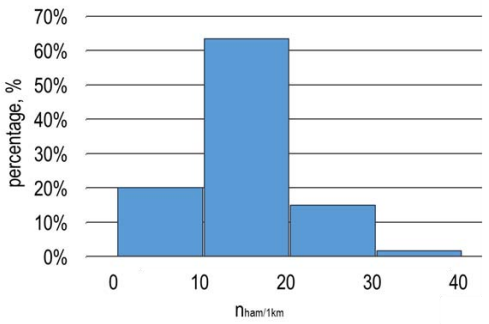

Fig. 4. Distribution of braking events per km ($n_{ham/km}$) in test routes

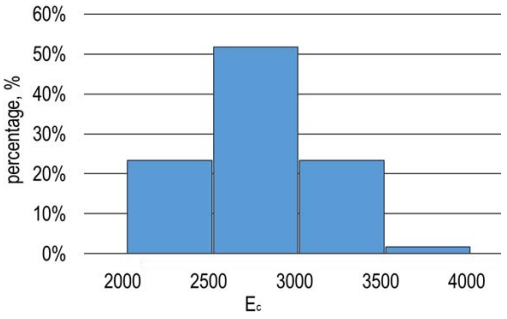

Fig. 5. Distribution of energy consumption (E_c) in test routes

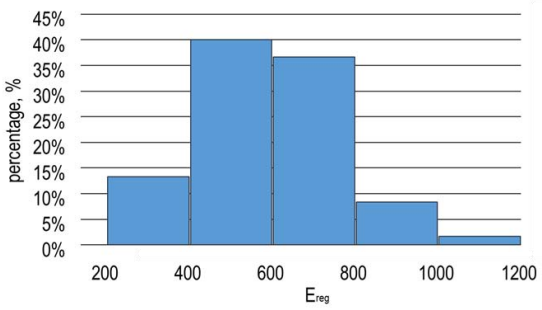

Fig. 6. Distribution of recovered energy values (E_{reg}) in test routes

On average, 595.42 kJ (0.17 kWh) of energy was recovered per trip. The range of recovered energy values was 710.71 kJ. The highest recorded value of recuperated energy during braking in the analysed trips was 1026.64 kJ (0.29 kWh). This particular trip also showed the highest energy consumption.

The number of braking events in urban driving reflects traffic dynamics; intense traffic and frequent stops lead to greater energy recovery. In areas with numerous stops (e.g., city centres), higher recuperation efficiency can be expected. It is evident that the amount of recovered energy increases with the number of braking events. In the analysed trips, these parameters exhibit a linear relationship. A correlation coefficient (r) equal to 0.9 indicates a very strong positive correlation between the number of braking events and the energy recovered (Fig. 7).

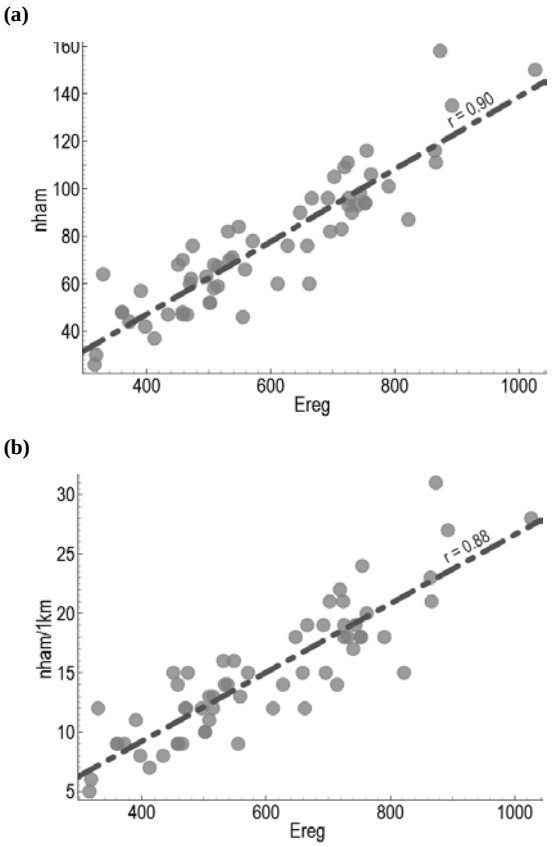

Fig. 7. Scatter plots of total energy recovered during braking and number of braking events (a), and number of braking events per 1 km (b) in a trip

The kinetic energy a vehicle possesses – and can potentially recover – is directly tied to its mass and initial braking velocity. Consequently, even minor increases in velocity lead to a significant rise in the energy available for recuperation. Deceleration reflects the dynamics of the braking process – that is, the rate at which vehicle velocity changes. Intense braking with high deceleration leads to a faster conversion of kinetic energy, requiring an appropriate response from the recuperation system to effectively recover the energy.

For each recorded braking manoeuvre, the initial braking velocity and deceleration were estimated. An average of these values was then calculated for each individual trip. Figure 8 presents the distribution of the average initial braking velocity (v_{hsr}), and Fig. 9 presents the average deceleration (d_{sr}) across the analysed trips. Figure 10 shows scatter plots of the total energy recovered during braking, along with the average braking velocity and average deceleration values.

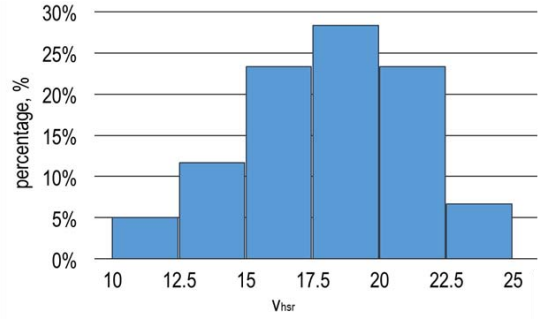

Fig. 8. Distribution of average initial braking velocity (v_{hsr}) in test routes

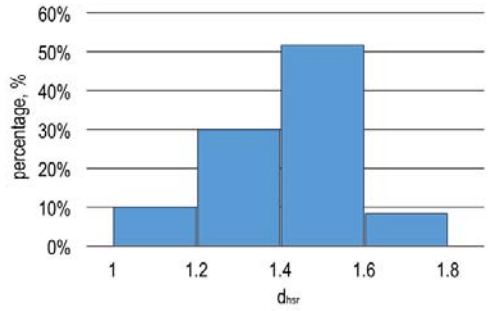

Fig. 9. Distribution of average deceleration (d_{sr}) in test routes

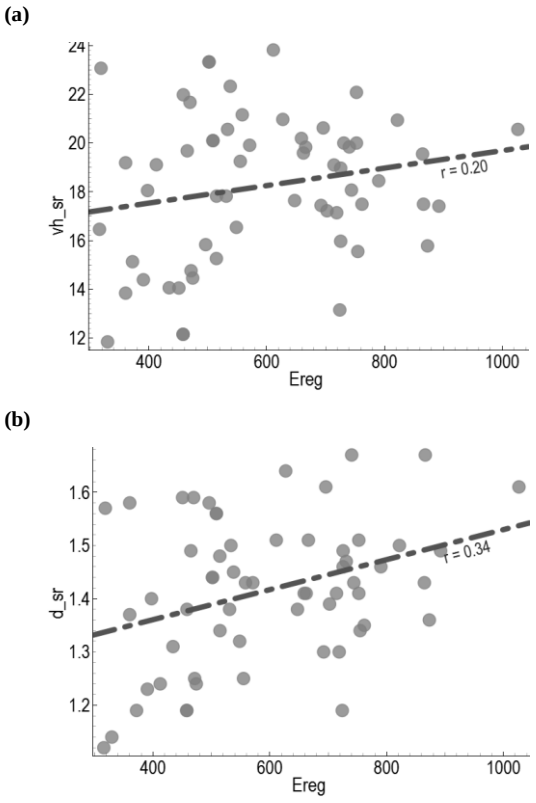

Fig. 10. Scatter plots of total energy recovered during braking and average initial braking velocity (a), and average deceleration (b) in a trip

For the analysed trips, the average initial braking velocity was 18.24 km/h, with an average deceleration of 1.42 m/s^2. Analysis of the averaged deceleration and initial velocity values for each trip indicated only a weak influence of these parameters on the total recovered energy. The trend line exhibits a slight positive slope, suggesting that increased average braking velocity could lead to a minor rise in recuperated energy. This is largely attributable to the fact that higher initial velocity inherently offers more kinetic energy for recovery. However, average braking deceleration shows a stronger correlation with the amount of recovered energy than the average initial braking velocity.

For each braking manoeuvre during the trips, the braking force was estimated. Figure 11 presents the distribution of averaged maximum braking force (F_{h_max}) values for each completed trip.

Braking force is a critical factor in the recuperation process as it dictates how effectively a vehicle's kinetic energy can be converted into electrical energy. The average braking force for the analysed trips was 1749.07 N. The averaged braking force values per trip show a moderate correlation with the energy recovered. An increase in braking force allows for a greater amount of energy to be recovered during electric vehicle braking (Fig. 12).

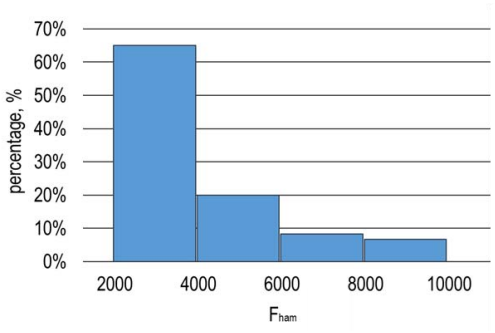

Fig. 11. Distribution of averaged maximum braking force (F_{h_max}) in test routes

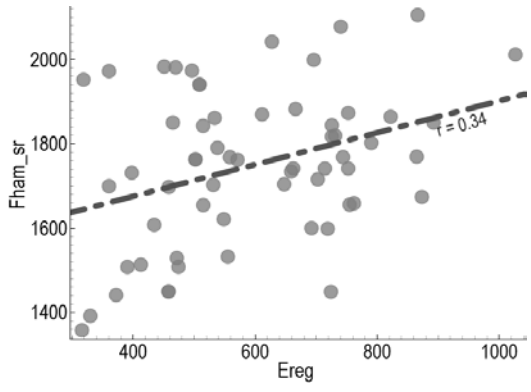

Fig. 12. Scatter plots of total energy recovered during braking averaged maximum braking force

Urban conditions offer substantial potential for effective recuperation, with braking force and dynamics being key factors influencing energy recovery. Based on averaged values for initial braking velocity, deceleration, and braking force, the foregoing analyses aim to elucidate the general influence of these parameters on the total energy recuperated during a trip.

The obtained results indicate that initial braking velocity influences the amount of kinetic energy available for recovery. A higher initial velocity during a braking manoeuvre presents an increased potential for energy recovery; however, the correlation observed at the trip level is weak, which may be attributed to the significant variability in prevailing road conditions and the diversity of braking scenarios encountered. The deceleration during braking is associated with the dynamic characteristics of the braking event. A moderate correlation indicates that more aggressive braking manoeuvres may result in enhanced recuperation efficiency. Simultaneously, braking force, being directly proportional to the kinetic energy conversion into electrical energy, exhibits a moderate reliance on the overall energy recovered throughout a given trip.

3.2. K-Means clustering of routes based on recuperation patterns

Another objective of this research was to identify energy recovery patterns during braking in electric vehicles and to segment routes based on key braking parameters using the K-Means algorithm. This algorithm partitions data into k clusters by minimizing the sum of squared distances between observations and centroids. The dependent variable was the total energy recovered during braking per trip (E_{reg}).

The following parameters were utilized in the study:

- number of braking events in trip (n_{ham})
- number of braking events per kilometer ($n_{ham/1km}$)
- average initial braking velocity (v_{h_sr}) in trip
- average deceleration (d_{sr}) in every trip
- averaged braking force (F_{h_max}) values for each completed trip.

To ensure data comparability and mitigate issues arising from differing units and value ranges, all data underwent standardization, scaling them to a mean of 0 and a standard deviation of 1. This standardization was crucial because the K-Means algorithm utilizes a Euclidean metric, where variables with larger values could otherwise dominate the analysis and skew the results.

The initial centroids were established using a method of maximizing the distance between them, which promotes a better separation of natural clusters. The optimal number of clusters (k = 4) was determined by analysing the "elbow method" and the silhouette coefficient. Each trip, represented as a feature vector, was assigned to its nearest centroid using Euclidean distance. Subsequently, the centroids were updated as the mean of the vectors assigned to their respective clusters. This iterative process continued until convergence was achieved (i.e., minimal changes in centroid positions). All computations were performed using Statistica software.

The data from 60 trips were divided into four distinct groups (Fig. 13), suggesting the presence of four clear behavioural patterns related to braking parameters and the energy recovery system. Trips within each cluster (C) exhibit comparable characteristics, specifically regarding the number of braking events, braking events per kilometre, average initial velocity, average deceleration, and average maximum braking force recorded for each trip.

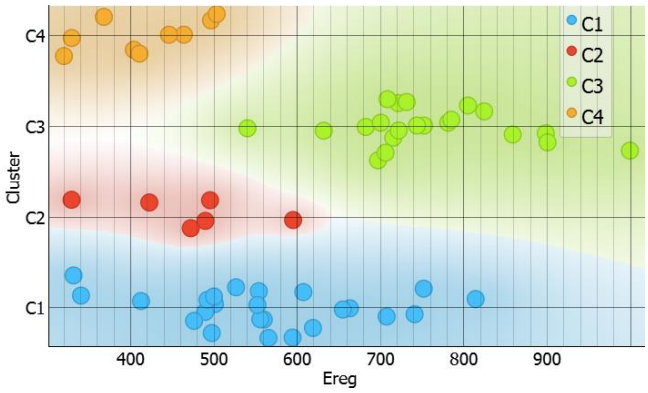

Fig. 13. K-Means clustering results for E_{reg}

Verification of the four-cluster division's capacity to accurately represent significant differences in the analyzed variables' behavior was achieved through an Analysis of Variance (ANOVA), performed on all quantitative variables (Table 2). A significance level of 0.05 was adopted. The effect size was calculated based on the F-statistic and the sums of squares (*SS*).

The ANOVA results demonstrated that the differences between clusters are statistically significant ($p < 0.001$ for most variables). The K-Means segmentation is thereby confirmed to effectively differentiate trips based on braking and energy recovery parameters. The exceptionally high F-statistic values observed for the chosen parameters underscore their critical role in distinguishing trips by their energy recuperation characteristics.

Table 2. ANOVA test results

Parameter	Between-Group SS	Within-Group SS	F-statistic	p-value
E_{reg}	37.86	21.14	33.42	0.0000
n_{ham}	40.11	18.89	39.64	0.0000
n_{ham}/1 km	39.58	19.42	38.05	0.0000
v_{h_sr}	26.85	32.15	15.59	0.0000
d_{sr}	31.28	27.72	21.06	0.0000
F_{h_max}	42.14	16.86	46.67	0.0000

To verify the stability of the results, 10-fold cross-validation was applied, and outliers that could distort the clustering outcomes were removed. The final error in the training sample was 0.371, indicating a relatively good quality of dependent variable assignment to the clusters.

The subsequent stage of analysis involved evaluating the energy recovered within the four clusters generated by the K-Means algorithm. This analysis specifically considered key braking process parameters: average braking velocity, average braking deceleration, and maximum braking force. The study aimed to identify the correlations between these variables and the total recovered energy. Figure 14 visually represents the E_{reg} values in relation to these parameters across the 4 clusters.

Cluster 1 (C1) comprises trips with the lowest energy recovery, ranging from 315.93 to 514.54 kJ. These trips are characterized by a low average braking velocity (11.84–16.46 km/h), slight deceleration (1.12–1.48 m/s²), and moderate braking force (2227.78–4192.34 N). The low number of braking events (26–76 per trip) suggests a smooth driving style. This cluster likely represents trips conducted under lower traffic density, which consequently limits the effectiveness of energy recuperation.

In Cluster 2 (C2), the recovered energy ranges from 318.50 to 822.03 kJ, indicating greater recovery efficiency than in Cluster 1. The average braking velocity falls between 15.83 and 23.82 km/h, with average deceleration ranging from 1.24 to 1.64 m/s^2. Braking force values (2624.99–6391.37 N) suggest more dynamic braking maneuvers. These trips are characterized by more frequent stops (30–87 braking events). This cluster likely includes both midday trips and those conducted under higher traffic density.

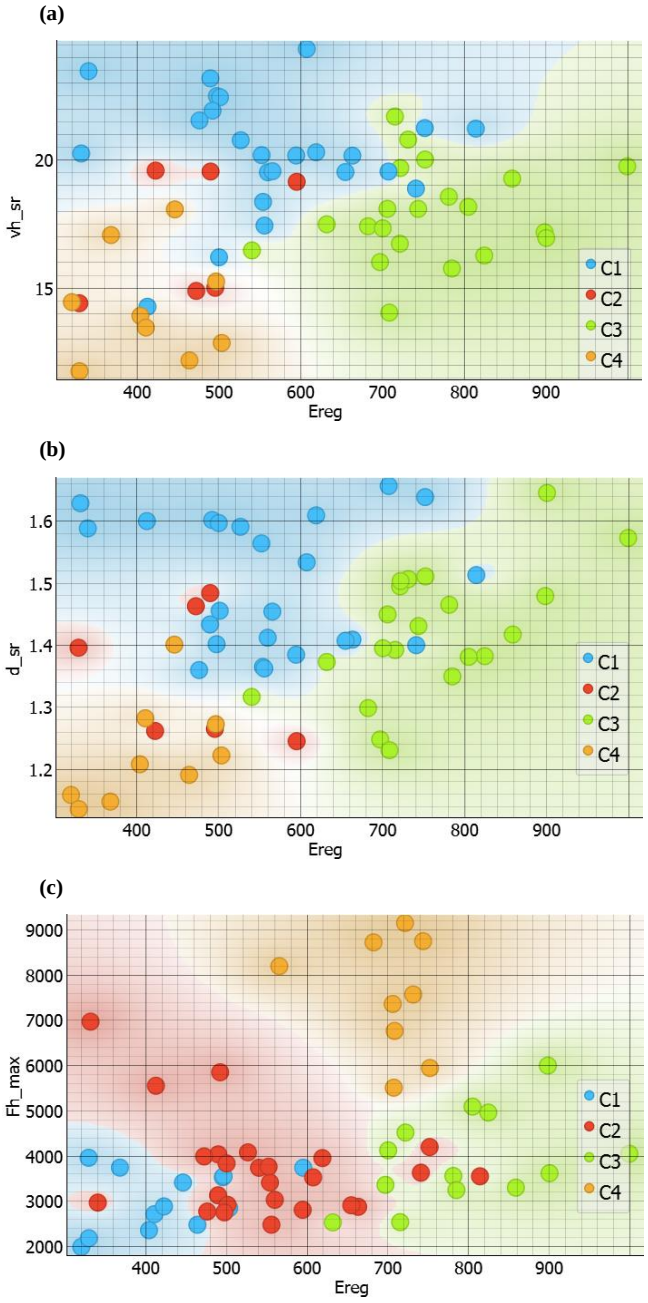

Fig. 14. Clustering of E_{reg} in 4 clusters based on average braking velocity (a), average braking deceleration (b), and maximum braking force (c) in analyzed trips

Cluster 3 (C3) exhibits significantly higher energy recovery, ranging from 450.80 to 752.47 kJ, compared to the first two clusters. Braking events in this cluster are more intense, with an average velocity of 14.05–20.56 km/h and greater deceleration (1.3–1.67 m/s^2). The maximum braking force values are the highest among all clusters, recorded between 5432.10 and 8737.75 N. The high frequency of braking events (68–98 per trip) suggests driving conditions typical of heightened urban traffic during the afternoon rush hour.

Cluster 4 (C4) exhibits the highest energy recovery, ranging from 548.51 to 1026.64 kJ. Despite braking velocity (13.15–22.08 km/h) similar to those in C2 and C3, the critical factor is the very high number of braking events (84–158 per trip). Braking in this cluster is frequent but not excessively intense, as indicated by maximum braking force values between 2612.34 and 6280.18 N. These trips likely occurred under conditions of the highest traffic density, necessitating frequent stops and accelerations.

In summary, the highest energy recovery was observed under conditions of intensive urban traffic, characterized by frequent, though not necessarily abrupt, braking (C4). Conversely, the lowest recovered energy values were recorded during trips defined by smooth driving with infrequent braking (C1), which corresponds to off-peak driving conditions.

To further analyse the efficiency of the recuperation system in electric vehicles under varying urban driving conditions, the percentage recuperation efficiency (η_{reg}) was evaluated for each of the four clusters identified by the K-Means method. This efficiency was defined as the ratio of energy recovered (E_{reg}) to the total energy consumed per trip (E_c), expressed as a percentage, according to the following formula:

$$\eta_{reg}\,[\%] = \left(\frac{E_{reg}}{E_c}\right) \cdot 100 \tag{1}$$

The recuperation system's effectiveness in transforming the vehicle's kinetic energy into electrical energy across varying urban driving conditions can be assessed using this metric. The percentage energy recovery efficiency (η_{reg}) for the four identified clusters is presented in Fig. 15.

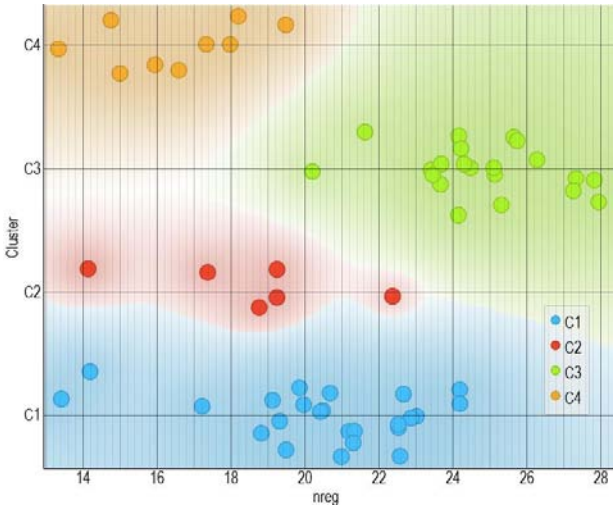

Fig. 15. Percentage of energy recovery efficiency (η_{reg}) by cluster

A direct relationship between energy recovery efficiency and the number of braking events is evident, notably within C4, where the combination of frequent, albeit moderate, braking in high-traffic scenarios optimizes recuperation. In contrast, C1 and C3, characterized by fewer braking events, demonstrate reduced efficiency. This diminished efficiency in C3, despite more intense braking, may suggest the occurrence of energy dissipation during abrupt manoeuvres.

The impact of initial braking velocity and maximum braking force on overall energy recovery efficiency is notably constrained. This observation implies that traffic dynamics, rather than the intensity of isolated braking events, constitute the predominant factor. Such findings are instrumental in guiding the further optimization of recuperation systems, especially in the development of control algorithms designed for the specificities of urban driving.

4. Discussion

This study significantly contributes to understanding the dynamics of energy recovery in electric vehicles under urban driving conditions, focusing on the relationships between braking parameters and recuperation efficiency. A key finding is the strong correlation between the number of braking events and the energy recovered, underscoring that urban traffic with frequent stops is an optimal environment for recuperation. K-Means cluster analysis revealed four driving patterns, with Cluster C4 demonstrating the highest recuperation efficiency (23.16%). This cluster was characterized by the highest number of braking events (84–158) and moderate dynamics within intensive traffic. Conversely, Cluster C1, marked by smooth driving and a limited number of braking events (26–76), exhibited the lowest efficiency (18.45%). This highlights the crucial role of braking frequency in the recuperation process.

The presented results align with the fundamental physical principles governing recuperation systems. This alignment is further corroborated by existing literature [1, 6, 17], which concludes that a higher frequency of braking cycles translates to more efficient recovery of a vehicle's kinetic energy during deceleration.

Comparing our findings with existing literature, the average recuperation efficiency of 21.47% falls within the typical range for electric vehicles operating in urban environments, thereby confirming the robustness of our methodology [8, 10, 20]. However, this study's detailed segmentation of routes using K-Means clustering and the analysis of varied speed profiles differentiate it from standard research based on predefined cycles like WLTP. This approach offers deeper insights into the impact of real-world traffic conditions. Notably, Cluster C3 exhibited lower efficiency (18.52%) than Cluster C4, despite a substantial number of braking events (68–98) and significant braking forces (5432.10–8737.75 N). This discrepancy may suggest energy dissipation due to abrupt braking, wherein kinetic energy is converted into heat within the mechanical braking system.

The presented results have practical implications for both electric powertrain designers and electric vehicle users. For engineers designing recuperation systems, it is recommended to focus on maximizing the efficiency of regenerative braking under frequent, low-intensity braking

conditions, such as those observed in Cluster C4. This may involve adjusting braking system control algorithms to prioritize recuperation in such scenarios. From the perspective of drivers, this study suggests that anticipating situations requiring stops and employing gentle braking can contribute to increased energy recovery efficiency, thereby extending vehicle range. Such driving strategies may be particularly beneficial in urban driving conditions, where numerous stops are necessitated by traffic infrastructure and density.

Several limitations warrant consideration within this study. Primarily, the exclusive use of a single driver for all trips constrained the diversity of driving styles, which, in turn, may limit the broader generalizability of the findings. It is acknowledged that variations in driving technique could potentially influence both braking dynamics and energy dissipation. Secondly, the AVL Cruise simulations were performed under consistent conditions of battery state of charge (SOC = 75%) and ambient temperature. This does not fully represent the complete range of real-world operating environments, given that a reduced SOC or colder temperatures can adversely affect battery performance. Finally, the analysis was confined to the Hyundai Kona Electric model, thus precluding a comprehensive assessment of design differences, such as vehicle mass or drivetrain type, across other electric vehicle models.

This study corroborates that frequent, moderate braking within high-density urban traffic optimizes energy recovery in electric vehicles. These findings have the potential to propel the development of more efficient recuperation systems and encourage driving techniques that extend vehicle range, thereby contributing to the advancement of electromobility. Continued research, encompassing a wider array of variables, will facilitate a more precise adaptation of this technology to authentic operational conditions.

5. Conclusions

This study, which investigated the influence of braking parameters on energy recovery in electric vehicles under urban driving conditions, confirmed our hypotheses and led to the following conclusions:

- Statistical analysis revealed a very high correlation (r = 0.9) between the number of braking events and the amount of energy recovered, confirming the crucial role of braking frequency in the recuperation process.
- The application of the K-Means clustering method identified four distinct regenerative braking patterns. The highest recuperation efficiency (23.16%) was achieved in the cluster characterized by the greatest number of braking events (84–158) and moderate braking force, whereas the lowest efficiency (18.45%) was observed in the cluster with fewer braking events (26–76) and a high average trip velocity.
- The average recuperation efficiency observed under the studied urban conditions was 21.47%, which aligns with the typical operational range observed for electric vehicles.

It can therefore be concluded that the key factor in maximizing recuperation is the frequency of braking events, along with their moderate intensity, which enables the efficient conversion of kinetic energy into electrical energy.

The findings of this study have broad applicability, extending beyond fully electric vehicles to include hybrid electric vehicles, which also utilize recuperation systems for energy recovery during braking. The study's key insights, such as the significance of braking frequency and characteristics for recuperation efficiency, are universal and can be directly applied to HEVs. Optimizing braking strategies based on the patterns identified in Cluster C4 could enhance energy recovery, thereby improving overall vehicle efficiency. In the context of hybrid vehicles, this could directly translate to reduced fuel consumption.

In conclusion, this study offers a significant contribution not only to the progression of electric drivetrain technology but also by providing universal insights directly applicable to hybrid vehicles, thereby fostering enhanced energy efficiency and promoting sustainable development within the automotive sector.

Nomenclature

d_{sr}	average braking deceleration
E_c	total energy consumption in test route
E_{reg}	total regenerated energy in test route
EV	electric vehicle
F_{h_max}	average maximum braking force
GPS	global positioning system
HEV	hybrid electric vehicle
NEDC	New European Driving Cycle
n_{ham}	number of braking events
n_{ham}/1 km	number of braking events per 1 kilometr
η_{reg}	percentage recuperation efficiency
r	Pearson correlation coefficient
RBS	regenerative braking systems
SOC	state of charge
v_{hsr}	average braking velocity
WLTC	Worldwide Harmonised Light Vehicles Test Procedure

Bibliography

[1] Berjoza D, Pirs V, Jurgena I. Research into the regenerative braking of an electric car in urban driving. World Electr Veh J. 2022;13(11):202. https://doi.org/10.3390/wevj13110202

[2] Borucka A, Stopka O, Kozłowski E. Analysis of electric vehicles in the context of the world's largest economies. The Archives of Automotive Engineering – Archiwum Motoryzacji. 2024;106(4):65-82. https://doi.org/10.14669/AM/196877

[3] Boukhari M, Bouzidi R, Ghadbane I, Khaled B, Bendib A, Abdelhammid K. Real-time implementation of ESOGI-FLL-based speed-sensorless control for induction motor drives within electric vehicle systems. The Archives of Automotive Engineering – Archiwum Motoryzacji. 2025;107(1):82-101. https://doi.org/10.14669/AM/202568

[4] Christoforidis C, Christakis I, Kotzasavva F, Fousekis G, Rimpas D. Electric vehicles charging stations and their influence on the electricity utility grid. The Archives of Automotive Engineering – Archiwum Motoryzacji. 2025;107(1):102-126. https://doi.org/10.14669/AM/202569
[5] Dongmin K, HuiZhi N, Kitae J. The analysis of traffic variables for EV's driving efficiency in urban traffic condition. 2022 IEEE 25th International Conference on Intelligent Transportation Systems (ITSC); 2022 Oct 8-12. Macau, China. https://doi.org/10.1109/ITSC55140.2022.9921918
[6] Faghihian H, Sarkar M, Sargolzaei A. A novel energy-efficient regenerative braking system for electric vehicles. SoutheastCon; 2024 Mar 15-24. Atlanta, USA. https://doi.org/10.1109/SoutheastCon52093.2024.10500159
[7] He Q, Yang Y, Luo C, Zhai J, Luo R, Fu C. Energy recovery strategy optimization of dual-motor drive electric vehicle based on braking safety and efficient recovery. Energy. 2022;248: 123543. https://doi.org/10.1016/j.energy.2022.123543
[8] Kropiwnicki J, Gawłas T. Evaluation of the energy efficiency of electric vehicle drivetrains under urban operating conditions. Combustion Engines. 2023;195(4):28-34. https://doi.org/10.19206/CE-169492
[9] Lee G, Park J, Park S, Yoon SH. Study on the necessity of real-world driving tests for passenger electric vehicles. International Journal of Automotive Technology. 2024;25:1323-1330. https://doi.org/10.1007/s12239-024-00108-5
[10] Lee G, Song J, Han J, Lim Y, Park S. Study on energy consumption characteristics of passenger electric vehicle according to the regenerative braking stages during real-world driving conditions. Energy. 2023;283:128745. https://doi.org/10.1016/j.energy.2023.128745
[11] Li Z. Traffic density, road gradient and grid composition effects on electric vehicle energy consumption and emissions. Innovations in Applied Engineering and Technology. 2023; 2(1):1-8. https://doi.org/10.62836/iaet.v2i1.264
[12] Liu M, Niu S, Lu C, Cheng S. An optimization study on transesterification catalyzed by the activated carbide slag through the response surface methodology. Energ Convers Manage. 2015;92:498-506. https://doi.org/10.1016/j.enconman.2014.12.074
[13] Lučić M, Lukić J, Grujić I. Statistical analysis of trends in Battery Electric Vehicles: Special reference to vehicle weight reduction, electric motor, battery, and interior space dimensions. The Archives of Automotive Engineering – Archiwum Motoryzacji. 2024;104(2):63-96. https://doi.org/10.14669/AM/189962
[14] Mei P, Yang S, Xu B, Sun K. A fuzzy sliding-mode control for regenerative braking system of electric vehicle. 2021 7th International Conference on Control, Automation and Robotics (ICCAR); 2021 Apr 23-26. Singapore. https://doi.org/10.1109/ICCAR52225.2021.9463463
[15] Pielecha I, Cieślik W, Szałek A. Energy recovery potential through regenerative braking for a hybrid electric vehicle in urban conditions. IOP Conf Ser: Earth Environ Sci. 2018;214: 012013. https://doi.org/10.1088/1755-1315/214/1/012013
[16] Prasanth B, Kaliyaperumal D, Jeyanthi R, Brahmanandam S. Real-time optimization of regenerative braking system in electric vehicles. Electric Vehicles and the Future of Energy Efficient Transportation. 2021:26. https://doi.org/10.4018/978-1-7998-7626-7.ch008
[17] Quan VH, Ngoc NA, Tien NM, Van Khai V, Khanh ND. Surveying the regenerative braking energy of the braking system on the Vinfast VF8 electric vehicle through simulation cycles. 2024 7th International Conference on Green Technology and Sustainable Development (GTSD); 2024 Jul 25-26. Ho Chi Minh City, Vietnam. https://doi.org/10.1109/GTSD62346.2024.10675193
[18] Sun B, Zhang Q, Wei N, Jia Z, Li C, Mao H. The energy flow of moving vehicles for different traffic states in the intersection. Physica A. 2022;605:128025. https://doi.org/10.1016/j.physa.2022.128025
[19] Szumska E, Jurecki R. The analysis of energy recovered during the braking of an electric vehicle in different driving conditions. Energies. 2022;15(24):9369. https://doi.org/10.3390/en15249369
[20] Szumska E, Skuza A, Jurecki R. The analysis of energy recovered by an electric vehicle during selected braking manoeuvres. The Archives of Automotive Engineering – Archiwum Motoryzacji. 2023;99(1):18-29. https://doi.org/10.14669/AM/162079
[21] Velu A, Chellammal N. An optimization-based neural network for estimating regenerative braking force in EVs for maximal energy recovery. Cybernet Syst. 2022;54(8):1375-1396. https://doi.org/10.1080/01969722.2022.2157604
[22] Wendeker M, Grabowski Ł. Investigations of the city bus powertrain efficiency. Combustion Engines. 2024;196(1):134-139. https://doi.org/10.19206/CE-172819
[23] You D, Luo X, Sun Z, Wu H, Wei G, Cheng Y et al. Correlation between braking strategy and regenerative braking energy of electric vehicle. 2022 41st Chinese Control Conference (CCC); 2022 Jul 25-27; Hefei, China. https://doi.org/10.23919/CCC55666.2022.9902868
[24] Zhang Y, Xie H, Song K. An optimal vehicle speed planning algorithm for regenerative braking at traffic lights intersections based on reinforcement learning. 2020 4th CAA International Conference on Vehicular Control and Intelligence (CVCI); 2020 Dec 18-20. Hangzhou, China. https://doi.org/10.1109/CVCI51460.2020.9338590
[25] Zhou M, Bi S, Dong C, He C. Regenerative braking system for electric vehicles based on genetic algorithm fuzzy logic control. ICIC Express Letters, Part B: Applications. 2014;5(3): 689-695.
[26] Zakrzewska D, Chłopek Z, Szczepański K. The criteria for qualifying fuels as a replacement fuels for internal combustion engines. Combustion Engines. 2024;199(4):60-6. https://doi.org/10.19206/CE-186848
[27] Zimakowska-Laskowska M, Kozłowski E, Laskowski P, Wiśniowski P, Świderski A, Orynycz O. Vehicle exhaust emissions in the light of modern research tools: synergy of chassis dynamometers and computational models. Combustion Engines. 2025;200(1):145-154. https://doi.org/10.19206/CE-201224
[28] Zimakowska-Laskowska M, Laskowski P. Comparison of pollutant emissions from various types of vehicles. Combustion Engines. 2024;197(2):139-145. https://doi.org/10.19206/CE-181193

Emilia Szumska, DSc., DEng. – Faculty of Mechatronics and Mechanical Engineering, Kielce University of Technology, Poland.
e-mail: *eszumska@tu.kielce.pl*

Adriana Skuza, MEng. – Faculty of Mechatronics and Mechanical Engineering, Kielce University of Technology, Poland.
e-mail: *askuza@tu.kielce.pl*

Czołowy producent agregatów prądotwórczych w Polsce

FOGO®

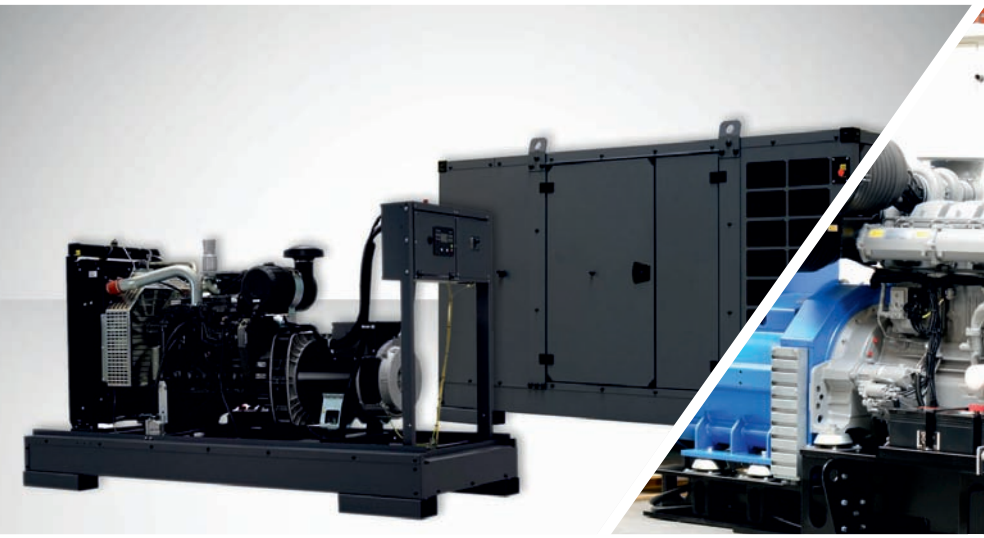

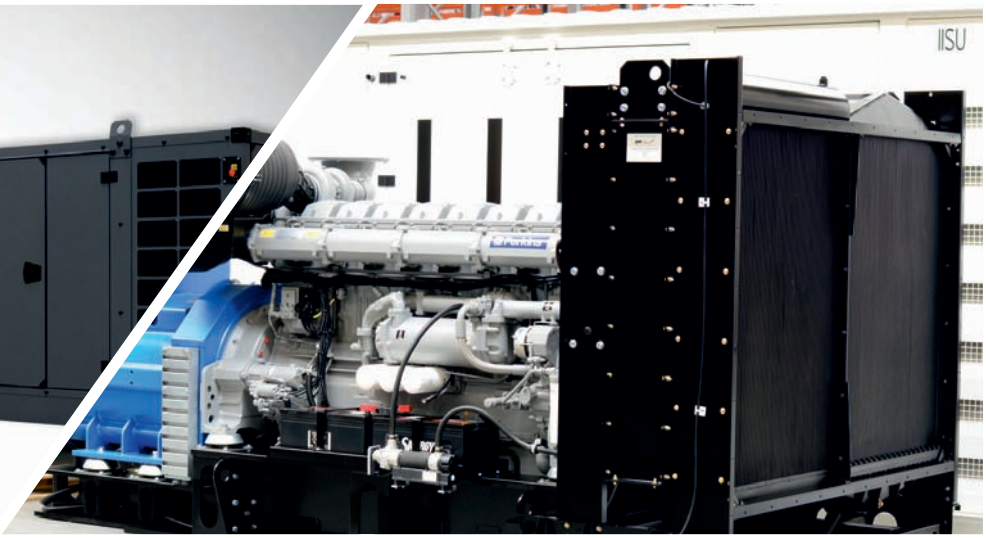

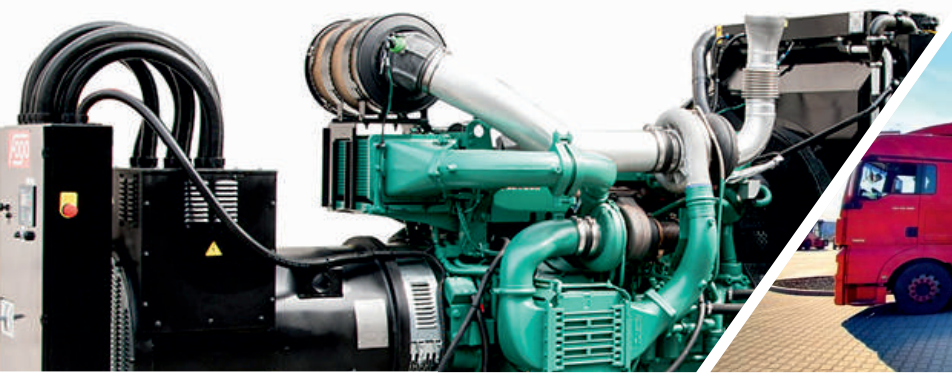

pewna **ENERGIA**

www.fogo.pl

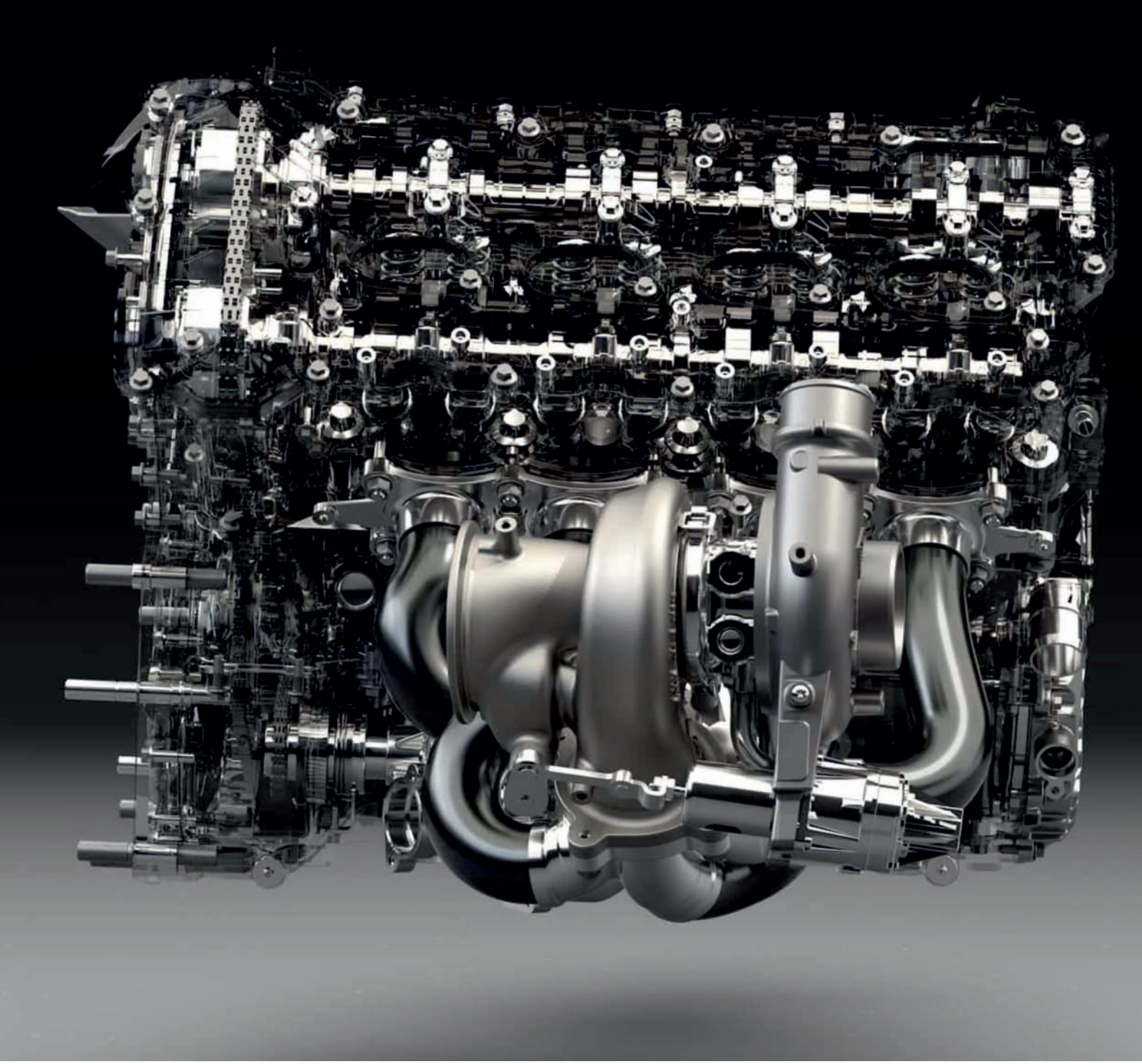

Publisher:

Polish Scientific Society of Combustion Engines

ISSN: 2300-9896
eISSN: 2658-1442

Combustion Engines

Polskie Towarzystwo Naukowe Silników Spalinowych

www.combustion-engines.eu